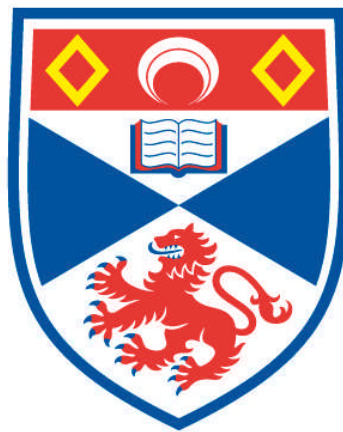


# **OBJECTIVE-PRISM AND SLIT-SPECTRA REDSHIFTS IN A STUDY OF THE DISTRIBUTION OF GALAXIES**

**QUENTIN ANDREW PARKER**

**A Thesis Submitted for the Degree of PhD  
at the  
University of St Andrews**



**1986**

**Full metadata for this item is available in  
Research@StAndrews:FullText  
at:**

**<http://research-repository.st-andrews.ac.uk/>**

**Please use this identifier to cite or link to this item:**

**<http://hdl.handle.net/10023/4650>**

**This item is protected by original copyright**

**This item is licensed under a  
Creative Commons License**

Objective-prism and slit-spectra redshifts  
in a study of the distribution of galaxies

by

Quentin Andrew Parker

A thesis submitted to the University of St. Andrews  
in application for the degree of Doctor of Philosophy

St. Andrews

March 1986



CERTIFICATE

I certify that Quentin Andrew Parker has spent nine terms in research work at the University Observatory, St. Andrews, that he has fulfilled the conditions of Ordinance General No.12 and Senate Regulations under Resolution of the University Court, 1967, No.1, and that he is qualified to submit the accompanying dissertation in application for degree of Ph.D.

A rectangular area of the document is completely blacked out, obscuring the signature of the certifier.

P.W.Hill

DECLARATION

The research detailed in this thesis and the composition of this thesis are entirely my own work except where explicitly mentioned in the text. No part of this work has been previously submitted for another degree at this or any other University. I was admitted to the Faculty of Science of the University of St. Andrews as a research student on 1st. October 1982, under Ordinance General No.12, to undertake an investigation of the large-scale distribution of galaxies. I was accepted as a candidate for the degree of Ph.D. on 1st. October 1983, under Resolution of the University Court, 1967, No.1.

A handwritten signature in dark ink, which has been obscured by a thick black rectangular redaction mark.

Quentin. A. Parker

## ACKNOWLEDGEMENTS

I am extremely grateful to my supervisors Drs.P.W.Hill and H.T.MacGillivray for their support, help and guidance throughout the course of this work. Also, at some stage or other, either wittingly or unwittingly, both staff and research students at St.Andrews University Observatory and the Royal Observatory Edinburgh have assisted me in numerous ways, in particular Drs A.C.Davenhall and R.G.Clowes. I would especially however, like to express my thanks to Dr.S.M.Beard not least for useful discussions but also for the software packages INTERZED and GALPLOT which have been extremely useful.

I would like to extend my thanks to Professor D.W.N.Stibbs for useful discussions on various aspects of this work and for making available the facilities of the University Observatory.

I gratefully acknowledge the use of the Computing equipment of the University of St.Andrews Computing centre and the STARLINK facilities at the Royal Observatory Edinburgh. I thank the Director and staff of the South African Astronomical Observatory for use of telescopes and equipment and PATT for generous allocations of observing time.

Finally I thank the Science and Engineering Research Council for travel funds for conferences and observing trips, for the excellent facilities at the Royal Observatory Edinburgh, in particular the plate library and Cosmos machine, and for financial support in the form of a post-graduate studentship.

I acknowledge that in submitting this thesis to the University of St. Andrews I am giving permission for it to be made available for use in accordance with the regulations of the University library for the time being in force, subject to any copyright vested in the work not being affected thereby. I also understand that the title and abstract will be published, and that a copy of the work may be made and supplied to any bona fide research worker.

To Mum

## ABSTRACT

A thorough and detailed investigation into the accuracy, reliability and consistency of the objective-prism redshift technique with changes in plate material, measuring machine and reduction techniques has been undertaken. Providing that the limitations of the procedures involved are appreciated, useful 3-D information, accurate to  $Z \sim \pm 0.01$ , for large numbers of faint galaxies may be obtained from single UKST fields. A surface brightness correction has enabled the technique to be extended to galaxies as bright as  $b_j \sim 15.8$ . The validity of the results were confirmed by external calibration with slit-spectra. The slit-spectra results obtained have more than doubled the size of the calibration sample available and have further vindicated the applicability of the technique.

Analysis of the 107 slit-spectra redshifts determined revealed the existence of considerable structure in the field studied, with significant density enhancements and voids being apparent. This structure has been confirmed on larger scales and to greater depths with the subsequent analysis of  $\sim 1,500$  objective-prism redshifts from COSMOS data of the field. Two large superclusters were discovered. The first centred at  $Z \sim 0.05$  but extending for at least  $150 h^{-1} \text{Mpc}$ , and the second a projected filament of connecting clusters at  $Z \sim 0.11$  and  $23 h^{-1} \text{Mpc}$  long. A selection of 2-D and 3-D statistical analysis techniques have been used to describe the observed large-scale galaxy distribution in this field.

A by-product of this work has been the discovery of a new and powerful means of star/galaxy separation based on magnitude comparisons between paired objects from both the direct and objective-prism plates. This technique has revealed  $\sim 20\%$  stellar contamination in the star/galaxy separation based on direct plate data

Chapter 6 Analysis of the galaxy distribution in SERC field 349

6.1	Introduction.....	302
6.2	The Distribution of Bright Galaxies in Field 349 with $b_j \leq 16.5$ .....	304
6.2.1	Preliminary Investigation.....	304
6.2.2	Application of Hierarchical Clustering Analysis.....	320
6.2.2.1	Basic Concepts and Theory.....	320
6.2.2.2	The Adopted Co-ordinate System.....	324
6.2.3	The Results of the Hierarchical Clustering Analysis Performed.....	328
6.2.3.1	Results for the Major Grouping with $6,500 \leq v \leq 10,000$ km/s.....	328
6.2.3.2	Results for the Second Major Redshift Distribution with $11,800 \leq v \leq 19,000$ km/s.....	350
6.2.4	General Conclusions from the Analysis of the Galaxies with $b_j \leq 16.5$ .....	369
6.3	The 2-D distribution and analysis of galaxies to $b_j=20.5$ .....	371
6.3.1	Preliminary results.....	371
6.3.2	The 2-D statistical analysis of the projected galaxy distribution.....	378
6.3.2.1	Simple binning analysis.....	378
6.3.2.2	Application of the angular two-point correlation function.....	381
6.3.2.3	Results from a Power Spectrum analysis of the galaxy distribution.....	396
6.3.2.4	Application of Meads analysis to the galaxy distribution in field 349.....	410
6.3.3	Analysis of the objective-prism galaxy redshift results to $b_j=18.7$ .....	421
6.3.3.1	Comparison of the objective-prims redshift sample with a random simulation.....	422
6.3.3.2	Study of the objective- prism redshifts of selected clusters.....	430
6.3.3.3	Examination of the 'whole plate' objective-prism redshift sample.....	437

Chapter 7 General conclusions and future suggested work.....455

References.....

alone. In conclusion, objective-prism galaxy redshifts are valuable information for complementing 2-D data in the study of the large-scale distribution of galaxies from COSMOS measures of large numbers of UKST plates. To this end an automatic technique of objective-prism redshift determination should be developed.

Acronyms and abbreviations used in thesis.

AAT	: Anglo-Australian Telescope
ARGS	: Advanced Raster Graphics System
B.D.	: Baker Density
bj	: direct plate COSMOS magnitude (IIIaj/G395 emulsion & filter)
buj	: prism plate COSMOS magnitude (IIIaj emulsion only)
CC	: characteristic curve
cdf	: cumulative distribution function
Cosmos	: Automatic, fast microdensitometer for obtaining Co-ordinates, Sizes, Magnitudes, Orientations and Shapes of astronomical plate images
ECO	: emulsion cut-off
edf	: empirical distribution function
E2D	: software package for graphical interactive manipulation of COSMOS data
HAGGIS	: Handling and Analysis of Graphical data in a General Interactive System
IAM	: Image Analysis Mode (from COSMOS machine)
ITS	: Image Tube Spectrograph
INTERZED	: Interactive technique of objective-prism redshift determination from COSMOS data
J-L	: Joyce-Loebl microdensitometer
MM	: Mapping Mode (from COSMOS machine)
ROE	: Royal Observatory Edinburgh
RPCS	: Reticon Photon Counting System
SAAO	: South African Astronomical Observatory
SC	: Supercluster of galaxies
SERC	: Science and Engineering Research Council
SGP	: South Galactic Pole
SPICA	: System for Programmable Interactive Computer analysis (for reducing spectral data)
UKST	: United Kingdom Schmidt Telescope

## TABLE OF CONTENTS

### Chapter 1 Large Scale Structure in the Universe - a review

1.1	Outline.....	1
1.2	Rationale.....	1
1.3	Historical Background.....	3
1.3.1	Results from the Lick Survey.....	6
1.3.2	Results from the POSS.....	6
1.4	Concepts and Observational Difficulties.....	7
1.4.1	Homogeneous Terminology.....	7
1.4.2	Cluster Definition.....	7
1.4.3	The Problem of the Field Component.....	11
1.4.4	Determination of Cluster Population and Extent.....	12
1.4.5	Absorbtion and Obscuration.....	14
1.5	The Local Supercluster.....	15
1.6	General Superclustering?.....	18
1.6.1	Analyses of the Projected 2-D Galaxy Distribution.....	18
1.6.2	Advances in Statistical Techniques.....	22
1.7	The 3-D Distribution of Galaxies.....	25
1.7.1	Highlights from 3-D Studies - Elucidating SC Structure.....	26
1.7.2	Hierarchical Structure or Continuous Clustering.....	31
1.8	Recent Advances.....	36
1.9	N-body Simulations.....	40
1.10	The Applications of Fast Measuring Machines to Studies of Large Scale Structure in the Universe.....	41
1.10.1	The Cosmos Machine.....	42
1.10.2	The Objective-Prism Redshift Technique.....	44
1.11	Summary of Supercluster Properties.....	45
1.12	Cosmological Implications.....	47
1.13	Conclusions.....	50

### Chapter 2 Determination of slit-spectra redshifts for 107 galaxies in a magnitude limited sample in SERC field 349

2	Summary.....	51
2.1	Introduction.....	52
2.2	The Target Sample.....	54
2.3	Observations and Instrumental Configuration Used.....	56
2.3.1	Observing Procedure.....	58
2.4	Date Reduction Techniques.....	60
2.4.1	Flat-Fielding.....	62
2.4.2	Sky-Subtraction.....	63
2.4.3	Wavelength Calibration.....	64
2.4.4	Rebinning the Data to Co-ordinates Linear in $\ln(\lambda)$ .....	69
2.4.5	The Cross-Correlation.....	70
2.4.6	Emission Line Measurements.....	71
2.5	Results.....	74
2.5.1	Emission Line Results.....	74
2.5.2	Results from Cross-Correlation Analysis.....	76
2.5.3	Redshift Results.....	77
2.5.4	Comparison of Recession Velocities from Emission Line Measures and from the CCF Technique.....	83

2.6	Assessment of the Internal Precision and External Accuracy of the Results.....	86
2.6.1	Internal Errors.....	86
2.6.1.1	Direct Measure of Night Sky Emission Lines.....	86
2.6.1.2	Results from Repeat Observations of the Same Object.....	87
2.6.1.3	Results from Cross-Correlation of an Object Spectrum against a Series of Stellar and Galaxian Templates.....	87
2.6.1.4	Error Estimate in the CCF Peak Position.....	90
2.6.1.5	Dispersion in Individual Emission Line Velocities.....	92
2.6.1.6	Overall Assessment of the Internal Errors.....	93
2.6.2	External Errors.....	95
2.7	Conclusions.....	99

Chapter 3 Empirical Studies of Objective-Prism Redshift Determinations from the 2480 Å/mm UKST Prism

3.1	Introduction.....	100
3.2	Redshift Determination from the Objective-Prism Spectra.....	102
3.2.1	Redshift Accuracy and Measurement Precision.....	102
3.2.2	Positional Stability of the 4000Å Feature.....	104
3.2.3	The Emulsion Cut-Off Wavelength and Positional Stability....	105
3.2.4	Data Base.....	107
3.3	The Photographic Process and Machine Reduction.....	108
3.4	Differences in the Redshift Values from Intensity and Non-Intensity Converted Cosmos Data.....	114
3.5	Stellar Redshift Results.....	119
3.6	Comparisons between Intensity Converted E2D/INTERZED Results and those for the J-L.....	124
3.7	Implications of a Strong Magnitude/Redshift Relation in Stellar Spectra.....	135
3.8	Use of other Spectral Features in UKST Low Dispersion Objective-Prism Spectra.....	138
3.9	A Repeatability and Consistency Assessment of the Redshift Results.....	146
3.10	Comparison between Cosmos and Joyce-Loebl Results.....	153
3.11	Effect of Variations in Instrumental Settings on the Results and Reproductions of Objective-Prism Spectra.....	159
3.11.1	The Joyce-Loebl Microdensitometer.....	159
3.11.2	The Cosmos Measuring Machine.....	164
3.12	The Photographic Copying Process.....	169
3.13	Comparison between J-L Measures of Objective-Prism Spectra for Stars and Galaxies from Original and Copy Plate Material.....	177
3.14	Comparison between Cosmos Data INTERZED Measures of Objective-Prism Spectra from Original and Copy Plate Material.....	182
3.14.1	Differences in the Spectral Reproduction from Copy and Original Plates.....	182
3.14.2	Comparisons of Copy and Original Plate Magnitude Estimates.....	189
3.14.3	Redshift Comparisons between Original and Copy Plate Cosmos Measures.....	191
3.15	Comparisons between Objective-Prism Results from Cosmos in its pre- and post-phase 1 Update Configuration.....	194
3.16	Stellar INTERZED Redshifts from Cosmos Measures of Field 475.....	197
3.17	Conclusions from the Empirical Studies Described in this Chapter.....	201

Chapter 4 Calibration of objective-prism galaxy redshifts with slit spectra results

4.1	Introduction.....	205
4.2	Previous Calibrations Performed.....	207
4.2.1	Calibration with J-L Measures Performed by J.Cooke.....	207
4.2.2	Calibration from J-L and Cosmos INTERZED Measures Performed by S.M.Beard.....	210
4.2.3	Calibration from clusters of galaxies.....	211
4.3	Calibration Data Obtained for this Thesis.....	215
4.3.1	J-L Objective-Prism Measures of Bright Galaxies in Field 349 Calibrated with Slit Spectra.....	216
4.3.2	INTERZED Measures of the Bright Galaxies in Field 349 Calibrated with Slit Spectra Redshifts.....	225
4.4	General Conclusions for the Calibration Data Obtained.....	237

Chapter 5 The reduction of Cosmos measures of the direct and prism plates of Serc survey field 349

5.1	Summary.....	241
5.2	The Plate Material.....	242
5.3	Intensity Conversion of the Prism Plate Data.....	243
5.4	Running the Cosmos Analyser on Objective-Prism MM Data.....	249
5.5	Magnitude Calibration of the Direct and Prism Plate Images.....	250
5.5.1	Direct-Plate Magnitudes.....	250
5.5.2	Prism Plate Magnitude from UJ6535P.....	251
5.6	The Star/Galaxy Separation of the Direct Plate.....	252
5.7	The Pairing of the Direct and Prism Data.....	262
5.7.1	Rationale.....	262
5.7.2	Basic Pairing Technique.....	264
5.8	Method and Results of Actual Match Performed.....	267
5.9	Comparison between Direct and Prism Plate Image Attributes.....	273
5.9.1	Matched Prism/Direct Magnitudes as a Means of Star/Galaxy Separation.....	273
5.9.2	Comparison of other Attributes from the Paired Sample.....	282
5.10	Check on the Positional Stability of the Co-ordinate Transformation.....	285
5.11	Extraction of the Prism Spectra.....	287
5.12	Measurements of the Objective-Prism Spectra in Field 349....	289
5.12.1	Stellar spectra results.....	289
5.12.2	Galaxy measures.....	294

Chapter 6 Analysis of the galaxy distribution in SERC field 349

6.1	Introduction.....	302
6.2	The Distribution of Bright Galaxies in Field 349 with $b_j < 16.5$ .....	304
6.2.1	Preliminary Investigation.....	304
6.2.2	Application of Hierarchical Clustering Analysis.....	320
6.2.2.1	Basic Concepts and Theory.....	320
6.2.2.2	The Adopted Co-ordinate System.....	324
6.2.3	The Results of the Hierarchical Clustering Analysis Performed.....	328
6.2.3.1	Results for the Major Grouping with $6,500 < v < 10,000$ km/s.....	328
6.2.3.2	Results for the Second Major Redshift Distribution with $11,800 < v < 19,000$ km/s.....	350
6.2.4	General Conclusions from the Analysis of the Galaxies with $b_j < 16.5$ .....	369
6.3	The 2-D distribution and analysis of galaxies to $b_j=20.5$ .....	371
6.3.1	Preliminary results.....	371
6.3.2	The 2-D statistical analysis of the projected galaxy distribution.....	378
6.3.2.1	Simple binning analysis.....	378
6.3.2.2	Application of the angular two-point correlation function.....	381
6.3.2.3	Results from a Power Spectrum analysis of the galaxy distribution.....	396
6.3.2.4	Application of Meads analysis to the galaxy distribution in field 349.....	410
6.3.3	Analysis of the objective-prism galaxy redshift results to $b_j=18.7$ .....	421
6.3.3.1	Comparison of the objective-prims redshift sample with a random simulation.....	422
6.3.3.2	Study of the objective- prism redshifts of selected clusters.....	430
6.3.3.3	Examination of the 'whole plate' objective-prism redshift sample.....	437

Chapter 7 General conclusions and future suggested work.....455

References.....

large-scale structure in the Universe -a review.

1.1. Outline.

The aim of this introductory chapter is to expound what I consider to be the most significant advances that have occurred in the study of the large-scale distribution of visible matter in the Universe from the work of the early pioneers up to the present day. It is hoped that the reader will be afforded as representative a picture of the development and present understanding of the subject as is feasible so that the potential of the work detailed in this thesis will be better appreciated. The problems and controversy that have bedevilled research in this field will be described and the potential that fast measuring machines such as Cosmos have for improving our understanding of the large scale matter distribution will also be discussed.

1.2. Rationale.

The assumption that the Universe is homogeneous and isotropic when considering large scales (the so called "Cosmological Principle"), has had a profound effect on modern Cosmology. However, if such a principle applies, the important question becomes what is the threshold scale beyond which homogeneity sets in? The study of the large-scale matter distribution is helping to answer this and other questions of fundamental importance to our understanding of the Universe.

Specifically:-

- 1). Are clusters of galaxies the largest 'real' building blocks of the Universe or are clusters of clusters, so called 'superclusters' (SC's) physically meaningful?
- 2). Is there a significant field component or do all galaxies ultimately belong to larger structures?
- 3). Does clustering occur on all scales or is there a hierarchical progression?
- 4). Are all SC's connected in some sort of 'cosmic net' separated by large voids?
- 5) Are there non-random trends in the orientation of galaxies in clusters and of cluster semi-major and minor axes in SC's?

The nature of the large-scale matter distribution has profound implications for galaxy and cluster formation theories. The study of SC's may yield information on the nature of any density fluctuations that occurred in the early Universe and give an indication of the way the largest agglomerations in the Universe may have originated. Furthermore, measurement of the motions of galaxies in the periphery of a SC relative to its gravitational centre may furnish an estimate of the SC mass and of the mean matter-density in the Universe (since we expect the Hubble flow to be decelerated due to the mass excess in the SC).

The observational evidence accumulated to address these questions, together with the development of techniques of statistical analysis and theoretical scenarios has progressed at an ever increasing rate over the last 30 years. To give justice to this and earlier work we shall consider these questions initially within the framework of an historical review.

### 1.3. Historical Background.

A number of review articles describing some of the background and concept of second-order clustering and the notion of a local supercluster have been written over the years, the most notable of these being Abell (1965, 1974), de Vaucouleurs (1960, 1971), and Oort (1984). This exposition is intended to complement these efforts but also to incorporate personal views on the way our present knowledge has grown out of the controversy, confusion and contradiction that has existed in this field even to the present.

The phenomenon that galaxies congregate into groups, clouds and clusters is a well determined observational fact. The possibility that these clusters might themselves be organised into second-order clusters only emerged in the 1950's. However this notion can be traced back to eighteenth century philosophers who considered a hierarchical Universe built up of systems of ever increasing size and content.

A Swedish astronomer, Charlier (1922), plotted the numbers of "nebulae" listed in the NGC catalogue of Dreyer as a function of galactic latitude and noticed a large excess in the number of nebulae per unit area in the general direction of the North Galactic Pole. This was the first real hint at the possible existence of what is now known as the local supercluster, though Charlier's data were affected by inclusion of all types of nebulae and the effects of interstellar absorption.

Between 1920 and 1930 several workers began to perform more detailed investigations of the galaxy distribution over the sky, noticeably Seares (1925), Lundmark (1927), and Reynolds (1921-1934), who described the significant clustering of "extragalactic nebulae" in both hemispheres but without taking the discussion further. In 1932 Shapley and Ames at Harvard published a catalogue containing 1,250 entries for galaxies brighter than the thirteenth visual magnitude (updated by Sandage and Tammann, 1979). A plot of these galaxies strongly supported the clustering found by Reynolds and by 1933 twenty-five clusters had been catalogued by Shapley.

Later Hubble (1934), undertook a fundamental investigation of the galaxy distribution over the sky. He suggested that after correction for interstellar absorption, galaxies appeared to be distributed homogeneously and isotropically on the large-scale, yielding the first observationally comprehensive support for the Cosmological principle. Nevertheless it was evident that at least small scale fluctuations in the galaxy distribution were present and that clusters of galaxies did exist.

The apparent general prevalence of clustering led Zwicky (1938), to propose a model for galaxy distribution in which all galaxies are in clusters and in which space can be regarded as divided up into cluster cells with a mean diameter of 75 Mpc. (for  $H_0 = 50 \text{ Km/s/Mpc}$ ). At around the same time Holmberg (1937), by analysing the distribution of double and multiple galaxies, provided the first quantitative evidence that there might be a large scale density excess or "metagalactic cloud" including the local group. This was confirmed by Reiz (1941), who investigated the spatial distribution of over 4,000 galaxies within  $40^\circ$  of the north galactic pole (NGP). He found distinct evidence for areas of high galaxy densities which he attributed to a large number of "metagalactic" clusters situated

around the NGP and which might form a "metagalactic supercluster".

Thus, by the 1940's, the picture of general clumpiness in the galaxy distribution had become well established, mainly as a result of the work of Shapley and his collaborators at Harvard. They discovered large transverse gradients in galaxy counts to the 17th magnitude in the SGP (Shapley, 1938). Furthermore the idea of a possible supercluster (SC) incorporating the local group had been formulated. Even so it must be remembered that extra-galactic astronomy was coloured at this time with the search for a possible edge to the entire metagalactic system which was then considered to be the Universe. Consequently the possibility that there might be some intermediate hierarchy between simple clustering and clouds of galaxies and the whole Universe was overlooked.

So far all investigations had mainly dealt with galaxies brighter than the thirteenth magnitude. What was required was an extensive deep survey to faint limiting magnitudes to extend the volume of space available for investigation. This material became available when two photographic surveys of the sky were commissioned; the Lick 20" Astrographic survey and the National Geographic's Palomar Observatory Sky survey (POSS). These surveys demonstrated conclusively that clusters of galaxies were extremely numerous, more so than anyone had imagined.

### 1.3.1. Results from the Lick Survey.

Using the Lick material Shane and Wirtanen (1954, 1967), from counts of individual galaxies to the 18th magnitude, produced catalogues and charts of the surface density of galaxies per square degree. They drew attention to more remote clusters and clouds of galaxies and even to apparent superclusters. The Lick counts were analysed statistically under the direction of Neyman, Scott and Shane (1953, 1954), and Scott, Shane and Swanson (1954). They found that the serial correlation between counts in square degree areas appeared to persist to  $4^\circ$  and had almost the same values in both galactic polar caps. Comparison of a synthetic 'field' (which assumed that all galaxies were in randomly distributed clusters), with the actual distribution showed an obvious similarity except that the actual fields displayed a slightly greater clustering tendency. Typical clusters seemed to have populations of around 100 galaxies and diameters of around a few million parsecs.

### 1.3.2. Results from the POSS.

Abell (1958), undertook a statistical analysis of the Palomar counts of distant clusters to the 20th magnitude. He catalogued 2,712 clusters and classified them into six groups according to estimated distance which he obtained by comparing the magnitudes of the tenth brightest cluster members in clusters of known redshift with those in unknown clusters. Of these, 1,682 were considered to form a homogeneous statistical sample for investigation. According to Abell the redshifts of these clusters lay in the range 0.02-0.20, and were at great enough galactic latitudes that interstellar absorption did not inhibit their identification. The distributions of these clusters are seen by plotting their positions on an Aitoff equal area projection, figure 1, after Abell (1958).

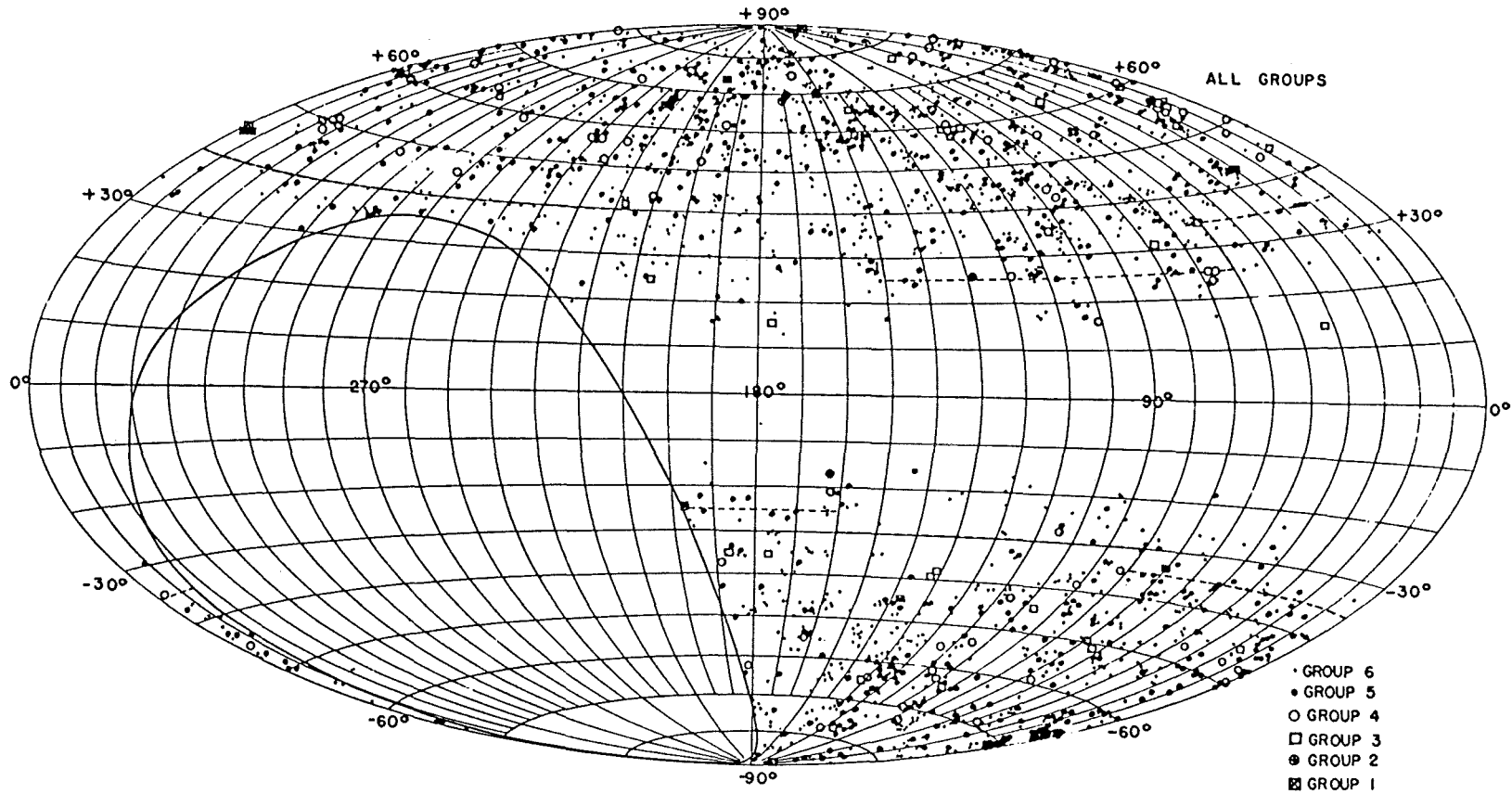


Figure 1.1 The distribution in old galactic co-ordinates of Abell clusters. The empty oval region is the area not covered by the Palomar Sky Survey. The plot is an equal area projection.

Abell maintained that even a cursory examination of this plot reveals an obvious clustering of the clusters themselves. He tested the significance of this possible superclustering by dividing the area covered by the survey into grid cells of various sizes and determining for each sized cell the frequency distribution 'F(t)' of cells containing 't' clusters each. This was compared to the Poisson distribution expected for a random arrangement of non-interacting objects using the Chi-square test.

Abell determined 'F(t)' as a function of cell size and the dependence of F(t) on cell size was derived separately for clusters in different distance groups to try and learn something of the linear scale of fluctuations in the cluster distribution. The analysis showed that for clusters of each distance group, the probability that the observed frequency distribution was a random sampling from a Poisson distribution passed through a highly significant minimum. The linear size of a SC was given as 87 Mpc for  $H_0 = 50 \text{ Km/s/Mpc}$ . Abell (1961), states that around fifty apparent SC's can be identified from his catalogue and he describes 16 of these groupings in more detail. The mean cluster membership was given as 11, although this only referred to rich clusters. He suggested that the total number of clusters and groups of various kinds in a typical SC might be at least an order of magnitude higher. The average diameter of the 16 groups was 78 - 24 Mpc with the total mass of a typical SC maybe as large as  $10^{16} \text{ Mo}$ . In conclusion Abell was convinced of the reality of second order clustering.

Zwicky (1957), admitted that the surface distribution of clusters was non-random, but interpreted this as the result of intergalactic obscuration, and asserted that SC did not exist.

In response, Abell (1961), confessed that Galactic obscuration could account for some of the non-uniformity, particularly at low galactic latitudes. He even agreed with the possibility of extragalactic absorption, as Zwicky had suggested, within the rich clusters themselves but nevertheless maintained that neither Galactic nor extragalactic obscuration could account for the majority of the clumpiness observed. If apparent clumps of relatively nearby clusters were just parts of a uniform or random distribution of clusters seen through holes in an absorbing medium, then one would expect to see groups of more remote clusters through these 'windows' but certainly not between them as was actually observed. Abell suggested that a misunderstanding could exist amongst astronomers as to what is meant by a second-order cluster or SC. He remarked that the mean diameter of one of Zwicky's "cluster cells" had a value of 75 Mpc, a value surprisingly close to the size Abell himself had assigned to second-order clusters!

Hence at this time the whole question of meaningful large-scale agglomerations in the Universe was being vigorously debated and the existence of second-order clustering was not proven. Unfortunately a considerable number of observational difficulties and complexities exist which have made the study of the large-scale distribution of matter far from straightforward. It is appropriate to consider some of these problems so that it is possible to appreciate why the development to our current level of understanding has been so difficult.

#### 1.4. Concepts and observational difficulties.

Before the reality of superclustering can be discussed, the building blocks with which such a SC would be composed have to be considered, e.g., clusters, groups, clouds and individual galaxies. It is at this level that many of the difficulties arise:-

##### 1.4.1. Homogeneous terminology.

Loose terminology has played its part in generating confusion. What some astronomers have called groups others have termed clusters and vice versa. For instance the Fornax system has been described by De Vaucouleurs as a nearby group whereas Welch et al. (1975), refer to it as a cluster. Also what constitutes a cluster for some astronomers is what others would describe as a multicluster or even a SC, e.g. earlier arguments between Abell and Zwicky. Zwicky devised a nomenclature where there are three types of cluster; open, medium compact and compact; whilst Abell considered more regular, centrally condensed clusters.

##### 1.4.2. Cluster definition.

Exactly what constitutes a cluster has led to some confusion as already seen. Clusters of galaxies range from rich aggregates of >10,000 members to poorer aggregates which some classify as groups. Indeed a clear distinction between a cluster and a group does not yet exist, although an attempt to rationalise the definition of groups was made by Turner and Gott (1976). A few clusters approach spherical symmetry but generally a host of configurations are observed. Some clusters appear elongated or elliptical, others irregular and diffuse; some have obvious sub-condensations provoking the question as to whether they should be considered as individual clusters themselves (Geller and Beers, 1982). Size, structure, number density and shape are all variables which make categorisation difficult. What is required is a set of standard criterion for cluster description.

#### 1.4.3. The problem of the field component.

From the 1930's onwards the concept of a general field of galaxies and of extensive clustering has been debated. According to de Vaucouleurs (1961), the notion of a general field of isolated galaxies was the product of the small-field Newtonian telescope while the concept of a cluster field was the result of the coverage afforded by Schmidt telescopes and wide-field astrographic cameras. At present, even though clustering has been shown to be quite general the exact meaning or content of a field component is still unknown. Do any truly isolated galaxies exist at all? This is an important question, having direct implications for Cosmology, since any theoretical galaxy, cluster, supercluster formation scenario should be compatible with the observed matter distribution if it is to be realistic.

Turner and Gott (1976), concluded that 40% of galaxies belonged to the general field whereas de Vaucouleurs (1975), and Soniera and Peebles (1977), agreed on only 5%. Tully and Fisher (1978), however, claimed that there was no evidence for a significant number of field galaxies. Clearly the whole question of field galaxies is inextricably linked to the cluster membership/population problem which has yet to be satisfactorily resolved.

#### 1.4.4. Determination of Cluster population and extent.

Stating with certainty whether particular objects in the region of a cluster are actually members of that cluster is not always possible. Though obvious foreground galaxies can be identified, the wide range of intrinsic luminosity and physical dimension means that very luminous background galaxies or very faint foreground galaxies, superimposed along the line of sight to a cluster, may be mistakenly assigned cluster membership. Often accurate radial - velocity determinations resolve the problem. Even so radial velocities do not always provide an unambiguous answer because of the internal velocity dispersion within a cluster and the dispersion in the velocity-distance relation. According to Abell (1974), cluster populations should only be considered statistically. Furthermore we must define:-

(a).The magnitude range concerned.

(b).How the cluster is presumed to be bounded. (presumed because outer boundaries of clusters are usually difficult or impossible to establish)

(c).How corrections are applied for the possible field of foreground and background objects. (we have already seen that the entire question of the field component is unsettled.)

It was because of these difficulties that astronomers tackled the problem in a variety of ways. In the catalogue of "Galaxies and Clusters of Galaxies" (CGCG), Zwicky considered the population of a cluster to be the number of galaxies visible on the red POSS plate where the surface density was twice that of the surrounding field. The cluster counts were then corrected for the mean count in the field. Unfortunately cluster populations are not distance independent, since a greater magnitude range is counted in nearby clusters than in more remote ones. Moreover, because an isopleth only

contains that part of a cluster within which the surface density is twice that of the field, the whole cluster population is not included, even for the magnitude range considered. Scott (1962), and Abell (1962), showed that the eye estimated isopleth contained a smaller fraction of the projected image of a distant cluster than a nearby one.

Abell (1958), determined cluster populations in a completely different manner that depended on the number of galaxies brighter than  $M_3+2$ , where  $M_3$  was the photo-red magnitude of the third brightest cluster member. All the counts were made on the red POSS plates and galaxies were included in the chosen magnitude range if they were contained within a circle centred on the cluster image whose radius was given by  $4.6 \times 10^5 / CZ$  mm. The recessional velocity CZ (in Km/s), was estimated by comparing the tenth brightest cluster member with the tenth brightest members of clusters of known redshift.

Both techniques are far from ideal and are prone to a variety of selection effects. Also because of the different ways Zwicky and Abell defined their populations their data on cluster richness were not easy to compare. Consequently, considering the problems encountered in defining clusters of galaxies and their populations, proving that clusters may themselves be clustered into superclusters was difficult. Furthermore the cluster populations may be affected by variable interstellar and intergalactic absorption.

#### 1.4.5. Absorption and Obscuration.

The effect of variable amounts of absorption and obscuration is perhaps the most serious yet difficult to determine quantity affecting the investigation of large-scale structure, especially when projected galaxy distributions are concerned. This is because the presence of a patchy absorbing medium can lead to a false impression of galaxy clumpiness (Seldner and Uson 1983). Holmberg (1974), focussed attention on the effects of absorption and stressed the need to combine an analysis of the cluster distribution with an analysis of the effects of variable absorption if realistic results were to be obtained. However, Holmberg confessed that comparisons between lists of Zwicky and Lick counts indicated quite pronounced galaxy grouping tendencies that could only partly be accounted for by local variations in Galactic absorption.

Recent work by McFadzean, Hilditch and Hill (1982), from uvby $\beta$  photometry of 572 O-F stars within  $15^\circ$  of the SGP, indicated that there was no interstellar extinction (reddening) out to 400pc from the Sun in this region. This result was in agreement with the HI column density maps of Burstein and Heiles (1982), which are a good means of highlighting the distribution of interstellar material. Such results vindicate the choice of a high galactic latitude field to study the galaxy distribution for this thesis, which should be less prone to the effects of absorption. However McFadzean et al. admit that regions of significant reddening ( $E(b-y) > 0.1$ ), do exist at high galactic latitudes and indeed the HI maps reveal the generally patchy nature of the interstellar material. Dall'Oglio et al. (1985), have investigated the correlation of infra-red dust emission, galaxy counts and Hydrogen column densities and conclude that only 25% of the observed fluctuations in galaxy counts at latitudes between  $10^\circ$  and  $80^\circ$  may be accounted for by patchy dust distribution. Ideally a detailed

knowledge of both interstellar and intergalactic absorption would be required to eliminate these effects from 2-D projected analyses.

Perhaps the best way to continue is with a discussion on the local supercluster since this was the first supercluster "recognised" and also because it is the one we know the most about.

#### 1.5. The Local Supercluster.

We have already considered the early work on the distribution of bright galaxies that suggested the presence of a large-scale local inhomogeneity. The development of this concept proceeded largely with the contributions of Gerard de Vaucouleurs, who, in a series of papers, (de Vaucouleurs 1953, 1956, 1958, 1960) tried to establish the reality of a Local Supercluster (LSC). Studies of the distribution of bright galaxies (de Vaucouleurs, 1956), led him to conclude that the local group of galaxies was merely an outerlying system in a flattened supersystem centred on the Virgo cluster but which also includes the Ursa-Major cloud, the majority of bright galaxies, and many thousands of fainter ones to the 16th magnitude. Irregularities and subcondensations appeared to be the predominant features in the internal structure of the system which he estimated to have an overall diameter of  $\sim 50$  Mpc. De Vaucouleurs took the observed flattening as indicative of rotation since this would be expected if the LSC was a real physical entity held together by gravitation. Furthermore he suggested that the velocity data then available from the extensive catalogue of Humason, Mayall and Sandage (1956), was consistent with the hypothesis that the LSC was both rotating and expanding. The question of rotation however, is still unresolved and is complicated by the observed asymmetry and the problems of resolving the effects of systematic motions and distance.

More recently de Vaucouleurs and Corwin (1975), showed that the distribution of intergalactic HI clouds appeared to be dictated by the LSC. A number of papers followed which threw doubt on the reality of the LSC itself as the debate on the existence of meaningful large scale galaxy aggregates continued. For example Jones (1976), re-examined the LSC on the basis of existing data for the purpose of mapping out the spatial distribution of galaxies within 15 Mpc of the Local Group and to fit a simple spherical mass-distribution centred on the Virgo cluster. He pointed out that although several studies of the distribution of galaxies in the LSC had been made, e.g. van den Bergh (1960), Sandage et al. (1972), and De Vaucouleurs (1972, 1974), none had really quantified the structure in terms of specific mass distribution models. Also there had been dynamical studies such as those of Rubin (1954), de Vaucouleurs (1972), and Stewart and Sciama (1967). Jones maintained that their results for significant deviations about the mean of the Hubble flow were a consequence of not taking proper account of the effects of the inhomogeneity in the mean density in the volume of space considered. He cited the findings of Sandage et al. (1972), in which no significant deviations from the Hubble flow were obtained. The expected deviation from the Hubble flow had been evaluated by Silk (1975), for some simple models of SC formation. Jones suggested that a detailed study of the Hubble flow in the LSC, together with corresponding evolutionary models like those of Silk or the numerical models of Peebles (1972), may provide some strong constraints on the value for the deceleration parameter  $q_0$ . Jones concluded that the impression of an extensive LSC was partly the result of a deficit of material in the direction away from the Virgo cluster and asserted that the local group was in a 'hole' in the cosmic matter distribution rather than in the outer regions of a SC. Thus, as yet, there was no agreement as to the actual form, size or content of the LSC even among those who believed in its reality.

Eastmond and Abell (1978), obtained a significant quantity of new data for galaxies in a large portion of the LSC. Eastmond determined total magnitudes for around 3,000 elliptical and lenticular galaxies complete to  $M \sim 16.5$ . The Hubble diagram for the spirals of known radial velocity and distance moduli was examined. A strong correlation of velocity with distance was noticed, even though the sample was dominated with Virgo cluster spirals. The Hubble diagram for the groups considered yielded a straight line consistent with a uniform expansion of the LSC. Hence, though they considered the LSC to be a reality as far as spatial inhomogeneity was concerned, they admitted that there was no evidence for any local inhomogeneity in the Hubble flow in agreement with Sandage et al. (1974), and Jones (1976). As a result of their findings they considered the LSC to be gravitationally unbound and expanding as rapidly as the Universe in general (within 20% uncertainties).

De Vaucouleurs (1978), gives a review of the LSC describing its properties. Large numbers of radial velocities have now been obtained for galaxies in the LSC and Yahil et al. (1980), and Tully (1982), have detailed a description of the LSC based on the radial velocity information in the Revised Shapley-Ames catalogue and the Atlas and Catalogue of Nearby Galaxies. The most recent description of our understanding of the LSC is given by Oort (1984).

## 1.6. General Superclustering?

Having discussed the development of the notion of the LSC we shall now return to the concept of general second-order clustering. The availability of deep sky surveys such as the POSS in the Northern hemisphere and the U.K. and ESO Schmidt surveys in the Southern hemisphere, together with larger numbers of radial velocities for faint and more distant galaxies, has meant that more detailed studies of the general galaxy distribution to faint limiting magnitudes became feasible.

### 1.6.1. Analyses of the projected 2-D galaxy distribution.

After the work on the Lick and POSS surveys in the late 1950's the notion of general second-order clustering was under active debate. The main opponents to the idea of meaningful 'superclustering' at this time were Zwicky and his collaborators who, between 1963 and 1971 in particular, continued to argue against the existence of such structures. The publication of the 'Catalogue of Galaxies and clusters of Galaxies' (CGCG) was the basis for much of their work.

Zwicky and Rudnicki (1963), undertook a statistical analysis of the areas of sky covered by various types of galaxy cluster found at various distances, using the data in the CGCG. Their analysis attempted to take into account the effects of interstellar and intergalactic absorption and other systematic "falsifying" effects which they considered to be inherent in their data. Their results purported to show that the notion of second-order clusters had no physical reality and that the idea originated in a lack of understanding of the nature of the "inevitable fluctuations of the galaxy distribution in stationary clusters". Zwicky regarded the evidence of density fluctuations in the observed distribution not as supporting the concept of superclustering but rather as the action of

the "Kinematic agitation" within the cluster to break it up into parts!

Rudnicki (1964), tackled the problem of second-order clustering using the morphological method developed by Zwicky (1959). He recognised the problems of cluster definition and thus undertook an analysis of all possible kinds of cluster description using the morphological method. He concluded that papers claiming to confirm the existence of superclustering were based on no strict definition (e.g. Shane 1956) or based on a definition of Abell's cluster types which he considered to be unsuitable. Furthermore, a series of six papers over the period 1966-1971 by Zwicky, Berger and Karpowicz (e.g. Zwicky and Berger, 1965) based on the data in the six volumes of the CGCG, confirmed essentially all their earlier conclusions on the non-existence of superclustering. Their analysis of the data was performed using the method of dispersion-subdivision curves (Zwicky and Rudnicki, 1966).

Abell and Seligman (1965, 1967), also analysed the data in the CGCG in a similar way to that done on the POSS. Almost identical results to those in Abell's catalogue were obtained. Three different statistical tests performed on the data revealed extremely significant departures from that expected for a random distribution of objects, in complete contradiction with the results obtained by Zwicky and his collaborators.

The cause of this contradiction was rooted in the conceptual differences in what was understood at that time by the term 'supercluster' and by different assumptions about the importance and extent of absorption and the interpretation of the significance of the statistical evidence.

Karachentsev (1966), in an independent statistical study of the data in the CGCG, obtained results in fair agreement with those of Abell and Seligman. Kiang (1967), applied the statistical methods developed by Neyman and Scott (1953, 1954), to the 'problem' of second-order clustering. From an analysis of the 'index of clumpiness' he believed that there were indications that galaxies were clustered on all scales with no preferential size and with little physical individuality; his concept of continuous clustering was based on irregularities or non-random fluctuations in the matter distribution on all possible scales. Kiang pointed out that his picture of indefinite clustering fitted in with McCrea's (1964), concept of 'continual creation'.

Yu and Peebles (1969), used a new statistical approach to analyse the 2-D distribution of rich compact clusters in an attempt to obtain an independent test for the existence of superclustering. From results of their 'Power Spectrum Analysis' they concluded that any tendency towards superclustering was hardly above that expected for a random distribution. They recognised that the distribution of clusters was manifestly non-random but suggested that this effect could be entirely due to systematic errors such as obscuration, atmospheric extinction, confusion by the Galaxy and even plate flaws. Nevertheless they did not dismiss the possibility that superclusters may exist.

Kiang and Saslaw (1969), computed serial correlations of Abell clusters in 50 Mpc cubic cells to try to determine the 3-D cluster distribution. They found correlations over scales at least as large as 100 Mpc. Their conclusions differed from those of Zwicky because they followed Abell's definition of a cluster. Also they suggested that there are serious projection effects in 2-D data which can eliminate almost any sign of spatial clustering.

Fullerton and Hoover (1972), re-analysed the 2-D distribution of clusters using the same technique as Abell (1961), in order to examine the angular scale of apparent superclustering as a function of his distance class estimates for galaxy clusters but found no correlation. They confirmed the suggestion of Yu and Peebles (1969), that Abell's test was apparently insensitive to systematic errors. In order to see whether superclustering was evident from visual inspection they generated a stereoscopic pair of 3-D perspective plots of Abell's catalogue. There appeared to be a preference for certain 'digits', plainly visible as concentric shells of clusters which they explained as the result of systematic errors in estimating the magnitude of the tenth brightest cluster members used by Abell to estimate the redshift of a cluster. Even so there were still two outstanding apparent superclusters visible in each hemisphere although their reality was questioned since they were at the same distance as the two most conspicuous shells of clusters. They contended that the results of Kiang and Saslaw (1969), may well have been influenced by these shells. In conclusion they stated that the bulk of statistical evidence for the reality of superclustering rested on the two outstanding 'superclusters' mentioned earlier. There was no conclusive proof for clustering of rich clusters in 3-D and they called into question the validity of a number of statistical tests which were influenced by selection effects (e.g. Chi-square test).

Thus, by the late 1960's, many analyses of the 2-D distribution of rich clusters of galaxies from the data in the published catalogues had been undertaken but the controversy over the reality of second-order clustering remained unresolved. The limitations of the 2-D data and the uncertainties over the seriousness of various selection effects, coupled with the difficulty in interpreting the significance and applicability of certain statistical tests, meant that wildly different conclusions were drawn. Scott, Shane and Swanson (1954), had shown that analysis of projected counts on photographic plates could be misleading w.r.t 3-D clustering. The initial lack of large numbers of radial velocities meant that statistics on projected cluster distributions had been the only way of attempting to elucidate the large scale distribution of visible matter in the Universe.

#### 1.6.2. Advances in statistical techniques.

By the early 1970's new, careful and detailed statistical analyses of the three important catalogues of extragalactic objects had been carried out by a group of researchers at Princeton, e.g. Peebles (1973, 1974a), Hauser and Peebles (1973), and Peebles and Hauser (1974). Their sources were the Abell (1958), catalogue, the CGCG of Zwicky et al. (1961-68), and the galaxies catalogued by Shane and Wirtanen (1967), from the Lick astrographic plates. They realised that in the study of the 2-D distribution of galaxies and clusters on the celestial sphere the influence of personal judgement on the results was hard to quantify. They obtained a more objective approach by studying the general correlation between the spatial configurations of galaxies by using the so called two-point correlation or 'covariance' function  $E(r)$ . This can be defined by:-

$$N(r) = \{ 1+E(r) \} \cdot \langle N \rangle$$

where  $\langle N \rangle$  is the average density and  $N(r)$  is the space number density of galaxies at a distance 'r' from any given galaxy. They reported

significant evidence for superclusters with small angular scale and a membership of two or three clusters.

Much work has now gone into investigations of the 2-D and 3-D galaxy distribution using such techniques which have shown correlations in the positions of galaxies and clusters over distances of up to 100 Mpc but were not conclusive over larger scales. Several investigations (e.g. Peebles 1974, Davis and Geller 1976) using various samples, have all led to similar results for 'E(r)' which appeared to obey a power law over a large range of 'r' (a remarkable fact on its own), i.e.:-

$$E = (r/r_0)^{\gamma}$$

The power index for small scales ( $0.1 < r < 10$  Mpc) was found to be  $\gamma=1.8$ . The correlation function has been found to be very useful in furnishing a unified description of the observed clumpiness in the galaxy distribution although it does not account for the chains and filaments encountered in superclusters, nor the existence of large voids. Peebles was perhaps the main driving force behind the effort to develop a description of galactic clustering in probabilistic terms and to put it within a cosmological context.

The results from these correlation studies indicated that the distribution of galaxies in space could be interpreted as a hierarchy of clustering in scales from 0.1-10 Mpc. Furthermore, estimates of the three- and four-point correlation functions indicated that the distribution was indeed hierarchical (Soniera and Peebles, 1978). The results suggested the absence of a preferred clustering scale. Sersic (1980), interpreted this as a natural consequence of gravitational instability since Newtonian attraction lacks a preferred scale.

Some studies, e.g. Rainey (1977), have indicated that correlations such as those described above do not extend to distances much beyond 100 Mpc. Webster (1976), concluded that faint radio sources appeared to be arranged isotropically and dismissed spatial density fluctuations of as much as 10% over a scale of 1000 Mpc. Similarly, the observed isotropy of the microwave background rules out any indefinite clustering hierarchy.

Karachentsev (1976), criticised the 'global' methods used to analyse the cluster distributions in which local fluctuations in the number density of clusters are correlated to one another over large areas of sky. He suggested that any real clustering of clusters could be masked by the effects of patchy obscuration in the Galaxy and the unavoidable photometric inhomogeneities of the observational material. He asserts that 'Global' methods give an overestimate of SC size and membership. The method of differential counts was applied to Abell clusters of various richness and distance class within ' $r \ll 6^\circ$ ' around clusters and around random centres which confirmed the reality of spatial clustering of galaxies. However the mean population of a SC was found to be only  $2.10 \pm 0.11$  clusters. He therefore regarded the term 'supercluster' as unfortunate and preferred the term 'multicluster'. It was also suggested that the clustering effect in clusters depended on the total number and morphological type of the cluster members.

Bogart and Wagoner (1973), used a different approach and performed a 'nearest neighbour' analysis on Abell clusters to test for angular correlations between sets of galaxies. Their analysis showed that the distribution of nearest neighbour distances from half of the clusters (referred to as sources) to the other half (referred to as objects) had a significantly smaller mean than the corresponding distribution obtained when a set of random points were used as

sources. This was taken as an indication that rich clusters are significantly clustered. Furthermore, they regarded their method as being free from many of the problems associated with other techniques. Rather surprisingly they found some evidence for an anti-correlation between the less distant and more distant clusters, implying that clusters separated along the line of sight seem to avoid each other in the sky. At the time they were unable to explain this effect although this observation now fits in well with the superclustering scenario envisaged by Joeveer et al. (1978), (see later).

### 1.7. The 3-D distribution of galaxies.

In the early seventies analyses of the 3-D galaxy distribution began to usurp 2-D statistical analyses of the projected galaxy distribution when larger numbers of radial velocities became available for galaxies outside the confines of the LSC (i.e at distances  $> 50$  Mpc). This was due to the application of more efficient imaging devices and solid-state detectors. More recently the CfA redshift-survey, Davis et al. (1981), Huchra et al. (1983), gave accurate radial velocities for all galaxies to  $M < 14.5$  in the North and South Galactic caps above declination  $0^\circ$ . This has led to a dramatic fourfold increase in the volume of space in which the redshifts of galaxies are known and should lead to a substantial improvement in our understanding of the large-scale 3-D galaxy distribution.

Consequently the emphasis changed from statistical studies to prove that SC's actually existed to studies of the actual 3-D nature of individual cluster clouds and SC'S. Direct detection of SC's with characteristic sizes of  $\sim 40$  Mpc in relatively narrow cones of 3-D space came from the statistically homogeneous redshift surveys of Chincarini and Rood (1975, 1976), Tifft and Gregory (1976), Gregory and Thompson (1978), on the 'Coma' supercluster; Tifft and Gregory

(1977), Gregory et al. (1981), on the 'Perseus' supercluster; and Tarenghi et al. (1978, 1979, 1980), on the Hercules supercluster. Furthermore the redshift survey of Kirschner et al. (1978, 1979), in 8 fields in the Galactic polar caps, though not directed in regions of particular interest, nevertheless found indications of large amplitude fluctuations in the density of galaxies of up to  $50 h^{-1} \text{Mpc}$ . By restricting the sample to a solid angle of about 120 sq.deg they were able to obtain redshifts for galaxies about 1.5 magnitudes fainter than for the CfA redshift survey and hence sample to twice the distance. Also, since the fields were selected without regard to the nature of the galaxy distribution, a fair and unbiased sample of the Universe should be obtained.

It now became possible to assign clusters, clouds and groups of galaxies to a SC on the basis of redshift and not only on the projected angular separation. The above studies also revealed the existence of vast voids in the Universe, devoid of visible matter and of a size comparable to that of the superclusters themselves. The results of the above work, together with similar contributions, constituted a significant advance in our understanding of the 3-D structure of the Universe.

#### 1.7.1. Highlights from 3-D studies elucidating SC structure.

Chincarini and Rood (1976), confirmed earlier findings that a large percentage of so called 'field' galaxies were spirals and noticed too the similarity between the luminosity function of field galaxies (Shapiro 1971) and the luminosity of galaxies in rich clusters. They claimed that this could be because all galaxies were ultimately members of superclusters.

Tifft and Gregory (1976), considered the Coma cluster in detail using a sample of 310 galaxy redshifts complete to  $M = 15.7$  to a  $3^\circ$  radius from the cluster centre and complete to  $M = 14.9$  to a  $6^\circ$  radius. They stressed that a statistical approach, when specific data on galaxy distances are lacking, is obviously limited when dealing with small, low - density populations and can say little about small groups and isolated galaxies. They assert that with direct observations, using redshifts, some of the important questions unanswered in the statistical studies can be addressed.

It was found that when the galaxy sample considered was grouped by redshift and position on the sky, almost all the galaxies appeared to belong to groups or clusters with isolated galaxies being very rare. In conclusion they tentatively surmised that two major structures could be identified as populating intergalactic space. The first being small groups of galaxies occupying perhaps 1% of space, exhibiting low redshift dispersion, little concentration and with a tendency to possess emission lines (indicative of spiral morphology). The second structure was that of major cluster-complexes that could consist of one or more major clusters in an extended 'shred' of material. The outerlying material could extend for several tens of Mpc and have various subcondensations.

Gregory and Thompson (1978), claimed to be the first to show that the rich Coma and A1367 clusters formed a unified system or SC from a redshift-based technique to study the 3-D distribution of a large number of galaxies in the region. A problem which they recognised was that there was no widely accepted definition of the term 'supercluster'. Originally a SC was taken to be a large agglomeration of clouds and clusters of galaxies that could be considered as being physically related and gravitationally bound. However, a SC may now be considered to be the manifestation of initial large scale

perceptions in the previous major observation that have been 'frozen in'. The individual clusters themselves may be only weakly gravitationally bound if at all. If gravitational forces between members of second-order clusters are negligible, then these unrelaxed systems must be expected to be expanding at least with the rate of the general universal expansion.

At this time, observational studies of SC's were largely subjective, based on the distance and angular proximity of cluster centres. In the case of the Coma and A1367 clusters Gregory and Thompson believed that in order to show that these clusters were members of the SC it was only sufficient and necessary to demonstrate the presence of a population of galaxies linking the two clusters which was itself a region of enhanced density. They found that groups of galaxies in the SC had separations much larger than their radii and that the inter-group space was nearly devoid of galaxies. The presence of large voids containing no detectable clusters, groups or galaxies was established with the void radii being greater than 10 Mpc (Gregory et al. 1981, examined the SC surrounding the Perseus, A347 and A262 clusters and discovered even larger voids!). Either these regions were really empty or there was mass in these 'holes' in some form other than bright galaxies. If the first explanation were true then severe constraints would be placed on the theories of galaxy formation. They suggested that the SC formed by the Coma and A1367 clusters was morphologically different from other SC's investigated so far. Moreover, since important physical processes could manifest themselves by morphological properties they speculated that a classification scheme for SC's would become necessary and even went as far as devising such a scheme based on examples of SC's so far discovered.

Similarly, Tarenghi et al. (1978, 1979, 1980), performed an in depth study of the Hercules SC whose main constituents were purported to be the A2147, A2151 and A2152 clusters. From redshifts obtained in the Hercules region they confirmed that galaxies were agglomerated into large asymmetric structures, groups and SC's. A sample of  $\sim 150$  redshifts for galaxies brighter than  $M_{pg} = 15.8$  were considered in a 28 sq.deg. field in Hercules. This sample populated a 60,000 cubic Megaparsec conical volume containing the Hercules SC near  $V_0 = 11,000$  Km/s. A large void of 100Mpc in depth was found in front of the SC. Tarenghi pointed out that it was not yet known if the velocities of clusters in SC's were primarily virial or cosmological. Rood and Dickel (1976), had found that the virial mass-to-light ratio for the best defined groups of galaxies was proportional to the  $1.6 \pm 0.3$  power of the virial velocity dispersion. Tarenghi showed that this relationship held for the rich clusters in his sample too. It was also pointed out that regular clusters with a relaxed appearance exhibited clustering of E-S0 galaxies yet had a uniform distribution of spirals, and also that the number density in clusters decreased in proportion to the inverse of the distance from the cluster centre (this would be in agreement with an isothermal distribution). In a qualitative way they suggested that the above observations were in agreement with a model where clusters exist at the location of the SC density perturbation and in fact came into existence because of these perturbations which are still reflected in the observed galaxy distribution.

On a different vein, Chincarini and Rood (1979), considered the redshift distribution of a homogeneous sample of ScI-ScII galaxies ( $M_{pg} = 14.0-15.0$ ) obtained by Rubin and Ford (1976), in an attempt to elucidate the large-scale galaxy distribution. Galaxies from the sample were placed at their galactic locations on an equal-area projection of the celestial sphere. From the corresponding redshift map, together with other auxiliary maps with narrower redshift windows, they illustrated the existence of the Hydra/Centaurus and Hercules/A2199 SC's. Furthermore their investigations revealed that the Coma cluster was part of a structure which could extend for more than 200 Mpc!

They noted that although many of the studies outlined above have increased dramatically our understanding of the 3-D structure on large scales, they were, nonetheless, somewhat limited. Specifically:-

- 1). Studies of surface distributions cannot recover the full detail of the 3-D distributions.
- 2). It is not possible to fully recover the broad-scale structure of the Universe from views of a few narrow cones.

To derive the 3-D structure of a cosmologically significant sample of the Universe they considered it desirable to have a complete all-sky redshift survey of all galaxies brighter than some faint limiting magnitude (The CfA redshift survey to  $B < 14.5$  has now gone some way to fulfilling this requirement). They maintained that an improved view of the Universe could be provided by a homogeneous all-sky redshift survey of a specific type of galaxy in a chosen apparent-magnitude interval. The data of the Rubin and Ford (1976) survey were considered to be such a sample.

From the redshift maps in various redshift ranges, they gained the impression that the Universe was like an irregular 3-D 'net' consisting of chains and clumps of galaxies separating vast voids. This impression persisted in the radial direction as well as across the sky, as shown by polar plots of redshift versus galactic longitude. They pointed out that this model was in general agreement with that proposed by Joeveer et al. (1978), (see below).

It was suggested by Doreshkevich and Shardarin (1978), that the Rubin and Ford galaxies were located primarily in two supercluster 'pancakes' moving with different velocities relative to the LSC. They concluded that the typical peculiar velocities of the pancakes were in agreement with the anisotropy found by Rubin et al. (1976). However, Sandage and Tammann (1975), Fall and Jones (1976), and Schechter (1977), pointed out that spurious anisotropies could result from various uncertainties including the biases introduced by ignoring the inhomogeneous galaxy distribution in the Universe.

The work detailed above has highlighted the structures of individual superclusters and illustrated the differences in morphological content, size and component velocity dispersion that seem to prevail between them.

#### 1.7.2. Hierarchical structure or continuous clustering?

The idea of a hierarchical Universe was introduced by Charlier (1922), and has resurfaced periodically since then (e.g. Wertz 1971), but until quite recently few theoretical studies had been done. Peebles (1974 a,b), considered a model for continuous clustering suggested by the fact that the covariance function he obtained for galaxy distribution varied smoothly, like a power law, over a wide range of separations. Consequently he considered whether superclusters could be regarded as entities in some way

distinguishable from clusters, groups or even individual galaxies!

Rudnicki and Zieba (1978), were drawn to the concept of continuous clustering (Kiang, 1967) after attempting to describe whole regions of the sky by listing individual clusters and possible superclusters but finding it impossible to see any notion of a cluster as an individual. They stated that the controversy over the existence of higher-order clusters or SC's and the assertion that there was a smooth transition between a SC and a single regular cluster of the same size (e.g. Zwicky's cluster cells), could be resolved by the notion of continuous clustering, i.e. clustering on all scales with no preferred size.

Kalinkov et al. (1978), developed a process for searching for second-order clusters which consisted of smoothing and filtering 2-D discrete fields defined on a lattice. Their material consisted of a metacatalogue made up of entries of Abell and Zwicky clusters, Zwicky galaxies, Lick counts, Jagellonian counts and some others. Though such a sample was mixed their findings lent support to the continuous clustering picture as proposed by Kiang, Saslaw, Peebles and others. However, the clustering tendency they found did appear to exhibit preferred sizes of 40-50, 90, 120-150 and 300 Mpc, together with a density contrast that decreased with increases in the characteristic size of the high-order clustering.

In a review article, Peebles (1978), considers clustering on scales  $< 20$  Mpc ( $H_0 = 50$  Km/s/Mpc) and raised the question of whether the power-law hierarchical clustering pattern with the density within clusters of size 'r' scaling as  $r^{-\gamma}$ , observed at  $r < 20$  Mpc, might simply be extrapolated to arbitrarily large scales. This extrapolation would imply that if galaxies were counted in cells of fixed size randomly placed in the sky then the expected r.m.s. fluctuations in the counts of galaxies brighter than 'm' say, would be

independent of 'm'. However this is not what is observed. This picture could change when adequate quantities of redshift for more remote clusters become available. Before this, where only crude estimates of individual galaxy distances were used, a major problem was that the angular distribution of a sample at great depth appears very close to random because we are seeing many clusters in projection. Consequently, a small systematic error in the angular distribution could be translated into a large error in the estimate of the spatial clustering.

Materne (1978), considered a 'new' method of classifying groups which he referred to as "hierarchical clustering". Dendrograms or tree diagrams could be constructed which give some indication of how the hierarchy is built up. Materne applied this technique to a well-defined sample of galaxies in the Leo region with encouraging results. Five clusters of galaxies were recognised which had already been shown to be physical groups by four independent tests.

However, Materne noted that the definition of what constituted a cluster or group had so far always contained a strong subjective component which had occasionally led to misleading results (e.g. Tully and Fisher 1976). Materne stated that since the properties of groups of galaxies depends strongly on the correct membership assignment (a non-trivial problem), it was vital to classify the groups correctly by a 3-D method. He stated that the advantage of the "hierarchical clustering" was the possibility to see the substructure of a cluster or to see which clusters might form larger systems such as superclusters. Further details of this technique are given in chapter 6.

By the late seventies, the reality of large-scale inhomogeneities in the Universe was becoming generally accepted although controversy over what clustering scenario best fitted the observed distribution still raged. No agreement as to the exact nature and properties of 'superclusters' existed and a few still questioned whether the term 'supercluster' was realistic.

Ford et al. (1980), concluded that although superclusters were 'real' they may be less rich than imagined because of projection effects. They reported observations of two superclusters from the list generated by Murray et al. (1978), that led them to conclude that either superclusters were spherical, bound agglomerations or they were flattened systems seen face on.

Perenod and Lesser (1980), obtained redshifts for 26 galaxies in a high-multiplicity SC. They found that the redshifts occurred in three distinct groups which they interpreted as implying that the apparent SC seen on the sky was actually composed of three separate low-multiplicity groups of clusters with large voids in between. Consequently they suggested that real clusters in 3-D space are often formed from members of different apparent clusters in 2-D space. Furthermore, they found that galaxies which apparently belonged to the same Abell cluster in reality belonged to different physical clusters! This highlights the inherent dangers in analysis of the projected 2-D galaxy distribution.

Fesenko (1979a), went as far as to suggest that "the discovery of so-called superclusters of galaxies was due to the unjustified neglect of various distortions of the data". He surmised that the main reasons for the observed fluctuations in the number densities of galaxies were the result of changes in the conditions of observation as one passes from one field to another (Fesenko 1979b) and the non-uniformity in the absorption of light. He asserts that large scale fluctuations are produced by the Zodiacal light! Fesenko questions the existence of "a large number of rectilinear chains of galaxies extending along the edges of cells of the Universe" as postulated by Joeveer et al. (1978). He stated that the existence of such chains was not confirmed when the cluster triplets described by Karachentsev et al. (1978), are examined. Moreover he considered the "problem" of the LSC to be unresolved, questioning the reality of the system by the connection he obtained between the light of bright galaxies and the surface density of interstellar neutral hydrogen (Fesenko 1977).

Although Fesenko's arguments deserve attention, it must be remembered that his criticisms failed to take into account the large number of 3-D investigations of the last few years based on more extensive redshift information. Even though the data contained in the Abell, Zwicky and Shane galaxy catalogues have been used, advanced statistical tests such as correlation functions and power spectrum analysis have been applied whilst the systematic effects believed to affect the data were taken into account.

More recently Fesenko (1983), has devised a statistical technique based on random departures of the observed cluster count from the theoretical number in various radial-velocity intervals which it is suggested might indicate the average SC multiplicity. Applying this technique to the galaxy cluster catalogue of Abell (1958), he maintains that the results are compatible with a complete absence of superclustering. However, because of the large random errors and possible truncation of hypothetical multiclusters by redshift interval boundaries, he only confidently excludes SC's with a mean multiplicity of 2-2.5! The possible effects of interstellar extinction are also stressed.

#### 1.8. Recent Advances.

We have already seen that the existence of large 'voids' is becoming a regular feature of the large-scale matter distribution. Perhaps one of the most significant contributions with regard to describing the observed large-scale matter distribution to emerge in recent years was that by Joeveer, Einasto, Saar and collaborators, who, in a series of papers have developed their so called "cell structure" scenario (e.g. Einasto et al. 1975, Joeveer et al. 1978, and Tago et al. 1984). Their preliminary results indicated that clusters of galaxies and 'field' galaxies were concentrated in flat aggregates with typical diameters of 100 Mpc ( $H_0 = 50 \text{ km/s/Mpc}$ ). Apparently the space between superclusters is sparsely populated. The whole picture resembles 'cells' with the cell interiors being almost devoid of galaxies while the superclusters themselves form the cell walls. Some clusters of galaxies appeared in chain like structures. Joeveer and Einasto (1978), studied the distribution of Abell and Zwicky clusters, groups, pairs and even individual galaxies. The Second Reference Catalogue of Bright Galaxies (de Vaucouleurs et al. 1976) was used as one source of radial velocities while radial

velocities for the Abell clusters came from compilations by Corwin (1974), and Faber and Dressler (1976). Only objects with  $V \leq 15,000$  Km/s were studied. It was discovered that clusters were not randomly distributed but tended to form long chains such as those in Perseus, Coma, Hercules and Fornax. Small groups tended to form disk-like aggregates. The densely populated regions seemed to be separated by large 'holes'. It was suggested that the so called 'cell structure' found could be considered as third-order clustering. They concluded that superclusters may have the form of distorted triangles (as in the case of the Perseus SC) surrounded by chains of clusters. Disks of apparent superclusters intersected at  $\sim 90^\circ$  forming cell walls with a mean diameter for the superclusters and voids of  $\sim 100$  Mpc.

Numerical experiments have generally shown that their proposed cell structure cannot be formed by random clustering. Furthermore this cell structure sets severe restrictions on the theory of galaxy formation. Consequently they believe that the observed structure is of a primordial nature. Sunyaev and Zeldovich (1972), and Doreshkevich et al. (1978), have proposed a theory of galaxy formation which results in the formation of cell structure with a predicted diameter of  $\sim 100$  Mpc in good agreement with the 'observed situation' as seen by Joeveer and co-workers.

Einasto, Joeveer and Saar (1980), studied the spatial distribution of clusters and galaxies in the southern galactic hemisphere using Zwicky clusters as the principle tracers of large-scale structure. Their aim was to use structural and morphological data to study supercluster formation. They noted that the definition of what constituted a SC had not been a trivial problem in the past. Superclusters may form a continuous network so that it is difficult to determine where one ends and the next begins. They consider the existence of large holes to be the most important property in the

large - scale distribution of galaxies and cite the independent studies of Tully and Fisher (1978), Tarenghi et al. (1979, 1980), Tifft and Gregory (1978), and Chincarini (1978), as confirming this result.

Studies such as those described above have indicated that the vast majority of galaxies belong to cluster chains or are located in their vicinity. A typical chain may consist of one rich cluster and seven poor clusters and may be 80 Mpc long. Cluster chains were visible in the computer-processed Shane-Wirtanen counts (Seldner et al. 1977). Groth and Peebles (1977), attempted to check the reality of these chains by calculating a 3-pt angular correlation function but found no statistical evidence for such chains. However, Einasto pointed out that this is to be expected since most cluster chains are poorly populated and cannot be recognised in Shane-Wirtanen catalogues which integrate up to 1,000 Mpc over the line of sight and rich clusters occur seldomly and may be lost in noise. Furthermore Groth and Peebles' results concerned small scales where no galaxy chains were expected.

Giovanelli and Haynes (1982), considered the distribution of galaxies in the Lynx-Ursa Major region and discovered the outlines of a previously unrecognised filamentary structure which extended for over 3 hours in R.A. and was characterised by a surface density contrast of  $\sim 3.7$  with respect to its immediate surroundings. They pointed out that there was a distinct similarity between the redshift range observed in the Perseus/Pisces supercluster chain and that of the Lynx-Ursa Major filament. Both structures were separated only by the zone of avoidance into which they both merge. Since the alignment of the filamentary axes and the significant preference of galaxies in that region of the zone of avoidance for the redshifts that characterize the two SC filaments were so similar, they suggested that these filaments are but two halves of a single connected

superstructure that stretches from horizon to horizon. If this super-filament could be confirmed then its sheer size would have important implications for theoretical models of the large-scale structure! A substantial improvement of the somewhat fragmentary statistical quantity of the available observational material is required to confirm this remarkable feature.

Kuhn and Uson (1982), describe a statistic which is sensitive to filamentary structure in the galaxy distribution in the Shane-Wirtanen catalogue and is sensitive to differences between this and similar random catalogues with the same low-order galaxy auto-correlation functions. They find statistical evidence that the observed Shane-Wirtanen galaxy distribution has significantly more filamentary structure than has previously been found by the two- and three-point correlation functions. Moody, Turner and Gott (1983), have also developed a filamentary-clustering mapping algorithm which they claim is successful in identifying those filaments which the eye picks out in the Shane-Wirtanen catalogue and thus provides an objective means of studying these structures. They stress that it is not yet clear whether the Shane-Wirtanen filaments can be understood in terms of simple hierarchical galaxy-clustering models.

Fontanelli (1982), and Bingelli (1982), have found evidence that cluster major axes are significantly correlated with those of their closest neighbours, especially if within 50 Mpc. Furthermore these cluster orientations seem to trace out observed filamentary structure in some SC's (e.g. the Perseus and Coma SC's). Struble and Peebles (1985), carried out a new application of Bingelli's test for large scale alignment of galaxy clusters and confirmed the Bingelli result but at a lower level of significance. They concluded that the mean value of the relative position angles cannot differ from isotropy by more than 5%.

A further important property to emerge from these 3-D surveys is the segregation of galaxy types within SC filaments. Giovanelli et al. (1982), discovered that early-type galaxies highlighted the Perseus SC filament much more clearly than later types. Although such segregation has been found in galaxy clusters, the existence of a similar trend in an unrelaxed sparsely-populated SC filament has important cosmological implications.

#### 1.9. N-body Simulations.

The observed galaxy distribution in the Universe is, to a large extent, explicable by considering the gravitational interaction between protogalaxies. Multi-particle simulations based on the mutual gravitational forces between points initially distributed at random have demonstrated how clustering on all scales up to 10Mpc can be produced, e.g. Aarseth et al. (1979), Efstathiou and Eastwood (1981). By an appropriate and judicious choice of initial conditions such as starting epoch, the observed correlation functions of the galaxy distribution can be mimicked. Miller (1984), using integrations for 100,000 particles, has been able to reproduce not only the observed small-scale clustering but also the formation of filamentary structures and spherical voids as detected by Tago et al. (1983). Because of the similarity between the results of such simulations and the observed galaxy distribution the question arises as to whether it is necessary to invoke large-scale adiabatic perturbations at all. In fact the epoch required at which protogalaxies could have become separate entities and the subsequent limitations on the range of expansion imply that no structures of SC size could have evolved from such a gravitational mechanism. Furthermore, such a mechanism cannot readily explain the observed segregation of galaxy types in SC filaments nor the alignment of cluster major axes in such filaments (Binggelli, 1982, and Giovanelli

et al. 1982). Nevertheless, gravitational interactions must have a significant bearing on the distribution of galaxies and clusters within the SC's themselves even if they cannot explain the existence of these SC's.

1.10. The application of fast measuring machines to studies of large scale structure in the Universe.

So far, investigations into the 2-D projected distribution of galaxies and clusters have relied on catalogues generated from visual inspection of Schmidt camera plates, e.g. the cluster catalogue of Abell (1958), the 'CGCG' of Zwicky (1961-68), and the Lick galaxy catalogue, Shane and Wirtanen (1967). The most recent study of the Lick galaxy counts in the Shane-Wirtanen catalogue was by Shectman (1985), who found that the 2-pt angular-correlation function for Shane-Wirtanen clusters was a factor of 2 weaker than that for Abell clusters with distance class  $< 4$ .

Inevitably, such catalogues will suffer from observer inconsistencies, effects of plate variations and other selection effects which may be quite severe and thus make the catalogues highly subjective. Even when redshifts have been sought for galaxy clusters in order to elucidate the 3-D structure, the galaxy selection was made with respect to these visual catalogues. Consequently, the results and conclusions from such investigations must necessarily be tempered by the inadequacies and selection effects inherent in such catalogues. Lack of a clear understanding of the extent and seriousness of such effects on the galaxy distribution has led to considerable dispute in the past (see above).

The advent of extremely fast, automated microdensitometry, allowing measurement of large numbers of Schmidt plates, provided an opportunity to circumvent some of the major problems that have beset the analysis and interpretation of results from visually generated catalogues. Machines such as the APM at Cambridge (Kibblewhite et al. 1984) and Cosmos at Edinburgh (MacGillivray and Stobie, 1985) are powerful photographic-plate-scanning microdensitometers which enable completely objective, large scale, systematic and very high speed investigations of the properties of detected plate images to be performed. Data are transferred from machine to tape and thence to computer for reduction and analysis. The work of the Cosmos machine will be described as this is the machine from which data were collected for this thesis.

#### 1.10.1. The Cosmos machine.

The potential that the Cosmos machine has for generating a Lick-type galaxy catalogue from the wealth of photographic material made available in the UKST southern sky survey was soon realised. A collaborative project aimed at generating such a catalogue has recently commenced and some preliminary results have already been obtained (MacGillivray and Dodd, 1984, a,b). Such a machine-based survey does not suffer from the inconsistencies of human judgement found in early catalogues and puts the catalogue generation on a much more objective basis. The advantages of such a survey are many-fold. Specifically:-

- (1). Consistent and uniform selection criteria can be placed on the data acquisition which is therefore controlled and objective, e.g constant magnitude limit and calibration.
- (2). Comparison of the overlap regions between adjacent fields and study of the sky background fluctuations means that it is much easier to obtain a quantitative measure of the selection effects and to

account for them.

Ultimately, a homogeneous galaxy catalogue to faint magnitudes (e.g.  $B \sim 22.5$ ) should be obtained for hundreds of fields in the southern sky. This will allow the formulation of a galaxy cluster catalogue analagous to Abell's northern sky catalogue but which is much more objective. Such a catalogue should provide a wealth of information for the purposes of statistical investigation into the 2-D large-scale matter distribution which is free from many of the falsifying effects in the earlier visual catalogues. Cosmos data have already been used in the study of the form of the 2-point correlation function from the projected galaxy distribution in a number of fields, e.g. Hewett (1982), Shanks (1983), MacGillivray and Dodd (1984, a,b), and Stevenson et al. (1984, 1985). Such investigations have confirmed the power-law nature of the 2-point correlation function (Peebles, 1978), although the scale at which the function goes consistently negative is inconclusive but generally is at smaller values ( $\sim 3-5 h^{-1} \text{Mpc}$ ) than that found from the Lick galaxy data ( $\sim 9 h^{-1} \text{Mpc}$ ).

However, although careful statistical analysis of a Cosmos Lick-type galaxy catalogue should provide a less biased insight into the large-scale galaxy distribution, the very 2-D nature of the catalogue limits its usefulness. A slit-spectra survey of the brighter galaxies in the rich clusters and groups detected in the catalogue would help to overcome the 2-D inadequacy but would necessitate vast amounts of telescope time. The advent of the fibre-optic system on the AAT, Gray (1983), and the development of a similar system on the UKST itself, Dawe and Watson (1984), would alleviate this problem somewhat and would be ideally suited to this work since large numbers of galaxy spectra could be obtained in a single exposure. At present however, although a fibre system is

operational on the AAT, such a system to take advantage of the wide angular coverage of the UKST is still far from being realised.

Fortunately there is another technique currently available which can determine large numbers of crude galaxy redshifts from measures of UKST objective-prism plates.

#### 1.10.2. The Objective-Prism Redshift Technique.

The basic method has been described at length by Cooke (1981), Beard (1983), Cooke et al. (1983), and Parker et al. (1982), and in chapter 3 of the present work. Briefly the redshift is determined by measuring the change in relative position of a gross spectral feature (rest wavelength =  $\lambda_{3990} \pm 10\text{\AA}$ ) in low-dispersion objective-prism spectra with respect to the emulsion cut off, which is used as the wavelength reference point.

Unfortunately the measurement accuracy, ( $Z \approx 0.01$ ), is insufficient to enable detailed properties of the galaxy distribution to be obtained but the results do allow large-scale density enhancements, rich clusters and importantly large 'voids' to be detected, as well as verification of cluster classification in the Bautz-Morgan (1970), scheme. The advantage of the technique lies in the huge numbers of crude redshifts that may be obtained from Cosmos measures of objective-prism plates. Either semi-interactive techniques already developed (Beard, 1983), or more practically the automatic technique being developed by Cooke (1984), would be used. Objective-prism redshifts, being more easily obtainable for early-type galaxies, could help to trace SC filaments, (Giovanelli et al. 1982), sheets and 'cells' across many Schmidt fields. The aim of such a study would be to provide a systematic survey of an extensive area of sky which can be used in conjunction with the faint galaxy survey from direct plates (MacGillivray and Dodd, 1984).

Preliminary results from this investigation, Parker et al. (1984, a,b), have indicated the existence of a possible large, filamentary supercluster at  $Z = 0.11$  in SERC survey field 349 with a physical size of  $\sim 20 h^{-1} \text{Mpc}$ . Also Beard (1983), has investigated the Indus supercluster region and found evidence for an extended tail. The further investigation of the large scale galaxy distribution in field 349 is the basis of this thesis.

#### 1.11. Summary of Supercluster properties.

The wide variety in the observed properties of SC's has made it difficult to produce a theoretical model that satisfies all these differences at the same time. Clusters which were once considered to be isolated have been found to have connecting bridges to other clusters thus forming wisps and chains. It has been suggested that all galaxies ultimately belong to groups, clusters and superclusters by ties of spatial proximity and/or gravitational interaction. The scale on which the 'Cosmological Principle' applies has had to be readjusted upwards to hundreds of Mpc. Moreover it is not known how large a volume of space must be to give a fair value for the mean matter density of the Universe since any such volume must be considerably larger than the size of the largest inhomogeneities. Vast voids containing no or few detectable galaxies have become apparent from the analyses of the 3-D galaxy distribution which has also revealed a complex picture of cluster groups and chains. Superclusters have been shown to be individual in their observed properties and yet they may be connected by filaments to neighbouring SC's which together form a cosmic 'net'.

Geller and Beers (1982), have shown how as many as 40% of rich clusters have subconcentrations on scales  $> 0.12$  Mpc ( $H_0 = 50$  Km/s/Mpc) with many others showing elongation. They stress that failing to take subclustering into account biases both the gravitational scale length and the velocity dispersion upwards.

Studies have shown that although individual SC's so far investigated display a wide variety of properties the range of some characteristics which seem to be fairly typical can be listed.

- (1). Supercluster sizes are typically 50-100 Mpc ( $H_0 = 50$  Km/s/Mpc)
- (2). Many seem to be flattened or elongated, possessing filamentary agglomerations of clusters, groups and individual galaxies which may form a continuous network.
- (3). Velocity dispersions are generally small, i.e. between 300 and 500 Km/s.
- (4). SC's are unrelaxed structures as their size and velocity dispersions imply that crossing times, which range from  $\sim 1-5 \times 10^{11}$  years, exceed the estimated age of the Universe. Consequently extensive mixing cannot have occurred.
- (5). Usually there is no significant central concentration or symmetry (with the possible exception of the LSC).
- (6). There is evidence that the major axes of clusters in SC's tend to be aligned to their nearest neighbours and may trace out SC chains.
- (7). The space between SC's seems to be devoid of visible matter. Such voids may have diameters  $> 100$  Mpc.
- (8). There is evidence of a morphological segregation within SC's.
- (9). Masses are probably of the order of  $10^{16}$   $M_{\odot}$ .
- (10). There are indications that SC's may have existed as early as  $Z \sim 3.0$ .

### 1.12. Cosmological Implications.

Complex hierarchical, relativistic models have been explored by Wesson (1975). Theoretical models for the origin and evolution of superclustering in general and of the LSC in particular have been discussed within the framework of the gravitational instability picture (e.g. Peebles 1974, Doreshkevich et al. 1976), the adiabatic collapse or 'pancake' scenario (e.g. Zeldovich 1978) or the primeval turbulence or 'whirl' theory (Ozernoy 1974). In all these 'scenarios' the crucial question that needs to be answered is what is the epoch of galaxy formation or more precisely "were supercluster structures the first to form and did the galaxies form from within these structures, or were the galaxies the first to come into existence, and did they gather into superclusters subsequently?" (Oort, 1984). The solution to this question will only come from the careful and extensive observation and analysis of the observed 3-D distribution of matter, such as the investigations described so far. A detailed discussion of the origin of superclustering, addressing the conflicting cosmological scenarios, is given by Oort (1984).

Ozernoy (1974), considered the dynamics of superclusters which he contended might be a powerful way of obtaining an insight into the way in which galaxies form. He believes that traces of the nature of the pre-galactic structure may manifest themselves on the scale of superclusters and that at least some of the initial conditions that characterized the pre-galactic medium may be 'frozen in' to the dynamical properties of superclusters.

Einasto et al. (1984), compared the observed distribution of galaxies with two models that represented the hierarchical and adiabatic scenarios of galaxy formation. Correlation and multiplicity analysis and percolation theory were used to demonstrate that the adiabatic scenario has the closest agreement with the observed galaxy distribution.

Theorists tend to favour an adiabatic scenario of some sort and indeed the weight of observational evidence also favours this picture, although an isothermal or mixed scenario cannot yet be excluded. The existence of filaments, voids and flattened structures are compatible with scenarios where SC's originate from a truncated spectrum of fluctuations with an excess of power on large scales (e.g. adiabatic fluctuations of massive neutrinos or baryons). However, it is difficult for such structures to be formed in a hierarchical fashion from isothermal fluctuations in the baryon number density (or even adiabatic fluctuations if the Universe is dominated by cold, weakly interacting particles).

Differences between the major scenarios might be expected to manifest themselves in the actual form and structure of the SC's, Zeldovich, Einasto and Shandarin (1983). Dekel et al. (1984), stressed that in order to discriminate between the various theoretical models it is essential to be able to obtain an objective and quantitative measure of the apparent flattening observed in many SC's. As already seen the tendency for cluster axes to be correlated with those of their nearest neighbours in SC filaments, Bingelli (1982), and the morphological segregation that also appears to exist in some cases, Giovanelli et al. (1982), are both strong indications in favour of an adiabatic scenario.

A severe problem though is the observed isotropy in the microwave background radiation. If SC pancakes formed first in the early Universe then the overdensity of matter at the time of decoupling (assumed to be at  $Z = 1,000$ ) which would be required to produce these SC's should lead to larger fluctuations in the  $3^\circ\text{K}$  background than have actually been observed, e.g.  $DT/T = 10^{-4}$ . This 'problem' may be resolved if the matter density in the Universe is dominated by weakly interacting particles such as neutrinos with a mass of about  $10\text{eV}$ . If such was the case, then perturbations may have commenced when these particles are no longer relativistic at an epoch much earlier than that at which baryons decouple from radiation. As a consequence adiabatic fluctuations could collapse at early enough epochs without necessitating large perturbations in the baryon density at decoupling. Fluctuations in  $DT/T$  could then be well below the limit indicated from observations. An alternative process by which the dilemma may be resolved is to invoke a re-heating of the intergalactic medium after decoupling. The resulting dense, ionized gas could then scatter the background radiation sufficiently that the  $DT/T$  fluctuations would be smoothed out. For this to be an effective mechanism any re-ionization would have to occur at a fairly early epoch, say  $Z > 10$ , when the density was still high. However, this alternative has to account for the existence of the ionizing radiation in the first place! Since quasars were born too late, ultra-violet sources that existed in the early universe would be required. As Oort (1984), states, this makes the 'scattering' hypothesis much less attractive than that of heavy neutrinos.

### 1.13. Conclusions.

From the above exposition it is hoped that a representative picture of the development and current understanding of the large-scale matter distribution has been given. The development of this field has been rapid, irregular and controversial, fraught with observational difficulties and changing conceptions. No consensus on the detailed nature of the cosmic galaxy configuration yet exists although a convergence of views on many aspects has taken place over the last decade. The twentieth century has seen a fundamental shift in our vision of the Universe from that of our place in a single all encompassing super-galaxy to the discovery that most nebulae were "island universes" in their own right, separated by vast distances. These nebulae have themselves been shown to congregate into clusters and groups which in turn may form part of an even larger structure or supercluster. The properties of these larger aggregates have been found to be diverse, making it difficult to reconcile these varied supercluster properties with a theoretical description of the distribution of matter on the largest scales.

The fundamental "constants" that govern the nature of the Universe, e.g. Hubble's constant, the deceleration parameter and the cosmic density parameter, remain insufficiently well determined for us to be certain of both the size and future history of the Universe. Painstaking research, both observational and theoretical, is still required to give us a better indication of these parameters and consequently an improved understanding of the physical Universe and its contents. The work detailed in this thesis should help to further elucidate the nature of the large-scale galaxy distribution and hopefully our understanding of its form.

## CHAPTER 2

### Determination of slit-spectra redshifts for 107 galaxies in a magnitude limited sample in SERC field 349.

#### Summary

Redshifts are presented for a magnitude limited sample ( $b_j = 16.5$ ) of 107 galaxies detected from scans with the Cosmos machine in the ESO/SERC southern sky survey field 349 (centred at:-  $00^h 00^m$ ,  $-35^\circ 00'$ , 1950 co-ordinates). Spectra at a dispersion of  $\sim 210 \text{ \AA/mm}$  were obtained with the 1.9m telescope of the South African Astronomical Observatory (SAAO), using the Image tube Spectrograph and Reticon Photon Counting System (RPCS). Both cross-correlation techniques against filtered templates and direct measures of emission lines (if present) were used to obtain radial velocities to an accuracy of  $\pm 75 \text{ Km/s}$ .

The observed sample represents a completeness of  $\sim 80\%$  for all the galaxies detected by Cosmos down to  $b_j = 16.5$  and provides a significant data base for analysis of the brighter end of the galaxy distribution in this field. The remaining unobserved galaxies were generally fainter than  $b_j \sim 16.0$ , although three were of low surface brightness. This survey, going  $\sim 2.0$  magnitudes fainter than the CfA survey, is compatible with the Durham/AAT redshift survey (Shanks et al. 1983) and should provide further insight into galaxy clustering.

## 2.1. Introduction.

The size and nature of any large-scale anisotropy in the 3-D distribution of galaxies is still little understood (for an excellent review of the subject see Oort, 1984). Recent studies of galaxy redshifts have indicated that large fluctuations in the matter distribution from tens up to several hundreds of Megaparsecs may exist (e.g. Tarenghi et al. 1979; Chincarini et al. 1981; and Kirschner et al. 1983). The picture emerging from such investigations is one in which there are large regions of space seemingly devoid of visible matter, while galaxies themselves appear to exist mainly in elongated filaments or sheets, Giovanelli and Haynes (1982), Kuhn and Uson (1982). However, actual evidence for this picture is as yet inconclusive. For example it is not yet known if "holes" are a general feature of the distribution of galaxies (Einasto et al. 1980; Tago et al. 1984), nor if categorisation of all galaxies eventually into "superclusters" is realistic. Clearly, further work is required in this area and this was a prime motivation for this investigation.

A major problem affecting the results of previous studies is that subjective effects have undoubtedly influenced the selection of objects, and consequently any findings must take into account the effect of possible biases. We are currently engaged in a collaborative project to study the large-scale 2 and 3 dimensional distribution of galaxies from objective measurements made with the Cosmos machine at the Royal Observatory, Edinburgh (ROE). The data were obtained from both deep direct and objective-prism plates taken with the U.K. Schmidt telescope (UKST). The area of sky examined covers a large region containing both the South Galactic Pole (SGP) and UKST survey field 349. Field 349 is a particularly important field in this work because a wealth of photometric data was obtained by Carter (1980), from PDS scans of an Anglo-Australian telescope

(AAT) direct plate of the rich southern cluster at  $00^{\text{h}}04.8^{\text{m}}, -35^{\circ}00'$  (1950 co-ords). These data have been compared with photometry obtained from Cosmos measures, (MacGillivray and Dodd, 1982) which indicate that galaxy magnitudes can be obtained to an accuracy of  $\pm 0.1$  with Cosmos, which is satisfactory for statistical analysis of the luminosities and distribution of galaxies.

Preliminary work by Parker et al. (1984,a,b), on objective-prism spectra in field 349, indicated the existence of a complex of structures evidenced by co-incidences in the location of galaxies in both 2-D and 3-D space. In particular a possible "supercluster" composed of at least 5 clusters at  $Z \sim 0.11 \pm 0.01$  was identified. However, the problem with the objective-prism determinations, apart from their low accuracy, is that the results can only be obtained for galaxies with magnitudes in the range  $16.0 \leq b_j \leq 19.0$  (Beard et al. 1985) but with most redshifts being furnished at  $b_j \leq 18.0$ . This is due to the effects of image size on the plate, the dynamic range limitations of the measuring machines, and noise limitations on photographic plates at faint magnitudes. This has led to a serious gap in the study of this field.

Hence, slit spectra were sought to allow redshifts to be obtained for the brighter galaxies in this field. Furthermore, since the slit spectra are at a much higher dispersion the accuracy of the results is much greater than their objective-prism counterparts, allowing a more exact and detailed analysis.

This chapter is concerned with the determinations of the slit spectra redshifts for the galaxies observed so far in field 349. Analysis and discussion of the redshift results are given in chapter four. Section 2 explains how the galaxy sample was selected, section 3 details the observations and instrumental configuration, section 4 deals with the reduction process employed and section 5 is a presentation of the results. Finally section 6 is a description of the error assessment of the redshifts and in section 7 the conclusions are presented.

## 2.2. The target sample.

The choice of magnitude limit for the survey was made with a number of considerations in mind:-

- (1). To try to reach as faint as is practically possible with the available telescope and instrumentation, without jeopardizing efficiency.
- (2). To go faint enough to overlap with the useful range of the objective-prism redshift technique, i.e. at least as faint as  $b_j \sim 16.0$ , and hence provide valuable calibration of the objective prism technique at the bright end.
- (3). To be compatible with the Durham/AAT redshift survey in depth (Shanks et al. 1983).
- (4). To provide a reasonably sized sample for observation which would yield a good chance of attaining a high level of completeness.
- (5). Recognition that a deep sample with a high level of completeness in a small field can be as useful as a shallower survey over a larger area of sky.

A magnitude limit of  $b_j \leq 16.5$  was chosen as this satisfied the above criteria well ( $b_j$  is the blue magnitude appropriate to the IIIaj/GG385 emulsion-filter combination, e.g. see Shanks et al. 1984).

The Cosmos machine was used to scan the UKST direct plate J3406 of field 349 in image-analysis mode (see MacGillivray and Stobie, 1985). This mode provided a list of 18 image parameters describing characteristics of each image detected above a given threshold. These parameters include an estimate of each object's magnitude which can be calibrated against external photometry, in this particular case using the same objects as in Carter (1980), see MacGillivray and Dodd (1982). Star-galaxy separation was performed using standard algorithms developed for Cosmos data (MacGillivray and Stobie, 1985). Selection of galaxies detected with magnitudes  $b_j \leq 16.5$  resulted in an initial sample of 138 objects over the  $5.35^\circ$  by  $5.35^\circ$  field measured. A plot of the X,Y positions of this selected magnitude-limited sample was then made and a match up with actual images on the direct plate sought.

After careful scrutiny, 133 images were directly identified as single galaxies. There remained 5 erroneous identifications which on inspection were found to be merged images of one form or another, e.g. very close pairs of fainter stars or a faint galaxy/star merger, and in one case a tight knot of 3 faint galaxies which would individually be below the magnitude limit imposed. It is very difficult to develop an algorithm to discriminate between the various types of merged image and a discrete galaxy image. However this problem ought to be alleviated somewhat in the near future with the installation of the proposed blended image software package on Cosmos. Nevertheless a 97% success rate in the correct identification of galaxy images in the present Cosmos selected bright sample was achieved. There also appeared to be a few cases of galaxies brighter than the magnitude limit which were not correctly identified by the star/galaxy separation algorithm due to their non-symmetrical form. The 3 most obvious cases were included in the target list. As this number is small compared with the total galaxy sample the objectivity of the

galaxy selection should not be significantly affected (these galaxies are identified in table 2.4 by their lack of magnitude estimate). Figure 2.1 is a finding chart for this galaxy sample. The filled circles refer to those galaxies observed thus far.

A list of radial-velocity standard stars and galaxies with accurately determined velocities was drawn up for use as templates for the cross-correlation analysis (see table 2.1). These templates were chosen so as to be easily accessible at the beginning and end of a night's observation.

### 2.3. Observations and instrumental configuration used.

The observations were performed over the period Oct.1983-Oct.1984 encompassing 3 separate 1 week allocations of dark time on the 1.9-metre Radcliffe reflector of the South African Astronomical Observatory. The Image-Tube Spectrograph at the Cassegrain focus was used with the slit oriented East-West together with the RPCS as the detector (S-20 cathode). A grating with an effective blaze of  $\sim 4600\text{\AA}$  and giving a wavelength coverage from  $\sim 3300\text{-}7500\text{\AA}$  was used for the observations with a reciprocal dispersion of  $\sim 210\text{ \AA/mm}$  in the first order. The slit width was set at  $300\text{ }\mu\text{m}$ , a typical setting for this grating, corresponding to  $\sim 1.8''$  on the sky ( at the Cassegrain focus,  $f/18$ , the plate scale is  $\sim 6''/\text{mm}$  ).

A spectrograph Dekker plate was used to isolate 2 holes along the length of the slit. These were adjusted to fall centrally upon the 2 parallel diode arrays of the reticon where simultaneous observations of object and sky are made. Each diode array is  $\sim 28\text{ mm}$  long and  $375\text{ }\mu\text{m}$  wide with no gap between and consists of 936 diode elements each of  $30\text{ }\mu\text{m}$ . Logic centring in the electronics enables photon pulses to be positioned to  $1/2$  a diode so that there are in fact 1872 pixels in each array.

●:observed    ○ unobserved

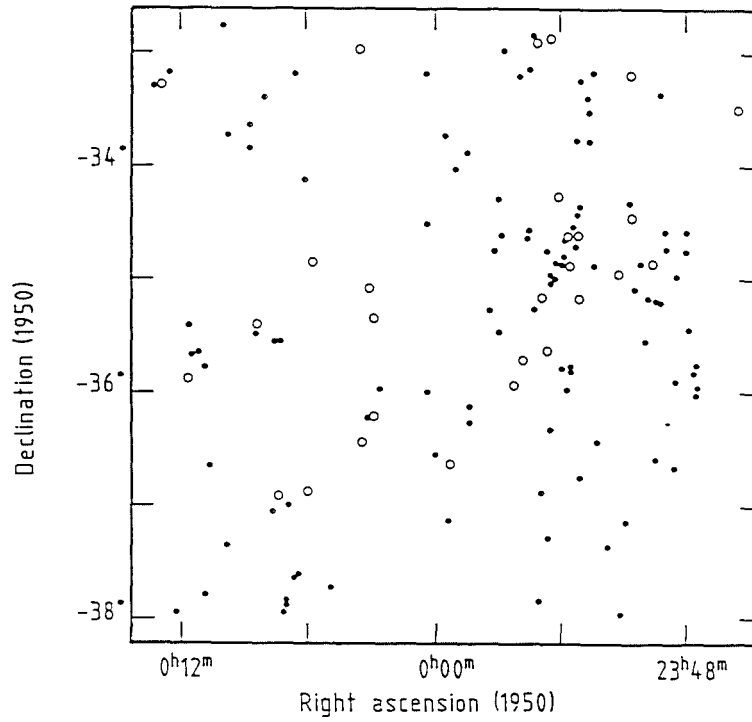


Figure 2.1 Projected distribution of the COSMOS selected galaxy sample with  $b_j \leq 16.5$ , in SERC survey field 349.

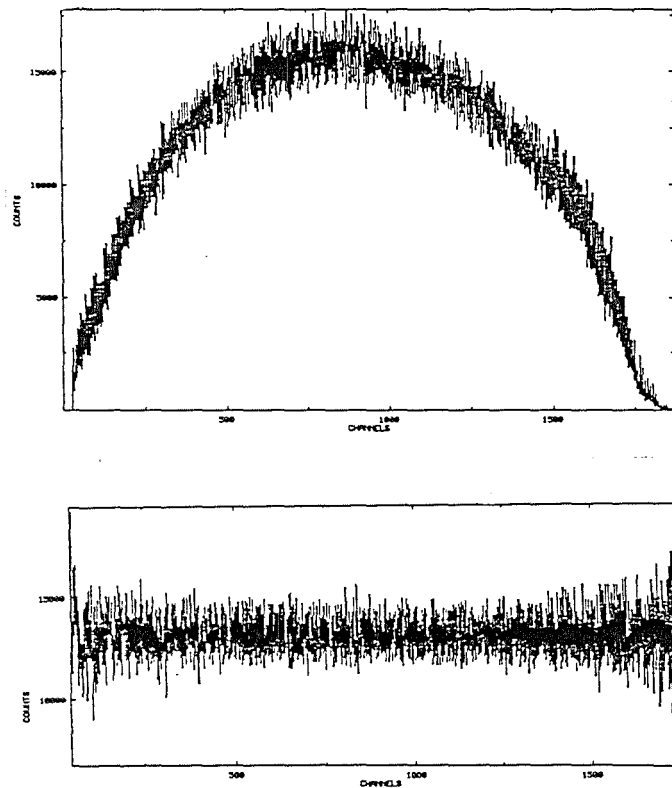


Figure 2.2 An example of the 'raw' and normalised flat-field exposures.

A dekker with a slit width of  $6.0''$  on the sky was employed. The same slit width and position angle and the same Dekker and Dekker setting were used throughout.

This instrumental configuration resulted in an average dispersion of  $\sim 3\text{\AA}/\text{pixel}$  (channel). The typical FWHM of an arc line was  $\sim 2.5$  channels ( $8\text{\AA}$ ) or  $\sim 450$  Km/s at  $5000\text{\AA}$ . Data were stored initially on cartridge tapes with disk backup for later transfer to 9-track tapes in Cape Town in FITS format. In most respects the instrumental set-up was very similar to that used by Tonry and Davis (1979), for their CfA redshift survey, except that they used a higher dispersion to study a brighter sample of galaxies.

### 2.3.1. Observing Procedure.

The RPCS suffers from pattern noise and small-scale sensitivity variations across the two diode arrays so that it is necessary to obtain flat-fields in order to try to normalise these effects out. Unfortunately flat-field exposures are unsatisfactory when using the  $210\text{\AA}/\text{mm}$  grating due to the spectral range of the grating exceeding that of the quartz-iodine calibration lamp. Hence it was necessary to use a higher-dispersion grating which complicated and lengthened the observing procedure. Flat-field exposures of 10,000 seconds were made at the beginning and end of each night's observations.

A typical observation of a target object consisted of object exposures in each array separated by 100 second Cu-Ar arc exposures.

The object exposures taken in each array ranged from ~400 seconds to a maximum of 1,200 seconds, depending on the galaxy being observed. In cases of low count rate, due either to poor observing conditions or a low surface brightness or faint galaxy, two exposures in each array were performed with arc exposures in between. This was a necessary step if wavelength calibration consistency was to be maintained because of flexure problems with the spectrograph and RPCS detector head which would be exacerbated by longer exposures. The separate object exposures could be summed to form a composite spectrum later.

It was possible to examine spectra under observation in either array building up in real time on a display unit. Some basic processing of the data could be performed, such as dividing by stored flat fields, subtracting the contents of one array from the other (sky subtraction), and smoothing the spectra to make spectral features easier to distinguish. This proved to be a useful means of determining a suitable exposure time for each observation. A general rule of thumb was to obtain for each object ~100 counts/pixel in the peak on S/N considerations alone, or at least to continue an exposure until spectral features such as CaII H and K or Mgb become recognisable. If strong emission lines were present in galaxy spectra then the integration was curtailed when the emission lines had become unmistakable. After sky subtraction the average counts per pixel along the central, most sensitive region of the reticon for the observed galaxies was:-  $52.5, \sigma_{n-1} = 19.5, N = 95$ , after exclusion of emission line objects with low S/N in the continuum. Nine non-template objects had sky-subtracted counts of  $> .90$  counts/pixel.

Since a cross-correlation technique was used to obtain the radial velocities it was necessary to observe a selection of stellar and galaxian templates with accurately determined radial velocities. Generally one or two radial velocity standard stars of spectral types F,G,K were observed each night to correspond to the dominant light contribution from the bulk of galaxy spectra. Also four galaxy templates were observed over the 3 weeks of allocated time as well as two spectrophotometric standard stars. Table 2.1 gives details of the stellar and galaxian templates used.

#### 2.4. Data reduction techniques.

Reduction of the data was facilitated using the STARLINK computer at ROE and the 'SPICA' package, (a suite of STARLINK software developed for handling spectral information of this nature). Two techniques were used to obtain an object's redshift:-

- (1). Cross correlation of an absorption spectrum against filtered templates of known radial velocity.
- (2). Direct measurement of emission line wavelengths in those galaxies possessing such features.

Essentially the same reduction process, (with minor differences) as described by Tonry and Davis (1979), for their CfA survey was followed, developing the appropriate procedures from within SPICA. As far as the Fourier analysis of spectral data is concerned, details of the correct methods are given by Brault and White (1971), with a review by Ridgway and Brault (1984). An excellent description of how the cross-correlation technique can be successfully and realistically employed is given in the Tonry and Davis paper, to which the reader is referred for greater detail. A summary of the principal steps required to prepare the data for the cross-correlation or direct measurement of emission lines is now given.

Table 2.1

Details of the stellar and galaxian templates employed.

(a). Stellar Templates.

Star name.	R.A. (1950) h m s	DEC. o ' ''	Mag.	Spectral type.	Vpub. Km/s	Ref.
HD693	00 08 43.2	-15 44 33	5.0	dF5	+14.7	a
HD8779	01 23 53.6	-00 39 29	6.5	gK0	-5.0	a
HD35410	05 21 56.3	-00 56 16	5.2	gK0	+20.5	a
HD157457	17 22 05.7	-50 35 24	5.2	K1	+17.4	b
HD171391	18 32 15.6	-11 01 04	5.2	gK7	+6.9	a
HD203638	21 21 19.6	-21 03 56	5.5	gK2	+21.9	b

(b). Galaxy Templates.

Galaxy name.	R.A. (1950) h m s	DEC. o ' ''	Mag.	Morph. type.	<Vpub.> Km/s	error Km/s	Ref.
NGC7793	23 55 15	-32 52 06	9.7	.SAS8.	214	9.6	RC2&RVG
NGC6909	20 24 09	-47 11 36	12.8	.E6.	2680	80	RC2&RVG
NGC7329	22 36 56	-66 44 36	13.0	SB	3189	25	RC2&RVG
IC5175	22 09 50	-38 22 30	13.5	S	10762	32	WEST
IC5135	21 45 21	-35 11 12	13.1	.P.	4823	49	RC2&RVG

References:-

a. Transactions of the IAU, 1955, 9, 442 and Fehrenbach and Duflot, Astron. and Astrophys. Suppl., 1980, 39, 311

b. Evans, Menzies and Stoy, 1959, Mon. Not. R. Astr. Soc., 1959, 119, 639

RC2. Second reference catalogue of bright galaxies, de Vaucouleurs, G., de Vaucouleurs, A., and Corwin, H.G., 1976, Univ. Texas press.

RVG. Catalogue of radial velocities of galaxies, Palumbo, G.G., Tanzella-Nitti, G., and Vettolani, G., 1983, Gordon and Breach Science pub.

West. West, R.M., and Barbier, b., 1982, Astron. and Astrophys., 106, 53

Notes.

(1). The stellar template velocities are accurate to  $\sim 1$  Km/s.

(2). The galaxy morphological types are on the "Handbuch der Physik" system, Vaucouleurs, G.de, 1959, in Hdb.d.Physik, 53, 275.

(3). The galaxy magnitudes are Harvard photographic apparent magnitudes (H.A., 88, 2) except for IC5175 which is on the 'B' system and from Vaucouleurs, G.de., and A., 1972, Mem.R.Astr.Soc., 77, part.1.

(4). The galaxy velocity for IC5175 was erroneously corrected for the solar motion using equation  $V = 300 \cdot \cos l \cdot \sin b$  by WB instead of the correct equation 2.5. The raw uncorrected velocity is given above.

Firstly all object, night sky, and arc exposures from each reticon array are divided by the appropriate normalised flat field. Sky subtraction of the object exposures is performed after which they are wavelength calibrated and rebinned to co-ordinates linear in wavelength (i.e "scrunched"). Separate object exposures are then summed, at which point the data is suitable for measurement of emission lines. Any strong emission lines or residual night sky lines are then removed and a suitable wavelength section of the spectra is rebinned to co-ordinates linear in  $\log(\text{wavelength})$ . The continuum and discontinuity between the beginning and end of the spectrum are then excised and finally the spectra are Fourier filtered by means of a bandpass filter. The spectra are now ready for cross-correlation against a similarly treated template.

In principle the above procedure is straightforward but in practice the situation was complicated by a number of problems associated with the data acquisition and reduction. This necessitated careful investigation if the best possible results from the data were to be obtained. Details of the actual reduction procedure used are given below.

#### 2.4.1. Flat fielding.

This was necessary to try to eliminate the pattern noise and small scale sensitivity variations along the reticon arrays. Inevitably, not only were there small scale sensitivity variations along each array individually, but there were also differences between the two arrays of the reticon. Hence, in order to account for these differences between the arrays the following procedure was performed:-

- (1). The two flat fields for the nights observations were averaged, each array done separately.
- (2). The averages for array A and B were then themselves averaged and heavily smoothed.

(3). The average flat fields for the night from array 'A' and that for array 'B' were then divided by this smoothed average from arrays A and B.

(4). The arc, object and sky exposures in each array were then divided by the normalised flat field for that array.

This procedure should result in a better sky subtraction that is not affected by any sensitivity differences between the 2 reticon arrays. An example of the "raw" and "normalised" flat fields is given in figure 2.2.

#### 2.4.2. Sky Subtraction.

This process was complicated by the fact that there was an approximately constant shift of  $\sim 2.0$  channels ( $\sim 6\text{\AA}$ ) between the two reticon arrays, so that if straight subtraction were performed the night sky lines and spectrum would not cancel satisfactorily. The solution to this particular problem was to cross-correlate the sky spectrum with the object spectrum and rely upon the strong night sky lines visible in the long exposures of both spectra to dominate and provide a strong cross-correlation peak. A St. Andrews modification of the cross-correlation function within SPICA was used. This provided the shift in channels between the two spectra as well as giving the height of the cross correlation function (CCF) peak, the width and an estimate of the error in the peak's centre position ' $\delta$ '. For simplicity, exposures, whether they were of object or sky, were always shifted relative to the same array prior to subtraction of the sky spectra. This technique proved to be very successful except in the stellar template exposures which were of very high S/N and of short exposure time. In these cases the sky subtraction is not critical but was still performed after shifting the data in one array by an amount which was the average shift found from the other cases.

### 2.4.3. Wavelength calibration.

This proved to be the most difficult and yet crucial step in the entire reduction process since the final accuracy of the results rests heavily upon good wavelength calibration of each spectrum. The first step is to identify lines in a template arc spectrum from a list of wavelengths of known lines in this spectrum. The SPICA arc calibration procedure was then used to obtain a best fit set of quintic co-efficients which describe the global wavelength/channel-number relationship for this arc spectrum, assuming the correctness of the line identifications. Poorly matched lines affect the polynomial fit for the entire spectrum and can give large discrepancies between the actual wavelengths and calculated wavelengths. Hence the list of identified lines was modified until the discrepancy between the laboratory wavelengths of the remaining lines and the calculated wavelengths from the same fitted lines are acceptably small. Nineteen arc lines were eventually used to define the wavelength/channel-number relationship for the 'template' arc spectrum with rms residuals for the calculated fit being  $\sim 0.2\text{\AA}$ .

Measurements of arc lines in a typical wavelength calibrated arc spectrum using a Gaussian fitting routine within SPICA (GAUSS hereafter) gave an average residual between measured and actual wavelengths of the lines of  $\sim 0.205\text{\AA}$ ,  $\sigma_{n-1}=0.131$ ,  $N=19$ . The average error given by the GAUSS function for the positional precision with which individual lines can be determined was  $\sim 0.249\text{\AA}$ ,  $\sigma_{n-1}=0.131$ ,  $N=19$ , in very good agreement with the average residual. Essentially, then, the accuracy of the wavelength calibration of the arc spectra is constrained by the accuracy of the gaussian fitting to individual lines on a fractional pixel basis. For spectra at this low dispersion this translates to a velocity uncertainty of  $\sim 15$  Km/s at  $5000\text{\AA}$ . The accuracy of the wavelength calibration of the object spectra depends

on whether the observed inter-arc shift either side of an object exposure is uniform with time. If this is even approximately true then the calibration will be good to  $\sim 20$  Km/s.

Once a good template arc line list had been compiled it could be used to wavelength-calibrate all other arc exposures using a comparison function within the arc calibration procedure. Since we are dealing with 2-D data each arc exposure is a summation from both arrays after correcting for any inter-array shifts. This practice not only simplified the calibration procedure by obviating the necessity for calibrating each array separately but also provided a higher S/N arc spectrum and consequently better definition of weak lines in the less sensitive regions of the reticon arrays. This was an important factor in providing a good calibration over the largest range of wavelengths. An investigation into the consistency and dispersion of this inter-array shift was desirous to assess the necessity of determining these shifts individually for each exposure or whether a constant value could be employed without unacceptably degrading accuracy. Figure 2.3 is a plot showing the internal shifts of the positions of arc lines in one array relative to those in the other array for each arc exposure made during 4 nights observations. As can be seen, this shift is not constant but varies in a random fashion. The average shift was 1.969 channels ( $\sigma=0.012$ ) and a range of 0.06 channels ( $\approx 0.18\text{\AA}$  or 11 Km/s at  $5000\text{\AA}$ ). This range of shift values is close to the calibration accuracy of the spectra, and consequently the actual shift between the arrays may in fact be constant. However, it was decided to obtain the inter-array shifts individually prior to summation to maintain the utmost precision in the data reduction process since this could be done easily.

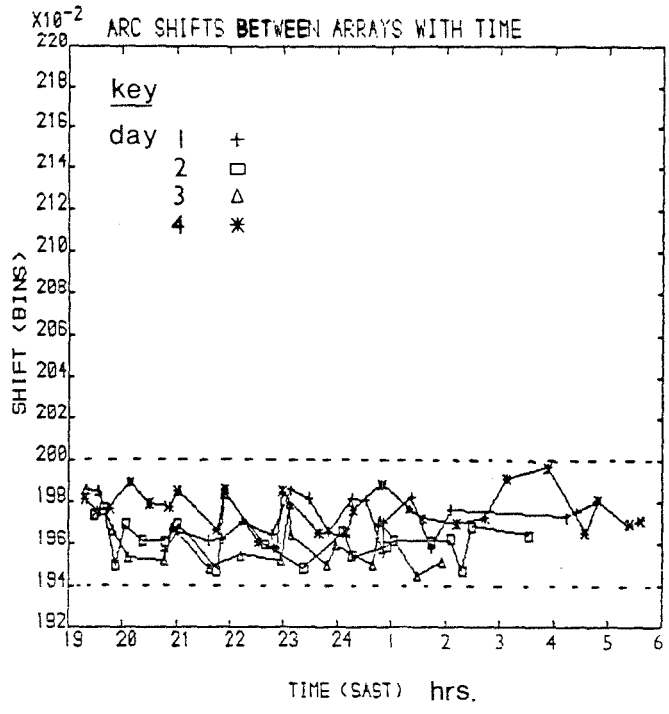


Figure 2.3 The internal shifts of arc line positions in one array relative to the other for each arc exposure made during 4 nights of observations.

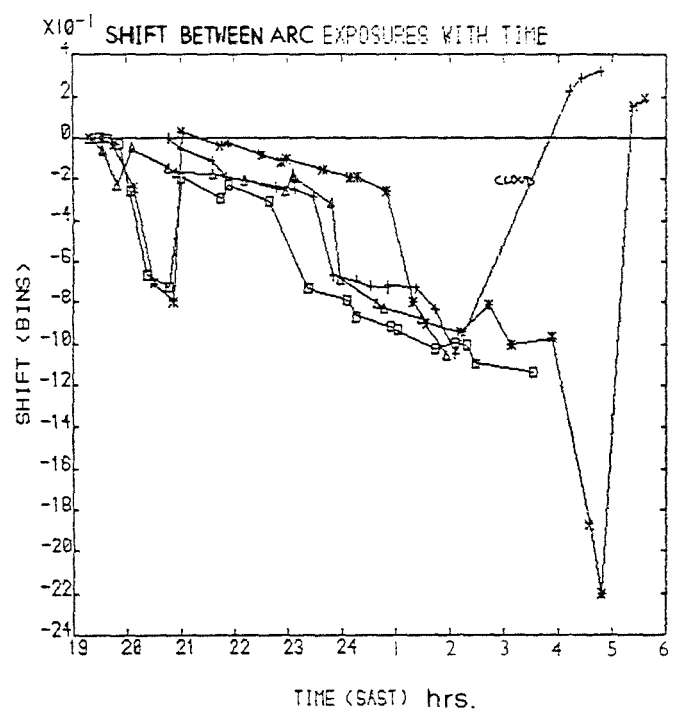


Figure 2.4 Channel shifts between arc exposures made over 4 nights of observations relative to the first arc exposure of each night.

It must be remembered that although the spectral data is non-continuous, i.e. is in discrete pixels, fractional channel numbers are legitimate and are obtained by parabola fitting the CCF peak. The correction for the inter-array shifts was performed because the range of shifts was greater than the precision with which the shifts were provided.

The next step was to wavelength calibrate the object exposures by associating the wavelength/channel-number relation obtained for the arc exposures with the object exposures. Now in each case there is an arc exposure both before and after each object exposure, with no slewing of the telescope in between (because of flexure). Apart from the  $\sim 2.0$  channel inter-array shift there are also time-dependent channel shifts between different arc exposures in the same array, i.e. either side of an object exposure. Excluding shifts of several channels that may follow a long slew in declination the stability of the RPCS is high. The expected shift with time is less than 0.02 channel/hour. This effect was investigated by seeing how the shift of each arc done during a night's observation relative to a template arc, (the first arc of the night) varied with time. The results from four nights observations are given in figure 2.4. In practice the effect was found to be generally  $\leq 0.02$  channel/hour but was somewhat irregular. In most cases the inter-exposure arc shifts for those arcs either side of an object exposure are quite small ( $\sim 0.05$  channels), but for certain exposures could be as large as 0.2 channels ( $\sim 36$  Km/s at  $5000\text{\AA}$ ), even though no telescope slewing had occurred! This effect was accounted for in the following way.

If it is assumed that the inter-exposure channel shifts are linear with time, then the arc exposures before and after the object exposure can be shifted each by half the shift found between them but in opposite directions so as to correspond to the mid-point exposure time for the object. The arcs can then be summed to yield an arc spectrum whose wavelength/channel-number relation should be the best possible relation for associating with the object exposure.

A problem with the calibration process was that the arc spectra had very few identifiable lines shortward of 4000Å and longward of 6000Å, although an arc line at  $\lambda 3729.3\text{\AA}$  was sufficiently well defined for inclusion in the template arc spectrum. For  $\lambda > 6000\text{\AA}$  the situation was exacerbated by the variability of line strengths for the few weak lines in this region. Hence the wavelength calibration at wavelengths  $> 6000\text{\AA}$  is less well defined than for the region  $\lambda 3600-6000\text{\AA}$  because of the small differences between the individual arc spectra and the template arc used for the comparison at longer wavelengths. For the cross-correlation technique this region is not important due to the lack of any strong absorption features in this range although wavelength measures of the  $H\alpha$ , [SII] and [NII] emission lines must be suspect. After the wavelength co-efficients for the arc exposures had been associated with the object exposures the spectra were rebinned into co-ordinates linear in wavelength. A judicious choice of start wavelength and wavelength increment (i.e. the wavelength to be covered by each channel in the scrunched data) was made to encompass the most sensitive range of the reticon arrays and incorporate the most useful wavelength range in the object spectra. These values were then used for all spectra. At this stage the spectra were measured for any emission lines and separate object exposures were summed to form composite spectra.

2.4.4. Rebinning the data to co-ordinates linear in  $\ln(\lambda)$ .

In preparation for the cross-correlation analysis a suitable wavelength subset of the data was mapped to 2048 bins with co-ordinates linear in  $\ln(\lambda)$ .

$$\text{i.e. } N = A \ln(\lambda) + B \dots \dots \dots 2.1$$

A subset of  $\lambda_{3600-6000\text{\AA}}$  was chosen as this region contains most of the spectral features visible in the original spectrum and avoids the suspect wavelength calibration at  $\lambda > 6000\text{\AA}$ . The scale was such that a velocity of  $\sim 65 \text{ Km/s}$  shifts a feature by one bin. The data were rebinned in this manner for the following reason:-

The usual form for the Doppler relation is given by:-

$$\frac{\lambda - \lambda_0}{\lambda_0} = \frac{V}{C} \text{ or } \Delta\lambda = \frac{\lambda_0 V}{C}$$

which implies that the change in wavelength  $\Delta\lambda$  is a function of both the velocity and wavelength.

If we take logarithms though:

$$\begin{aligned} \ln \lambda - \ln \lambda_0 &= \ln(1 + V/C) \quad (V \ll C) \\ \Rightarrow \Delta \ln \lambda &= \ln(1 + V/C) \dots \dots \dots 2.3 \end{aligned}$$

Hence the shift in bins between a template spectrum and an object spectrum can be related to a redshift directly, where  $\Delta \ln \lambda$  is linearly related to the shift in bins.

Thus:

$$\begin{aligned} \text{Exp}(\Delta \ln \lambda) &= 1 + V/C \\ \Rightarrow V &= (\text{Exp}(\Delta \ln \lambda) - 1) \times C \dots \dots \dots 2.4 \end{aligned}$$

i.e. the Doppler shift is a function of redshift alone when expressed in terms of  $\ln \lambda$ .

The next stage of the reduction process was to eliminate any emission lines and uncanceled night-sky lines by interpolation of the continuum across such features. This was necessary since the templates are absorption spectra and the cross-correlation should be performed between objects with similar spectral characteristics if it is to work satisfactorily.

The continuum and discontinuity between the beginning and end of the spectrum are then removed followed by the application of a Fourier filter which is the final step in the preparation of a spectrum for cross-correlation. This filtering was performed for two main reasons:-

- (1). To remove any residual curvature of the continuum. (low frequency)
- (2). To attenuate the highest spatial frequency components which are usually due to noise and are beyond the instrumental resolution.

After obtaining an initial value of the high-frequency cut to apply by examination of the power spectra of a number of object spectra of different S/N, the object spectra were repeatedly cross correlated against a set of templates. The value of the high-frequency cut was slightly altered until the most consistent set of results between the different templates and the best combination of peak height and width were obtained.

#### 2.4.5. The Cross-Correlation.

A St. Andrews modified version of the SPICA cross-correlation routine was employed which includes an error estimate in the cross-correlation function (herein after CCF) peak's position based on the method used by Tonry and Davis (1979).

The largest peak in the CCF is selected and fitted by a parabola and the peak centre position ( $r$ ), height ( $h$ ), FWHM ( $w$ ) and peak position error estimate ' $\delta$ ' ( $\delta$ ) are returned. This selection is performed automatically from within the SPICA CCF procedure with no external interference and is therefore independently chosen in each case. The shift in the peak relative to the template (in channels) gives the velocity of the object since a redshifted spectrum is a uniform linear shift because of our choice of binning to  $\ln(\lambda)$ . Hence CCF redshifts can be calculated for each observed galaxy.

Figure 2.5a-f gives examples of each of the reduction steps described above for a typical galaxy spectrum (e.g. sky subtraction, wavelength calibration, rebinning and cross-correlation against a filtered template).

#### 2.4.6. Emission line measurements.

After the object spectra had been sky subtracted, wavelength calibrated and 'scrunched', they were individually scanned for the presence of emission lines or uncanceled night sky lines. Any uncanceled night sky lines were then excised and any remaining 'spikes' in the spectrum were measured. The GAUSS function was used which fitted a Gaussian to the selected emission feature. An error estimate of the observed line centre wavelength is given as well as an error estimate of the SIGMA and FWHM values (the latter in Å and Km/s). Consequently for each suspected emission line wavelength obtained there is an associated estimate in the uncertainty of the line's central wavelength, SIGMA and FWHM from the fitted Gaussian profile.

Figure 2.5 (a-f)

Plots illustrating the series of reduction steps performed in obtaining a cross-correlation function velocity for a typical target galaxy.

(a). Flat-fielded data from both arrays of the reticon for a single object exposure. The object spectrum is in the first array and the sky exposure in the second.

(b). The single exposure object spectrum after sky subtraction.

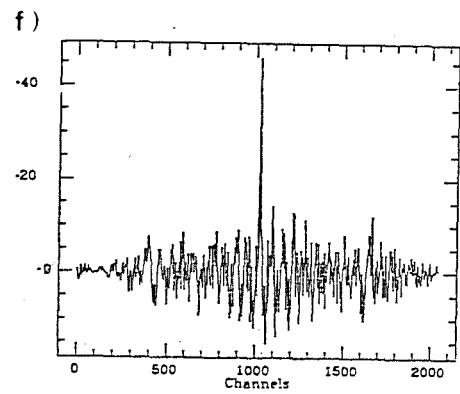
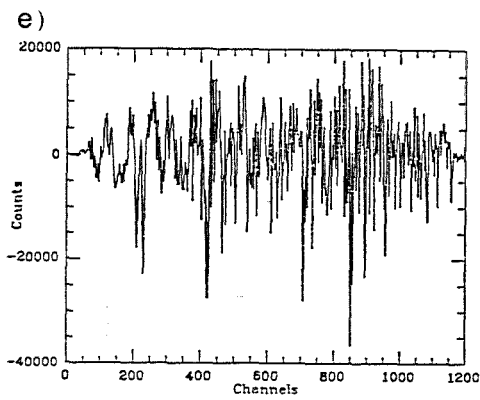
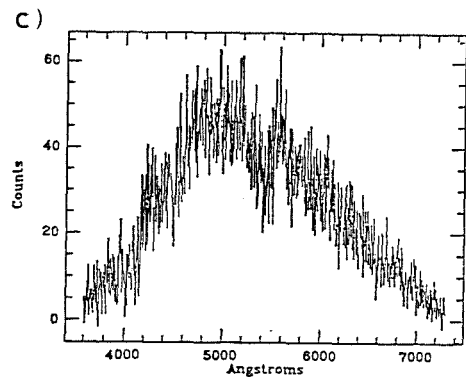
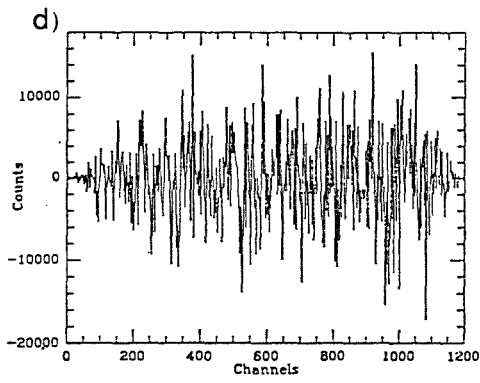
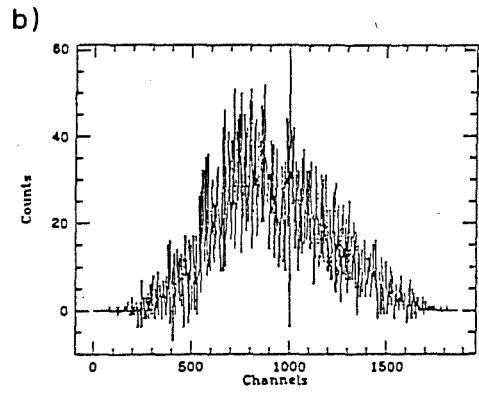
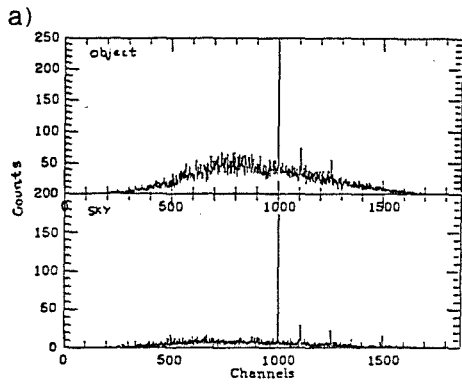
(c). The same object spectrum after wavelength calibration, summation of the separate object exposures and removal of any residual uncanceled night sky emission lines.

(d). Again, the same summed object spectrum after "scrunching", rebinning to  $\text{Log}(\text{wavelength})$ , subtracting the continuum and applying a Fourier filter.

(e) Example of a typical high signal-to-noise stellar template spectrum after being processed as in steps (a)-(d). The object spectrum will be cross-correlated against this filtered template.

(f) The resulting cross-correlation function given by cross-correlating the galaxy spectrum in (d) with the stellar template. A shift of the CCF peak 'N' channels to the right corresponds to a linear change in redshift due to the rebinning of the data to  $\text{log}(\text{wavelength})$ .

figure 2.5 a-f



## 2.5. Results.

Measurement of both absorption line redshifts from the cross correlation technique and emission line redshifts from direct measures of individual lines is an important consideration. Emission lines can be produced in non-nuclear regions of a galaxy and can thus exhibit velocities which differ significantly from the CCF redshifts.

### 2.5.1. Emission line results.

Out of a total observed sample of 107 galaxies in field 349, 44 had suspected or definite emission lines. This sample, obtained by careful examination of each galaxy spectrum, was subdivided into 3 categories:-

- (a). Spectra which have strong, easily identified emission lines. The number of such cases was 17. (=16% of total sample)
- (b). Spectra which have probable emission lines, although there were no strong lines present to put identification beyond doubt. The number of spectra in this category was 16. (=15% of total sample)
- (c). Spectra which had no obvious strong lines but which may have weak emission lines or whose match of possible lines against a set of standard, likely galaxy emission lines resulted in an unlikely line identification (from matching emission line redshifts with CCF redshifts). The number of spectra in this case was 11. (=10% of total sample)

Table 2.2 outlines these findings, giving the rest wavelengths of identified lines and the frequency of occurrence in each of the three categories above.

Table 2.2

Details of the number and confidence of the various species of emission line identified from the observed galaxy spectra.

Rest $\lambda$ Angstroms	Line Identity.	Definite	Probable	Possible
3425.8	[NeV]	-	-	1
3727.0	[OII]	14	9	1
3797.9	H10	-	-	1
3868.74	[NeIII]	2	1	2
3889.9	H8+HeI	-	-	1
4363.2	[OIII]	1	1	2
4861.33	Hbeta	11	5	-
4958.91	[OIII]_N2	3	1	-
5006.84	[OIII]_N1	8	3	1
5875.63	HeI	2	-	1
5977.0	HeII	-	-	1
6300.3	[OI]	-	1	-
6548.10	[NII]	5	-	1
6562.81	Halpha	5	4	1
6583.60	[NII]	7	5	-
6717.00	[SII]	-	1	1
unidentified lines:		13	24	-

Table 2.3

Average cross-correlation velocities from repeat observations of stellar and galaxian templates and three target galaxies.

Object identity	Number of Observations	Av.CCF vel. all templates	Dispersion in repeat Observations
(a).Stellar templates.			
HD157457	8	-12.3	19.6
HD35410	11	-5.8	27.6
HD171391	5	-33.7	52.2
HD203638	4	-5.3	8.7
(b).Galaxy templates.			
IC5175	3	2778	31
NGC7793	3	237	50
(c).Target galaxies.			
NGC7812	2	6767	5
QP37	2	14605	37
QP72	2	14614	59

N.B. Velocities in column 3 are in Km/s.

The identification of emission lines of a particular species in galaxy spectra, except for very strong lines, was somewhat qualitative and clearly subjective. In making such an assessment a number of factors were considered:-

- (a). Strength of the line concerned.
- (b). Whether the line velocity matches that for other lines that may be present in the same spectrum or matches the CCF velocity. (within a certain tolerance)
- (c). Whether the line is a 'likely' identification. (e.g.[OII]3727 c.f. H10)

All these factors were considered in conjunction before a decision regarding line identification was made.

#### 2.5.2. Results from cross-correlation analysis.

Once object spectra had been suitably prepared they were cross-correlated against a set of radial-velocity standard stars and galaxies with good published redshifts. (see table 2.1)

Up to 5 stellar templates and 3 galaxy templates were used, each template yielding its own CCF peak parameters for 'r', 'h', 'w' and ' $\delta$ '. This was an important exercise not only because of the varying morphological type of the galaxy spectra but because in cases of low S/N spectra it becomes difficult to identify the true peak of the CCF from surrounding noise peaks of comparable size. Use of a selection of templates of different spectral types can help to resolve doubt and ambiguity in these cases. Those templates yielding the most consistent velocities, largest CCF peak heights and narrowest peak widths are given greater weight. Obvious mis-matches, i.e. large negative velocities or velocities which are wildly different from those obtained for the majority of templates, are excluded. Occasionally only one template would yield sensible and acceptable

peak parameters, further vindicating the use of a selection of templates.

The velocities calculated from the shifts given by the CCF are formal heliocentric velocities  $c \cdot Z$ , corrected for the velocity of the template and for the annual and diurnal motions. A further correction for the motion of the sun relative to the centroid of the Local Group (the Solar Motion) was also applied. The Solar Motion correction is given by:-

$$V_{\text{corr}} = 300 \cdot \sin l \cdot \cos b \quad (\text{Km/s}) \dots \dots \dots 2.5$$

Average velocities from using just the stellar templates, just the galaxy templates and from combining all the templates were formed, the latter being the velocities presented herein.

### 2.5.3. Redshift results.

Details of the CCF velocities, emission velocities and other relevant data are given in table 2.4. This gives in successive columns:-

#### (1). Galaxy sequence number.

In cases where there is a corresponding catalogue identification this is then given in table 2.5.

#### (2). Equatorial co-ordinates. (1950)

Calculated from Cosmos image positions and accurate to 1-2 arcseconds.

#### (3). Morphological Classification.

A crude classification on the revised Hubble sequence based on individual scrutiny of sample galaxies on the direct plate. 'Seo' refers to a suspected edge on spiral while a question-mark indicates that whole or part of the classification is doubtful.

#### (4). Magnitude Estimate $b_j$ .

Calibration of Cosmos object magnitudes with the photometry of Carter (1980), which gave accuracy to  $\pm 0.1$  magnitudes on the  $b_j$  system.

However, for NGC7793, because of its large physical size on the plate, the Cosmos background array was affected in the vicinity of this image and was not removed by the spatial filtering applied. As a result the luminosity for this galaxy is underestimated.

(5). Heliocentric Recession Velocity, c-Z, (Km/s).

Average recession velocity from cross-correlation of each object spectrum against a set of templates, correcting for the velocity of the template and for annual and diurnal motion.

(6). Dispersion in Vhel. (Km/s).

Sample standard deviation of the radial velocities from cross-correlation against the different templates. The standard error in the mean radial velocity would be obtained by dividing this value by  $\sqrt{N}$ , where N is the number of templates against which each object spectrum is cross-correlated. However, since use of such a value is only really meaningful for large samples, e.g.  $N > 20$ , the standard deviation is preferred.

(7). Heliocentric recession velocity

As in column 5 but corrected for relativity and solar motion.

(8). Average height of the CCF peak.

Individual CCF peaks are normalised to unity for an autocorrelation.

(9). Average width of the CCF peak.

Both the peak height and width give some indication of the quality of the observed spectrum and the match of the template.

(10). Average error in the CCF velocity.

Calculated from the method of Tonry and Davis (1979).

(11). Average emission line velocity.

With associated standard deviation. Corrections applied as in column 5.

(12). Combined object exposure time. (both arrays, in minutes)

(13). Date of observation.

(14). Remarks. If asterisk in this column see table 2.5.

Cross-correlation velocities, emission line velocities and other results pertaining to the observed galaxy sample.

Table 2.4

No. s	R.A. (1950)				DEC	Morph	$b_T$	V <sub>ccf</sub>	$\sigma_{V_{ccf}}$	V <sub>corr</sub>	<Ht>	<Wid.>	<Err>	Ven.	$\sigma_{V_{em}}$	Exp.	Date	Remark	
	h	m	s	o															''
QP1	23	47	25.2	-35	57	34	E3	15.4	12955	121	12673	0.39	8.73	28	-	-	33	30/1-10-83	
QP140	23	47	26.9	-35	45	21	E0	-	12778	81	12505	0.29	7.86	30	-	-	27	23/24-9-84	
QP2	23	47	28.3	-36	1	33	Sb(r)	15.5	12975	89	12692	0.21	6.14	32	-	-	33	30/1-10-83	
QP4	23	47	36.5	-35	49	54	Sc	16.3	12751	122	12479	0.15	4.07	28	12811	68	27	23/24-9-84	
QP5	23	47	51.6	-35	26	35	E3	16.4	14831	144	14464	0.22	7.64	46	15039	-	40	24/25-9-84	
QP6	23	47	56.9	-34	34	50	E0	16.1	17349	146	16853	0.36	8.45	29	-	-	20	29/30-8-84	
QP7	23	47	59.0	-34	45	24	Sa	16.2	18648	162	18073	0.22	8.38	40	18305	-	23	23/24-9-84	
QP8	23	48	25.9	-34	58	36	S	16.0	13204	80	12916	0.18	5.18	32	-	-	32	21/22-9-84	
QP10	23	48	30.7	-35	54	4	Sb	15.8	16816	168	16343	0.26	6.85	30	-	-	27	24/25-9-84	
QP12	23	48	32.4	-36	39	49	S(c-d?)	15.8	13913	56	13585	0.18	5.02	33	-	-	33	1/2-10-83	
QP139	23	48	57.8	-34	43	54	E1	-	17217	256	16727	0.26	8.76	38	-	-	23	22/23-9-84	
QP13	23	48	59.0	-34	34	39	S0?	15.7	16880	91	16409	0.26	10.34	44	-	-	33	18/19-9-84	
QP15	23	49	12.7	-35	12	28	E7/Seo?	16.2	9957	25	9792	0.18	3.10	18	9336	61	23	23/24-9-84	
QP14	23	49	14.9	-33	22	39	S(c?)	15.9	12014	123	11782	0.23	7.12	36	-	-	30	20/21-9-84	
QP16	23	49	26.2	-35	11	26	Sbb	15.0	13148	110	12861	0.17	4.24	26	-	-	17	28/29-8-84	*
QP18	23	49	26.6	-36	35	34	Sb	15.8	15784	124	15364	0.16	7.02	45	-	-	32	18/19-9-84	*
QP19	23	49	47.8	-35	10	18	Seo/E7?	16.1	13789	133	13474	0.27	6.79	30	-	-	37	19/20-9-84	*
QP20	23	49	56.4	-35	33	6	Sbc	15.8	12864	26	12588	0.18	8.04	52	13042	-	17	18/19-9-84	*
QP21	23	50	10.1	-34	51	58	E0	15.6	13317	60	13023	0.39	6.76	23	-	-	27	18/19-9-84	*
QP23	23	50	27.1	-35	5	19	Sc	16.3	13137	0	12850	0.23	4.61	22	13215	-	58	24/25-9-84	*
QP25	23	50	40.6	-34	19	50	E1	14.9	16881	190	16410	0.32	7.91	29	16848	534	13	23/24-9-84	*
QP26	23	50	51.8	-37	8	28	Sb(r)	16.1	13691	84	13379	0.23	4.86	23	13764	-	32	22/23-9-84	*
QP28	23	51	8.9	-37	57	13	S0?	16.0	13165	99	12878	0.23	5.83	28	13202	-	18	22/23-9-84	*
QP29	23	51	44.6	-37	21	20	E2	16.2	17251	260	16745	0.22	10.11	56	-	-	33	22/23-9-84	*
QP32	23	52	13.4	-36	26	14	Sb	15.8	13853	154	13527	0.18	4.50	29	-	-	20	21/22-9-84	*
QP31	23	52	22.6	-34	52	47	Sb(r)	14.9	16002	126	15577	0.32	7.55	28	-	-	47	1/2-10-83	*
QP30	23	52	25.7	-33	11	15	E1	15.2	17308	179	16818	0.24	7.43	34	16922	-	33	28/29-8-84	*
QP33	23	52	34.8	-33	32	4	S(Ba?)	16.3	22038	352	21236	0.18	9.36	54	21620	-	40	22/23-9-84	*
QP34	23	52	35.3	-33	47	10	Sbb	16.1	17425	224	16925	0.27	9.28	45	-	-	33	22/23-9-84	*
QP35	23	52	41.5	-33	24	34	S(Bc-d?)	15.6	17872	179	17348	0.21	6.65	36	-	-	33	29/30-8-84	*
QP36	23	53	0.2	-33	15	14	E7/Seo?	16.3	17331	235	16838	0.23	7.58	36	17595	-	25	23/24-9-84	*
QP42	23	53	1.9	-36	45	12	S(B(r)?)	16.3	15289	113	14891	0.22	5.96	31	-	-	40	24/25-9-84	*
QP37	23	53	2.4	-34	22	9	E2	16.4	14631	100	14278	0.32	7.19	28	-	-	30	28/29-8-84	*
QP40	23	53	8.6	-34	26	14	E0	15.9	15025	179	14651	0.27	8.51	36	14654	-	32	28/29-8-84	*
QP38	23	53	10.3	-33	47	9	S0	16.4	17291	168	16798	0.24	7.18	31	-	-	33	22/23-9-84	*
QP43	23	53	13.4	-34	43	16	E3?	16.1	13934	178	13611	0.26	6.29	26	-	-	15	21/22-9-84	*
QP44	23	53	19.4	-34	32	2	Seo/E7?	16.0	14677	86	14320	0.30	6.29	26	-	-	31	22/23-9-84	*
QP46	23	53	26.6	-35	48	53	E1	16.0	14573	141	14215	0.29	9.16	34	-	-	18	21/22-9-84	*
QP47	23	53	29.8	-35	46	18	Sbc	15.9	14115	354	13779	0.18	9.29	59	14603	112	40	19/20-9-84	*
QP50	23	53	38.6	-35	58	47	E0?	16.5	-	-	13783	0.13	-	-	14115	85	29	31/1-9-84	*
QP49	23	53	43.4	-34	39	12	E2	16.2	17117	305	16630	0.18	8.37	54	17581	-	21	21/22-9-84	*

QP51	23	53	48.2	-34	48	17	E0	15.8	13908	188	13586	0.28	8.66	38	13557	-	13	21/22-9-84	
QP51R	23	53	52.8	-34	52	39	E0	0.0	14208	85	13871	0.31	6.90	28	-	-	10	21/22-9-84	*
QP52	23	53	54.5	-35	46	36	S	16.5	22724	666	21860	0.17	9.05	57	-	-	40	24/25-9-84	*
QP53	23	53	55.0	-35	47	9	Sn	15.8	10093	128	9919	0.22	7.92	44	10140	-	30	19/20-9-84	
QP55	23	54	9.4	-34	51	19	SRb	16.3	16211	204	15773	0.15	6.27	47	16178	-	67	24/25-9-84	
QP56	23	54	14.6	-34	59	32	E1	16.5	14725	161	14363	0.29	7.91	32	-	-	27	22/23-9-84	
QP59	23	54	25.7	-35	2	19	E3	15.9	14800	142	14434	0.26	9.30	40	14794	-	17	21/22-9-84	*
QP58	23	54	25.9	-34	57	33	Sb-c	14.6	12489	156	12229	0.24	6.33	29	-	-	28	19/20-9-84	*
QP60	23	54	29.5	-36	19	25	E3	15.7	13707	121	13387	0.40	6.47	18	14014	-	30	28/29-9-84	
QP64	23	54	36.0	-37	16	53	SRb(r)	15.7	18749	329	18152	0.19	10.79	61	18705	-	33	30/1-10-83	
QP62	23	54	38.2	-34	45	3	E7/Seo?	16.1	9927	180	9763	0.23	6.29	30	10063	98	37	21/22-9-84	
QP67	23	54	55.7	-36	52	50	E2?	16.2	8363	85	8237	0.23	8.58	41	8292	135	12	21/22-9-84	
QP70	23	55	1.4	-37	50	38	E3?	16.4	16853	189	16366	0.33	8.64	32	-	-	15	23/24-9-84	
QP69	23	55	11.5	-35	16	12	E3	16.2	14850	201	14480	0.32	8.84	35	-	-	58	1/2-10-83	
N7793	23	55	14.9	-32	52	1	Sb	10.9	185	123	193	0.42	5.58	23	-	-	13	20/21-9-84	*
QP71	23	55	25.7	-33	9	29	Irr/Sd	15.1	12910	391	12639	0.18	8.77	50	12568	501	33	33/1-10-83	*
QP72	23	55	26.9	-34	34	10	E2	15.1	14656	166	14299	0.28	7.96	32	-	-	25	19/20-9-84	*
QP73	23	55	33.4	-34	38	38	E1?	16.2	7131	113	6798	0.23	6.08	32	7395	-	33	22/23-9-84	
QP74	23	55	53.3	-33	13	17	Seo	15.6	12339	86	12092	0.24	4.63	22	12933	-	17	20/21-9-84	*
QP78	23	56	38.6	-32	59	30	E2	16.3	12612	266	12354	0.25	7.76	35	-	-	23	23/24-9-84	
QP79	23	56	47.3	-34	36	36	E2?	16.3	14824	141	14458	0.20	4.59	26	-	-	45	31/1-9-84	
QP81	23	56	53.0	-35	27	44	E1	15.6	14909	154	14535	0.34	8.50	33	-	-	23	19/20-9-84	
QP80	23	56	54.5	-34	17	29	SRb(r)	15.2	8521	72	8402	0.20	4.91	29	8649	451	30	20/21-9-84	
QP82	23	57	5.8	-34	45	11	Seo	15.8	16968	193	16487	0.20	8.23	43	-	-	17	21/22-9-84	
QP83	23	57	7.2	-34	43	60	E3	15.9	3573	115	3551	0.21	8.17	49	3540	80	48	1/2-10-83	
QP84	23	57	18.2	-35	16	24	E1	16.4	14342	142	13996	0.33	7.41	26	-	-	30	28/29-8-84	
QP85	23	58	18.2	-36	7	22	E2	15.7	15633	81	15218	0.28	9.83	46	-	-	33	29/30-9-83	
QP86	23	58	19.2	-36	15	55	E1	15.9	14943	158	14562	0.36	8.47	31	-	-	33	29/30-9-83	
QP87	23	58	24.7	-33	53	29	Sb	14.1	6836	34	6760	0.20	5.78	32	-	-	33	30/1-10-83	*
QP88	23	58	58.8	-34	2	16	E2	16.2	6893	88	6815	0.24	7.03	33	-	-	13	23/24-9-84	
QP90	23	59	19.4	-37	7	43	S(b(r)?)	15.3	15117	158	14723	0.19	5.24	30	15384	-	17	21/22-9-84	*
QP91	23	59	30.0	-33	44	44	SRc	15.3	8755	146	8629	0.27	6.75	28	8794	92	20	19/20-9-84	*
QP92	23	59	59.3	-36	33	17	Sb	15.6	13680	1898	13355	0.14	5.93	44	14629	-	33	29/30/9/83	
N7812	0	0	20.9	-34	30	50	Sb	14.5	6842	108	6762	0.22	9.23	49	-	-	67	28/29-9-83	
QP94	0	0	21.2	-36	0	4	E2	16.1	14750	480	14379	0.23	13.71	67	-	-	33	30/1-10-83	
QP95	0	0	21.5	-33	11	50	E2	16.4	9421	44	9277	0.20	5.09	29	9560	28	15	30/1-10-83	
QP96	0	2	33.7	-35	58	26	E2	15.0	8575	67	8444	0.39	7.51	23	-	-	12	20/21-9-84	*
QP100	0	3	8.7	-36	13	46	S(b?)	14.9	9320	3159	9161	0.15	6.44	43	8490	-	25	18/19-9-84	*
QP103	0	4	53.7	-37	43	46	E7/Seo?	15.4	36720	1811	34464	0.17	5.06	33	-	-	30	20/21-9-84	*
N0010	0	6	2.3	-34	8	11	SRb	12.9	6846	104	6766	0.33	6.63	24	6195	-	13	18/19-9-84	*
QP107	0	6	26.0	-37	36	33	S(Bb?)	15.7	8703	59	8558	0.34	6.79	23	-	-	20	20/21-9-84	*
QP109	0	6	31.2	-33	11	32	Sn	15.1	6940	99	6861	0.21	8.19	50	7512	-	48	19/20-9-84	*
QP108	0	6	35.3	-37	38	13	E4	15.1	8658	115	8515	0.26	5.62	25	8768	35	27	20/21-9-84	*

Table 2.4 continued

QP111	0	6	52.5	-36	59	44	S	16.2	4567	165	6478	0.32	6.61	25	-	-	19	23/24-9-84	
QP110	0	6	57.0	-37	52	43	S(b?)	15.8	19384	295	18738	0.18	7.78	52	19176	-	33	21/22-9-84	*
QP112	0	6	58.5	-37	49	55	S(c?)	14.9	8686	77	8540	0.28	11.46	60	-	-	33	30/1-10-83	*
QP113	0	7	6.9	-37	56	35	E0	15.2	8763	94	8614	0.41	7.52	25	-	-	40	1/2-10-83	*
QP115	0	7	14.8	-35	33	12	E2	15.0	14648	319	14281	0.27	7.68	33	-	-	17	20/21-9-84	*
QP117	0	7	31.9	-35	33	12	SBa(r)	16.3	15127	176	14737	0.28	6.68	28	-	-	33	29/30-8-84	
QP116	0	7	35.1	-37	3	16	E2	14.8	6886	57	6791	0.46	7.21	19	-	-	13	21/22-9-84	*
QP118	0	7	59.6	-33	24	47	E5	16.5	7807	134	7697	0.30	6.86	25	8144	-	27	23/34-9-84	
QP121	0	8	25.5	-35	29	12	S(r)	15.4	14910	198	14529	0.30	7.04	30	-	-	17	20/21-9-84	*
QP122	0	8	40.9	-33	51	25	Sa	14.1	7842	115	7736	0.43	7.00	21	-	-	33	1/2-10-83	*
QP123	0	8	42.1	-33	39	31	E3	16.1	7706	63	7605	0.25	6.25	30	7656	-	13	22/23-9-84	
QP125	0	9	43.2	-33	44	33	E7/Seo?	16.2	7661	355	7560	0.16	9.84	61	7562	164	67	29/30-9-83	*
QP124	0	9	47.9	-37	21	35	E3	15.8	15313	86	14903	0.24	6.31	30	-	-	17	21/22-9-84	
QP126	0	9	54.1	-32	46	32	S?	15.5	7440	76	7350	0.17	5.90	35	7630	-	33	18/19-9-84	
QP127	0	10	34.1	-36	39	31	E3	16.5	21822	205	20733	0.31	8.56	32	-	-	30	23/24-9-84	
QP129	0	10	48.2	-35	47	15	E2	16.0	27743	368	26451	0.27	7.81	35	-	-	20	23/24-9-84	
QP128	0	10	48.9	-37	47	37	E3	15.3	15236	84	14827	0.33	7.43	27	-	-	13	20/21-9-84	*
QP130	0	11	4.0	-35	38	53	S(r)	16.3	14724	102	14351	0.30	6.95	28	-	-	18	23/24-9-84	
QP131	0	11	24.6	-35	40	22	S(a?)	15.8	8850	67	8707	0.27	6.27	27	-	-	30	19/20-9-84	
QP132	0	11	32.2	-35	24	29	S?	15.7	8699	523	8561	0.17	6.66	52	-	-	30	21/22-9-84	*
QP134	0	12	10.6	-37	56	8	Sa-b	14.5	8335	70	8196	0.23	5.65	28	-	-	27	20/21-9-84	*
QP136	0	12	28.5	-33	11	19	Sb	15.3	18349	213	17787	0.19	5.39	29	-	-	27	20/21-9-84	
QP138	0	13	13.2	-33	18	30	SB	14.6	7363	70	7269	0.31	5.53	21	7401	-	23	18/19-9-84	*

Table 2.4 continued

Table 2.5

The following list gives those galaxies in table 2.4 for which there is a corresponding entry in an existing catalogue.

Sequence No.	Alternative Identification(s).
QP68	NGC7793; SVEN459; MCG-06-01-009
QP106	NGC0010; MCG-06-01-024
QP93	NGC7812; MCG-06-01-016
QP71	SVEN460; HELW505
QP74	SVEN461
QP21	MCG-06-01-001
QP25	MCG-06-01-002/3
QP31	MCG-06-01-004
QP30	MCG-06-01-005
QP51B	MCG-06-01-006
QP58	MCG-06-01-007
QP59	MCG-06-01-008
QP72	MCG-06-01-010
QP87	MCG-06-01-013
QP90	MCG-06-01-014
QP91	MCG-06-01-015
QP93	MCG-06-01-016
QP96	MCG-06-01-019
QP100	MCG-06-01-021
QP105	MCG-06-01-023
QP107	MCG-06-01-025
QP108	MCG-06-01-026
QP109	MCG-06-01-027
QP112	MCG-06-01-028
QP110	MCG-06-01-029
QP113	MCG-06-01-030
QP115	MCG-06-01-031
QP116	MCG-06-01-032
QP121	MCG-06-01-033
QP122	MCG-06-01-034
QP128	MCG-06-01-035
QP134	MCG-06-01-036
QP138	MCG-06-01-037

References for catalogues:-

a). NGC Number; The Revised New General Catalogue of Non-Stellar Astronomical Objects, Jack.W.Sulentic and William.G.Tifft, University of Arizona Press, 1973.

b). MCG Number; The Morphological Catalogue of Galaxies. V., Trudy Gos. Astron. Inst. Shternberga (USSR), Vol.46, No.1, 67pp. (in Russian)

2.5.4. Comparison of recession velocities from emission-line measures and from the CCF technique.

Table 2.6 gives details of this comparison. The format of the columns is given below:-

- (1).The galaxy identity (sequence number).
- (2).The discrepancy between the average CCF velocity from all templates "Vccf" and the average emission-line velocity "Vem" in the sense (Vccf-Vem).
- (3).The combined error from the uncertainties in the peak positions of individual emission lines, as given by the GAUSS function.
- (4).and (5). The sample standard deviations in the average CCF and emission-line velocities.
- (6).The average error in the CCF peaks position in Km/s.
- (7).The number of emission lines used to obtain each emission-line velocity.
- (8).A reliability flag for the emission - line identification.  
'D':=definite emission lines present; 'P':=probable emission lines present; 'U':=possible weak or unlikely emission lines present.

Although we might expect differences between the emission line velocity and the CCF velocity the size of this discrepancy is quite large in a few cases. The occurrence of some of the larger discrepancies is probably the result of the combination of one or more of the following effects:-

- (a). Large uncertainties in emission-line positions in some cases, as given by the GAUSS function (see column 5 table 2.6).
- (b). Lines that were only tentatively identified and chosen only because they yielded reasonable agreement with the CCF velocities (see column 8 table 2.6).

(d). The observed emission-line velocity may hinge solely on the identification of lines such as  $H\alpha$ , [NII] and [SII] at longer wavelengths where the wavelength calibration is suspect.

(e). Strong emission lines and good emission-line velocities may mean a poor absorption spectrum because of a shorter integration period or simply absence of absorption features in these spectra.

Ignoring the above considerations and including all the emission-line velocities yields an average discrepancy ( $V_{ccf} - V_{em}$ ) of  $-24$  Km/s with  $\sigma_{n-1} = 296$ . In general, except in those cases where definite, strong emission lines were identified, the cross-correlation velocities are given greater weight. If only galaxies which exhibit strong emission lines and small emission-line positional errors are considered which also have well-determined CCF velocities (i.e. small dispersion in  $V_{ccf}$ ) then the discrepancy becomes  $-42$  Km/s;  $\sigma_{n-1} = 74$ ;  $n=19$ . This is a considerable improvement in result consistency and a fairer description of the agreement between the CCF results and the emission line results. The observed discrepancy indicates that there may be a small systematic difference between the velocity results obtained from the two techniques, although the size of this discrepancy is not serious and may simply reflect 'real' differences in the velocities of the emission and absorption spectra, as found for example in Seyfert galaxies.

Table 2.6

Comparison of recession velocities from emission-line measures and from the cross-correlation technique for those galaxies yielding velocities from both methods.

IDENT	Vccf-Vem (Km/s)	combined error (Km/s)	Sigma Vccf (Km/s)	Sigma Vem (Km/s)	Error CCFPK (Km/s)	No.of emission lines.	Emission flag
QP4	-60	30	122	6	28	2	D
QP5	-208	-	144	-	46	1	P
QP7	344	26	161	-	40	1	U
QP15	620	30	25	61	18	3	D
QP20	-178	38	26	42	52	5	D
QP23	-78	29	-	-	22	1	D
QP25	33	29	190	534	29	2	P
QP26	-73	236	84	-	23	1	P
QP28	-37	14	99	-	28	1	U
QP30	386	123	179	-	34	1	U
QP33	418	-	352	-	54	1	P
QP36	-264	-	235	-	36	1	U
QP40	370	38	179	-	36	1	U
QP47	-488	24	354	112	59	2	P
QP49	-464	26	305	-	54	1	D
QP51	351	25	188	-	38	1	P
QP53	-47	19	128	-	44	1	P
QP55	33	127	204	-	47	1	P
QP59	5	44	142	-	40	1	D
QP60	-307	125	121	-	18	1	U
QP62	-136	16	180	98	30	4	D
QP64	44	113	329	-	61	1	P
QP67	71	76	85	135	41	2	D
QP71	342	64	391	501	50	3	P
QP73	-264	84	113	-	32	1	P
QP74	-594	28	86	-	22	1	P
QP80	-128	361	72	451	29	2	P
QP83	33	24	115	8	49	3	D
QP90	-267	20	15	-	30	1	P
QP91	-40	46	146	92	28	2	D
QP95	-139	24	44	28	29	4	D
QP106	651	80	104	-	24	1	U
QP108	-110	12	115	35	25	4	D
QP109	-572	9	99	-	50	1	U
QP110	209	6	295	-	51	1	U
QP118	-337	59	134	-	25	1	U
QP123	50	-	63	-	30	1	D
QP125	98	9	355	164	61	2	D
QP126	-190	-	7	-	35	1	D
QP138	-38	41	70	-	21	1	P
QP50	-	29	-	85	-	5	D
*IC5135	-3	19	-	37	-	5	D

\*N.B. The velocity difference in column 2 for IC5135 is with the published velocity as given in Table.1.

2.6. Assessment of the internal precision and external accuracy of the results.

2.6.1. Internal Errors.

Estimates of the size of the internal error and consistency of the results for this redshift sample are possible from a number of sources, each of which is considered individually below.

2.6.1.1. Direct measures of night-sky emission lines.

Radial velocities of night-sky lines from a selection of 52 object exposures made over the 3 weeks of observations were obtained from direct measures of such lines in the object spectra. Only the lines  $\lambda 5577.35\text{\AA}$  [OII],  $\lambda 5891.94\text{\AA}$  (NaI) and  $\lambda 6300.23\text{\AA}$  [OI] were prominent in the observed spectra. The results of such measures are given in table 2.7.

Table 2.7

Velocity results from measures of night-sky emission lines in the observed galaxy sample.

Sky-Line rest-wavelength	<Vel> Km/s	dispersion in Line velocity	No.lines measured.
5577.35 $\text{\AA}$ (OI)	28	19.7	52
5891.94 $\text{\AA}$ (NaI)	-15	42.3	44
6300.23 $\text{\AA}$ (OI)	134	95.0	48
5577.35 $\text{\AA}$ & 5891.94 $\text{\AA}$	8	38.4	96

The results for the  $\lambda 6300.23\text{\AA}$  [OI] line are systematically different from the results for the other two lines. The average wavelength discrepancy ( $\lambda_{\text{lab}} - \lambda_{\text{obs}}$ ) is  $-2.82\text{\AA}$  ( $\sigma_{n-1} = 1.99$ ,  $N = 48$ ). This is due to the imperfect wavelength calibration at  $\lambda > 6000\text{\AA}$  and so the results for the [OI] line are ignored. The average velocity from the two other night-sky lines was  $+8.4$  Km/s ( $\sigma_{n-1} = 38$  Km/s,  $N = 96$ ), a much better result. The standard deviation in the mean night-sky-line velocity is one estimate of the internal error which tests the consistency not only of the wavelength calibration but also of the reliability of the GAUSS measures performed.

#### 2.6.1.2. Results from repeat observations of the same object.

Repeat exposures of stellar and galaxian templates (high S/N) were performed as a matter of course. However 3 target objects were also re-observed (low S/N), usually because an earlier integration was curtailed due to deteriorating observing conditions. In all, multiple exposures of 4 stellar templates, 2 galaxy templates and 3 target galaxies were obtained. The average deviation of the residuals from the mean velocity for all re-observed objects was 38.5 Km/s ( $\sigma_{n-1} = 26.7$ ,  $N = 9$ ).

The results for the re-observed objects are given in table 2.3. The velocity dispersion associated with the object velocities from repeat observations (final column table 2.3) is generally smaller than the dispersion in the object's velocity from single observations and obtained by cross-correlation against a series of templates (column 6 table 2.4). This illustrates that there are no significant systematic differences in the results obtained for the same object over prolonged time scales, indicating consistent observing practice, wavelength calibration, reduction technique and instrumental stability.

#### 2.6.1.3. Results from cross-correlation of an object spectrum against a series of stellar and galaxian templates.

Since each object spectrum is cross-correlated against a series of filtered templates, the radial velocities presented are averages of the results from the individual templates. Averages (together with their associated dispersions) were formed from :- (a) cross-correlating the object spectrum against the stellar templates only, (b) just the galaxy templates and (c) using all the templates. The results are given in table 2.8 item 3.

Table 2.8

A summary of the internal error estimates in the derived galaxy velocities from the various measures described in the text.

1). Comparison of CCF velocity with Emission line velocity.

$$\langle V_{ccf-Vem.} \rangle = -42 \text{ Km/s. ; } N = 19 ; \sigma_{n-1} = 74 \text{ Km/s.}$$

2). Measures of night sky emission lines.

$$\langle V_{ns} \rangle = +8.4 \text{ Km/s. ; } N = 96 ; \sigma_{n-1} = 38 \text{ Km/s.}$$

3). Average velocity dispersions from all observed objects, giving the results from using the different types of template separately.

$$\begin{aligned} \langle \text{SIGVH} \rangle &= 163 \text{ Km/s. ; } N = 114 ; \sigma_{n-1} = 110 \text{ (all templates)} \\ \langle \text{SIGVH} \rangle &= 83 \text{ Km/s. ; } N = 114 ; \sigma_{n-1} = 87 \text{ (stellar templates)} \\ \langle \text{SIGVH} \rangle &= 136 \text{ Km/s. ; } N = 114 ; \sigma_{n-1} = 150 \text{ (galaxy templates)} \end{aligned}$$

4). Results from repeat observations of the same galaxies.

Average deviation of residuals from the mean:-

$$= 38 \text{ Km/s. ; } N = 10 ; \sigma_{n-1} = 27 \text{ Km/s.}$$

5). Mean error in CCF peak from all objects.

$$\langle \text{error\_CCF} \rangle = 35 \text{ Km/s. ; } N = 114 ; \sigma_{n-1} = 11 \text{ Km/s.}$$

6). Average dispersion in emission line velocities from individual dispersions in measures of 2 or more lines.

$$\langle \text{SIGVEM} \rangle = 69 \text{ Km/s. ; } N = 13 ; \sigma_{n-1} = 49 \text{ Km/s.}$$

7). Average combined error obtained from the same emission line sample.

$$\langle \text{Comb.error} \rangle = 29 \text{ Km/s. ; } N = 13 ; \sigma_{n-1} = 17 \text{ Km/s.}$$

It is apparent from table 2.8 that the stellar templates give more consistent results than their galaxy counterparts even though a larger number of templates were used in forming the average velocity. This can be partly accounted for by the fact that the stellar template velocities are known to within 1 Km/s whereas the mean error associated with the galaxy template velocities was 37 Km/s. Furthermore the galaxy templates were of lower S/N than the stellar templates and consequently often give worse CCF peak parameters. Cases of skewed CCF peaks are hence more likely when using the galaxy templates. This would lead to small errors in the central position of the true peak and hence to a larger discrepancy with the true object velocity. Finally, the morphological differences between the galaxy templates observed compared with those exhibited by the stellar templates of spectral type F-K, could also affect the characteristics of any match. Even so, the velocity dispersion resulting from using the different templates is greater than the average errors in the CCF peak positions (see later).

If we consider the mean discrepancy between the average object velocity obtained from using only the stellar templates and only the galaxy templates we obtain:-

$$\langle V_{hel}(\text{star}) - V_{hel}(\text{galaxy}) \rangle = 136 \text{ Km/s}, \sigma_{n-1} = 149 \text{ Km/s}$$

This is not an insignificant value. However, the final object velocity, obtained from using all the templates averaged equally, smoothes this effect since more stellar templates were used than galaxy ones. We shall see in the section on external errors how the average object velocities from using all the templates may yield more reliable results than considering the results from cross-correlating against the stellar templates and galaxy templates separately. A further possible source of discrepancy between the results from the stellar and galaxian templates is that in good seeing the template stars might not completely fill the slit. Hence, because of guiding

errors, the star may spend more time on one edge of the slit than the other and consequently lead to systematic velocity errors compared to galaxies. Although the seeing was generally worse than 2" and the slit width corresponded to ~1.8" on the sky, non-uniform guiding of stars on the slit may still account for this discrepancy. However, if this explanation was accurate, we might expect large dispersions in the average stellar template velocities themselves and in the average object velocity from just using the stellar templates. This is not what is actually observed.

2.6.1.4. Error estimate in the CCF peak position.

Essentially the same method as described by Tonry and Davis (1979), was used to obtain a reliable measure of the internal error associated with the peak of the CCF. The antisymmetric component of the CCF is used and the error in the peak position 'E' is provided by the modified SPICA CCF routine.

The error in the CCF peak is given by:-

$$E = ( N/8B ) \times ( 1/(1+r) ) \dots\dots\dots 2.6$$

where N = 2048, the number of bins in the CCF.

and 'B' is the highest wavenumber where the Fourier transform has appreciable amplitude, i.e. the half-maximum point.

'r' is the peak significance parameter given by:-

$$r = h/\sqrt{2} \sigma_a \dots\dots\dots 2.7$$

where 'h' is the height of the CCF peak (which is normalised so that h = 1 for an autocorrelation) and  $\sigma_a$  is the rms of the antisymmetric component of the CCF.

Ultimately the precise value of the factor multiplying (1/(1+r)) should be adjusted so that the predicted error fits external errors wrt independently known velocities.

'B' can be shown to be  $2N \times \ln 2 / \pi W$  where W is the FWHM of the CCF peak. Hence:-

$$E = 0.2833 \times W / (1+r) \dots\dots\dots 2.8$$

Thus the error is tied not only to the peak significance parameter but also to the observed width of the CCF which would be larger if the peak was skew.

The error in the peak position 'E' is then transformed to an error in Km/s (column 11 of table 2.4), and is the average value from all the templates used. The largest errors come from cases of low S/N spectra where the 'true' peak height has been surpassed by other peaks in the CCF. This results in the wrong peak being chosen which can give potentially very large redshift errors. In such cases the error estimate 'E' is totally inappropriate.

The mean error in the CCF peak position (in Km/s), from all the objects observed was 35 km/s,  $\sigma_{n-1}=11$ . In most cases the average 'error' in the CCF peak position for each object is less than the velocity dispersion for the same object from cross-correlating against the different templates. This is to be expected. The error in the CCF peak position is an internal error and depends solely on the precision with which the CCF peak's position can be determined and not on whether this peak is at the correct position to yield the object's 'true' velocity. The actual position of the CCF peak is subject to a number of sources of external errors such as the uncertainties of the wavelength calibration, incorrect guiding on the slit, errors in the published velocities of the templates and the effect of cross-correlating against templates of varying spectral type.

Generally speaking, we can expect the CCF results to become increasingly unreliable as the value of the CCF peak height and peak significance parameter fall below a certain level. A value of the CCF peak height of  $h=0.18$  was selected as being the level at which the CCF results become suspect. Below this limit the cross-correlation of the object spectra against the template spectra begins to yield wildly different velocities as inconsistent peaks were selected. Out of the total sample observed, however, only 12 galaxies had CCF peak heights which were  $\leq 0.18$  for the averages from both stellar and galaxian templates. Of these 12, seven had good emission-line velocities, indicating that the exposure was probably cut short for this reason. There remained 5 galaxies for which there is no reliable handle on the redshift from either the CCF or emission lines. Nevertheless the tentative results for these galaxies are still included in table 2.4 since the correct CCF peak may still have been chosen (see table 2.5 for the identity of galaxies in this category). For instance the CCF peak heights for galaxies 4 and 126 were both  $\leq 0.18$  but they had good emission-line velocities which tied in very well with their CCF results.

#### 2.6.1.5. Dispersion in individual emission line velocities.

Although the majority of galaxy emission-line velocities rested on the identification and measurement of only 1 line, some were average results from 2 or more emission lines. In these cases there is an associated dispersion in the average emission-line velocity together with the combined error estimates of the internal precision with which the GAUSS function can determine each line's position. If we assume that the galaxy emission lines have been correctly identified, that they originate in the same region of the galaxy and also that the wavelength calibration was consistent, then we might expect that the observed sample standard deviation in the emission-

line velocity for a galaxy with 2 or more emission lines would be of comparable size to the combined error from the same lines as given by GAUSS. Any inconsistencies in the wavelength calibration or non-uniform guiding on the slit would, however, tend to increase the observed dispersion in the emission-line velocities whereas the size of the positional errors would remain the same.

Reference to table 2.6 indicates that this is in fact the observed situation. Out of the sample of 16 galaxies with 2 or more measured emission lines only 10 had line velocity dispersions ( $\sigma_{\text{vem}}$ ) less than 100 Km/s, 3 had  $100 < \sigma_{\text{vem}} < 200$  Km/s and 3 had  $450 < \sigma_{\text{vem}} < 550$  Km/s. In the last 3 cases the emission lines had only been identified as 'probable' lines. Excluding these 3 doubtful cases, we obtain for the average velocity dispersion  $\langle \sigma \rangle = 69.5$  Km/s;  $\sigma_{n-1} = 49.3$ ;  $N=13$  (which includes data for QP50 and IC5135, an emission line template, which have no CCF velocities because of the lack of an absorption spectrum). This compares with the average combined error in the emission-lines positions (for the same sample) of  $\sim 30$  Km/s;  $\sigma_{n-1} = 18$ ;  $N=12$ . Nevertheless the emission line results are still consistent and the observed average dispersion compares favourably with the observed dispersion and average discrepancy between the emission line and CCF velocities.

#### 2.6.1.6. Overall assessment of the internal errors.

We have seen that there are a number of different methods of estimating the internal precision of the spectral data. Table 2.8 is a summary of these estimates. Comparisons between the velocity results from repeat measures of the same objects (table 2.3) reveal agreement to  $\pm 38$  Km/s. It is significant that the dispersion in the average night-sky emission-line velocity, mean error in the CCF peak and combined error estimate in emission-line positions are all between

30 and 40 Km/s. Most of these estimates reflect the positional precision of the data and are independent of the actual velocity of the object. What is encouraging is the low dispersion in the night-sky line results indicating broad consistency in the wavelength calibration for all the data (at least over the range covered by the sky lines), and also the good agreement between repeat measures of the same spectra, whether they were high S/N templates or lower S/N target objects.

The largest velocity discrepancies were obtained when the results from more than one emission line or the results from cross-correlating against more than one template were considered. Here the velocities obtained yielded a dispersion more than twice that from the other estimates. This is not surprising since other factors apart from simple positional errors of any feature in a spectrum must be taken into account. The increased dispersion in the emission - line velocities over that found for the night-sky lines probably indicates the effects of non-uniform guiding on the slit which would effect the velocities of individual galaxy emission lines but not the night-sky lines. Other possibilities are that there are real differences between the galaxy emission-line velocities because of projection effects and because the lines may originate from different non-nuclear regions and have different contributions from the galaxy rotation curve. Also, since the observed galaxy emission lines may span the whole wavelength region  $\lambda 3600-6000\text{\AA}$ , any slight inconsistencies in the calibration would show up as greater velocity differences for galaxy lines than for night-sky lines which only span the region  $\lambda 5577-5891\text{\AA}$ .

The observed dispersions from use of different templates are even greater than for the emission lines. The dispersion from using the stellar templates is also considerably less than from using the galaxy templates and the actual spread of individual dispersion values is also more uniform. As discussed earlier, these dispersion values reflect the effects of S/N variations and morphological match differences which affect the CCF peak position more than the precision with which the peaks position can be determined.

#### 2.6.2. External Errors.

Sandage (1978), has indicated that the true errors in most redshift determinations are virtually always greater than the estimates of the internal errors. For our sample an estimate of the external error can be obtained by comparing our results with those already obtained by others.

Apart from the stellar and galaxian templates which have accurately determined, published radial velocities, a few of the brighter target galaxies in field 349 have also been observed by Menzies, Coulson and Sargent (herein after MCS, private communication) as part of a large project to extend the CfA redshift survey in the Southern hemisphere. There were 5 galaxies which had so far been observed in common. A comparison with their results for the same target objects can be made, as well as comparisons with the published velocities for the stellar and galaxian templates observed. The results of this comparison are presented in table 2.9. The agreement is generally very good and ties in with the velocity differences obtained from repeat measures of the same objects.

Table 2.9

Estimates of the external error in the observed galaxy sample from comparisons with galaxies with previously determined and published velocities.

Object identity	Average CCF velocity	Observed vel. dispersion	Published Velocity	Vpub-Vccf
HD157457	-12.3	19.6	17.4	30.1
HD693	96.4	135	14.7	-81.7
HD8779	4.0	38	-5.0	-9.0
HD35410	-5.8	27.6	20.5	26.3
HD171391	-33.7	52.2	6.9	40.6
HD203638	-5.3	8.7	21.9	27.2
NGC6909	2778	84	2680+/-80	-98
IC5175	10797	31	10762+/-34	-35
NGC7793	237	50	214+/-10	-23
NGC7329	3205	100	3189+/-25	-16
*IC5135	4826	37	4796+/-16	-30
QP59	14800	142	14812+/-15	12
QP122	7842	115	7903+/-10	61
QP140	12778	81	12782+/-15	4
NGC0010	6846	104	6813+/-15	-33
QP64	18749	329	19176+/-12	427

\* Our results for IC5135 come from measures of emission lines and the quoted error in the velocity is from the observed dispersion in the emission line velocities for each line.

All velocities are in Km/s.

The comparison velocities in the last part of the table were provided from unpublished list by Menzies, Coulson and Sargent. (see text)

The average discrepancy between the observed velocities and those given in other sources, whether they were for target objects or for stellar and galaxian templates, was  $-8.3$  Km/s. ;  $N=15$  ;  $\sigma_{n-1}=46$  km/s. Considering the comparison for just the stellar templates gives:-  $\langle V_{pub.-V_{ccf.}} \rangle = 5.6$  Km/s. ;  $N=6$  ;  $\sigma_{n-1}=50$  km/s, whilst just the galaxy templates yields:-  $\langle V_{pub.-V_{ccf.}} \rangle = -40.5$  Km/s. ;  $N=5$  ;  $\sigma_{n-1}=32$  Km/s.

In the case of the stellar template observations, the average velocities from cross-correlating against other stellar templates leads to better agreement with published velocities than for either just the galaxy templates or all the templates averaged (except for HD8779 which gives closer agreement if all the template results are averaged). When considering the galaxy template CCF results, the average velocities from cross-correlating each galaxy template against all the other templates yields much closer agreement with the published velocities than for using either just the stellar or remaining galaxy templates separately. The results from those target galaxies which have also been observed by MCS are also more consistent with their results if the averages from all the templates are considered.

Generally speaking, the average object CCF velocities formed from the results of cross-correlating against all the templates provides better agreement with published velocities than averaging the results from just the stellar and galaxian templates. In the former case the results will be weighted in favour of the stellar templates since more stellar templates were used, while in the latter case the stellar template and galaxy template results were given equal weight.

In conclusion it has been shown empirically that better agreement with published velocities is obtained if the velocity results from both stellar and galaxian templates averaged are used in preference to either group separately. Furthermore this agreement is usually to within 75 Km/s indicating that this is the expected external accuracy of the CCF velocities obtained in this programme. Larger discrepancies may exist in some cases where the CCF parameters are weak but there are few candidates in this category. The data represented in tables 2.4 and 2.5 are sufficiently detailed to enable an individual assessment of the likely error associated with each object velocity. The largest discrepancy between the results of this study and those obtained by others is in the case of target object 'QP64'. Here the disagreement with the velocity obtained by MCS was 427 Km/s. The MCS results were also obtained using the SAAO 1.9m and the same basic instrumental configuration except that a higher dispersion grating was employed. However, since an emission line velocity has also been obtained for this target galaxy in this sample which agrees to within 44 Km/s with the CCF velocity, the validity of the MCS result must be considered, although the observed velocity dispersion from the CCF results is rather high ( $\text{SIGVH} = 328 \text{ Km/s}$ ). It is worthwhile to note though, that the MCS results quoted are derived by cross-correlation against a single 'a'-quality Mt. Wilson standard star of type K. Hence the large velocity discrepancy for 'QP64' may be because the MCS template used was not a good match to this particular object spectrum.

## 2.7. Conclusions.

Radial velocities can be obtained to an accuracy of  $\sim 75$  Km/s for galaxies to  $b_j \leq 16.5$  using the image-tube spectrograph and RPCS on the SAAO 1.9m telescope. This accuracy compares favourably with that obtained by Corwin and Emerson (1982), who used the same telescope, grating and spectrograph but employed photographic plates. Furthermore the accuracy also compares well with that obtained by Tonry and Davis (1979), whose reduction technique was closely matched in this survey. The power of the cross-correlation technique is again demonstrated as is the usefulness of using a selection of different templates.

The velocities obtained represent a significant sample in one UKST field and to a high level of completeness (80%) for the magnitude limit employed. The analysis of the results presented here is given in chapter 6, where clustering properties are investigated. The data is also compatible with the Durham/AAT redshift survey and will be a valuable addition to the investigations of the large scale distribution of galaxies fainter than  $B=14.5$ , the limit of the CfA redshift survey.

Empirical Studies of Objective-Prism redshift determinations from the 2480Å/mm UKST prism.

3.1. Introduction

Emerson, in a series of internal reports of the ROE, has performed simulations of stellar and elliptical galaxy low-dispersion objective-prism spectra to examine the variations of magnitude, colour and redshift on the emulsion cut-off (hereafter ECO) and 4000Å feature positions. The behaviour of perfect intensity spectra and simulated Cosmos spectra was investigated. These simulations are invaluable as indicators of the effects of magnitude, colour and redshift changes on any real machine-measured sample.

This chapter describes attempts to determine empirical estimates for the consistency, reliability and limitations of objective-prism measures of stellar and galaxian spectra as measuring machine and plate material are varied, comparing the results where appropriate with Emerson's simulations. As yet no proper evaluation of the susceptibility of objective-prism redshift determinations to changes in measuring technique and plate material has been made. The integrity of the results must be shown to be sufficiently independent of the measurement technique and of plate material used, before objective-prism redshifts can be confidently employed. If significant differences are revealed, then it is necessary to understand the causes and ascertain the most reliable estimates. For this purpose an intimate knowledge of how photographic information on an original plate is affected by use of a copy plate is desired, as well as an understanding of the likely effects of using the Cosmos machine to scan the plates. Such studies are essential if a realistic appraisal of objective-prism redshift determinations is to be made, thereby

paving the way for a meaningful analysis of large machine-determined samples with any automatic technique.

Much work has already been done on low-dispersion objective-prism galaxy - redshift determinations, e.g. Cooke et al. (1981), and Beard (1984). It is hoped that the present studies will vindicate the findings of these authors and help to unravel the complications of measuring objective-prism redshifts with machines such as Cosmos and the Joyce-loebl microdensitometer (hereafter J-L).

Currently there are a number of techniques used to determine objective-prism galaxy redshifts:

- (a) Manually, with a J-L tracing of a spectrum (Cooke, 1980).
- (b) Interactively using the "E2D" software and Cosmos MM data (Parker, 1983).
- (c) Interactively using the "INTERZED" procedure on Cosmos MM data (Beard, 1984).
- (d) Automatically using the pattern matching technique of Cooke (1984), with Cosmos MM data. This technique, while being potentially the most useful, has yet to be satisfactorily implemented.

The findings of this chapter will be concerned with techniques (a)-(c) but should prove invaluable in the assessment and refinement of the automatic process in the hope of obtaining an optimum algorithm. Work by Clowes (1985), and Palmer (1984), show that a co-ordinate transformation from the position of late-type, faint stars on the direct plate to those on the prism plate, is probably a better wavelength standard than the ECO, which is prone to colour, magnitude and redshift effects. Ultimately this method is to be preferred and will be used with any automatic technique (see chapter 5).

### 3.2. Redshift determination from the objective-prism spectra.

#### 3.2.1. Redshift accuracy and measurement precision.

Ideally, if objective-prism plates could be taken in perfect seeing, the fundamental limit on storage of spectral information is set by the emulsion grain size, typically  $1.5 \mu\text{m}$  for IIIaj (the IIIaj emulsion is actually capable of a resolving power of 200 line pairs/mm). In practice the spectral resolution is limited by the seeing disc size during the exposure. For seeing of  $1''$  FWHM this corresponds to  $15 \mu\text{m}$  on the plate (the plate scale of the UKST is  $67.14''/\text{mm}$ ) equivalent to a wavelength increment of  $30\text{\AA}$  at  $4000\text{\AA}$ . This implies a velocity resolution of  $2,000\text{km/s}$ . Such resolution is further degraded by object colour and magnitude effects on the relative positions of continuum features and ECO in stellar spectra, and the effects of redshift and finite image size in galaxy spectra.

Previous studies of galaxy objective-prism redshifts, e.g. Cooke (1980), Beard (1984), have quoted an accuracy of  $\Delta Z = \pm 0.01$ , based on comparisons with slit-spectra redshifts. However, such calibration is still sparse and does not span the full magnitude range over which galaxy objective-prism redshifts are deemed measurable. There is also an important distinction between the measurement precision and the intrinsic redshift accuracy from objective-prism galaxy measures using the various manual and interactive techniques. Chapter 4 deals with the calibration of the technique using newly acquired galaxy slit spectra in fields 349 and 145.

The basic technique for determining galaxy redshifts from objective-prism spectra relies on the change with redshift of a prominent spectral feature at 4000Å from its rest wavelength position. This feature is present in the spectra of many elliptical and early spiral galaxies and is due to the blend of CaII H and K and other metal lines. Measurements are made with respect to the mid-point in density or intensity of the ECO, which is taken as the wavelength standard. For the unfiltered IIIaj emulsion this has been determined by Cooke as  $5380 \pm 30\text{Å}$ . The dispersion of the prism with IIIaj emulsion is such that 'D', the displacement of a feature of wavelength  $\lambda$  from the ECO, is given by:-

$$D = A/(\lambda - \lambda_0)^{1.2} - D_0 \dots\dots\dots 3.1$$

where  $D_0 = 727.48$ ;  $\lambda_0 = 1313.41\text{Å}$  and  $A = 15591900$ . The precision of the ECO to 4000Å feature separation varies with each technique used. Repeat measures of the same spectra using the same measuring technique and intercomparison with the results from other techniques yields information only on how consistently the same features and same feature positions are manually or interactively chosen and also how consistently the same spectra are reproduced by each measuring machine. These techniques incorporate no allowance for variations in ECO wavelength with object colour, redshift or magnitude which obviously affect the true accuracy of the results. The effect on the intrinsic redshift accuracy of using copy plates, as opposed to original plate material, is also insufficiently well determined. These considerations were a prime motivation for the present studies.

In assessing the accuracy of objective-prism galaxy redshifts the stability of the positions of the zero redshift 4000Å feature in stellar spectra and that of the ECO needs to be ascertained for variations in colour and magnitude.

### 3.2.2. Positional stability of the 4000Å feature.

Using the spectrophotometry of Pritchett and Van den Bergh (1977), and of Fay, Stein and Warren (1974), Emerson (internal report, ROE, 1982) simulated UKST stellar objective-prism spectra and found that the 4000Å feature position was generally fixed for spectral types F6-K2, but changed by  $\sim 10\text{Å}$  to longer wavelengths at F0 (equivalent to a radial velocity change of  $\sim 750\text{km/s}$  or  $DZ=0.0025$ ). Also no significant difference in the measured positions of the feature in density and intensity spectra for faint stars was found, although the density 4000Å feature is about  $2\text{Å}$  shorter in wavelength than the corresponding intensity feature for stars of  $b_{\text{uj}} < 15.0$  (assuming measurement with a Joyce-Loebl type microdensitometer). Cooke (1980), investigated the size of this magnitude dependent difference using a sample of stellar spectra covering a range of density on the plate. He concluded that no correction between density and intensity spectra was required for densities up to 1.3 above the sky background and only 0.2mm on J-L tracings from densities 1.3 to 1.7 above sky! (0.2 mm on a J-L tracing corresponds to  $\sim 4\ \mu\text{m}$  on the plate or  $\sim 10\text{Å}$  at HV, with a ratio arm setting of 50:1). Thus, since the magnitude and colour effects on the 4000Å feature position are expected to be relatively small, a 4000Å feature wavelength of  $3990 \pm 10\text{Å}$  was adopted for these studies in concordance with the value determined by Cooke (1980).

### 3.2.3. The emulsion cut-off wavelength and positional stability.

The spectral response of hypersensitised, unfiltered IIIaj emulsion (Clowes 1983), covers the region from  $\lambda 3200\text{\AA}$  to  $\lambda 5300\text{\AA}$  where the fall-off in intensity is particularly sharp. The dispersion curve of the objective-prism, Nandy et al. (1977), indicates that energy will be increasingly piled up at longer wavelengths so that an objective-prism spectrum, which is a convolution of the dispersion curve, the emulsion sensitivity curve, the seeing disc and the actual object spectrum, has a characteristic "tadpole like" appearance with a dense "head". The long wavelength edge of this "head", where there is a steep decline in density, is called the ECO. The ECO is important because it provides the wavelength reference point needed for a redshift estimate. The mid-intensity (or-density) point of the ECO, i.e. half-way between the sky level and the ECO peak, is the chosen wavelength reference point. Cooke (1980), and Emerson (1983), have shown that the effect of the image profile on continuum feature positions in spectra is least if the mid density or intensity points of each feature are taken. This is not so important in spectra of fainter objects where the ECO slope is generally quite sharp, but can become important in brighter spectra and the spectra of extended objects where the ECO slope is less steep due to the smoothing effect of the image profile.

The actual wavelength of the ECO mid-point varies significantly with object colour, much more so than for the  $4000\text{\AA}$  feature. Emerson's simulations of stellar intensity spectra indicate variations in the ECO from  $\lambda 5340\text{\AA}$  at B0 to  $5400\text{\AA}$  at M0 (equivalent to  $DZ=0.015$ ). No magnitude dependence is expected when using intensity spectra. With density spectra however, such as produced with the J-L, the ECO centroid is different from that measured in intensity spectra. Emerson found variations of  $10\ \mu\text{m}$  for images from  $buj \sim 15-19$  ( $25\text{\AA}$  at HY)

which is however, a less severe effect than the colour dependence. Cooke (1980), using J-L density spectra, ignored the magnitude and colour effects on the grounds that for faint objects the difference between the half maximum position in intensity and density is very small compared with the measurement precision. Also, late-type stars were used to define the ECO wavelength, which yielded  $\lambda_{\text{eco}} = 5380 \pm 30\text{\AA}$ . This 30Å scatter compares favourably with the 40Å variation expected from Emerson's simulations for F5-K5 stars. Late-type stars exhibit strong 4000Å features, as do elliptical galaxies and the nuclei of early spirals up to Sb, whose light will be dominated by such stars. Thus the ECO wavelength for late-type stars could be argued as being the appropriate value to use when measuring galaxy spectra. Furthermore, Cooke (1980), performed a series of tests to check the consistency of the wavelength scale. He concluded, for his sample limits in colour and magnitude, that this scale did not vary with position on a single plate nor from plate to plate and that the measurement errors were also independent of positional and magnitude effects. In fact, from measures of ~80 stars of different magnitudes in 16 areas of plate, Cooke (1980), surmised that for  $D < 1.2$  above sky, no correction of the ECO position was required when using density instead of intensity converted spectra. At higher densities however, the ECO-feature separation is overestimated so that a correction factor needs to be applied to the J-L results.

In all the above discussion, manual measurement with a J-L was assumed. Hence conclusions about ECO wavelength stability to magnitude, colour and plate variations are only appropriate to the J-L measures made and for the limited sample of spectra chosen. This chapter is concerned not only with J-L measures but also with the analysis of Cosmos scans of objective-prism plates to see how well the J-L results are reproduced from measures of Cosmos data. Stellar and galaxy prism spectra over the widest possible magnitude range were

measured with the J-L and interactive techniques that utilise Cosmos MM data. These measures should help to highlight any measuring machine and magnitude effects and help to determine the useful magnitude range over which reliable results from each technique can be expected before saturation and S/N problems become too severe.

#### 3.2.4. Data base

The data base for these studies comes from a number of sources:

(a) Joyce-Loebl tracings of  $\sim 100$  stars and  $\sim 100$  galaxies selected in and around a rich cluster of galaxies in SERC survey field 349 and covering a 1sq inch region on the plate. The plate material was UJ5402P (original plate, unfiltered IIIaj) and UJ5402P P2N1 (copy).

The same sample of spectra were measured in each case.

(b) Cosmos MM scans of the same small area from the copy plate UJ5402P P2N1 and from the original plate UJ5402P. The Cosmos data can be tackled using either the "INTERZED" or "E2D" interactive techniques for reduction of objective-prism spectra. The E2D technique (Cooke and Kelly, 1981), can measure the raw Cosmos transmission spectra (equivalent to the J-L density spectra), or the MM data can be intensity converted to measure intensity spectra. The interactive INTERZED technique measures intensity converted spectra.

(c) Cosmos MM scans of a relatively small region of field 475, containing the cluster A140, from the original plate UJ4543P and reduced using INTERZED.

The above data base provided a wealth of objective-prism results for the same objects from different plate material, (original and copy plates and plates of different exposure times), for different measuring machines and for different reduction processes. Details of the prism plates used are given in table 3.1. Study of these results should help us to understand and tackle the consistency, reliability and limitations of objective-prism redshift determinations.

### 3.3. The photographic process and machine reduction.

Ideally, the mid-intensity points of the 4000Å and ECO features of objective-prism spectra should be measured, as opposed to their mid-points in density space. This is because the photographic density variations along an objective-prism spectra are not, in general, linearly related to the number of incident photons but varies in a manner dependent on the type of emulsion used. Hence density spectra do not accurately represent the strengths of spectral energy variations with changing density on the plate. The 'characteristic curve' (hereafter CC) of the emulsion describes how the photographic density varies with exposure (log[intensity] usually). Knowledge of the form of the CC, obtained from measures of sensitometer spots impressed on the plate, enables conversion from photographic density, (transmission values in Cosmos data), to the incident light intensity, (in principle!). This is because the photographic density of these spots corresponds to a known relative intensity.

Plate number	Programme or survey codes	R.A. h m	dec o	Date of exposure	LST	Emulsion and filter	Exposure time	Grade
J 6145	J 349	00 00.0	-35 00	80-07-19	23:35	III AJ GG 395	65.0	A12
UJ 5402P	P 354 349	00 00.0	-35 00	79-10-16	: 1	III AJ NONE	60.0	B2 1S
UJ 6535P	P 354 349	00 00.0	-35 00	80-10-31	23:30	III AJ NONE	50.0	AE2 1W
UJ 4543P	P 207 475	01 06.0	-25 00	78-10-02	:37	III AJ NONE	60.0	B14 1N

Table 3.1

Details of the objective prism and direct plates used in this thesis (originals).

Cooke (1980), argued that for faint objects of similar colour, the differences in using J-L density spectra instead of intensity spectra can be neglected. For a large sample however, attempting measures over the widest possible magnitude range, a quantitative assessment of any differences should be made. Differences are expected and will grow with density as the true strength of the ECO peak above sky is increasingly underestimated due to non-linear regions of the CC being encountered. The ECO mid-point in density space will therefore have a lower relative position above sky than in intensity space. As already stated this difference is slight for faint objects since the ECO slope is so steep. Nevertheless, as the ECO slope is non-zero, underestimates in the true ECO mid-point will result in a larger ECO to 4000Å feature separation and hence to a more negative redshift. This situation is further complicated by the effects of object colour and measuring machine used.

Emerson (1983), assumed that for IIIaj emulsion the CC takes the form:

$$D - \alpha\gamma(D - 2.4)^3 = \gamma \log(I) + C \dots \dots 3.2$$

where 2.4 is taken as the mid-point density of the CC and  $\gamma$  is the slope of the straight-line portion of the curve near the mid-point. This form was considered an accurate representation of the true curve to densities 0.75. Clowes (1983), states that the linear portion of the CC of hypersensitised IIIaj emulsion is generally accurately linear between densities of 1.5 and 3.0, so that the CC is often taken as linear for simplicity. The "Baker density" form of the CC is often chosen as it linearises the curve over a larger density range. The Baker density form is given by:

$$\log(I) = \gamma D_b + C \dots \dots 3.3$$

where 'I' is the incident intensity,  $D_b$  is the Baker density,  $\gamma$  is the

slope of the relation and C is a constant.

The IIIaj fine grained emulsion (hypersensitised) can cope with densities as high as 4.0 before saturation. Typical sky backgrounds for original IIIaj plate exposures are at photographic densities of  $\sim 1.3$  while the chemical fog level is at a typical density of 0.3. Ultimately though, the recoverable information is a consequence not only of the limitations imposed by the emulsion but also of the dynamic range limitations of the measuring machine used to scan the plates.

For the J-L this is dictated essentially by the density wedge used. With routine measures of objective-prism galaxy spectra, the 'D117' wedge was employed. This has a slope of 0.087D/cm and a useful range of 1.6D. When measuring the sensitometer spots on the original and copy plates the 'J253' wedge was used with a slope of 0.168D/cm and a useful range of 3.04D. The Cosmos machine on the other hand saturates at  $D \sim 2.5$  where the machine error begins to dominate the signal, giving a useful range of only 1.5D (MacGillivray and Stobie, 1985).

The great advantage of Cosmos, apart from its ability to scan a plate in a few hours, is that it is possible to convert large areas of plate from simple Cosmos transmission values (density space) to, in principle, intensity space, via knowledge of the CC. Also other manipulations of the data can be performed with relative ease. The Baker density form of the CC is used since this helps to linearise the 'toe' of the curve near the sky background. For Cosmos data it has the form:-

$$\text{Log}(I) = \gamma \text{Log} [ (T_c - T_b) / (T - T_b) - 1 ] + C \dots \dots 3.4$$

where 'I' is the incident intensity, 'T' is the transmission of the ith pixel, 'Tc' and 'Tb' are the transmissions for clear and blackened plate and  $\gamma$  is the slope of the CC. If Cosmos were a perfect

measuring machine and exact representation of the CC was possible, the accuracy of the intensity conversion would be limited only by plate saturation. In practice measuring - machine limitations and inaccuracies in intensity conversion mean that the full information on the plate is never completely recovered.

In attempting to understand the likely effects of using Cosmos to measure objective-prism plates, the simulations of objective-prism spectra of elliptical galaxies by Emerson (1983), prove useful. Most of the simulations assume that spectra were measured by Cosmos in its pre-update configuration. However, Cosmos has since undergone an extensive electronics rebuild (termed the phase 1 improvements) which has resulted in S/N improvements at low and high densities, MacGillivray and Stobie (1985). How the improvements have affected the Cosmos objective-prism data is described in section 3.15. The Cosmos machine though, is in almost continuous development, with both software and hardware enhancements planned. Consequently it is difficult to ascertain the compound effects of these changes on the quality of any Cosmos objective-prism plate measures performed in the future, although further S/N and dynamic - range improvements are expected.

Emerson showed that any magnitude effects due to the complex addition of sky light to galaxy light and of using the Baker density form of the CC to convert transmissions to intensity, as compared with the non-linear shape of the true CC, are small compared with the effects of using the Cosmos machine itself. Ideally, the properties of the plate emulsion, i.e. photon-grain statistics and corresponding emulsion-sensitivity variations, should be the dominant error source in any measurements. Unfortunately the accuracy and stability of the measuring machine, together with the effects of digitisation, are the major limitation. The Cosmos user manual details results of

experiments on the machine performance. Results are mainly affected via the spot size used to scan the plate and its associated halo. This halo still has 1% of the total spot flux at 1000  $\mu\text{m}$  from the spot centre! Consequently the halo transmits light even if the scanned pixel is completely black. This results in an overestimate of the true transmission since the extensive halo accounts for 5% of the total spot flux. It is this halo which restricts the maximum density which Cosmos can handle. The halo contribution to the overall transmission becomes 50% at density 2.3 so that Cosmos essentially saturates here, only 1.3D units above sky! If the spot halo could be eradicated then the finite number of transmission levels (0-255) would lead to saturation when  $T=1$  was reached at a density of 3.2. Emerson points out that the Cosmos spot averages transmission over a finite area which is greater than the pixel size (16  $\mu\text{m}$  for these studies). Hence we might expect this to smear spectra along the dispersion direction, resulting in a lowering of the peak intensity and a loss of resolution. This will cause an underestimate in the mid-intensity peak height.

Complications arise because transmission not intensities are averaged by Cosmos, a process which underweights points of high density. For instance, for a linear flux cut-off, averaging in intensity space will not affect the mid-point intensity, but averaging in transmission will be weighted to low-density points such that when transmissions are converted to intensities too low a value will be given. Furthermore the halo effect is reduced by the spot size and by extended images resulting in increased transmission for any central pixel measured. As Emerson notes, the resulting Cosmos intensity spectra depends on the complicated convolution of the effects of galaxy size, apparent magnitude, spot size and the properties of the spot halo.

Bearing in mind the above considerations, the findings of empirical studies of objective-prism redshift determinations from Cosmos MM data, using intensity and non-intensity converted spectra, are now discussed.

#### 3.4. Differences in the redshift values from intensity and non-intensity converted Cosmos data

The expected variation in the ECO mid-point position from using J-L density instead of intensity spectra is  $10 \mu\text{m}$  for images with  $b_{\text{uj}} \sim 15-19$ . This results in redshift differences of 0.0047, in that brighter objects give more negative redshifts in density space than in intensity space. The effect on the redshifts of using intensity and non-intensity converted Cosmos data was investigated to compare with the J-L measures.

The Cosmos data was reduced using the E2D interactive technique developed by J.Cooke and B.D.Kelly at ROE and described by Parker et al. (1983). Briefly, 512 by 512 pixel frames of Cosmos prism plate MM data were projected onto an ARGS screen. These could be the raw transmission values or processed intensity converted frames. Individual spectra could be isolated manually using a box-cursor. ECO and  $4000\text{\AA}$  feature positions chosen for each spectrum could be positioned to  $1/2$  a pixel ( $8 \mu\text{m}$  on the plate). This precision for isolating features led to a quantisation in the redshift results obtained, i.e.  $DZ=0.003$  at  $Z=0.000$  going to  $DZ=0.007$  at  $Z=0.20$ , the changing resolution being the effect of the varying dispersion along a spectrum. The same sample of stellar and galaxy spectra, identified from visual inspection of the direct plate, were measured with E2D on intensity and non-intensity converted MM frames. The Cosmos data was from the objective-prism high-quality copy plate UJ5402P P2N1 of field 349, for a small area near the plate centre containing a rich

cluster of galaxies at  $00^{\text{h}}03^{\text{m}}.5$ ,  $-35^{\circ}00'$  (Carter, 1980).

Figure 3.1 is a plot of the redshift results from the E2D measures using post-phase1 update intensity and non-intensity converted Cosmos data. For both stars and galaxies, the redshifts from the intensity converted data are more positive than their non-intensity converted counterparts. The circled points indicate instances of obvious feature mis-match between the two measures. Feature mis-match can occur in faint galaxy spectra of low S/N where  $4000\text{\AA}$  feature identification is difficult or in cases where galaxy spectra exhibit more than one  $4000\text{\AA}$  feature candidate, e.g. some galaxies have a pronounced 'Balmer jump' discontinuity which can be confused with the  $4000\text{\AA}$  feature. However, these ambiguous spectra would have been assigned low weight. A subjective weighting assessment of likely redshift reliability was applied which reflected spectral properties such as S/N, ECO uniformity, feature slope, strength and ambiguity. Weight 1 was assigned to high-confidence spectra and weights 2 and 3 to low confidence spectra. For stellar results, redshift discrepancies between spectra assigned high weights in both measures is a different problem, related to the intensity conversion and to saturation and contrast reduction problems with the copy plate and Cosmos data at high densities. Compression of the  $4000\text{\AA}$  feature in bright density spectra may lead to features in less saturated regions of the spectra being preferentially chosen, whereas in the equivalent intensity converted spectra, the recovery of intensity information may be sufficient to more clearly resolve the true  $4000\text{\AA}$  feature.

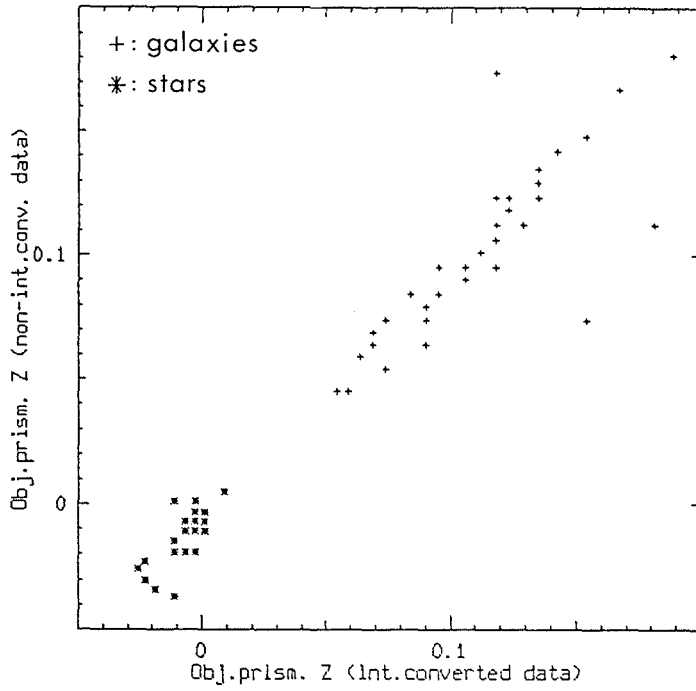


Figure 3.1 Comparison of objective-prism redshifts from non-intensity and intensity converted COSMOS data.

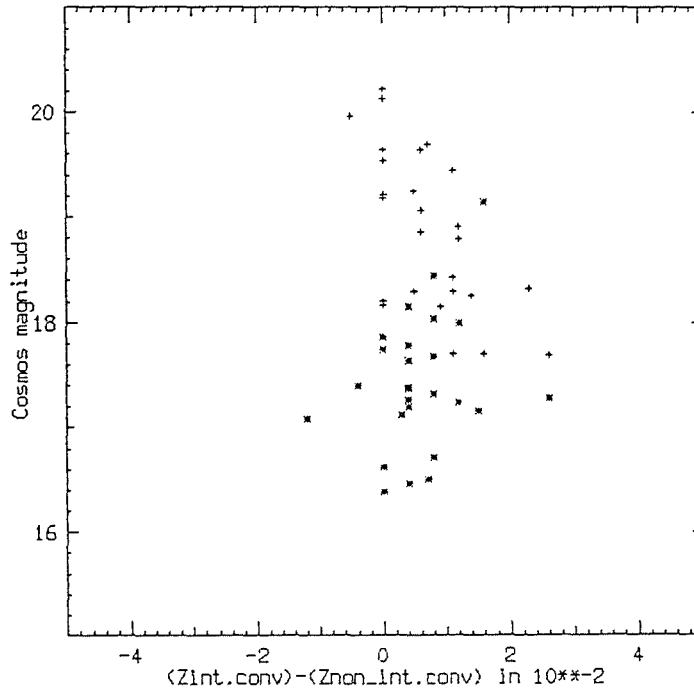


Figure 3.2 COSMOS prism magnitude against the difference between objective-prism redshifts from intensity and non-intensity converted COSMOS data.

Returning to figure 3.1, the average redshift difference between the results for stellar spectra was:

$$DZ=0.0062 ; \sigma =0.0059,$$

where  $DZ = Z(\text{intensity converted}) - Z(\text{non-intensity converted})$

Excluding the four worst discrepant points as being due to mis-matched features, this became:-

$$DZ=0.0043 ; \sigma =0.0033$$

For the galaxy results, again rejecting obvious cases of mis-match, the average difference was:-

$$DZ=0.0048 ; \sigma =0.003,$$

in good agreement with the stellar results. Hence the average discrepancy between the redshifts from measuring intensity and non-intensity converted spectra is essentially the same, irrespective of whether stars or galaxies are considered. Furthermore, the redshift differences appear approximately constant with redshift until  $Z=0.15$ , when the discrepancy is reduced. Though the number of points is sparse in this region, the result is not surprising since the highest redshift objects are usually the faintest and we might expect better agreement because the intensity conversion is not so crucial.

Figure 3.2 gives estimated prism object magnitude versus the redshift difference between intensity and non-intensity converted spectra. The crude magnitude estimates are obtained from the images detected by Cosmos above a given threshold (usually 7% of the night sky level) and by normalising to the relative sky brightness. The standard relation for Cosmos data was used:-

$$\text{COSMAG} = -2.5 \log[\sum(I - I_{\text{sky}})] + 2.5 \log[I_{\text{sky}}/\text{PIXARE}] \dots 3.5$$

Here 'I' is the intensity of the ith pixel, 'I<sub>sky</sub>' is a derived, smoothed background intensity and PIXARE is the pixel area in arcseconds. This raw COSMAG can be calibrated using the equation below:-

$$buj' = \text{COSMAG}/100.0 + 2.5\log(\text{Isky}) -$$

$$5.0 \log(\text{stepsize} \times \text{platescale}/1000.0) \dots\dots 3.6$$

where stepsize = 16  $\mu\text{m}$  and platescale = 67.14"/mm. Hence the calibrated COSMAG 'buj' is related to the apparent magnitude of an image by the relation:-

$$buj = \text{Msky} + buj' \dots\dots\dots 3.7$$

An Msky zero point of 22.2 was adopted in forming the apparent magnitude estimates, which is a typical value for deep IIIaj exposures. The exact value of Msky is not critical at this stage, since we are only concerned with the relative brightness of each image. In any case, since the objective-prism plate was taken without a filter, the magnitude estimates buj are not in any standard photometric band (see chapter 5 section 5.5 for a more detailed discussion of magnitude calibration).

Figure 3.2 shows, that for these copy plate measures, a significant, approximately constant, discrepancy exists between the redshifts from intensity and non-intensity converted Cosmos data of -0.004, which seems independent of magnitude from buj = 16.0-20.0. The non-intensity converted results are systematically more negative. This observed discrepancy is sufficiently large for intensity conversion of all Cosmos data to be recommended.

Figure 3.1 also reveals that redshifts obtained for many of the stellar measures of intensity and non-intensity converted data deviate markedly from the zero redshift we might expect, considering stars are essentially at rest when compared with the redshift resolution of the objective-prism technique. To investigate this effect further a sample of 100 stellar spectra were measured, covering a wide range of magnitude.

### 3.5. Stellar redshift results

Cooke (1980), determined the wavelength of the ECO, used as the wavelength reference point, by measurements of a relatively small sample of faint, late-type stellar spectra. It was hoped that ECO wavelength variations caused by object colour and magnitude changes would be small. Emerson's simulations of perfect intensity spectra have show that the effects of object colour on the ECO position will cause a wavelength variation from  $\lambda 5340\text{\AA}$  at B0 to  $\lambda 5400\text{\AA}$  at M0, corresponding to a redshift difference of  $-0.015$ . This effect was expected to be more serious than that of object magnitude variation. Here a difference in redshift of  $\sim 0.004$  was anticipated from simulations of J-L density spectra, for objects from buj  $\sim 15$  to  $19$ , in that bright objects give more negative redshifts.

The size of the negative stellar redshift effect in figure 3.1 could not solely be explained by changes in intrinsic stellar colour and magnitude for perfect intensity spectra. We might expect the stars measured to exhibit a mixture of colour but the majority will probably be late-type (Reid and Gilmore, 1982). Furthermore, late-type stars have strong  $4000\text{\AA}$  features and so they are preferentially chosen as yielding reliable measures, unlike spectra of early types which are more likely to be rejected because of insufficiently strong, ambiguous, or absent  $4000\text{\AA}$  features. Consequently most of the colour effect should be confined to yielding negative redshifts not in excess of  $-0.006$ , (calculated by Emerson from perfect intensity spectra where there was no effect due to the magnitude of the object).

Inevitably, real measures always give some imperfections in the intensity conversion due to limitations of the measuring machine used. Thus the Cosmos machine is one likely source of the effect found for stellar spectra in figure 3.1, although use of a copy instead of an original plate must also be investigated (see sections 14.12-14.14).

Figure 3.3 gives results of measuring a sample of stellar spectra with both the J-L and with E2D non-intensity converted data. Hence both sets of measures are, in principle, performed on density spectra. Any differences should therefore be due to effects of the measuring machine on the actual form of the spectra. The J-L spectra are manually reduced by measuring the separation on a paper tracing between chosen ECO and feature mid-point positions. The same instrumental settings and D117 wedge recommended by Cooke (1980), were used. Because a ratio arm of 50:1 was employed, the observed separation had to be scaled to that actually existing on the plate. A measurement precision of  $\pm 0.2$  mm on the tracings was achieved, equivalent to  $4 \mu\text{m}$  on the plate. This corresponds to a redshift measurement precision of  $\pm 0.003$  ( $\pm 1,000$  km/s).

There is a distinct trend in figure 3.3 for the J-L results to yield consistently more positive redshifts than their E2D counterparts for the 30 or so spectra deemed to exhibit reasonable  $4000\text{\AA}$  features from both measures. The scatter about the  $45^\circ$  line is  $\pm 0.01$  in redshift. The discrepancy between the J-L and E2D results is significant and must be explained. Furthermore the J-L results also yield redshifts considerably more negative than expected for stars, although the situation is not as severe as for the equivalent E2D measures. The cause of the discrepancy between the J-L and E2D results is at least partly due to the narrower dynamic range of the Cosmos machine.

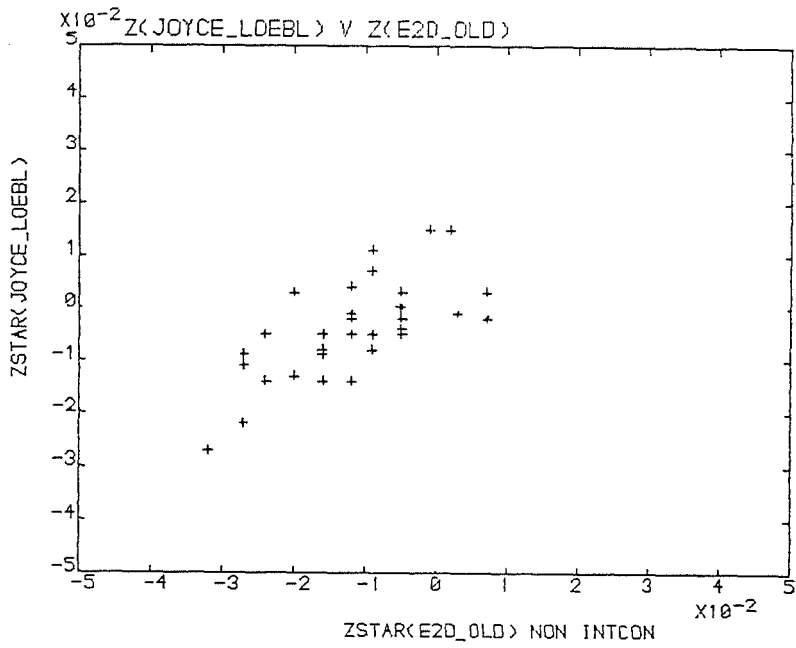


Figure 3.3 Comparison between stellar objective-prism redshifts from density Joyce-loebl tracings and from E2D non-intensity converted COSMOS data.

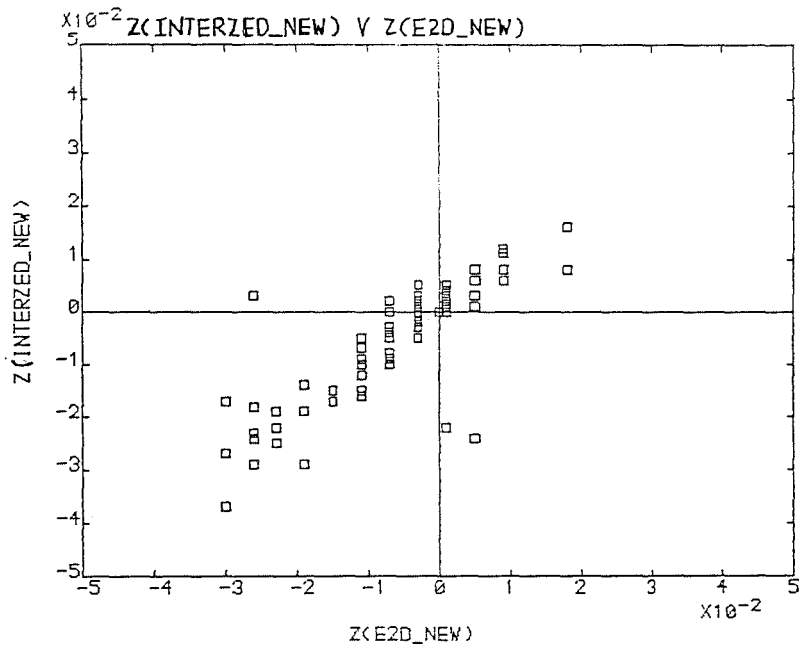


Figure 3.4 INTERZED against E2D objective-prism stellar redshifts from intensity converted COSMOS data.

The maximum density measurable in an image from Cosmos data is given by:-

$$D_{\max} = D_{\text{sky}} + \Delta D \dots \dots \dots 3.8$$

where 'Dsky' is the plate background density and  $\Delta D$  is  $\sim 1.3$  (MacGillivray and Stobie, 1985). Now the copy plate emulsion saturates at  $D = 2.0$ , within the dynamic range of the J-L, depending on the wedge employed. However, for a Dsky on a typical copy plate of  $\sim 0.3$ , the maximum Cosmos density that can be accommodated is  $D_{\max} \sim 1.6$ . Hence, even with copy plates of low sky background, the Cosmos dynamic range is exceeded for the brighter spectra. A result of saturated Cosmos pixels is that the photographic densities on the copy plate are underestimated compared with results for the brighter J-L spectra. Hence the observed sky to ECO peak distance in E2D density spectra is also underestimated, leading to lower ECO mid-points and thus greater ECO to  $4000\text{\AA}$  feature separations. The redshifts of brighter, non-intensity converted Cosmos objective-prism spectra are thus more negative than the corresponding J-L measures.

For a clearer indication of what is happening with the stellar measures, since the results could have important consequences for any galaxy copy plate measures, a sample of  $\sim 100$  stellar spectra were selected from a central 1 square inch area of copy plate UJ5402P P2N1. The pure stellar sample, identified by reference to the direct plate, covered a wide magnitude range and was measured with the J-L and with the interactive E2D and INTERZED techniques. The INTERZED technique, developed by Beard (1984), uses a suite of software to extract all spectra above specified percentage and area cuts from Cosmos MM data of an objective-prism plate. A 128 by 128 pixel box is centred around each spectrum. Intensity conversion is performed from supplied values of  $T_c, T_b, \gamma$  and  $C$ . The resulting spectra are summed perpendicular to the dispersion direction to form 1-D intensity spectra suitable for interactive reduction. The capability to fit third order polynomials

to features with this technique results in improved positional resolution to 2-3  $\mu\text{m}$  over the E2D technique (8  $\mu\text{m}$ ), yielding a redshift resolution of  $\pm 0.001$ .

Quantisation in the E2D results is clearly seen in figure 3.4, where consistency of the stellar redshifts from E2D and INTERZED is demonstrated. The Cosmos data was intensity converted in both cases. Good redshift agreement to within  $\pm 0.01$  was obtained although there is a slight tendency for the INTERZED redshifts to be less negative. This trend is more clearly illustrated in figure 3.5, a plot of estimated prism magnitude versus redshift difference between the E2D and INTERZED results. Two features of figure 3.5 are of note. Firstly the redshift discrepancy between the techniques are independent of magnitude estimate over the range covered, and secondly 2/3 of the points lie left of the zero redshift line. The average redshift difference was 0.0014,  $\sigma = 0.003$ .

A probable explanation for the discrepancy lies in the measurement precision of the E2D technique itself. In E2D we might expect the cursor to be sometimes positioned 1/2 a pixel to the left or right of the true ECO mid-point position due to the cursor positional resolution. Although the frequency with which the cursor is placed longward of the true ECO position should, on average, be the same with which it is placed shortward, the resulting redshift difference will not be the same because of the rapidly decreasing dispersion of the objective-prism near the ECO. However, this effect is unlikely to cause a trend to negative redshifts in excess of -0.001, insufficient to explain the size of the observed effect. The coarser resolution of the E2D technique, though, means that if the mid ECO position was being preferentially chosen longward of the ideal position by 1/2 a pixel (8  $\mu\text{m}$ ), this is sufficient to account for the observed effect. Further inter-technique comparisons were carried out

for both stars and galaxies to verify the findings of figures 3.4 and 3.5 (see later) using data from Cosmos in its post-phase 1 update configuration.

3.6. Comparisons between the intensity converted E2D/INTERZED results and those for the J-L.

A comparison between results from E2D transmission spectra and J-L density spectra has already been made (figure 3.3). Figure 3.6 is a plot of the results from E2D measures of intensity converted spectra versus the Joyce-Loebl measures for a sample of 60 stars. Comparison with figure 3.3 illustrates clearly how converting the Cosmos data to intensity has improved agreement between the results of the two techniques. This was expected from the results given in figure 3.1. Though 1/5 of the points lie outside the  $\pm 0.01$  redshift bounds either side of the  $45^\circ$  line, it appears that density J-L spectra yield very similar results to intensity converted Cosmos data reduced with E2D.

Neglecting the few instances of obvious feature mis-match, closer examination of figure 3.6 indicates that the scatter about the  $45^\circ$  line may be non-random. At near zero redshifts the E2D results seem to be more positive than their J-L counterparts, while at larger negative redshifts the J-L results seem to be more positive. Again, the effect of the E2D cursor resolution is evident.

To check that the trend in figure 3.6 was not an anomaly of the E2D cursor resolution a sample of 100 stellar spectra were measured using INTERZED, which afforded a higher measurement precision. Of this sample 95 had measurable  $4000\text{\AA}$  features. Eighty three spectra from the same sample were also measured with the J-L. For the brighter stellar spectra, the slit height was matched to the width of the spectrum. Only 77 of these 83 spectra had sufficiently well identified  $4000\text{\AA}$  features.

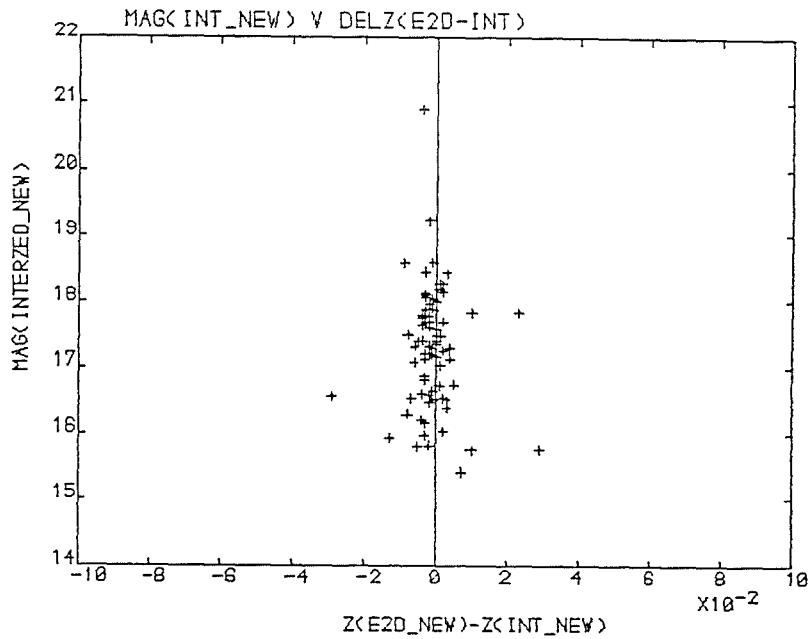


Figure 3.5 COSMOS prism magnitude against the difference between objective-prism redshifts from the E2D and INTERZED interactive measurement techniques.

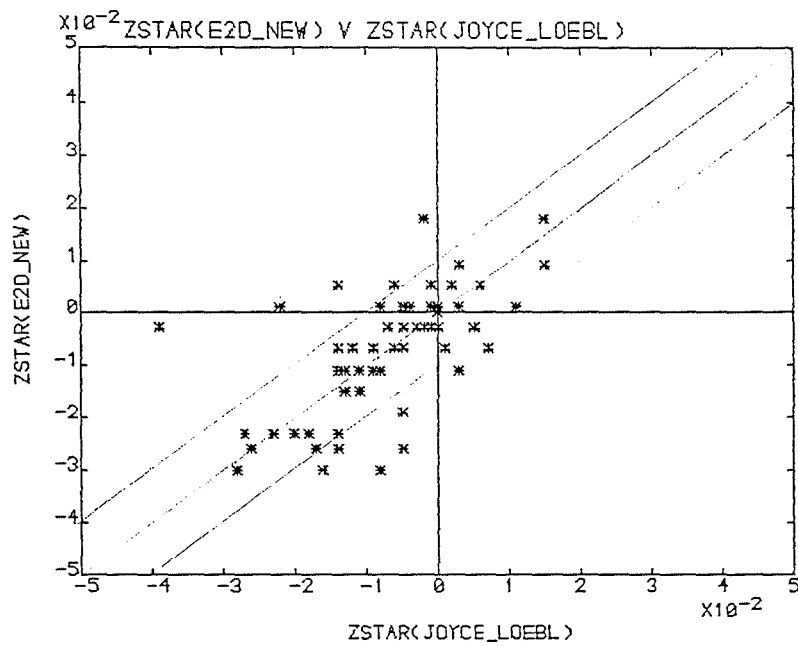


Figure 3.6 Stellar objective-prism redshifts using the E2D technique on intensity converted COSMOS data against the corresponding Joyce-loebl results.

Hence 6 spectra deemed to yield measurable features with INTERZED were not considered suitable from their J-L tracings. There are a number of possible explanations for this disparity:-

- (a) Human inconsistency in switching from J-L to INTERZED measures.
- (b) The selection criteria applied to feature identification in the J-L tracings could have been more stringently applied than for the INTERZED measures. Hence spectra at the low weight end accepted by INTERZED may have been rejected in the J-L sample.
- (c) Real differences in the appearances of the spectra from using the different measuring machines could have led to enhanced or submerged spectral features in some instances.

Examination of the appropriate J-L and INTERZED spectra helps to clarify this point (see below).

Study of the assigned 4000Å feature weights between the INTERZED and J-L spectra gave the following results for the 77 spectra measured in common (Dwt = weight assigned J-L spectra - weight assigned to the INTERZED spectra).

Number with Dwt= 0 was 36; Number with Dwt= 1 was 35

Number with Dwt= 2 was 3; Number with Dwt= 0.5 was 3

Hence 47 % of the sample gave no weighting difference while 45% had a weighting difference of  $\pm 1$ . Only 3 objects had a weighting difference of 2. Thus 92% of the assigned sample weights agreed to 1 weighting division which, for a completely subjective assessment of feature and spectral quality, is remarkable. Of the 6 spectra rejected by the J-L examination, 2 were assigned weight 1, 2 weight 2 and 2 weight 3 within INTERZED. Considering the good weighting assignment consistency between the two techniques, it seems that real differences in spectral appearance is the cause of the disparity in sample size chosen from the same parent population, although manual inconsistencies cannot be ruled out.

Comparison of the INTERZED stellar redshifts with the equivalent J-L measures is given in figure 3.7. As in figure 3.6, most points lie within the  $\pm 0.01$  redshift bounds of the  $45^\circ$  line, but more importantly the slight evidence of a non-random trend in figure 3.6 is enhanced in figure 3.7. There are definite indications that at measured redshifts near zero, INTERZED gives more positive redshifts than those from the J-L. However, the J-L results are systematically less negative than those from INTERZED when both techniques yield larger negative redshifts.

In attempting to understand the likely causes of the observed effect a number of factors should be considered.

(a) Intensity converted Cosmos MM data, reduced with INTERZED, is being compared with measures of J-L density spectra.

(b) The dynamic range of the J-L exceeds that of Cosmos which saturates at  $\sim 1.3D$  above the sky background (due to transmission of light through the spot halo). This corresponds to a density of  $\sim 1.6D$ , assuming a copy-plate sky background of  $\sim 0.3D$ .

(c) Although intensity conversion of the Cosmos data is worthwhile, since it decreases the negative redshifts from non-intensity converted data by 0.004 (on average), saturation problems are encountered at densities in excess of 1.6D on the copy plate. At such densities, present in brighter stellar and galaxian spectra, overestimates in the Cosmos transmission values are carried through the intensity conversion since it is impossible to recover the true incident light intensity from a saturated pixel. Furthermore, even if reliable Cosmos transmission values were available at higher densities, the intensity values obtained are probably slightly erroneous due to differences between the true CC, which deviates significantly from linearity at densities  $> 3.0$ , (original plate), or 1.9, (copy plate) and the Baker density form actually used.

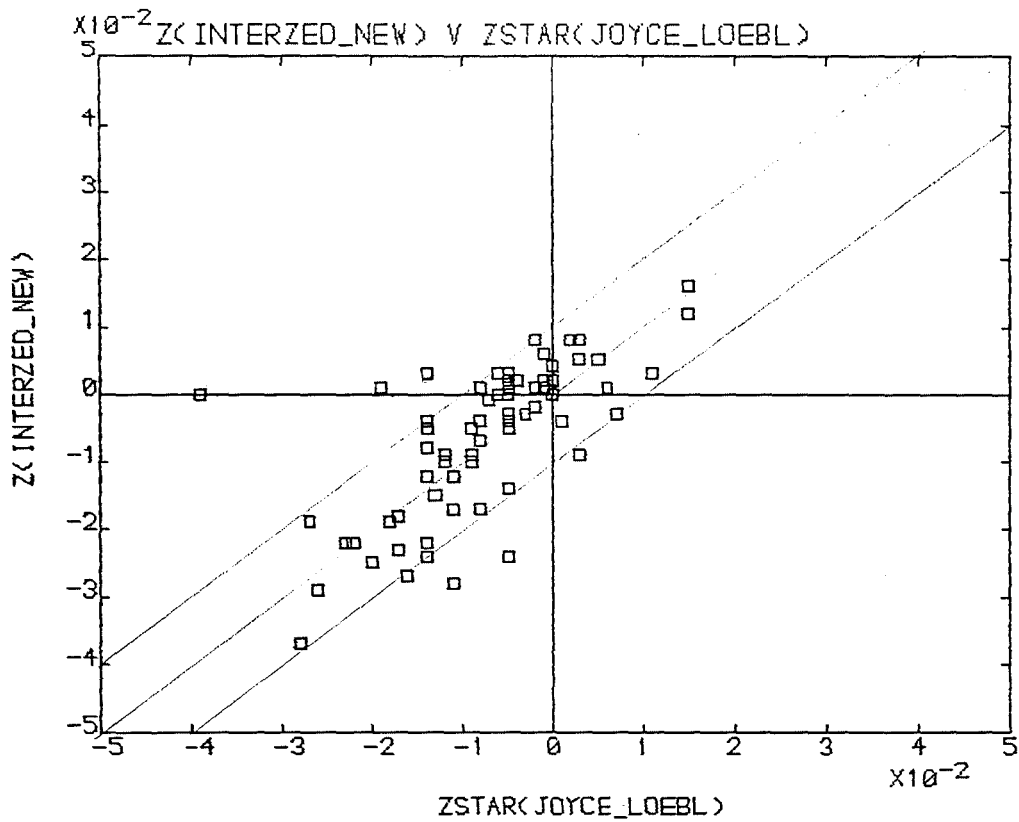


Figure 3.7 Stellar objective-prism redshifts using the INTERZED technique on intensity converted COSMOS data against the corresponding Joyce-loebl results.

Bearing these factors in mind, a satisfactory explanation of the observed trend in figure 3.7 can be obtained by assessing the competing effects of Cosmos data intensity conversion and the extra dynamic range of the J-L at higher densities on the copy plate. For spectra fainter than magnitude, 'M', say, the intensity conversion of the Cosmos data gives a more accurate representation of the object spectrum than the equivalent J-L density spectrum. As more information about the spectrum is recovered a more appropriately scaled tracing results. The ECO mid-point is consequently nearer its true position. Since the ECO slope is non-zero, the feature-to-ECO separation will thus be less than for the equivalent density spectrum, yielding more positive redshifts. As photographic density increases however, intensity conversion becomes more fruitless as the Cosmos machine saturates. There then comes a point when no more information about the true intensity in the object spectrum is recoverable. The equivalent J-L spectra are not so saturated, so the J-L mid-density point becomes a more accurate representation of the spectrum than the intensity converted Cosmos spectrum, at least for densities between 1.6D and 2.0D (where the copy plate emulsion itself saturates). The J-L ECO mid-point position, though not as far above the sky level as it would be if it was intensity converted, is nevertheless higher up the ECO than the equivalent Cosmos intensity spectrum. Thus the J-L spectra ECO-to-feature distance, whilst still underestimated due to contrast reduction at higher densities on the copy, is still smaller than that for the equivalent Cosmos intensity spectra, resulting in a less negative J-L redshift.

The remaining check on the validity of the above argument is to show that the redshift results at the faint and bright limits tie up with the redshift comparison between J-L and INTERZED results (figure 3.7), i.e. it is the faint objects where the INTERZED results give the more positive redshifts and the bright objects where the J-L results yield the less negative redshifts.

Figure 3.8 gives a plot of estimated object magnitude against INTERZED stellar redshift. The expected trend to negative redshift with decreasing magnitude is evident, as is the tendency to small positive redshifts at faint magnitudes. Figure 3.9 is the corresponding plot for the J-L results. The same magnitudes for the matching spectra were used for convenience instead of J-L peak density above sky. The magnitude/redshift effect (mag/Z hereafter), for the brighter spectra is less severe than in figure 3.8, although it is still present. Fainter than  $\text{buj} \sim 17.5$  the points appear evenly distributed about  $Z = 0.0$ . Brighter than  $\text{buj} \sim 17.5$  though, the majority of points have increasingly negative redshifts. Beard (1984), for a sample of 50 J-L stellar spectra, found no trend to negative redshift for brighter spectra, although a few faint spectra had their redshifts overestimated. This was possibly due to the top of the  $4000\text{\AA}$  feature becoming less well defined. The results of figure 3.9 contradict these findings but this may be because the trend in Beard's data was masked by scatter and would not have become obvious until his sample was extended to brighter spectra. Hence the earlier discussion on J-L/INTERZED redshift comparisons is further vindicated by figures 3.8 and 3.9.

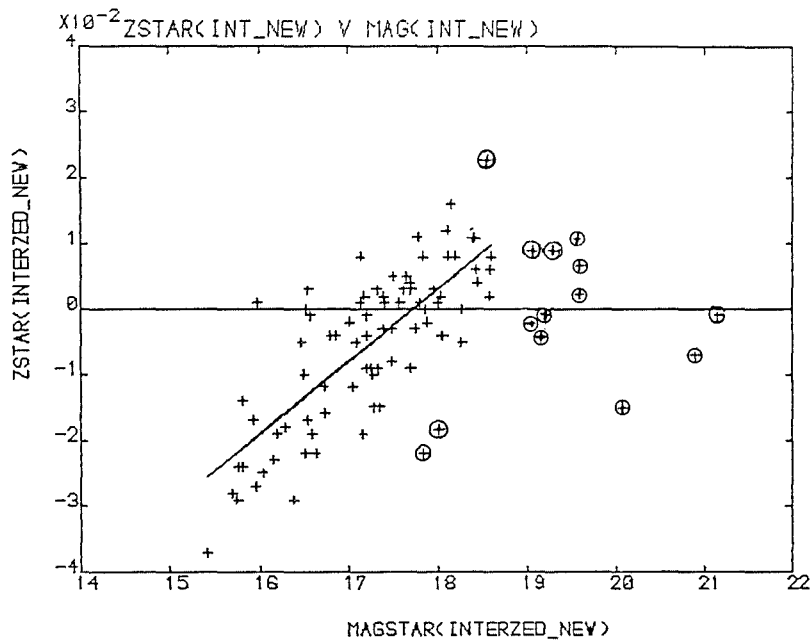


Figure 3.8 Stellar redshifts from INTERZED measures versus COSMOS prism magnitude together with overlaid least squares fit.

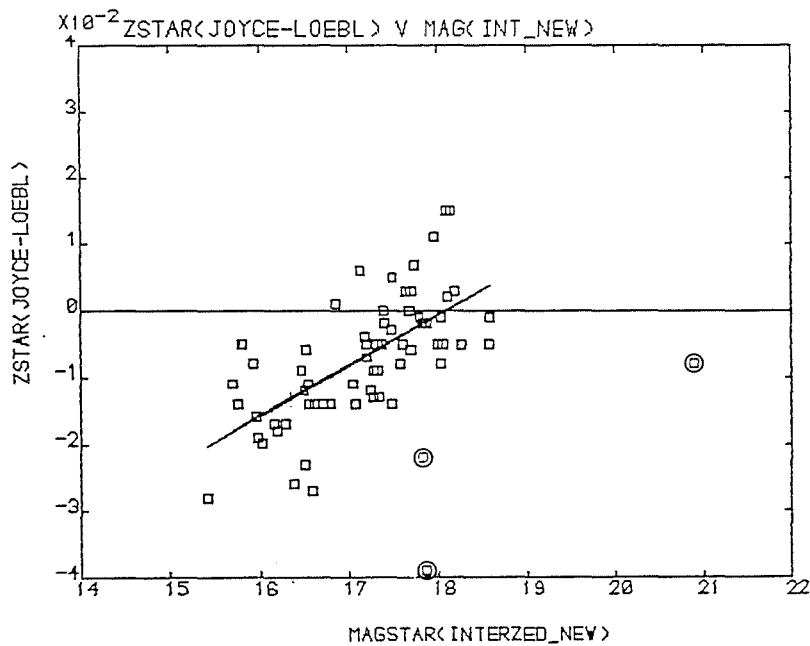


Figure 3.9 Stellar redshifts from Joyce-loebl measures versus estimated prism magnitude together with overlaid least squares fit.

Returning to figure 3.8 an interesting property of the plot is evident. Though considerable scatter exists, the relationship between redshift and magnitude estimate appears to be approximately linear between  $b_{uj} = 15.5$  and  $18.5$ . After  $b_{uj} = 18.5$  the few faint stellar results indicate that this relationship flattens out, though there are too few points to say anything conclusive. The lack of points at faint magnitudes was not due to any deficiency in the numbers of identified faint stars but is an indication of how difficult it was to unambiguously identify the  $4000\text{\AA}$  feature above the background noise in such low S/N spectra. This flattening in the Mag/Z relationship is expected as spectra are no longer saturated.

An important factor when considering the 'linear' Mag/Z relationship in figure 3.8, is that the magnitude estimates are increasingly unreliable for denser spectra due to the saturation effects described earlier. This results in unknown underestimates of the true magnitude of object spectra at bright limits. In photometric work this would be a severe problem, although calibration for the less saturated spectra could be attempted by obtaining Cosmos magnitude estimates of a selection of stars of known apparent magnitude. At this stage however, the exact magnitude values are not crucial (see chapter 5 section 5.5). Providing consistent magnitude estimates are derived, the effects of increasing image brightness on redshifts can be adequately described qualitatively if not quantitatively. It is sufficient to show how the observed redshift measures are affected by changing Cosmos determined magnitudes.

The 'linear' mag/Z relation in figure 3.8 is only applicable for the specific post-phase 1 update Cosmos measures of the copy plate UJ5402P P2N1. For different plates a similar plot would have to be generated from measures of a similar sample of stellar spectra. Indeed figure 3.9 gives a slightly different mag/Z relation for the J-L redshifts, even though the same plate material was utilised. Again a roughly linear relationship exists, with scatter, though the best-fit line to the data yields a different slope to that of figure 3.8. A linear least-squares regression was applied to the data in figures 3.8 and 3.9 after excluding obviously discrepant points that would adversely affect the fit. Instrumental, ( $\sigma[y]$ ), weighting was applied to the redshift values in an attempt to account for the measurement errors. The results of the fits to the data in figures 3.8 and 3.9 is given in table 3.2. The size of the linear correlation coefficient in both cases, reveals that a straight line is a reasonable representation for both sets of data, though the fit is somewhat better for the INTERZED results. Values calculated for the gradients of the fits, indicate the shallower trend to negative redshift with increasing image brightness for the J-L data.

The scatter of  $\pm 0.01$  in redshift in figures 3.8 and 3.9 may be partly attributable to positioning errors on the ECO and feature mid-points and partly to small colour effects which may smear the trend to negative redshift with decreasing magnitude. Points remote from the main data stream are from mis-identification of the  $4000\text{\AA}$  feature. There is also a possibility that compact elliptical galaxies with a strong Balmer-jump discontinuity may be mistaken for a stellar spectrum with a  $4000\text{\AA}$  feature. This is because at faint limits they are very difficult to distinguish from stars, even on the direct plate. The numbers of such mis-classified objects is likely to be small.

Table 3.2

Results of linear least-squares fit to the data in figures 3.8 and 3.9

(a) Results for fit to data in figure 3.8

Gradient : 0.01110, std.devn.: 0.00104  
Constant : -0.19677, std.devn.: 0.01787

Linear correlation co-efficient : 0.77698  
Reduced Chi-square of fit : 0.00005  
value of f-test of fit : 114.252

(b) Results for fit to data in figure 3.9

Gradient : 0.01180, std.devn.: 0.00132  
Constant : -0.21320, std.devn.: 0.02275

Linear correlation co-efficient : 0.71559  
Reduced Chi-square of fit : 0.00009  
value of f-test of fit : 79.7582

### 3.7. Implications of a strong magnitude/redshift relation in stellar spectra

The relationship exhibited by stellar measures in figure 3.8 could have significant consequences for galaxy redshifts from Cosmos data, since the redshifts for brighter galaxy spectra should be similarly affected, i.e. redshifts will be underestimated by an amount dependent on the object surface brightness. In figure 3.8 the mag/Z effect becomes significant for objects brighter than  $b_{uj} \sim 17.0$ . Hence objective-prism galaxy redshifts from Cosmos copy-plate data with  $b_{uj} < 17.0$  may be significantly underestimated (Cooke 1980, quotes a useful magnitude range of  $16.0 \leq b_{uj} \leq 19.0$ ). Since the relation in figure 3.8 seems quite well behaved, at least for this sample, it may be possible to quantitatively correct the underestimated redshifts from the brighter galaxy spectra.

Cosmos magnitudes are calculated by addition of all contiguous image pixels above user defined background percentage and area cuts. Due to their extended and diffuse nature the image sizes of galaxy spectra of magnitude 'bg' will generally be greater than that of a stellar spectrum of the same magnitude. Thus, because of the lower surface brightness of galaxy spectra compared to stellar spectra of the same isophotal magnitude, the mag/Z effect for galaxies may not be so severe as for stellar spectra. The galaxian magnitudes come from a larger number of lower-intensity pixels compared with the smaller number of higher-intensity pixels for stellar spectra. The difference may not be too large on plates of moderate seeing however, because the low-intensity pixels which give many objective-prism galaxy spectra their fuzzy appearance contribute little to the overall magnitude of the object, especially when considering the blurring effect of the seeing disk.

A further item to consider for galaxy spectra is the effect of image size along the dispersion direction. This results in a decrease of spectral resolution and a lowering of the peak intensity. Emerson's simulations show that for an elliptical galaxy image profile with an effective radius of 6.0" (=180  $\mu\text{m}$  on the plate), convolved with seeing of  $\sim 1.5''$ , the ECO position should be shifted by 15 $\text{\AA}$ . This is equivalent to a redshift difference of only 0.002. Hence we shall assume that the Cosmos mag/Z effect is dominant for bright galaxy objective-prism spectra on copy plates of originals with good seeing, with image profiles perpendicular to the direction of dispersion of  $\leq 200 \mu\text{m}$  diameter.

To test the validity of correcting galaxy objective-prism redshifts for the mag/Z relation found for stellar spectra, some comparison with a galaxy with an accurate slit-spectrum redshift and an objective-prism redshift is required. Fortunately, the central cD galaxy in the cluster in the measured sample has a published slit-spectrum redshift of  $0.114 \pm 0.001$  (Carter, 1980). Furthermore the objective-prism spectrum of this galaxy has a good 4000 $\text{\AA}$  feature. Consequently it has been measured a number of times with the J-L, E2D and INTERZED techniques during the course of these studies. Four separate E2D and three separate INTERZED measures of this cD galaxy from pre-phase 1 update Cosmos data yielded  $Z(\text{average}) = 0.082$ ,  $\sigma = 0.003$ . The Cosmos magnitude of this spectrum was  $b_{uj} = 16.32$ . A best-fit straight line through the Mag/Z relation for stellar spectra in the same sample implied that a correction of +0.023 should be made to galaxy redshifts with  $b_{uj} \leq 16.5$ . This correction is the amount by which a star of the same magnitude is less than zero redshift. This gives a corrected cD galaxy redshift of  $Z = 0.105$ , in much better agreement with the slit-spectrum redshift than the uncorrected value.

The J-L result for the cD galaxy was  $Z = 0.107$ . Reference to figure 3.9 indicates that a correction of only +0.013 should be applied to compensate for the weaker mag/Z effect in the J-L stellar results. A corrected value of  $Z = 0.120$  results which is no closer to the published redshift. In this case the correction factor applied has not improved the agreement with the slit-spectrum redshift though neither has it made it worse. We expect the mag/Z effect to be less severe for the J-L data because of the J-L's wider dynamic range. Indeed reference to figure 3.9 shows that correction for the mag/Z relation in J-L spectra becomes significant only at  $\text{buj} \leq 16.5$ . Hence, because of the scatter in figure 3.9, no real advantage in applying the correction to the J-L results is achieved until  $\text{buj} \sim 16.5$ .

The result for correcting the cD galaxy redshift when using Cosmos data is encouraging. Before firmer conclusions can be made regarding the validity of this correction procedure, a larger sample of galaxies with good objective-prism and slit-spectra redshifts is required for comparison. Chapter 4 details the calibration of the objective-prism redshifts with slit-spectra redshifts using results for the slit-spectra observations in chapter 2. Attempts to correct the galaxy prism redshifts from these bright spectra based on magnitude and mean surface brightness considerations are described. Both J-L and Cosmos INTERZED results were obtained. Also a co-ordinate transformation was obtained to see if this alleviated the mag/Z effect.

### 3.8. Use of other spectral features in UKST low dispersion objective-prism spectra

Only the strongest features in objective-prism spectra remain consistently identifiable with wide variations in magnitude, since weaker features are washed out by saturation effects for bright spectra and would become indistinguishable above the noise in faint spectra.

The 4000Å feature was often strong enough in many stellar spectra for unambiguous identification. However, the 4000Å feature was not always the only prominent visible feature. A less significant but sharp feature was evident at shorter wavelengths in the spectra of a significant number of the stellar sample. Examples of stellar spectra exhibiting these features is given in figure 3.10. Examination of photoelectric spectral scans of stellar spectra by Foy, Stein and Warren (1974), indicate that this feature is probably the Balmer limit at  $\lambda 3646$  which is particularly strong in G,K and M giants. This 'Balmer-jump' continuum drop in many of the stellar spectra studied affords the opportunity to corroborate the 4000Å feature redshifts.

Consequently, those stars in the sample with significant secondary features were re-measured with INTERZED. The results are plotted in figure 3.11, which gives INTERZED redshifts, as determined from the separation between the Balmer jump and the ECO, versus Cosmos magnitude estimate. A mag/Z effect is again evident. Comparing with figure 3.8, the corresponding results from the 4000Å feature, this effect is not obvious until  $b_{uj} \sim 17.0$ , (c.f.  $b_{uj} \sim 17.5$  in figure 3.8). Scatter in the Balmer-jump results though, does seem worse. Differences between the the 4000Å feature and Balmer-jump results are highlighted in figure 3.12, which gives INTERZED, Balmer-jump stellar redshifts versus the equivalent 4000Å feature redshifts.

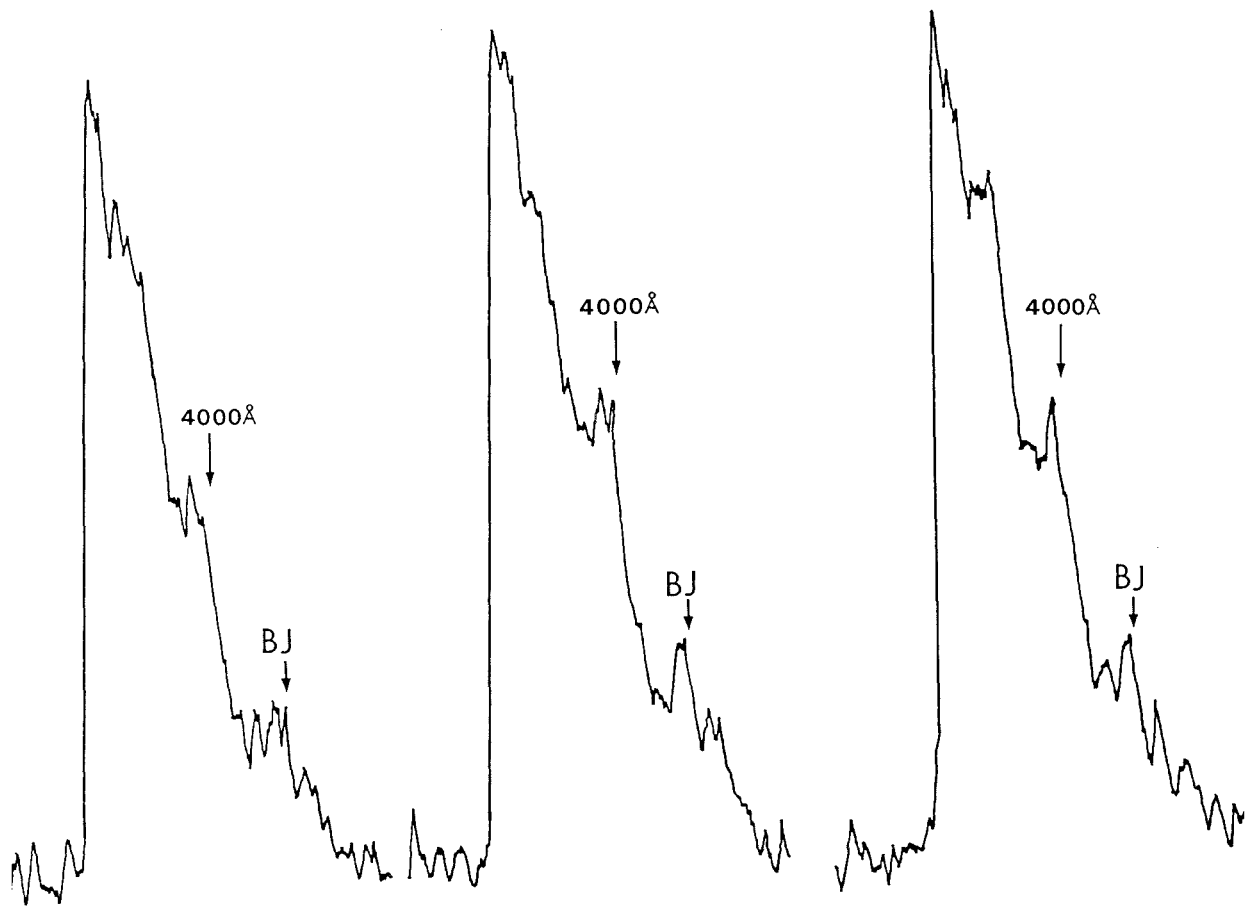


Figure 3.10 Some examples of stellar spectra exhibiting both 4000Å and Balmer-jump features.

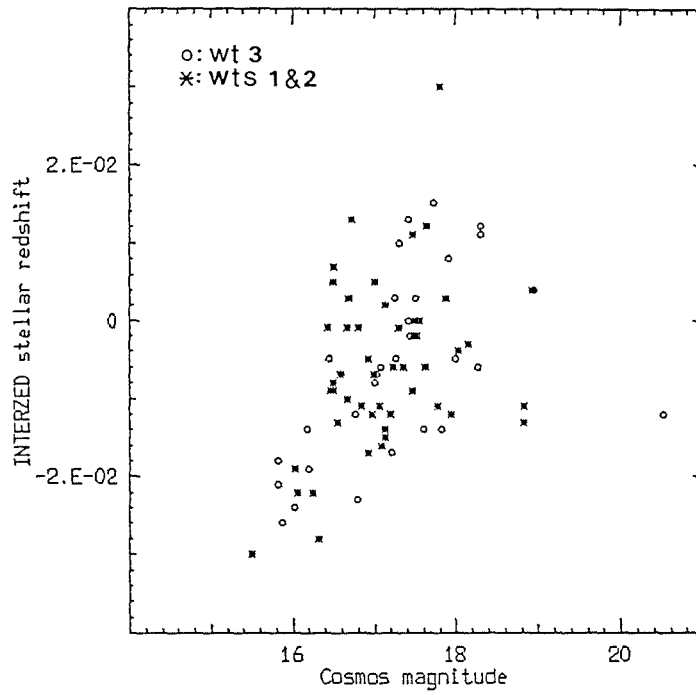


Figure 3.11 INTERZED stellar redshifts versus COSMOS prism magnitude. The redshifts were from measurement of the Balmer-jump feature.

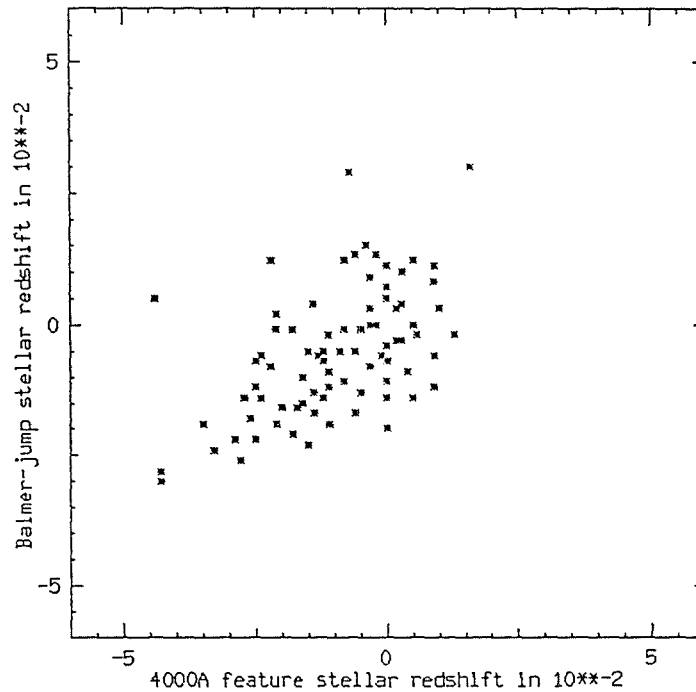


Figure 3.12 Comparison between the stellar INTERZED redshifts from measurement of the 4000Å and Balmer-jump features, (all weights considered).

Although the scatter in this plot is  $\sim 0.15$  at redshifts near zero, it is obvious that at increasingly negative redshifts the Balmer-jump values are more positive than their 4000Å feature counterparts. This diagram indicates that the Balmer-jump redshifts are not as severely affected by the mag/Z effect as the 4000Å feature results.

Explaining this effect is not easy. The major causes of the trend to negative redshift with increasing image brightness are the use of copy-plate material and Cosmos dynamic-range limitations. Consequent improper intensity conversion affects the ECO mid-point determination and hence the redshift (the effect of using copy plates instead of the original plate is investigated later). Hence we might expect that the choice of feature used would have little effect on the stellar redshift results. A possible explanation lies in the measurement technique. Within INTERZED, once the ECO position has been chosen, the programme arrows the expected zero redshift for the current choice of feature wavelength. The user may then be influenced to choose any conspicuous feature close to the arrowed position. There is little chance of confusion with the 4000Å feature because its size usually dominates all other spectral discontinuities apart from the ECO itself. The Balmer-jump feature though, is not so prominent and there is sometimes more than one possible feature candidate. Consequently some feature other than the true Balmer jump may be chosen because of its proximity to the arrowed position. This would lead to preferential selection of an apparently less negative redshift feature. For example there is a feature at  $\lambda 3720\text{Å}$ , due to blends of H14, FeI and TiI, which is fairly prominent in the spectrophotometry of Fay, Stein and Warren (1974).

We might therefore expect that Balmer-jump features assigned a high weight, because there is little ambiguity in feature identification, will have more consistent agreement with the 4000Å feature results. Figure 3.13 is the result of choosing only the obvious Balmer-jump features. It is apparent that the trend in figure 3.12 has not diminished.

A possible contributor to the Balmer-jump and 4000Å feature redshift discrepancy is small positional errors in the feature mid-points. This would not affect the Balmer-jump redshifts as much as the 4000Å feature because of the higher dispersion at shorter wavelengths. This might be expected to reduce the scatter for the Balmer-jump results but in practice the improvement is minimal, i.e.  $Z \sim 0.0001$ , because the errors in the ECO mid-point determination dominate.

Misplacing the 4000Å feature mid-point randomly about its ideal position would, in a large sample, result in slightly higher positive redshift values longward of the true mid-point than negative values shortward of it. This would work against the effect seen in figures 3.12 and 3.13. In practice, although the changing wavelength dispersion along a spectrum results in a slowly changing redshift resolution, (the positional resolution remains constant) this has no significant effect on the results. This is because the magnitude of this change with each positional movement is a small fraction of the redshift difference caused by the positional resolution itself. Furthermore the Balmer jump is often a shorter, sharper feature in stellar spectra so that determination of its exact mid-point is less critical.

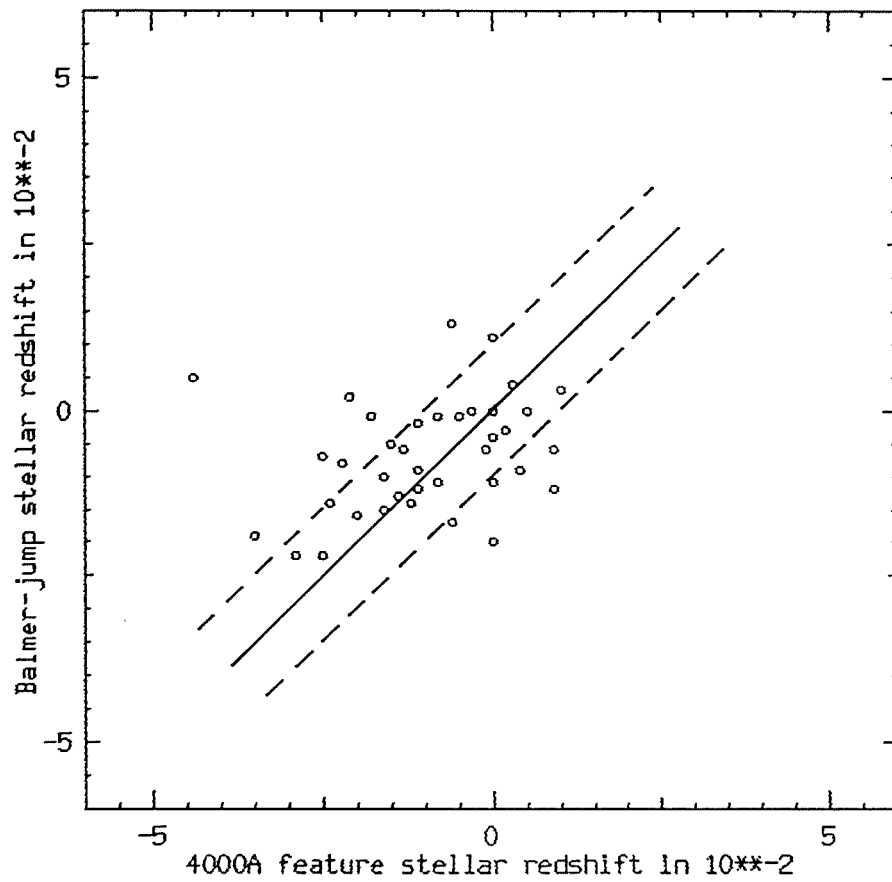
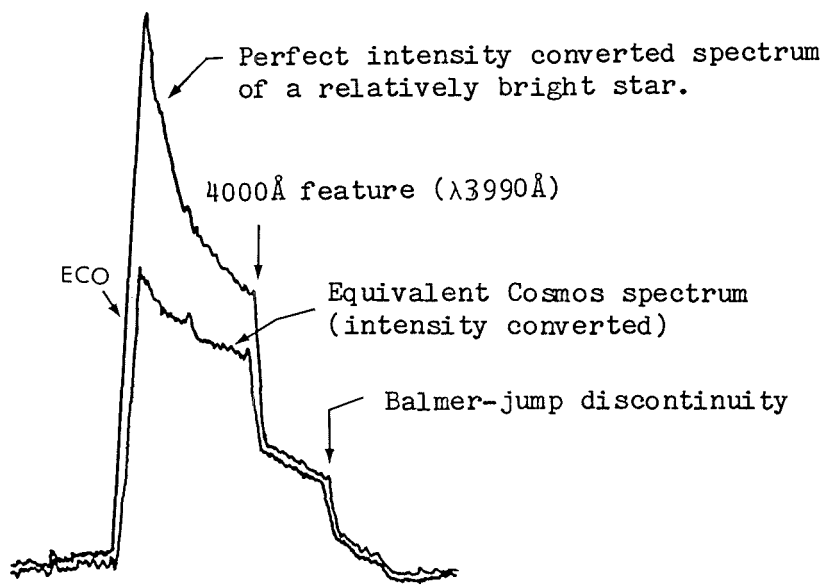


Figure 3.13 As Figure 3.12 but for just those spectra possessing top weight features.

The most plausible explanation for the Balmer-jump and 4000Å feature - result discrepancy comes from a consideration of the saturation problems of Cosmos. Examination of brighter, stellar, intensity converted, Cosmos copy plate spectra, reveals that although many spectra still possess strong 4000Å features they appear more rounded. This is a consequence of Cosmos dynamic range limitations and the use of a copy plate. The 4000Å feature appears higher up the continuum nearer the ECO peak than it would in an unsaturated spectrum. This is not due to any intrinsic variation in the relative positions of feature, sky level and ECO peak, but reflects the vertical compression of spectral information at higher photographic densities due to Cosmos saturation and contrast reduction in copy plates. The true strengths of 4000Å features in semi-saturated stellar spectra are thus underestimated, since the transmission values at higher densities are being overestimated. The mid-point of such a feature would be at a lower intensity value than in a perfect intensity converted spectrum. As the feature slope is non-zero this results in larger ECO to feature separations and thus to more negative redshifts.

So, in the brighter stellar spectra, the "observed" ECO and 4000Å feature positions both contribute to negative redshift estimates. The position of the shorter wavelength Balmer-jump though, is considerably further down the continuum at lower densities. Hence, even in bright stellar spectra, the Balmer-jump is unlikely to be affected by saturation. The above effect is demonstrated schematically in figures 3.14a-b. They show a bright, idealised, perfect intensity converted stellar spectrum with the corresponding Cosmos intensity converted spectrum superimposed. To illustrate how this leads to the "negative redshift effect" the slopes of the ECO and features have been grossly exaggerated.



Subscripts 1 and 2 refer to the mid points of the emulsion cut-off (ECO), 4000Å feature (4F) and Balmer-jump (BJ), as determined from perfect intensity converted and COSMOS intensity converted stellar spectra.

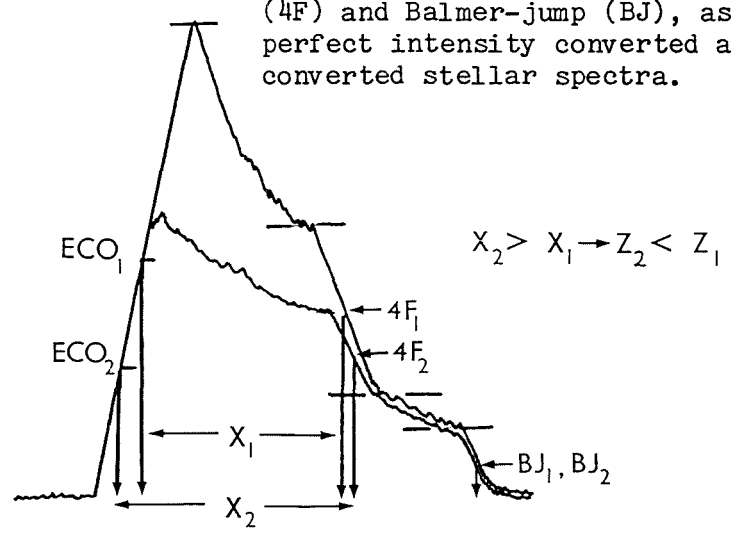


Figure 3.14 Schematic representation of how objective-prism spectral features and the ECO position is affected by image brightness.

In the idealised situation above it can be seen that the Balmer-jump mid-point position is unaffected by using measures from a Cosmos intensity converted spectrum for a bright star, implying that the resultant negative redshift is caused solely by underestimates of the true ECO position. Using the 4000Å feature, however, results in an even larger negative redshift estimate in the Cosmos spectra.

Hence the Balmer-jump may give a better redshift estimate if it can be unambiguously identified in object spectra. Restricting the sample to spectra possessing strong Balmer jumps would result in a considerable reduction in redshifts obtained. The 4000Å feature will therefore remain the prime redshift handle in manual/interactive reductions. The Balmer-jump though will serve as a useful check on redshifts obtained in spectra exhibiting both features.

### 3.9. A repeatability and consistency assessment of the redshift results

All redshifts obtained so far from J-L measures and from INTERZED/E2D measures of pre- and post-phase 1 update Cosmos data have been freely inter-compared. Redshift accuracy has been assumed to be limited by the positional resolution of each technique. No serious thought had been given to repeatability of any one set of measurements using the same technique, over prolonged time intervals, nor of the result consistency for both stars and galaxies between the various techniques. Obviously, with any manual or interactive technique, where features are user defined, the result integrity and consistency must be investigated. Any limitations or reliability problems of manual or interactive measures must be assessed and understood. The bounds for realistic deductions of properties of the measured redshifts should then be known.

Figure 3.15 is a plot of average galaxy redshifts from three, and in some cases four, separate E2D measures of the same sample, against corresponding averages from three separate INTERZED measures. Note that the effect of the coarser positional accuracy of the E2D data has been masked by the averaging. The averages were obtained from repeat measures of pre-update Cosmos data over a two and a half year period. The results from the repeat measures yield very good agreement. The majority of points lie within the  $\pm 0.01$  redshift bounds of the  $45^\circ$  line. A few points are remote from the  $45^\circ$  line. Since each point comes from 3 or 4 separate measures, where small redshift differences would be smeared in the averaging process, the large discrepancies indicate instances where different  $4000\text{\AA}$  features were consistently chosen by each technique. This usually occurs only where spectra have more than one  $4000\text{\AA}$  feature candidate, thus introducing identification ambiguity. As is the case for the wayward points in figure 3.15, the redshifts had been assigned very low weights (average weight = 3.1).

The mean of the E2D/INTERZED average redshift differences has a small positive value but is less than half the size of the population standard deviation. Specifically (excluding obviously discrepant points):-

$$DZ(\text{average}) = 0.032; \quad \text{Sigma} = 0.0072; \quad n = 46$$

This is a slightly larger discrepancy than that found for the stellar results (figure 3.4), which had yielded:-

$$DZ(\text{average}) = 0.0015; \quad \text{Sigma} = 0.0031; \quad n = 68$$

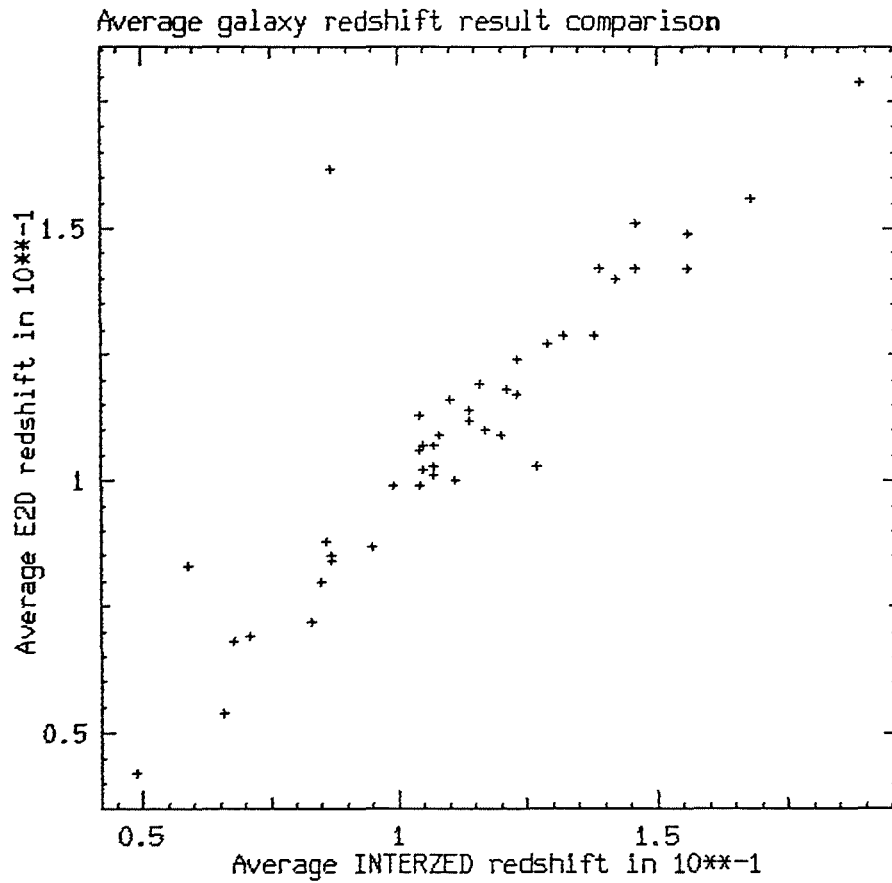


Figure 3.15 Comparison between average objective-prism redshift results for galaxy spectra from the E2D and INTERZED techniques.

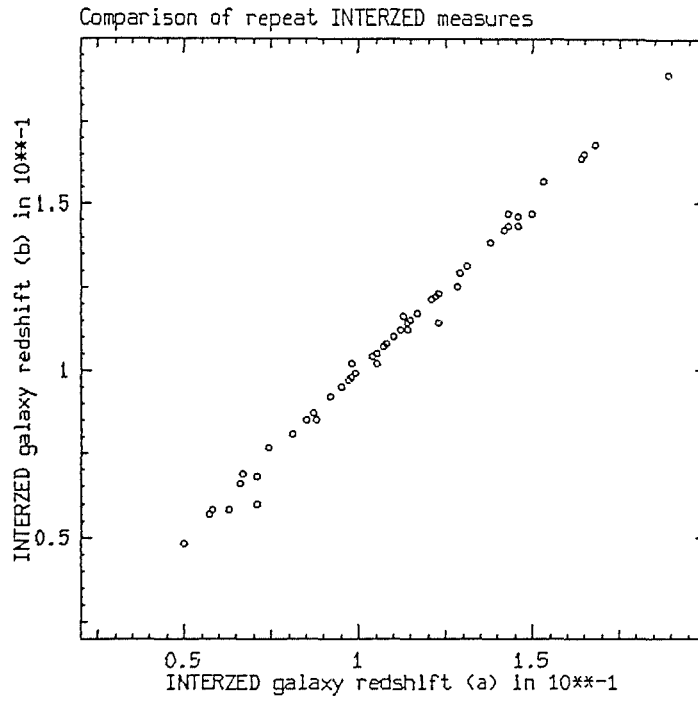


Figure 3.16 INTERZED result consistency from repeat measures of the same spectra.

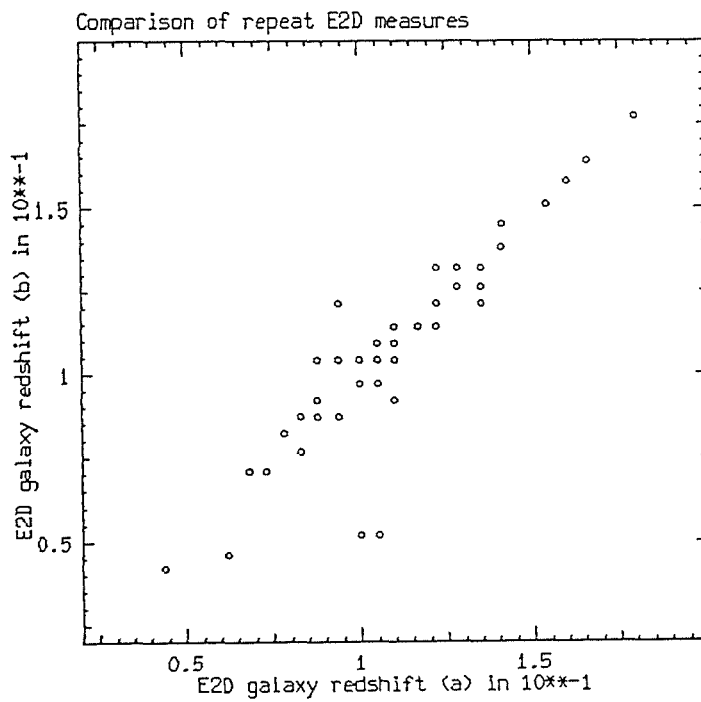


Figure 3.17 E2D result consistency from repeat measures of the same spectra.

Hence, though there is evidence for a slight positive offset between the INTERZED/E2D stellar and galaxian results in that the INTERZED results yield slightly more positive redshifts than the E2D results, the magnitude of this trend is 1/3 that of quoted objective-prism redshift accuracy assessments of  $\pm 0.01$  (e.g. Cooke, 1980), and not as significant as the differences found between intensity and non-intensity converted Cosmos data (figure 3.1). In conclusion, although the E2D/INTERZED redshift results may be slightly technique-dependent the size of the discrepancy is small enough to cause no real concern.

Consistency of repeat measures from the different techniques can also be illustrated independently. Figure 3.16 is a plot of INTERZED results for the same galaxy sample measured twice over a 6-month period. There is excellent agreement between the repeat measures, illustrating consistent feature choice and feature mid-point choice in the same spectra over prolonged time intervals. The equivalent plot for the repeat E2D measures is given in figure 3.17. There is also very good agreement between the repeat measures, again made 6 months apart. The one discrepant point had been assigned low weight. The agreement is not as tight as in figure 3.16 but this is expected because of the coarser E2D positional resolution. Also a polynomial fit was applied to the ECO within the INTERZED technique which gave the same ECO mid-point position for separate re-measures. The necessity for manual ECO determination with the E2D technique provides a further source of redshift inconsistency over that of INTERZED where only the 4000Å feature position has to be determined interactively. Hence the INTERZED technique is a more consistent means of obtaining objective-prism redshifts from Cosmos data. The advantage of E2D is that prism plate image areas from Cosmos MM data can be examined on the ARGS screen. Hence identification of individual 2-D spectra is possible. Beard (1984), relied on visual classification of INTERZED

spectra into stars or galaxies. Cases of overlapping spectra are also less of a problem since the interactive positioning of a 'box' around each selected spectrum can be carefully made to obtain a 1-D spectrum in cases where the INTERZED technique would have failed. Furthermore, the size of the box could be varied quickly, unlike the 128 by 8 pixel box currently hardwired into the INTERZED software. A larger redshift sample may thus result with the E2D technique.

Comparison between the INTERZED and E2D results for a selection of stars and galaxies from post-phase 1 update Cosmos data is given in figure 3.18. The consistency between the results is again extremely good, and can be compared with figure 3.15 (averaged results from pre-phase 1 update Cosmos data). A number of discrepant points do exist where different features have been chosen. The discrepant points account for 11% of the galaxy sample, a higher percentage than for the stellar sample since 4000Å feature identification in galaxian spectra is often more difficult, hence leading to more cases of ambiguity. Being too severe in feature identification would drastically reduce the sample of galaxy redshift estimates. Selecting only the best 4000Å features would certainly yield a higher proportion of reliable redshifts but only for 20% of galaxies deemed to have measurable features. For measures of galaxy spectra in rich clusters, in the trade off between quality and quantity, the inclusion of a few discrepant redshifts from cases of feature mis-identification is acceptable. In such cluster studies, well suited to the manual and interactive techniques, individual galaxy redshift estimates are not important but only the determination of the cluster redshift peaks. Parker et al. (1984a,b), in an objective-prism redshift study of 13 rich clusters in field 349 using Cosmos data, found that the distribution of redshifts assigned weights 3 essentially mimicked that from weights 1 and 2. Hence, although the numbers of discrepant redshifts in a sample is generally unknown, they are likely to be a

small fraction of the total because of the general agreement between cluster peak redshifts from high- and low-weight features.

With the advent of a completely automatic objective-prism redshift technique, feature mis-match between repeat measures would be removed along with other manual inconsistencies. This does not imply that all redshifts will be reliable. Great care must be taken in the development of an optimum automatic reduction technique since over an entire Schmidt plate the possible numbers of discrepant redshifts may not be inconsiderable. Indeed Cooke et al. (1983,1984), gives results of an initial comparison between a preliminary automatic technique and a manually determined sample of 2000 galaxian objects identified from their spectral appearance, Beard (1984). A plot of automatic versus INTERZED redshift revealed parallel sequences  $\pm 0.08$  in redshift above and below the  $45^\circ$  line. This effect was partly due to contamination by 15% stars in Beard's sample and partly due to difficulties with the automatic technique with spectra of low S/N. Faint, late type stars can exhibit a feature at  $\lambda 4470 \pm 80\text{\AA}$  which can give the appearance of a galaxy at a redshift of 0.10-0.14 (Beard, 1985). Also some galaxy spectra possess a prominent Balmer jump at  $\lambda 3650\text{\AA}$  which may also be mistaken for the  $4000\text{\AA}$  feature, in which case a redshift estimate which is 0.10 too low is obtained. This mis-match of identified features could explain the parallel sequences found in plotting automatic redshifts against corresponding manual estimates. If the automatic technique chose the true  $4000\text{\AA}$  feature whilst the manual measure had used the Balmer jump by mistake, then the automatic result would be 0.10 in Z higher than the manual result. Conversely, if the automatic method had erroneously used the Balmer jump feature whilst the manual measure had used the true  $4000\text{\AA}$  feature, then the automatic technique would yield a redshift 0.10 lower than the manual measures. The redshift difference in choosing the Balmer jump as the  $4000\text{\AA}$  feature is only a slowly changing

function of increasing redshift, i.e. from 0.096 at  $Z=0.01$  to 0.107 at  $Z=0.09$ . Hence the parallel sequences in fact diverge slowly with increasing redshift. This trend is not marked over the redshift range covered ( $Z=0.0-0.20$ ) and would probably be smoothed by scatter.

### 3.10. Comparison between Cosmos and Joyce-Loebl redshift results

Consideration is now given to the result consistency achieved from using Cosmos post-phase 1 update data with INTERZED and E2D and from J-L measures of the same spectral sample. We might expect poor agreement since the J-L gives density not intensity spectra and because the different machine characteristics may affect the reproduction of spectra.

Figure 3.19 is a plot of E2D redshifts versus their J-L counterparts for a sample of stars and galaxies, whilst figure 3.20 is the corresponding comparison between INTERZED and J-L results. Figure 3.18 reveals substantially better agreement between results from the interactive methods using Cosmos data than between J-L measures and either of the other techniques. The scatter in figures 3.19 and 3.20 is twice that of figure 3.18. The majority of points lie within  $\pm 0.02$  of the  $45^\circ$  line. The agreement is marginally improved for the stellar results. Figure 3.20 has evidence of the parallel sequence where a significant number of feature mis-matches exist between INTERZED and J-L results. Feature mis-matches are probably due to inconsistencies in human judgement and in spectral reproduction by the different measuring machines. A considerable amount of experience of visual examination of objective-prism spectra of stars and galaxies is necessary even to obtain the consistency illustrated from repeat measures of the same data from the same machine.

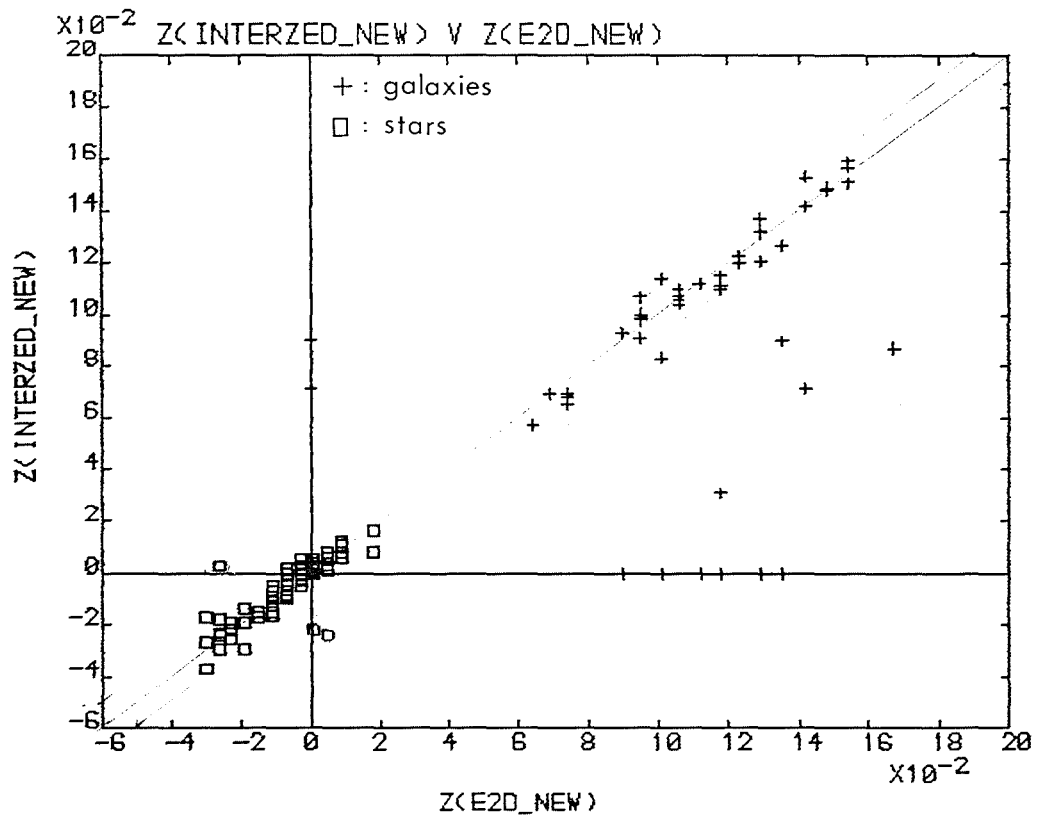


Figure 3.18 INTERZED versus E2D redshift results for a selection of stars and galaxies from intensity converted, post-phase 1 update, COSMOS data.

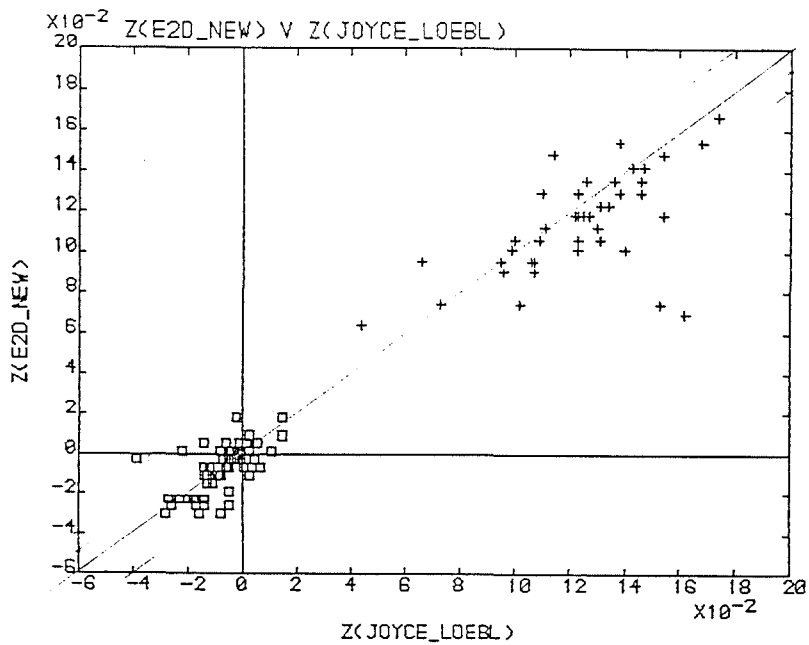


Figure 3.19 E2D versus Joyce-loebl objective-prism redshifts for a selection of stars and galaxies.

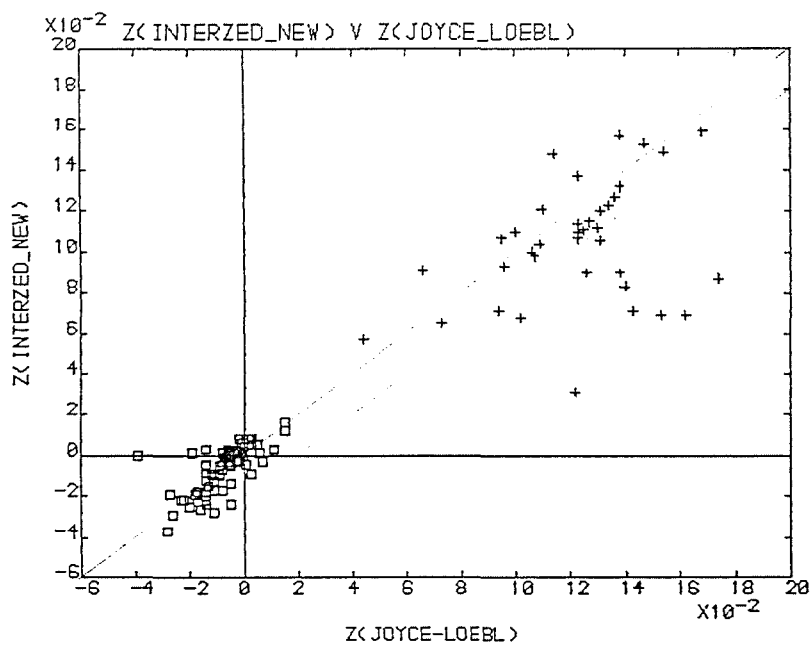


Figure 3.20 INTERZED versus Joyce-loebl objective-prism redshifts for a selection of stars and galaxies.

Another feature of figures 3.19 and 3.20 is that the J-L results appear to yield a higher proportion of more positive redshifts, even for fainter galaxy spectra. This result is expected for brighter spectra (see figure 3.7) but is contrary to expectations for fainter spectra. Here intensity conversion and Cosmos dynamic range limitations are not so important since the spectra lie in the unsaturated régimes of both machines. This effect must be due to some other factor. Figure 3.21 is a plot of magnitude estimate versus the redshift difference between the J-L and E2D redshifts. We might expect the faintest low S/N objects to be more prone to feature mis-match as 4000Å feature identification becomes difficult. Discrepant points in fact occur over a wide magnitude range. An interesting feature of figure 3.21 is that nearly all the discrepant points arise from J-L spectra being assigned higher redshifts than their INTERZED equivalents. Five of the twelve discrepant points have redshift differences of  $DZ = 0.08-0.10$ , which is what one would expect if the Balmer jump had been mistaken for the 4000Å feature.

The significant number of discrepant redshifts and greater dispersion between the Cosmos and J-L results than between repeat measures of each technique separately may all be symptoms of the way the photographic spectral information is reproduced by the different measuring machines. The appearance of the spectral tracings from INTERZED and E2D are substantially similar but both differ markedly in some cases from corresponding J-L tracings. For stellar spectra these differences are not too severe because the 4000Å feature is often very strong and unmistakable, even though the spectra may be quite different in appearance in other respects. In fact the scatter in the stellar results is not unreasonable considering the different machine dynamic ranges and comparing density and intensity converted spectra.

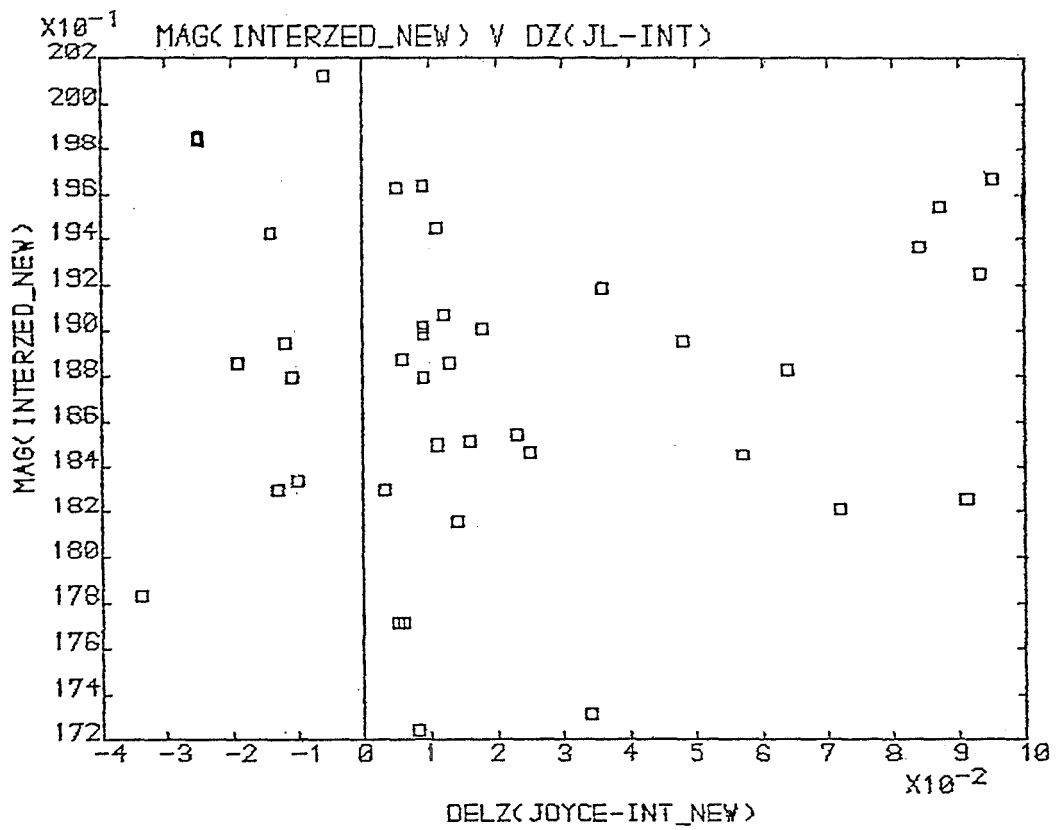


Figure 3.21 COSMOS prism magnitude versus the difference between objective-prism redshifts from the Joyce-loebl and INTERZED techniques.

For the lower S/N galaxy spectra though, the situation is somewhat different. This lower S/N means that the position, slope, strength and general form of any 4000Å feature is more sensitive to variations in the way each spectrum is reproduced by each technique. This is particularly true in comparisons between the J-L and INTERZED/E2D spectra where noticeable differences are often evident. In assessing the causes of redshift discrepancies between each method the following factors prove to be important:-

For relatively bright spectra of high S/N, the redshift anomalies are caused by effects of saturation on ECO and feature mid-point positions due to the different machine dynamic ranges and the effects of comparing density with intensity spectra. For fainter, lower S/N spectra, the gross redshift differences are due to complete feature mis-match between separate measures as it is more difficult to unambiguously identify the correct feature. Differences are also due to the measuring machines affecting the way each spectrum is reproduced, since the noise characteristics of each machine will affect the appearances of features in lower S/N spectra. This could account for both the large and small discrepancies.

Obviously, these factors will affect the sample size of examined spectra deemed to have measurable features, particularly at the low weight end. Intercomparison with the E2D and INTERZED methods revealed that for independent re-measures over the same plate area, substantially the same sample of objects yielded redshifts. However, comparison between these methods and the J-L method revealed that consistency of sample size was a more serious problem. From a sample of ~100 galaxy spectra about 13% assigned redshifts from the J-L measures had been considered unmeasurable with INTERZED. Also 20% of those features assigned redshifts in the INTERZED case had been unmeasurable with the J-L. Examination of the weights given to these spectra showed, that as expected, they were nearly all low weight

features. This analysis indicated that 50% of the INTERZED sample that had weights 3 or 3+ would not have been given a redshift in the J-L sample.

Initial conclusions are that sample-size-and-redshift-result consistency are quite sensitive to the measuring machine used. The major contribution to the sample size and redshift anomalies come from measures of spectra assigned low weights within each technique. These are usually fainter, low S/N spectra whose features and spectral quality can be adversely affected by the influence of the measuring machine instrumental profile. A few examples of INTERZED and J-L galaxy tracings from the copy plate UJ5402P P2N1 are given to illustrate some of the points raised above (figure 3.22 a-c). How spectra are extracted from J-L plate measures and from Cosmos MM data is now described.

### 3.11. Effect of variations in Instrumental settings on the results and reproduction of objective-prism spectra

#### 3.11.1. The Joyce-loebl microdensitometer

When measuring objective-prism spectra, regardless of technique, it is desirable to recover the maximum spectral information. Cooke (1980), on experiments with J-L instrumental settings, derived what he concluded to be optimum values of slit height and width for obtaining the best noise characteristics and information recovery of faint galaxy spectra. Obviously the J-L slit height and width defines the plate area sampled by the microdensitometer system at any one moment. The intensity of light projected through this aperture onto the plate is matched by the step wedge and translated into a recording of the average density of the plate at that point.

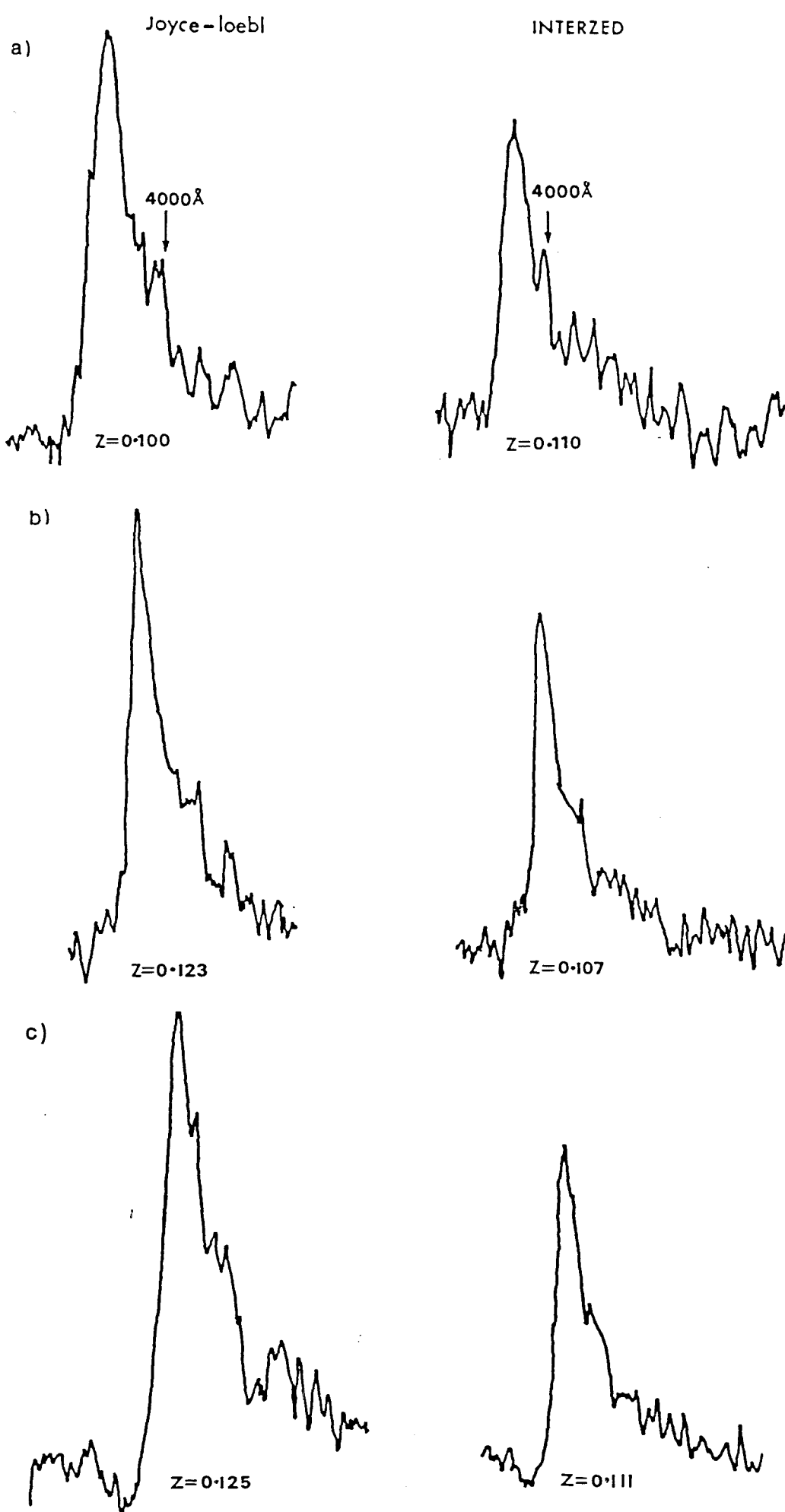


Figure 3.22a-c Examples of objective-prism spectral tracings from measures with the INTERZED and Joyce-loebl techniques on the copy plate UJ5402P P2N1.

As the plate is moved continuously across the path of the beam, a running average of relative plate density is produced and recorded by a pen tracing, incorporating the smoothing effects of the slit settings. A ratio arm of 50:1 was used to get the maximum scaling of the spectral tracings. Cooke found that when the slit area was small, machine noise became dominant because the light intensity reaching the photomultiplier is small. Too narrow a slit would average transmissions of only a small number of emulsion grains, giving rise to correlated noise due to grain clusters and Poisson noise from the electronics etc. A widened slit averages out this noise but also reduces the resolution. The slit height determines what regions of the total spectrum are sampled. This is an important variable because of the range of widths of objective prism spectra; e.g. a narrower slit height centred on the nuclear regions of a spiral galaxy will give a better 4000Å feature than a slit height which encompasses the entire spectrum, since it is the late-type stars in the nucleus which produce the 4000Å feature. Cooke's optimum choice of slit height and slit width of 34 μm and 50 μm on the plate were generally used with J-L galaxy spectra measures as checks using combinations of these settings usually vindicated his choice, at least for relatively faint galaxies. An advantage of using constant slit height is that the relative densities of different spectra can be compared. The ECO peak height above sky can be related to a relative density above sky by using the density gradient of the step wedge. This parameter can assess the relative brightness of each spectrum in a crude fashion over a limited density range.

In reality, an optimum combination of J-L slit parameters exists to best represent each object's spectrum. Galaxies are extended objects and therefore have spectral diameters which are dependent not only on the luminosity of the object but also on the projected angular diameter. For fainter galaxy spectra, information is at a premium so the slit height should contain all exposed galaxy grains and exclude all background sky which degrades the S/N noise. Some flexibility in chosen slit height is necessary since using a slit height appropriate for faint galaxies may mean that in measures of brighter spectra valuable information is being discarded. Furthermore, as already noted, concentrating on the nuclear regions of early spiral galaxy spectra can highlight a 4000Å feature that would otherwise be swamped. Ideally the optimum slit parameters would be used for each given spectrum. This is impractical with the J-L measures because of the time required but may be possible with the Cosmos machine. Work along these lines has already commenced with the APM facility at Cambridge.

For measurement of stellar spectra a variety of slit heights were employed. Stars are assumed point sources so their spectral diameters on the plate perpendicular to the dispersion direction depend on their magnitudes. Bright stars exhibit a wider spectrum than fainter ones. Tapering of the spectrum's width from the long-wavelength to the short-wavelength region also occurs and is a function of object colour. Consequently the slit height was matched to the physical diameter of the stellar spectrum to obtain good tracings. With too narrow a slit the dynamic range of the J-L would be exceeded and no tracings could be obtained. A more dense wedge would need to be employed to attempt to alleviate this problem.

A complication with J-L measures is scattered light around the edges of spectra. This causes premature saturation in some brighter images if the J-L iris setting does not match the slit height, as noted by Cooke (1980). The need to adjust the iris setting for each spectrum lengthens the time for manual measurements. To ascertain if the iris setting was an important factor affecting the redshifts from brighter spectra a selection of stellar spectra were measured with the iris both wide open and closed down to the slit height. We might expect any underestimate in the peak density on the plate due to scattered light to manifest itself in an underestimate of the ECO mid-point position. In fact the redshifts from the separate measures indicated that a significant but small effect was present. The 'open iris' configuration yielded more negative stellar redshifts than the corresponding 'iris closed' measures; on average by  $-0.036$  ( $\sigma = 0.036$ ,  $N=20$ ). Consequently, for manual J-L measures of objective-prism spectra, it is good practice to modify the iris setting to match the slit height as this alleviates, but does not eliminate, the trend to negative redshifts with increasing image brightness.

Tracings were made of a few stellar spectra of various magnitudes and with various slit heights. These measures revealed that the separation between ECO mid-point position and  $4000\text{\AA}$  feature was essentially independent of slit height. This justifies use of wider slits for stellar spectra. If the slit height used for galaxian spectra was used for measures of brighter stellar spectra the amount of transmitted light reaching the photomultiplier would often be insufficient to accommodate the J-L density wedge used and no tracing could be obtained. Increasing the slit height for these spectra, so that the entire width of the spectrum is sampled, results in satisfactory tracings. The new slit-height settings would be closer to the  $128\ \mu\text{m}$  width box used by INTERZED and E2D.

### 3.11.2. The Cosmos measuring machine

The quality of spectra produced with Cosmos is determined not only by the machine dynamic-range limitations and the pixel size but also by the box size placed around spectra before summation to 1-D. For the Cosmos measures described so far a 16  $\mu\text{m}$  spot and 16  $\mu\text{m}$  increment were used as these values have been found to produce the best prism MM data. Hence the MM data consist of an array of contiguous 16  $\mu\text{m}$  square pixels, each with a transmission value between 0 (clear plate) and 255 (blackened plate). Each transmission value is an average of the emulsion grain densities in each pixel so this effectively limits the information resolution.

To extract the spectra from a prism-plate MM file for measurement by INTERZED, percentage threshold and area cuts are applied (see the Cosmos user manual). The values chosen affect the sample size of extracted spectra. The pixel area cut is chosen to be large enough so that large numbers of spurious images are not extracted. The percentage cut applies an isophotal threshold to the data which determines whether pixels a certain intensity fraction above the night sky are deemed to belong to an image. Hence, for a given area cut, increasing the percentage cut will exclude more faint images, e.g. for a small MM area, 360 spectra were extracted with a 5% cut and only 284 with a 7% cut. However, use of different percentage cuts hardly affects the selected object magnitudes while the redshift results still give excellent agreement. Small changes in the parameters used to extract prism spectra from a MM file do not therefore affect the resultant objective-prism redshifts significantly.

Most INTERZED and E2D results were obtained using a 128 by 8 pixel box centred around each detected or chosen spectrum. Ideally instrumental settings ought to be modified according to the spectrum considered as already stated. An algorithm which automatically places an optimum box size around each detected spectrum would be desirable. For instance, faint spectra, whether they are stellar or galaxian, tend to be narrower than for brighter objects. Consequently, in summation from 2-D data to 1-D within each 128 by 8 pixel box, more background sky pixels are included. Spectra of low S/N may therefore be adversely affected by inclusion of significant numbers of sky pixels in summing to 1-D. Weak features may be submerged and false features may arise due to chance coincidences of noise spikes. Conversely, brighter spectra with strong features are little affected by inclusion of moderately large numbers of background pixels.

After most INTERZED and E2D measures had been performed the E2D software was upgraded to allow different box sizes. Also a sample of spectra extracted using a 128 by 16 pixel box were measured using INTERZED. A comparison between the results from using different box sizes was made to see if the predicted effects are observed (the default box width of 8 pixels, equivalent to  $128 \mu\text{m}$ , compares with the J-L "optimum" slit height of  $34 \mu\text{m}$ ).

First, the effect on measured redshifts of using a 128 by 8 and 128 by 4 pixel box with E2D was considered. The results, mostly for galaxy spectra, are given in figure 3.23. There is good agreement with virtually all points evenly scattered and lying within the  $\pm 0.01$  redshift bounds of the  $45^\circ$  line. Use of a narrower box does not seem to have had a great effect on the results obtained. Examination of the weights assigned and comments associated with the measures however, revealed that feature ambiguity was resolved in some cases and introduced in others. This affected the weights given but not

usually the redshifts. Experience showed that altering the box width did have an advantageous effect in some instances where a doubtful feature was enhanced. Occasionally an apparent feature disappeared or ambiguity was introduced. Generally if a feature is enhanced on narrowing the box width then it is likely to be genuine whereas if increasing the box width brings out a feature then it is more likely to be due to chance noise fluctuations from inclusion of more background pixels.

To highlight the effects of including too many sky pixels in forming 1-D spectra, a comparison was made between INTERZED results from spectra extracted with 128 by 8 and 128 by 16 pixel boxes. The results are shown in figure 3.24. The stellar redshifts are little changed because the high S/N features are not significantly affected by inclusion of quite large numbers of background pixels. The galaxy results though do occasionally exhibit substantial discrepancies since the lower S/N features are more sensitive to inclusion of extraneous pixels. Figures 3.25a-c give examples of how 3 galaxy spectra are modified after summing to 1-D from 128 by 8 and 128 by 16 pixel boxes. A larger width box (16 pixels) was used than would normally be employed to illustrate the effect more clearly. Obviously instances of overlapping spectra are increased by using wider boxes. The above convincingly shows that galaxy spectra redshifts are sensitive to both the machine used and the manner in which the spectra are extracted.

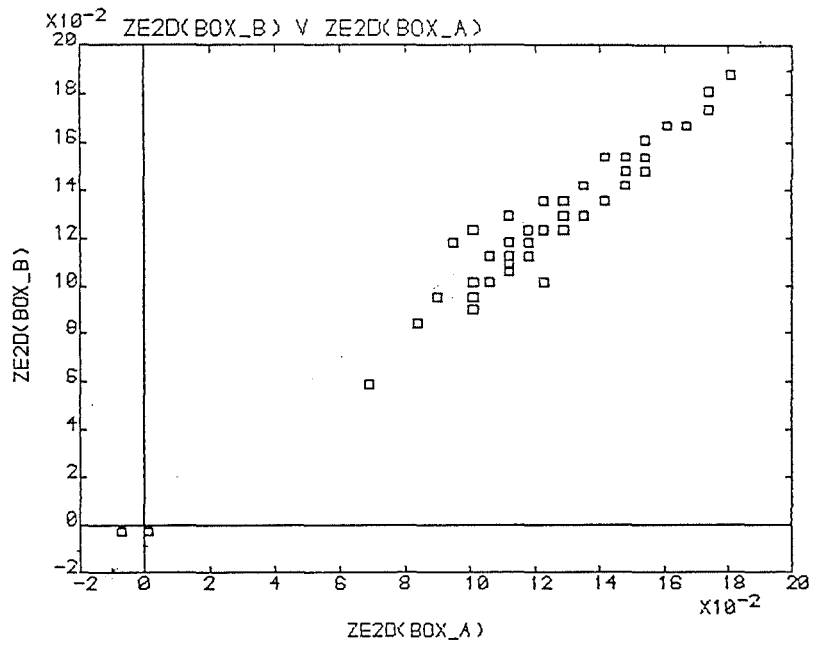


Figure 3.23 Comparison of E2D redshifts from using a 128 X 4 and 128 X 8 pixel box within which to sum the 2-D data to a 1-D spectrum.

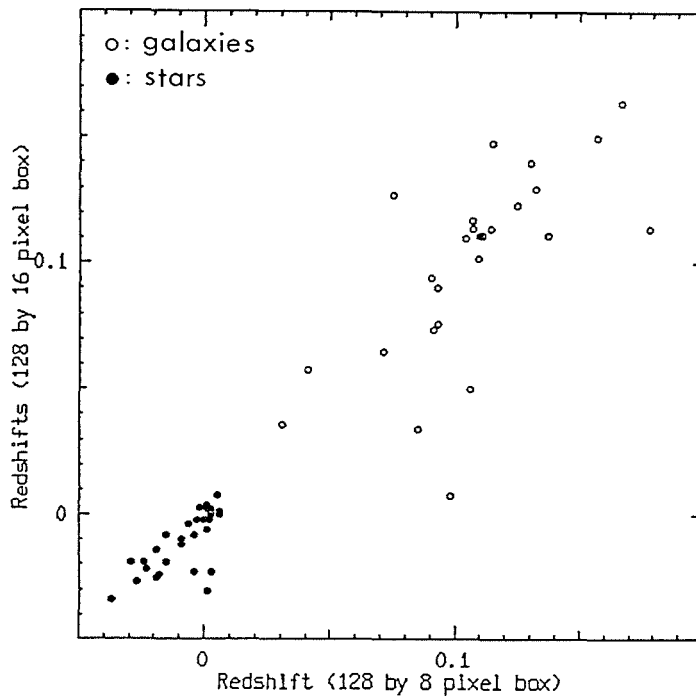
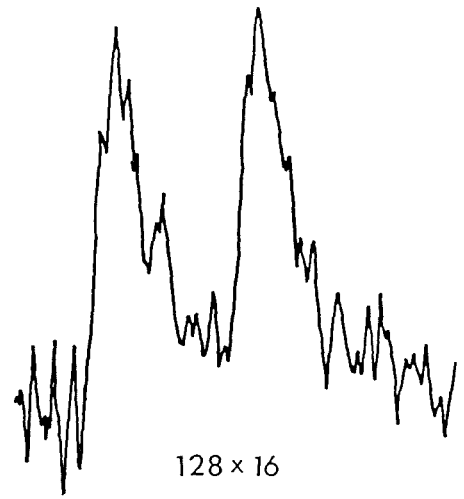
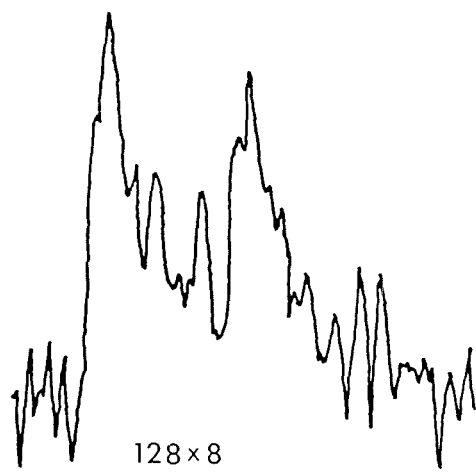
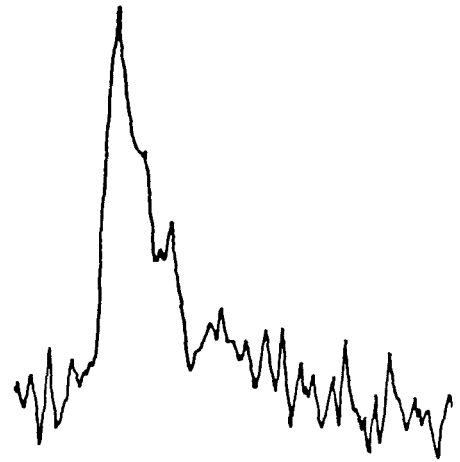
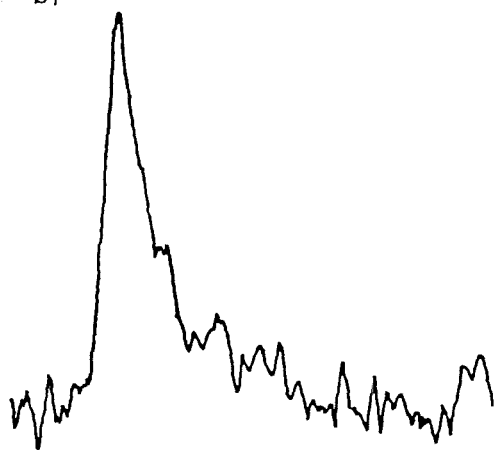


Figure 3.24 Comparison of INTERZED redshifts from using a 128 X 16 and 128 X 8 pixel box within which to sum the 2-D data to a 1-D spectrum.

a)



b)



c)

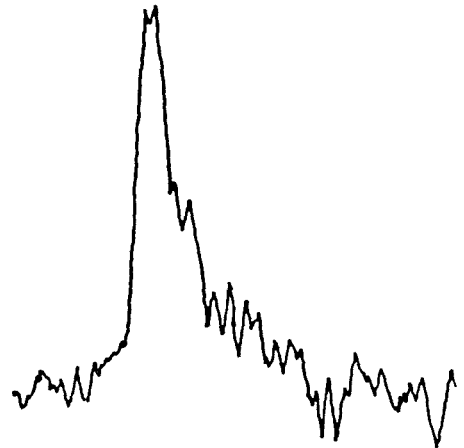
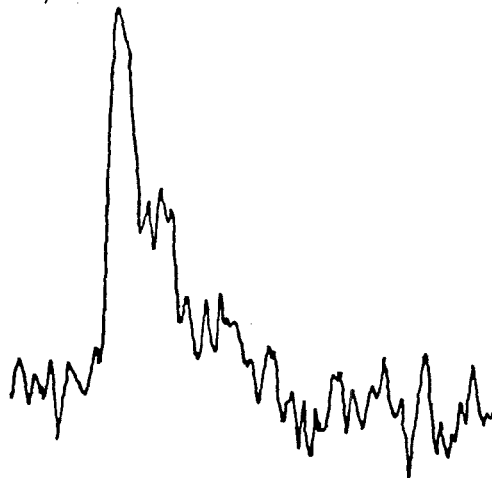


Figure 3.25a-c Examples of objective-prism spectra summed to 1-D when a 128 X 8 and a 128 X 16 pixel box was used.

All results from J-L and Cosmos measures of objective-prism spectra have so far been performed on a high-quality copy plate of the original UJ5402P. The quality of this plate was verified by plate library staff at ROE. Often original plates are unavailable for measurement because they are atlas quality or are abroad or damaged. Use of high-quality copy plates has been encouraged for many astronomical projects. Beard (1984), based his work on the Indus supercluster from measures of objective-prism spectra from copy plates. Generally good agreement was found for the objective-prism redshifts from both copy and original plate. However, the greater noise characteristics of some copies could exaggerate spectral features. Hence many features not accepted on the original plate were taken to be real on the copy. He concluded that it is easy to mis-identify  $4000\text{\AA}$  features on plates to which the observer is unaccustomed.

The effect of using copy plate instead of original plate material for the objects studied was also investigated after the return of the original plate from Australia. Before discussing the comparison it is appropriate to describe the photographic process for creating copy plates. This may help in understanding the likely effects of using copy plates with regard to the fidelity of objective-prism spectra.

### 3.12. The photographic copying process.

Details of making glass and film copies of original UKST plates are given by Standon and Tritton (1979), Eccles, Sim and Tritton (1983), and Bruck and Waldon (1984). The ideal of any plate copying process is not to change the astronomical information from original to copy. This ideal is never realised. For UKST plates the aim is to reproduce as closely as possible the properties, positions etc of all faint images in a consistent and heterogeneous manner over the entire

plate. That is, the copying process is optimised for the faintest images. This has serious consequences for the brighter images which may be reproduced at very low contrast.

The IIIaj emulsion has a wide dynamic range. Ansi diffuse densities  $\sim 4.0$  can be recorded. Unfortunately no photographic process yet available can maintain a linear relationship between density and exposure over such a range. Instead the 'characteristic curve' describes how recorded plate density varies with exposure ( $\log[\text{intensity}]$ ) for any particular emulsion. This curve deviates from linearity at both high and low densities.

Copy plates are produced first by making contact intermediate positives, and then by obtaining a negative copy of the positive. For typical UKST original plates the chemical fog density is  $\sim 0.4D$  while the sky background is generally  $\sim 1.3D$ . On the positive copy, to retain the information on the original, a sky background density of  $\sim 2.0D$  would be needed. In fact most positives are reproduced with a sky background of only  $1.5D$ , since higher background densities on the intermediate positive would require prohibitively long exposure times. This lower background density of  $1.5D$  is a compromise between conflicting requirements to have this value as large as possible so that a larger range of densities can be linearly copied and of impracticably long exposure times. The final copy-plate-background density is usually  $0.5D$ , chosen so that visual inspection of faint objects is easier. The copying gamma is given by  $dD_a/dD_b$  where  $D_a$  is the original plate density and  $D_b$  that of the final negative copy. If this copy gamma could be made unity over the whole original plate density range then the densities of original and copy would agree everywhere.

In practice it is impossible to exactly reproduce the density and contrast of an original plate. Information is lost in obtaining the intermediate positive because of the long exposure times that would be needed to get the high sky-background density. Since the astronomical purpose of the copying process was to produce a very deep survey, the copying gamma was kept close to unity at the sky density to reproduce faint images as faithfully as possible. Unfortunately the copying emulsion saturates at 2.0D, so that copies only have a density range of 0.5 to 2.0D. This leads to a loss in contrast at higher densities. Consequently we might expect to have a copy plate that recovers information on faint images, has the same slope of the linear portion of the characteristic curve as the original (i.e. copying  $\gamma$  of  $\sim 1$ ) over a density range that includes the sky density but which does not cover the full density range of the original. To demonstrate the effect this will have on the information content of bright spectra, schematic representations of characteristic curves of original and copy plate are shown in figures 3.26 and 3.27.

Consider an object which is 1.7D above sky at its peak on the original plate, i.e. at a density of 3.0D. By reference to figure 3.26, this object still lies on the straight line portion of the CC. On the copy plate though, the same object lying 1.7D above sky is on a portion of the curve that deviates significantly from linearity. In this region the contrast is drastically reduced. This could result in a loss of 0.6 magnitudes at the bright end of the density range between original and best copies (Bruck and Waldon, 1984). Consequently, feature resolution in bright copy-plate spectra may be considerably reduced compared with the original plate. Furthermore, because light is scattered in the emulsion when making a copy plate, and since the original plate grain pattern is also 'copied', the copy plate S/N characteristics are likely to be worse than for the original. The S/N properties of the measuring machine used to scan

the plates should also be considered. Thus, because measuring machines generally have poor S/N characteristics at high densities, the combined S/N of plate and measuring machine might be superior for bright objects on a good-quality copy plate made at reduced density than for an original.

When comparing objective-prism tracings from original and copy plates, a number of competing factors influence the resultant spectrum. For bright copy-plate spectra features will be compressed due to the reduced contrast. This results in less distinct features appearing higher up the continuum relative to the peak and also in relatively smooth spectra because of the contrast reduction and because of the reasonable S/N characteristics. For the original plate a larger density range is linearly accommodated so that features in brighter spectra are more clearly resolved and more accurately positioned up the continuum relative to the peak density. However, the S/N properties of the measuring machine may begin to dominate at high densities so that denser regions of the spectra become noisy.

For fainter spectra, the differences between copy plate and original plate measures are expected to be slight since the copying process was optimised to recover information for faint images. Nevertheless, for very faint spectra, the combined S/N of the measuring machine and plate may be worse for the copy than for the original. This S/N difference may be sufficient to affect the strength and appearance of spectral features in these spectra. This could have important consequences for galaxy objective-prism redshifts since the bulk of the galaxy spectra are relatively faint.

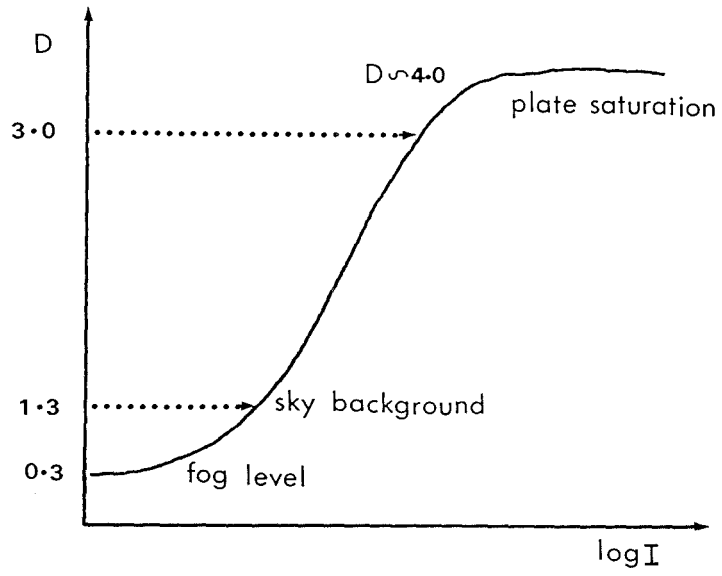


Figure 3.26 Schematic representation of the characteristic curve from an original plate.

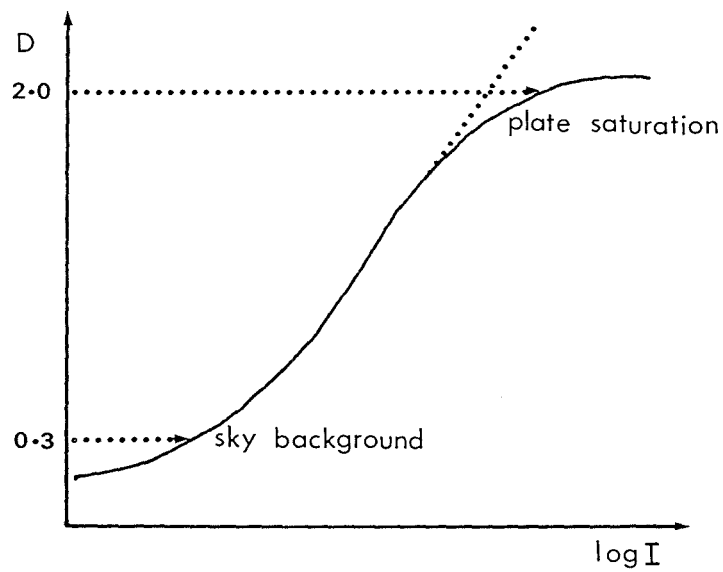


Figure 3.27 Schematic representation of the characteristic curve from a copy plate.

From the above discussion, an investigation into the effects of using copy and original objective-prism plates on galaxy spectra redshifts is very important. The strong mag/Z effects found from copy plate stellar measures with Cosmos data, and, to a lesser extent, with J-L data, are partly due to effects of copy plate reduced contrast in bright images and partly due to machine dynamic range limitations and the problems of correctly converting Cosmos data to intensity. More importantly, if copy plates are to be an acceptable medium for objective-prism redshift studies, then the copy-plate results must be in good agreement with those from the original or at least a clear understanding of the causes of any discrepancies must be obtained so that the bounds of compatibility can be determined.

Before discussing the findings of this investigation the results of scanning the sensitometer steps on the copy and original plate are presented. Figures 3.28a-b refer to J-L measures of the north seven step wedge on the original and copy plates UJ5402P and UJ5402P P2N1. Differences in the relative heights of each step above chemical fog are evident, especially between the most dense steps 1 and 2 where the reduction in contrast between original and copy is obvious.

The sensitometer spots on the original plate come from exposure to light of known relative intensity. Hence the photographic density of each spot can be related to the relative intensity of incident light during the exposure. The  $\text{Log}(\text{relative intensity})$  values for each step in the wedges on the plate are given in the UKST handbook. Characteristic curves can be drawn from a knowledge of the density slope of the J-L wedge used and the tabulated  $\text{Log}(\text{rel.intensity})$  values for the measured steps. Comparison of the CC from the step wedge on the original plate with that from the copy plate should indicate how well the information content of the original is reproduced on the copy with changing density.

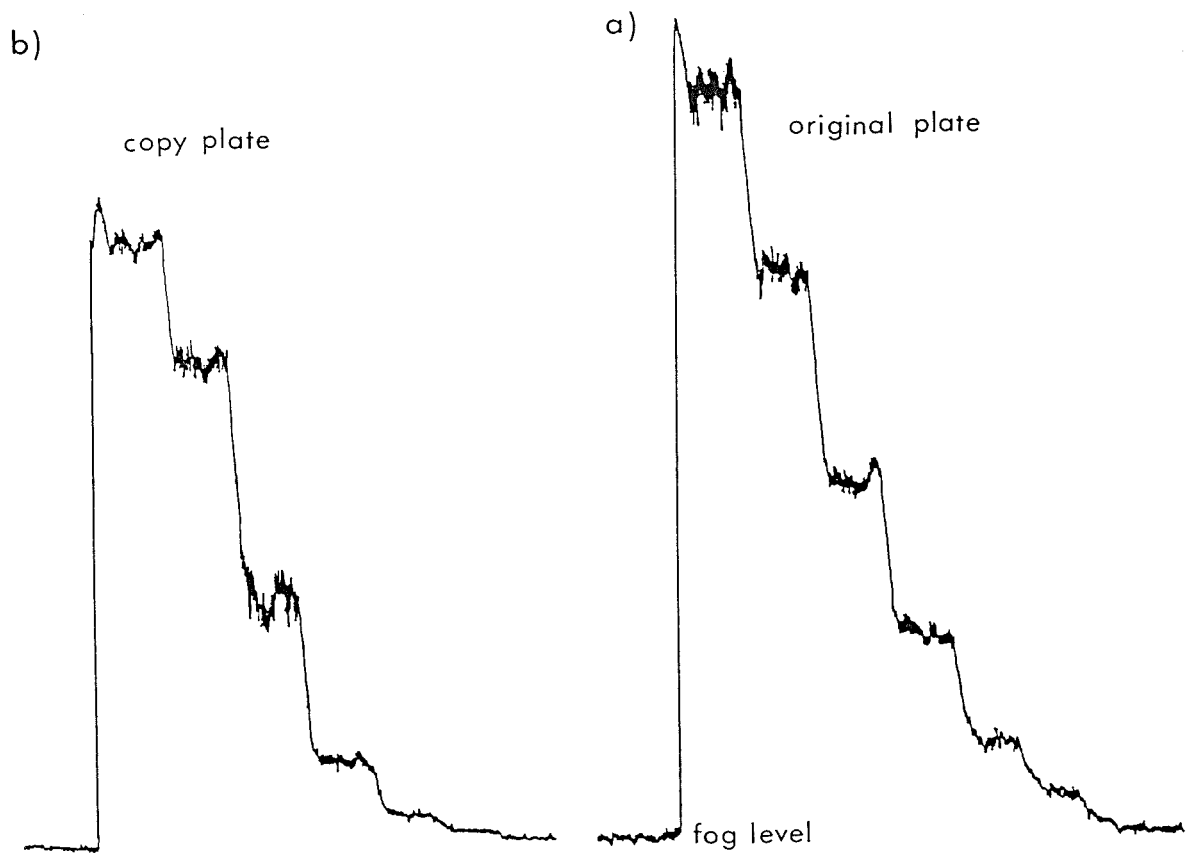


Figure 3.28a-b Joyce-loebl tracings of the north 7-step wedge on the original plate UJ5402P and the copy plate UJ5402P P2N1.

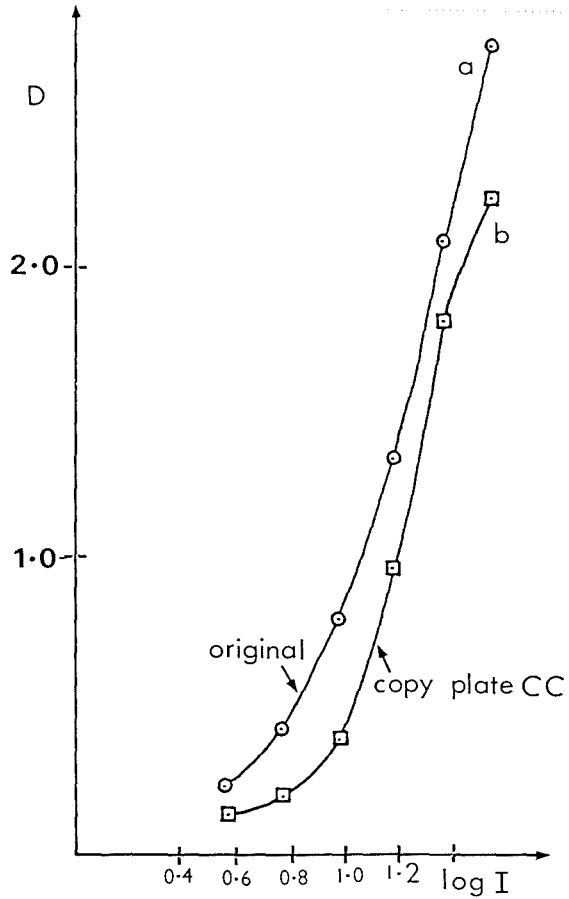


Figure 3.29a-b The characteristic curves derived from the step-wedge tracings in Figure 3.28a-b.

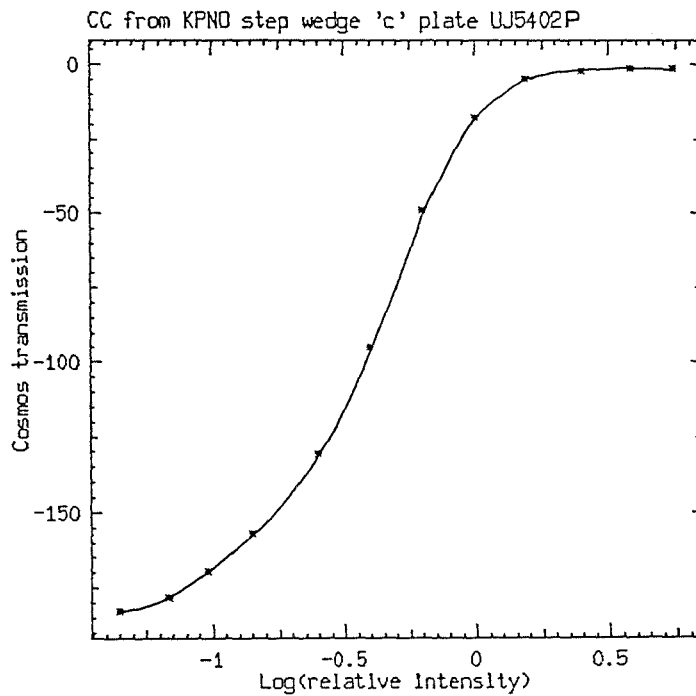


Figure 3.30 The characteristic curve derived from Joyce-Loebl measures of the 16 step KPNO wedge on original plate UJ5402P.

These curves, from measures of the seven step wedge with the J-L, are given in figures 3.29a-b. These figures reveal that for the copy plate the CC is already deviating from linearity at  $\sim 1.9D$  above sky whereas the original plate CC continues to be linear up to the last plotted point. As anticipated, the copy plate straight-line portion of the CC covers a somewhat narrower density range. Also the slopes of the straight line portions of the curves do not agree, although they are in much closer agreement near the sky background on both plates. The original plate CC from measures of the 16 step KPNO wedge is given in figure 3.30.

Having discussed the likely effects on prism spectra from using copy instead of original plate material, real measures of the original plate were performed both with the J-L and with Cosmos. The comparisons from using J-L measures are presented first.

### 3.13. Comparison between J-L measures of objective-prism spectra for stars and galaxies from original and copy plate material.

Plates UJ5402P and UJ5402P P2N1 were employed. The same sample of stars and galaxies measured on the copy plate were re-measured on the original. The results from the two different plates are illustrated in figure 3.31. Very good agreement in the stellar results is evident and reasonable agreement exists between the galaxy measures. The strong trend to negative redshifts for bright stars is still found in original plate data using J-L density spectra. Figure 3.32 gives a plot of estimated object magnitude versus redshift difference between copy and original plate results. This diagram shows that:-

- (a) The results agree to within  $\pm 0.01$
- (b) There is no significant magnitude dependence on the redshift difference.

(c) There is an indication that the copy plate measures yield more positive redshifts for the stellar spectra

This last effect, though weak, is opposite to what we might have expected from our earlier discussion. Using original plate stellar spectra measures has not led to a decrease in the trend to negative redshift with decreasing magnitude; if anything the opposite is true. Perhaps the sample of stars measured were not sufficiently bright that contrast loss in the copy plate spectra was enough to significantly affect the mid-point positions of the ECO and 4000Å feature in the J-L density spectra.

A possible cause of this marginal trend is obtained by examining the appropriate J-L tracings of the same spectra from both copy and original plate. It must be remembered that the copy-plate sky level is at a density of  $\sim 0.3D$  whereas that on the original is  $1.3D$ . Figures 3.33a-b are J-L tracings of a relatively bright star from the copy and original plates. Note that the observed sky to peak distance for the copy plate spectra is greater than for the original and that the 4000Å feature size also appears greater for the copy. However, the actual peak photographic density of the copy-plate spectrum is less than for the original because of the different sky-background densities of the plates. Consequently, the trend for the original J-L stellar results to yield more negative values could be because density not intensity converted spectra were reduced. This gives an exaggerated description of ECO and 4000Å feature strengths in the copy plate because of the low sky background. Simple J-L density spectra are unsuitable for measures of brighter spectra in any case, but galaxy results could be calibrated by reference to stellar redshifts or better still the spectra could be intensity converted, Cooke (1980).

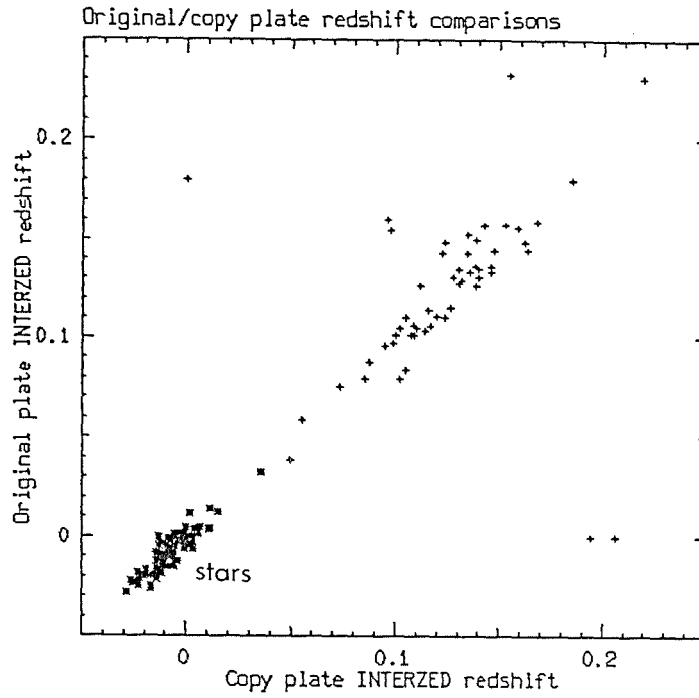


Figure 3.31 Comparison between Joyce-loebl redshifts from measures of the same sample of stars and galaxies on the original and copy plates UJ5402P and UJ5402P P2N1.

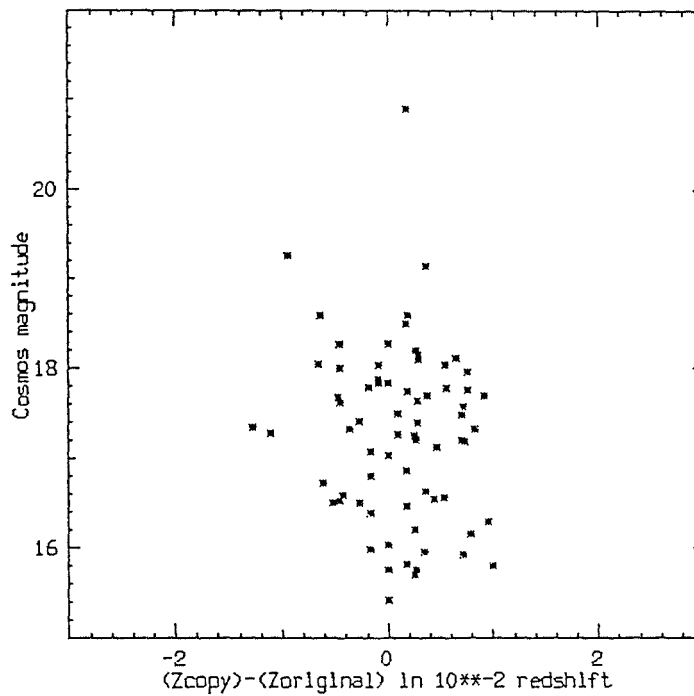


Figure 3.32 COSMOS prism magnitude versus the redshift difference between measures of the copy and original plate.

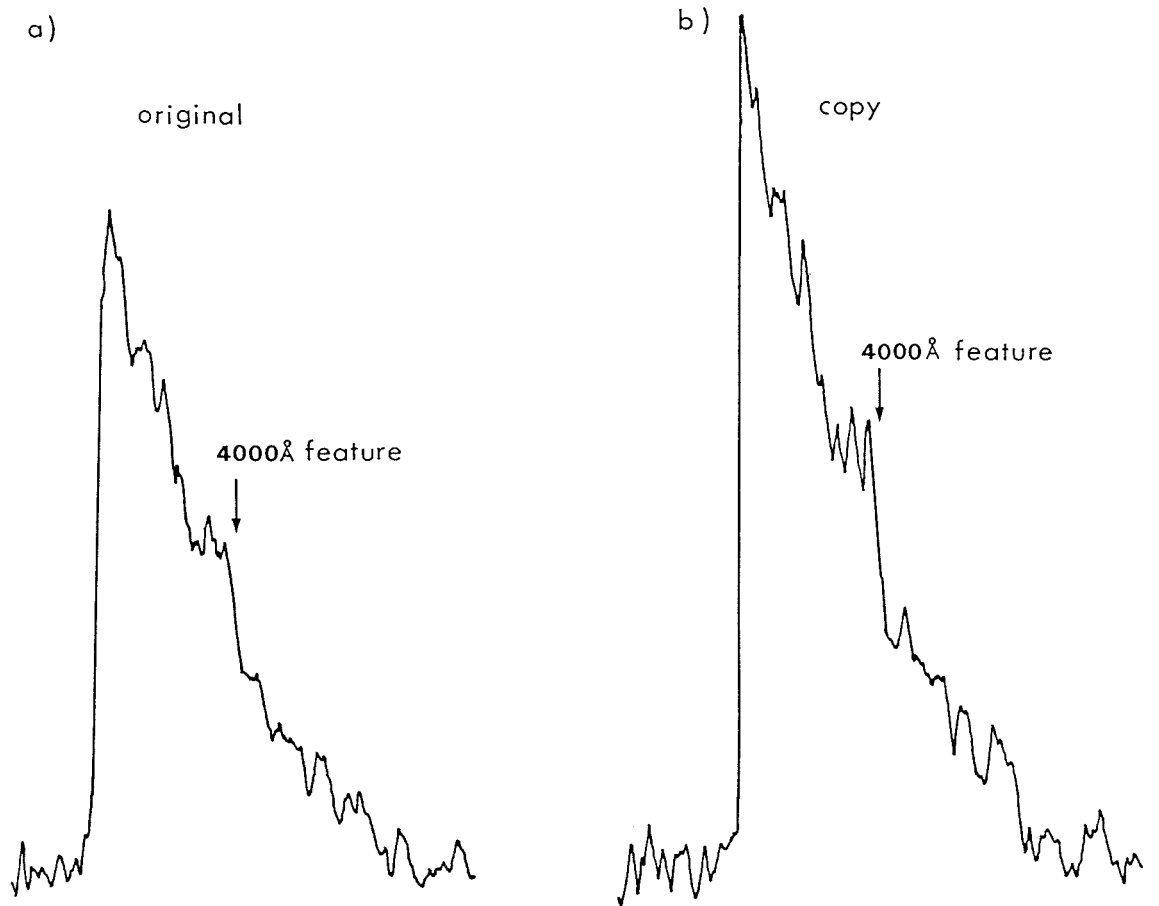


Figure 3.33a-b Joyce-loebl density tracings of the same star from the original and copy plates UJ5402P and UJ5402P P2N1.

For the galaxy results of figure 3.31, which are the prime concern, agreement between copy and original plate redshifts is not so good. Some degradation is expected because of the worse S/N of most galaxy spectra. There are a few instances of feature mis-identification which results in large redshift discrepancies. These cases probably arise because of the worse S/N characteristics in the copy-plate spectra affecting judgement of feature position and also because of ambiguous features. The number of discrepant points is no worse than from repeat measures of the same plate. Most of the galaxy points appear evenly distributed within  $\pm 0.01$  in redshift of the  $45^\circ$  line. The overall spread in galaxy redshifts, while being worse than for stellar spectra, is still less than that found when comparing Cosmos results with J-L measures, even though the same plate material was utilised. The differences between Cosmos and J-L data from the same plate seems to be a more serious problem than the resulting differences between copy and original plate using the same measuring technique. This result is not solely due to using simple density spectra in the J-L case (see figure 3.3), since even faint spectra, where intensity conversion is not important, exhibit the differences. It is more likely a reflection of fundamental differences in the way the photographic information is extracted by the different measuring machines.

Hence, for J-L measures of faint galaxy spectra, using a good-quality copy plate instead of the original does not have a serious effect on the redshift results and would not significantly effect any galaxy-cluster-redshift peaks determined. The effects of using Cosmos data from the original and copy plates is now described.

3.14. Comparison between Cosmos data INTERZED measures of objective-prism spectra from original and copy plate material.

The Cosmos data was obtained after the Phase 1 improvements had been carried out. The same area of original plate was again scanned by Cosmos as for the copy plate. Intensity conversion of the raw Cosmos transmission values was performed in both cases.

3.14.1. Differences in the spectral reproduction from copy and original plates.

The intensity spectra for the same object from original and copy plate will differ because neither intensity conversion nor the copying process are entirely satisfactory. The similarity of spectra produced by intensity converting copy and original plate material actually depends on a number of interdependent factors such as object magnitude, accuracy of the intensity conversion in each case, the range on the copy plate for which information is linearly copied from the original and the combined S/N characteristics of plate and Cosmos machine. Because of contrast loss in brighter copy-plate spectra, intensity conversion of these spectra is less successful than for equivalent original-plate spectra. This leads to lower peak intensities, and compression and smoothing of features at higher intensities in the copy-plate spectra. Due to peak intensity under-estimates in brighter copy plate spectra, the ECO mid-point will be biased to longer wavelengths and result in greater ECO to 4000Å feature separation and hence to more negative redshifts. Conversely, improved intensity conversion on the original plate yields more appropriately scaled spectra for the brighter objects, important if an attempt at rough spectral classification is considered. For very bright spectra Cosmos runs into saturation problems and the machine S/N begins to dominate.

Intensity converted spectra which lie on the straight portions of the CC on both original and copy plate should have a similar form. With very faint spectra near the sky background, two further problems exist. Firstly, the copy-plate S/N in faint spectra is likely to be lower than that for the original. Secondly, the S/N characteristics of Cosmos, which is poor at both high and low densities, will be worse for spectra near the sky background on the copy plate than on the original because the sky background is considerably lower on the copy. The overall appearance of these faint spectra might therefore be significantly affected by changes in the S/N, resulting in spurious, split or distorted features. These problems would be aggravated by intensity converting the spectra.

A comparison between copy- and original-plate objective-prism redshifts for faint galaxy spectra should indicate how much the S/N variations affect feature identification between the samples. A faint magnitude limit, where relatively consistent estimates from both plates are obtained, could then be deduced.

To illustrate the points discussed above, examples of original and copy-plate stellar spectra, of widely different magnitudes, from intensity converted Cosmos data are presented in figures 3.34a-b. The same sequence of spectra is presented from both copy and original plate. Individual spectral plots are scaled to fill the same area box. Magnitude estimates and redshift measures for each spectrum are also given. Ideally, zero redshifts are expected for these stellar spectra. From reference to figures 3.34a-b, original and copy plate spectra with magnitudes fainter than  $b_{uj} \sim 17.5$  have very similar appearances, with most spectral variations being faithfully reproduced (e.g. sequence No.90 figure 3.34a and sequence No.5 figure 3.34b).

a) Original plate

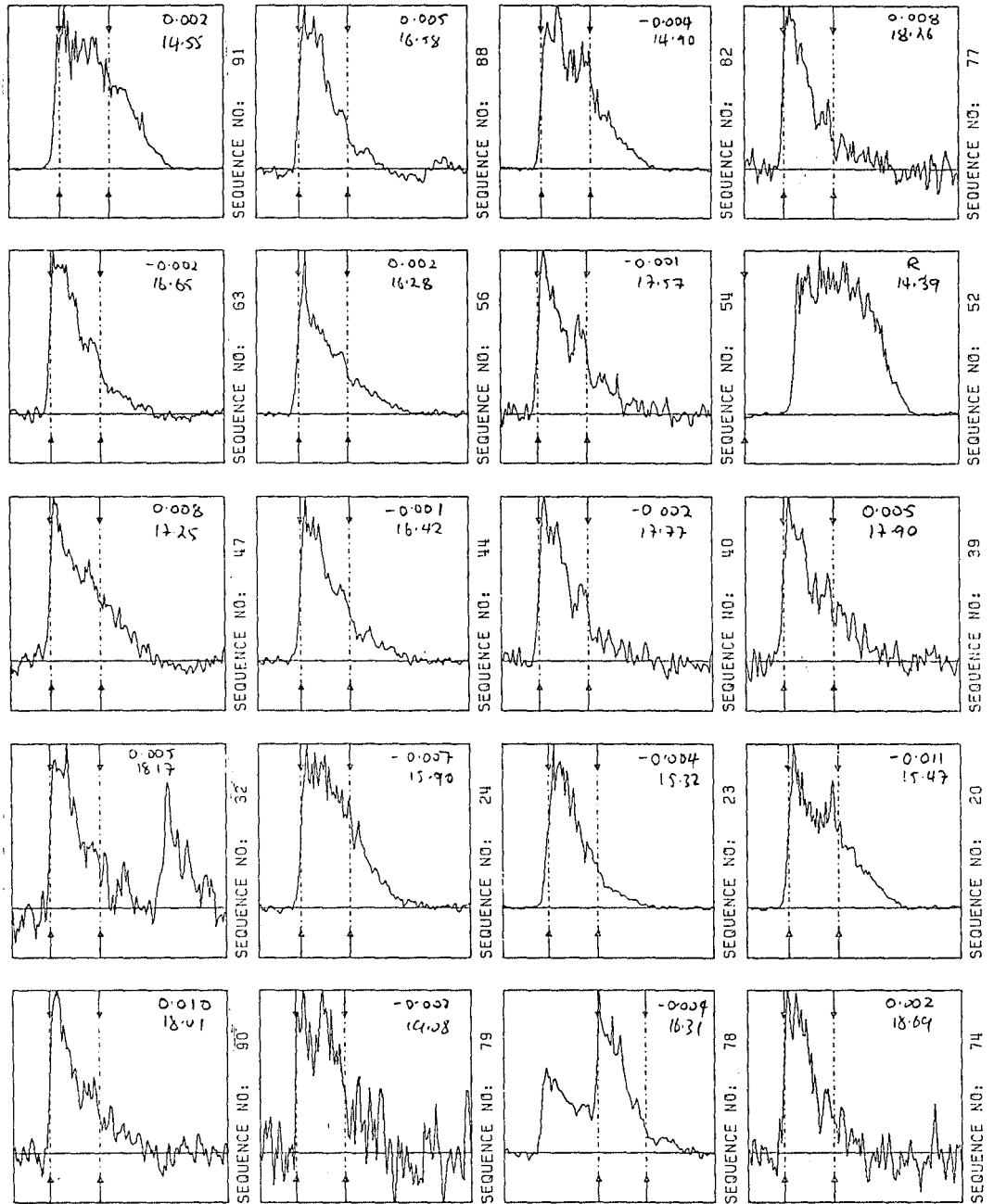


Figure 3.34a-b Examples of a variety of stellar spectra of different magnitudes from intensity converted COSMOS data of the original and copy plates UJ5402P and UJ5402P P2N1.

b) Copy plate

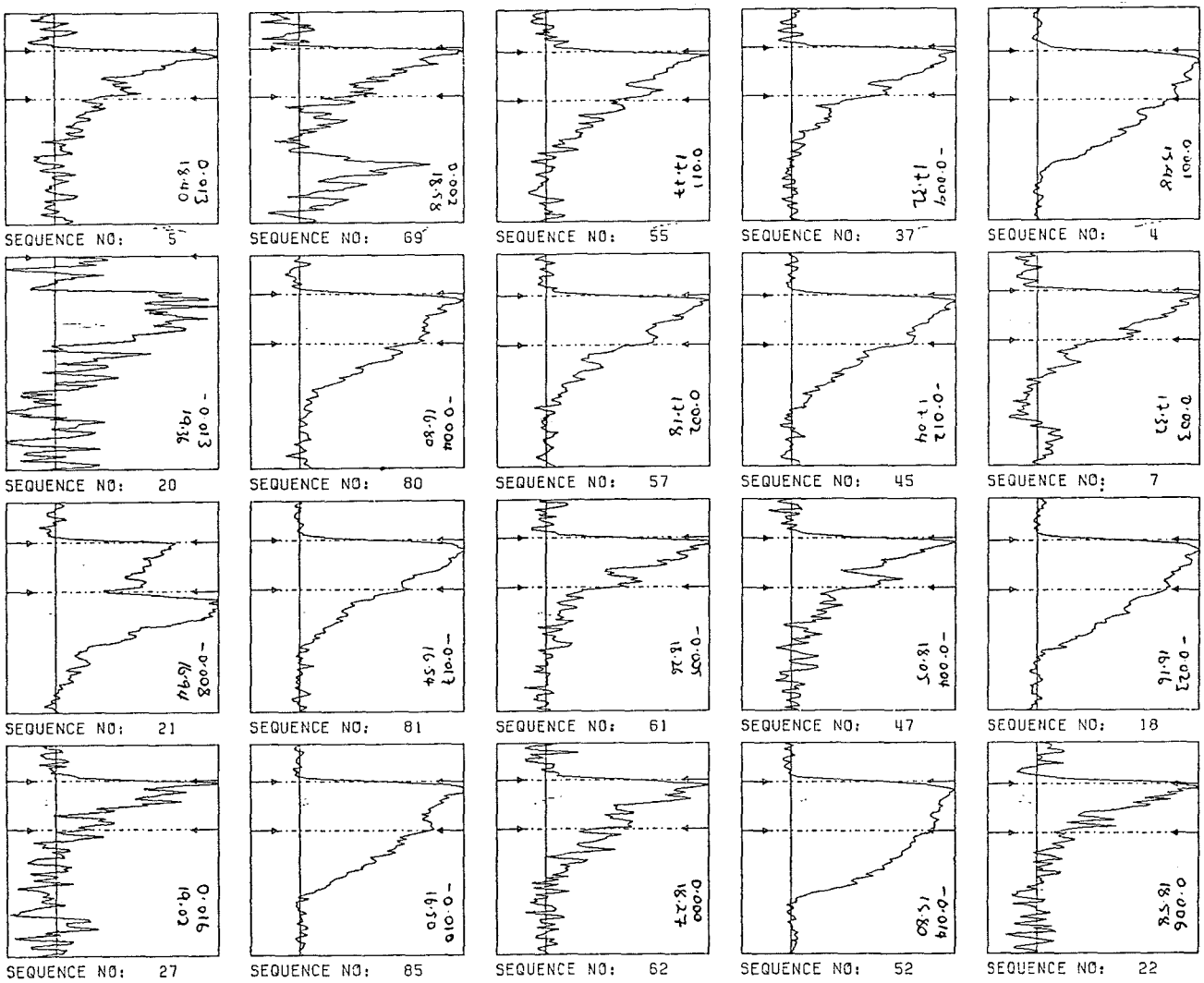


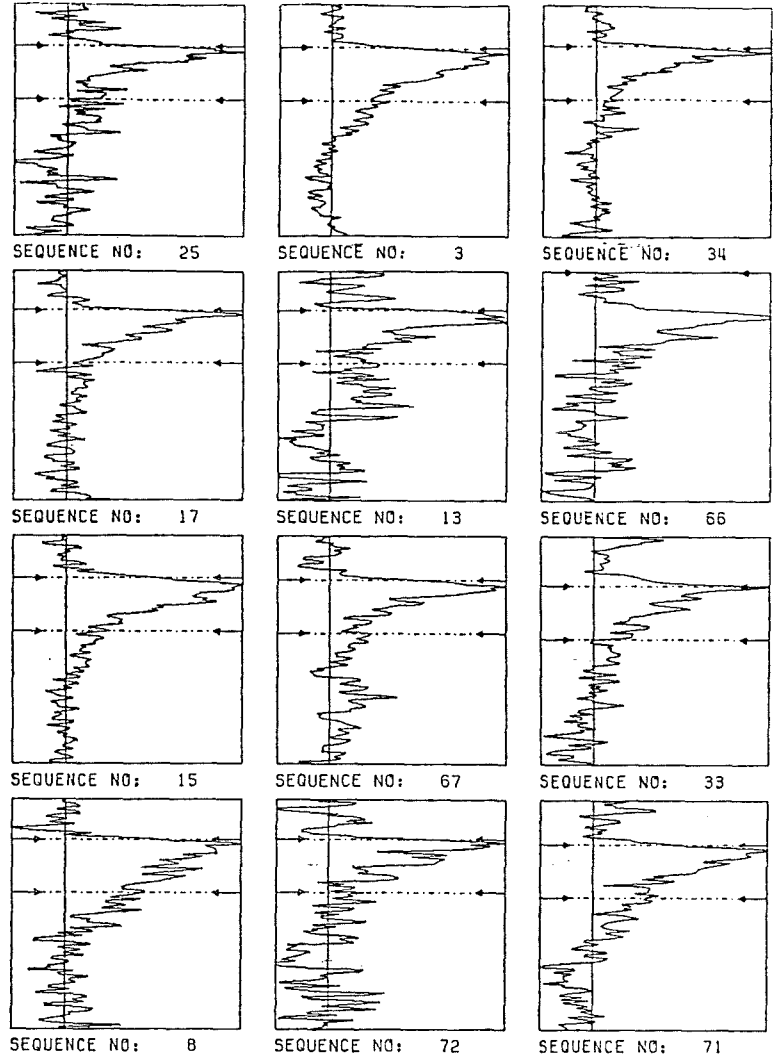
Figure 3.34b

The sky noise in these spectra are comparable, indicating that intensity-converted spectra from copy-and original-plate data are well matched. For spectra fainter than  $\text{buj} \sim 19.0$ , differences in the amplitude of the S/N variations become more distinct. This could partly be the effect of scaling the spectra until the spectrum's maximum intensity just fills the box. However, since the spectra are faint and near the sky background, their densities lie on the straight portions of the CC's. This implies that the intensity conversion of faint spectra is also fairly well matched between original and copy plate. Hence the S/N degradation in faint copy spectra over the original is real and is expected; see sequence No.79 figure 3.34a and sequence No.20 figure 3.34b.

At brighter magnitudes, the predicted scaling and compression of spectral resolution between copy and original plate spectra is indeed seen, e.g. sequence No.56 figure 3.34a and sequence No.45 figure 3.34b. The  $4000\text{\AA}$  feature is evident in both spectra but the general form of the spectra is quite different. The  $4000\text{\AA}$  feature in the copy-plate spectrum appears much higher up the continuum near the ECO peak, whereas that of the original is more appropriately positioned. The sky-background variation in each case gives some indication of the improved intensity conversion for the original plate spectrum, i.e. the difference in the apparent size of the sky variation is here due to scaling, since the recovered intensity of the original spectrum is much greater than for the equivalent copy-plate spectrum.

For very bright objects the S/N of Cosmos at high densities decreases. This is not so serious for copy-plate data because of the lower density limit ( $D \sim 2.0$ ), but can affect original spectra which can go to much higher densities ( $D \sim 4.0$ ), though Cosmos saturates well before this density is attained. For instance sequence No.52 figure 3.34a and sequence No.52 figure 3.34b are original and copy plate spectra of the same bright star. The original plate spectral tracing seems quite noisy at high intensity values and the intensity peak is not at the ECO peak. This may partly reflect the stars spectral type but is primarily due to the poor S/N of Cosmos at high density (and therefore intensity on conversion) dominating the spectrum. The copy plate spectrum is much smoother in appearance and its intensity and ECO peaks coincide. There is also an apparent '4000Å' feature high up the continuum. This is an artefact of improper intensity conversion for bright copy-plate images because of contrast loss. This results in compression of spectral features and gives undue weight to lower intensity features further down the continuum. No such feature is present in the original plate spectrum, possibly because it is masked by the poor S/N at high intensities. The apparent feature in the copy plate spectrum is therefore unlikely to be real. The largest negative stellar redshifts from bright copy-plate spectra may be due to identification of similar spurious features caused by contrast reduction, apart from the effect that the reduced contrast has on the ECO position itself. This problem is not serious in the J-L measures evidenced by the very good agreement between the copy and original plate results.

a) ORIGINAL PLATE



b) COPY PLATE

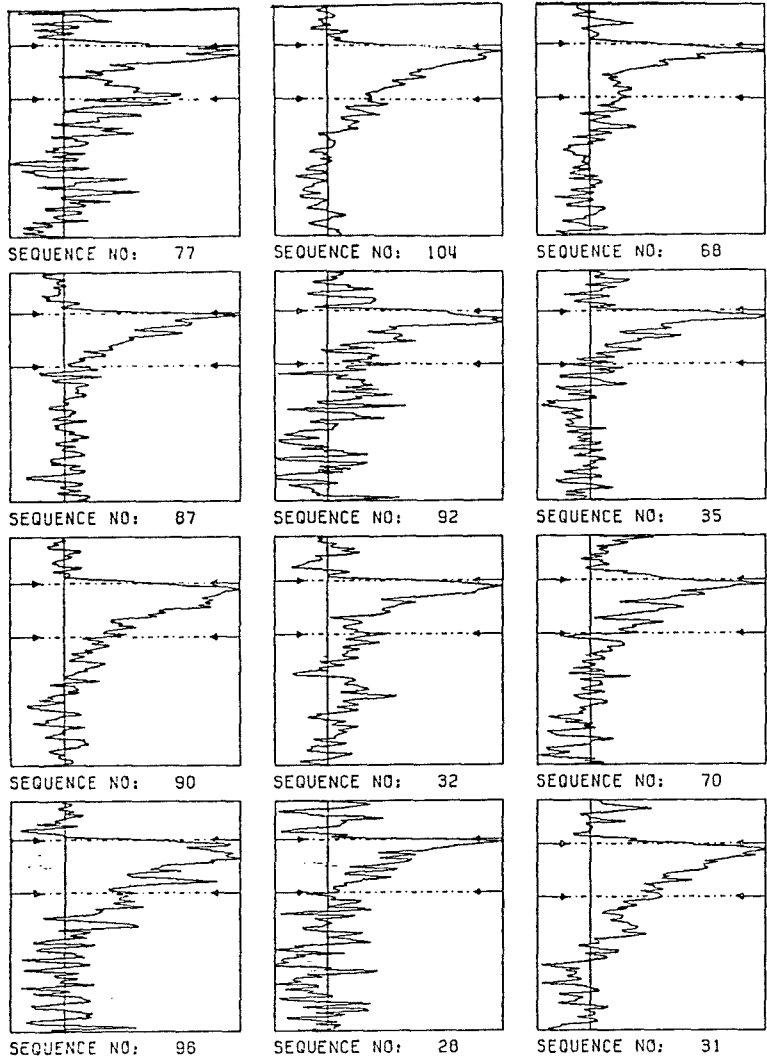


Figure 3.35a-b As for Figure 3.34a-b but for galaxy spectra.

Having considered original- and copy-plate stellar spectral tracings from Cosmos data, some examples of galaxy spectra are presented. Although measures of high S/N stellar spectra are important for determining the zero point, and for revealing problems such as the mag/Z effect (which we assume affects bright galaxy spectra also), the main concern is with determining galaxy redshifts. Consequently the stability of spectral features and redshifts to changes in plate material for low S/N objective-prism galaxy spectra must be assessed. Figures 3.35a-b are a random sample of Cosmos galaxy spectra from the original and copy plates. Examination of these spectra revealed substantial differences in the appearance of the 4000Å features in some cases, e.g. sequence No.3 figure 3.35a and sequence No.104 figure 3.35b. This can lead to complete feature mis-identification giving gross redshift discrepancies. The results for other spectra may also be modified by effects of S/N variations altering the size, shape and mid-point positions of presumed features.

#### 3.14.2. Comparisons of copy and original plate magnitude estimates.

Figure 3.36 gives the original-plate versus corresponding copy-plate Cosmos-magnitude estimates for a sample of 89 galaxy and 69 stellar spectra. A tight relation exists between the estimates but in almost every case copy plate magnitudes are fainter than their original plate counterparts. The discrepancy is worst for brighter spectra but decreases uniformly with increasing magnitude. This is more clearly seen in figure 3.37, a plot of magnitude difference between copy and original plate estimates versus original plate magnitudes. The expected effect of contrast reduction in brighter images on the copy plate and the subsequent intensity underestimates for the denser pixels on intensity conversion is seen. This results in an overestimate of the copy-plate object magnitudes. For fainter spectra the copy-plate contrast loss becomes less severe.

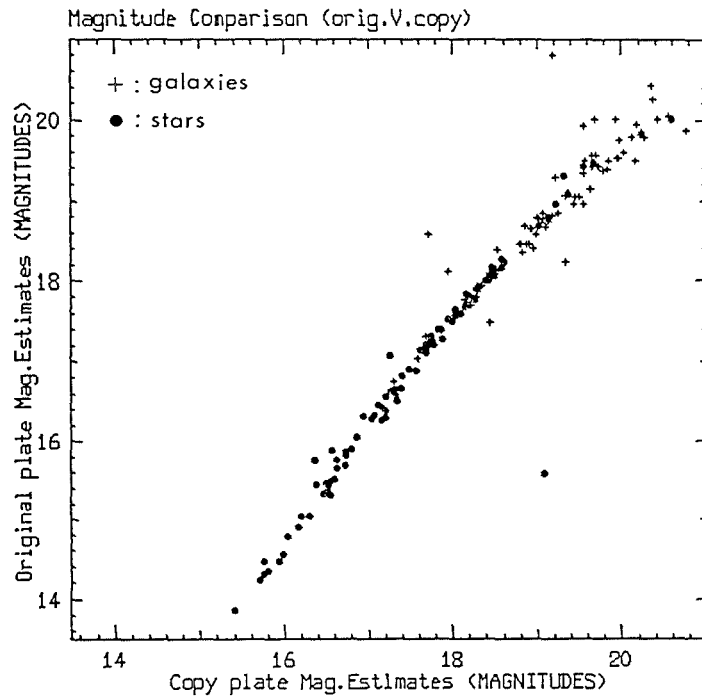


Figure 3.36 Original versus copy plate objective-prism COSMOS magnitude estimates.

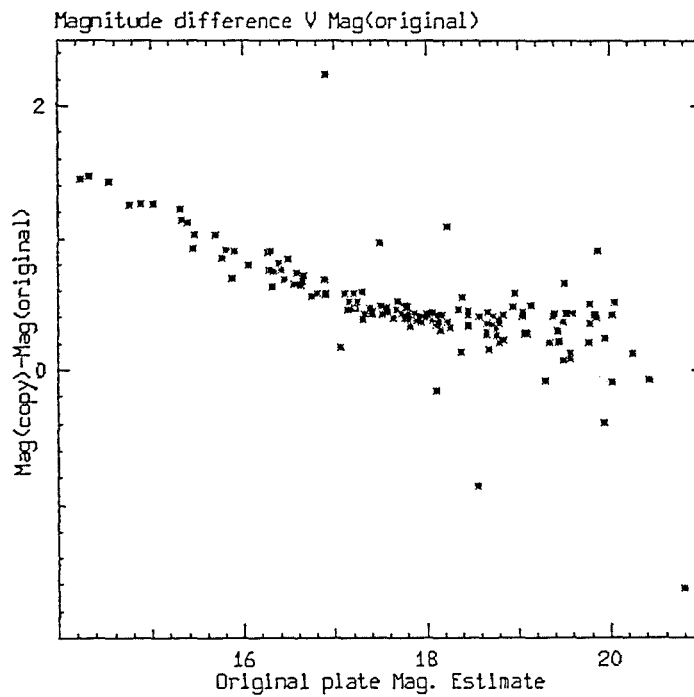


Figure 3.37 Magnitude difference between the copy and original plates against the magnitude estimates from the original plate.

Hence the copy-plate magnitudes converge to those of the original plate as the overall magnitudes are increased. At original plate magnitudes of 17.4 the convergence stops and the relation runs parallel to, but below, the 1:1 correspondence line. There is then an approximately constant 0.4 magnitude overestimate in the copy-plate magnitudes compared with original-plate measures though the scatter increases. At faint limits neither original-nor copy-plate spectra are saturated so they ought to lie on the straight portions of their respective CC's. Since Cosmos magnitudes are given as estimates above sky (section 3.3), and since the same sky background magnitude ( $M_{\text{sky}} = 22.2$ ) was adopted for both copy and original plate measures, the near constant magnitude discrepancy for fainter spectra is probably due to differences in the intensity conversion parameters used. Reference to figure 3.29a-b indeed indicates different slopes for the straight portions of the CC's obtained from J-L measures of the seven step wedges on the copy and original plates.

### 3.14.3. Redshift comparisons between original and copy plate Cosmos measures.

Redshifts from measures of copy-and original-plate spectra are now considered. This comparison has important consequences for the use of copy-plate material in performing objective-prism redshift surveys with Cosmos, e.g. Beard (1984). Figure 3.38 is a plot of original-versus copy-plate objective-prism redshifts for a sample of 158 galaxy and stellar spectra measured with INTERZED, regardless of assigned feature weight. There is some scatter about a straight line, especially for lower S/N galaxies. If only features assigned top weights 1 and 2 from both measures are considered, then the dispersion is reduced considerably. However, the total sample size is also reduced by 50%. Only 20% of the remaining galaxies and 25% of the stars now lie outside the  $\pm 0.01$  redshift bounds of the  $45^\circ$  line.

Significantly, most discrepant stellar points are due to original plate estimates being less negative than copy plate estimates. Only 4 of the 15 points lying outside the  $\pm 0.01$  redshift bounds are due to cases where a high-redshift feature has been mistaken for the  $4000\text{\AA}$  feature in the original-plate spectra but has been correctly identified in the copy plate spectra. There are no cases of the converse situation. Also in figure 3.38, 4 galaxy spectra yielded near zero redshifts in the original sample but had high redshifts for the copy-plate spectra, indicating that a low-redshift feature was mistaken for the  $4000\text{\AA}$  feature in the original-plate case. Ignoring cases of obvious mis-matches, the sample in figure 3.38 reveals a noticeable trend for original stellar spectra to yield less negative redshifts than for copy-plate spectra. Such an effect is expected because of the improved intensity conversion of original-plate high S/N spectra over the reduced-contrast copy-plate equivalents. Figure 3.39 gives Cosmos prism magnitude estimates versus prism redshifts for a sample of stars from original-and copy-plate measures. The mag/Z effect (see section 3.6) is again present for both sets of data and is approximately linear in both cases. However, as expected, the relation is steeper for the original-plate results which are less affected by contrast reduction and saturation problems. Consequently it is much more important to apply a redshift correction to the copy plate, bright galaxy results than for the original plate where the mag/Z effect only becomes significant at  $\text{buj} \leq 16.0$ .

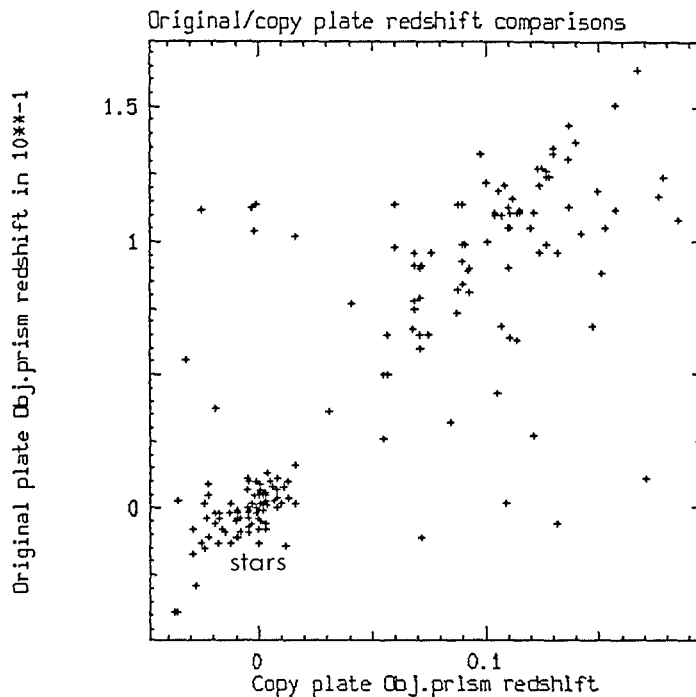


Figure 3.38 Original versus copy plate INTERZED redshift results for a random selection 158 stars and galaxies of all feature weights.

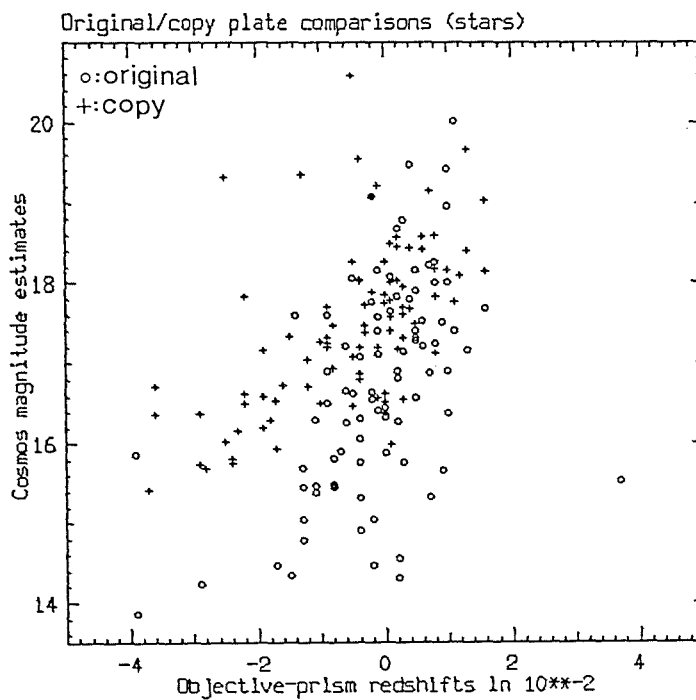


Figure 3.39 COSMOS prism magnitude estimates against objective-prism redshifts for a sample of stars and galaxies from original and copy plate measures.

3.15. Comparisons between objective-prism results from Cosmos in its pre- and post phase 1 update configuration.

Previous sections have described the effects on reproduction of objective-prism spectra of stars and galaxies of variable S/N, as measuring machine, plate material and reduction technique are changed. During the course of these studies, the Cosmos machine underwent an extensive electronics rebuild which resulted in S/N improvements of a factor of 2 near the sky background (MacGillivray and Stobie, 1985). Measurements of the same objective-prism spectra from pre- and post-phase 1 update Cosmos data should indicate how these improvements have affected the objective-prism results. Improved S/N should lead to better object magnitude estimates as it should be easier to discriminate background from image pixels. Furthermore, S/N enhancements in faint spectra may lead to better prism redshifts and fewer cases of feature mis-match.

A sample of 66 stellar and galaxian spectra were found that had been measured with INTERZED from pre- and post-update Cosmos data. Of this sample 16 were deemed to have no measurable features from both samples, and a further 3 objects were rejected in the pre-update sample but were assigned redshifts in the post-update sample. Figure 3.40 is the pre- versus post-update INTERZED redshifts for the remaining sample. The agreement is generally good, although 7 discrepant points exist and these are marked on the plot. If their individual weights and object identifications are examined it becomes clear that the pre-update measures are causing most discrepancies. All but one of the discrepant points are for faint objects where the improved S/N should make the most impact.

Some objects were assigned low weights in the pre-update sample but high weights in the post-update sample. Here effects of better S/N in the post-update sample may be leading to improved feature resolution in faint spectra. Of the 7 discrepant objects, 3 had redshifts which indicated stellar origin in one case and galaxian in the other. Object identifications from the direct plate were occasionally overruled by the redshift result for a conspicuous feature being incompatible with the identification. More confidence can be attached to the post-update results for the discrepant points because of their generally improved feature-weights and because where the object was classified as stellar in one case and galaxian in the other (on the basis of feature redshift), the post-update results agree with the direct plate object identification.

Figure 3.41 gives the magnitude comparisons between the pre- and post-update Cosmos prism sample. At the bright end the post-update estimates are fainter than their pre-update counterparts, whereas at fainter limits ( $b_{uj} > 18.0$ ), the converse is true. This effect must be due to the improved S/N in the post-update data. The fact that the pre-update magnitudes at the bright end are brighter than the post-update values is not easy to explain unless a zero-point offset between the estimates is assumed. Such an offset could arise from an improved sky-background determination which, on intensity conversion, would affect the magnitudes. The fact that a copy plate (UJ5402P P2N1) was used may also have some bearing on the situation. The brighter post-update estimates at fainter limits are probably due to the inclusion of more pixels in the image because of better discrimination from background pixels.

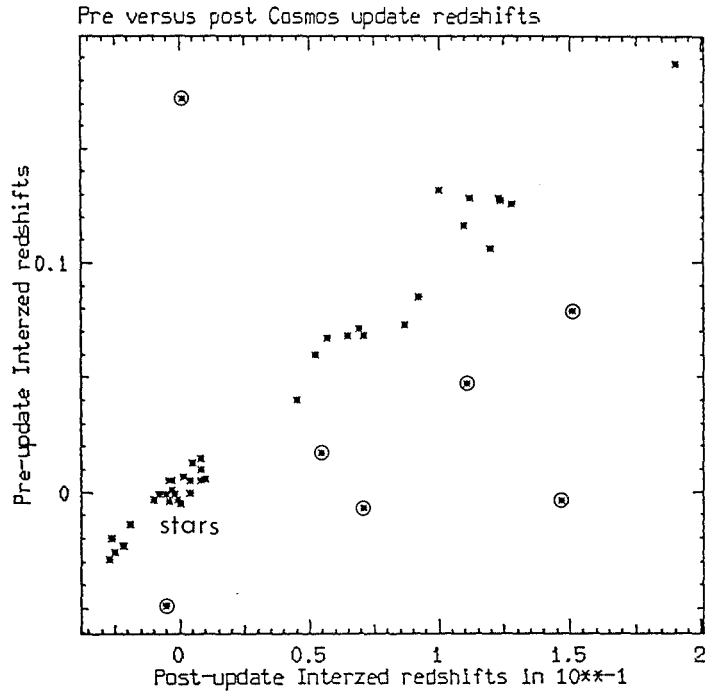


Figure 3.40 INTERZED redshift results from pre- and post phase 1 update COSMOS data from measures of the copy plate UJ5402P P2N1.

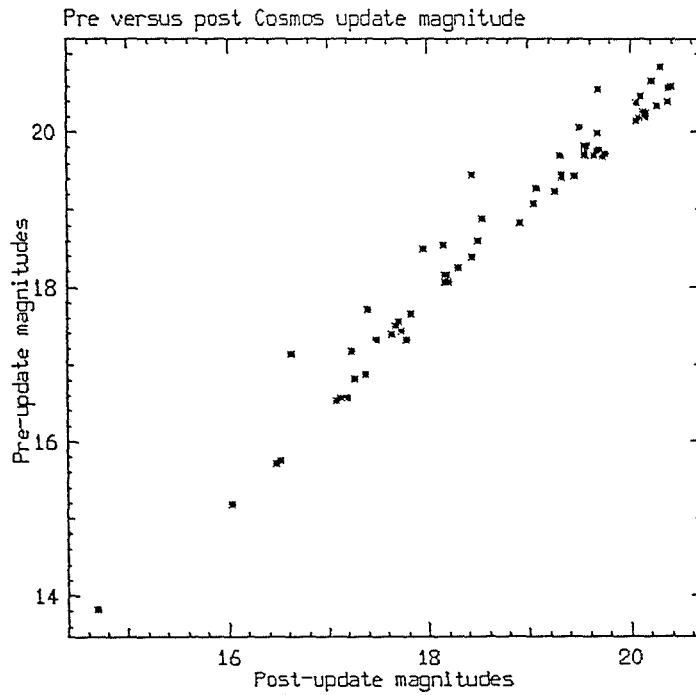


Figure 3.41 Magnitude comparison between objective-prism spectra from pre- and post phase 1 update COSMOS data.

The relation in figure 3.41, is approximately linear but a zero point offset alone would not explain the relation since the slope is not  $45^\circ$ . Figure 3.42 is a plot of redshift difference (pre-post) versus post-update prism magnitude estimate. No trend with magnitude is evident indicating consistent redshift estimates with magnitude from both samples, although, as expected, the numbers of discrepant points increases at fainter limits.

In conclusion, the redshifts and magnitude estimates have been shown to be quite sensitive to changes in the Cosmos machine. The redshifts are generally consistent for the higher S/N spectra but significant discrepancies between the samples exists for the fainter objects. The S/N improvements have had an effect on the redshift results for the fainter objects which should lead to a more reliable redshift sample. Again these results have shown the susceptibility of objective-prism redshifts for faint objects to small changes in the S/N.

### 3.16. Stellar INTERZED redshifts from Cosmos measures of field 475.

All the results described so far have been obtained from copy and original plates of field 349. This has enabled the consistency and reliability of the objective-prism redshifts to be determined as measuring machine, reduction technique and plate material have changed. This was because the same sample of stars and galaxies were measured. However, results from a different field should be considered since the mag/Z effect, for example, may depend significantly on the properties of any individual plate as well as on the measuring machine, data reduction technique and whether original or copy plates were used.

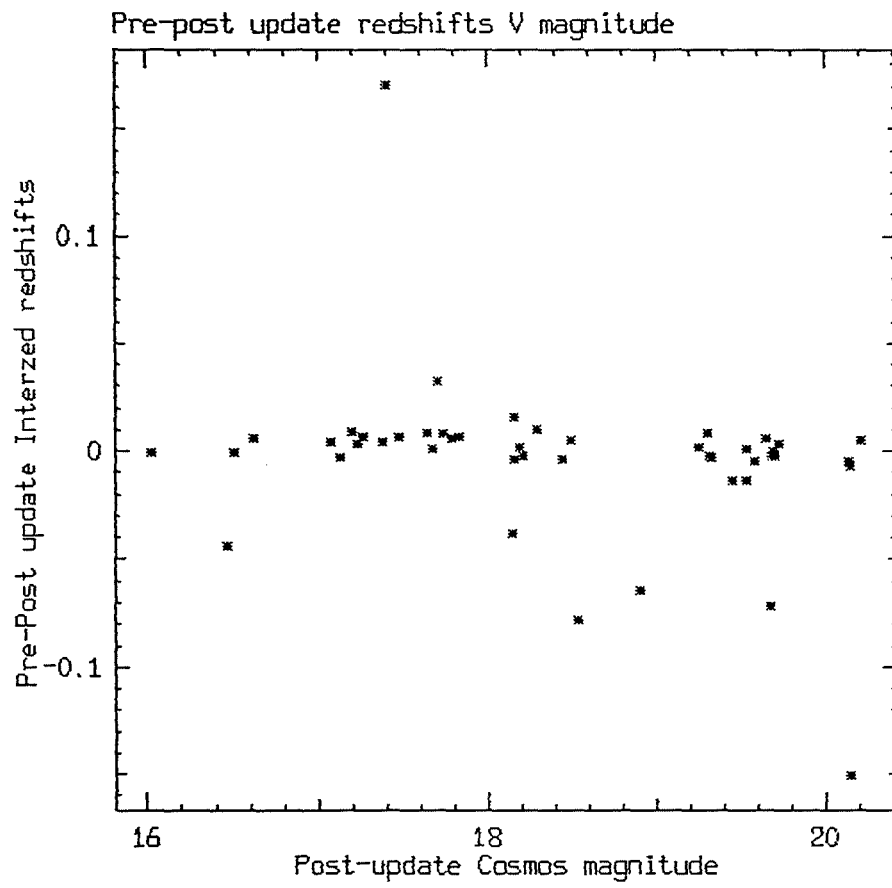


Figure 3.42 Redshift difference between results from pre- and post phase 1 update data versus post update COSMOS prism magnitudes.

Figure 3.43 is a plot of stellar redshift versus prism magnitude for a random sample of 103 stars extracted from around the galaxy cluster A140 in field 475 and measured using INTERZED. The data comes from Cosmos scans of the original plate UJ4543P. The stellar redshifts are randomly scattered about the zero redshift line over the magnitude range  $b_{uj} \sim 21.0-15.5$ , with the majority of points lying within  $\pm 0.01$  in of the zero redshift value. This is compatible with the zero redshift for stars and the expected accuracy of the objective-prism redshift technique. However, at  $b_{uj} \sim 15.2$  a mag/Z effect does become apparent. These results can be compared with figure 3.44, the equivalent plot for INTERZED stellar measures from field 349. The plots are very similar with the mag/Z effect becoming stronger at bright limits although there is a noticeable but weak mag/Z effect over the whole magnitude range in figure 3.44. There may also be a residual magnitude offset between the two plots because the magnitudes have not been externally calibrated. The same background magnitude of  $b_{uj} = 22.2$  was assumed for both original plates, a typical value for deep IIIaj exposures. Since the magnitudes were derived in a consistent manner any offset is unlikely to be more than a few tenths of a magnitude.

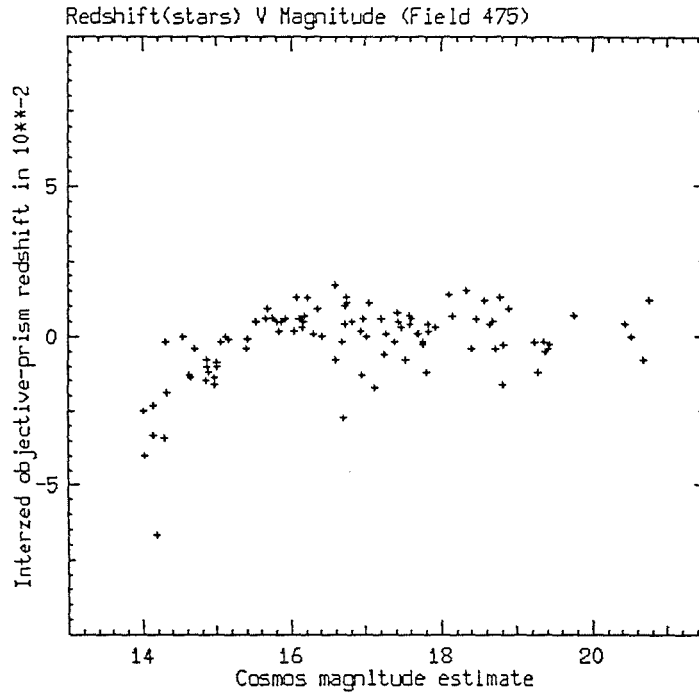


Figure 3.43 Stellar objective-prism INTERZED redshifts versus prism magnitudes from COSMOS measures of an original plate of field 475.

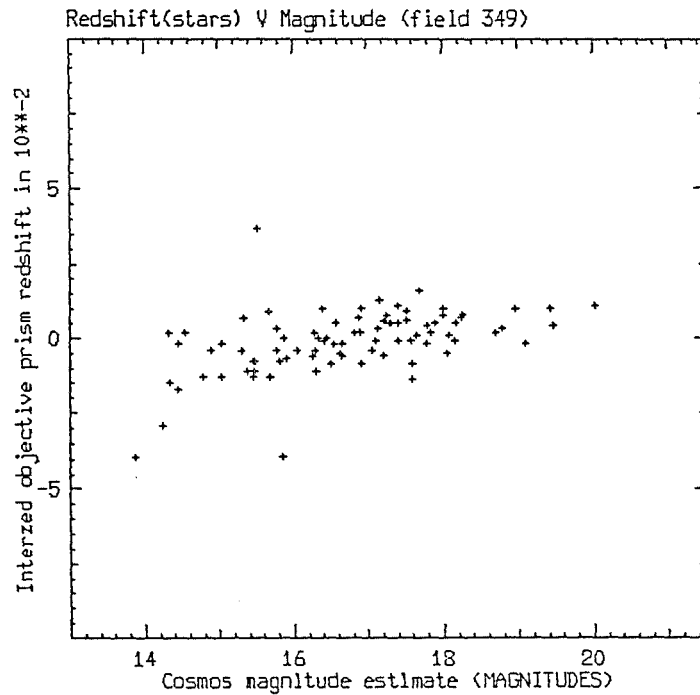


Figure 3.44 As for Figure 3.43 but for measures of original plate UJ5402P of field 349.

The general agreement between the stellar redshifts from Cosmos data of two different original plates of two different fields is encouraging. Such agreement indicates that, for high S/N spectra at least, consistent results can be obtained with Cosmos data. The main cause of result discrepancy found is thus dependent on whether original or copy plates are used, which measuring machine is used to scan the plates, and how the spectra are finally reduced.

### 3.17. Conclusions from the empirical studies described in this chapter.

A thorough and detailed discussion of the various means of determining objective-prism redshifts from different plate material and from different measuring machines using different reduction techniques has been given. The results of these empirical studies have demonstrated that the objective-prism redshift technique cannot be applied without regard to the effects that measuring machine and plate material have on the integrity, consistency and reliability of the redshifts obtained. Galaxy objective-prism redshifts are susceptible to a variety of external influences outwith the photographic information on the plate, and to whether copy or original plates are used. The main findings of the empirical studies carried out in this chapter are summarised below:-

(1). The recovery of photographic information from an objective-prism plate is dependent on the measuring machine used to scan the plate. The reproduction of the spectra can differ significantly. At high plate densities the machine - dynamic - range limitations limit the recovery of information and lead to improper intensity conversion in the case of the Cosmos machine. Use of copy plates with reduced contrast exacerbates the situation. This results in improperly-scaled intensity spectra which can lead to feature ambiguity and mis-match,

as well as affecting the position of the observed feature and ECO mid-points. At low densities the S/N variations of the J-L and Cosmos machine affect the spectral quality in different ways, especially since density and intensity spectra are being compared. Hence the positions, strengths and form of any 4000Å features are affected. This results in feature ambiguity and redshift discrepancy between the results from the two machines.

(2). There is a significant magnitude/redshift effect evident in copy plate measures of stellar spectra. If uncorrected this would lead to underestimates in the redshifts from brighter, higher S/N, galaxy spectra. This effect, found for both density J-L spectra and intensity-converted Cosmos spectra measured with E2D and INTERZED, was approximately linear with magnitude. However, the slopes of the relations were different, even when simple Cosmos transmission spectra were compared with the J-L results. This effect, being different for both machines, leads to redshift discrepancies between the same sample of spectra. When the original plate was measured by Cosmos the mag/Z effect was considerably reduced but not eliminated completely. The combination of contrast loss on the copy plate at higher densities and the S/N limitations of the Cosmos machine, affects the ECO and feature mid-point determinations and is the likely cause of the strong mag/Z effect in copy-plate measures. Similar measures from an original plate of a different field yielded good agreement with the original plate measures of field 349, confirming that the copy plate is causing the trouble. With care, the mag/Z effect can be calibrated out to yield a more reliable galaxy redshift sample (see chapter 4).

(3). There is good agreement between the redshift results from J-L measures of stellar and galaxian spectra of the original and copy plate whilst considerable discrepancies exist between the equivalent Cosmos measures. The spectral tracings produced with Cosmos data differ considerably in many cases, again because of the effects of contrast loss and machine S/N variations. The scatter in the original/copy plate redshift comparisons is reduced considerably if only top-weight features are considered, but this results in a reduction of sample size of ~50%. The problems caused by using a copy plate and the Cosmos machine are sufficient to recommend that only original plates should be used for doing objective-prism galaxy redshift surveys. Most galaxy spectra are of low S/N and the original plate Cosmos measures are more resilient to the effects of improper intensity conversion and machine S/N limitations since the sky background density is much higher. Differences between Cosmos and J-L data from measures of the same copy plate are more serious than differences found between original and copy plate using the J-L technique.

(4). The consistency between repeat measures of the same sample using the same technique over prolonged time intervals has been shown to be very good as is the consistency between measures of the same sample using the different interactive techniques that use Cosmos data. Any technique dependence is within the expected uncertainties. The subjective weighting assessment applied to the spectra to indicate feature quality has also been shown to be in surprisingly good agreement between the repeat measures. Consistent redshift samples can therefore be obtained if the intensity conversion and measurements are performed carefully.

In conclusion, as long as the limitations of the plate material and measuring machine are properly understood and allowed for wherever possible, the objective-prism redshift technique can be a useful tool for providing relatively large numbers of crude redshifts from a single UKST plate. The problems of using the observed ECO as the wavelength reference point should be alleviated when a co-ordinate transformation is employed (see chapter 5). Although this should reduce the mag/Z effect found for copy, and to a lesser extent, original plate data, other problems such as feature mis-match and ambiguity will remain for the lower S/N objects. The most consistent results have been obtained from the highest S/N spectra and the most problems encountered with the low S/N galaxy spectra not surprisingly. Unfortunately it is the low S/N spectra which are of the most interest as they are the most numerous and come from the most distant galaxies. These studies have indicated that if copy plates are used the useful magnitude range of the objective-prism redshift technique may well have to be brought to brighter limits.

Calibration of objective-prism galaxy redshifts with slit spectra results.4.1. Introduction.

In this chapter the calibration of objective-prism galaxy redshifts with corresponding slit-spectra velocities is discussed. Chapter 3 has shown that measures of stellar spectra of different magnitude across a plate, whose redshifts are essentially zero, exhibit a significant magnitude/redshift effect. Measures of brighter spectra yielded progressively more negative redshifts and not the zero value expected, although at fainter magnitudes the stellar results were zero to within the expected uncertainties ( $\pm 0.01$  in  $Z$ ). This effect was found to be dependent on both plate material and measuring machine, being less serious for the J-L measures than for Cosmos measures. Such an effect, discussed in chapter 3, is expected to be reduced considerably when the ECO position is determined from a co-ordinate transformation provided by pairing the direct and prism plates. It may not be eliminated completely however, because saturated  $4000\text{\AA}$  features also contribute to the effect (see chapter 3 section 3.8), especially for copy-plate material. This independent calibration of objective-prism redshift accuracy from stellar measures revealed that redshift results from brighter galaxy spectra will be underestimated. The results may be corrected in some sense for this trend by reference to stellar spectra of the same magnitude. In such cases it is hoped that the diffuse nature of galaxy images will not seriously affect the size of the correction needed. This is more likely true for J-L measures because corrections for the mag/ $Z$  effect are made on the basis of similar peak densities in the spectral tracings between star and galaxy. For Cosmos measures though, correcting the galaxy redshift by the average amount that stellar

spectra at the same magnitude were negative, may result in over-compensation for this effect. If the prism plate was taken in good seeing this is especially true since magnitudes are isophotal and differences between stellar and galaxy images are not so smoothed by the blurring effects of the seeing disc.

Nevertheless, the crucial test of the objective-prism redshift technique is to determine how well the galaxy redshifts obtained match up with their corresponding accurate slit-spectra values. Without such tests the validity of the technique is questionable. Samples of faint galaxy spectra with both good objective-prism redshifts and slit-spectra redshifts are required from single UKST fields. At present the size of this sample is small. A problem is that the useful range over which objective-prism redshifts can be determined (i.e.,  $16.5 \leq B \leq 19.0$ , Cooke, 1980), even at the bright end, is fainter than the limits of most slit-spectra galaxy redshift surveys, e.g. the CfA redshift survey to  $B \leq 14.5$ , Davis et al. (1981), and Huchra et al. (1983). Most other faint samples of galaxy redshifts amount to one or two galaxies in the centres of rich clusters, e.g. Sarazin et al. (1982), with rarely more than a couple of redshifts per UKST field.

This chapter describes previous calibrations of the technique from J-L and Cosmos data (Cooke, 1980, and Beard, 1984), and discusses the problems and results obtained. Furthermore, considerable extra data was obtained for this thesis and these results are also presented. The results of these calibrations should give a better indication of the general validity of the objective-prism redshift technique and the success of correcting for the observed mag/Z effect, as well as the effects of plate material and measuring machine variations on the calibration reliability. A realistic appraisal of the technique and its limitations can then be made and its usefulness determined.

## 4.2. Previous calibrations performed.

### 4.2.1. Calibration with J-L measures performed by J.Cooke.

Cooke (1980), in his PhD thesis, obtained only 19 calibration points comparing slit spectra redshifts with those determined from J-L measures of objective-prism spectra. Seven of these points came from one cluster, A2670, which fortuitously had 10 slit-spectra redshifts determined by Oemler (1973). The A2670 calibration is given in Cooke (1981), from measures of the prism plate UJ4551P, which covers the area containing A2670. The resultant dispersion in ( $V_{\text{prism}} - V_{\text{slit}}$ ) was 2,000 Km/s, which is what was expected from the feature and ECO measurement precision from the J-L density spectral tracings (see chapter 3 section 3.2). This initial calibration was encouraging, even though density not intensity J-L spectra were used. However, the results are only for one cluster, from one plate, over a limited magnitude range.

Cooke (1981), applied the objective-prism redshift technique to a faint cluster of galaxies, A140, of unknown redshift, in SERC survey field 475 (plate UJ5443P). The cluster redshift was determined to be 44,500 Km/s, but the velocity dispersion from the 12 galaxies yielding prism redshifts was 3,800 Km/s. Since cluster velocity dispersions are  $< 1,500$  Km/s (e.g. Faber and Dressler, 1977 and Yahil and Vidal, 1977), and since the objective-prism redshift accuracy was thought to be  $\sim 2,500$  Km/s, Cooke suggested that to explain the size of the prism cluster velocity dispersion, A140 may in fact be two clusters superposed along the line of sight. Other possible causes of the large velocity dispersion were rejected because of the wavelength scale consistency tests that had been carried out on a selection of prism plates, e.g. Cooke (1980).

Chapter 3 however, has shown that the derived objective-prism redshifts are sensitive to S/N effects at faint limits and variations in plate material and measuring machine. Such factors affect the actual form of the prism spectral features and may consequently influence choice of feature and ECO mid-point positions. This will in turn affect the derived redshift, irrespective of the measurement precision. Since cluster A140 is faint on the prism plate, the contribution of the above effects to the size of the observed cluster velocity dispersion cannot be ignored, although Cooke's original conclusion may also be valid. Furthermore, for higher redshift galaxies, measurement errors lead to larger redshift uncertainties due to the decreasing dispersion in objective-prism spectra at longer wavelengths.

Cooke (1980), augmented the small calibration sample for A2670 by slit-spectra results for a further 12 galaxies. These came mainly from observations on the SAAO 1.9m, carried out specifically for calibration of galaxies in the area of objective-prism plates then available. All objective prism measures were performed with the J-L microdensitometer. The total dispersion between the slit and prism redshifts was  $\sigma = 2,975$  Km/s, a larger value than obtained for A2670, but a better indication of the technique's accuracy. The average discrepancy ( $V_{\text{slit}} - V_{\text{prism}}$ ), was +541 Km/s. The total error in the slit-spectra velocities, after applying various corrections, was determined to be  $\sim 300$  Km/s, small when compared to the inherent crudeness of the objective-prism redshifts. Cooke surmised that to get slit spectra for faint galaxies that lie in the useful magnitude range of the objective-prism redshift technique, observations on a larger aperture telescope such as the AAT would be required.

The results for the 19 calibration points from Cooke's J-L measures are given in figure 4.1, with the data taken from Cooke (1980). The expected error bounds of  $\pm 0.01$  in redshift are superimposed. As can be seen, although the number of points is limited, the agreement between the slit and prism redshifts is about what is expected from measurement precision and the uncertainties in the 4000Å feature and ECO wavelengths. Since the prism results for the two lower-velocity objects in this figure (which are the brightest), are underestimated with respect to the slit spectra results, this could reflect the influence of the mag/Z effect. Many more calibration points, over the full useful magnitude range from different plates, are required before firmer conclusions on the reliability of the objective-prism redshifts can be made.

For measures of large numbers of objective-prism spectra, the time-consuming nature of J-L manual measurements makes this technique impractical. Scans with the Cosmos machine however, can provide MM data of the central  $5.35^\circ$  by  $5.35^\circ$  area of a UKST objective-prism plate in a matter of a few hours. Software has been written which can extract prism spectra from the MM data and process them. Interactive techniques of objective-prism spectra reduction, such as INTERZED and E2D (see chapter 3), which use Cosmos data, are generally preferred over the J-L technique. This is because it is possible to process and manipulate larger numbers of spectra in a shorter time period and also provide an intensity conversion from the simple density data. Ultimately, a completely automatic objective-prism redshift reduction technique will replace these interactive techniques and should remove the inconsistencies introduced by manual judgement of ECO and feature positions (e.g. see Cooke, 1984).

Since the future of objective-prism redshifts lies with data from scans of prism plates by some fast, automated microdensitometer such as Cosmos, it is essential to obtain a significant sample of calibration points for prism-redshift measures from Cosmos data over a wide magnitude range. Unfortunately, the empirical studies of chapter 3 have shown that objective-prism redshifts are quite sensitive to whether J-L or Cosmos data is used. Moreover, Cosmos data are also more sensitive to changes in plate material, viz copy or original, than J-L measures whose dynamic range is also somewhat greater. The J-L spectra are consequently less susceptible to the S/N problems inherent in Cosmos data. Consequently it is necessary to determine how seriously the effects discovered in chapter 3 affect the calibration, and if corrections for the mag/Z effect are worthwhile.

4.2.2. Calibration from J-L and Cosmos INTERZED measures performed by S.M.Beard.

Beard (1984), in his PhD thesis, gives details of further calibration points obtained during the course of his work. Three calibration points were redshifts from slit spectra obtained on the AAT (Tritton, 1982, private communication), which were of galaxies on available UKST prism plates. The equivalent galaxy prism-spectra were measured by Cooke on the J-L. Four more calibration points were obtained by Beard from an observing run with an experimental fibre-optic system developed on the AAT (Gray et al. 1982). This system seemed ideally suited for calibration purposes and galaxy cluster work. The system has now been considerably improved (see Carter et al. 1984, and Ellis et al. 1984). Consequently a further run using this fibre system (Ellis and Sharples, 1983, private communication to S.M.Beard), provided a further 14 calibration points for galaxies in two clusters. This brought the total fibre calibration redshifts to 18. All the corresponding prism redshifts

were obtained by Beard from INTERZED measures of Cosmos data from objective-prism copy plate material of the Indus supercluster area. Figure 4.2 gives the results for these 18 calibration points, with the data taken from Beard (1984). The agreement is poor, with the r.m.s. scatter in the Ellis and Sharple's points alone of 6,000 Km/s, even after excluding 2 points because the prism 4000Å features were mis-identified. Furthermore, Beard was convinced that in most cases the 4000Å feature had been correctly identified in the objective-prism spectra. Beard's calibration from Cosmos measures is much worse than that obtained from the J-L measures (see figure 4.1) obtained by Cooke (1980). The standard deviation of the Cosmos calibration described above was 6539 Km/s which compares with 3,995 Km/s from all the J-L measures. Beard surmised that the poor agreement in the Cosmos results was due at least in part to the brighter galaxies having their redshifts underestimated due to the mag/Z effect.

#### 4.2.3. Calibration from clusters of galaxies.

The calibration data described thus far has come from matching individual objective-prism redshifts with those from slit spectra. The results from the Cosmos data in particular, suffer from a significant mag/Z effect, as well as effects of poor intensity conversion and dynamic range and S/N limitations which are exacerbated by use of copy-plate material (see chapter 3). Such effects could explain the poor agreement found by Beard for individual calibration points from Cosmos measures of a copy plate.

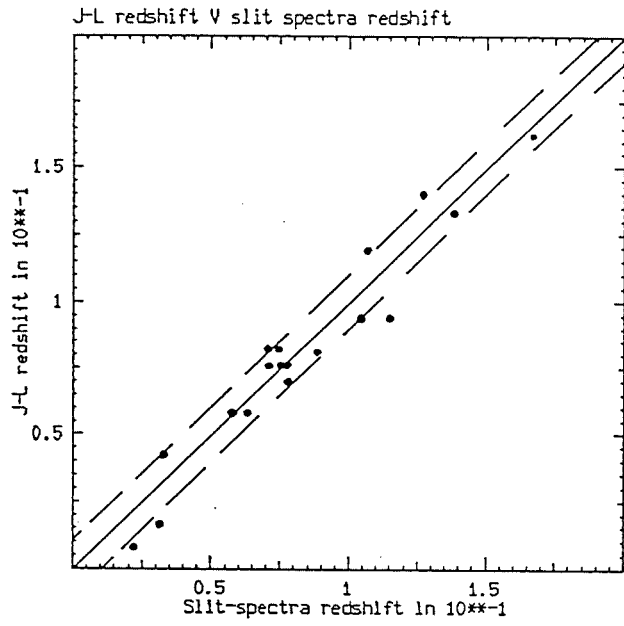


Figure 4.1 The 19 Joyce-Loebl calibration points from Cooke (1980).

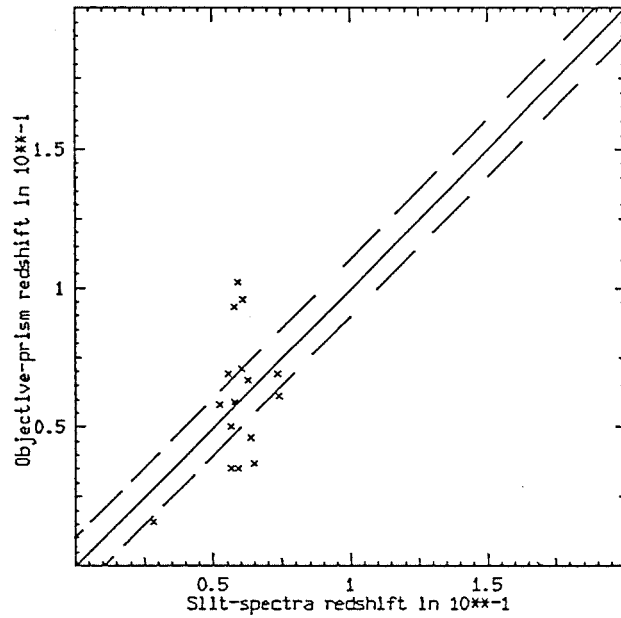


Figure 4.2 The 18 INTERZED calibration points from Beard (1984).

Because of the associated uncertainties, objective-prism redshifts should perhaps be given little individual weight. Collectively however, prism redshifts become more meaningful when numbers obtained for cluster galaxies are significant. For galaxy clusters, the objective-prism redshifts for galaxies in the cluster direction should be dominated by cluster members. Since cluster velocity dispersions are  $\leq 1,500$  Km/s (e.g. Yahil and Vidal, 1977) and usually much less, and since the redshift measurement precision for the objective-prism technique is 2,000-3,000 Km/s, then if the redshifts are binned into 0.01 intervals, the cluster redshift should manifest itself as a distinct peak, with a possible spread over 3 bins due to measurement error and factors such as the mag/Z effect. A significant number of objective-prism cluster redshifts may be necessary to highlight the cluster peak, e.g. Parker et al. (1984a,b).

Although 14 of the calibration points given by Beard (1984), were in 2 clusters (9 in one, 5 in the other) there were still too few points to pick out the cluster peaks in this way. Furthermore, these calibration points spanned 3.5 prism magnitudes from  $b_{uj} = 15.5-19.1$  so that the mag/Z effect may be a significant factor in the observed prism cluster velocity spread obtained. Indeed, reference to the prism velocities for the brightest cluster members given by Beard (1984), reveals significant underestimation by 7,000 Km/s compared with the slit-spectra results. The discrepancies for fainter galaxies are much larger in some cases but here the problem is more likely due to complete  $4000\text{\AA}$  feature mis-identification in these lower S/N prism spectra. This is not unexpected when faint spectra from Cosmos scans of a copy plate are utilised. In fact the results from chapter 3 recommend that copy plates should not be used for objective-prism redshift work if possible.

Determining cluster peak redshifts is probably the most useful and reliable application for the objective-prism technique and has been shown to yield good agreement with slit-spectra results. For instance, Parker et al. (1984a,b), obtained a significant number of objective-prism galaxy redshifts in the direction to the rich galaxy cluster near the centre of field 349, (1950 co-ordinates  $00^{\text{h}}04^{\text{m}}.8, -35^{\circ}00'$ ). The central cD galaxy has a slit-spectrum redshift of  $0.114 \pm 0.001$ , as determined by Carter (1980). The prism redshift for this cD galaxy using Cosmos data of the copy plate UJ5402P P2N1 was underestimated by 0.02, presumably because of the mag/Z effect since this galaxy is quite bright. Indeed, when correction for this effect is applied, the objective-prism redshift is in much better agreement. The cluster peak determined from the rest of the prism redshifts though, was  $Z = 0.11$ , in good agreement with the cD slit spectrum velocity. Cooke (1981), also obtained good agreement for cluster A2670 as already described. Beard (1984), obtained objective-prism measures from Cosmos data from a copy plate of the Indus supercluster region for 3 clusters on the plate. The redshift results for one of these clusters was swamped by background galaxies but peaks for the other 2 clusters were evident. Compared to the average cluster-slit-spectra redshifts as determined by Corwin (1981), the brighter cluster members had their prism redshifts underestimated, again because of the mag/Z effect. After correcting for this trend the mean cluster objective-prism redshifts were in good agreement with the average slit spectra values.

These results demonstrate that cluster redshifts can be determined to an accuracy of  $\pm 0.01$  in  $Z$  from objective-prism measures using both the J-L technique and Cosmos data, provided the limitations of the measuring machines are appreciated and any corrections for the mag/Z effect applied carefully.

#### 4.3. Calibration data obtained for this thesis.

As already stated, the amount of absolute calibration available for objective-prism redshifts is insufficient to justify complete confidence in the technique. Apart from the extra calibration point for the cD galaxy described above, the slit-spectra observations of 107 galaxies in this field with  $b_j < 16.5$  (see chapter 2) afford an opportunity to obtain many more calibration points. Furthermore, the wealth of prism-plate material for this field (see chapter 3 table 3.1), enables an absolute comparison of the accuracy of prism redshifts from different original and copy plates, at least at the bright magnitude end. A firmer indication of the reliability of prism redshift measures from different plates and for data from different measuring machines should be obtained.

Unfortunately, these slit spectra observations are at the extreme bright limit of the objective-prism redshift technique as determined by Cooke (1980), and many are beyond this limit. It will be interesting to determine how many of these slit-spectra results have a suitable  $4000\text{\AA}$  feature redshift. The mag/Z effect should be present in objective-prism measures where manual selection of ECO and  $4000\text{\AA}$  features is made, since these brighter galaxies have image profiles with an effective radius large enough to shift the ECO mid-point. Allowing for this effect may enable the technique to be pushed to brighter magnitudes than determined by Cooke (1980), although this is likely to depend on plate quality and measuring machine employed. Furthermore, Cosmos measures of the A-grade prism plate UJ6535P of field 349, and its pairing with images on a direct plate of the field (see chapter 5), provided a co-ordinate transformation between the plates. This gave a wavelength reference - point independent of the observed ECO. Hopefully this should significantly reduce the mag/Z effect and allow a more direct calibration of the bright-galaxy prism-

redshifts.

The remainder of this chapter is devoted to increasing the objective-prism redshift calibration from the slit - spectra observations described in chapter 2, using the available prism - plate material. Both J-L measures of a selection of prism plates and INTERZED measures from Cosmos data of plate UJ6535P were made. The merits of the respective reduction methods at bright limits can then be assessed. In order to apply a correction for the mag/Z effect it was necessary to measure a significant number of stellar spectra on the different plates using the J-L and INTERZED techniques.

4.3.1. Joyce-Loebl objective-prism measures of the bright galaxies in field 349 for which slit spectra redshifts are available.

The 107 galaxies in field 349 with  $b_j < 16.5$ , observed on the SAAO 1.9m (chapter 2), were identified on the original objective-prism plates UJ5402P and UJ6535P of this field. Details of these plates, viz exposure time, quality, dispersion direction etc, are given in chapter 3 table 3.1. These plates were measured on the J-L microdensitometer at ROE. The same instrumental J-L configuration recommended by Cooke (1980), was employed, except that the slit height was adjusted to 5 different values depending on the width of the prism spectrum scanned (i.e. 34, 45, 68, 90 and 114  $\mu\text{m}$ ). A small region in the centre of a UKST plate of a few square centimetres and a 3 cm strip along the plate edges remained inaccessible due to the translational limitations of the J-L plate carriage. Since the bright galaxy slit-spectra sample was selected from measures of the direct plate of this field by the Cosmos machine, which could only access the central  $5.35^\circ$  by  $5.35^\circ$  plate area, the loss of area available for scanning by the J-L was not severe.

Joyce-Loebl measures were first performed for plate UJ5402P. Ninety-five of the 107 slit-spectra galaxy sample were scanned, with the remainder being inaccessible or too bright. The number of resultant prism spectra which were not too saturated and which exhibited spectral features, were used as the basis for the J-L measures of plate UJ6535P. However, because the dispersion direction for this plate was  $90^\circ$  south of that for plate UJ5402P, some of these spectra were inaccessible for measurement or lay in regions of step wedges etc so that the sample for UJ6535P was smaller. Finally, a selection of these galaxies with reasonable  $4000\text{\AA}$  features from plate UJ5402P, were also measured on the copy plate UJ5402P P2N1. Details of the number of spectra scanned on each plate, those yielding  $4000\text{\AA}$  feature redshifts and the numbers assigned feature weights 3, 2 or 1, are presented in table 4.1.

The number of scanned bright-galaxy spectra assigned top  $4000\text{\AA}$  feature confidence (weight 1) was not insignificant. Almost 60% of the sample measured on plate UJ5402P yielded objective-prism redshifts and 52% of these were assigned weights 1 or 2. The total number of bright galaxies with J-L objective-prism redshifts from this plate corresponding to the slit-spectra sample, more than doubles the calibration points previously available. Obviously this is an important and valuable increase in the available calibration data for this technique. Figure 4.3 gives examples of bright-galaxy spectra measured by the J-L which possessed  $4000\text{\AA}$  features from all three plates.

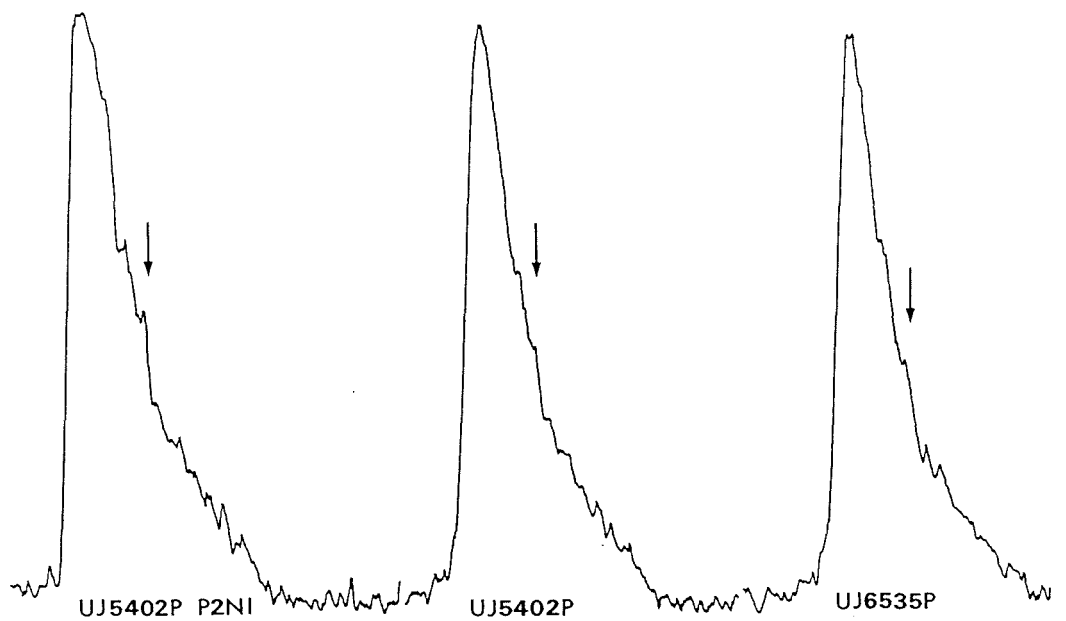
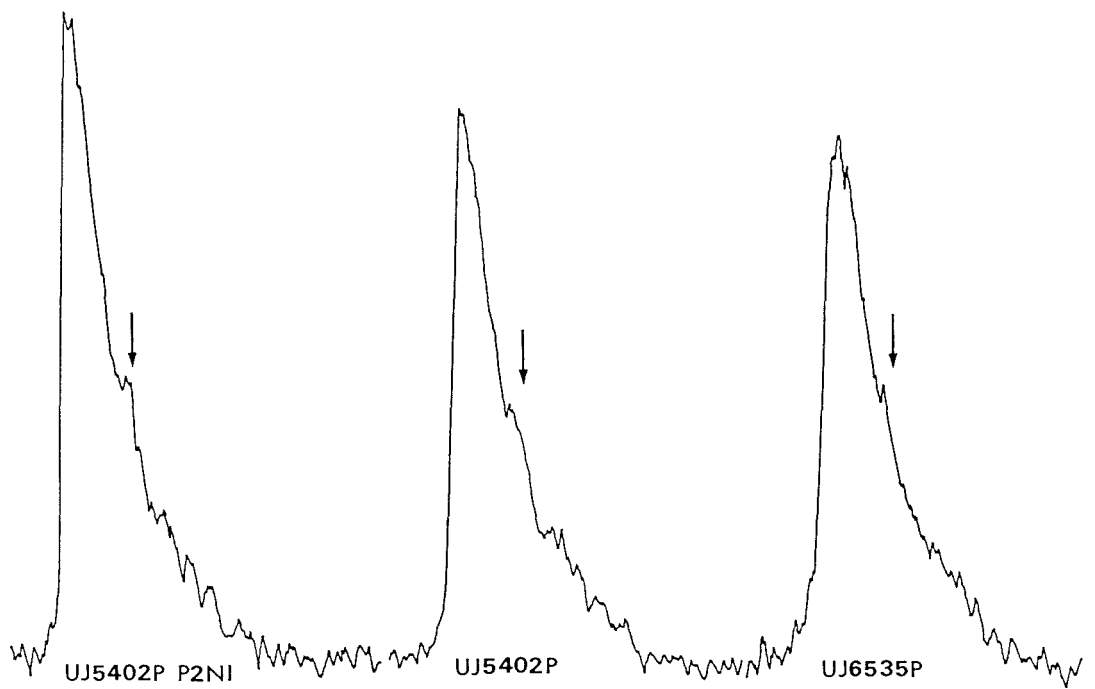


Figure 4.3 Examples of bright galaxy objective-prism spectra possessing  $4000\text{\AA}$  features, as measured with the Joyce-Loebl microdensitometer, on all three plates considered.

Chapter 3, section 3.6 illustrated that a mag/Z effect does exist for brighter objective-prism spectra measured with a J-L, although it is not as marked as for Cosmos data and its size depends on the plate material employed (see chapter 3, figures 3.44a-b). Consequently the brighter-galaxy spectra measured with the J-L are expected to exhibit this effect. Any resultant redshifts should therefore be corrected if possible, or else their values will be underestimated. To this end about 80 late-type stars with good 4000Å features were measured with the J-L from plates UJ5402P, UJ5402P P2N1 and UJ6535P and their prism redshifts obtained. The measures were performed at a variety of J-L slit heights to accommodate the brighter, higher-density spectra which have wider spectral profiles on the plate. The stellar redshift averages for those measures at a given slit height on each plate were calculated. These results are presented in table 4.2. It is apparent that for brighter stellar spectra, indicated by larger slit-height values, the average prism redshifts become increasingly negative. Furthermore, at a given slit-height, the average negative offsets from zero redshift for the 3 different plate measures, are in reasonably close agreement, i.e. to within the expected uncertainties. These offset values were applied to the results for the bright galaxy sample measured on each plate with the equivalent slit-height settings. This correction process is inherently crude since the scatter in the average offset values is not insignificant. However, because the mag/Z effect is real and larger than the redshift uncertainties at brighter limits, the application of a correction for this effect was thought worthwhile.

Table 4.1

Joyce-loebl measures of bright objective-prism galaxy spectra with  $b_j < 16.5$  in field 349 which have corresponding slit-spectra redshifts.

Plate	No.spectra measured	No with redshift	Wt.3	Wt.2	Wt.1
UJ5402P	95	55 : 58%	26	15	14
UJ5402P P2N2	38	20 : 52%	8	2	11
UJ6535P	46	34 : 74%	10	15	9

Table 4.2

Variation in average negative redshift offset with slit-height (together with dispersion), for Joyce-loebl measures of stellar spectra from the 3 objective-prism plates considered.

Slit.Ht. (mm)	UJ5402P	N	UJ5402P P2N1	N	UJ6535P	N
0.75	-0.0004 (0.0095)	28	-0.0025 (0.0100)	30	-0.0091 -	1
1.00	-0.0078 (0.0065)	19	-0.0064 (0.0056)	20	-0.0057 (0.0037)	10
1.50	-0.0102 (0.0093)	13	-0.0129 (0.0061)	12	-0.0141 (0.0058)	30
2.00	-0.0190 (0.0051)	9	-0.0166 (0.0050)	10	-0.0164 (0.0067)	20
2.50	-0.0179 (0.0040)	5	-0.0102 (0.0045)	5	-0.0180 (0.0078)	6

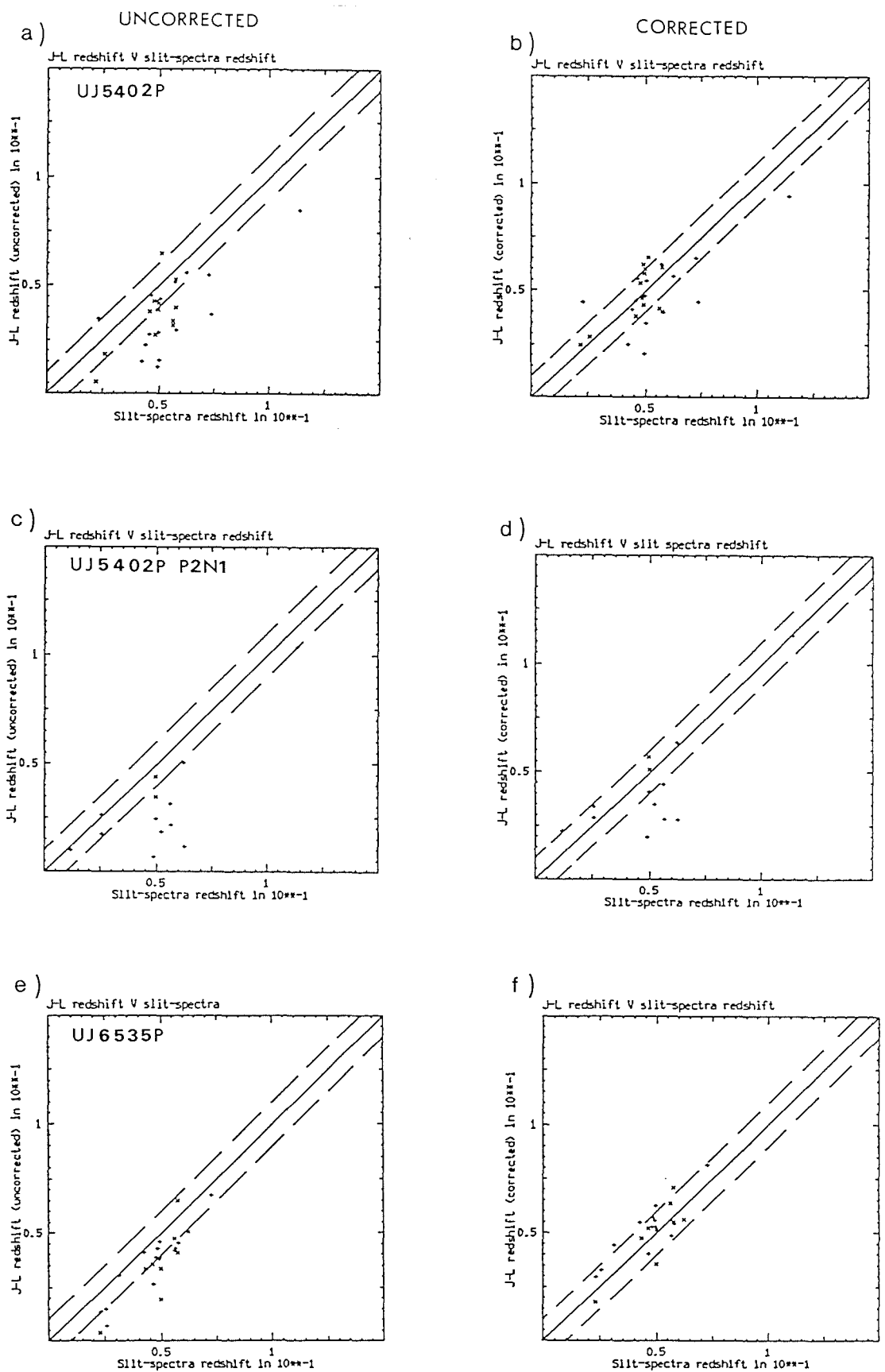


Figure 4.4a-f Calibration plots for the Joyce-Loebl, bright galaxy, objective-prism redshifts versus their slit-spectra values, both before and after the magnitude/redshift corrections were applied (weights 1 and 2 only). Results are from the three prism plates considered.

Figures 4.4a-f show the calibration plots for the J-L bright-galaxy prism redshifts versus their slit-spectra values from the 3 prism plates considered both before and after the mag/Z corrections were applied. The results are for those prism spectra with 4000Å features assigned weights 1 and 2. The improvement in the calibration from the corrected prism data is marked and vindicates the validity and usefulness of the correction procedure. The  $45^\circ$  line and  $\pm 0.01$  in redshift error bounds are super-imposed on the plots. Most of the corrected J-L prism redshift values from all 3 plate measures now lie within the expected uncertainties. These plots demonstrate that good agreement between slit-spectra redshifts and J-L objective-prism redshifts for bright galaxies with  $b_j \leq 16.5$  is possible, as long as the mag/Z effect is allowed for. This is true even for the reduced-contrast, bright, copy - plate, prism spectra. Figures 4.5a-c are the calibration plots for the corrected J-L measures obtained from all three prism plates considered for all feature weights. This illustrates that even low-weight features can yield good agreement.

Figure 4.6 is a histogram of the calibrated direct magnitudes for those bright galaxies in field 349 with slit-spectra redshifts and with J-L redshifts from plate UJ5402P. The shaded region indicates prism -spectra redshifts assigned weights 1 or 2. It is evident that even spectra as bright as  $b_j \sim 15.5$  can yield reasonable 4000Å features and hence redshifts on correction for the mag/Z effect. Similar results were found from the other prism plates considered. Figure 4.7 is a plot of the redshift difference between slit spectra and corrected J-L prism spectra results from plate UJ5402P, versus the direct plate calibrated  $b_j$  magnitude estimates provided by H.T.MacGillivray (private communication). No obvious residual trend in the redshift difference is evident with magnitude for the 51 points plotted.

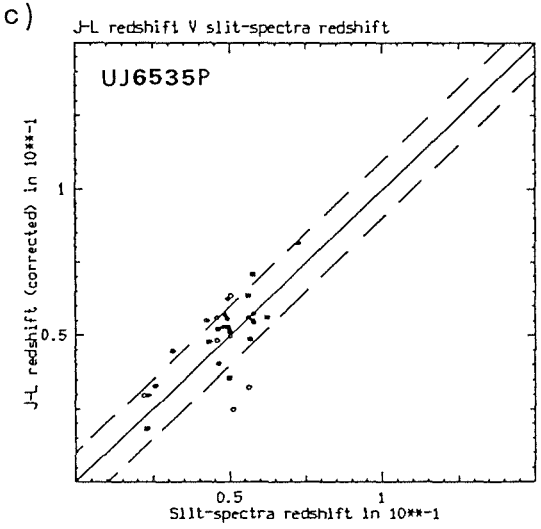
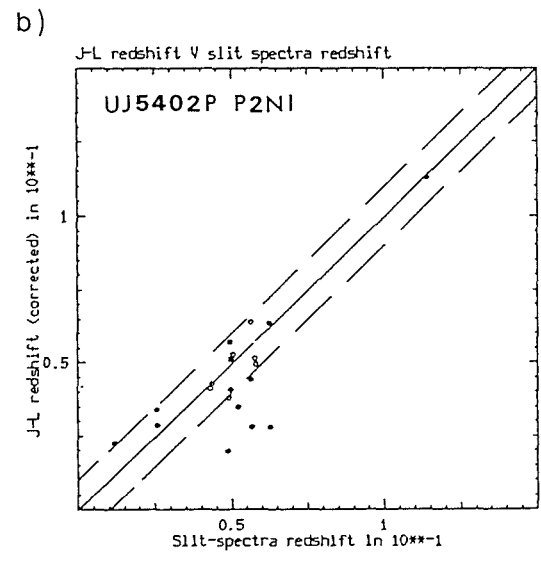
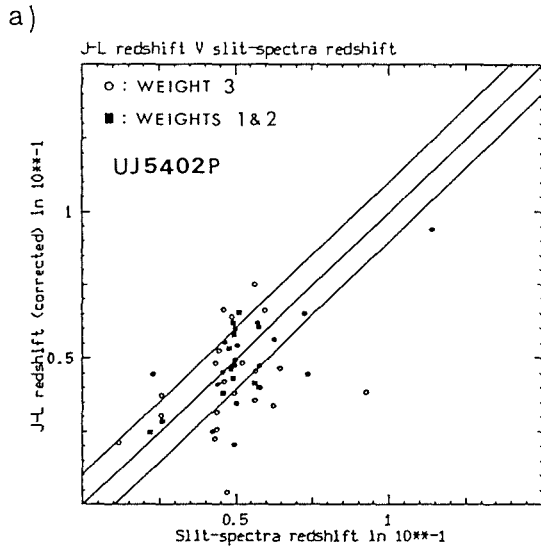


Figure 4.5a-c Calibration plots for the corrected Joyce-loebl measures obtained for this thesis from plates UJ5402P, UJ5402P P2N1, and UJ6535P, all feature weights.

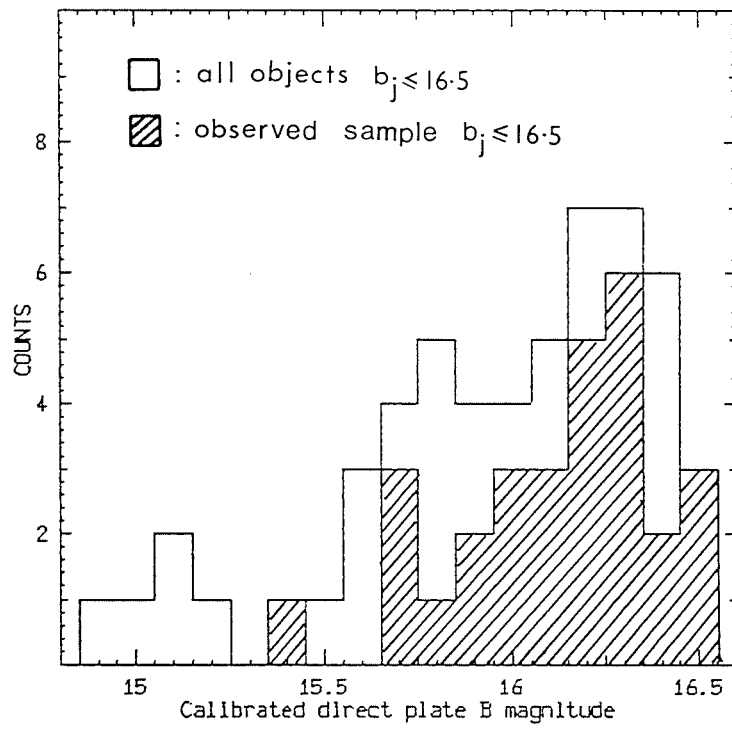


Figure 4.6 Histogram plot of the calibrated direct magnitudes for those bright galaxies in field 349 with slit spectra redshifts and with Joyce-Loebl redshifts from plate UJ5402P.

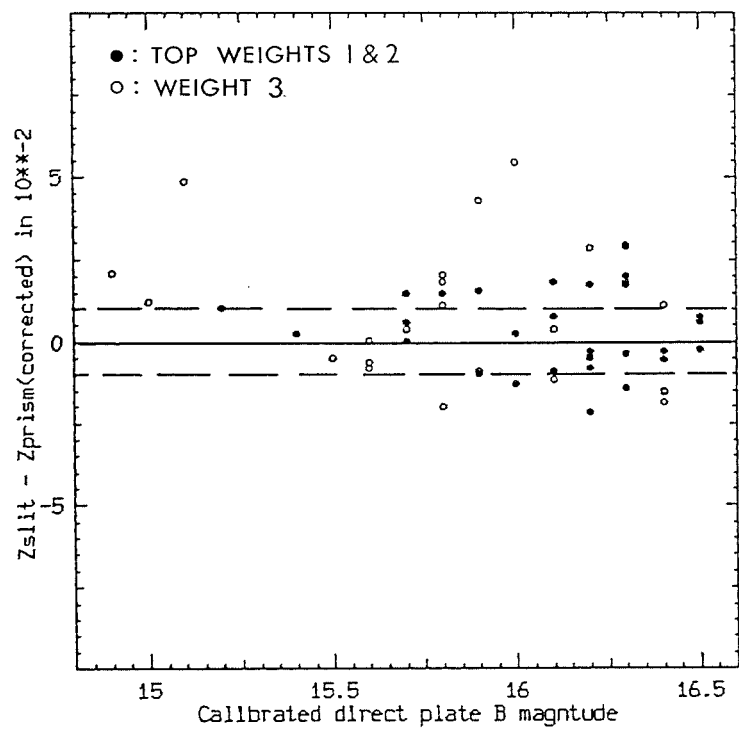


Figure 4.7 Plot of the redshift difference between slit spectra and corrected objective-prism spectra results for plate UJ5402P versus direct plate calibrated  $b_j$  magnitudes.

This is evidence that the objective-prism redshift technique can be pushed to brighter limits ( $b_j \leq 15.5$ ) than that given by Cooke (1980), of  $B \sim 16.0-16.5$ , at least for the corrected J-L measures. However, the direct plate  $b_j$  magnitudes are generally a couple of tenths of a magnitude brighter than the Johnson B magnitudes specified by Cooke (see chapter 5 equation 5.2).

#### 4.3.2. INTERZED measures of the bright galaxies in field 349 and comparisons with their slit-spectra redshifts.

Chapter 5 describes the pairing of a direct plate with the prism plate UJ6535P for field 349 and the subsequent co-ordinate transformation performed. This provides a wavelength reference point for the matched prism spectra independent of the observed ECO. Such a reference point comes from a co-ordinate system defined by the image centroids of faint stars on the direct plate, and should not suffer as severely from the effects of magnitude and colour variations on the observed ECO position nor those of improper intensity conversion or saturation problems with the Cosmos machine data. Hence the mag/Z effect in previous measures of brighter Cosmos objective-prism spectra (see chapter 3), should be considerably reduced. The resulting INTERZED measures of the bright, prism-galaxy spectra with corresponding slit-spectra redshifts should therefore not require correction.

However, redshifts were also obtained from an automatic polynomial fitting to the observed ECO as well as from using the wavelength reference-point provided by the co-ordinate transformation. The resulting calibration from these Cosmos measures should give a comparison between applying a mag/Z correction to redshifts determined from manual ECO positioning and from redshifts obtained using a co-ordinate transformation.

The slit-spectra, bright-galaxy sample was extracted from the matched direct/prism plate and star/galaxy separated data by pairing the equatorial co-ordinates available for both samples. This resulted in 81 spectra matching up from the two samples. This sample was not larger because of cases of overlapping spectra on the prism plate and because the step-wedge positions on the prism plate masked off regions which contained galaxies selected from the direct plate. The objective-prism spectra for this matched sample were then reduced interactively using INTERZED. This resulted in 55 prism-spectra redshifts, with 8 assigned weight 1 and 14 weight 2. Examples of some of these Cosmos data spectra are given in figure 4.8. Comparison of these with the equivalent J-L tracings in figure 4.3 illustrates the improved feature resolution in the brighter spectra from the J-L over those from Cosmos because of the wider J-L machine dynamic range.

Measures of 400 stellar spectra from the Cosmos data of plate UJ6535P, where the wavelength reference-point is provided by the co-ordinate transformation, indicated that the Mag/Z effect had been eliminated, (see chapter 5, figure 5.31). However, a constant negative offset from zero redshift of  $-0.021$  was evident. Furthermore, the redshift scatter at a given magnitude was larger than the equivalent scatter in the redshift/magnitude plot for stellar measures obtained from using an automatic polynomial fit to the observed ECO, even though a significant, apparently linear, mag/Z effect is present (see chapter 5, figure 5.32). Figure 4.9 is the resultant calibration plot from the INTERZED prism redshifts (all weights), corrected for this negative offset. The agreement with the slit-spectra results is not nearly as satisfactory as for the equivalent J-L measures. Many points lie well outside the expected uncertainties about the  $45^\circ$  line.

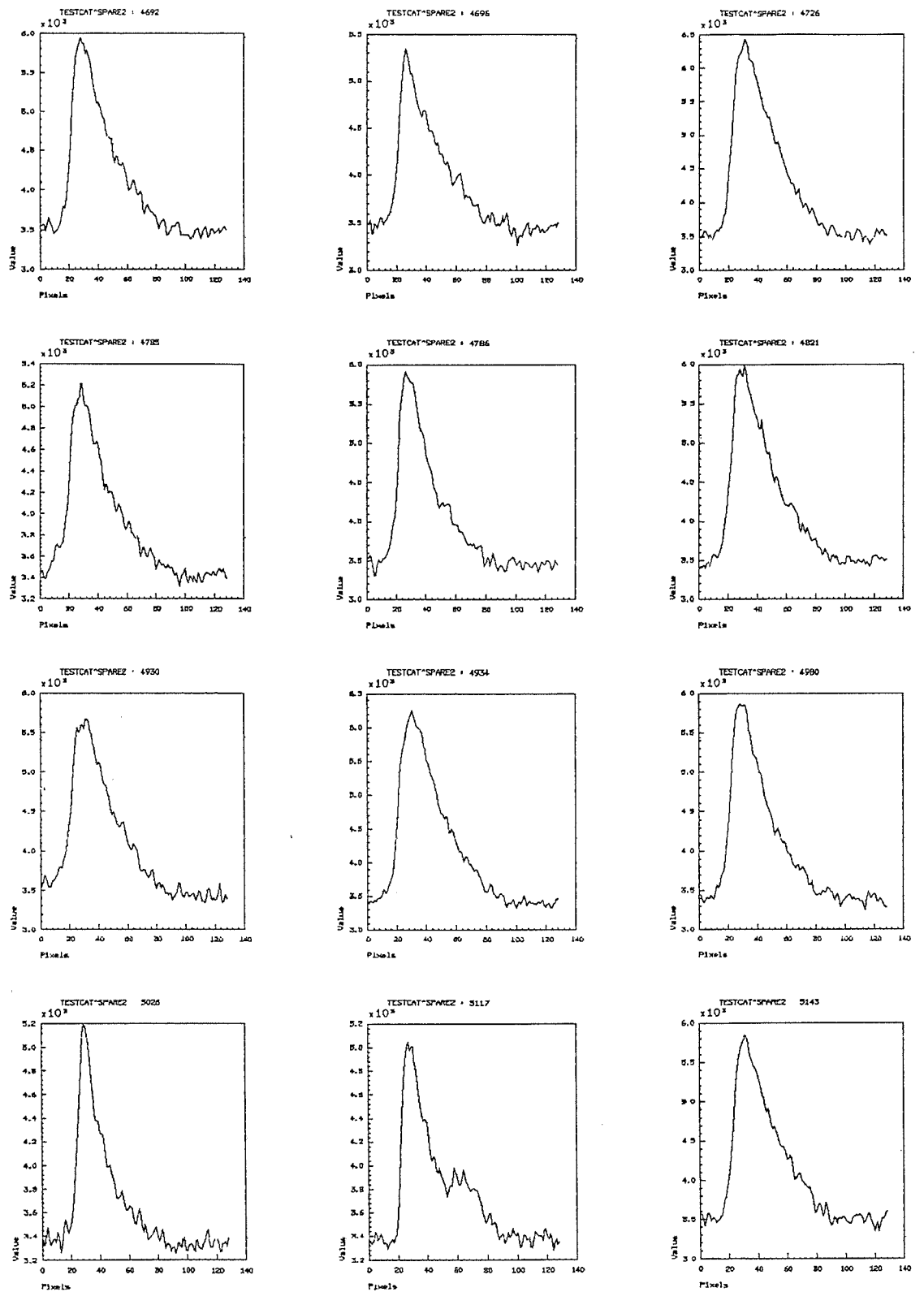


Figure 4.8 Examples of COSMOS INTERZED bright galaxy spectra from plate UJ6535P

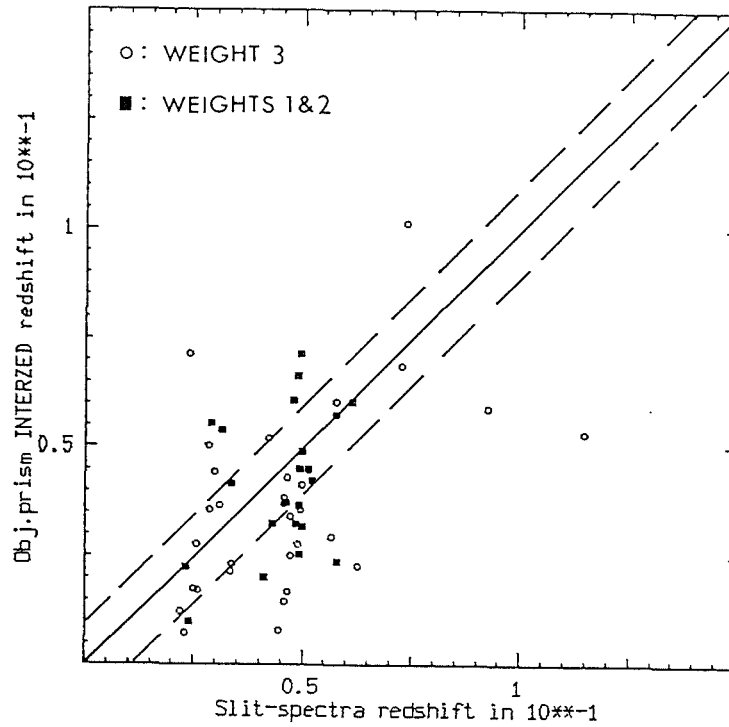


Figure 4.9 INTERZED objective-prism redshifts versus slit spectra redshifts, for the bright galaxy sample.

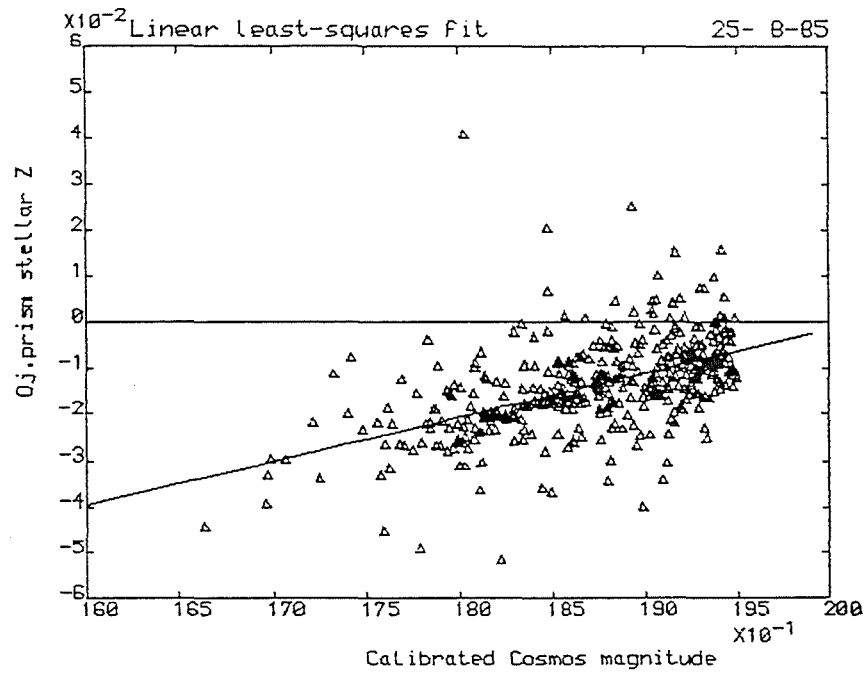


Figure 4.10 INTERZED stellar objective-prism redshifts versus COSMOS magnitude estimates, with linear least squares fit superimposed.

If only those INTERZED measures with top weight are considered however, the agreement is good, with 7 of the 8 points lying within  $\pm 0.01$  in redshift of their slit-spectra values. The proportion of the measured INTERZED sample of all weights yielding good agreement with the slit-spectra results is significantly smaller than for the equivalent J-L measures (i.e. 43% of the INTERZED sample yielding prism redshifts compared to 76% of the J-L redshifts).

Hence, even though the INTERZED results are from an A-grade, high-quality prism plate, only the very best identified features for the bright-galaxy sample yield good agreement with the slit-spectra results. Many of the identified features in the INTERZED spectra from Cosmos data may thus be affected by saturation and feature compression problems (as described in chapter 3) because of the high plate densities of these bright-galaxy spectra. In fact the calibrated direct-plate  $b_j$  magnitude estimates of the 7 INTERZED spectra assigned redshift weight 1 are all  $b_j \gg 15.8$ . This is probably the brightest limit that the objective-prism technique can be pushed to with Cosmos data for this particular plate. Even so this is still  $\sim 0.5$  magnitudes brighter than the limit given by Cooke (1980).

For comparison purposes, the same INTERZED sample of bright-galaxy spectra were re-measured using a wavelength reference-point determined from an automatic polynomial fit to the observed ECO. This was the technique formerly employed before the advent of the plate pairing and co-ordinate transformation method described in chapter 5, which provides a wavelength reference-point automatically. For these measures of bright galaxies we might expect the resultant INTERZED redshifts to be underestimated because of the mag/Z effect. In order to account for this expected effect, a large sample of stellar spectra were measured using the same INTERZED technique.

Figure 4.10 is the resultant plot of INTERZED stellar redshift versus Cosmos magnitude estimate. An approximately linear mag/Z effect is evident in the data. The dispersion in redshift at a given magnitude estimate is  $\pm 0.01$ . Brighter than  $b_j \sim 17.5$  there are too few points to say anything conclusive about the continuing trend to negative redshift with increasing image brightness although it seems reasonable to assume that the downward slope continues. A linear least-squares fit was applied to this data and the result overlaid on the plot. The basic code for this program was taken from Bevington (1969), and adapted for this work by the author. Details of the fit are given in table 4.3. The characteristics of the fit indicate that the straight-line relation is a reasonable representation of the data trend, adequate for correction purposes. Using the calculated gradient and intercept of the fit, the INTERZED galaxy redshifts from using the observed ECO mid-point-to-feature separation were corrected.

Figure 4.11 is a plot of the INTERZED measures of the bright galaxy sample assigned top feature weights versus their slit-spectra results, where ECO position was determined interactively. The filled circles are the raw, uncorrected prism redshifts whilst the open circles refer to the prism values after allowing for the mag/Z effect seen in figure 4.10 above. Note that 6 of the 8 top weight uncorrected prism redshifts lie within  $\pm 0.01$  of their slit-spectra values. However, the majority, including the 2 discrepant points, do lie below the  $45^\circ$  line indicating that their prism redshifts are indeed underestimated as would be expected from a mag/Z effect. It is obvious from this plot that the uncorrected INTERZED redshifts give better agreement with the slit-spectra values than the 'corrected' INTERZED redshifts which seem to have overcompensated for any mag/Z effect in the galaxy measures.

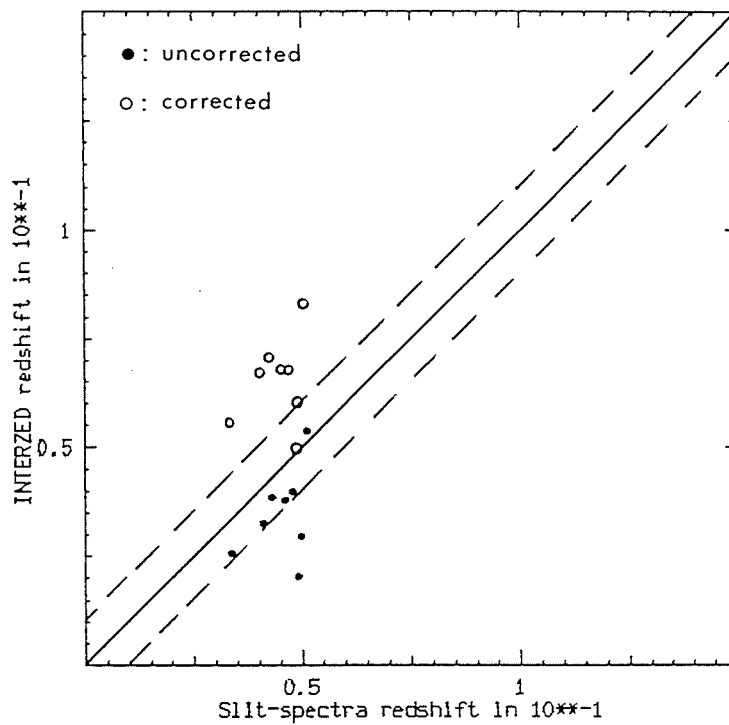


Figure 4.11 INTERZED measures of the bright galaxy sample assigned top feature weights versus their slit-spectra redshifts (ECO position was determined interactively).

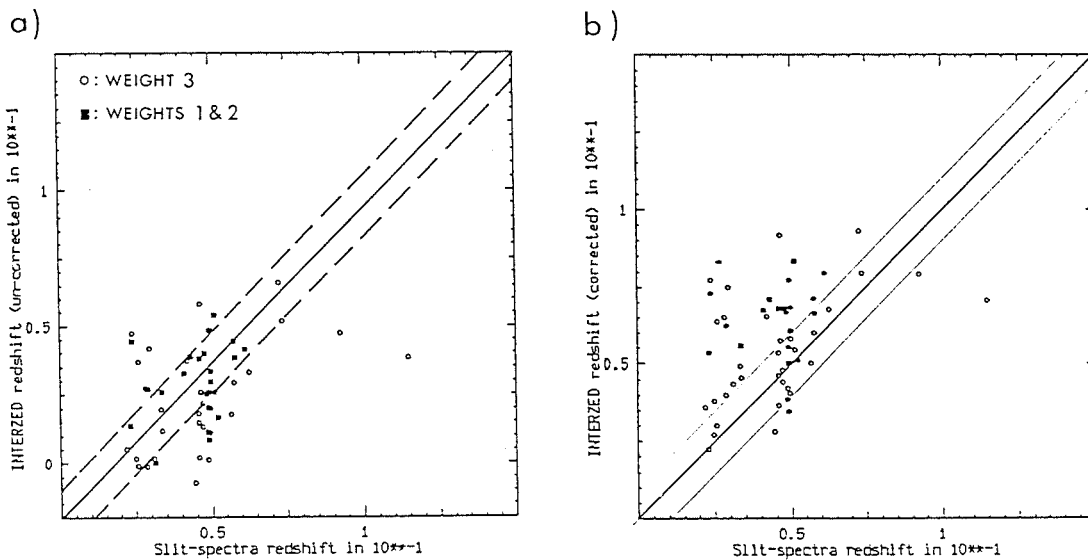


Figure 4.12a-b INTERZED objective-prism galaxy redshifts (all weights) versus their slit-spectra values before and after a magnitude/redshift correction was applied.

Table 4.3

Characteristics of linear least squares fit to the data in figure 4.11. Instrumental ( $\sigma$  [y]), weighting was applied to account for the measurement errors of the objective-prism redshift values.

Gradient : 0.00952, std.dev.: 0.00155

Constant : -0.19193, std.dev.: 0.02856

Multiple linear correlation co-efficient: 0.399

Reduced Chi-square of fit : 1.094

Value of f-test fo fit : 37.532

Table 4.4

As above but for the data in figure 4.14.

Gradient : 0.06039, std.dev.: 0.01288

Constant : -0.02537, std.dev.: 0.00192

Multiple linear correlation co-efficient: 0.292

Reduced Chi-square of fit : 1.191

Value of f-test fo fit : 18.4513

This effect is even more pronounced if the results from all weights are considered. For instance, figure 4.12a-b is the INTERZED galaxy redshifts (all weights) versus their slit-spectra values before and after a magnitude/redshift correction was applied. Furthermore, reference to figure 4.9 indicates that the uncorrected INTERZED results, where an interactive ECO determination was used, give better agreement with the slit spectra values than the INTERZED results where the ECO position is determined from the co-ordinate transformation. More calibration points lie within  $\pm 0.01$  of their slit-spectra redshifts. This indicates that for bright-galaxy spectra at least, uncorrected INTERZED measures from plate UJ6535P, using an interactive ECO determination, give a better calibration than using an ECO position provided from the co-ordinate transformation. The filled circle points in figure 4.11, if compared with the equivalent results from the co-ordinate transformed INTERZED measures, yield good agreement to within the expected uncertainties. The overcompensation applied to the galaxy redshifts using a correction based on the negative offsets of stars of the same isophotal direct-plate magnitudes is not an altogether surprising result.

As plate UJ6535P was taken in good seeing, starlight is concentrated into a smaller spectral image area than on a plate taken in moderate seeing (e.g. plate UJ5402P), since the blurring effect of the seeing disk is reduced. For galaxies the diffuse nature of these images will also be more apparent to fainter limits. Consequently, for a galaxy and star of the same direct isophotal magnitude, the actual mean density of pixels scanned by Cosmos in the equivalent prism-plate spectra will be higher for the stellar spectra than for the galaxy spectra and the image area smaller. This effect is enhanced when the blurring effects of the seeing disc on the spectral image profiles is less severe. The causes of the mag/Z effect in Cosmos data, e.g. saturation and intensity conversion problems (see

chapter 3), will be more pronounced in the stellar prism-plate spectra because of their more concentrated nature. As a result, the observed mag/Z effect found in INTERZED stellar redshift measures from plate UJ6535P cannot simply be applied to galaxy spectra of the same direct isophotal magnitude. This is because of the difference in mean surface brightness between stellar and galaxy prism spectra which is exacerbated by the good prism-plate quality. Thus a larger correction than was actually necessary was applied (e.g. in figure 4.11).

Nevertheless, since a trend similar to that found for stars probably exists in the brighter galaxy prism spectra measured with INTERZED, where an interactive ECO determination is used, it would be desirable to apply a correction to the redshifts if possible. To circumvent the problem of applying an appropriate correction to these galaxy INTERZED redshifts using magnitude comparisons, a mean surface brightness parameter 'S' was calculated for both stellar and galaxian objects. This was obtained by dividing the Cosmos calibrated direct-plate magnitudes with the corresponding direct-plate image area (as provided from the image parameters for each object from running the Cosmos analyser on the MM data of the direct plate). Direct magnitudes and image areas were utilised because stellar objective-prism image areas are significantly dependent on object colour as well as magnitude. Hence, for a star and galaxy of the same isophotal magnitude 'M' say,

$$M/(\text{area})_{\text{gal}} < M/(\text{area})_{\text{star}} \dots \text{i.e. } S(\text{galaxy}) < S(\text{star})$$

where 'S' is in units of magnitudes per pixel. A better correction factor may thus be obtained if galaxy redshifts are corrected by the amount that stellar spectra with the same 'S' value are offset from zero redshift.

Figure 4.13 gives the results of plotting INTERZED stellar redshifts (from using an interactively determined ECO position), versus the mean surface-brightness parameter 'S' for a selection of  $\sim 400$  stars brighter than  $b_j \sim 18.7$ . The stellar sample with  $18.2 < b_j \leq 18.7$  is indicated by filled squares whilst the sample with  $b_j \leq 18.2$  is represented by open circles. For fainter objects the value of 'S' increases. The plot also reveals an approximately linear relation between stellar redshift estimate and surface-brightness parameter (cf. figure 4.10). The linear least-squares fit to these data is overlaid on the plot and the characteristics of the fit given in table 4.4. This fit was subsequently used to calculate the 'new' redshift corrections to apply to the INTERZED galaxy results with the same 'S' value.

The effect of applying this 'new' correction is given in figure 4.14, which can be compared with the previous correction based solely on magnitude considerations in figure 4.12b. A significant improvement is evident, with INTERZED redshifts at a given slit-spectra redshift now straddling the  $45^\circ$  line instead of mainly lying above it. This technique does seem to yield a more appropriate means of correcting INTERZED galaxy redshifts when using an interactive ECO determination than a simple correction based on object magnitude alone. The actual improvement in the calibration over that from using the raw, uncorrected INTERZED redshifts (figure 4.12a) is however marginal. No overall improvement in the calibration is obvious. Nevertheless this correction technique may prove valuable for any future measures from different lower-quality prism plates.

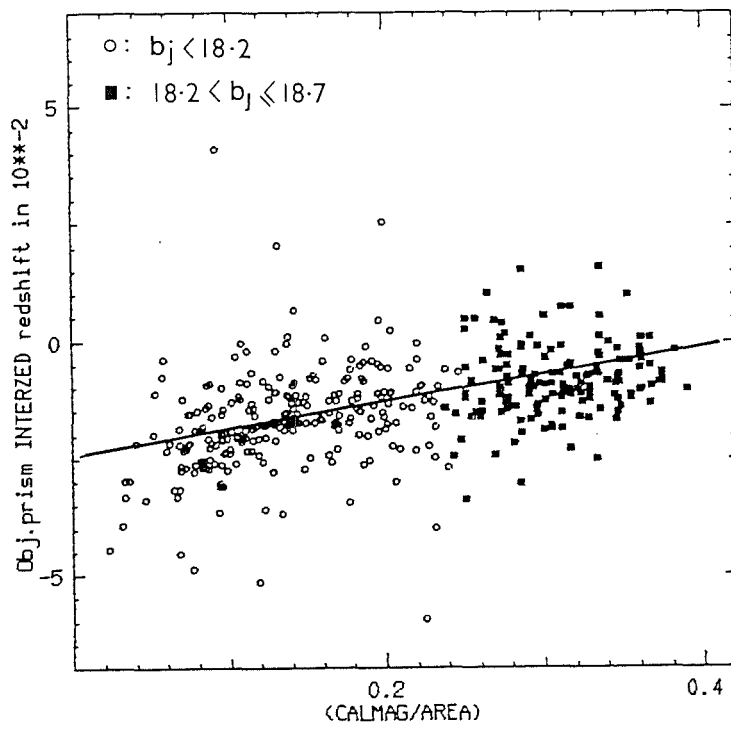


Figure 4.13 INTERZED stellar objective-prism redshifts from an interactively determined ECO position against the mean surface brightness parameter 'S', together with an overlaid least squares fit.

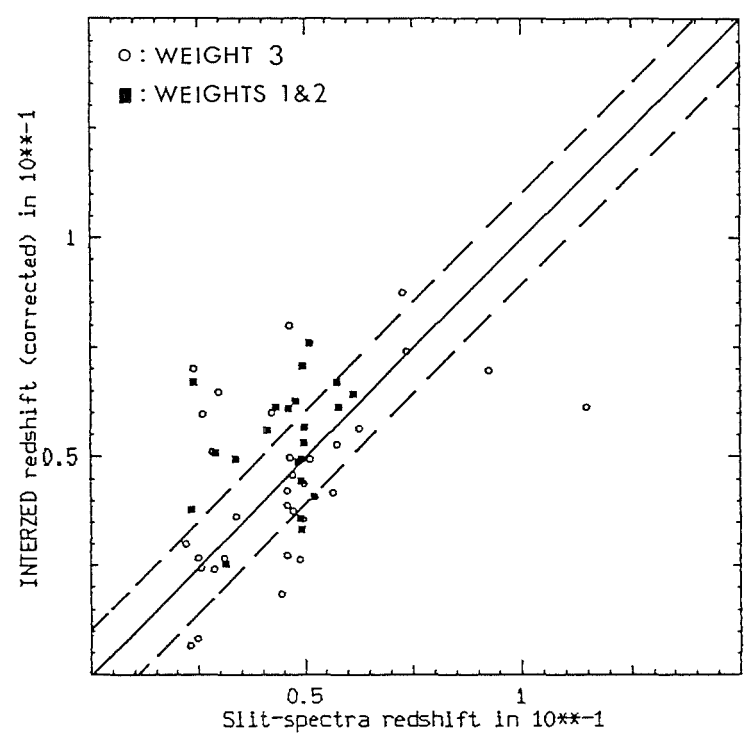


Figure 4.14 Corrected INTERZED galaxy redshifts against their slit-spectra counterparts.

#### 4.4. General conclusions for the calibration data obtained.

The number of calibration points for the objective-prism redshift technique from both J-L and Cosmos data has been significantly enlarged, (i.e. by a factor of two), over that previously available. Unfortunately these extra points are for galaxies with  $b_j < 16.5$ , at the extreme bright limit of the technique as determined by Cooke (1980). Consequently much more slit-spectra data for fainter galaxies at higher redshifts are required to improve the calibration between  $16.5 < b_j < 19.0$ . Such an observational programme would be ideally suited to the fibre-optic spectroscopy system on the AAT (see section 4.2), or a similar system currently under development for the UKST (Dawe and Watson, 1984). The main findings from the calibration work described above will now be summarised.

(1) A larger sample of calibration points was obtained from measures of bright galaxy objective-prism spectra using the J-L than from using Cosmos data, even though essentially the same parent population was considered. However, it was necessary to apply a correction factor to the J-L results to account for the mag/Z effect. The correction procedure employed proved to be successful. No correction for the INTERZED measures, where the ECO position is provided from a co-ordinate transformation, should be necessary. The larger calibration sample for the J-L measures is due to the wider plate density coverage of the J-L compared with Cosmos, which suffers from S/N limitations, and saturates only 1 density unit above the scanned plate sky-background. Details of these problems are given in chapter 3.

(2). The J-L technique can obtain objective-prism redshifts accurate to within  $\pm 0.01$  of their slit-spectra values for galaxies as bright as  $b_j \sim 15.5$ , provided the mag/Z effect is allowed for. This is  $\sim 0.5$  magnitudes brighter than the limit specified by Cooke (1980). The exact limit at the bright end may depend somewhat on plate quality, although the 2 original and 1 copy prism plates considered all confirmed this brighter limit.

(3). Calibration from using INTERZED redshifts (on COSMOS data), determined from the separation between an observed  $4000\text{\AA}$  feature and the interactively-determined ECO position, is better than that provided from using the ECO position given by the co-ordinate transformation. This is true even though no correction for the expected mag/Z effect was applied. Such a result is contrary to expectations but probably reflects the larger redshift dispersion at a given magnitude obtained for the stellar results when using the co-ordinate transformation to define a wavelength reference point (see chapter 5 figure 5.31), even though the mag/Z effect appears to have been eliminated.

(4). Applying a correction to the INTERZED redshifts for the mag/Z effect (where an interactive ECO position was used), which is based solely on the object magnitude leads to an overcompensation for any such effect in the galaxy results. This is not surprising because galaxies are extended objects and their mean surface brightnesses are lower than a star of the same direct isophotal magnitude. These differences are enhanced by the good seeing on plate UJ6535P.

(5). A correction based on mean object surface brightness (in magnitudes per pixel) applied to the INTERZED results reduces the overcompensation found from using a magnitude based correction alone. The improvement in the calibration over that from the uncorrected measures is however, marginal for this plate.

(6). The best, most consistent set of calibration points from the INTERZED measures described above come from those bright galaxy prism spectra assigned top feature weights. Good agreement to  $\pm 0.01$  in redshift with the slit-spectra results is then obtained from INTERZED redshifts where the ECO position is determined directly (figure 4.11), and also where it is provided by the co-ordinate transformation. Unfortunately, the number of such points is small.

(7). The use of the objective-prism technique as means of determining cluster redshifts to  $\pm 0.01$  has been confirmed. This is perhaps the most worthwhile and fruitful application of the technique as a dependence on the individual accuracy of the prism redshifts is not crucial.

Finally figure 4.15 gives a composite plot for three sets of calibration points now available for the objective-prism redshift technique. The 18 AAT fibre-optic calibration points described by Beard (1984), are excluded because a rather poor-quality objective-prism copy plate was used. However the plot does include a further 12 points obtained from survey field 145 in the Indus supercluster. The objective prism redshifts had been determined by Beard (private communication), using INTERZED, and the slit-spectra observations were performed by the author and Dr. Beard on the SAAO 1.9m telescope and were reduced by the author as described in chapter 2. Further details for this sample are given by Parker and Beard (1985, in preparation). The other plotted calibration points are the J-L results from plate UJ6535P obtained for this thesis and the J-L calibration points obtained by Cooke (1980).

J-L Obj.prism redshifts v slit-spectra redshifts.

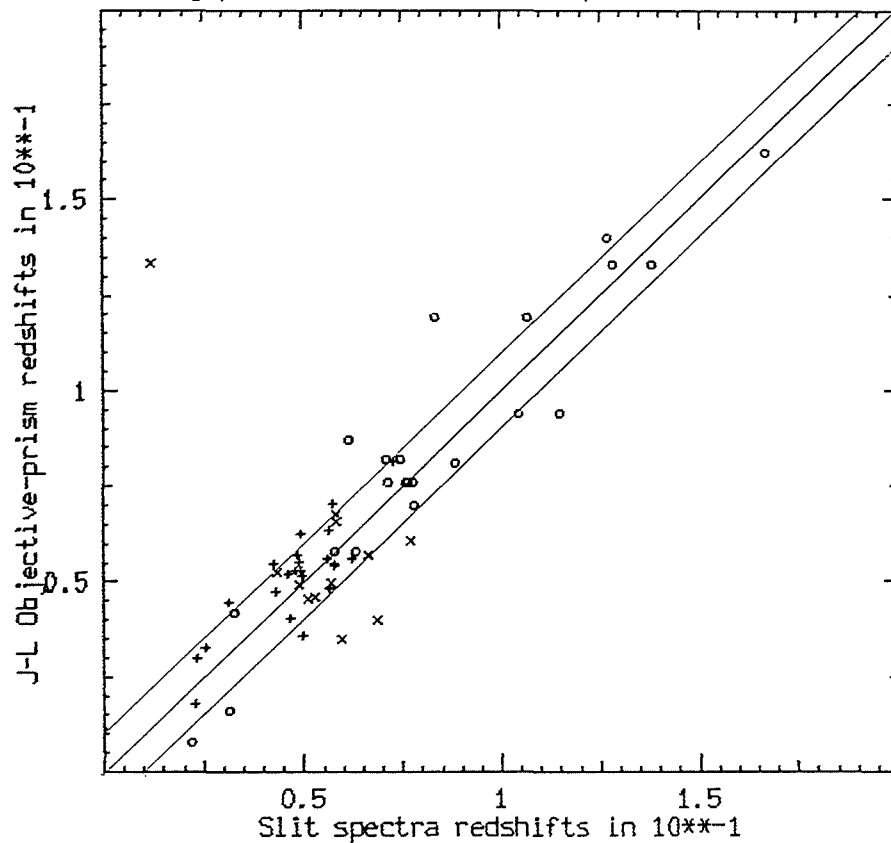


Figure 4.15 Composite objective-prism redshift calibration plot (see text for details).

Key.

- O : JAC Joyce-loebl calibration points.
- + : QAP Joyce-loebl calibration points for field 349
- X : SMB Interzed calibration points for field 145

The reduction of Cosmos measures of the direct and prism plates of SERC survey field 349.

5.1. Summary.

This chapter describes measures performed by the Cosmos machine on the direct plate J6145 (copy) and prism plate UJ6535P (original) of SERC survey field 349, how the data was reduced, and how a match between images on the direct and prism plates was obtained. This match enabled objective-prism galaxy spectra to be extracted and measured for redshift. Chapter 3 has illustrated the problems associated with consistent reduction and measurement of objective-prism spectra and the potential that objective-prism redshifts have for highlighting gross features in the large-scale galaxy distribution. Work on objective-prism galaxy spectra in field 349, Parker et al. (1984,a,b), has already been performed, but only for restricted samples in the environs of rich clusters. This chapter details how objective-prism spectra for all galaxies to specified magnitude limits over the entire plate area accessible to the Cosmos machine were extracted for measurement. The match between images on the direct and prism plates enables, in principle, a 'pure' galaxy sample of objective-prism spectra to be selected, since each object was classified and flagged from the star/galaxy separation performed on the direct plate. A co-ordinate transformation from the direct plate, produced by the image pairing, was used to define a wavelength reference point in preference to the ECO (see later). The data obtained from the direct and objective-prism plate Cosmos measures form the basis of the statistical 2-D and crude 3-D analyses of the faint galaxy distribution in this field (see chapter 6).

## 5.2. The plate material.

Table 3.1 chapter 3, gives details of the plates scanned by Cosmos to provide data for the analysis of the faint galaxy distribution in field 349. Cosmos has since undergone enhancements both in hardware and software (Macgillivray and Stobie, 1985, hereafter referred to as MS), so that data are now extracted in 14-bit words instead of the 8-bit words formerly used. The main advantage of the 14-bit capability is that 16,384 transmission levels are now possible for each pixel compared with the 256 levels previously available. This improved resolution in transmission space should lead to better intensity conversion. The Cosmos 8-bit data was used in this thesis, however, because the 14-bit capability was not available in time.

Since an 'A' grade original, objective-prism plate was used it was hoped that even better prism spectra would be provided than from plate UJ5402P, which was employed for the earlier tests (chapter 3). The good seeing on this plate should give less resolution loss from the blurring effects of seeing along the dispersion direction. A general S/N improvement, especially for fainter galaxies, is also expected since the galaxy light will be concentrated into fewer pixels. Unfortunately, a copy of the direct plate J6145 was used because the original high-quality direct plate was unavailable at the time. Plate J6145 is the accepted survey plate for this field. Differences in photographic information on a quality copy plate compared with an original have been detailed in chapter 3 section 3.12. However, since copy plates are optimised to recover information for faint images, the star/galaxy separation should not be seriously affected. Ideally both high quality, original direct and objective-prism plates should be used.

The prism plate was scanned in mapping mode (MM) using a  $16\ \mu\text{m}$  increment and  $16\ \mu\text{m}$  spot size. The total plate area scanned was  $17,920$  by  $17,920$  pixels ( $1\ \text{pixel} = 16\ \mu\text{m}$ ) corresponding to the central  $5.35^\circ$  by  $5.35^\circ$  square degrees. This gave  $\sim 320$  Mbytes of 8-bit data which required 10 magnetic tapes for storage (see MS). These 10 tapes of MM data were spooled up to the Cosmos Vax at ROE for subsequent processing. This entailed application of the Cosmos analyser programme to detect the objective-prism spectra, together with their extraction.

The direct plate was scanned in thresholded mapping mode (TMM) which only uses information for pixels a given threshold above the plate sky background intensity. Details of this process are given by MS. The thresholded pixels are subsequently read into an off-line pattern analyser (Thanisch et al. 1984), which provides a list of image parameters based on moment analysis of the image pixels (Stobie, 1980). This is referred to as image analysis mode (IAM). These image parameters, such as image area and isophotal magnitude estimate, form the basis for the star-galaxy separation. The next reduction step was to provide an intensity conversion for the prism plate.

### 5.3. Intensity conversion of the prism-plate data.

Chapter 3 section 3.4 demonstrated that good intensity conversion of MM data was a vital part of preparing objective-prism spectra prior to their measurement, especially if a direct fit to the ECO is made. Even though the co-ordinate transformation provided by the direct/prism plate match will provide an automatic spectral ECO position, it is still essential to obtain a transmission to relative intensity conversion for the prism plate. This enables a uniform isophotal threshold to be set over the entire plate at a fixed fraction above the sky background, regardless of any local variations

in the background caused by changes in emulsion response and edge effects such as vignetting. A controlled sample of spectra can then be extracted in an objective manner. Furthermore, spectral isophotal magnitude estimates can be obtained by integrating the intensity of each image pixel and using formula 3.5 and 3.6. Although such magnitudes are not in any standard photometric band, since no filter is used when taking prism plates, they can be compared with the direct plate magnitudes in the paired sample. An important point is that good intensity conversion leads to proper scaling of the relative positions of spectral features, making identification of  $4000\text{\AA}$  features less ambiguous. The same features in Cosmos density spectra would be compressed, particularly for brighter objects.

For the intensity conversion of UJ6535P the plate step-wedge areas were scanned by Cosmos in MM with data written to magnetic tape. To retain adequate density resolution with the 256 transmission levels available, the gain on the output signal from the photomultiplier (which detects transmitted light from the CRT spot through the plate in the Cosmos machine) could be set to any of 4 values. The step wedge scans were repeated at all 4 density gains to cover the largest possible density range of the sensitometer spots. The gain setting for the actual plate measurement was chosen to obtain the best possible resolution over the most useful plate density range. This depends on the sky-background plate density, which varies with exposure time, and if an original or copy plate is being scanned. A small overlap between the density ranges given by the gain settings exists so it is possible to maximise the transmission resolution for the plate measurement and to allow slight zero-point adjustments (as described by MS).

The prism plate was scanned at gain 3 so only step wedge information for the first three gain settings was relevant. Data for the 16 step KPN0 alpha wedge (UKST handbook p6.1.3) for gains 3,2 and 1 was spooled to disk using the Cosmos software 'costep'. This gives a STARLINK BDF file for each step wedge scan which can then be displayed as STARLINK images. The 'stepwedge' command in E2D was used to obtain average transmission values for the 16 steps in the KPN0 wedge by using a 40 by 40 pixel box centred on each step. This was repeated for each wedge scan. Table 5.1 gives the average transmission values from these measures, together with the relative intensity for each spot. Resolution in transmission space for the different steps was relatively poor, even when they were not saturated. The fractional pixel values are an averaging artefact so differences between average transmission values for steps 2,3,4 and 5, as measured at gain 3 for instance, are not meaningful. In fact, at gain 3, only three measurements were not saturated. Psuedo-transmission values for some of the saturated steps can be obtained by using the ratio between transmission values for the same unsaturated steps at different gains. This ratio should be constant if the correct transmission value for a totally blackened pixel 'Tb' is added to the higher gain measure before dividing by the lower gain measure (ideally Tb should be zero). The value of Tb was actually modified until a constant ratio between the reliable transmission values from corresponding steps at the different gains was obtained. A value of Tb = 3 was found to give the best agreement.

Table 5.1

The average transmission values obtained from measures of the KPNO step wedge on plate UJ6535P, together with the relative intensity for each spot.

Step	Log(rel.I)	Gain 1	Gain 2	Gain 3
1	0.76 ± 0.02	-	-	2.15
2	0.53 0.02	-	-	3.28
3	0.40 0.02	-	-	3.72
4	0.15 0.01	-	-	3.89
5	0.00 0.01	-	-	3.91
6	-0.15 0.02	-	0.96	4.90
7	-0.30 0.02	-	1.01	6.80
8	-0.55 0.02	2.09	10.28	43.80
9	-0.85 0.03	15.66	64.05	251.60
10	-0.97 0.04	25.92	104.40	-
11	-1.14 0.05	33.76	135.30	-
12	-1.38 0.05	41.28	165.50	-
13	-1.58 0.05	40.43	162.10	-
14	-1.74 0.05	41.77	167.50	-
15	-1.90 0.06	43.18	173.10	-
16	-2.14 0.06	44.87	179.90	-

Table 5.2

Details of the variation in the number of images detected from the prism plate UJ6535P with changing area cut.

Area cut (pixels)	Images retained
20	61,292
27	50,390
43	40,037
74	29,934
142	19,909
267	9,836
1000	593

Once a suitable set of KPNO step wedge transmission values were obtained, a plot of  $\log(\text{relative intensity})$  versus transmission was made. A cubic spline fit was attempted using the 'coscal' routine, provided for generating a look-up table for converting transmission to relative intensity. This can be globally applied to the entire plate. The attempted spline fit is given in figure 5.1. The best fit remained an unsatisfactory representation of the relation between  $\log(\text{relative intensity})$  and transmission. Beard (1984), found that the step-wedge calibration technique was unsatisfactory for providing an accurate intensity conversion because insufficient step levels were falling within the density range of the Cosmos machine, as is indeed the case for this plate. Furthermore, practical difficulties exist in generating an accurate step wedge on the plate itself due to source illumination fluctuations over prolonged time intervals. Alternative possibilities for calibration are discussed by Beard (1984), but for our purposes the step-wedge technique was the only practical means of obtaining a relative calibration. Indeed, this technique is still the one normally employed. Examination of a few random 512 by 512 pixel frames of prism-plate MM data indicated that transmission values for the darkest image pixels were  $T \leq 14$ . Only 3 points on the curve in figure 5.1 appear not to be affected by saturation problems and have average transmission values  $T > 4$ . Thus, considering the useful T range on the plate and the difficulty in obtaining a believable spline fit, a straight-line Baker density fit was felt to be the best means of obtaining a reasonable intensity conversion for this data. This resulted in values of  $T_c = 360$ ,  $T_b = 3$ ,  $\gamma = 0.23$ , and  $C = 2.23$ . These can be used with formula 3.4 to provide intensity conversion on a pixel by pixel basis.

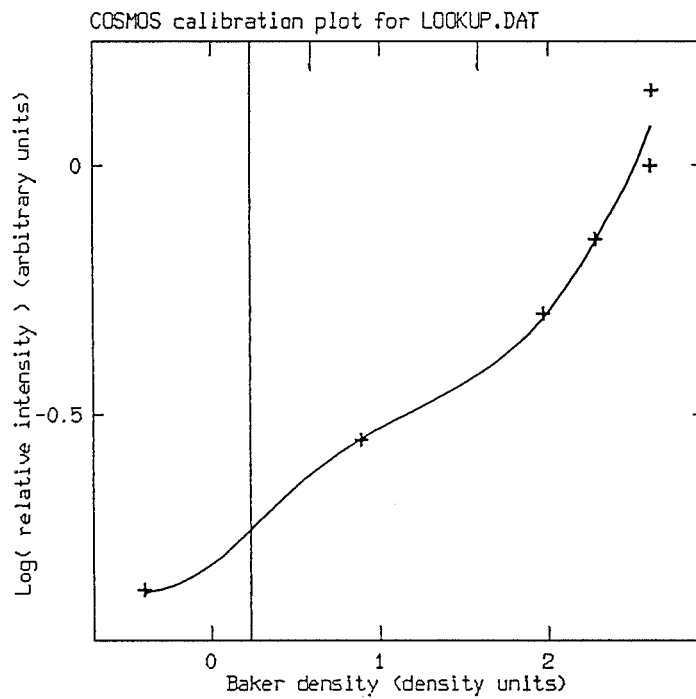


Figure 5.1 Spline fit to the log(relative intensity) transmission data (gain 3).

#### 5.4. Running the Cosmos analyser on the objective-prism MM data.

The next reduction stage was to decide on percentage threshold and area cuts to apply to extract the most useful information from the prism-plate MM data.

A few 512 by 512 pixel frames of MM data were extracted and intensity converted using the parameters derived above. The IAM software was then run on these individual STARLINK frames. The background intensity was chosen from a histogram of intensity levels of all pixels in each frame. Various values of the area and percentage cuts above the night sky were applied. The Cosmos analyser was then run to produce details of the number of images detected given these cuts. The results were compared with the original intensity converted frame. In this way, optimum values for the percentage and area cuts were chosen, albeit subjectively, to retain the maximum useful MM information. The average relative intensity of sky background pixels was found to be 442 and an area cut of 20 pixels and a threshold cut of 5% were used. The entire MM file for the prism data was then put through the Cosmos analyser. This resulted in 61,292 spectra being detected compared with 199,014 images from the direct plate. A larger area cut is used for prism than for direct data because of the dispersed nature of prism images. The chosen area cut should be small enough to retain the bulk of real spectral images and yet large enough to exclude spurious, low S/N images. Table 5.2 details the variation in detected image numbers with changing area cut. The same numbers of images from both the prism and direct plates are not expected because object surface brightness is reduced by the prism. With IIIaj sky limited exposures the penetration is typically 2.5 magnitudes less for a prism plate than for the corresponding direct plate (see UKST handbook p5.6.3-4).

Figures 5.2 and 5.3 are contour plots of sky background intensity variations over the prism and direct plates. The contours are in units of  $\log(\text{intensity})$ . Positions of step wedges and bright images, e.g. the galaxy NGC7793, are evident as series of closely spaced contours. No serious sky background fluctuations are present although vignetting at the plate corners is revealed.

#### 5.5. Magnitude calibration of the direct and prism plate images.

##### 5.5.1. Direct plate magnitudes.

The Cosmos IAM software calculates a raw isophotal magnitude 'COSMAG', for each image using formula 3.5. These COSMAG estimates are for images with pixels above the applied thresholds, normalised to the relative sky brightness. These raw magnitudes are calibrated using formula 3.6. Consequently a calibrated COSMAG of zero corresponds to an image with thresholded intensity the same as for the sky background and an object 1 magnitude brighter than sky would have a COSMAG value of -1 etc. Direct IIIaj exposures are generally taken with a GG395 filter which only transmits at wavelengths longward of  $\lambda 3950\text{\AA}$  until the ECO at  $\lambda 5380\text{\AA}$  (UKST handbook p5.3.1). A magnitude  $b_j$ , appropriate to the IIIaj/GG395 emulsion-filter combination, is obtained by adding a sky background magnitude estimate to the calibrated COSMAG values, e.g.:-

$$b_j = \text{calib.COSMAG} + b_j(\text{sky}) \dots 5.1$$

The brightness of the night sky on the direct plate ( $\sim 22.22$  mag/sq arc second for deep IIIaj exposures) was estimated as  $22.0 \pm 0.1$  by H.T.MacGillivray, (private communication), who also performed the intensity conversion of the direct plate data. The resultant ' $b_j$ ' magnitude is related to the Cousins photometric B and V passbands (e.g. Cousins, 1980) by the approximate relation:-

$$b_j = B - (0.28 \pm 0.04) \times (B-V) \dots 5.2$$

as determined by Blair and Gilmore (1982). Calibration of the direct magnitudes meant that controlled, magnitude-limited samples could be extracted from the IAM direct data. Such Cosmos  $b_j$  magnitudes can be calibrated against external photoelectric photometry, e.g. Beard (1984, PhD thesis). According to MacGillivray and Dodd (1983), agreement to  $\pm 0.2$  magnitudes can be obtained between photometry from both Cosmos measures and PDS measures down to  $b_j \sim 21$  on UKST plates.

#### 5.5.2. Prism plate Magnitudes from UJ6535P.

A similar process to that described above was performed on the prism-plate IAM data using formula 3.6, to yield prism isophotal magnitudes 'buj'. These magnitudes cannot be directly related to B or V magnitudes because prism plates are usually taken without a filter. The emulsion is consequently exposed from the ECO at  $\lambda 5380\text{\AA}$  to wavelengths dictated by the telescope optics and UV atmospheric cut off at  $\sim \lambda 3200\text{\AA}$ . Furthermore, the dispersed nature of objective-prism images means it is more likely for image pixels to lie below the applied thresholds and lead to underestimates of the prism magnitude, especially for fainter images. The actual prism object magnitudes are therefore dependent on the percentage threshold and area cuts applied, as well as the S/N limitations of the Cosmos machine. Object colour variations affect the length of prism spectra (see UKST prism handbook p.28 and Krug et al. 1980), and consequently the area into which the image flux is dispersed. This can lead to loss of image pixels below the threshold which is colour dependent. Final Cosmos prism magnitude estimates are a convolution of thresholding effects, image brightness, pixel saturation, object colour, and for galaxies, redshifts (as this reddens the intrinsic colour of the object). How these magnitudes compare with their matched direct equivalents is described in section

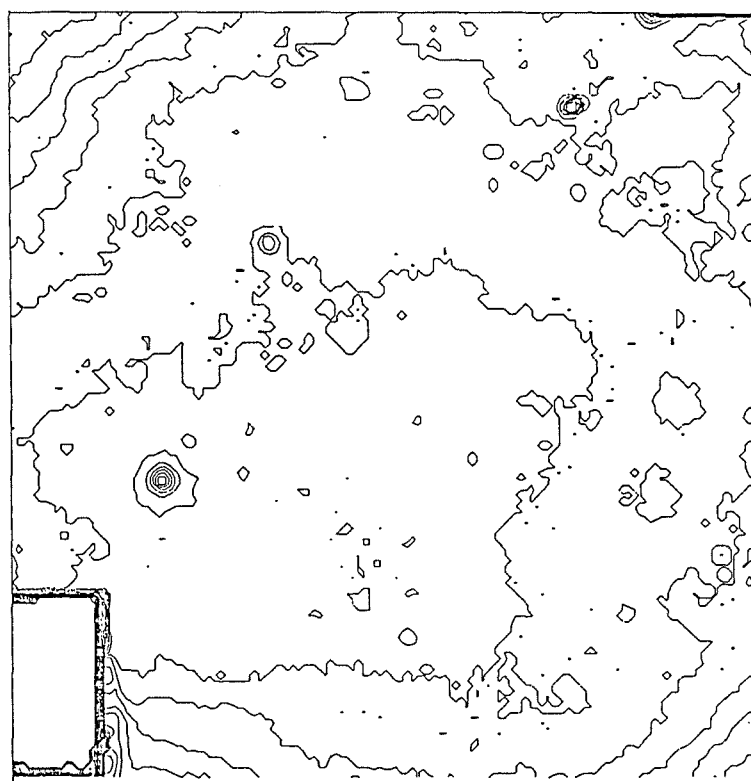
5.6. The star/galaxy separation from the direct plate.

The star/galaxy separation from the direct plate data of field 349 (performed by H.T.MacGillivray), was essential for the 2-D statistical investigation of the galaxy distribution and for providing a sample of objective-prism galaxy spectra for reduction. Such a sample would circumvent the necessity for individual scrutiny of prism spectra. Beard (1984), for his work on the Indus supercluster, used a sample of objective-prism spectra that had not been star/galaxy separated prior to their measurement. The visual appearance of the 1-D spectral tracings was used to make a subjective assessment of object identity. Such a technique is fraught with problems since, although the majority of stellar spectra are easy to recognise, it is difficult to distinguish all faint, late-type stars from galaxy spectra. Indeed Beard (1984), admits to the likelihood of ~15% stellar contamination in his galaxy redshift sample. Clearly, if a satisfactory star/galaxy separation could be performed before prism spectra measurement, then this source of contamination should be removed. This is important because an unnoticed stellar component in the galaxy sample could manifest itself as false peaks in the redshift distribution due to mistaking features in contaminant stellar spectra for a galaxy 4000Å feature.

Investigations into separating stellar and galaxian images from the direct plate IAM parameters were made initially by MacGillivray et al. (1976). Current techniques are based on this earlier work and are detailed in MS.



Figure 5.2 Contour plot showing the variation in sky-background intensity on the prism plate. The contours are in  $\log(\text{intensity})$ .



JOB: 688  
 PLATE: 349  
 DATE: 14 1 1985

XMIN: 145460  
 YMIN: 391620  
 XMAX: 3012660  
 YMAX: 3258820

INC 16  
 FTH 4  
 FSC 1

CONTOURS IN LOG (I)

LOWEST .21900E1  
 INTERVAL .10000E-1

MIN .21847E 1  
 MAX .27810E 1

Figure 5.3 Contour plot showing the variation in sky-background intensity on the direct plate. The contours are in  $\log(\text{intensity})$ .

Essentially 2 different methods are used depending on the magnitude range. From  $b_j \sim 17.0$  to faint limits ( $b_j \sim 21.5$ ) a plot of  $\log(\text{image area})$  versus  $b_j$  magnitude is employed. Figure 5.4 is such a plot for a subset of the direct data together with the star/galaxy discrimination line. This method relies on the lower surface brightness for galaxies compared with stars of the same isophotal magnitude. For a given magnitude, galaxies should occupy a different  $\log(\text{image area})$  space due to their larger number of image pixels. Intensity variations across stellar images are much more constant so they follow a much tighter sequence. Visual classification of selected objects from such a plot has indicated that this technique is a fairly reliable ( $\sim 95\%$ ) discriminator over the  $b_j \sim 17.0-21.0$  range (MS). At fainter limits image areas are so small that it is difficult to classify them even visually with a microscope. The non-circular nature of many galaxy images is washed out by seeing effects. Beard (1984), and Hewett (1983), have shown that this method breaks down at  $\sim 2$  magnitudes above the plate limit, i.e. at  $b_j \sim 20.0$  for deep IIIaj exposures. Examination of figure 5.4 indicates that it is also very difficult to choose a good discrimination line much beyond  $b_j \sim 20.2$  for this data. A faint limit for the star/galaxy separation of  $b_j \sim 20.5$  was consequently chosen for the direct plate data. At bright magnitudes the method also fails because diffraction spikes in stellar images become significant. Since only circular or elliptical images are produced by the IAM software, the presence of diffraction spikes determines the image area. Hence brighter stars could have mean surface brightness's which are comparable with many galaxies in the same magnitude range. At bright limits, i.e.  $b_j \leq 17.5$ , it was found that the best means of separating stars from galaxies was a geometric discriminator (e.g. Beard, 1984), defined as:-

$$(\text{Image area})/(\mathcal{I}\mathcal{I}\mathcal{A}\mathcal{u}\mathcal{B}\mathcal{u})\dots\dots 5.3$$

where 'Au' and 'Bu' are the unweighted semi-major and minor axes of each image. This technique works because many brighter galaxies have well defined elliptical images so that the geometric factor is always close to unity. Merged and stellar images with significant diffraction spikes though, yield factors which are generally much less than unity.

Figure 5.5 is a plot of geometric discriminator against  $b_j$  for a sub-sample of images to  $b_j = 17.2$  from the IAM direct data for field 349. The stellar objects are represented by crosses and the galaxies by open circles. The almost sinusoidal nature of the stellar sample is striking. At  $b_j < 17.2$  the stellar sequence decreases in a fairly well behaved way as diffraction spikes begin to become significant. The sequence veers up again when the circular halo, characteristic of brighter stellar images, begins to form. At very bright limits ( $b_j < 14.6$ ) the sequence turns down again as diffraction spikes dominate once more. The galaxy sample however, remains a fairly flat distribution with geometric factor  $< 1.0$  until  $b_j \sim 17.2$ . Here the discriminator breaks down and the  $\log(\text{area})/\text{magnitude}$  discriminator should be used. Figure 5.5 illustrates that this method seems a good means of separating stellar and galaxian images to  $b_j \sim 17.2$ , even though a copy direct plate was used which is optimised to recover information for faint images.

Hence, using the above techniques and a faint limit of  $b_j = 20.5$ , the star/galaxy separation of the 199,014 detected images from the direct plate yielded the following classification:-

Stars : 27,715, Galaxies : 25,812, Unknowns : 14 5,487

An identification flag was written to the IAM attribute list for each image. Most unidentified objects are for images  $\sim 1$  and 2 magnitudes above the plate limit as expected.

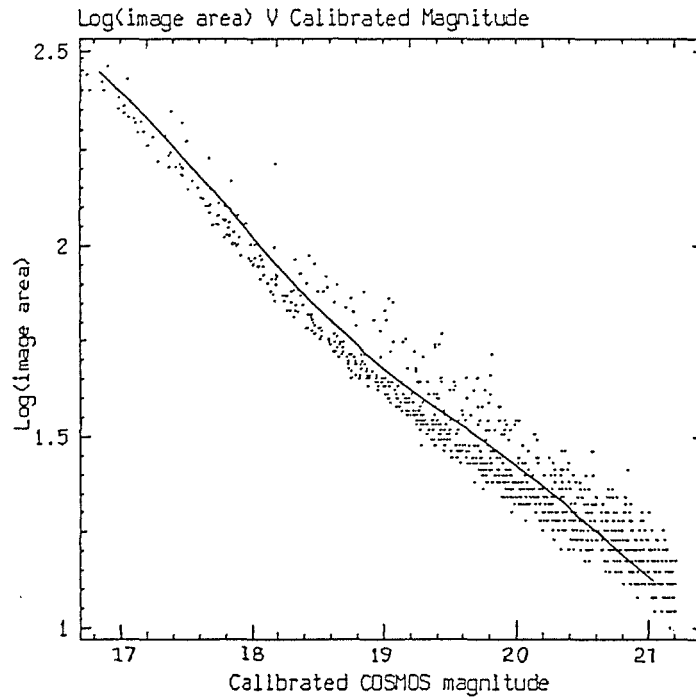


Figure 5.4 Log(image area) against  $b_j$  magnitude for a sample of images from field 349. The star/galaxy discrimination line has been drawn in.

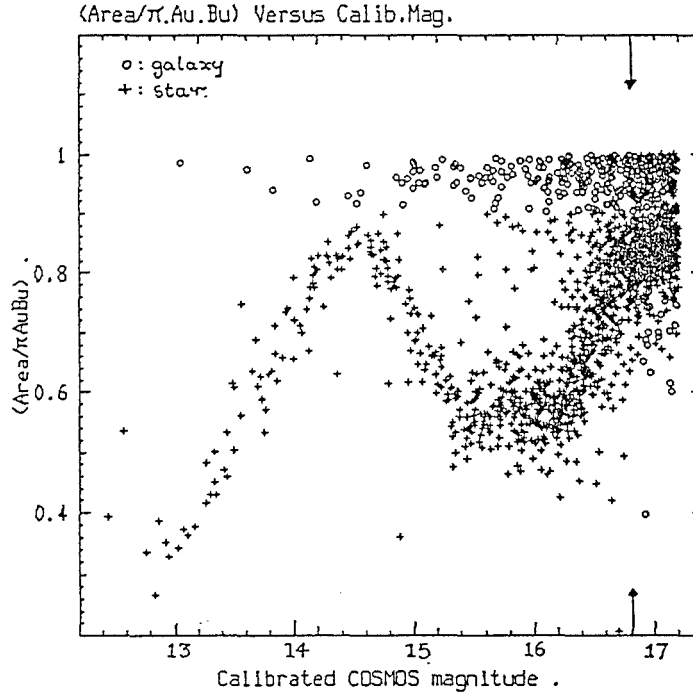


Figure 5.5 Geometric discriminator against  $b_j$  magnitude for a sub-sample of images to  $b_j = 17.2$  from field 349.

This is the practical limit of the star/galaxy separation on this plate. Simple astrophysical considerations dictate that the majority of unidentified objects will be faint galaxies, although some are spurious objects found by the Cosmos analyser when dealing with very bright images.

Figure 5.6 is a dot plot of all 199,014 detected direct plate images. Number density enhancements due to rich galaxy clusters can be seen as well as the locations of bright, extended images whose outlines are defined by large numbers of spurious image points. Small areas around these extended images should therefore be removed or 'drilled' prior to any analysis of the galaxy distribution. Figure 5.7 is a dot plot of all images classified as galaxian, again the non-random clumping of image points is evident. A contour map of this data is given in figure 5.8. The lowest contour is at a mean surface density of  $\sim 170$  galaxies per square degree and the contour interval is  $\sim 860$  galaxies per square degree. Such a map highlights the galaxy density enhancements and reveals the presence of rich clusters, such as the cluster labelled 'C' (Carter, 1980). Figure 5.9 is a 3-D surface density plot for the same data, again illustrating the clumpy nature of the projected galaxy distribution. The galaxy dot plot can be compared with the equivalent stellar plot in figure 5.10, which has a much more random distribution as one would expect.

The program 'COSRADEC', developed by N.M.Pratt at ROE, was run on the direct IAM data. This calculated right ascensions and declinations for all detected images accurate to within an arcsecond. This was a worthwhile step since matching with images in other astronomical catalogues based on the equatorial co-ordinates can be made. The calculated R.A. and Dec. for each image were read in to the IAM parameter list.

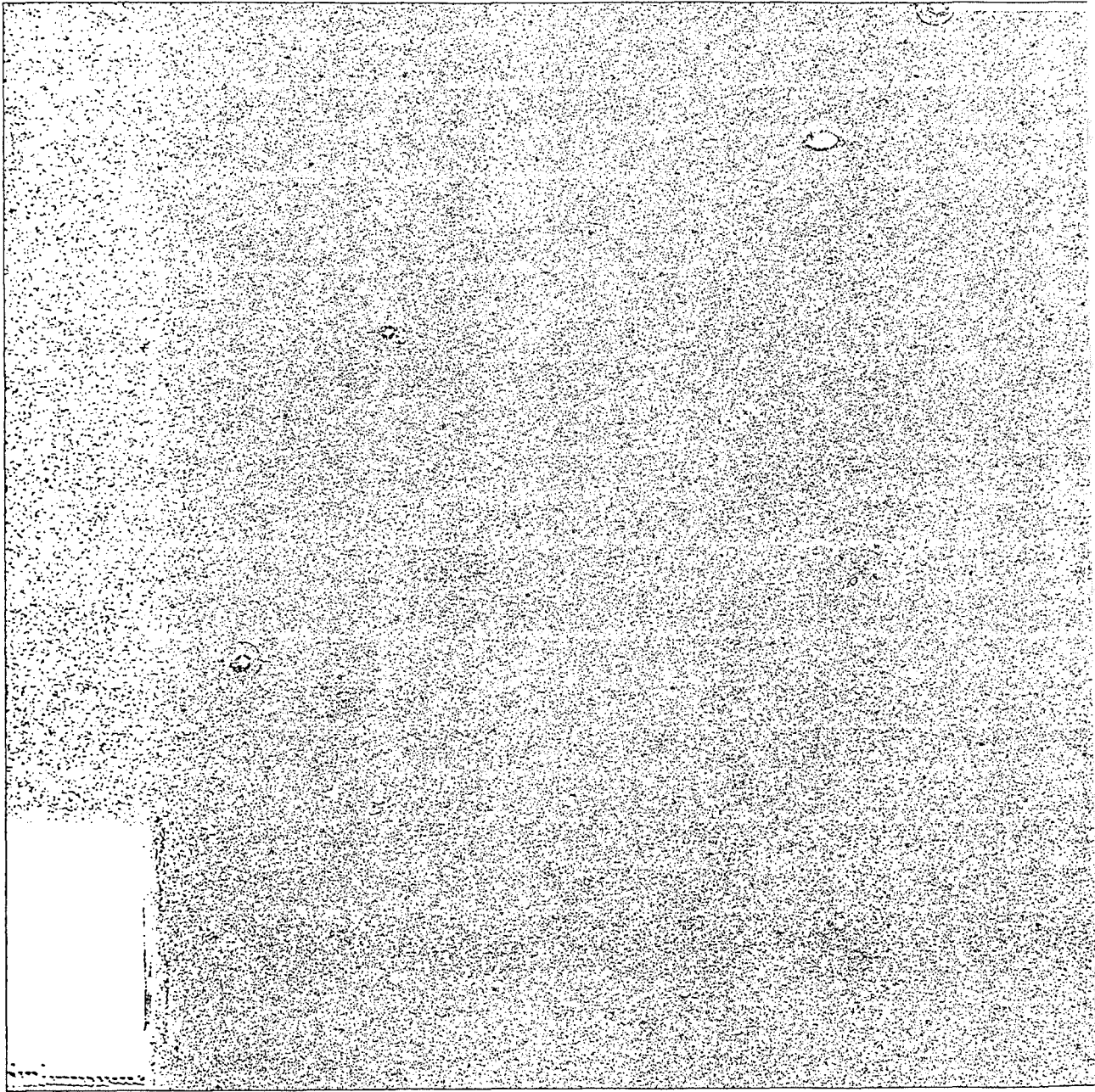


Figure 5.6 A dot plot of all 199,014 images detected by COSMOS from a scan of the direct plate J6145 (copy) of field 349.

Galaxy images detected Fld.349 (XY plot)

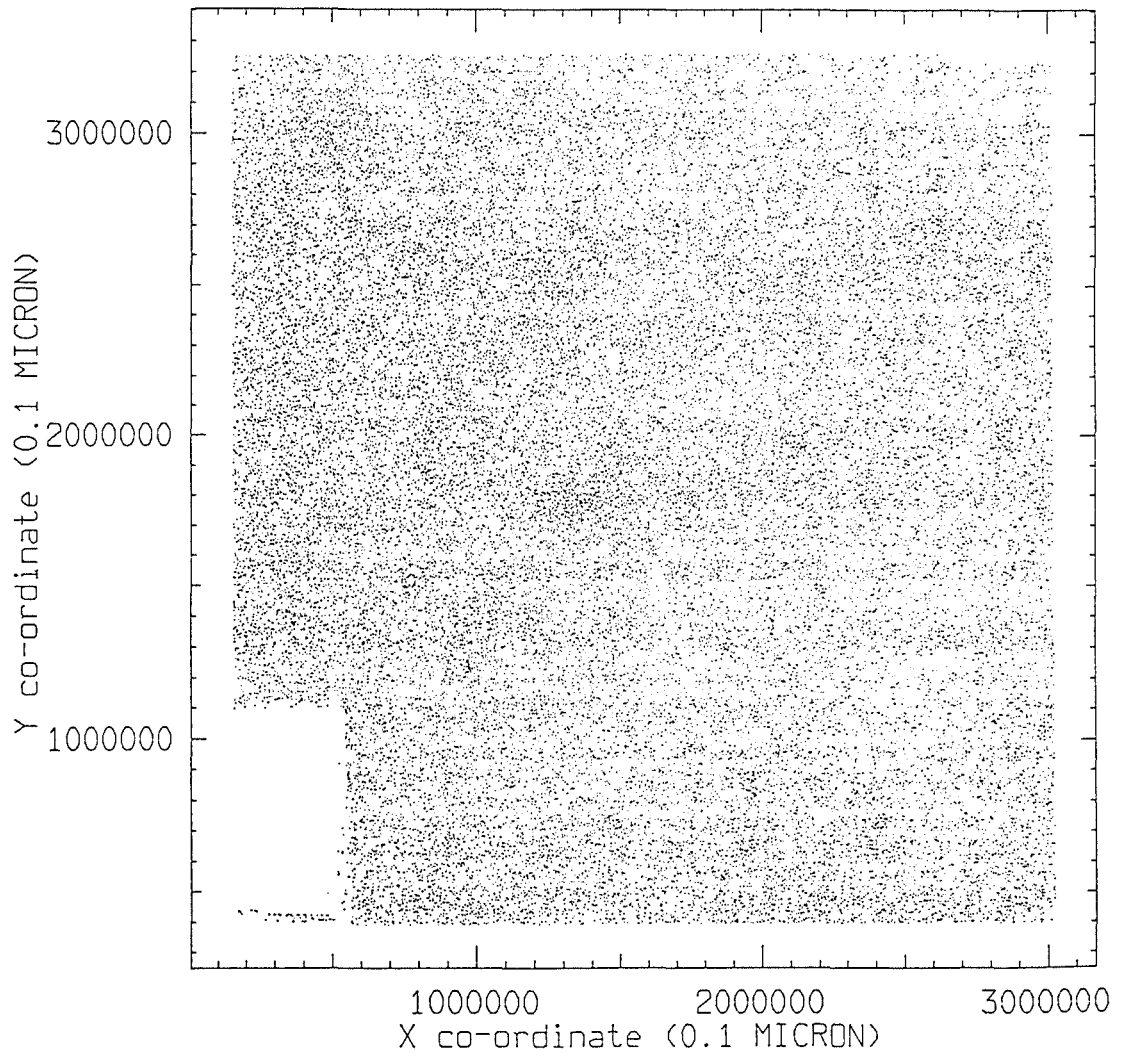


Figure 5.7 All galaxian images detected and identified from the star/galaxy separation on the direct plate.



Figure 5.8 Contour plot of all galaxian images detected from the star/galaxy separation on the direct plate.

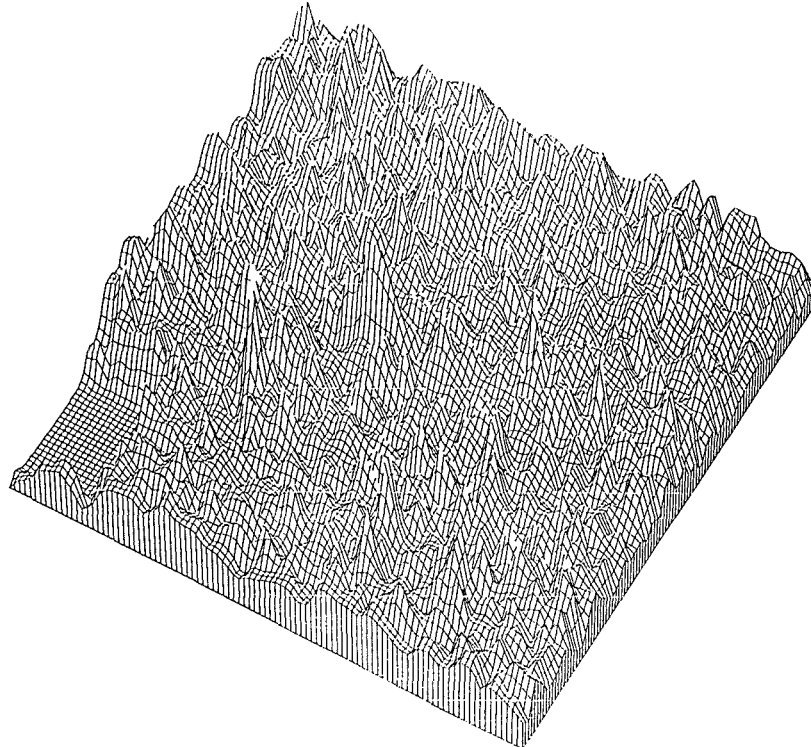


Figure 5.9 3-D plot of surface number density of galaxies in 5 square arcsecond cells for all galaxies detected on the direct plate.

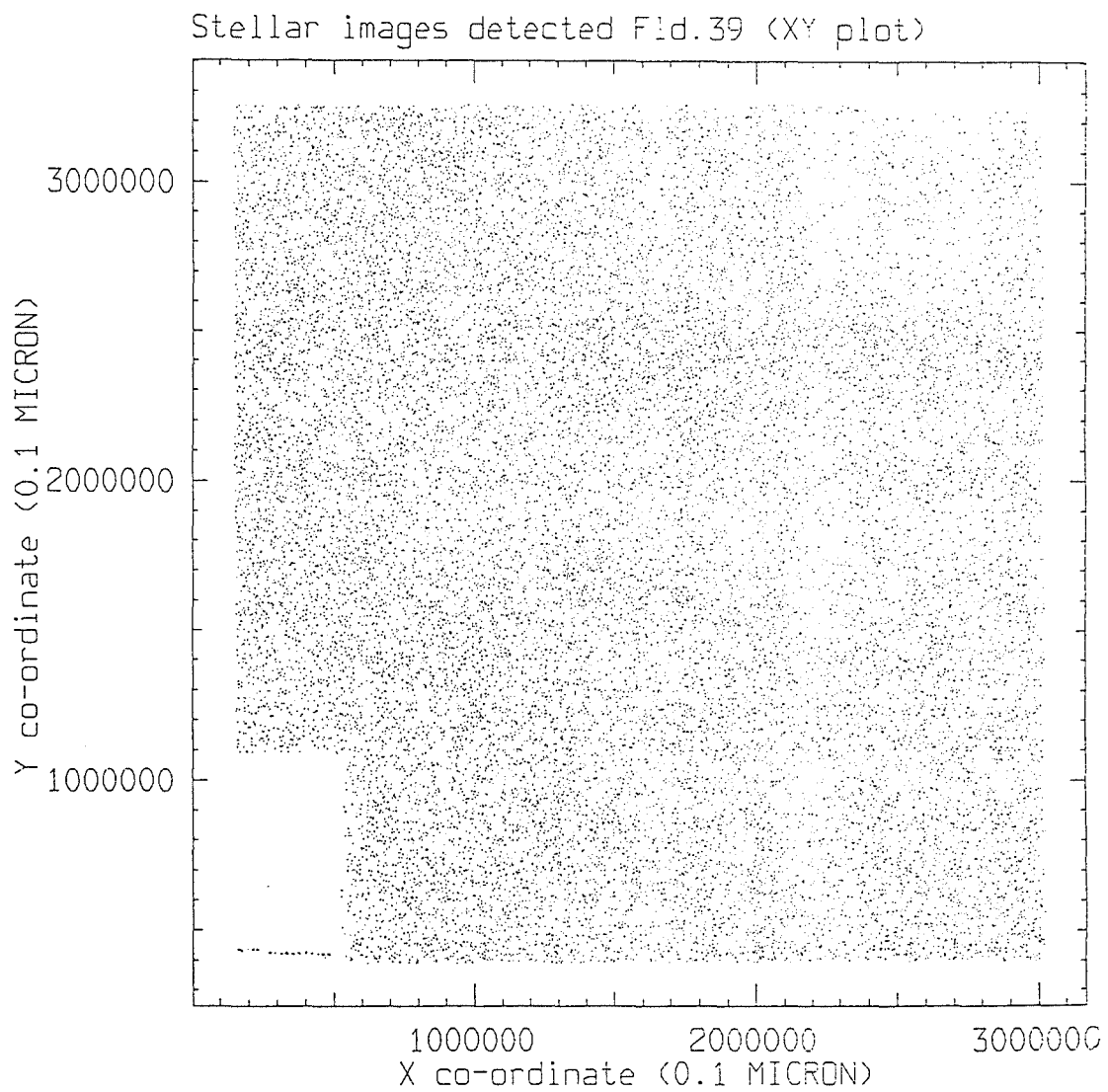


Figure 5.10 A dot plot of all stellar images detected from the direct plate and from the star/galaxy separation.

The direct and objective-prism IAM files were written to HAGGIS catalogues using a routine called 'COSDUMP'. The STARLINK HAGGIS software package is particularly useful for handling parameterised data of this form and has been used extensively for the manipulation, reduction and analysis of the data in this thesis. The potential uses of this package are detailed in the HAGGIS user manual. Briefly though, a catalogue can be created which can contain any number of values or 'attributes' which describe properties of each entry in the catalogue. The extremely flexible nature of this package enables arithmetic operations between different attributes for each catalogue entry to be performed (with the result written to a new attribute).

## 5.7. The pairing of the direct and prism data.

### 5.7.1 Rationale.

The next stage in the data reduction was to pair direct and prism plate images using their respective IAM files. This pairing is important for a number of reasons:-

- (1). The direct plate star/galaxy separation can be applied directly to the prism data enabling relatively pure samples of galaxy spectra to be extracted. When these spectra are measured for redshift, worries about stellar contamination should be largely removed.
- (2). Comparisons between Cosmos IAM parameters from the two plates can be made and positional and magnitude effects can be investigated (see later).
- (3). Perhaps most importantly, the pairing provides a co-ordinate transformation between the two plates. If done carefully, this gives a wavelength reference point for each objective-prism spectrum independent of the observed ECO. Chapter 3 has shown that manual, or even automatic polynomial fitting to the ECO in objective-prism spectra yields an ECO position that is sensitive to properties of plate and image. This applies particularly to object magnitude and

colour, but also to the quality of the intensity conversion, whether original or copy-plate material is used and on the combined S/N limitations of the plate and Cosmos machine at high and low photographic densities. Clowes (1985), and Palmer (1984), have shown that use of a co-ordinate transformation from direct to prism plate can provide a more consistent wavelength reference point than the ECO. Using such a transformation for this work should eliminate the strong mag/Z effect discovered when using the observed ECO, (see chapters 3 and 4).

Pairing techniques between direct UKST plates, for a number of astronomical investigations such as variable stars studies, are well established. Consequently software already exists, such as the STARLINK 'AIPS' package, which has been designed specifically for direct-plate pairing. The HAGGIS software also contains a routine for pairing attributes from different catalogues within given tolerances. The situation is more complicated for pairing prism and direct plates however, because prism image centroids along the dispersion direction depend strongly on object magnitude and colour. For the direct plate images, intensity weighted X and Y centroids were used as pairing co-ordinates, but for the prism plate, the minimum X value for the image was used, together with the intensity weighted Y centroid, since the prism spectra were dispersed in the +X direction.

A number of factors will affect the ease of any pairing between UKST plates. Specifically:-

(a). Slight differences in the orientations of the two plate co-ordinate systems may exist. This is more likely if one of the plates is a copy since the original may have been slightly mis-aligned with respect to the intermediate positive and final copy during the copying process.

(b). There will be slight offsets of the plate centres, even though

the same field was observed, because of the telescope setting accuracy.

(c). Small positional variations of a few microns occur over a plate in the IAM data due to limitations of the Cosmos measuring machine (see MS). These are however, systematic and repeatable for plates measured with the same orientation.

(d). Quite large differences in the X,Y co-ordinates for the plates may exist because of the way the plate is centred in the Cosmos machine, irrespective of the positional integrity between the plates.

(e). There will be a higher incidence of merged images on the prism plate which reduces the potential sample size for pairing. This is already substantially diminished by the brighter prism plate magnitude limit.

These problems must be overcome by any pairing procedure if it is to prove successful and match up the largest number of images.

#### 5.7.2. The basic pairing technique.

Clowes (1985), found it necessary to pair prism and direct plates whilst investigating automatic quasar detection (AQD). A software package was developed to pair up direct and prism plates and to generate a co-ordinate transformation to convert the direct-plate X,Y image positions to the prism-plate co-ordinate system. This software was kindly made available for this work by Dr. Clowes. The essential pairing steps recommended by Clowes are described below, prior to a discussion of the actual reduction performed.

(a). Firstly, a rough indication of the image translation between the 2 plates is obtained by comparing the X,Y co-ordinates of the brightest images. Files of X,Y co-ordinates for a selection of bright images are input to the Clowes 'FASTMATCH' program which is designed to find the coarse translation between the plates to the nearest 0.5 mm. A 0.5 mm search radius and increment was used to scan over a

large X,Y range to tie down the rough match. A rotation parameter, for accounting for any mis-alignment between the plates, was initially set to zero. A log file is created which is updated whenever a larger number of objects are paired as the X,Y translation is incremented. A successful pairing is indicated by a dramatic increase in paired images. The program terminates when it has attempted pairings at all X,Y shifts dictated by the range and increments chosen. The X,Y shifts, which provided the greatest number of paired images, is given in the log file.

(b). With the rough translation from 'FASTMATCH' a histogram of magnitude estimates for the prism plate images is made. For a good pairing, faint objects in a narrow magnitude range are selected so that their images are small enough to yield accurate centroid positions and yet bright enough to exclude spurious images (there are systematic variations in the calculated image positions which are magnitude dependent). Clowes recommends an interval of about 0.04 magnitudes  $\sim 1.0$  magnitude above the plate limit. The actual limit chosen however, depends on the applied area cut since a small area cut will result in large numbers of spurious images from the prism plate. A sensible choice can be made from careful examination of the prism magnitude histogram.

(c). The X,Y prism co-ordinates for objects in the chosen narrow magnitude interval are output to a file, as are all the stellar X,Y co-ordinates from the direct data. These are then read in to the final pairing routine 'MATCH'. Here the search radius is only 0.25 mm. Again suitable X,Y ranges are chosen to encompass the X,Y translation given by the 'FASTMATCH' program. Small X,Y increments are used ( $\sim 0.1$  mm) together with small angle increments ( $\sim 0.05^\circ$ ). The rotation parameter proved to be crucial (see later), since when using small search radii and X,Y increments, a rotation of only a fraction of a degree between plates gives positional shifts of a few mm's

across a plate. Again successful pairing is indicated by a sharp increase in paired objects written to the log file. Since a prism sample of both faint stars and galaxies was used in the 'match' programme, compared with just stellar images from the direct plate, we might expect about half of the prism sample to match up if the pair is successful, although this fraction is obviously dependent on the galactic latitude of the field.

(d). Once a matched sample has been obtained, X,Y co-ordinates for paired images from the faint prism and direct sample are read in to the routine 'TRANSFORM' which actually determines the co-ordinate transformation. An N-sigma cut can be applied to the paired co-ordinates so that objects with large residuals are removed. A refined list of co-ordinates is then re-submitted to the 'TRANSFORM' program and a new N-sigma cut applied. This cyclic process can be repeated until a stable set of paired co-ordinates is obtained and when the combined residuals from both co-ordinates are acceptably small (i.e.  $\sim 1$  pixel,  $16 \mu\text{m}$ ).

(e). The final stage in the process is to use the characteristics produced by the last application of the TRANSFORM program to transform the co-ordinates of all images on the direct plate to the same co-ordinate system as the prism plate. This can be achieved within the TRANSFORM program. The IXCEN, IYCEN positions for the direct plate images are read in to the 'TRANSFORM' program and a file of transformed co-ordinates is produced. These transformed co-ordinates IXTRAN, IYTRAN can be written to the HAGGIS catalogue containing the direct plate IAM data. If a linear transformation is used then it is of the form:-

$$X_{\text{direct}} = aX_{\text{prism}} + bY_{\text{prism}} + c \dots 5.4a$$

$$Y_{\text{direct}} = eX_{\text{prism}} + fY_{\text{prism}} + c \dots 5.4b$$

#### 5.8. Method and results of the actual match performed.

Essentially, the reduction process described above was used with minor differences. In actual fact a pair between the 5,000 brightest images from both the prism and direct plates was first attempted using the HAGGIS pairing routine on the IXCEN, IYCEN direct co-ordinates and the XMIN, IYCEN prism co-ordinates. An X tolerance of 1.0 mm and a Y tolerance of 0.5 mm were used. The success of this pairing depends entirely on whether the 2 plates were similarly centred in Cosmos prior to scanning, as this is what produces the bulk of the positional translation between the plates. Of these 5,000 objects, 3,398 were paired by the HAGGIS routine, indicating that some sort of match had been achieved. However, many objects may have been incorrectly paired because of the large tolerances used. The mis-matched objects are not important as long as sufficient numbers are correctly matched to enable a comparison. The integrity of this pairing was tested using a plot of prism versus direct magnitude. Mis-matched objects should produce a scatter diagram whilst correctly-paired objects should follow a well-behaved sequence. This plot (figure 5.11), indeed indicates contamination by mis-matched objects. The sample can be 'purified' by constructing a histogram of the magnitude difference between matched objects and selecting only those objects in a narrow magnitude range ( $\sim 0.4$ ) about the histogram peak (figure 5.12). This resulted in a refined sample of 1,933 paired objects. Using this matched sample, properties of the pairing could be investigated which may provide useful information for the proper plate match using Clowes's software. Figures 5.13 and 5.14 show the difference in X co-ordinates between these direct and prism paired images, versus the Y direct co-ordinate and of the difference in Y co-ordinates versus the X direct co-ordinate.

Mag.comparison for HAGGIS paired sample

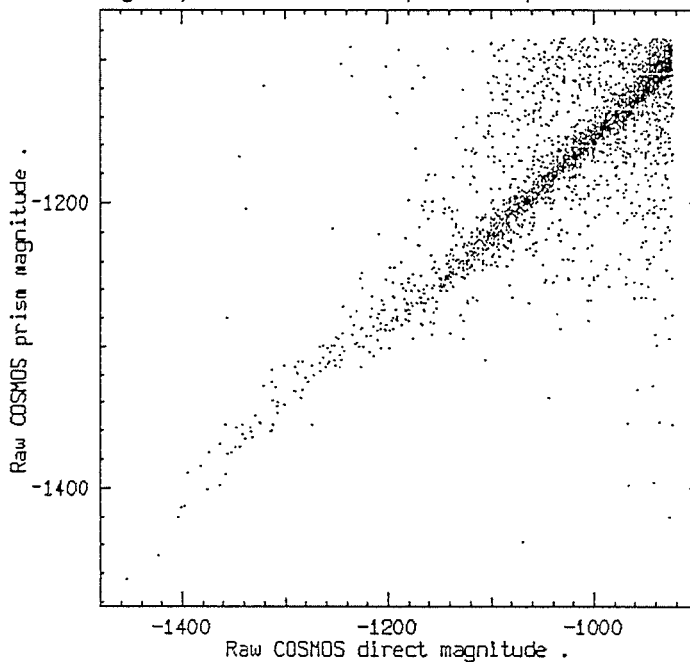


Figure 5.11 Prism versus direct plate COSMOS magnitudes for a sample of images paired using Haggis for the 5000 brightest images from both plates.

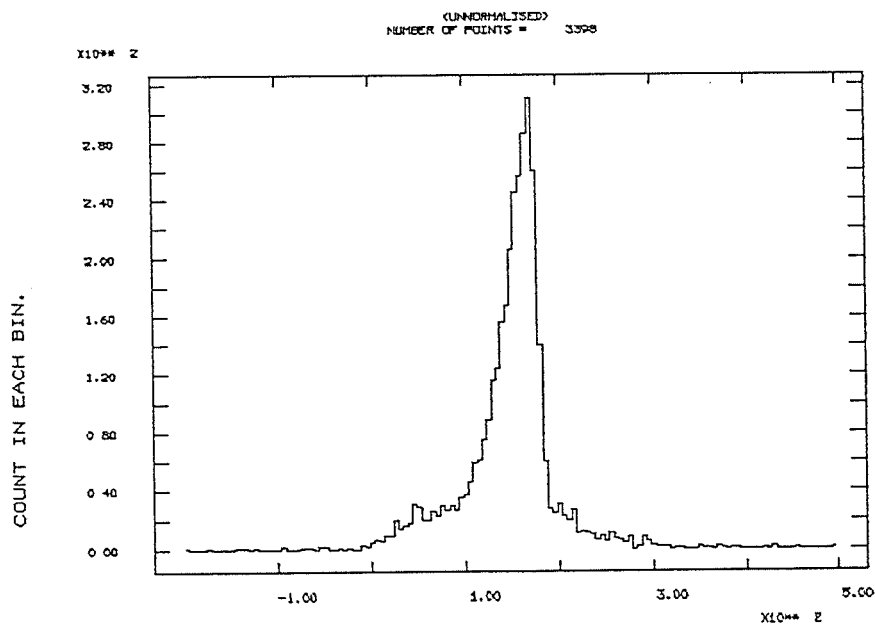


Figure 5.12 Histogram of the magnitude difference between the paired prism and direct sample of Figure 6.11.

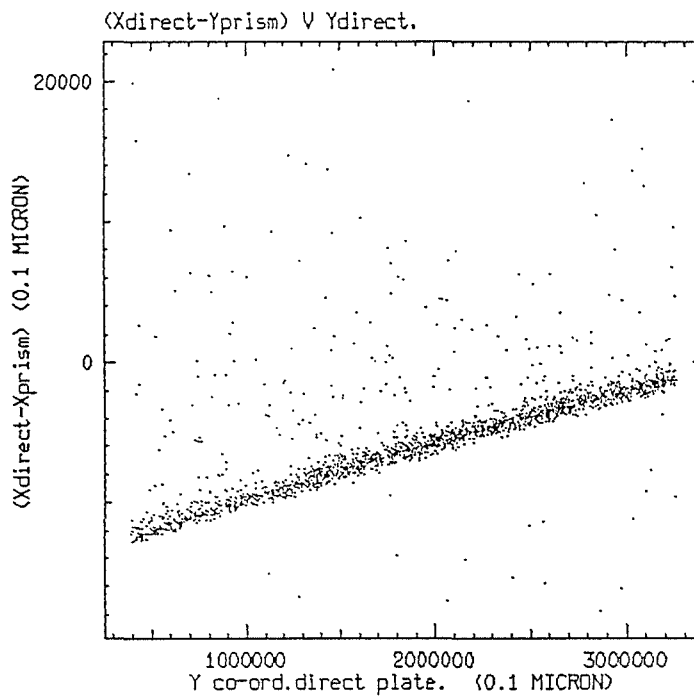


Figure 5.13 Difference in X co-ordinates between the direct and prism paired images versus the Y direct co-ordinate.

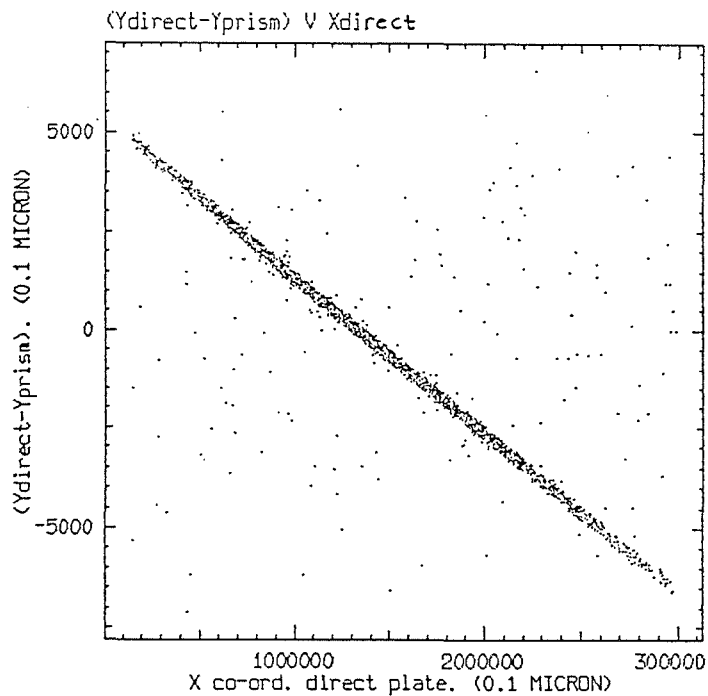


Figure 5.14 Difference in Y co-ordinates between the direct and prism paired images versus the X direct co-ordinate.

The relations exhibited in both plots are well-behaved, linear and of non-zero slope, although that of figure 5.14 is tighter than in figure 5.13. This is expected since diffraction spikes in brighter spectra cause positional variations of several mm's along the dispersion direction for the prism XMIN values. For this reason, the final pairing is done using faint objects. The plots also exhibit some scatter indicating residual mis-matched contaminants. The non-zero slopes of opposite sign in figures 5.13 and 5.14 can be explained as the effect of a rotation between the co-ordinate systems on both plates. This causes uniform shifts in the  $\Delta X$  or  $\Delta Y$  of up to  $\sim 1.0$  mm as X,Y position increases across the plates. The valuable result is that the rotation angle can be calculated from the gradients. Both give an angle of  $\sim 0.22^\circ$  (the sign depends on which plate is regarded as being fixed), e.g.:-

$$\tan \theta = |(\Delta X/Y_{\text{direct}})| = |(\Delta Y/X_{\text{direct}})| \dots \dots 5.5$$

What is also evident is that larger offsets exist between the X co-ordinates than the Y co-ordinates, i.e. ( $X_{\text{direct}} - X_{\text{prism}}$ ) is always  $< 0.0$ , whilst ( $Y_{\text{direct}} - Y_{\text{prism}}$ ) is between  $\sim -0.7$  and  $\sim 0.5$ .

The 5,000 brightest objects from the direct and prism plates were subsequently read in to the FASTMATCH program. A successful pairing of 4,015 objects resulted at an X shift of  $-0.5$ mm and a Y shift of  $0.0$ mm with respect to the direct plate (search radius was  $0.5$ mm).

The final plate pairing was performed using faint images. Figure 5.15 is a histogram plot of raw, uncalibrated Cosmos magnitudes for the 61,292 prism objects from the IAM data (now in a HAGGIS catalogue). The sharp upturn at raw COSMAG values  $\sim -700$  is a consequence of large numbers of spurious images detected at faint isophotes. This was because of the small area and threshold cuts applied to the prism MM data (see chapter 3, table 3.1). A faint magnitude limit was chosen from the histogram which excluded spurious

images since these would affect the pairing. A raw COSMAG range from -795 to -791 was chosen, which resulted in 519 faint prism objects being selected. The XMIN, IYCEN values for these objects and the IXCEN, IYCEN values for all the 28,414 stellar images detected from the direct plate provided the basis for the plate pairing and were read in to the MATCH program. A successful match was obtained with an X-shift of -1.4 mm, a Y-shift of 0.3 mm and a rotation angle of  $0.2^\circ$  (as predicted). The search radius was 0.25 mm, the X,Y increments were 0.1 mm and the angle increment was  $0.05^\circ$ . Only 283 of 519 faint prism spectra were matched with the stellar direct sample. This is about what we would expect since the faint prism sample was a mixture of stars and galaxies whilst the direct sample was only stars. The value of the X-shift changed by  $\sim 1.0$  mm in going from the bright to the faint sample. As described earlier this is the result of diffraction spikes in the brighter images and also perhaps thresholding effects at faint isophotes for the faint sample. The paired co-ordinates produced by MATCH were then read in to the TRANSFORM program to provide the co-ordinate transformation. An iterative 3-sigma cut was applied to excise paired objects with high residuals. After 12 iterations a stable set of 222 paired images with acceptable combined residuals of  $< 1$  pixel (16  $\mu$ m) remained. The final transformation residuals and co-efficients are given in table 5.3. The X-residual was  $\sim 5$ X the Y-residual, indicating the more consistent nature of the Y co-ordinates. Using this transformation, all images from the direct data were transformed to the prism plate co-ordinate system. The transformed co-ordinates IXTRAN, IYTRAN, were written as new attributes to the main catalogue.

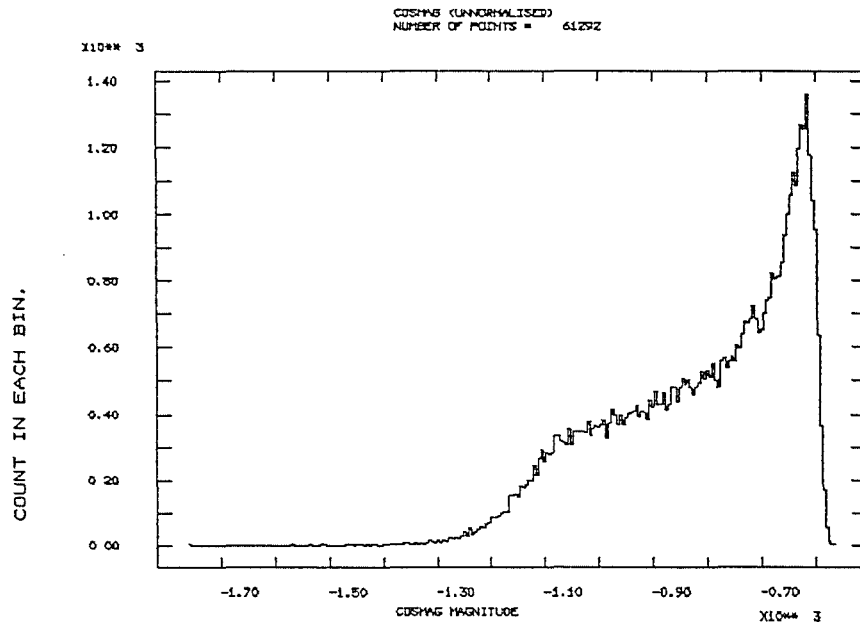


Figure 5.15 A histogram of the raw COSMOS magnitudes for the 61,292 detected prism images.

Table 5.3

Final transformation residuals and co-efficients for the co-ordinate transformation from the paired prism/direct data.

Co-efficients:-

a : 1.49646    e : -0.50197  
 b : 0.99971    f : 0.00397  
 c : -0.00389    g : 0.99987  
 (Refer to equations 6.4a-b)

r.m.s. Xt-residual        : 15.8156  $\mu\text{m}$   
 r.m.s. Yt-residual        : 3.5231  $\mu\text{m}$

Combined r.m.s. residual : 16.2033  $\mu\text{m}$  = 1pixel

As a result of this transformation, it was possible to pair up the 61,292 prism images with the 199,014 direct images using the HAGGIS pairing routine. The pairing was performed on the prism XMIN, IYCEN values and the direct ITRAN, IYTRAN values. Tolerances of 3 and 6 pixels were chosen, which resulted in 38,141 and 50,025 paired objects respectively. The larger sample was used for comparison purposes. Selected prism and direct-image attributes were then output to a new catalogue for all the paired images. The resultant paired sample enables properties of the prism and direct images to be investigated.

### 5.9. Comparison between direct and prism plate image attributes.

#### 5.9.1. Matched prism/direct magnitudes as a means of star/galaxy separation.

Comparison of the Cosmos calibrated magnitudes for the matched prism and direct images was made. The plot of direct against prism magnitude estimates for the 50,002 stellar and galaxian images matched using a 6-pixel tolerance is given in figure 5.16. A striking feature of this plot is its two component nature. The most obvious inference is that the two components are due to separation of stellar and galaxian images in the mag/mag plot. Since all paired objects were flagged as stellar or galaxian from the star/galaxy separation, this inference was easy to test. Figure 5.17 is the mag/mag plot for the stellar-classified sample and figure 5.18 is the equivalent for the galaxy-classified sample. The segregation by image type is clearly demonstrated. However, although a very tight stellar sequence is obtained, figure 5.18 shows that objects classified as galaxian exhibit the 2 component feature of figure 5.16, with the upper curve following that of the stellar sequence in figure 5.17. This would tend to imply significant stellar contamination of the supposed galaxy sample.

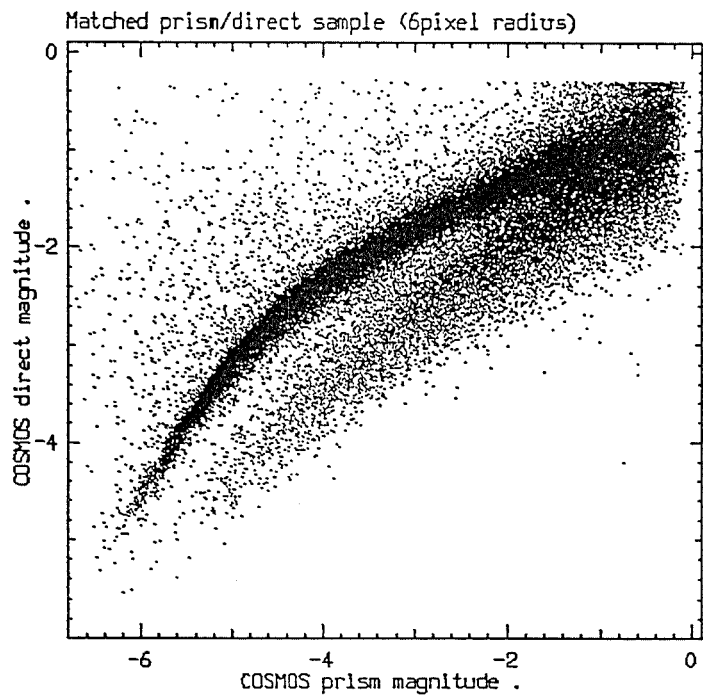


Figure 5.16 Direct versus COSMOS prism magnitudes for the final paired sample.

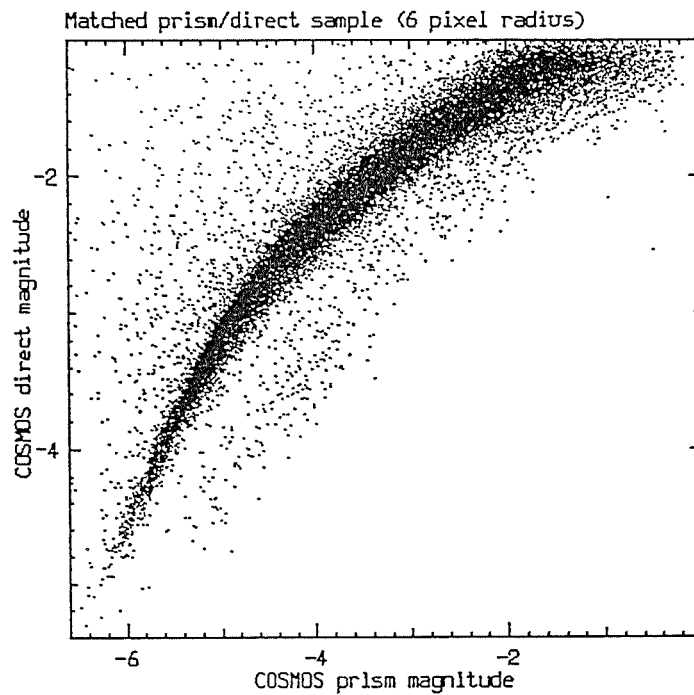


Figure 5.17 Direct versus COSMOS prism magnitudes for the paired sample classified as stellar objects.

From astrophysical considerations, we would not expect such an obvious splitting in the mag/mag plot for a pure galaxy sample. Whilst some objects on the upper curve in figure 5.18 may indeed be compact E0 or Seyfert type galaxies, which are difficult to distinguish from stars, we would not expect to observe such large numbers of these objects. Pence (1976), expects no more than ~23% to 27% of all types of galaxy to be elliptical or lenticular in the range  $b_j \sim 16.0-19.5$ , and only ~23% of these would be compact E0's (Freeman, 1975). Furthermore Huchra and Sargent (1973), found that only 5% of galaxies are Markarian in nature of which 10% are Seyferts.

If the stellar contamination is real, then this could have serious consequences for studies of galaxies which use a star/galaxy separation from UKST direct plates. Significant stellar contamination would not seriously bias correlation analyses since the stellar contaminants would simply add a random background, but number-magnitude counts could be significantly affected. Consequently conclusions drawn from such analyses e.g. MacGillivray and Dodd (1980), Shanks et al. (1984ab), and King and Ellis (1985), could be misleading in some respects.

The degree of stellar contamination in the galaxy-separated sample was determined from examination of their objective-prism spectra. Such measures were performed using INTERZED (see section 5.12). All 'galaxies' detected to  $b_j = 18.2$  were measured as well as a subset of galaxies down to  $b_j = 18.7$ . Reference to low dispersion objective-prism plots of stars of different spectral types, as given in the UKST objective-prism handbook, enabled stellar spectra to be identified in the supposed galaxy sample. In most cases, stellar contaminants were obvious and their nature confirmed by the derived redshifts from their  $4000\text{\AA}$  features. Of the 1,462 'galaxy' spectra to  $b_j = 18.2$ , 276 were identified as being definitely stellar, though many

more were of dubious identity. Furthermore, 103 of the 720 'galaxy' spectra measured from the sample of 1,220 between  $b_j = 18.2-18.7$  were also classified as stellar. The stellar contaminants were flagged as such in the data catalogue. A lower limit of  $\sim 19\%$  stellar contamination in the galaxy sample to  $b_j = 18.2$  was obtained. This figure agrees with the observed numbers on the upper curve in figure 5.18. Clearly the star/galaxy separation performed on the direct data using the  $\log(\text{image area})/\text{magnitude}$  discriminator is much worse for this sample than expected (MacGillivray and Stobie, 1985).

The final proof of the stellar content of the upper curve in figure 5.18 is given by individually identifying a selection of objects on this curve. Fortunately, since stellar contaminants were flagged during redshift measurement, they can be plotted with a different symbol in the prism/direct magnitude plot for this sample. Figure 5.19 is such a plot with identified stellar contaminants denoted with crosses. This conclusively demonstrates that the bulk of objects that lie along the upper sequence in figure 5.18 are stellar, as evidenced by their objective-prism spectra. There was no evidence that galaxies had been mis-classified as stars in figure 5.17. In fact examination of a few hundred stellar spectra down to  $b_j = 18.7$  only gave 2 obvious galaxy candidates. Nevertheless, the direct plate star/galaxy separation has at least provided a sub-sample that contains nearly all the galaxies detected on the plate, even if the sample does suffer from considerable stellar contamination.

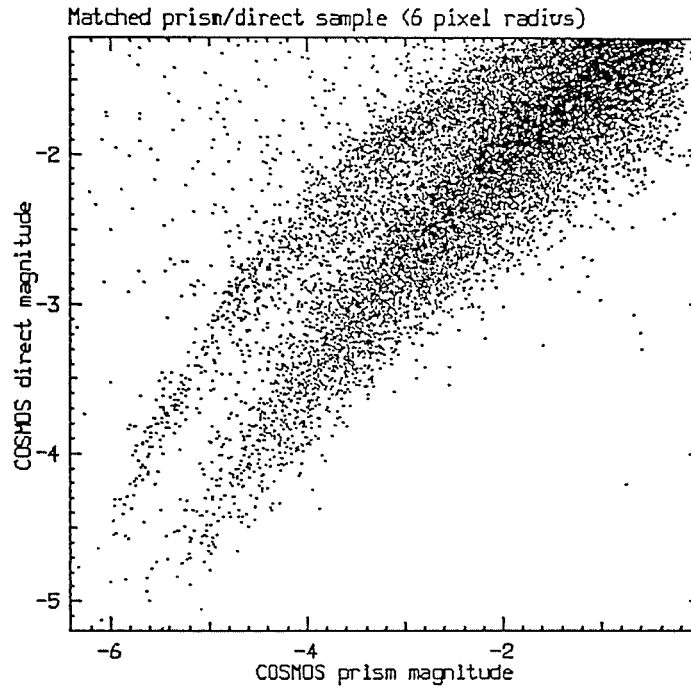


Figure 5.18 Direct versus COSMOS prism magnitudes for the paired sample classified as galaxies.

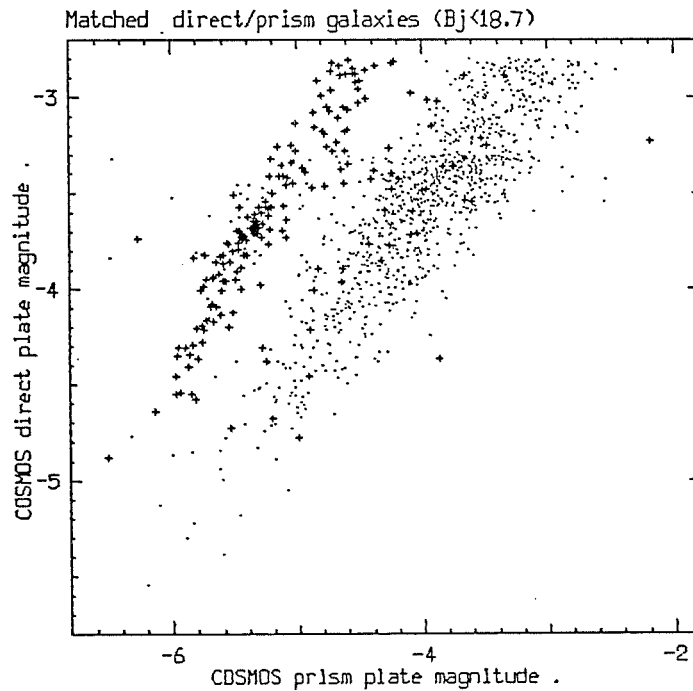


Figure 5.19 Direct versus prism magnitude for a sample of paired objects classified as galaxies from the direct plate star/galaxy separation. Objects identified as stellar from examination of their prism spectra are indicated with a cross.

These results strongly indicate that utilisation of magnitude estimates from both the direct and prism plates can provide a much more reliable means of star/galaxy separation. An improved discrimination is not surprising considering the extra information available from using both prism and direct plates. Obviously, differences between the surface brightnesses of the galaxy images compared with the stellar images, and the effect of dispersing these images into spectra on a prism plate, reveals more about the nature of an object than just using the direct data alone. This technique would not yet be practical for most investigations since prism plates are not yet available for a large enough number of fields and because of the difficulty in correctly pairing the plates.

In order to strengthen the above findings however, the technique should be applied to more plates (both copies and originals) and the results compared with a star/galaxy separation from the direct plate. Even so it is unlikely that the results of figures 5.16 to 5.18 are due to using copy plate material, since Beard (1984, 1985, private communication), found similar effects when pairing original prism and direct plates in different fields, although he did not attribute this to stellar contamination. Furthermore, even if the segregation in figure 5.16 is more pronounced because a copy direct-plate was used, a lot of work using star/galaxy separations from copy direct-plates has already been undertaken.

A disadvantage of using prism and direct-plate magnitude estimates as a means of star/galaxy separation is the brighter magnitude limit on the prism plate (typically by  $\sim 2.0$  magnitudes over the direct plate). However, direct plate star/galaxy separation has been shown to break down at  $\sim 2.0$  magnitudes above the plate limit, (Beard, 1984, Hewett, 1983, and this thesis), so this disadvantage is largely offset. A major advantage of the prism/direct magnitude

technique of star/galaxy separation is that it is applicable over a wide magnitude range. Consequently this circumvents the need to use different discriminators for certain magnitude ranges as required when performing the separation from the direct plate. A new potentially important use of prism plates has thus been found. If the effect in figure 5.18 is typical of star/galaxy separation from direct plates, then a strong case for pairing with prism plates to perform this separation is made.

Checking on the success of star/galaxy separation from the direct plate has relied on visual inspection of individual images and a subjective assessment of image identity. The main problem was thought to be the difficulty in identifying compact galaxies from stars. Examination of objective-prism spectra allows a much more unambiguous identification. Stellar spectra are relatively easy to identify, except those of type 'M', whose appearance can mimic that of a redshifted galaxy. However, even these can be identified with care. The stellar contamination thus revealed in the galaxy sample and the matching of this sample with the upper curve in figure 5.18 clearly demonstrates that some stars are being visually classified as galaxies from the direct plate. Stellar images on the direct plate may not be as sharp in all cases as has been supposed. The failure of the  $\log(\text{area})/\text{magnitude}$  discriminator in this case is due to the selected discrimination line being unable to provide a proper segregation.

From figure 5.16 it is evident that the stars and galaxies follow different curves. The stellar sequence is quite curved and merges into the galaxy relation at faint limits where image identification is difficult. The galaxy sequence, though, is broader and follows a more linear relation, even at the bright end. A problem on the direct plate is that due to saturation of stellar image pixels because of the relatively low Cosmos density range, the direct stellar isophotal

magnitudes may be significantly underestimated. Indeed, since a copy direct plate was used, the loss in contrast for bright images is more a limitation of the plate material itself (see chapter 3 section 3.12). For the prism plate though, object flux is spread over a larger number of pixels so they are less likely to be saturated. Consequently, though not on the same magnitude system, the prism, stellar isophotal magnitudes are less likely to be underestimated. The calculated magnitudes for galaxies from the direct plate will not suffer so much from saturation effects as a star of the same isophotal magnitude because of its dispersed nature. Hence the direct plate galaxy magnitudes are less prone to underestimation. This explains why, at the brighter end in figure 5.16, a star and galaxy assigned the same direct magnitude have considerably different prism magnitudes. The stellar direct value is considerably fainter than its prism value because of saturation, whilst the galaxy has a direct magnitude much closer to its prism value because of its much lower surface brightness. This effect is still present even at quite faint magnitudes, though the size of the discrepancy decreases.

The tight stellar sequence of figure 5.17 can be fitted with a polynomial to obtain an empirical relation between the stellar magnitude estimates. Obviously a new relation would need to be obtained for each set of plates paired. A simple quadratic or cubic gives a satisfactory fit to the stellar sequence in figure 5.17 if the prism magnitudes are taken as the independent variable. This is illustrated in figure 5.20. The characteristics and co-efficients of the quadratic fit are given in table 5.4.

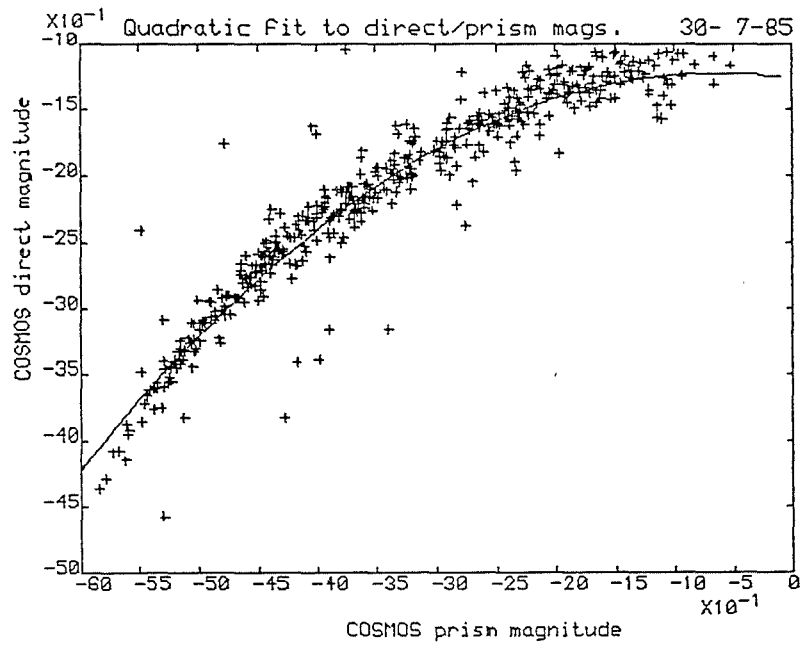


Figure 5.20 Quadratic fit to the upper stellar curve of Figure 5.17, buj taken as the independent variable.

Table 5.4

Characteristics of the quadratic fit to the data in figure 5.20.

Co-efficient (a): -0.131716, std.dev.: 0.060664

Co-efficient (b): -0.104315, std.dev.: 0.009329

Constant : -1.263222, std.dev.: 0.086976

Multiple linear correlation co-efficient : 0.9610

Reduced Chi-square of fit : 0.0473

Value of f-test of fit : 1189.5

Polynomial fits could be used as a means of performing automatic star/galaxy separation on paired samples by comparing the expected direct magnitude with that given by the polynomial in prism magnitude. Acceptable tolerances could be placed on the expected magnitudes and if the observed magnitudes are within these tolerances then the object can be flagged accordingly.

#### 5.9.2. Comparison of other attributes from the paired sample.

Various other direct/prism image attributes were compared but none gave as distinct a star/galaxy separation as for the mag/mag comparison. For instance, figure 5.21 gives prism image area against direct image area for the matched sample. There is evidence of separation by image type although it is not as marked as in figure 5.16. The stellar images alone (figure 5.22), do exhibit a tight sequence. Such segregation is not surprising as stellar images are more compact than galaxy images. For just the galaxian images (figure 5.23), which is more of a scatter diagram due to the wide range in galaxy image area and surface brightness, stellar contamination is less obvious than in figure 5.18. The steep slope of the stellar sample is indicative of colour variations which cause corresponding variations in objective-prism spectrum length, and hence the prism spectrum's image area. The relation flattens out considerably for brighter stars due to the onset of diffraction spikes which give an exaggerated stellar image area. For the galaxy sample, colour effects are less pronounced due to the composite nature of galaxy light and the effects of reddening due to redshift.

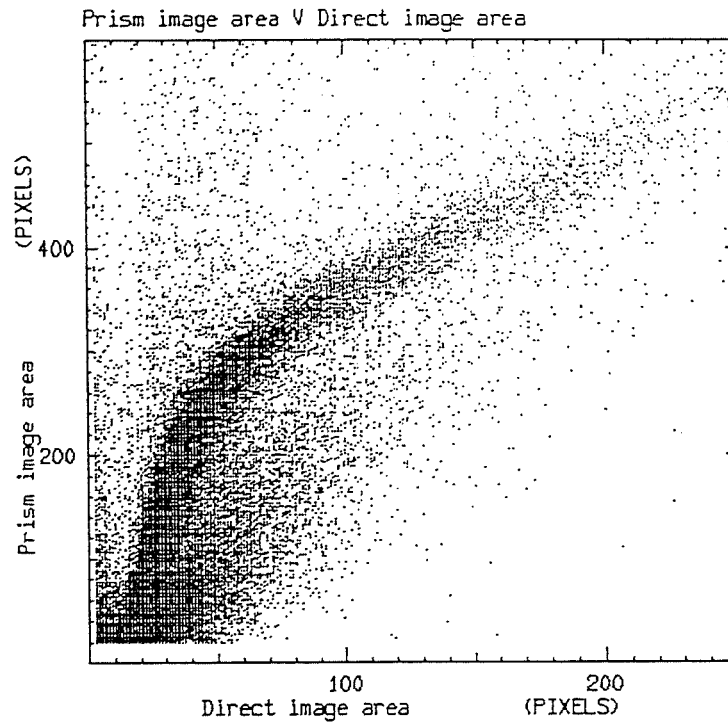


Figure 5.21 Prism image area versus direct image area for the paired sample.

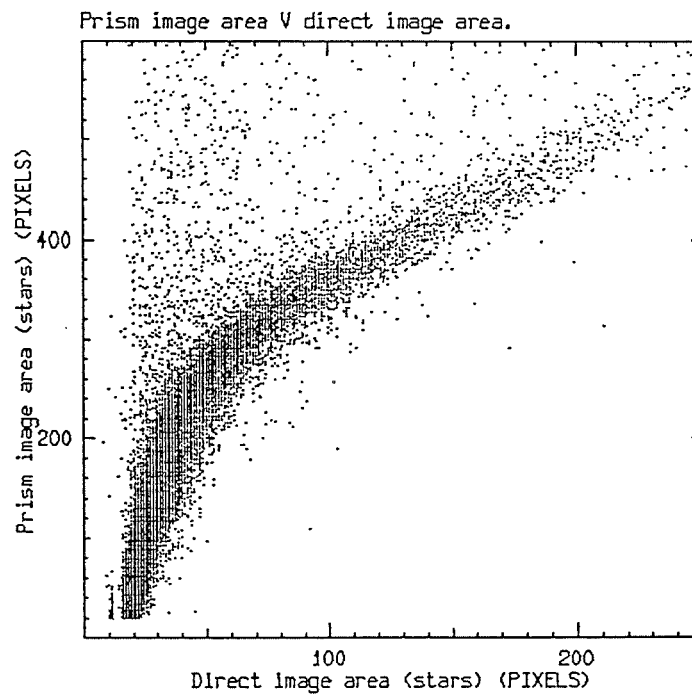


Figure 5.22 As for Figure 5.21 but for just the stellar images.

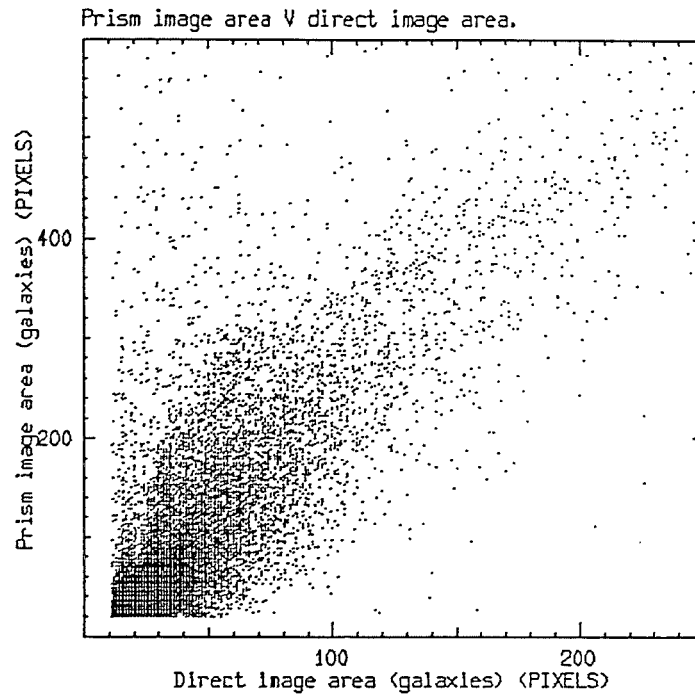


Figure 5.23 As for Figure 5.21 but for just the galaxy images.

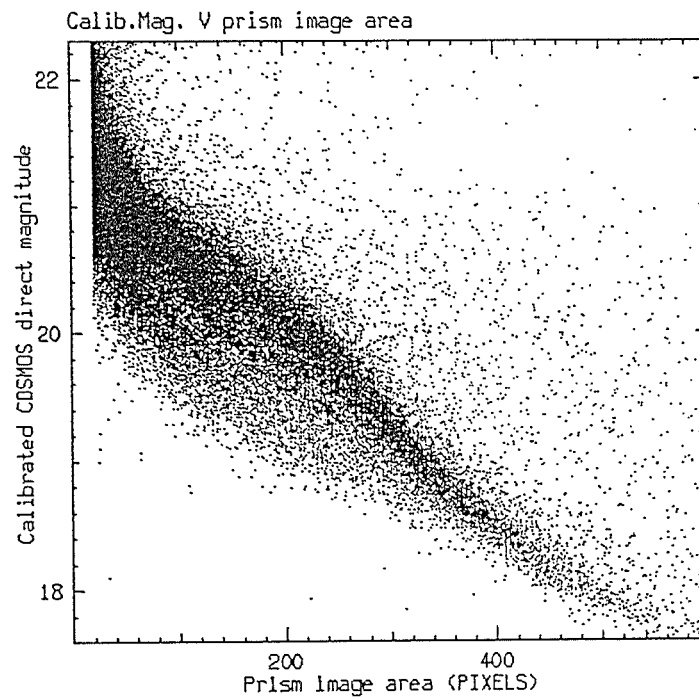


Figure 5.24 Calibrated COSMOS direct magnitude versus prism image area for the paired sample.

A comparison of calibrated Cosmos direct magnitude and prism image area was also made (figure 5.24), which is analogous to that of figure 5.5. We might therefore expect some segregation of image type to occur. However, the segregation is not as clear cut as in figure 5.16 and it would be difficult to choose an appropriate discrimination line. Furthermore, the stellar contamination of the galaxy sample demonstrated clearly in figure 5.18 is not obvious in this plot. Figure 5.24 is more useful for indicating stellar colour differences than for use as a star/galaxy discriminator since stars of different spectral types, but of the same isophotal magnitude, will have different prism image areas. A more thorough investigation of paired image attributes may provide further useful information and lead to identification of peculiar objects. Such a study however, is beyond the scope of this thesis.

#### 5.10. Check on the positional stability of the co-ordinate transformation.

Figures 5.25 and 5.26 give the differences between direct- and prism-X and direct- and prism-Y image co-ordinates as a function of Cosmos calibrated magnitude for the 50,025 paired images. The direct X,Y values have been transformed to the same co-ordinate system as the prism plate. The excellent agreement between the Y co-ordinates is clear. The rms scatter is  $\sim 0.01$  mm at the bright end, increasing to  $\sim 0.02$  mm at faint limits. This confirms the success of the pairing. The increasing discrepancy at fainter magnitudes is because of the difficulty in obtaining accurate Y-centroid positions when images are only a few pixels across. Figure 5.25 though, reveals quite large, systematic variations of  $\sim 0.1$  mm. Here  $\Delta X$  is the prism image X-minimum value subtracted from the transformed direct X-centroid co-ordinate.

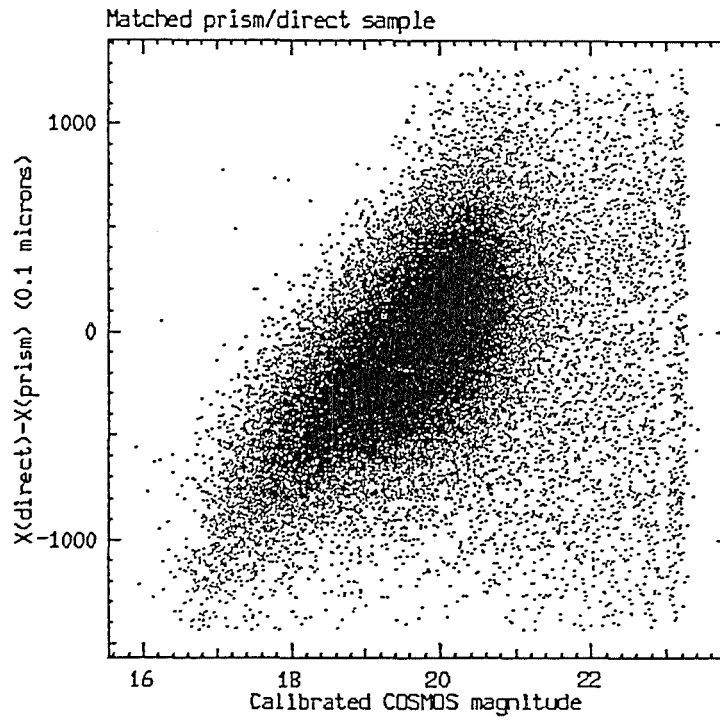


Figure 5.25 The differences between the transformed direct X co-ordinate and prism X co-ordinate as a function of calibrated COSMOS direct magnitude for the paired sample.

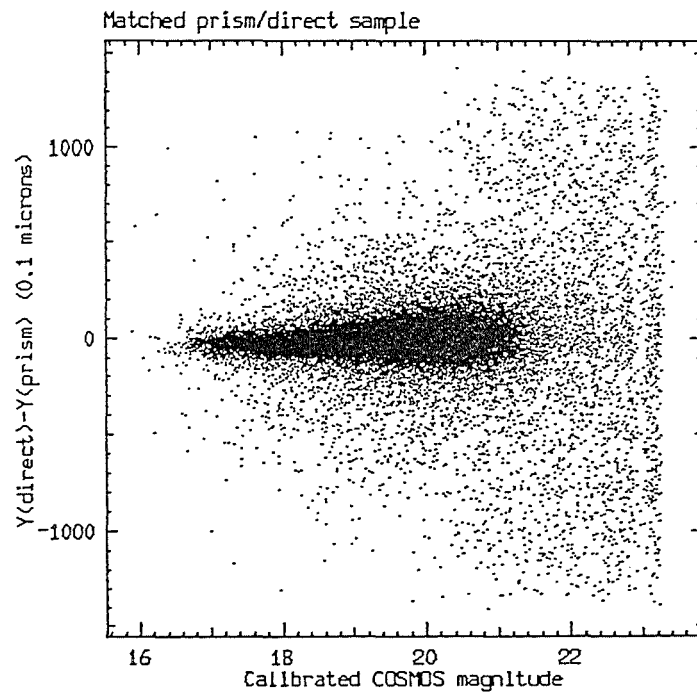


Figure 5.26 The difference between the transformed direct Y co-ordinate and prism Y co-ordinate as a function of calibrated COSMOS direct magnitude for the paired sample.

The rms scatter in  $\Delta X$  increases from  $\sim 0.02-0.06$  mm with increasing magnitude, as does the average  $\Delta X$  value itself from  $\sim -0.1$  mm to  $0.06$  mm (= 10pixels) in going from  $b_j = 17.0-21.0$ .

Assuming no severe systematic trends in the direct image X-centroids with magnitude (as expected from the results for the Y-centroids), then since the X co-ordinate was the dispersion direction, the systematic effects must be due to variations in the minimum X-positions of prism images which are a function of image magnitude, colour, type and surface brightness. The magnitude effect dominates and as the minimum X-position is directly related to the ECO position, use of the observed ECO accounts for the strong mag/Z effect found (see chapter 3 section 3.6 and figure 5.28). Using transformed direct plate X-centroid positions as the wavelength reference point should largely eliminate this effect.

#### 5.11. Extraction of the prism spectra.

A HAGGIS based software package called 'HOPS', developed by Dr.S.M.Beard, was used to extract and manipulate objective-prism spectra from the prism plate MM data. The transformed direct X,Y co-ordinates were used to define the ECO position in the prism spectra. The HOPS program 'OPSELECT' was then run which tests to see if a box of specified size can be placed around the X,Y co-ordinates without overreaching the bounds of the data. The box should be large enough to contain any objective-prism spectrum but should include enough sky pixels to determine the background sky-level immediately before and after the spectrum. The box should also be narrow enough to exclude unnecessary sky pixels which will decrease the S/N, especially for faint spectra. A 20 pixel offset was chosen in front of the ECO position for a 128 by 8 pixel box.

The OPSELECT program resulted in 197,284 of the 199,014 direct images lying within the bounds of the data set. These objects were flagged and written to an index of the main direct-data catalogue (index 'border'). Beard (1984), has shown that objective-prism redshifts can only be determined over the magnitude range  $16.5 \leq b_j \leq 18.5$ . However, the bright limit has been pushed back to  $b_j = 15.8$  for INTERZED measures and  $\sim 15.5$  for J-L measures, as described in chapter 4. Hence, only galaxy spectra brighter than  $b_j = 18.2$  were extracted from the MM data and written to a new index of the main catalogue. This resulted in 5,981 objects being selected.

The HOPS program 'OPEXTRACT' was then used to extract these 2-D prism spectra from the MM data which were subsequently written to a VMS file. The HOPS routine 'OPCUTFIX' was used to recover the ECO positions (as determined from the co-ordinate transformation) to a fraction of a pixel. This was necessary since the box around each spectrum was only positioned to the nearest pixel with OPEXTRACT. If uncorrected the ECO to box-edge distance would not be the same for each spectrum but would only be to the nearest pixel. The accuracy of any prism redshifts might then be affected.

Finally the HOPS 'OPSQUASH' program was used to convert to intensity the selected prism spectra (using the parameters given in section 5.3) and sum them perpendicular to the dispersion direction to form 1-D spectra. The results were written to a new VMS file. Since each object was flagged from the direct plate star/galaxy separation (or else was unclassified), separate catalogue indices containing just the stellar and galaxian samples were created. The INTERZED program (see chapter 3), modified by Dr. Beard to run within the HAGGIS environment, was then used to measure the spectra for redshift. Consequently a catalogue was produced which contained the IAM direct-image parameters, RA's and DEC's, objective-prism redshifts and feature

weights for each measured galaxy spectrum.

All 4,346 objects between  $b_j = 18.2$  and  $18.7^*$  were also output to a catalogue index of which 1,441 had been classified as galaxies. This fainter sample was chosen to test the objective-prism redshift technique to fainter limits and to ascertain what fraction yield redshifts. This was a worthwhile exercise, since although Beard (1984), limits the technique's useful magnitude range between  $b_j = 16.5$  and  $18.5$ , his results were from copy plates. In this work a high-grade, atlas-quality, prism plate was used which may enable the technique to be pushed somewhat fainter.

#### 5.12. Measurements of the objective-prism spectra in field 349.

##### 5.12.1. Stellar spectra results.

Stellar spectra are essentially at rest compared with galaxies and the inherent crudeness of the objective-prism redshift technique. Hence measures of stellar spectra may reveal any zero-point shifts that should be applied to the galaxy results. Any residual colour or magnitude effects not accounted for by using the co-ordinate-transformed direct-image X,Y centroid positions and any variations in redshift with plate position may thus be revealed.

Random samples of stellar spectra were selected from the 4,519 stars to  $b_j = 18.2$  and from the 2,905 stars between  $b_j = 18.2$  and  $18.7$  and were measured for redshift using INTERZED. Of the 180 stars selected to  $b_j=18.2$ , 140 had suitable  $4000\text{\AA}$  features whilst 240 of the 364 stars selected from the  $18.2 < b_j \leq 18.7$  sample yielded 'redshifts'.

\* See note at end of chapter.

The results for those stellar spectra assigned top feature weight from the two samples are plotted as a function of magnitude in figure 5.27. The wavelength reference point for these spectra was defined automatically from the co-ordinate transformation. The same stellar sample was also measured using an automatic polynomial fitting to the observed ECO. These latter results, given in figure 5.28 exhibit the expected mag/Z effect. Reference to figure 5.27 reveals that the mag/Z effect has been eliminated by using the co-ordinate transformed direct X,Y positions to define a wavelength reference point. However, the redshift scatter at a given magnitude is slightly worse and there is also a zero point offset of  $\sim -0.021$ . The mean 'redshift' for the 380 stellar spectra measured to  $b_j = 18.7$ , was  $Z = -2.115E-02$ ,  $\sigma = 1.024E-02$ . This zero point offset should be applied to the objective-prism galaxy redshifts. Furthermore the dispersion in the stellar redshifts of  $\sim 0.01$  ties in with the expected uncertainties of the objective-prism redshift technique.

Some of the stellar spectra measured are illustrated in figure 5.29. Figures 5.30 and 5.31 are plots of stellar redshift versus X,Y positions of spectra on the plate. The evidence of curvature in these plots, especially in figure 5.31, indicates that there may be some systematic positional variation between the co-ordinate systems not accounted for by the simple linear transformation used. This curvature suggests that a quadratic transformation may have been more appropriate. The trend is only noticeable near the plate edges and in figure 5.31 amounts to a redshift difference of  $\sim 0.015$  compared with the central regions of the plate. However, due to the time consuming nature of the pairing procedure, the effect was considered small and localised enough not to warrant a re-pairing, although it is probably contributing to the size of the observed dispersion in figure 5.27. Consequently the results from the linear transformation were used.

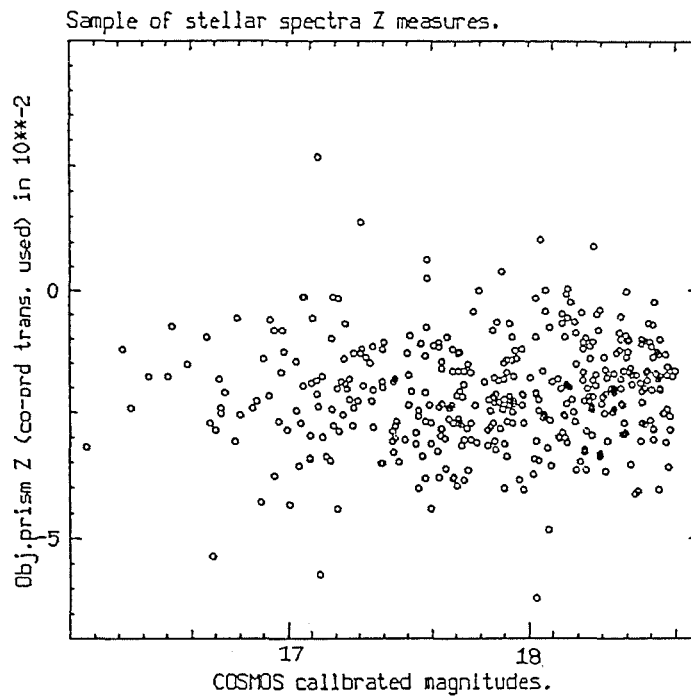


Figure 5.27 INTERZED stellar redshift versus COSMOS calibrated direct magnitude for a selection of stellar spectra measured to  $b_j=18.7$  and assigned top feature weights.

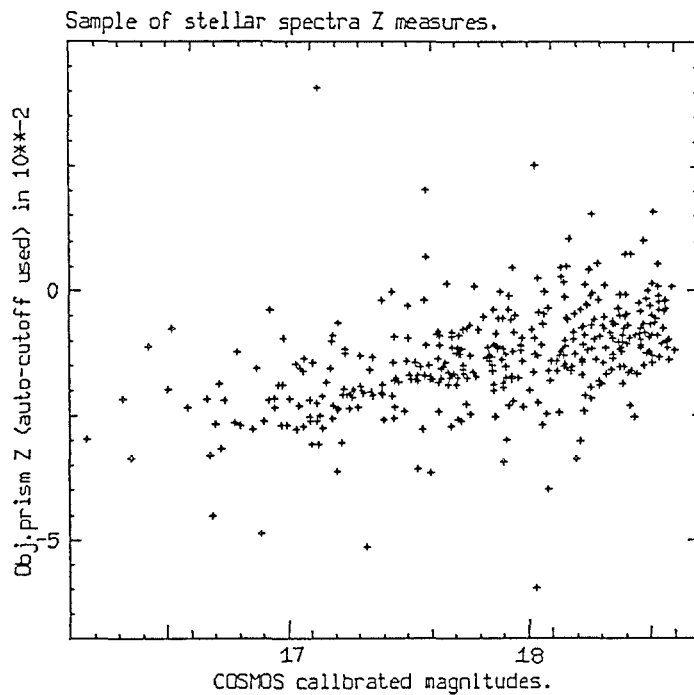


Figure 5.28 INTERZED stellar redshift against COSMOS calibrated direct magnitude for the same sample in Figure 5.27 except the wavelength reference point was determined from a polynomial fit to the observed ECO.

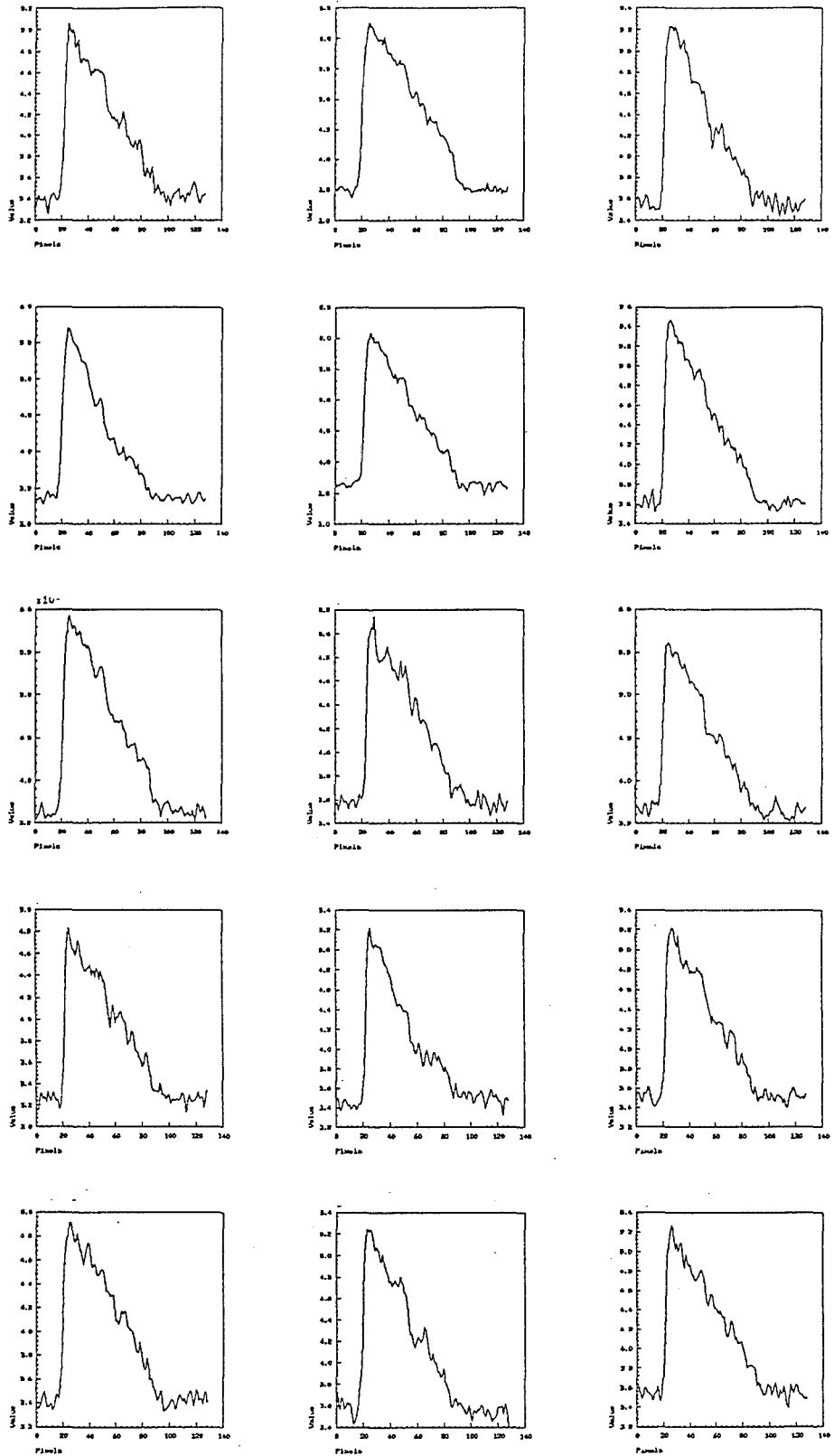


Figure 5.29 Random examples of stellar spectra measured by INTERZED from COSMOS MM data of plate UJ6525P.

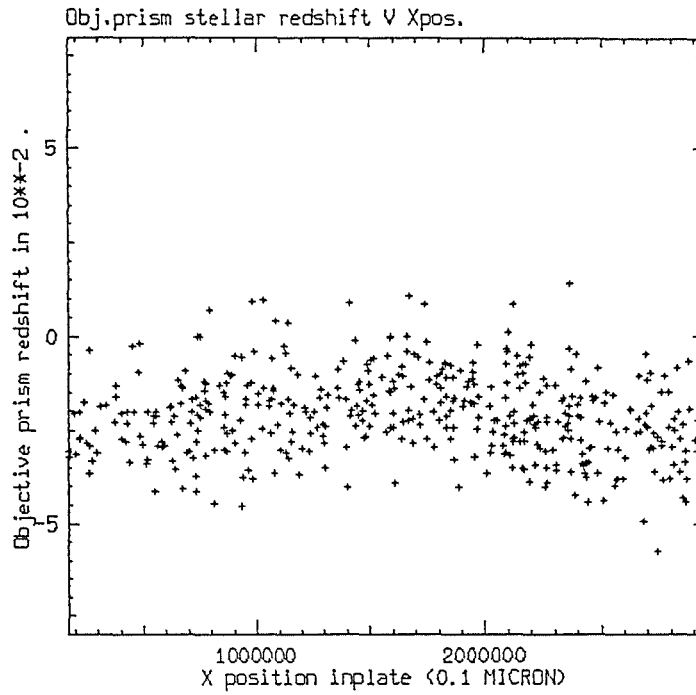


Figure 5.30 Stellar INTERZED redshift versus co-ordinate transferred direct X co-ordinate for these objects.

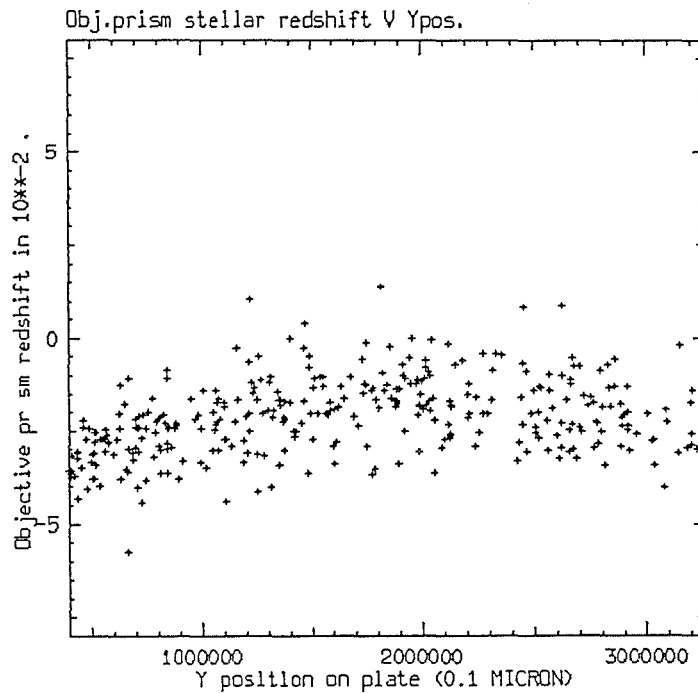


Figure 5.31 Stellar INTERZED redshift versus co-ordinate transferred direct Y co-ordinate for these objects.

### 5.12.2. Galaxy measures.

All 1,462 galaxy classified spectra to  $b_j = 18.2$  were measured with INTERZED. From the form of the spectra it became apparent that a significant number of stars were contaminating the galaxy sample. In all, 286 spectra were re-classified as stellar with confirmation from measurement of their  $4000\text{\AA}$  features. The following results were obtained:-

Number of stellar spectra yielding redshifts : 220

Mean stellar redshift : -0.0229

Sigma : 0.0117

These results, which are consistent with those from the stellar spectra measured earlier, imply a lower limit of  $\sim 19\%$  stellar contamination in the supposed galaxy sample (see section 5.9.1). Figure 5.32a gives spectral examples of these contaminants which can be compared with figure 5.29. A further 320 spectra (22% of the sample), were deemed too faint, noisy, ambiguous or without  $4000\text{\AA}$  features to warrant redshift determination. They include the 65 stellar contaminants identified with no measurable  $4000\text{\AA}$  feature. Nevertheless, 916 galaxy spectra (63% of the sample), did yield redshifts, of which 297 were assigned weight 1, 396 weight 2 and 223 weight 3. Four quasars were also identified. Examples of galaxy spectra assigned weight 1 to  $b_j = 18.2$  are given in figure 5.32b.

Figure 5.33a is a plot of the relative frequency of galaxies yielding redshifts (as determined from the separation on the direct plate), as a function of magnitude to  $b_j = 18.2$ . The data are binned into 0.1 magnitude intervals. The total number of contaminating stars identified is also included, as is the fraction of these with redshifts (the two lower curves in the diagram). The fraction of identified stellar contaminants peaks at  $b_j \sim 17.7$

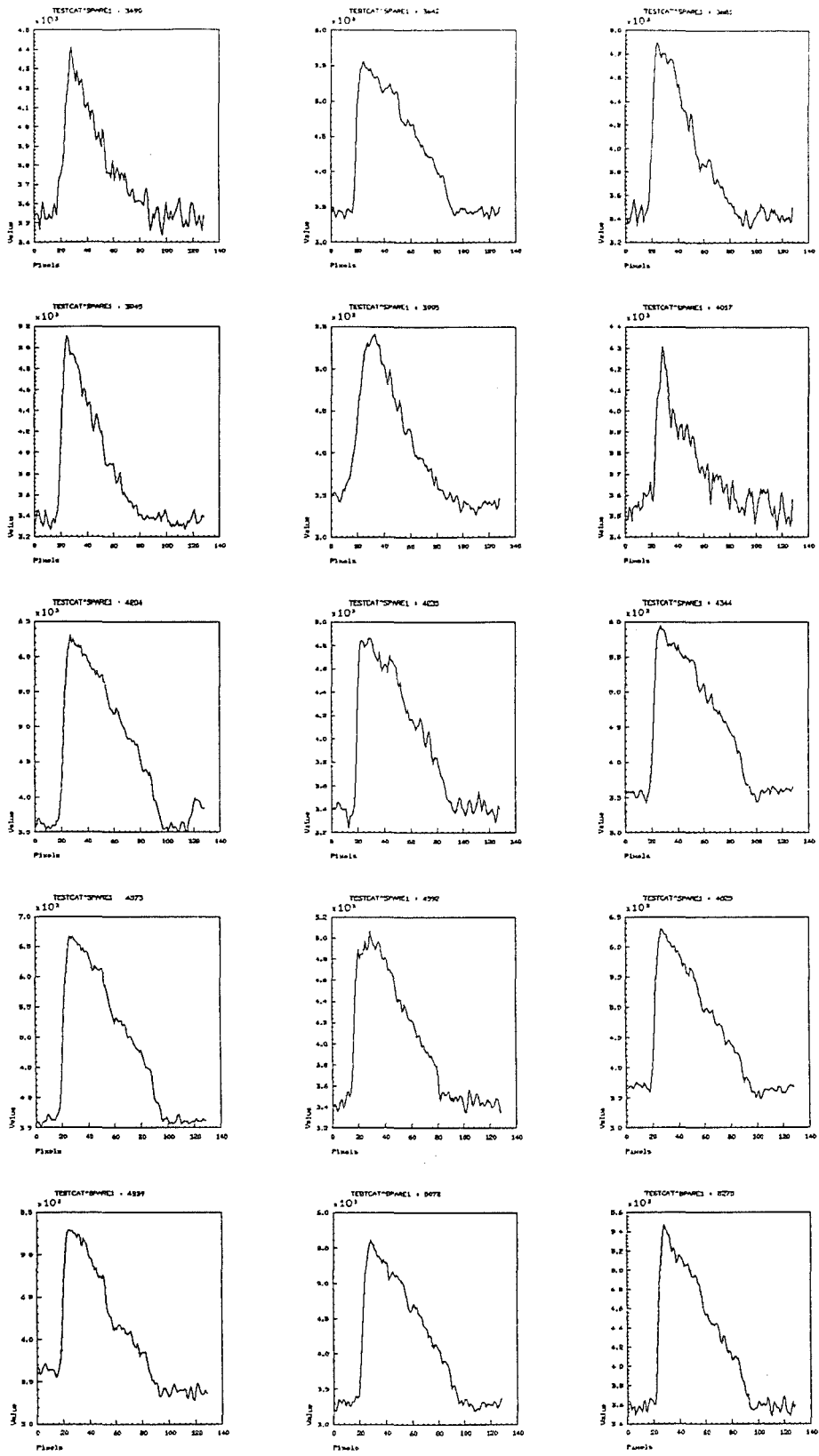


Figure 5.32a Random examples of stellar spectra contaminating the galaxy sample.

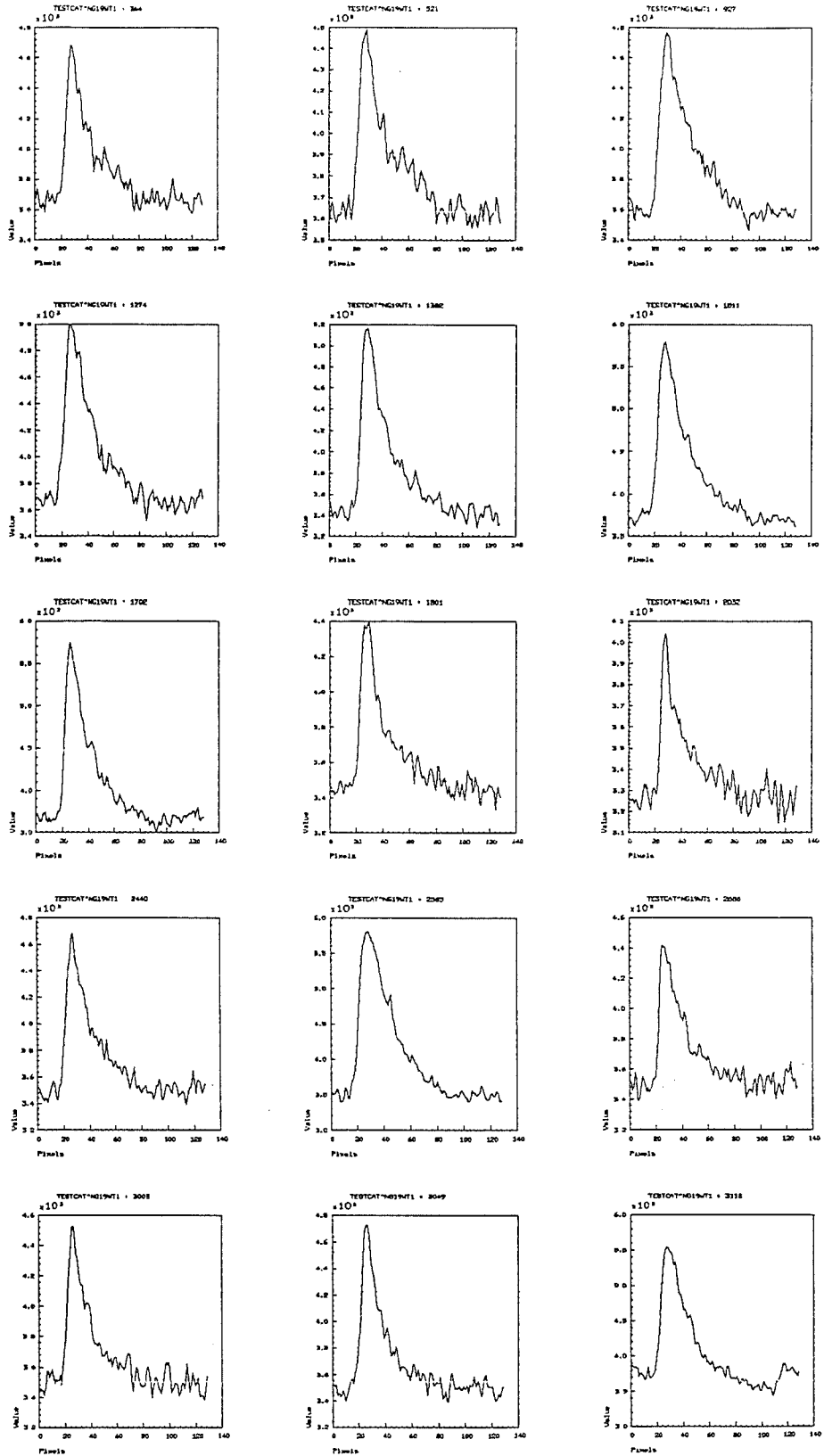


Figure 5.32b Random examples of galaxy spectra with  $4000\text{\AA}$  features assigned weight 1 from the sample with  $b_j < 18.2$ .

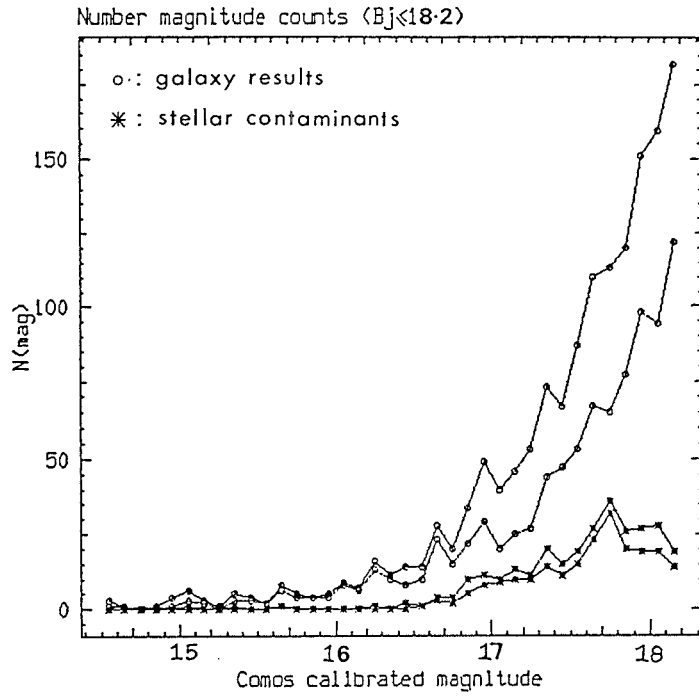


Figure 5.33a Relative frequency of galaxies yielding redshifts compared to the total galaxy sample, as a function of magnitude, to  $b_j=18.2$ .

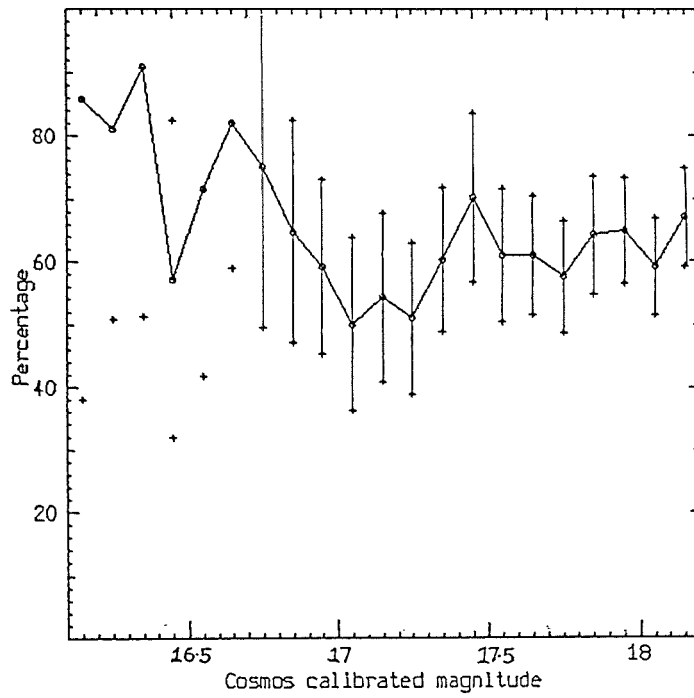


Figure 5.33b The percentage fraction of galaxies with redshifts (all weights) compared to the total galaxy sample as a function of magnitude, together with error bars.

The decrease thereafter is likely to be real because of the large parent population from which the contaminants were identified. This could be the peak of the selection function for identifying stellar contaminants in the supposed galaxy sample because of the effects of worsening S/N at fainter limits. The peak may also reflect the true maximum of stellar contaminants from the imperfections of the star/galaxy separation. Figure 5.33b gives the percentage fraction of galaxies with redshifts (all weights) compared to the total, as a function of magnitude, together with error bars. The fraction yielding redshifts does not vary by more than 10% between  $b_j = 16.7-18.2$  and the average is 61%,  $\sigma = 7$ . Brighter than  $b_j \sim 16.7$  the small numbers of objects make estimates unreliable.

Figure 5.34a gives the relative frequency of galaxies assigned redshifts (all weights) compared with those assigned top weights, again as a function of magnitude. Although the total fraction with redshifts remains fairly constant, the assigned weights change substantially with fewer high weight features at fainter limits. This is expected because of the effects of worsening S/N. The percentage fraction with top weights peaks at  $b_j \sim 17.3$  and thereafter decreases steadily until  $b_j = 18.2$ . This is shown in figure 5.34b. Figures 5.34a-b indicate that though the objective-prism galaxy-redshift selection function for top weight features had peaked, the overall fraction of galaxies yielding redshifts remained fairly stable to  $b_j = 18.2$ . Hence an attempt to obtain redshifts for a fainter galaxy sample to  $b_j = 18.7$  was made. The galaxy sample between  $b_j = 18.2$  and 18.7 (1,441 objects) was subsequently measured with INTERZED. Again a significant proportion (14%) were re-classified as stars. This is also a lower limit of contamination. Whether the percentage decrease in stellar contaminants on going to the fainter sample is real is not easy to ascertain.

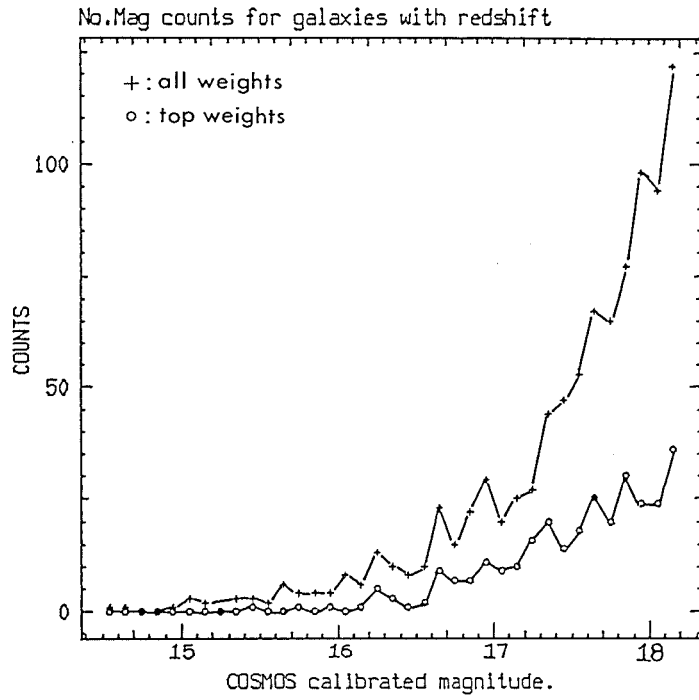


Figure 5.34a The relative frequency of galaxies assigned redshifts (all weights) compared with those assigned top weights, as a function of magnitude.

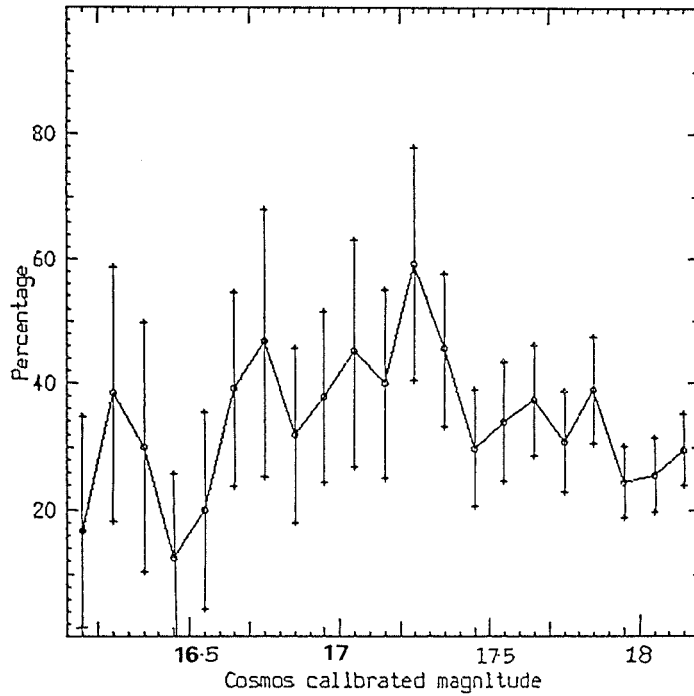


Figure 5.34b The percentage fraction of the total redshift sample assigned top weight as a function of magnitude, together with error bars.

It is just as likely a consequence of the worsening S/N which makes it difficult to unambiguously identify objects. In fact 53% of the measured sample were unsuitable for measurement, twice the percentage of the brighter sample. Even so, 43% (626 spectra) did yield redshifts of which 12% (169 spectra) were assigned top feature weight. This compares with 20% top feature weights for the brighter sample.

Figure 5.35 shows the relative frequency of galaxies with redshifts to  $b_j = 18.7$  compared to the total. The fraction with redshifts decreases significantly from 67% at  $b_j = 18.2$  to 33% at  $b_j = 18.7$ . This is still a significant percentage of the galaxy sample and implies, for this plate at least, that measures of fainter galaxy spectra to  $b_j = 18.7$  would be worthwhile. The most efficient magnitude interval for obtaining redshifts was  $b_j \sim 18.2$ . Beard (1984), found a somewhat brighter useful magnitude limit of  $b_j = 18.0-18.5$ , but this may reflect on his use of copy plate material compared to the original 'A' grade survey plate used in this study (see chapter 3).

Thus, with high quality plate material, substantial numbers of objective-prism redshifts can be obtained to  $b_j = 18.7$ . For the work of this thesis 1,543 redshifts from features of all weights and 464 redshifts from features assigned top weight were obtained in field 349. The analysis of these redshifts is given in chapter 6.

Note. The magnitude limits of the measured galaxy prism spectra of 18.2 and 18.7 were actually intended to be to  $b_j \sim 18.5$  and 19.0. However, the HAGGIS COSMAGCAL routine used to calibrate the raw Cosmos direct magnitudes, supposedly according to formula 3.6 (chapter 3), was later found to be erroneous. This resulted in magnitudes too bright by  $\sim 0.31$ . This software bug has since been fixed.

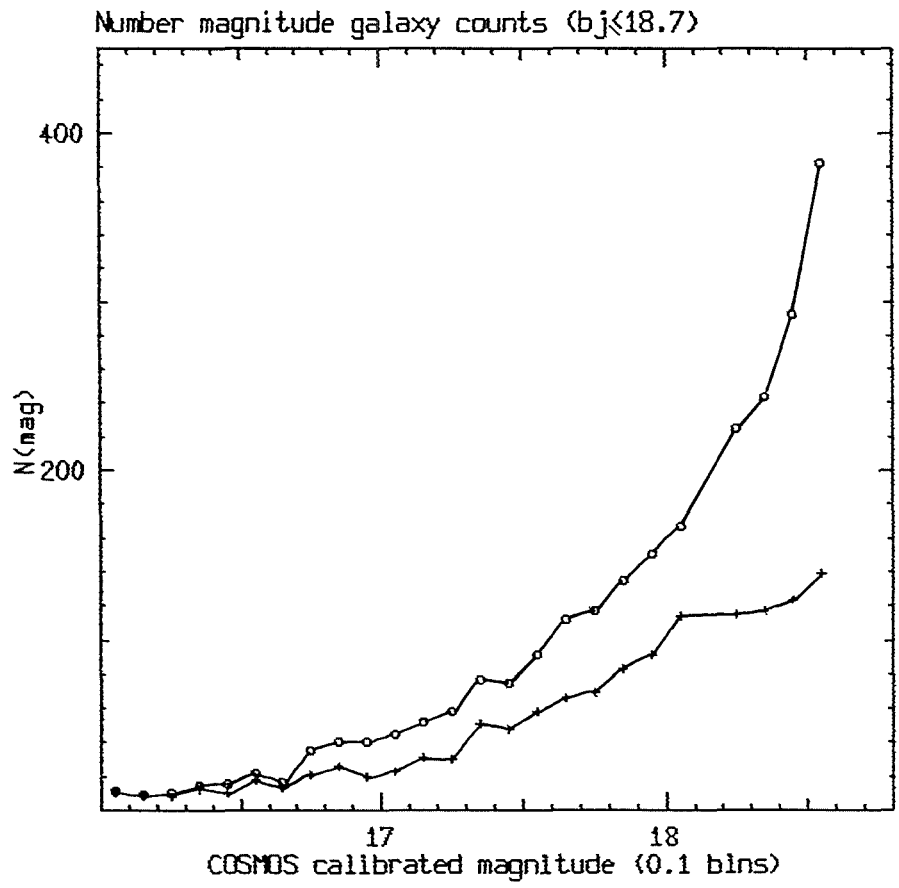


Figure 5.35 The relative frequency of galaxies with redshifts to  $b_j = 18.7$  compared to the total sample.

Analysis of the Galaxy distribution in SERC survey field 349.6.1. Introduction.

In the previous chapters, the techniques used to obtain crude objective-prism redshifts and accurate slit-spectra redshifts for a sample of galaxies have been described, together with the calibration and intercomparison of these data. This chapter is concerned with the analysis of the distribution of this galaxy sample in SERC sky-survey field 349, centred at  $00^{\text{h}}00^{\text{m}}, -35^{\circ}00'$  near the SGP. This analysis is the culmination of foundation work carried out in the earlier chapters, although it must be stressed that chapters 3 and 4 stand for themselves as follow-up studies to work on the objective-prism redshift technique pioneered by Cooke (1981), and Beard (1984).

The field under investigation is at a high galactic latitude so that effects of galactic obscuration and reddening should be at a minimum (see chapter 1, section 1.4.5). For the purposes of this work the effect of galactic extinction on the observed galaxy distribution is assumed negligible. Extinction values, 'Ab', of  $\sim 0.25$  magnitudes at the poles, have been obtained, e.g. Van den Bergh (1967), and Holmberg (1974). However, McFadzean et al. (1982), found no evidence for significant interstellar extinction at the poles. The remaining external effects on the observed clustering of galaxies in this field will be any non-uniformities in the sensitivity and response of the IIIaj emulsion, selection effects such as K-dimming, and any intergalactic absorption that may be present.

As yet there is no convincing evidence that intergalactic obscuration plays a significant role in galaxy counts, e.g. Shane (1976), although an interesting article by Rudnicki (1984), discusses the current status for the existence of intergalactic dust. The sky background variations and stellar number density from the Cosmos measures of the plate used for this field (see chapter 5 figures 5.2 and 5.10) indicate that any effects on the observed numbers of galaxies due to vignetting and emulsion properties are small and are ignored in this investigation. The significance of K-dimming is that the much larger K-corrections for early-type galaxies (ellipticals and lenticulars) cause them to fade out with distance much more rapidly than later types. Consequently, though intrinsically fainter, the later types can be seen to a greater distance. This is unfortunate since we have already discussed in chapter 1, section 1.8, that early-type galaxies may be important tracers of any filamentary structure in the galaxy distribution, (Giovanelli and Haynes 1982). Furthermore it is the early-type galaxies which possess the best  $4000\text{\AA}$  features.

This chapter is divided into two main sections. The first section deals with analysis of the spatial distribution for the magnitude-limited sample of bright galaxies with  $b_j \leq 16.5$ , for which an almost complete slit-spectra redshift list is available (see chapter 2). The second section deals with the statistical analysis of the fainter galaxies in this field to  $b_j \sim 20.5$ . Few accurate slit spectra-redshifts for this much larger, faint sample exist, so the projected 2-D distribution of these galaxies is studied. The measurement of large numbers of objective-prism galaxy spectra for these faint galaxies (see preceding chapter), also provides crude spatial information which is nevertheless sufficiently accurate to resolve voids more than 25 Mpc in depth (for  $H_0 = 100 \text{ Km/s/Mpc}$ ), to highlight regions of enhanced galaxy density, and to obtain cluster redshifts. The detection of large voids seems to be an increasing

feature of investigations into the 3-D galaxy distribution, as discussed in chapter 1.

## 6.2. The distribution of bright galaxies in field 349 with $b_j \leq 16.5$ .

### 6.2.1. Preliminary investigation.

The number of slit-spectra radial velocities obtained in the field, and their accuracy, is sufficient to allow a much more detailed investigation of the bright galaxy distribution than is possible with crude objective-prism redshifts. Indeed, an estimation of the luminosity function for this magnitude-limited, near-complete redshift sample is a potential derivative from these high quality data. Felten (1977), in an excellent review article, describes the standard procedure for deriving a galaxy luminosity function and also assesses the results, problems and consistency of previous determinations. A severe difficulty is that the techniques are sensitive to any spatial inhomogeneities in the observed galaxy distribution. As shall be shown later, anisotropy, at least for the bright galaxies, is particularly pronounced in this field. Kirshner et al. (1979), have suggested that the general luminosity function for galaxies does not differ substantially from the rather well-defined cluster-galaxy luminosity function whose analytical expression was developed by Schechter (1976). The radial velocities have in general been shown to be accurate to  $\sim 75$  Km/s, which is just sufficient to enable dynamical studies to be carried out on any identified galaxy groups. Virial radii and masses may be determined as well as M/L ratios given knowledge of the luminosity function (e.g. Gregory and Thompson, 1984 and Mezzetti et al. 1985). Such possibilities for the data, though of undoubted interest, are beyond the brief of this thesis wherein we are confined to the study of the spatial distribution of galaxies in this field. Further potential analyses will be discussed, along with other future work suggested, in the final chapter.

As described in chapter 2, radial velocities for 107 galaxies were obtained, amounting to 80% of all galaxies detected with  $b_j \leq 16.5$  in this field. Figure 6.1, a reproduction of figure 2.1 given again for convenience, illustrates the disposition of the remaining unobserved galaxies (denoted by open circles). The sample with radial velocities covers the entire field in a fairly uniform manner and indeed the intention was to attempt to observe a uniform sample from the parent population given the uncertainties in observing conditions etc. Even a cursory examination of figure 6.1 reveals that bright galaxies in this field appear non-randomly distributed, with an obvious concentration of projected objects to the right-hand side of the field centre. Figure 6.2 is the number-magnitude histogram for the magnitude-limited sample, binned into 0.1 magnitude intervals. The shaded region indicates the proportion of galaxies with redshifts at a given magnitude. It can be seen that the velocity sample is essentially complete to  $b_j = 15.9$  (there remain 3 low surface brightness galaxies which were unobserved). Fainter than  $b_j \sim 16.2$  the number of unobserved galaxies amounts to ~50% of the total sample at these magnitudes. The increasing incompleteness of the radial velocity data is clearly illustrated in figure 6.3, the integrated number-magnitude counts for the total sample and the subset with redshifts. Figure 6.4 gives the comparison between the number of observed galaxies at apparent magnitude  $b_j$  divided by the number of observed galaxies at  $b_j + \Delta b_j$ , as a function of magnitude interval ( $\Delta b_j = 0.1$ ). The horizontal line is the ratio of the number of galaxies expected to be observed in the intervals  $b_j$  and  $b_j + \Delta b_j$ , assuming that all galaxies have the same intrinsic luminosity, are uniformly distributed in Euclidean space and if the K-corrections and evolutionary effects are ignored, i.e. assuming that the galaxy number-magnitude distribution obeys the law:-

$$N(b_j) = 10^{0.6 b_j} \dots \dots \dots 6.1$$

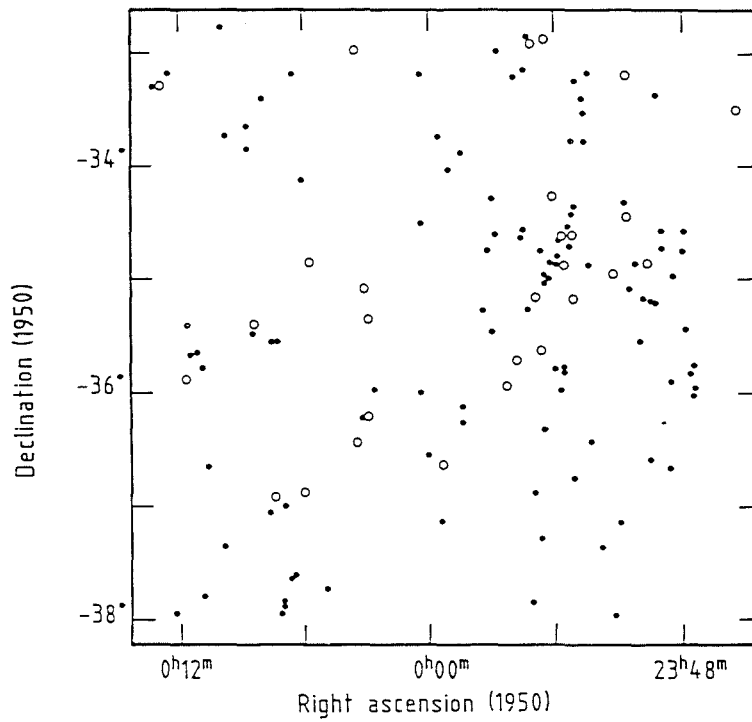


Figure 6.1 Reproduction of Figure 2.1. The projected distribution of galaxies with  $b_j \leq 16.5$  in field 349. Unobserved galaxies denoted by open circles.

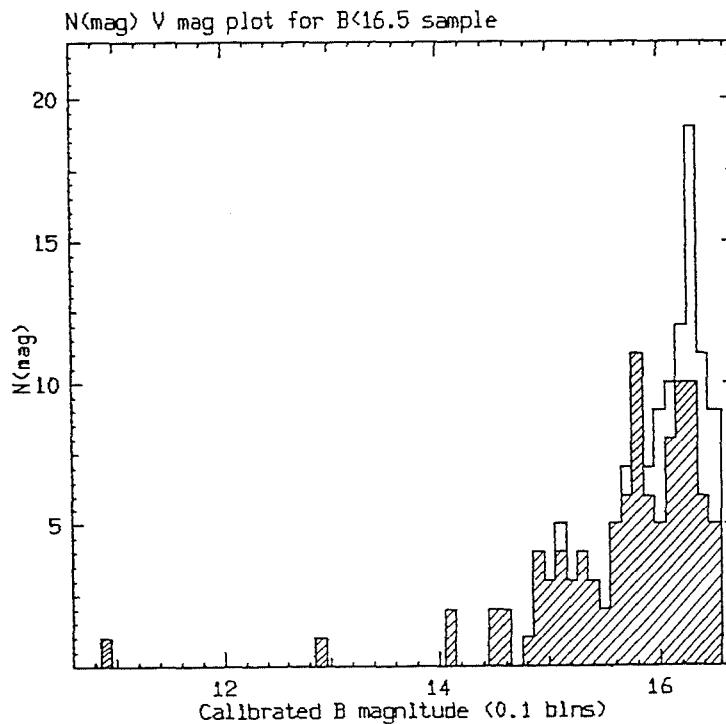


Figure 6.2 The number-magnitude histogram for the magnitude limited sample, binned into 0.1m intervals.

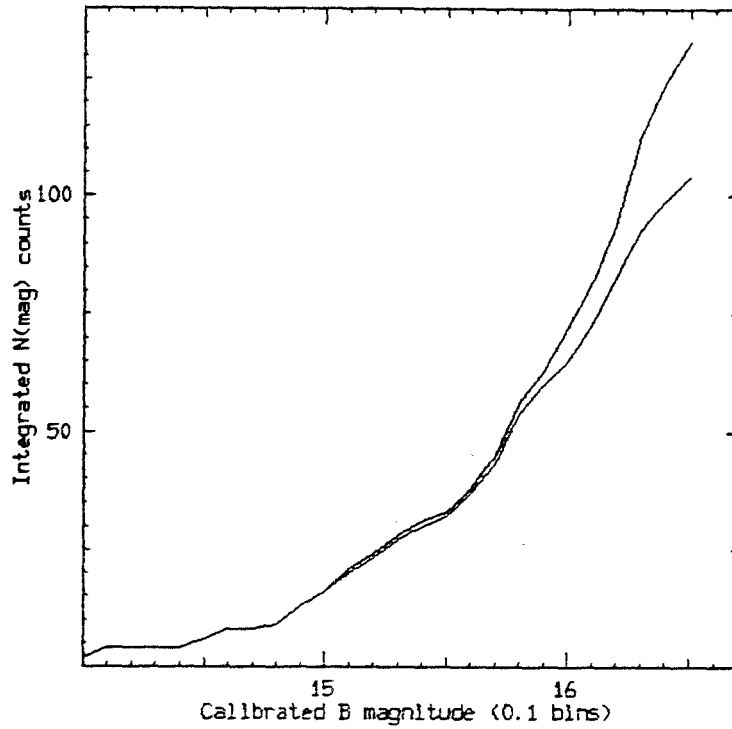


Figure 6.3 The integrated number-magnitude counts for the total sample and the subset with redshifts.

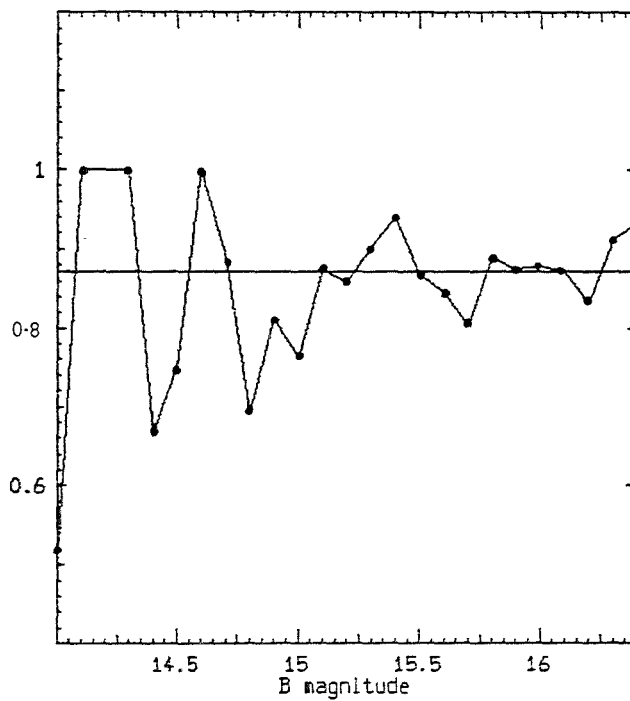


Figure 6.4 Number of observed galaxies at magnitude  $b_j$  divided by the number at  $b_j + \Delta b_j$  as a function of magnitude interval ( $\Delta b_j = 0.1$ ) compared with the ratio from the  $10^{0.6b_j}$  law.

The observed count ratio's and those expected from the formula 6.1 do agree to within the errors associated with each observed ratio value calculated on the basis of Poisson statistics. These errors are quite significant, i.e.  $\sim 0.36$  at  $b_j = 14.7$  to  $\sim 0.12$  at  $b_j = 16.5$ , being larger at the bright end because of the small numbers of objects at those magnitudes. Figure 6.5 is a simple histogram of the velocity data with 200 Km/s width bins. The most striking feature of this plot is that 2 broad redshift distributions are present which are mainly confined within the ranges  $6,500 \leq V \leq 10,000$  and  $11,800 \leq V \leq 19,000$  Km/s, although significant individual peaks are also evident. There is a gap of  $\sim 1,900$  Km/s between these broad distributions in which no galaxies are found over the entire area surveyed. The depth of this 'void' is  $\sim 19$  Mpc with a projected physical extent of at least 5 by 9 Mpc at the front end and 6 by 11 Mpc at the rear. The void volume is calculated to be  $\sim 1,100$  Mpc<sup>3</sup>.

All space volumes are calculated using equation 6.2 in spherical polar co-ordinates.

$$\int dV = \int_{r_1}^{r_2} \int_{\theta_1}^{\theta_2} \int_{\phi_1}^{\phi_2} r^2 \sin \theta \, d\theta \, d\phi \quad \dots\dots\dots 6.2$$

where 'r1' and 'r2' are the radial distances in Mpc of the volume element of the 'sphere' under consideration,  $\phi_1$  and  $\phi_2$  denotes the angular distance in radians subtended on the sky parallel to the RA co-ordinate axis and  $\theta_1$  and  $\theta_2$  covers the range of declination of the area concerned. The actual physical extent of the projected area on the  $5.35^\circ$  by  $5.35^\circ$  UKST plate in the RA and Dec directions obviously depends on the declination of the field. Hence the physical size of any projected redshift surface parallel to the RA direction is different at the low declination end than at the high declination end of the field:-

e.g.

$$X1 = r \sin \theta_1 \, d\phi ; \quad X2 = r \sin \theta_2 \, d\phi$$

whereas the physical extent in the declination direction at any redshift surface 'r' is just:-

$$Y1 = Y2 = r d\theta$$

where  $d\theta$  is the range in declination of the area. For simplicity, and because of the small angular size of the field, the physical dimensions of any sampled space volume in the RA direction are calculated using the field's mid-declination value.

From figure 6.5, the observed paucity of objects in the low and high velocity regions are not unexpected. At the low velocity end the volume of space sampled over the field is only  $\sim 450 \text{ Mpc}^3$  out to a distance of 6.5 Mpc where the first main redshift peak is present. At this distance only a 3.5 by 6 Mpc area is covered. Consequently, unless this field had been preferentially aligned with a nearby cluster, only a few galaxies from the LSC are expected in this volume.

At the high velocity end, i.e.  $V \geq 18,000 \text{ Km/s}$ , the observed paucity is due to the luminosity function which determines the numbers of objects that are intrinsically luminous enough to have such a high redshift and still remain in the magnitude-limited sample. Indeed, at this velocity, which samples to a distance of 180 Mpc, a galaxy with an apparent magnitude of  $b_j = 16.5$  would have an absolute magnitude of  $\sim -20.0$ . Such a galaxy would be at the bright, low relative-frequency region of the range of intrinsic luminosities exhibited by galaxies. For instance, the mean absolute B magnitudes for galaxies of types E, SO, Sab, and Sbc were found to be  $\langle B \rangle \sim -18.4$  from a statistical study of 1,500 bright galaxies (de Vaucouleurs, 1963). The brightest members of rich clusters may be as high as  $B \sim -21.5$ . Hence any intrinsic deficiency in the numbers of galaxies at higher redshifts would be severely masked by the incompleteness of galaxies that can be sampled in this magnitude-limited survey at these redshifts.

The immediate question arising from figure 6.5 is how significant is this 'void'? How likely is it that such a configuration could have arisen by chance if the galaxies are distributed randomly throughout space in this region? Intuitively, we might suppose that since the redshift sample is ~80% complete to  $b_j = 16.5$  (with the bulk of the remaining galaxies being at the faint end), and since the observed numbers of galaxies either side of this void are considerable, the probability that the observed paucity is due to the chance co-incident that the remaining unobserved galaxies populate this region is small.

To put this supposition on a much more objective basis, non-parametric statistical tests can be employed on the distribution as a whole. The Chi-square test can be used to test the goodness-of-fit of the observed grouped-velocity data to a normal distribution with the same mean and variance. This test, performed on the velocity data in 200, 500, 1,000 and 2,500 Km/s width bins, revealed that the null hypothesis  $H_0$ , that the observed distribution could have come from the assumed theoretical distribution, could be rejected in each case at the  $> 99\%$  confidence level, even though more and more resolution was being discarded at each re-binning. Any bins with expectation values ' $E_i$ '  $< 1.0$  were combined with adjacent bins since for small ' $E_i$ ' values the asymptotic Chi-square distribution may not be appropriate. No more than 20% of the  $E_i$ 's should be  $\leq 5.0$  and none should be  $< 1.0$  on theoretical grounds. Because the mean and standard deviation were estimated from the observed sample (which is assumed random) the number of degrees of freedom (d.o.f) must be reduced by 2, e.g. for  $N$  bins,  $d.o.f = N-1-K$ , where  $K$  is the number of parameters estimated from the sample. A histogram of the data in 500 Km/s width bins, together with the fitted Gaussian, is given in figure 6.6. An interesting point is that even if the data is binned into 2,500 Km/s width bins, the approximate accuracy of the objective-prism redshift

technique, the gap in the redshift distribution is still evident and significant (figure 6.7). Hence, although all substructure is washed out by the crude rebinning, we might still expect to resolve such voids with this technique.

A problem with the Chi-square test, apart from the fact that it is not distribution-free, is that potentially useful information is being discarded by grouping the data. Consequently statistics of the Kolmogorov-Smirnov type were also considered. For the K-S test all the data values are employed. The data are ordered and the empirical distribution function (e.d.f) is constructed from the sample data. The corresponding cumulative distribution function (c.d.f) for the hypothesized population against which the observed data were tested is superimposed. The largest departure  $D_n(\max)$  of the e.d.f.  $S_n(x)$  from the c.d.f  $F(x)$ , is then obtained, i.e.:-

$$D_n(\max) = \text{Sup } | S_n(x) - F(x) | \dots\dots 6.3$$

The advantage of this test is that the distribution of 'Dn' does not depend on  $F(x)$  as long as  $F(x)$  is continuous. The e.d.f for the radial-velocity data is given in figure 6.8. Notice the long "tread" length between ~10,000 and ~12,000 Km/s corresponding to the void described above. For this data the K-S test should not be used directly since the mean and variance of the hypothesized distribution are obtained from the sample data itself. Instead, a modification known as the Lilliefors test was employed. Normalised sample values 'Zi' are obtained from the individual data values 'Xi', e.g.:-

$$Z_i = ( X_i - \bar{X} ) / S \quad i = 1, 2, \dots, n \dots\dots 6.4$$

where  $\bar{X}$  and  $S$  are the mean and standard deviation of the data sample. The e.d.f. is constructed from the  $Z_i$  values in units of the standard deviation, and the c.d.f. overlaid is the standard normal distribution. The null hypothesis, 'Ho', is that the assumed random sample has the normal distribution with unspecified mean and variance.

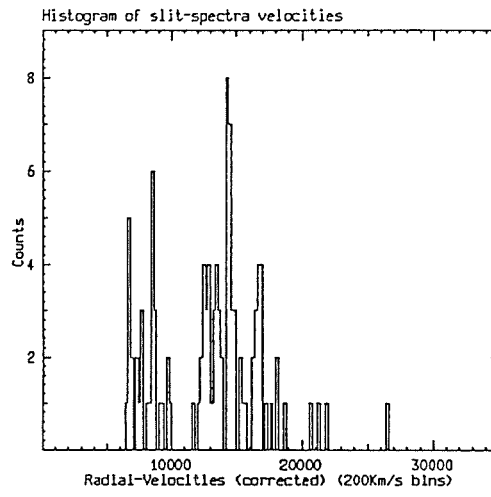


Figure 6.5 Redshift histogram for the sample data in 200km/s width bins.

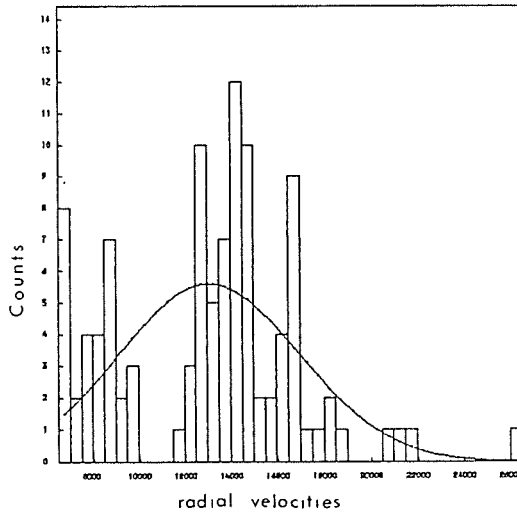


Figure 6.6 Redshift histogram, 500km/s width bins with overlaid Gaussian.

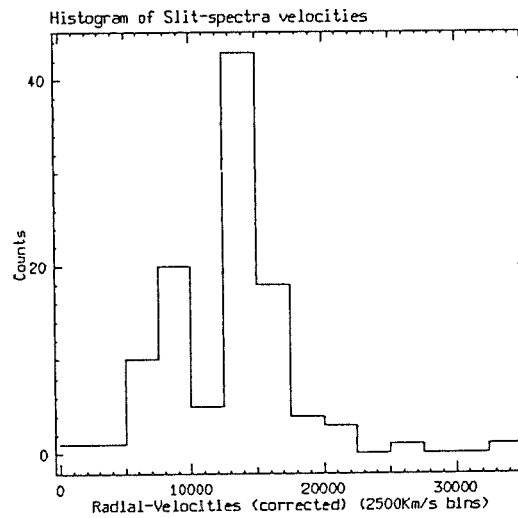


Figure 6.7 Redshift histogram, 2,500km/s width bins.

The modified e.d.f for the velocity data and the c.d.f. are given in figure 6.9. The test statistic 'T2' is then obtained :-

$$T2 = \text{Sup } | F(x) - S(x) | \dots\dots 6.5$$

where F(x) is the standard normal distribution and S(x) is the e.d.f of the Zi's. The Lilliefors test calls for rejection of Ho at a level of significance ' $\alpha$ ' = 0.01 if the test statistic T2 exceeds its 0.99 quantile. This is given by :-

$$W = 1.031 / \sqrt{N} \dots\dots 6.6$$

where N is the number of data values, (104 for this sample). This gave a W value of 0.1011. The actual value of T2 obtained was 0.1295. Hence the null hypothesis Ho could be rejected at the > 99% confidence limit.

Finally the Von-Mises global goodness-of-fit test was applied to the radial - velocity data. Again the assumption is that the observed sample is a random one from some larger parent population. In this case F(x) is a completely specified hypothesized distribution function and the null hypothesis is that the unknown distribution function from which the random sample was obtained is equal to F(x). As in the other cases, F(x) is taken to be the normal distribution with mean and variance given by the data. The data values X(i) are ordered from smallest to largest and then the test statistic T3 is formed where:-

$$T3 = 1/12N + \sum_{i=1}^n [ F\{X(i)\} - 2i-1/2N ] \dots\dots 6.7$$

A value of T3 = 0.4098 was obtained. The 90% quantile for this statistic was  $W_{0.9} = 0.37$  so we can reject Ho at a level of significance ' $\alpha$ ' = 0.10. However, for the 95% quantile,  $W_{0.95} = 0.461$ , so we are not able to reject Ho at this level. The results for this test did not reject the null hypothesis as strongly as the first two tests employed, possibly because a measure of global departure was obtained like the Chi-square test but from using the individual ungrouped data values like the Lilliefors test. In any event all three tests led to rejection of the null hypothesis at high levels of confidence.

Details of these tests and the tables of critical values associated with each statistic used are given by Conover (1971). The histograms, overlaid Gaussians and statistical tests described above were handled using an interactive statistical/graphics package developed by the author.

These tests give some quantitative credence to the significance of the paucity in radial velocities between  $\sim 10,000$  and  $\sim 12,000$  Km/s in showing that the observed distribution is non-normal. The void itself differs from the overlaid Gaussian by  $\sim 3$ -sigma for data in 500 Km/s width bins. The question of whether we would expect a normal or quasi-normal distribution of radial velocities if the objects in the surveyed area were randomly distributed, given the influence of the luminosity function and other selection effects, is not addressed. Ideally, it is the resulting distribution from the convolution of a random distribution of objects with the various selection effects which we would like to test against the observed distribution.

Returning to figure 6.5, it can be seen that apart from the deficiency of objects between  $\sim 10,000$  and  $\sim 12,000$  Km/s, the broad redshift distributions exhibit substantial sub-condensations with individual peaks and troughs evident. This demonstrates the tendency for certain preferential redshift ranges, irrespective of any spatial associations that may exist in the co-ordinates perpendicular to the radial direction. Such anisotropy is a well-known feature of the galaxy distribution on small scales. For instance, de Vaucouleurs (1974), from an extensive study of the space distribution of nearby ( $< 20$  Mpc) galaxies, found that  $\sim 85\%$  of the surveyed galaxies belonged to loose groups whose shapes were rather irregular but which had mean diameters of  $\sim 1.5$  Mpc with a range between 0.3 and 2.5 Mpc. Such groups had centres separated by  $\sim 7$  Mpc on average and occupied volumes of  $\sim 300$  Mpc<sup>3</sup>.

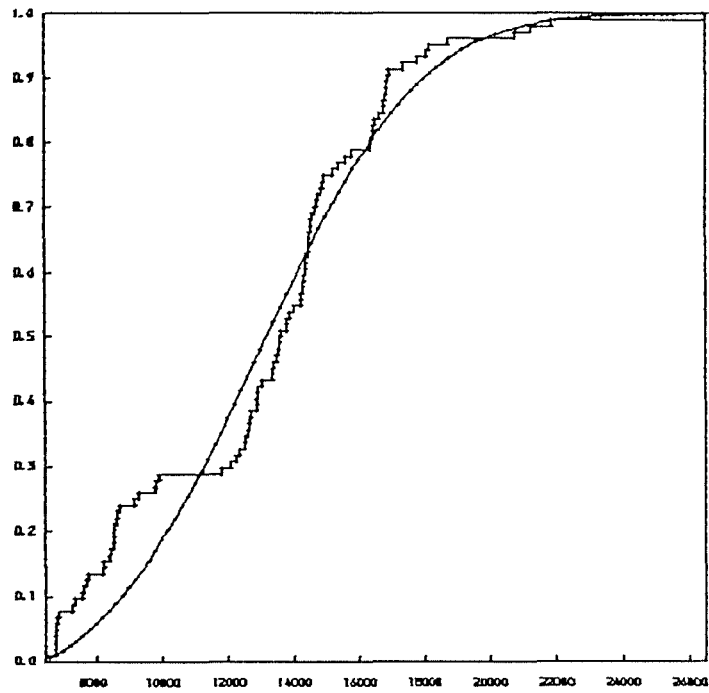


Figure 6.8 Empirical distribution function of the radial velocities together with overlaid cumulative distribution function for a normal curve.

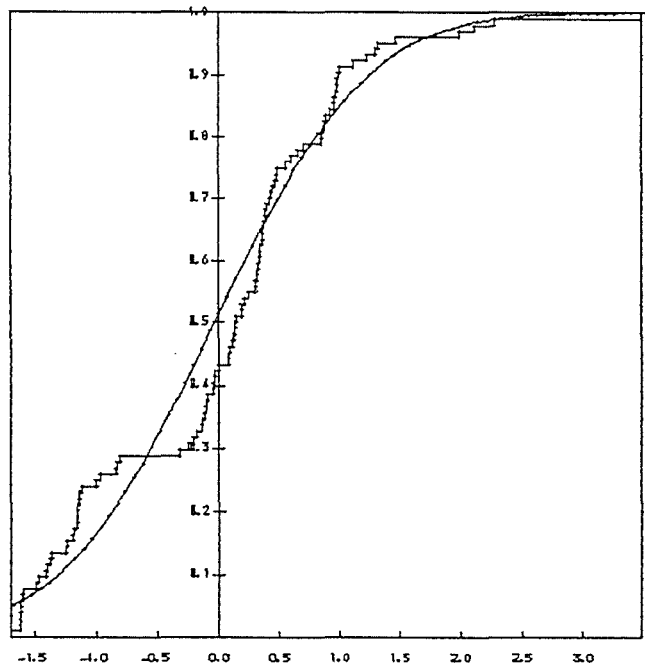


Figure 6.9 Empirical distribution function of standardised radial velocities and overlaid cumulative distribution function for standard normal distribution.

Although the differently binned histograms give a 'first glance' indication of the radial distribution of objects at different resolutions, a 3-D impression of the distribution of the magnitude-limited galaxy sample would be more revealing. Figures 6.10a-b are the cone diagrams of right ascension and declination against redshift. The circle size for each object increases with decreasing magnitude. These plots clearly illustrate the clumpy nature of the galaxy distribution in this field, further highlighting regions of enhanced and diminished density. An impression gained, which may be purely physiological, is of preferred alignments of galaxies into short filaments forming a crude lattice network, particularly noticeable in figure 6.10a. This is suggestive of the type of structures described by Tago et al (1984), see chapter 1 section 1.8. The regions at depths greater than  $\sim 180$  Mpc are sparsely populated because of incompleteness in the observed sample at higher redshifts.

Figure 6.11 gives the projected 2-D distribution of the radial velocity sample in RA and dec. Each object's position is plotted with a circle whose size is directly proportional to object redshift in the sense that nearby objects have larger circles than remote objects. There is a  $3^\circ$  by  $3^\circ$  region between dec =  $-32^\circ$  and  $-35^\circ$  and RA =  $0^h 0^m$  and  $0^h 12^m$  which is apparently devoid of objects with  $V \geq 10,000$  Km/s (the appropriate radial velocity for the larger plotted circles in that quadrant). If we assume the volume of space is well sampled to 180 Mpc, as implied by the redshift histograms, that the front end of the void is at  $\sim 10,000$  Km/s and that the mid-range in declination of this void is at  $-33^\circ 30'$ , then this void has a depth of  $\sim 80$  Mpc. It occupies a volume of  $\sim 2,437$  Mpc<sup>3</sup> with a physical extent of  $\sim 3$  by 5 Mpc at the front end and 5 by 9.5 Mpc at the rear. This void alone amounts to  $\sim 25\%$  of the total space volume sampled to 180 Mpc in this field of  $\sim 9,720$  Mpc<sup>3</sup>. However, space is being sampled in the radial co-ordinate  $\sim 10\times$  deeper than in the projected co-ordinates due to the

small angular extent of the field and the relatively faint magnitude limit employed.

The significance of such 'pyramid like' voids would be enhanced if it could be shown that their dimensions across the line of sight were similar to their radial extent. This is because the chance of large radial distances being covered before any objects are encountered is increased if the projected angular surface is decreased, even if objects were uniformly distributed throughout the volume. This is not to suggest that the observed clumpy distribution is not significant, since even the projected extent of the voids are greater than the average separation expected between groups.

So far, the redshift histograms, cone diagrams etc, have helped to illuminate the clumpy nature of the distribution of the bright galaxies even over the rather narrow cone sampled. Indeed, they have revealed the existence of tight knots of 3 or more galaxies together with looser aggregates of larger multiplicity. These are separated in some instances by regions apparently devoid of galaxies and extending for up to 80 Mpc in the radial direction. Such structure is in general agreement with that found by Gregory et al. (1981), and Tarenghi et al. (1980) for instance; see chapter 1, section 1.7.1. However, it is desirable to replace the rather qualitative description used till now with a more objective and quantitative method of describing the galaxy distribution. This is because properties of clusters and groups depends strongly on whether galaxies are correctly assigned to the appropriate association (Materne and Tammann, 1974). Consequently, a method of classifying such groups in 3-D in some meaningful, way would be of considerable value.

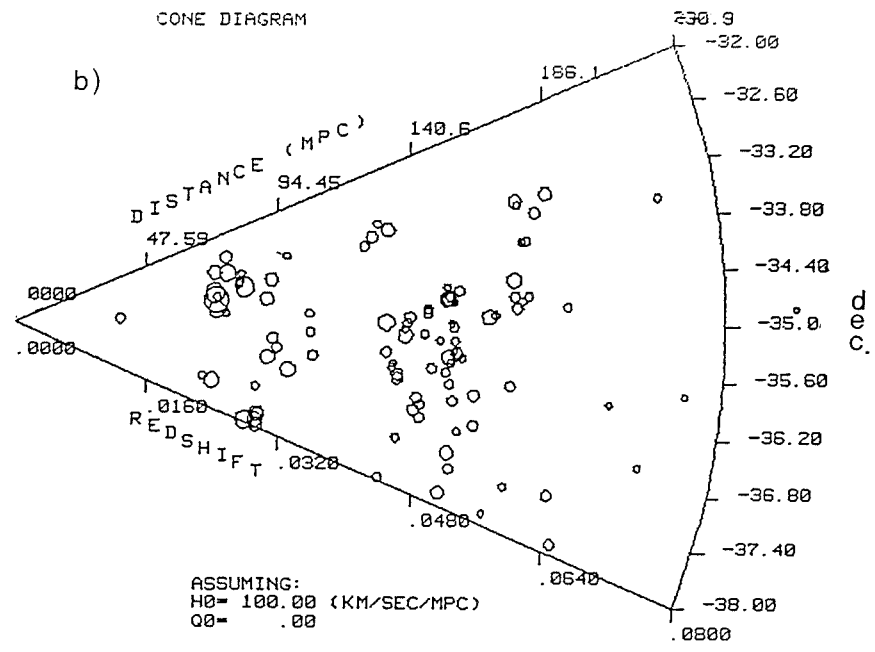
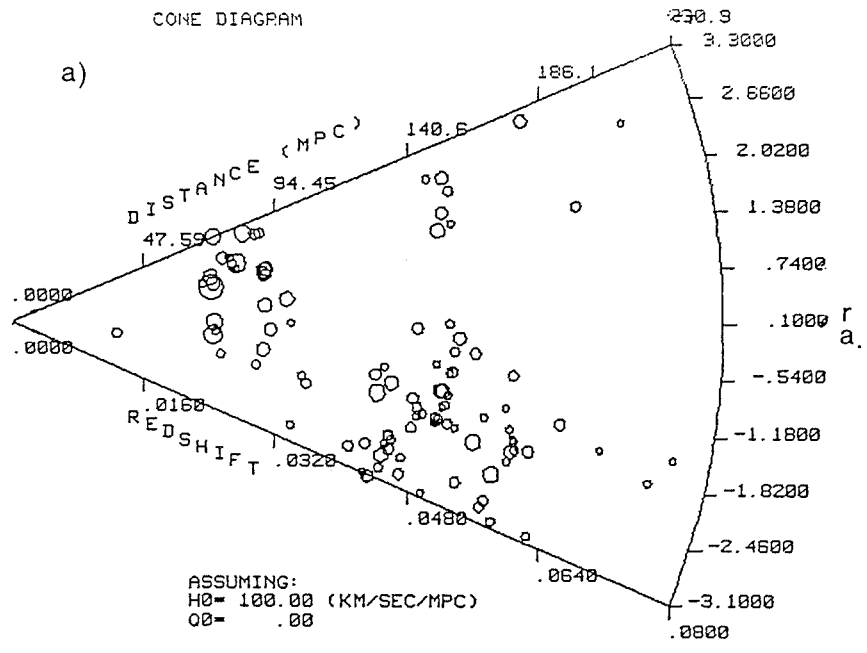


Figure 6.10a-b The cone diagrams of RA and Dec against redshift for the observed galaxy sample.

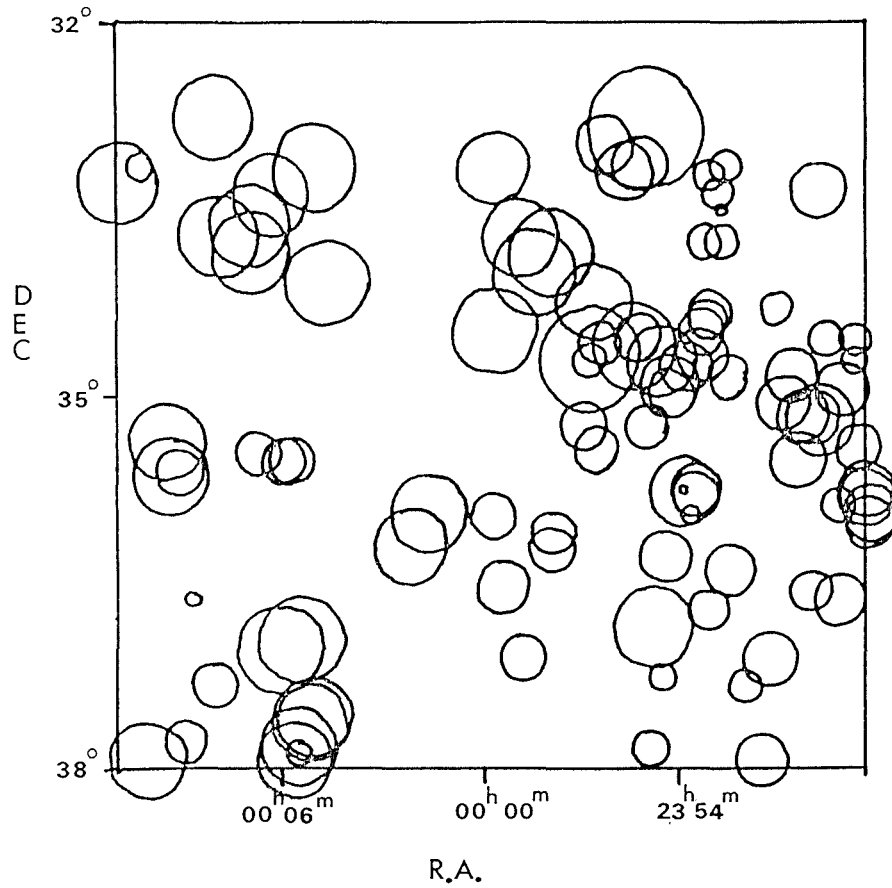


Figure 6.11 The projected 2-D distribution of galaxies with radial velocities. The plotted circle has decreasing radius with increasing distance of each galaxy.

To this end it was decided to apply agglomerative, hierarchical clustering analysis to the data. Such techniques were employed with some success by Materne (1978), on a well-defined sample of galaxies in the Leo region, and by Tully (1980). The advantage of these methods is that clusters and groups can be classified simultaneously in 3-D. No model assumptions about the clusters themselves are required beforehand.

### 6.2.2. Application of hierarchical clustering analysis.

#### 6.2.2.1. Basic concepts and theory.

Techniques of cluster analysis are extensive and varied. They have been widely used as a research tool of discovery and classification in many branches of science and social science from the 1960's. Such methods for revealing structure and associations in data, which may have been far from intuitively obvious, have unfortunately been rarely used in astronomy which is perhaps an ideal medium for such applications. The aim of clustering analysis is to categorise a sample of data into clusters or groups such that the amount of association between members of the same cluster is high whilst that between members of different clusters is low. Anderburg (1973), in his book "Cluster analysis for applications", describes the concepts, theory and methods of clustering analysis to which the reader is referred for greater background. For convenience, a summary of the basic concepts and a description of the clustering method employed for these data is given, following the nomenclature of Anderburg (1973).

The starting point is a set of units  $U_j$ ,  $j = 1, 2, \dots, N$  (galaxies in this case). Each unit is described by a data vector  $X_j$ , where:-

$$X_j = (X_{j1}, X_{j2}, \dots, X_{jm}) \quad j = 1, 2, \dots, m.$$

The  $X_{ji}$  refer here to the spatial co-ordinates of the galaxies. The techniques of clustering analysis use a triangular 'similarity matrix' which describes the strength of all pair-wise relationships among the variables or data units for each item in the data set. This is so that the set  $U = (U_1, U_2, \dots, U_n)$  can be distributed into a set of clusters  $G = (G_1, G_2, \dots, G_k)$ . In our context the term cluster is an inappropriate term to use as the membership of the classified galaxy associations was found to be  $\leq 10$ . Hence 'clusters' will be used when describing the clustering techniques employed but 'groups' will be used when discussing the properties and content of the identified galaxy associations. There are essentially three different methods of performing the clustering operation, but for our purposes the hierarchical technique was chosen since it provides the clearest insight into any group or cluster structure and because less well associated objects are easy to identify.

As the name suggests, the hierarchical clustering methods operate on the similarity matrix to construct a tree diagram or 'dendrogram' which depicts the relationship or degree of similarity between items in the data set in a hierarchical fashion. The technique used in this case is agglomerative in which entities are fused together according to some specified criterion to form a new cluster at some meaningful level 'E' which is referred to as the fusion coefficient of that level. More formally:-

- (1). The initial situation is where each item (galaxy) is a simple cluster
- (2). On some basis, such as physical proximity, the most similar clusters are fused together to form a new cluster by searching

the similarity matrix which is subsequently updated.

(3). This process is continued until only one cluster remains which is made up from all the items in the original data set.

Once the dendrogram has been constructed it is then up to the analyst to determine at what level(s) of 'E' the hierarchy is meaningful. This is a free parameter, inherent in all techniques of cluster classification where no specific model assumptions are made. The level 'E' associated with each fusion point and indeed the fusion itself, depends on the particular agglomerative method adopted at step (2) above for defining the most similar pair of objects from the similarity matrix and for updating the revised similarity matrix. In our case the clustering analysis will be on 3-D positional information for each galaxy. Hence the fusion coefficient could be based on some criteria such as the smallest distance between objects or on keeping the increase of the dispersion of distances to a minimum on fusing two clusters. Obviously the actual criterion chosen is in a sense defining what is meant by a cluster. Whichever formulation is adopted, the great advantage of the hierarchical technique is that it enables all levels of substructure and superstructure to be elucidated, e.g. from small groups or sub-condensations in rich clusters to possibly even superclusters.

Although there are a wide variety of hierarchical clustering methods available, they are all alternative representations of 3 basic clustering notions. Specifically:- linkage methods, centroid methods and error sum - of - squares methods (for details see Anderburg 1973). Each approach has its own advantages and limitations so the most appropriate technique for a given classification problem has to be chosen. In this study the minimum sum-of-variance methods were felt to be the best general techniques to employ and in particular the 'Ward' criterion was adopted as this seems to be the most efficient of

these. Wishart (1969), demonstrated that the Ward algorithm (Ward 1963), could be implemented through updating a stored matrix of squared Euclidean distances between cluster centroids. The following quantities are defined:-

$X_{ijk}$  is the score on the  $i^{\text{th}}$  of  $n$  variables (distance coefficients in this case), for the  $j^{\text{th}}$  of  $M_k$  data units (galaxies) in the  $K^{\text{th}}$  of  $h$  clusters.

$$\bar{X}_{ik} = \frac{1}{M_k} \sum_{j=1}^{M_k} X_{ijk} / M_k \dots 6.8$$

is the mean on the  $i^{\text{th}}$  variable in the  $K^{\text{th}}$  cluster.

$$E_k = \sum_{i=1}^N \sum_{j=1}^{M_k} (X_{ijk} - \bar{X}_{ik})^2 \dots 6.9$$

is the error sum of squares for cluster  $K$ , i.e. the sum of Euclidean distances from each cluster point in cluster  $K$  to the centroid of that cluster.

$$E = \sum_{k=1}^h E_k \dots 6.10$$

is the total within group error sum of squares for the collection of clusters.

The Ward objective is to find at each stage the two clusters which on merging give the minimum increase in the total within group sum-of-squares 'E'. This is in fact the fusion coefficient for that cluster. For instance if it is chosen to merge two clusters 'p' and 'q' to form a new cluster 't', then the increase in E is such that:-

$$\Delta E_{pq} = E_t - E_p - E_q \dots 6.11$$

Following Anderburg, this can be expressed as:-

$$\Delta E_{pq} = \frac{M_p M_q}{M_p + M_q} \sum_{i=1}^m (\bar{X}_{ip} - \bar{X}_{iq})^2 \dots 6.12$$

which must be minimised. Hence the minimum increase in the error sum of squares 'E', is proportional to the squared Euclidean distance between centroids of the fused clusters. The form of 'E' is a non-decreasing function which does not suffer from reversals (i.e. where the minimum distance between two clusters can decrease after a merging takes place), which is the main disadvantage of centroid clustering.

The actual hierarchical clustering of the magnitude-limited galaxy sample was facilitated using a flexible computer package called CLUSTAN. This package was originally developed by D. Wishart at the University of St. Andrews in the 1960's for the study of clustering analysis methods and their applications to problems of classification. An updated version was used for this investigation. Before details of the actual clustering analysis and results are presented, a brief discussion of how the positional information for each galaxy was defined is given.

#### 6.2.2.2. The adopted co-ordinate system.

Materne (1978), stated that the "naive procedure to divide velocities by the Hubble constant and transform the resulting polar co-ordinate system into a 3-D cartesian co-ordinate system" was unsatisfactory. This is because the effect of the velocity uncertainties and velocity dispersions is to extend the clusters into cigar shapes along the line of sight, the so called "finger of God" effect. Consequently, because the Ward criteria finds minimum-variance, spherical clusters, this would tend to fragment such elongated clusters too easily. This situation does not appear to be pronounced for this sample though, at least in part because of the good redshift accuracy. Materne (1978), however, did not transform the 3-D polar co-ordinate system ( $\alpha, \delta, v$ ), but treated  $\alpha$  and  $\delta$  simply as numbers whilst scaling the velocities. This was so all 3 co-ordinates would be in the same order of magnitude, essential if the clustering analysis is to proceed satisfactorily. Furthermore, he asserts that the application of this method is restricted to a limited velocity range if the clusters are to be studied in detail (e.g.  $\Delta V \sim 2,000 \text{ Km/s}$ ).

Applying such a procedure to this sample is not so straightforward because the depth of the survey is about ten times that of the greatest projected physical extent. This presents a few problems for any clustering analysis attempted on the whole sample. For instance, a compact group at high redshift would appear much more diffuse and open at low redshifts. Similarly, the 'pyramid' nature of the volume of space sampled to a given depth means that only parts of groups may be picked out at low redshift whereas the same group might be completely contained within the field if placed at high redshift. Hence the size, completeness and concentration of clusters identified by the clustering process might depend on the redshift of the clusters themselves. The clustering algorithm would need to identify loose groups at low redshift and tight groups at high redshift with equal clarity. It is difficult to see how the derived hierarchical clustering could be homogeneously applied.

A practicable solution is to divide the data into different velocity ranges and analyse these 'distributions' separately. Fortunately the distinct 'break' in the velocity distribution at  $\sim 11,000$  Km/s provides a natural choice for this partition. Objects with widely different velocities from the two major distributions, evident from the velocity histogram (figure 6.5), are excluded from the samples for analysis as their unrelated nature is self evident. Inclusion of these objects would lead to large dispersion values for any depth co-ordinate. This might bias the hierarchy and make substructure difficult to see in any plotted dendrogram, due to the very large fusion coefficients required. Hence the analysis of the data can be performed over much narrower ranges of velocity, e.g..  $6,500 \leq V \leq 10,000$  and  $11,800 \leq V \leq 19,000$  Km/s. This gives 30 objects in the first 'group' and 70 objects in the second, from the total sample of 107 galaxies with measured radial velocities. The velocity range of the second grouping, i.e.  $\sim 7,000$  Km/s, is quite

large but it was felt that further partition would be somewhat arbitrary as there is no pronounced gap in the velocity distribution. Also such a split may mask any clusters that cross the chosen partition. Once the two distributions for analysis had been chosen, the co-ordinate system for each group was defined.

The simple  $\alpha$  and  $\delta$  values and scaled velocities were not used. Instead, 3-D cartesian co-ordinate systems were constructed in which each co-ordinate is expressed as a distance in Mpc relative to a reference plane of redshift in the mid-redshift range of each sample and relative to the field centre. Firstly a program called 'project' (courtesy of Dr.R.Clowes) was used to obtain a tangent plane projection of the  $\alpha$  and  $\delta$  co-ordinate system in degrees relative to the field centre. The projected angular separation between the field centre and each object 'i' was obtained by pythagoras on the tangent plane ( $X\theta, Y\theta$ ) values for each point. E.g:-

$$\theta_i = (X_i\theta^2 + Y_i\theta^2)^{\frac{1}{2}} \dots 6.13$$

After selection of the reference redshift plane, the Z co-ordinate (i.e. the distance of each object above or below this plane) is given simply by:-

$$Z_i = D_o - D_i \cos \theta_i \dots 6.14$$

where 'Do' is the distance of the redshift plane from the observer and 'Di' is the distance of object 'i' from the observer. To get the X and Y distance for each object on the redshift reference plane we simply use:-

$$X_i = D_i \sin X_i\theta \quad ; \quad Y_i = D_i \sin Y_i\theta \dots 6.15$$

All distances 'Di' are obtained by simple division of object velocity 'Vi' by Hubble's constant. Hence physically meaningful 3-D co-ordinate systems (X,Y,Z), expressed in the same distance units, in a reference frame not centred on the observer, are obtained. Hopefully, this should help remove the ambiguity which seems to be present when 3-D clustering is performed on differently scaled

co-ordinates as used by Materne (1978). Obviously the uncertainty in the Z co-ordinate of  $\sim 0.75$  Mpc far exceeds that in the X,Y plane and will contribute to any elongation of clusters in the Z direction caused by velocity dispersions within clusters. However, expressing the co-ordinates in Mpc relative to the centres of two quasi-cubes does put all the co-ordinates on the same scale which is of the same order of magnitude in each co-ordinate. This circumvents, to an extent, the problem of a large range of values and hence variance for one co-ordinate (depth) relative to the other two (X,Y), without having to resort to a false scaling of the velocities and making the co-ordinates dimensionless.

Materne's scaling procedure in a sense standardised the data so that the similarity coefficients generated are not biased towards variables with large variance (e.g. the velocities). As Materne noted however, this restricts the application of the clustering analysis to a velocity range of  $\sim 2,000$  Km/s. Also, because standardised co-ordinates are given the same weight by the clustering analysis, this would mask the contribution to the actual hierarchy that may be present since the Z co-ordinate, which covers a larger range than the X,Y co-ordinates, is under-weighted. In fact we do wish to give due weight to the Z co-ordinate. If velocities were simply converted into distances from the observer then, if the raw data were used, the radial co-ordinate would have too much weight and spherical shells of clusters around the observer would be favoured, irrespective of any clustering in X and Y. By using the actual spatial information for each galaxy relative to the centre of a quasi-cube, then even though the accuracy in the Z co-ordinate is much worse than in (X,Y), the clustering analysis is likely to be more realistic and take into account the existence of real deficiencies and enhancements in 3-D more appropriately. The analysis should then be worthwhile so long as it is understood that the groups identified may form parts of larger

aggregates which lie outside of the field. Furthermore it is likely that the structure of the first grouping can be studied in more detail than the second where larger physical dimensions are covered by all three co-ordinates giving greater co-ordinate dispersions. However, a disadvantage of the hierarchical clustering technique, which seeks tight minimum variance, spherical clusters, is that it would not be sensitive to any branches or filaments which may exist in the galaxy samples. Such chains would be broken up by the clustering algorithm. Nevertheless, the existence of chains or linear groups might be indicated by the group dispersion in the co-ordinate which is in closest alignment with the filament direction exhibiting a larger value than for the other two co-ordinates.

### 6.2.3. The results of the hierarchical clustering analysis performed.

#### 6.2.3.1. Results for the major grouping with $6,500 \leq V \leq 10,000$ Km/s.

The galaxies NGC7793 and QP83 were excluded from the analysis because they are obvious foreground objects which are well separated from each other and the major grouping by  $\sim 3,000$  Km/s. Hierarchical clustering using Wards' method was applied to the 3-D distance co-ordinates, as defined above, for the 30 galaxies in the group. This was the same technique adopted by Materne (1978), for his galaxy sample and that recommended by the CLUSTAN user manual for data sets of this type and size. The resulting dendrogram is given in figure 6.12. The abscissa identifies individual galaxies whilst the ordinate gives the fusion coefficient calculated according to equation 6.11. From this dendrogram it is apparent that most meaningful associations of galaxies have occurred by  $E \sim 60$ . The first fusions are at low E values ( $< 2.0$ ) and are composed mainly of binaries (60% of the sample) and the odd triplet or quadruplet of galaxies. After the formation of pairs and triplets, subsequent fusions take place at relatively small and uniform increments in the fusion coefficient until 6 clusters

remain at  $E \sim 17$ . The next fusion to form 5 clusters does not occur until  $E \sim 32$ , double the previous  $E$  value, and then 4 clusters at  $E \sim 38$ . The fusion of the 6 clusters to form 4 can be considered as a higher level of agglomeration because of the distinct break in the hierarchy. Thereafter the groups are even more well separated, especially in  $Z$ , and do not fuse to form 2, 3 and finally 1 'cluster' until large values of  $E$ . Apart from the binaries and occasional triplet, the 6 groups formed at  $E < 17.0$  are probably the lowest meaningful classification of this sample using this hierarchical technique. Figure 6.13 is the plot of fusion coefficient ' $E$ ' versus the number of clusters remaining at that  $E$  value starting from the initial classification of single object clusters. The discontinuity in this plot at the level of 6 clusters is clearly evident which strengthens the case for applying a cut in the hierarchy at this point. This plot, and the dendrogram, give an excellent quantitative impression of how the structure for this sample is built up. However, before describing some of the properties of the groups identified so far, some further clustering analysis was performed to ascertain the reliability of this initial classification.

A procedure called 'RELOCATE' was run from within CLUSTAN on the Ward results. This process is designed to improve the error sum solution starting with Ward's part-optimum result. The procedure attempts to find a local optimum solution for ' $K$ ' clusters in relation to the chosen similarity criteria by 'iterative relocation'. A brief description of this process is given here, but for further details the CLUSTAN user manual should be consulted.

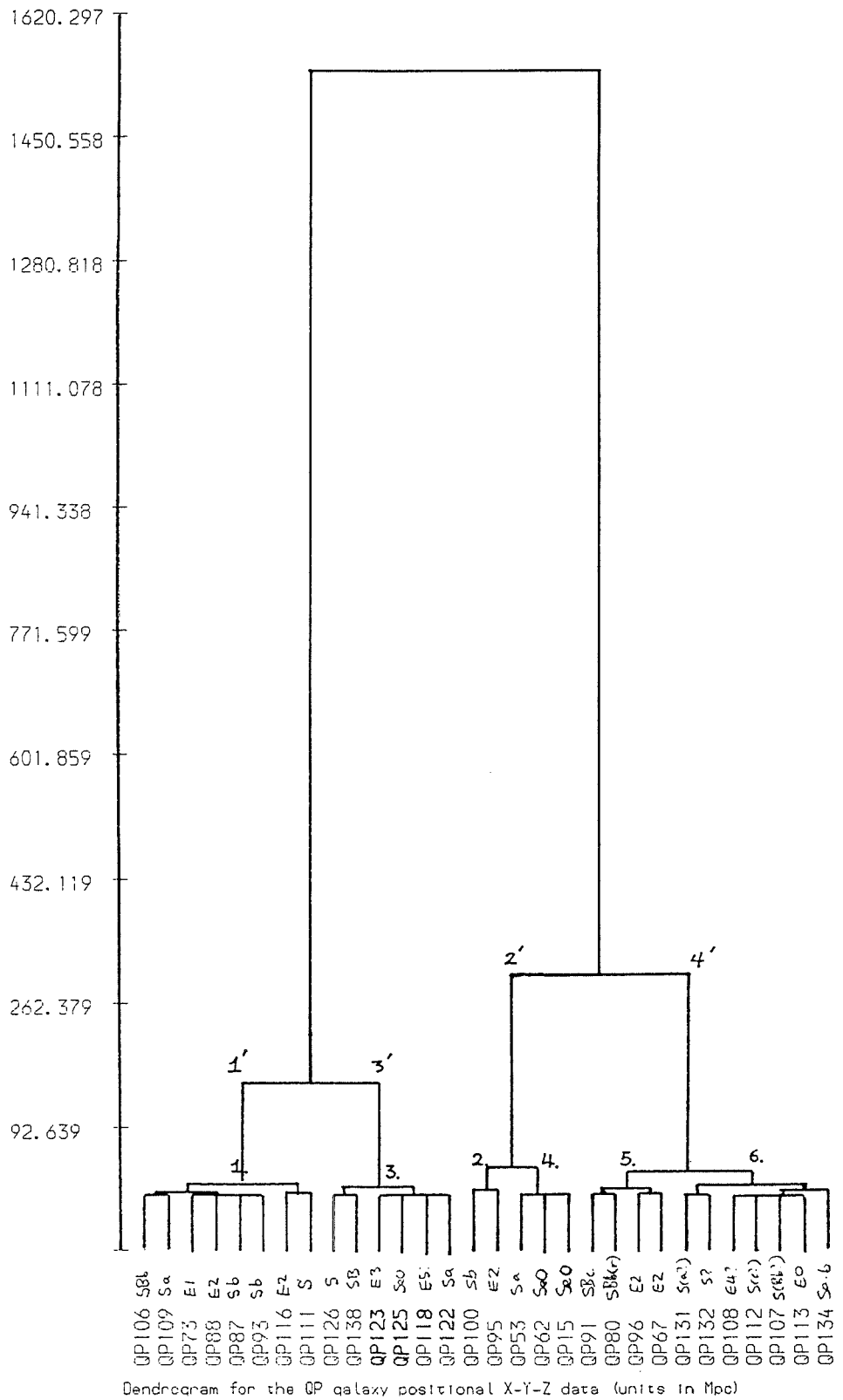


Figure 6.12 The dendrogram for the first major redshift grouping in the field.

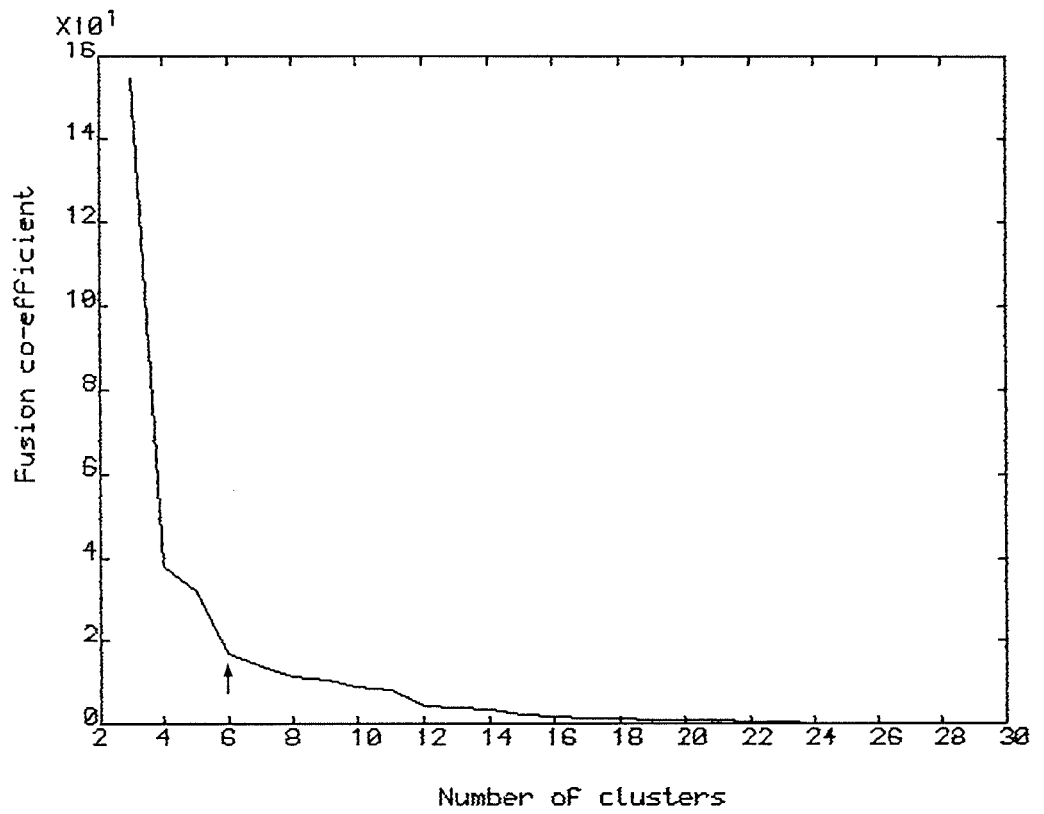


Figure 6.13 Plot of fusion co-efficient 'E' versus the number of clusters remaining at that E value for the first galaxy redshift sample.

Starting with 'K' clusters, during one relocation sweep each galaxy is sequentially considered and its similarity with the K clusters calculated. If the similarity between object 'X' say, and its parent cluster 'P' is  $S(P,X)$  and the similarity between X and any other cluster 'Q' is  $S(Q,X)$ , then if  $S(Q,X) > S(P,X)$ , X is relocated from cluster P to Q. The cluster characteristics are re-computed to allow for this switching. The population is repeatedly scanned until no objects are relocated during one full sweep. At this point a local optimum solution for 'K' clusters in terms of the similarity function 'S' will have been obtained.

The usual practice is to perform several runs of 'RELOCATE' with different initial conditions (e.g. assigning galaxies to 'K' clusters randomly). If the same cluster solution is still reproduced then it is likely that that a global optimum solution has been found. This is a good indication of the goodness of the similarity measure used (e.g. error sum of squares in this case). Running the iterative relocation procedure on the initial classification produced by Ward's method (choosing 10 clusters down to 2 clusters), and then re-running the procedure with a random assignment of the galaxy sample to 10 clusters of equal size, exactly reproduced the results from Ward's method. This indicated that a good, robust classification had been achieved.

A procedure called 'Mode analysis' was also applied to the sample. This is a technique for deriving 'natural' clusters by "estimating disjoint density surfaces according to a probabilistic model" (Wishart, 1973). Unlike the hierarchical analyses using Ward's criterion and the RELOCATE procedure, where tight, minimum variance clusters are favoured, the MODE analysis seeks natural clusters which do not have to be tight. The technique makes use of the K-nearest neighbours for each object. Again the CLUSTAN manual should be consulted for further details of the method and the probabilistic

interpretation. Briefly however, for a density parameter 'D', MODE computes the average 'A(I)' of the 2D smallest distance coefficients for each object 'I'. This value is a measure of the space density of galaxies in the immediate volume surrounding each galaxy. Small A(I) values are connected with points that lie in regions of high density. The A(I) values themselves are calculated from the K-nearest neighbours associated with each galaxy. The MODE analysis always has one cluster at both the start and end of the analysis. During the analysis though, the number of cluster nuclei identified increases to a maximum until the first fusion is performed. It has been suggested that this maximum number of clusters corresponds to the lowest natural level of classification which is possible. The maximum number of clusters so selected by the MODE analysis for this sample was 6. Furthermore, the 6 clusters identified are exactly the same as those produced by Ward's method and by the two RELOCATE runs when dealing with 6 clusters. This confirms the initial classification suggested from examination of the dendrogram and figure 6.13. Consequently, since the results from all the clustering techniques described above agree, then a really robust classification has been achieved.

Apart from the dendrogram, the clustering analyses provided other useful information and statistics for the individual clusters identified, e.g. such as K-nearest neighbours. The analyst is free to choose the maximum and minimum numbers of clusters that are likely to be of interest. Diagnostics for all maximum down to minimum clusters are then produced. This includes, in this case, the mean and standard deviations of the X,Y,Z co-ordinates for each cluster and their F-ratios, which are given by:-

$$F\text{-ratio} = V(c,j)/V(j) \dots\dots 6.16$$

where V(c,j) is the variance of variable 'j' for the subset of cases which form cluster 'c' and V(j) is the overall variance for variable 'j'. Small F-ratios indicate a co-ordinate with a comparatively low

variation within the cluster which is a good diagnostic. The diagnostics and other properties for the 6 groups which seem to form the lowest natural level of major association are given in table 6.1.

In each group the velocity dispersion is  $< 200$  Km/s and the dispersion values for the (X,Y,Z) distance co-ordinates are  $< 2.0$  Mpc (except in the case of the binary group 2 which is well separated in the declination direction by  $\sim 3.5$  Mpc). The F-ratio's for the (X,Y,Z) co-ordinates of each group indicate that they are all fairly well defined entities, except again for the binary group 2 whose large F-ratio reflects the large separation of the galaxies parallel to the declination axis. However, as previously stated, there is an inherent assumption of spherical clusters, at least in the hierarchical clustering analysis using Ward's criterion, so that any chain like structures might not be picked out using this technique.

Materne (1978), performs 4 basic tests on his galaxy groups, but their application here is restricted by the lack of independent distance estimates and luminosity classifications for galaxies in this sample. The dynamical stability of the identified groups could be determined according to Materne (1974). Essentially stability exists if :-

$$E = 2T + \Omega < 0.0 \dots \dots \dots 6.17$$

where T is the kinetic energy and  $\Omega$  the potential energy. However, the correct determination of the dynamical status of a group depends heavily on the accuracy of the observations. The assumptions involved in determining 'T' and ' $\Omega$ ' contain considerable uncertainty such as the adopted masses of the galaxies themselves, which are at best only a rough approximation, and morphologically dependent M/L ratios. Even for well-determined groups such as those studied by Materne (1974, 1978), where the velocity accuracy is even greater than for this sample, the possibility of considerable errors in 'T' and ' $\Omega$ ' make

statements concerning group dynamical stability somewhat tentative. Consequently, given the crudeness of the morphological classification of this sample, in many cases into basic types only, such an investigation was not considered worthwhile at this stage.

In order to test the physical significance of the 6 groups identified, the postulate that they can be regarded as discrete entities if their separations exceed their (X,Y,Z) dispersions by at least a factor of two, was considered.

The calculated distances in Mpc between the 'centroids' of each group was calculated from their mean (X,Y,Z) co-ordinates. The largest separation between any two group centres was  $\sim 31$  Mpc (groups 1 and 2) and the closest separation was  $\sim 4.5$  Mpc (groups 5 and 6). Obviously these group centres do not correspond to their centres of mass. Nevertheless, it is interesting to note that 5 inter-group separations were  $\sim 8$  Mpc, 3 were  $\sim 2 \times 8$  Mpc and 2 were  $\sim 3 \times 8$  Mpc. These are all multiples of the average separations found from studies of nearby galaxy groups (e.g de Vaucouleurs, 1974). The calculated group separations for this sample revealed that they were generally all well separated and can be considered distinct, although the physical separation of the binary group 2 brings into question its physical reality and they might best be considered as field galaxies. It must therefore be stressed that groups selected by these clustering techniques identify associations of galaxies whose co-ordinates are most similar to each other but do not necessarily indicate true physical association in all cases, although such a supposition seems likely. Furthermore the hierarchical clustering techniques employed would tend to split up any galaxy chains present into smaller sub-units.

Table 6.1

Group diagnostics and other properties for the '6' group classification of the first major redshift distribution.

GROUP	N	Morphology Spir. Ellip.	$\langle a \rangle$			$\langle \delta \rangle$			$\langle V \rangle$ Km/s	$\sigma_z$ Mpc	$\sigma_x$ Mpc	$\sigma_y$ Mpc	$F_z$	$F_x$	$F_y$
			h	m	s	o	'	''							
1	8	63% , 37%	00	02	32	-34	48	29	6754	1.17	1.32	1.69	0.013	0.360	0.520
			04	42		1	26	10	116						
2	2	50% , 50%	00	01	45	-34	42	48	9219	0.81	0.63	3.46	0.006	0.112	2.186
			01	58		2	8	38	82						
3	6	67% , 33%	00	09	42	-33	27	33	7536	1.91	0.45	0.47	0.035	0.057	0.041
			01	52			23	33	188						
4	3	100% , 0%	23	52	35	-35	14	53	9825	0.83	1.02	0.90	0.007	0.295	0.147
			02	57			31	07	83						
5	4	50% , 50%	23	59	29	-35	13	22	8428	1.63	0.97	2.14	0.026	0.263	0.835
			05	05		1	27	22	161						
6	7	70% , 30%	00	08	53	-37	08	54	8527	1.62	0.80	1.62	0.026	0.179	0.481
			02	39		1	06	32	159						

Tully (1980), in a study of galaxies in a region around NGC1023, applied a hierarchical clustering technique that merged entities sequentially on the basis of maximisation of the gravitational force, as well as the method adopted by Materne (1978) and used in this analysis. Tully considered his 'force' method to be a better physical approach for selecting real tidally-bound groups. However, this technique makes assumptions about the luminosity weights, which may contain considerable errors. The methods employed in this study do not require the assumption of a fixed relationship between mass and luminosity and may even reveal the existence of structure in instances where there are large departures from 'normal' values for the M/L ratios used.

Generally then, the results from this analysis are in good agreement with the average size and separation of nearby galaxy groups. The morphological content of the 6 groups is dominated by spirals, i.e. 66% spirals and 33% ellipticals. The morphological classification for the galaxies in this first major redshift distribution is often more detailed than that for the more remote distribution because of the larger angular extent that most of these galaxies subtend on the sky and therefore their size on the UKST plate examined. This makes distinguishing internal features of these galaxies somewhat easier. Even so, the morphology of one or two galaxies in this first distribution is dubious, since the small angular extent of even some of the low-redshift galaxies means that some galaxies classified as ellipticals may in fact be tightly wound spirals, since it is impossible to distinguish any internal structure in these cases.

Nine out of the total of 16 galaxies with definite detected emission lines in the complete redshift sample of 107 galaxies were in this first redshift distribution. This is almost a third of galaxies in this sample. Furthermore, 4 of these galaxies with emission lines were classified as ellipticals, 40% of the ellipticals present in this sample. One of the major visible emission lines in their spectra was  $\lambda 3727\text{\AA}$  [OII], present in 2 out of 4 elliptical galaxies with emission lines. This line is the primary indicator of ionized gas for spectra taken in the blue. Usually only the  $\lambda 6583\text{\AA}$  [NII] emission line is seen in elliptical and lenticular galaxies and indeed Burbidge (1970), in a review article of emission lines in galaxies, states that  $\lambda 3727\text{\AA}$  [OII] is only visible in 14-18% of all elliptical galaxies adequately studied.

Generally speaking, the frequency of emission lines in elliptical and lenticular galaxies, which usually originate in the nucleus, is comparatively low. The high percentage of ellipticals with emission lines in the first sample may be a statistical fluke or may indicate some peculiarity of the galaxies in this sample. However it is more likely a reflection of the mis-classification of tightly-wound spirals to ellipticals. All of the galaxies in this sample classified as E7/Seo (see chapter 2 table 2.4), also possessed emission lines. These galaxies were originally classified as E7/Seo because it was impossible to distinguish between such possibilities from examination of the UKST plate. They are more likely to be of a spiral nature though, because emission lines occur much more frequently in spiral galaxies and by simple considerations of the fraction by number of E7 galaxies which are likely.

Now that the significant groups in the first distribution have been identified on a quantitative basis it is pertinent to investigate some of their basic properties. Since a morphological classification, at least into spirals and ellipticals, is available for this sample, it may be possible to determine if any morphological segregation exists in these groups. Such segregation in galaxy clusters is well known (e.g. Oemler, 1974 and Dressler, 1980), and is potentially important in the development of theories of galaxy formation and evolution and the possible environmental influences on galaxy morphology, e.g. Giovanelli and Haynes (1982). Davis and Geller (1976), from an analysis of the UGC (Nilson, 1973), also discovered that ellipticals appeared to be more tightly clustered than spirals.

These properties of the distribution of galaxies have often been seen as evidence that all galaxies had a common origin but evolved from one type to another. For instance the development of a lenticular galaxy as a result of gas removal from a spiral galaxy (e.g. Gunn and Gott, 1972). Mechanisms such as galaxy-galaxy collisions, ram-pressure stripping and gas evaporation (Cowie and Songaila, 1977), have been proposed as means of removing the gas from spirals. Since such processes are more likely to occur in regions of high galaxy density they could explain the greatly enhanced proportions of ellipticals and lenticulars in rich clusters relative to the field. Alternatively, the morphological mix may be intrinsic to the galaxy formation process or reflect evolution at an early epoch (e.g. Gott and Thuan, 1976). Dressler (1980), found a well-defined relation between local galaxy density and galaxy type which gave an increasing fraction of ellipticals and lenticulars and a decreasing spiral component with increasing number density. However, he presented evidence that contradicts the hypothesis that these morphological gradients are the result of S0 production from the stripping of gas from spiral galaxies by an intergalactic medium.

Mezzetti et al. (1985), in a study of 39 galaxy groups identified by Geller and Huchra (1983), and based on complete redshift information, attempted to address the question of morphological segregation in groups as opposed to clusters. By studying the ratios of the mean pair-wise separations among spirals  $R_p(S)$ , ellipticals  $R_p(E)$  and all group members  $R_p(\text{all})$ , they concluded that when both ellipticals and spirals were present in groups the ellipticals are significantly more clustered than the spirals. Attempting to perform a similar analysis for the groups in this first sample is, perhaps, not so worthwhile from a statistical standpoint because of the small numbers of groups (6) and individual galaxies (30) concerned.

Nevertheless, all within-group pair-wise separations were calculated from the (X,Y,Z) distance co-ordinates for each galaxy. This resulted in 74 unique pairs. There were only 30 cases of within-group spiral-spiral separations and only 6 cases of elliptical-elliptical pairs. This is insufficient, at least in the case of ellipticals, to form any meaningful ratios. However, the mean pair-wise separations associated with the spirals and the entire sample, together with their associated errors, are:-

$$R_p(S) = 3.103 \text{ Mpc}, \quad \sigma = 1.498, \quad N = 30, \quad \sigma/\sqrt{N} = 0.273$$

$$R_p(\text{all}) = 2.942 \text{ Mpc}, \quad \sigma = 1.533, \quad N = 74, \quad \sigma/\sqrt{N} = 0.181$$

The ratio of the mean pair-wise separation between spirals only and between all galaxies was:-

$$R_p(S)/R_p(\text{all}) = 1.055 \pm 0.113$$

This value is not statistically significant given the sample size and the associated errors. The ratio tends to unity if there is no distinction between the concentration of pairs of spirals and pairs of galaxies in general. However the empirical distribution functions (e.d.f's) of the pair-wise separations for all within-group members and for just the spiral-spiral within-group pairs were constructed. Since the mean and standard deviation for each sample was determined

from the data itself, the Lilliefors test was applied to the data after it had been normalised (equation 6.3). This was done in order to test the hypothesis that the distribution of galaxy-galaxy separations was normal. A Kolmogorov-Smirnov test on the e.d.f rejected the hypothesis that the distributions were uniformly distributed at  $> 99\%$  confidence level. Using equation 6.4, the following statistics were obtained:-

$$D_n(\text{max})_{\text{all}} = 0.1218, \quad P_{0.99} = 0.1198$$

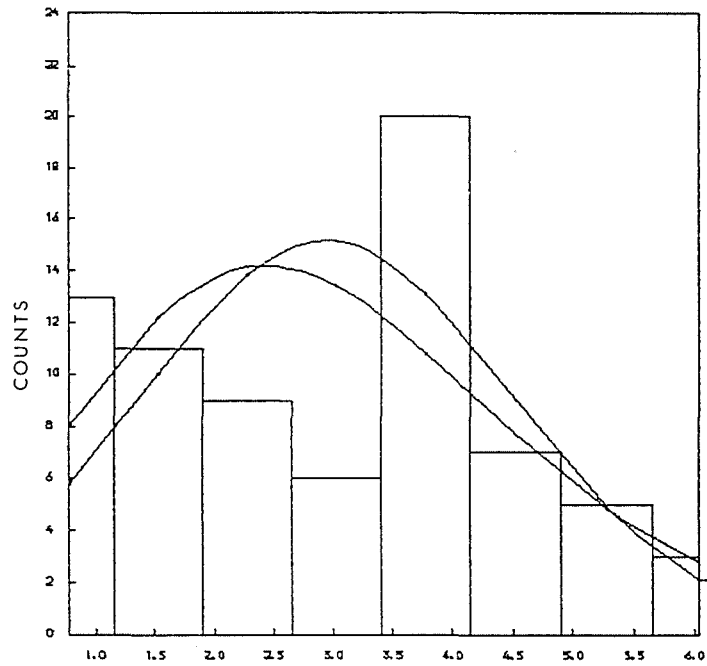
$$D_n(\text{max})_{\text{spirals}} = 0.14526, \quad P_{0.9} = 0.144$$

Hence the null hypothesis  $H_0$ , that the distribution of pair-wise separations among within group galaxies could have come from a normal distribution, can be rejected at the  $> 99\%$  confidence level for the case of all pair-wise separations, but can only be rejected at the  $\sim 90\%$  confidence level when considering the spiral-spiral within-group pairs. This implies that the spatial distribution of galaxies within the groups is highly non-normal for this sample. The chi-square test was also applied to the pair-wise separations for all the galaxies in 0.75 Mpc bins (the accuracy of the radial velocities when converted to Mpc), by testing against a Gaussian with the same mean and variance as the observed distribution. This again led to rejection of the null hypothesis  $H_0$ , at the  $> 99\%$  confidence level. Comparing with the equivalent data for just the spirals, the chi-square test leads to rejection of  $H_0$  at the 90% confidence level, but not the 95% confidence level. The histograms and the overlaid Gaussian and Poisson distributions are given in figure 6.14a-b. In figure 6.14a, the histogram for all the within-group galaxy-galaxy separations, a distinct peak is evident, indicating a preferential pair-wise separation of between  $\sim 3.4$  and 4.2 Mpc. The most striking feature of figure 6.14b, is the apparent paucity of cases where the pair-wise separation is between  $\sim 2.7$  and 3.4 Mpc, almost the opposite of the situation in figure 6.14a. This paucity is significant at the

> 2-sigma level. These results seem to imply that within-group galaxy pair-wise separations of  $\sim 4$  Mpc seem to occur more frequently than any other separation, whilst if only spiral-spiral pairs are concerned there seems to be a separation of  $\sim 3.0$  Mpc which is avoided. The relatively small numbers of pair-wise separations involved, at least for the spiral-spiral pairs, means that the reality of the paucity at  $\sim 3.0$  Mpc must be questioned. Such effects, if real, are difficult to explain.

Perhaps substructure in the 6 groups identified can explain the effect for spirals. If the spirals lie in the outer regions of a sub-group and a group is made up of 2 such sub-groups then preferential separations may occur. The apparent excess in figure 6.14a at  $\sim 3.7$  Mpc, whose results are based on a much more statistically significant sample, is more inexplicable. The observed peak seems to go against the general downward trend of the separations starting with larger numbers of pairs at small separations ( $< 1.0$  Mpc). The possibility that these effects are artefacts of the classification into 6 groups seems unlikely, given the well-behaved nature of the results from different clustering approaches. One possibility that might explain the excess of large within-group separations for the ellipticals might be if there was some contribution from chains of such galaxies. For instance, a chain in the Z direction, which is well defined in the X,Y plane, might be identified as a group by the hierarchical clustering analysis simply because the very tight agreement in the X,Y values for galaxies in the chain overcome the large dispersion in the Z co-ordinate. Long chains would be split up into smaller chains, but those that are placed in a 'group' may be contributing to the excess of large separations in figure 6.14a. The possibility that the observed effect is due to some other currently unknown selection effect cannot be overlooked.

a)



b)

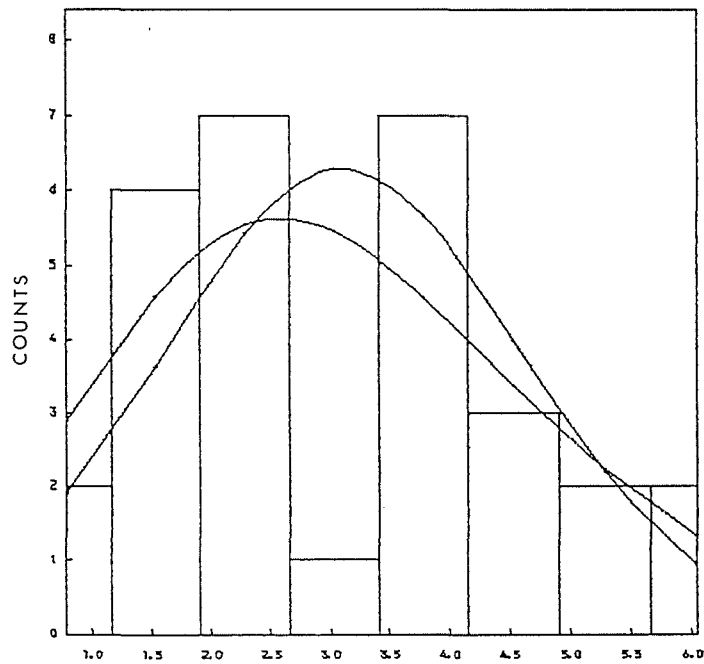


Figure 6.14a-b Histograms of the within-group galaxy-galaxy separations for (a) all galaxies, and (b) for just the spiral-spiral pairs, together with overlaid Gaussian and Poisson curves (bin width 0.75 Mpc).

A further test that was applied was to consider the separations of spirals and ellipticals relative to the calculated centroid of each group. Obviously, since the centroid is calculated from the individual (X,Y,Z) distance co-ordinates for each group galaxy, the centroid value will be weighted towards objects which have the most discrepant co-ordinates compared to other group members and not to the groups gravitational potential well. The seriousness of this effect is assumed to be small since, at least as far as the distribution of galaxies is concerned, obvious discrepant objects would be classified into separate clusters by the clustering analysis which sought tight, minimum variance, spherical clusters (Ward criterion). If the mean separations and standard deviations are significantly less for the ellipticals than for the spirals then this would indicate that the ellipticals are more tightly clustered than the spirals to the calculated group centroid. Such population gradients in rich clusters are well established (e.g. Melnick and Sargent, 1977). The following results for galaxy groups identified in this sample were obtained:-

$$S(r) = 1.97 \text{ Mpc}, \quad \sigma = 0.983, \quad \sigma/\sqrt{N} = 0.22, \quad N = 20$$

$$E(r) = 1.86 \text{ Mpc}, \quad \sigma = 0.808, \quad \sigma/\sqrt{N} = 0.25, \quad N = 10$$

and the ratio was:-

$$E(r)/S(r) = 0.94 \pm 0.16$$

The observed ratio is  $< 1.0$ , as would be expected if the ellipticals were more concentrated to the cluster centres. However, the result is not statistically significant considering the associated errors. The small numbers make firm statements on the significance of this trend impossible.

Finally, figure 6.15a-c are plots of the (X,Y), (X,Z) and (Y,Z) positions for all galaxies with slit-spectra determinations in the field with  $V \leq 10,000$  Km/s, plotted to scale, with individual galaxies identified and with the 'minimum spanning tree' (MST) superimposed. The minimum spanning tree or 'shortest dendrite' is the graph of (N-1) 'edges' which connects N points, has the least overall length and has no circuits (i.e. does not form a closed loop). This construction was also facilitated from within CLUSTAN. The reason for performing this operation was to see if the suggestive impression of apparent short filaments in the galaxy distribution from the cone diagrams would be enhanced in a more quantitative way with the MST construct, and also to see if any of the 6 groups identified above are actually chains of galaxies which are only well defined in 2 co-ordinates.

Barrow et al (1985), describe an application of the MST in both 2-D and 3-D to data in the CfA and Zwicky catalogues, and also to random samples and numerical simulations. They suggest that this technique enables the skeletal pattern of galaxy clustering to be highlighted in a quantitative manner and can be used as a filament detecting algorithm. The existence of filaments in the observed galaxy distribution has so far been a matter of speculation gained from a subjective visual impression only. Indeed, Barrow et al (1985), demonstrated that pattern recognition by eye is highly subjective and is sensitive to minor changes in the alignments and proximity of galaxies. The usual statistical techniques applied to studies of the large-scale galaxy distribution, such as the 2-point correlation function, (e.g. Peebles 1980), have been found to be quite insensitive to any filamentary structure that may be present. The existence of real filaments, even if demonstrated on a statistical basis only, would be an important feature of the galaxy distribution, since it has been suggested that the hierarchical and pancake scenarios of galaxy formation could result in significant differences

in the amount of filamentary structure that might be produced (Zeldovich et al, 1982). A variety of simple filament-finding algorithms have already been developed in an attempt to place filament detection on a much more objective and quantitative basis (e.g. Kuhn and Uson 1982, Turner and Gott 1983, and MacGillivray and Dodd 1984b), but these techniques have not been very successful to date. The MST technique is an alternative which may be better suited to the study of filamentary structure in the distribution of galaxies. It has the advantage of being able to select a well-defined subset of all possible connections between galaxies (termed nodes) which highlights the dominant pattern of 'connectedness' and which emphasises linear associations. Application of the MST technique to both random samples and the Zwicky catalogue by Barrow et al (1985), revealed that the MST's generated differed quite significantly. This was demonstrated by constructing a graph of the relative frequency of edge lengths (separations between galaxies) ' $F(l)$ ' against  $1/\langle l \rangle$ , which gave a Gaussian for the random sample, but which exhibited an exponential fall off with a significantly larger contribution at large and small  $1/\langle l \rangle$  for the Zwicky data.

Examination of figure 6.15a-c, where the edge lengths plotted refer to the actual physical distances between galaxies projected on to a 2-D surface, does not indicate any particularly pronounced filaments, although we might expect some elongation in the Z direction in any case because of the 'finger of God' effect. However, there is a line of eight galaxies connecting the 2 main groupings in figures 6.15b and 6.15c which extends for  $\sim 1,300$  Km/s and is well defined in both the X and Y directions. Hence this cannot be attributed solely to velocity dispersion effects. This 'filament' of  $\sim 13$  Mpc in length is labelled 'F1' in figures 6.15b and 6.15c. Furthermore, the innermost 6 galaxies of this chain constitute group 3 identified from the clustering analysis.

a)

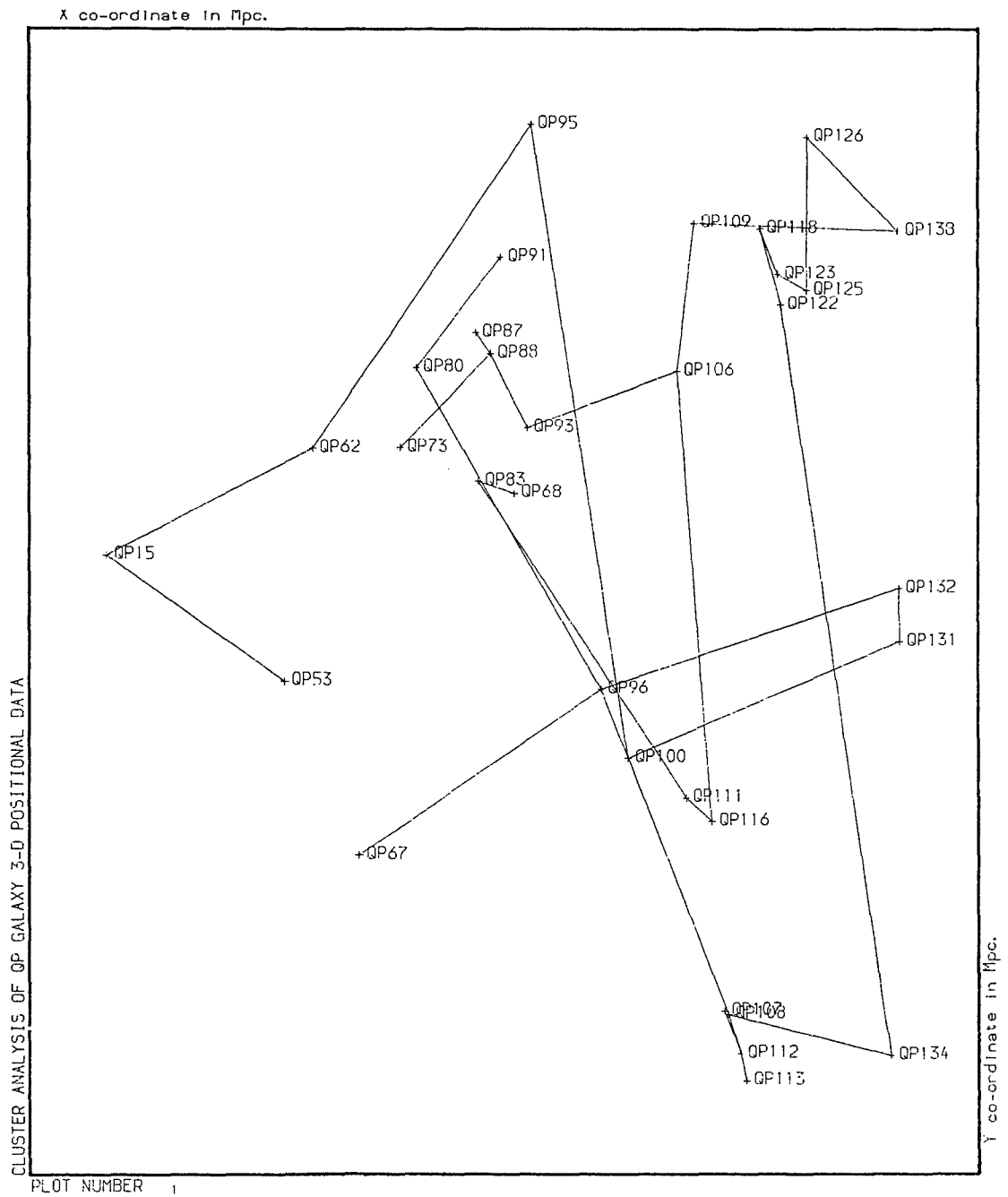
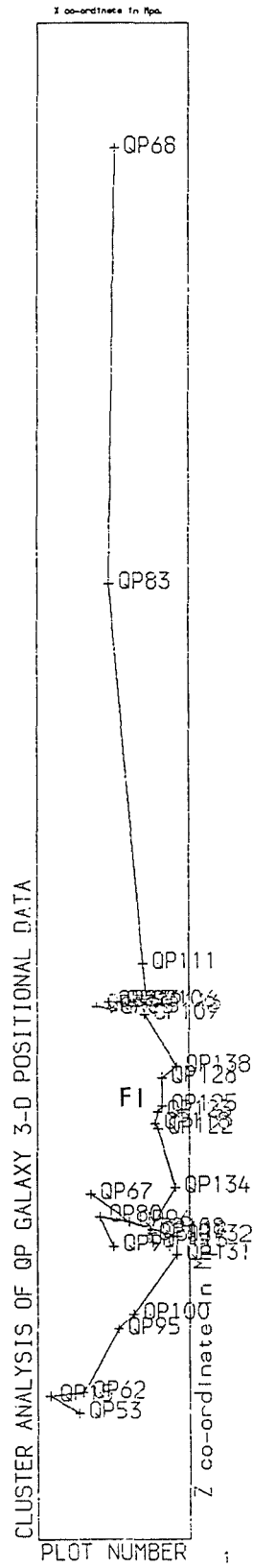
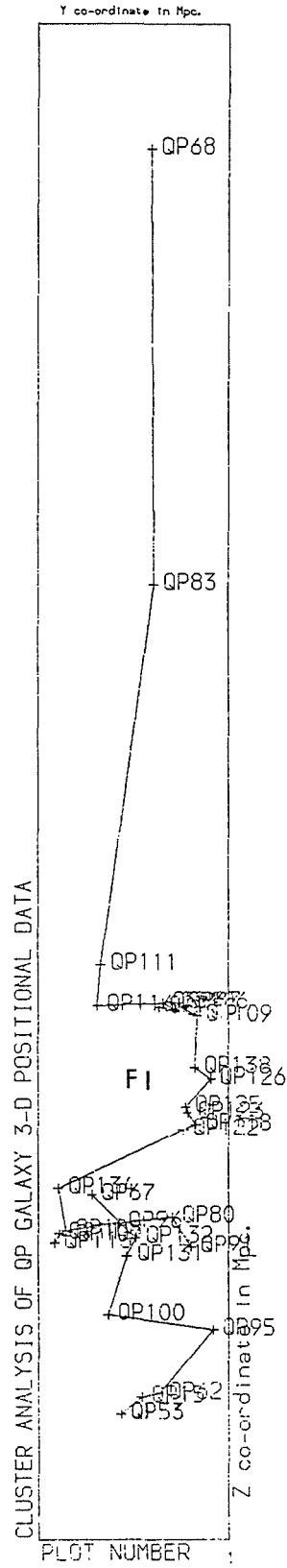


Figure 6.15a-c The (X,Y),(X,Z), and (Y,Z) co-ordinate plots for all galaxies in the first major redshift grouping together with the minimum spanning tree construct and case labels (to scale).

b)



c)



Reference to table 6.1 reveals, that as might be expected for such a chain extending in the Z direction, the dispersion values for the X,Y co-ordinates of group 3 are both  $< 0.5$  Mpc whereas that for the Z co-ordinate is a factor of 4 higher.

In conclusion, 6 'clusters' are identified which, from various clustering analyses seem to be well defined. These groups exhibit some sub-structure in the sense that they may be composed of binaries and tight groups of higher multiplicity. One of the groups, group 3, seems actually to be part of a chain of galaxies bridging the gap between groups 1 and groups 5 and 6. This is evidenced from the MST results which demonstrate the connectedness between the galaxies in this first distribution. The 6 groups only coalesce to form the next stage of hierarchy at much higher coefficients of fusion. The morphology of this first major redshift distribution in this field is dominated by spirals which account for 66% of the sample. This can be compared with the morphological mix for the brightest galaxies in the sky which was 79% spirals and 21% ellipticals and lenticulars, e.g. de Vaucouleurs (1963), and Sandage and Tammann (1981). A simple analysis of the within-group galaxy distribution seems to indicate preferential pair-wise separations of  $\sim 3.7$  Mpc for the galaxies in general and a possible paucity of spiral-spiral pairs with separations  $\sim 3.0$  Mpc. The current sample is too small to say anything conclusive about any morphological segregation that may exist or indeed if the ellipticals are more tightly clustered.

6.2.3.2. Results from the redshift distribution with  
 $11,800 \leq V \leq 19,000$  Km/s.

The same techniques of clustering analysis carried out on the first grouping were also applied to this sample. However, 5 galaxies were excluded because they were obvious background objects well separated from the second redshift distribution, i.e. galaxies QP103, QP33, QP129, QP127, and QP52 (see figure 6.5). This left 70 galaxies in this second sample. The resulting dendrogram is given in figure 6.16a. From examination of this dendrogram there appears to be  $\sim 12$  groupings with 2 or more members, a few well-separated single objects and a few binary systems. The structure at low fusion coefficients is difficult to see because of the large 'E' range encompassed by the total sample due to the larger (X,Y,Z) dimensions covered. Hence figure 6.16b is the dendrogram replotted with the ordinate on a log scale. This clearly illustrates how the hierarchy is built up from the first tight binary to form between QP2 and QP1.

If the fusion coefficient is plotted against the number of clusters remaining at that 'E' value (figure 6.17), then a discontinuity at  $\sim 16-18$  clusters is evident. The similarity of the general form of this plot with that of figure 6.12 from the first distribution is striking. Furthermore, if the cut in the hierarchy is applied at the level indicated by the discontinuity (arrowed in the diagram), then the fusion coefficient has about the same value as that obtained from the first grouping. The fact that there seems to be a natural break in the hierarchy between  $E \sim 20$  and  $E \sim 35$  for both major redshift distributions may be indicative of preferred levels of hierarchy for galaxies, at least in this field. Examination of figures 6.16a-b and 6.17 led to a choice for the cut in the hierarchy of  $E \sim 20$  at 18 clusters. This cut could have been applied somewhat freely between  $E \sim 20$  (18 clusters) and  $E \sim 23$  (16 clusters), since

the fusion coefficient increments on going from 18 to 16 clusters are small. The fusion to form 15 clusters at  $E \sim 27$  results in a binary forming between galaxies which are well separated in X and Y (5 and 3 Mpc) but which have similar redshifts. These should really be treated as discrete 'field' galaxies and so the hierarchy cut should be applied before this 'E' value.

The results from the different clustering approaches do not yield classifications which agree quite as well as for the analysis of the first sample, although the results from Ward's method are replicated by the RELOCATE procedure at the level of 6 'clusters'. The MODE analysis however, produces 'clusters' whose membership is slightly different than from the other techniques in a few cases. These differences may reflect the increase in sample size and the greater (X,Y,Z) range of the distance co-ordinates and also the existence of well-separated single objects which were absent from the first sample. The classification of 18 groups chosen from the results of the Ward technique was adopted. For these 18 groups, 4 are single objects and 4 are binaries. This leaves 10 groups with multiplicity  $> 2$ . The diagnostics and other properties of these groups are given in table 6.2. Their F-ratios seem, on the whole, as well behaved as for the first sample, indicating that most groups are well defined. The dispersions in the (X,Y,Z) distance co-ordinates are all generally  $< 2.0$  Mpc and in some instances are tighter than for groups in the first sample. Furthermore velocity dispersions for 11 of the 14 groups with  $\geq 2$  members are  $< 200$  Km/s and the remaining 3 have dispersions  $< 320$  Km/s.



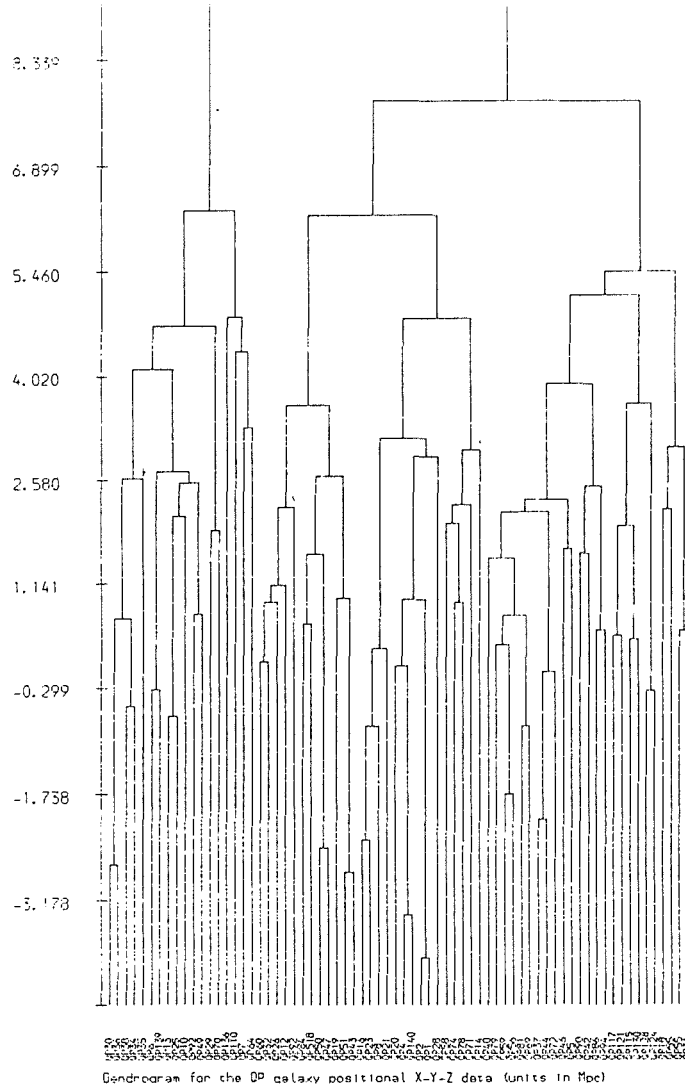


Figure 6.16b The dendrogram replotted with the ordinate on a log scale.

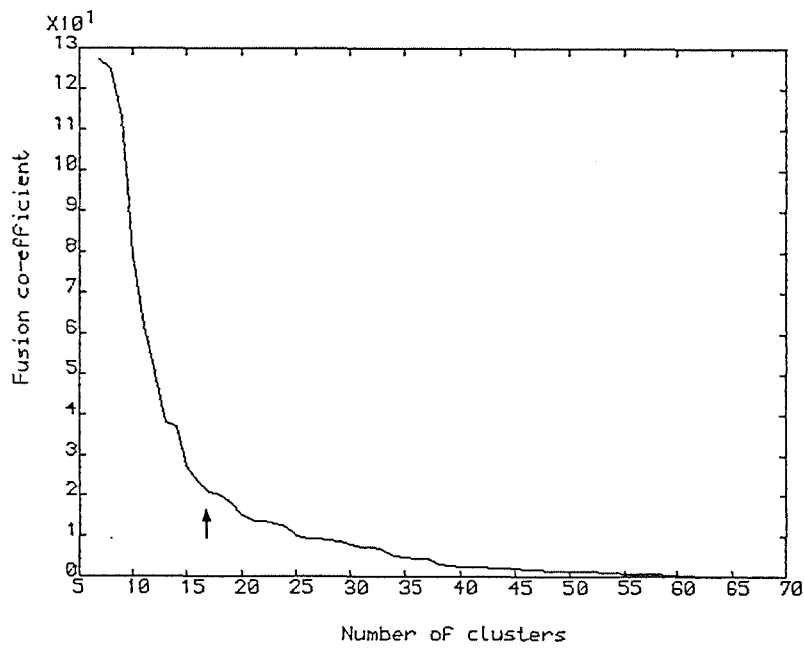


Figure 6.17 Plot of fusion co-efficient 'E' versus the number of clusters remaining at that E value for the second redshift sample.

Table 6.2

Diagnostics and other properties for those groups classified from the second redshift distribution with more than 1 member.

GROUP	N	Morphology Spir. Ellip.	<a>			<δ>			<V> Km/s	σ <sub>z</sub> Mpc	σ <sub>x</sub> Mpc	σ <sub>y</sub> Mpc	F <sub>z</sub>	F <sub>x</sub>	F <sub>y</sub>
			h	m	s	o	'	''							
1	5	60% , 40%	23	52	47	-33	29	04	16945	2.30	0.21	0.85	0.018	0.004	0.063
			00	18			17	12	230						
2	5	80% , 20%	23	53	13	-36	37	26	13447	1.03	2.06	0.75	0.004	0.385	0.050
			04	21			18	57	103						
3	11	91% , 9%	23	53	59	-34	57	29	14409	1.36	1.26	1.23	0.007	0.144	0.137
			02	27			29	23	127						
4	7	71% , 29%	23	53	36	-35	08	17	13729	1.83	1.03	1.17	0.012	0.097	0.123
			02	11			27	54	181						
5	7	71% , 29%	23	50	51	-34	47	23	16551	1.89	2.00	1.47	0.013	0.364	0.194
			03	22			30	34	190						
6	4	75% , 25%	00	08	34	-35	33	37	14474	2.05	0.87	0.18	0.015	0.068	0.003
			01	44			04	00	204						
7	4	75% , 25%	23	49	37	-35	01	24	12912	0.79	0.41	0.32	0.002	0.016	0.009
			00	54			08	24	79						
8	6	50% , 50%	23	48	30	-36	10	47	12636	1.43	0.73	1.99	0.007	0.048	0.358
			01	37			53	05	146						
9	2	50% , 50%	23	53	52	-36	21	28	15291	0.93	3.38	0.96	0.003	1.033	0.084
			06	16			19	56	103						
10	5	80% , 20%	23	54	20	-33	32	29	12219	3.19	1.23	1.73	0.036	0.138	0.271
			02	57			48	16	317						
11	2	0% , 100%	00	10	18	-37	34	36	14865	0.58	0.33	0.78	0.001	0.010	0.055
			00	43			18	24	54						
14	4	50% , 50%	23	57	45	-36	32	13	14638	2.15	1.70	1.33	0.016	0.261	0.160
			03	15			30	09	219						
15	2	0% , 100%	23	53	23	-37	35	58	16555	2.69	1.41	0.85	0.026	0.179	0.066
			02	19			20	43	268						
17	2	100% , 0%	23	53	16	-34	52	03	15675	1.41	0.67	0.06	0.007	0.041	0.001
			01	15			01	02	139						

The general properties of the 18-group classification are in good agreement with those from the first sample and in the same range as that found for nearby galaxy - groups (e.g. de Vaucouleurs, 1974). This implies that the clustering techniques employed still seem able to elucidate structure to the same degree as for the first sample, even though the Z co-ordinate range is twice as large. The expected degradation in resolution from an increase in the (X,Y,Z) co-ordinate dispersions does not appear to have occurred. This is perhaps because the range of the X,Y distance co-ordinates are also correspondingly larger so that the actual proportions of the co-ordinate ranges are about the same as for the first sample, i.e.  $X:Y:Z = 1:1:5$ .

However, there does appear to be certain differences between the galaxy groups identified compared with the earlier analysis. Specifically, the morphological mix has changed from being dominated by spiral galaxies in the first sample (66% spirals, 34% ellipticals), to approximately equal numbers of spirals and ellipticals in the second sample (49% spirals, 51% ellipticals). This difference may simply reflect the larger size of the second grouping compared with the first which may not be morphologically representative of the general galaxy population. The dominance of spirals in studies of nearby field galaxies (~80%) is well established, e.g. Sandage and Tammann (1979), so the results for the first grouping studied are in better quantitative agreement with these results. Alternatively the results may indicate a real shift in the proportions of different galaxy types for the higher redshift sample. More probably, the proportion of spiral galaxies in this second sample is a lower limit because tightly-wound spirals may have been mis-classified as ellipticals (see earlier). Nevertheless, the observed proportions of spirals and ellipticals compares reasonably well with that found by Shanks et al. (1984), for their redshift survey, of 43% elliptical and lenticulars and 57% spirals. This is a good comparison to make

because the same magnitude system and a similar magnitude limit was employed ( $b_j \leq 16.75$ ). The volume of space occupied by this second sample is  $\sim 8,240 \text{ Mpc}^3$ , with X,Y dimensions of 6 by 11 Mpc at the front end and 10 by 17 Mpc at the rear. The depth is 70 Mpc.

Another difference between the samples is that of the existence of single galaxies which do not coalesce with other groups until large values of E. These 'field' galaxies are all spirals and again may simply have been absent from the first sample because of its smaller size. The largest multiplicity 'cluster' identified in the second sample has 11 members, 10 of which were classified as ellipticals. The diagnostics for this group, from table 6.2, indicate that it is very well defined, much more so than many other looser groups of lower multiplicity. The dominance of elliptical galaxies in well-defined spherical clusters is a well-determined observational property, e.g. Butcher and Oemler (1978), and Strom and Strom (1979). In fact all groups identified in the second sample with multiplicity  $\geq 6$  are dominated by ellipticals and lenticulars, whereas all those with multiplicity  $\leq 5$  are dominated by spirals. De Vaucouleurs (1974), from a study of bright galaxies, showed that the population of small, loose groups was dominated by spirals. An interesting property of group 3 is that if all unique pair-wise separations are calculated for member galaxies then the resulting distribution of separations appears normal with mean 2.9 Mpc and standard deviation 1.17 Mpc. Performing the Lilliefors test on the e.d.f constructed from the standardised pair-wise separations led to acceptance of the null hypothesis,  $H_0$ , that the observed distribution is normal. The von-Mises global goodness-of-fit test yielded  $T_3 = 0.049$ , which indicates acceptance of  $H_0$  with  $> 90\%$  confidence. These results imply that significant substructure within the cluster is negligible as such structure would manifest itself as preferred - separation ranges. A bimodal distribution would result if the group was made up of two distinct

sub-groups for instance. There is a preferred galaxy-galaxy, within-group separation of  $\sim 3.0$  Mpc, the peak of the distribution. This is close to the peak found for the first sample although the data appears normally distributed in this case. Figures 6.18a-c are the (X,Y), (X,Z) and (Y,Z) plots for the 11 galaxies in group 3 with the minimum spanning tree drawn in and with the individual galaxies labelled. There are two main features of these plots. Firstly, the distribution of galaxies appears spherical to a first approximation since all three plots exhibit the same general form with no bunching or extension in any one co-ordinate relative to the others. Indeed, reference to table 6.2 reveals that the dispersion values in all 3 co-ordinates are almost identical (i.e.  $\sigma \sim 1.3$  Mpc). Secondly, although the whole group seems spherical in nature, figures 6.18b and 6.18c especially, indicate a possible bi-modal arrangement. There seem to be two sub-groups joined together by galaxies QP59 and QP56, which are themselves located near the projected centroid of the group in all three plots. Such bimodality should be incompatible with the observed normality in the within group galaxy-galaxy separations. To investigate this possible bimodality the Lilliefors test, von-Mises  $\omega^2$  test and the Chi-square test (with the data in 75 Km/s width bins), were applied to the velocity data for this group which has a low dispersion of only 127 Km/s. These tests were unable to reject the null hypothesis of normality with even moderate (75%) confidence. Consequently any bimodality within this group is marginal and in this instance may reflect a misleading MST construct.

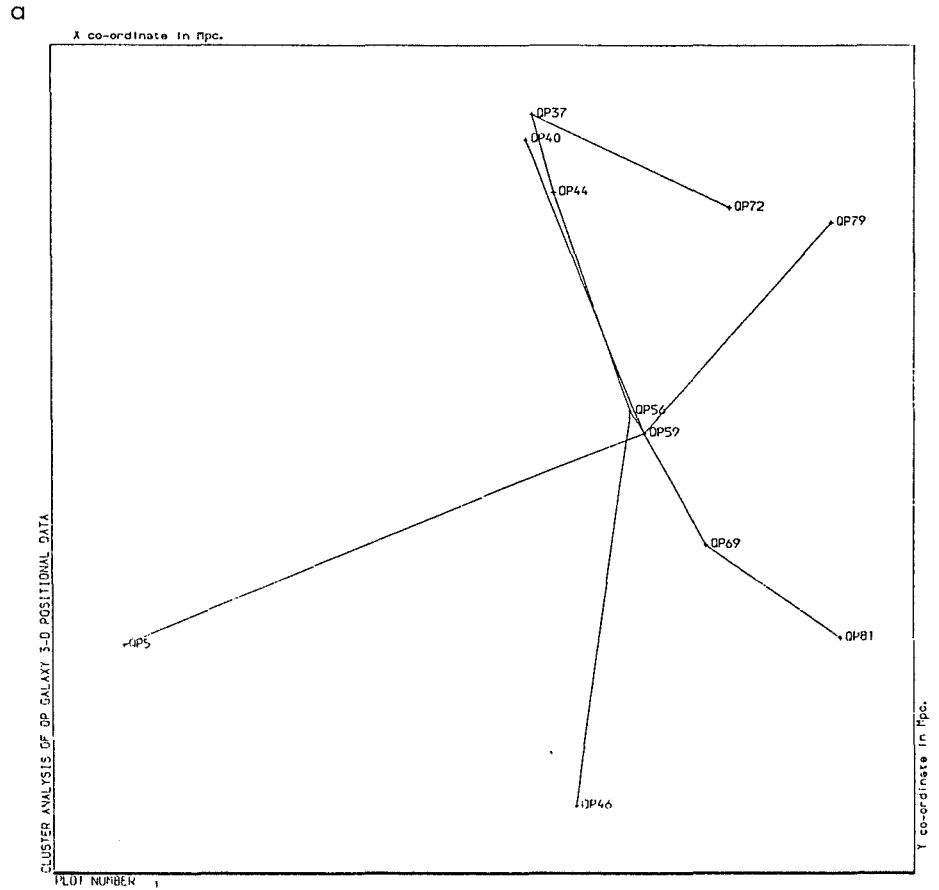
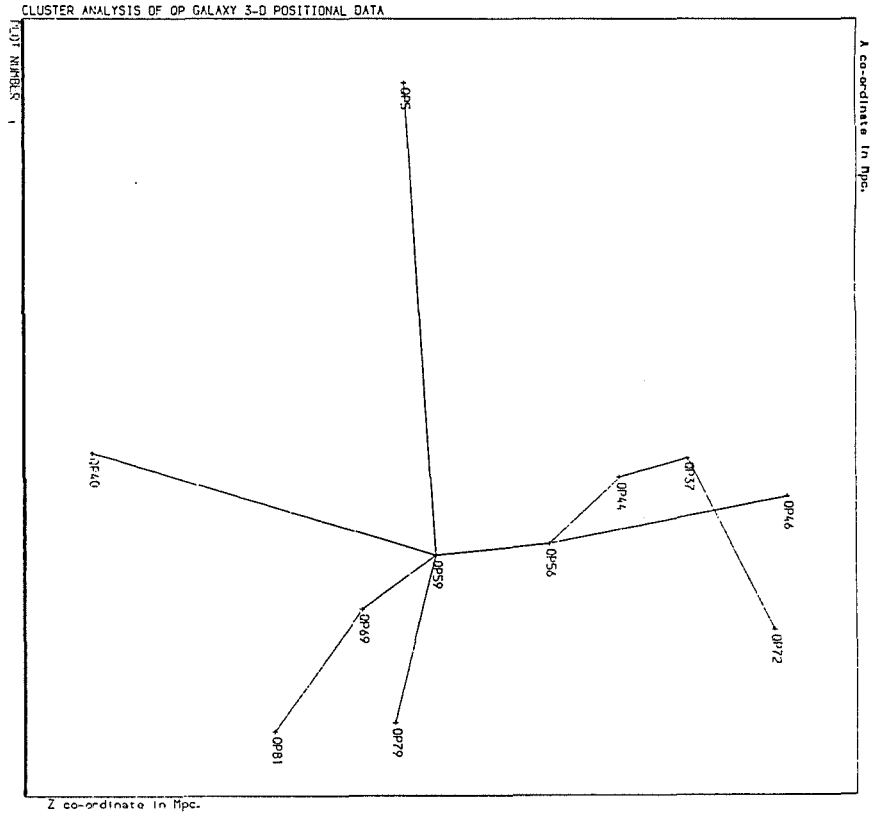


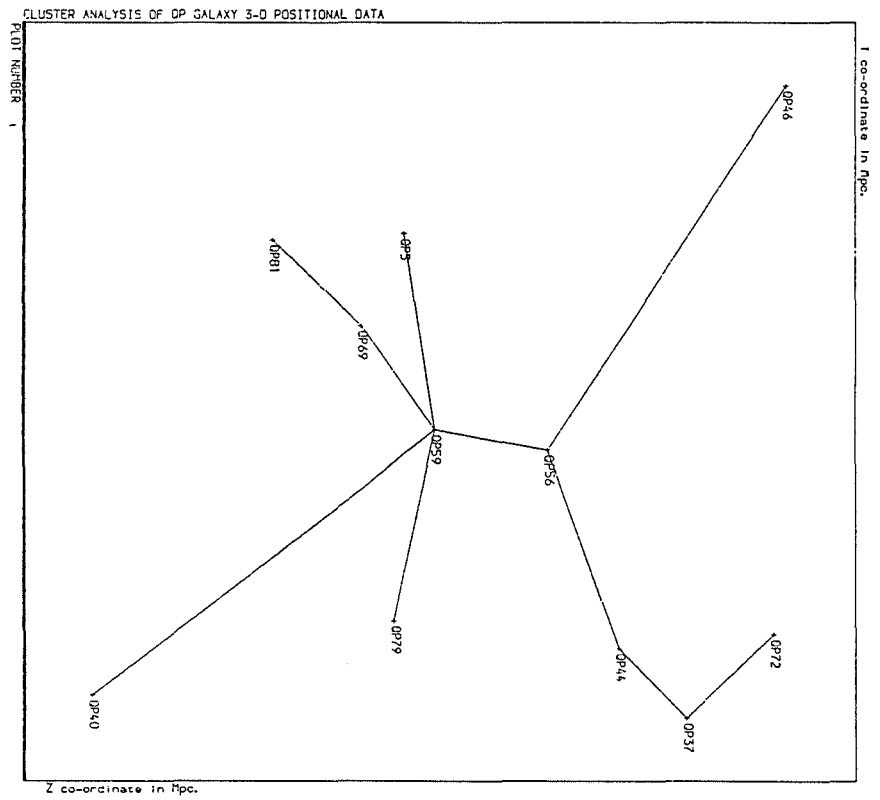
Figure 6.18a-c The (X,Y), (X,Z) and (Y,Z) co-ordinate plots for the eleven galaxies in group 3 together with the minimum spanning tree construct and case labels (to scale).

figure 6.18b & c

b



c



Yahil and Vidal (1977), have shown that a normal distribution is a good approximation for the velocity distribution in rich clusters, whilst Rood and Dickel (1978), found that the same was generally true for smaller galaxy groups. This merely reflects the fact that the 3-D velocity distribution is Maxwellian. However, the projected density distribution at the sky is not known for small galaxy groups. Materne (1979), in a follow-up of his paper on hierarchical clustering, assumed that the projected density distributions of the galaxy groups were also Gaussian. This distribution was simply chosen for demonstration purposes because of its simple analytical form, unlike a King model which might be a more appropriate fit to rich clusters. A multivariate, normal, probability density function was thus defined which was fitted to the observed group galaxy distribution by maximising the likelihood function. This was then used to obtain a quantitative membership probability for the galaxies in his sample. No such probabilistic analysis is attempted here because a realistic density function for these galaxy groups is not known. Nevertheless, the fact that the galaxy-galaxy pair-wise separations appear normal for group 3, may mean that Materne's initial assumption may not be too inaccurate for well-defined groups such as this.

If all within-group elliptical-elliptical separations are considered a similar result to that for group 3 above is obtained. The Lilliefors test again leads to acceptance of  $H_0$ , as does the von-Mises statistic  $T_3$  at  $> 90\%$  confidence. The e.d.f and the overlaid standard normal distribution pertaining to the 77 unique, elliptical-elliptical, within-group pairs is given in figure 6.19a. The histogram of pairs in 0.75 Mpc bins is given in figure 6.19b, together with the overlaid Gaussian fit. The mean separation was found to be 3.1 Mpc with  $\sigma = 1.23$  Mpc. Conversely, if only the spiral-spiral pair-wise separations are considered for those clusters containing at least 2 spiral galaxies, then there are only 28 unique

pairs. The mean separation was found to be 3.5 Mpc with  $\sigma = 1.93$  Mpc. The results from this somewhat smaller sample appear non-normal as the Lilliefors test leads to rejection of  $H_0$  at a level of significance  $\alpha = 0.15$ , although the von-Mises test only allows rejection of  $H_0$  at the 50% level. This may reflect the tendency for spiral galaxies to be outlying members of their groups. If we examine the histogram of the spiral-spiral pairs (figure 6.20) then a paucity at separations of  $\sim 3.0$  Mpc is again evident. Although the reality of this paucity must be questioned due to the small numbers involved, it is highly suggestive since exactly the same situation was uncovered for the spiral-spiral pairs from the first sample (figure 6.14b). Furthermore, as found for the first sample, this paucity co-incides with the maximum in the elliptical-elliptical pair-wise separations (figure 6.19b). The paucity in figure 6.20 is significant at  $> 2$ -sigma.

As in the first sample, we can look for evidence of morphological segregation in the groups identified by examining the ratios of the mean pair-wise separations among spirals, ellipticals and all group members. Unlike the first sample though, there are a sufficient number of elliptical-elliptical and spiral-spiral pairs to attempt a meaningful analysis. Table 6.3 gives the results for the mean pair-wise separations. The three ratios formed, together with their errors, are given below:-

$$R_p(E)/R_p(S) = 0.886 \pm 0.099$$

$$R_p(E)/R_p(\text{all}) = 0.958 \pm 0.056$$

$$R_p(S)/R_p(\text{all}) = 1.081 \pm 0.119$$

If ellipticals are more concentrated than spirals then the ratio  $R_p(E)/R_p(S)$  should be less than unity. These results are marginally significant and do indeed indicate that the ellipticals are more concentrated than the spirals, in agreement with the results of Mezzetti et al. (1985), for segregation in galaxy groups.

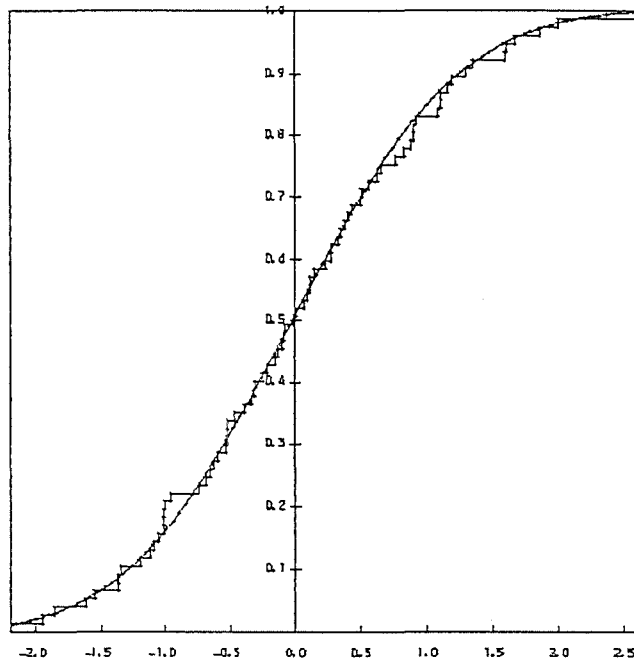


Figure 6.19a The empirical distribution function for the standardised elliptical-elliptical pair-wise separations for the second sample together with the overlaid standard normal distribution (the Lilliefors test).

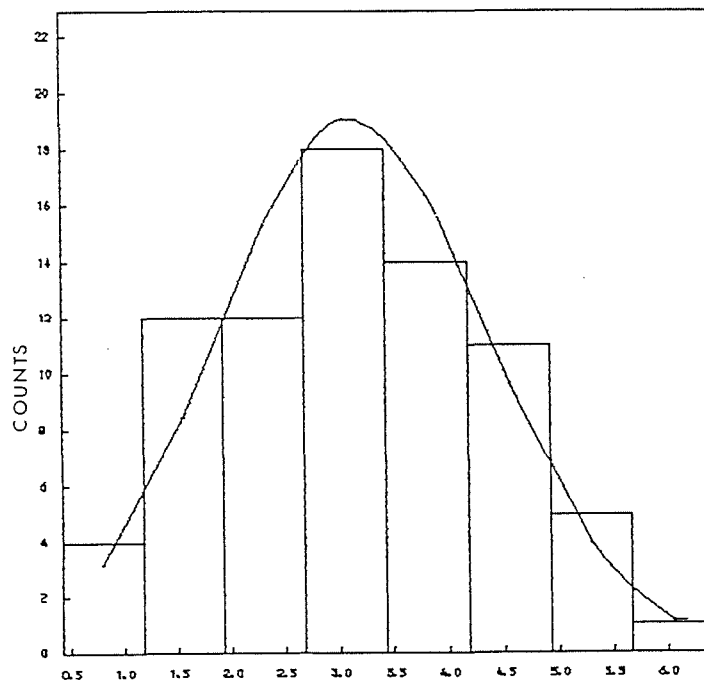


Figure 6.19b Histogram of the elliptical-elliptical pair-wise separations (with bin width of 0.75 Mpc), for the second sample, with overlaid Gaussian.

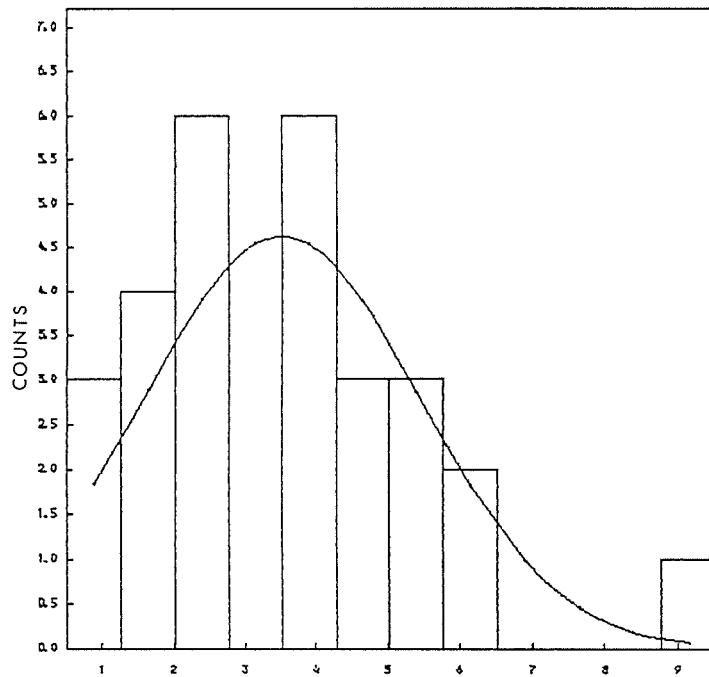


Figure 6.20 Histogram of the spiral-spiral pair-wise separations (with bin width of 0.75 Mpc), for the second sample, with overlaid Gaussian.

Table 6.3

Results for the mean pair-wise separations between all within-group galaxies, and for just elliptical-elliptical and spiral-spiral pairs.

Morph.	Rp(Mpc)	$\sigma$	N	$\sigma/\sqrt{N}$
All	3.26	1.60	164	0.125
Spirals	3.52	1.92	28	0.364
Ellip.	3.12	1.23	77	0.140

If, as in the first sample, the separations of within-group galaxies relative to their parent-group's calculated centroid is examined on a morphological basis, then it may be possible to determine if the ellipticals are more concentrated to the calculated group centres than the spirals. The following results were obtained:-

$$S(r) = 2.13 \text{ Mpc}, \quad \sigma = 1.27, \quad \sigma/\sqrt{N} = 0.39, \quad N = 30$$

$$E(r) = 1.97 \text{ Mpc}, \quad \sigma = 0.93, \quad \sigma/\sqrt{N} = 0.33, \quad N = 36$$

which gave a ratio:-

$$E(r)/S(r) = 0.92 \pm 0.23$$

We would expect this ratio to be  $< 1.0$  if the ellipticals were more concentrated and indeed the mean and standard deviation for the ellipticals are less than for the spirals. As was the case for the first sample, although the observed ratio is  $< 1.0$  the small numbers and associated errors make the above result no more than indicative.

Finally, the separations of the calculated group centroids from their nearest neighbours is considered for the 14 cases where group membership is  $\geq 2$ . The average separation between all unique inter-group pairs was  $\sim 26$  Mpc,  $\sigma = 15$ ,  $N = 153$ . The furthest separation was  $\sim 66$  Mpc, corresponding to the front and rear ends of the velocity range for this sample, and the closest separation was  $\sim 4$  Mpc. This was between groups 7 and 8 which individually exhibit good diagnostics but which also fuse to form one larger group at an 'E' value of 23.6, close to the applied cut in the hierarchy. In fact the properties of this merged group are still within the acceptable range exhibited by the other groups. The average nearest neighbour separations was  $\sim 7$  mpc,  $\sigma = 2$ ,  $N = 14$ , indicating that in general the identified groups are fairly well separated from each other and most can be considered as discrete entities.

However, as for the first distribution, it was considered prudent to consider the MST construct for this data, again to see if there is any obvious chaining in the galaxy distribution not revealed by the clustering analysis. Consequently, figures 6.21a-c give the (X,Y), (X,Z) and (Y,Z) co-ordinate plots for the galaxies in this second distribution with labelling and the MST construct superimposed. This exercise proved to be quite suggestive. Figure 6.21a highlights the pronounced  $3^\circ$  by  $3^\circ$  gap in the projected galaxy distribution corresponding to the large void discussed earlier, as well as the well defined, high-multiplicity group '3'. In this case the MST is not particularly revealing since most resolution is in the radial co-ordinate. Figure's 6.21b and 6.21c though, are more interesting. The major, higher multiplicity groups identified from the hierarchical clustering analysis are evident as tight clumps, but the striking feature of these plots are that these clumps seem to be chained together by linear associations of single galaxies. Furthermore the entire system is strung out in the radial direction over a fairly narrow window of X,Y in the field and extending to a depth of  $\sim 170$  Mpc (except for a small 'side chain' of 6 galaxies evident in figure's 6.21a and 6.21b). This elongation purely in the radial direction is somewhat suspicious. In fact the lining-up of the major groups in the radial direction is heavily dictated by the large void mentioned above so that the intervening galaxies are also constrained to lie over the same narrow interval in X and Y. Nevertheless the galaxies lying between the major groups still seem to be arranged in a more linear manner than one might expect by chance. Furthermore, these intervening chains are more extended than can be explained by the finger of God effect. In particular there is a distinctive chain of 4 galaxies between the high multiplicity group 3 and group 5, especially evident in figure 6.21b, which is in fact split up into groups 9 and 17 by the clustering analysis.

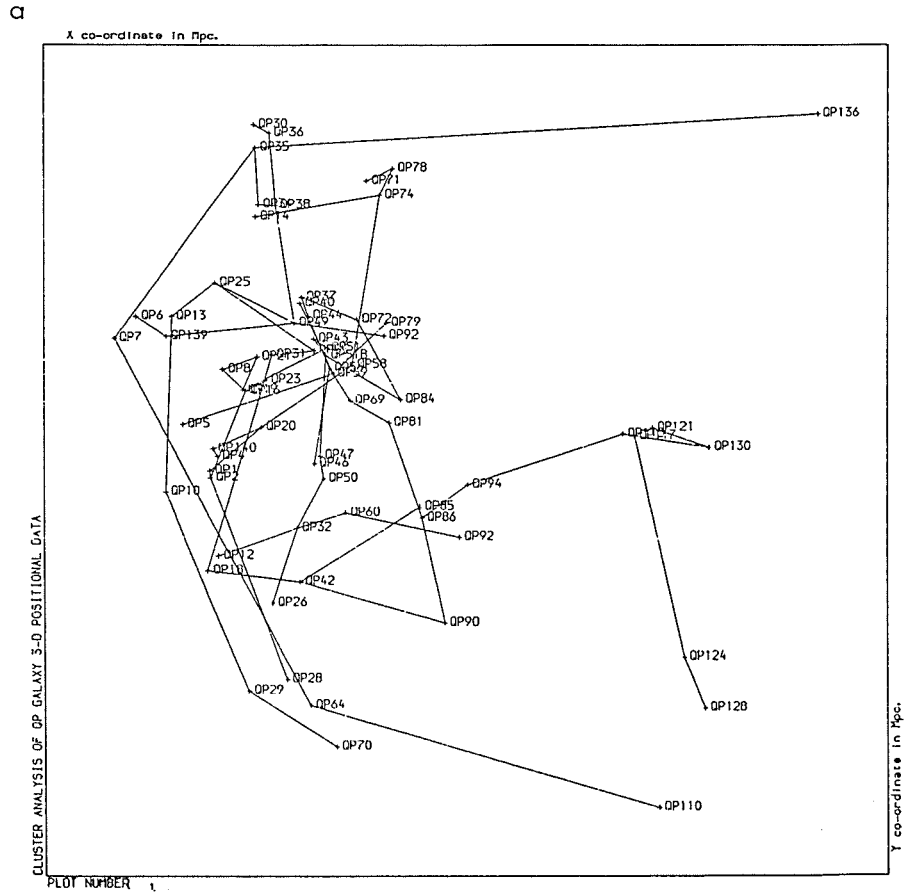
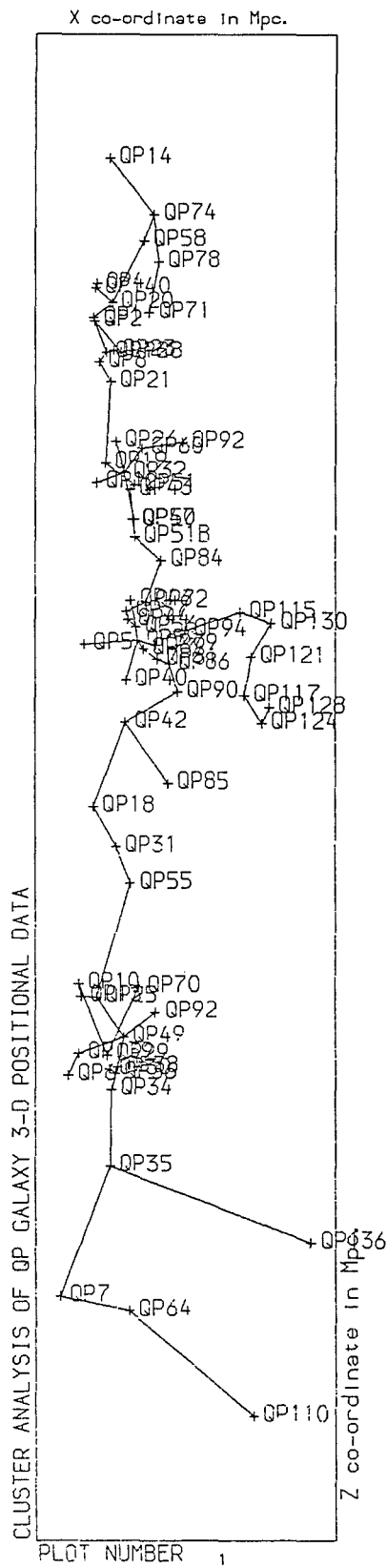


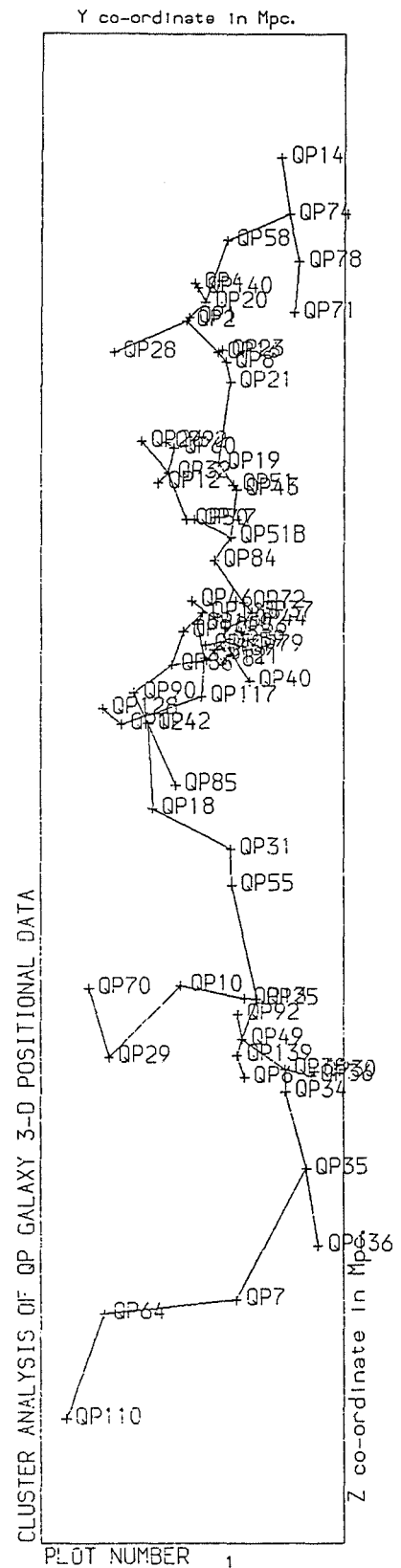
Figure 6.21a-c The (X,Y),(X,Z) and (Y,Z) co-ordinate plots for all galaxies in the second major redshift grouping together with the minimum spanning tree construct and case labels.

figure 6 21b&c

b



c



Another interesting feature in the MST construct is the linear chain of 4 galaxies at the low redshift end in figure's 6.21b and 6.21c. This was group 10 in the hierarchical classification. Reference to table 6.2 shows that the Z dispersion for this group is  $\sim 2.5X$  that of X and Y. The impression gained from these MST constructs is of unequally-spaced knots in a loose string. However, although the MST has revealed the connectedness between the galaxy-groups which is suggestive of some sort of chaining or bridging between the higher multiplicity groups (particularly groups 3,4 and 5), caution is advised in giving too much weight to this filamentary impression. In fact Barrow et al (1985), note that the MST gives a close correspondence to the subjective patterns isolated by the eye. Increasing the angular coverage in this area to adjacent fields would enable a decision on the validity of this 'chaining' to be made.

In conclusion, using techniques of hierarchical clustering, a number of well-defined groups have been identified in the galaxy distribution for this second sample which are generally well separated, so well as 4 discrete 'field' galaxies. This classification may not be quite as robust as that for the first sample as the results from the different clustering approaches employed do not generally agree as precisely. The classification from Ward's method was adopted. Nevertheless, the properties of these groups are generally in good agreement with those of the first sample and with the properties of galaxy groups identified using more traditional if somewhat intuitive methods (de Vaucouleurs, 1974). Some of the lower-multiplicity groups, such as groups 9 and 17, may form parts of chains of galaxies not identified by the hierarchical clustering analysis, but which seem to connect the higher-multiplicity groups. The larger sample size also enables a firmer statement on the morphological segregation that seems to be present in the galaxy groups. Again there is the possibility of avoided separations for within-group

spiral-spiral pairs in this sample and preferred elliptical-elliptical separations co-inciding with the spiral-spiral paucity. A suitable explanation for this effect has yet to be found.

6.2.4. General conclusions from the analysis of the galaxies with  $b_j \leq 16.5$  in field 349.

The most important and distinctive feature arising from the analysis of the bright galaxy distribution in this field, made with the aid of a significant sample of radial velocities, is the detection of large voids. In particular, 2 large voids were identified with depths of 20 and 80 Mpc and projected physical extent of  $6 \times 11$  and  $5 \times 9$  Mpc respectively. The space volume of the second void alone amounts to 25% of the total volume of space sampled to 180 Mpc. These void dimensions are minimum values restricted by the angular size of the field surveyed. Extension of the redshift survey to adjacent fields would enable the true size of these voids to be determined. The existence of these voids has highlighted the highly anisotropic nature of the galaxy distribution in this field on scales at least as large as 20 Mpc.

Two major groupings of redshifts were evident. These distributions were analysed separately using techniques of clustering analysis in general and hierarchical agglomerative methods in particular. Such techniques have been shown to be a powerful means of unravelling the structure of the galaxy distribution in a quantitative and objective manner. The dendrograms produced enable all levels of hierarchy, whether meaningful or not, to be seen. An encouraging property of the clustering analysis employed was the ability to identify not only well-defined groups, such as group 3 in the second sample, but also well-separated field galaxies. An interesting and perhaps important feature arising from the clustering analysis was the

break or discontinuity in the fusion coefficient for both samples at  $E \sim 20-35$  (figures 6.13 and 6.16). This was so significant as to be a natural choice for the cut in hierarchy to apply and may be an important property of the galaxy distribution in general. It must be remembered though, that dynamical stability of the identified groups is not addressed and that they may consequently contain members which are not in fact tidally bound to the group at all. The resulting classification did nevertheless select groups which generally appeared to be well defined and well separated, with velocity dispersions and physical dimensions compatible with those for 55 nearby groups identified from a study of bright galaxies (de Vaucouleurs, 1974). However, a drawback of the hierarchical clustering technique is its inability to identify filamentary structure or chains in the galaxy distribution. In this respect the minimum spanning tree has proved to be a useful visual tool for indicating that the larger multiplicity groups, especially in the second redshift distribution, may be connected by strings of single galaxies. There is slight evidence of morphological segregation in the identified groups, at least in the second, larger sample. The number of groups is too small to say anything conclusive about a concentration of ellipticals to the calculated group centroids. The most perplexing result from this analysis is the preferred pair-wise galaxy separations which seems to be a function of morphology. Both major redshift samples exhibit a paucity in the spiral-spiral within-group pair-wise separations at  $\sim 3.0$  Mpc. This paucity, somewhat suspiciously, co-incides with the peak in the elliptical-elliptical pairs which, at least for the second sample, are normally distributed.

6.3. The 2-D distribution and analysis of galaxies in field 349 to  $b_j = 20.5$

The rest of this chapter presents results from analysis of faint galaxies in field 349 to  $b_j = 20.5$ , the limit of "reliable" star/galaxy separation from the direct plate (see chapter 5 section 5.6). The analysis consists of various statistical tests developed over the years to address the question of large-scale galaxy clustering, its prevalence, scale and significance. Knowledge of how galaxies are distributed on the largest scales should reveal much about conditions in the early Universe and consequently guide current theories of Cosmology and galaxy formation into a form consistent with observation. In particular, a choice between the conflicting processes of continuous clustering or preferred scales of hierarchy associated with the gravitational instability or adiabatic perturbation theories of galaxy, cluster and supercluster formation could be made (see chapter 4). Correlation analysis, power spectrum analysis and Meads analysis were employed on the 2-D galaxy information to various limiting magnitudes. Furthermore, apart from the 2-D statistical tests, ~1,500 objective-prism redshifts were obtained for galaxies to  $b_j = 18.7$ . The crude spatial information afforded by these results was also assessed.

6.3.1. Preliminary results.

The basic data consist of positions, magnitudes and other image parameters for 25,812 galaxies and 27,715 stars to  $b_j = 20.5$  identified from a star/galaxy separation of the direct plate J6145 (copy) of field 349. This was supplemented by objective-prism redshifts for 1,539 galaxies measured using INTERZED on COSMOS data from plate UJ6535P (original) for galaxies to  $b_j = 18.7$  (see chapter 5).

Firstly number/magnitude, (N-m) histograms for the stars and galaxies selected from the direct plate to  $b_j = 20.5$  were constructed. Serious plate defects, vignetting or obscuration might be manifested as depressions or trend changes in the (N-m) histograms at fainter magnitudes since an occluded or less sensitive plate region would affect faint object counts before those for brighter objects. Furthermore, significant wiggles contrary to the overall trend in the galaxy (N-m) histogram could be due to the presence of strong galaxy clumping in the field. The (N-m) histograms for the stars and galaxies are given in figure 6.22a-b whilst figure 6.23 gives the integrated (N-m) plot for both. Figure 6.22a does seem to indicate a paucity of stars at  $b_j = 19.4-19.7$  which is more significant than the  $\sqrt{N}$  Poisson error bars for each bin. No corresponding feature in the (N-m) histogram for the galaxy results at similar magnitudes is seen which might be expected if the feature was due to one of the effects above. Consequently, unless there was an excess of galaxies over the same magnitude range which had co-incidentally filled in the paucity, the inference must be that the feature in the stellar counts is real. Indeed there is a slight excess in the (N-m) counts for the galaxies between 19.3 and 19.9 compared with the general curvature of the plot. Any such effects though, are smeared in the integrated (N-m) counts for the stars and galaxies in figure 6.23. The evidence of an excess in figure 6.22b could be due to some large-scale feature in this field. Preliminary work on the faint galaxy distribution in this field by Parker et al (1984a,b) has indicated the existence of a cell like supercluster at  $Z \sim 0.11$ . The possibility of large-scale anisotropy of the galaxy distribution on scales  $> 25 h^{-1} \text{Mpc}$  was a prime motivation for the more thorough investigation of this field described in this thesis.

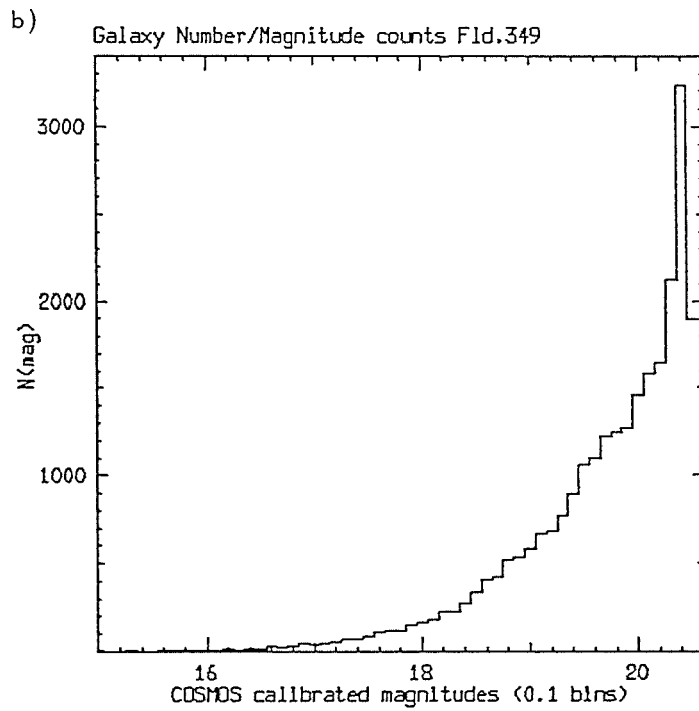
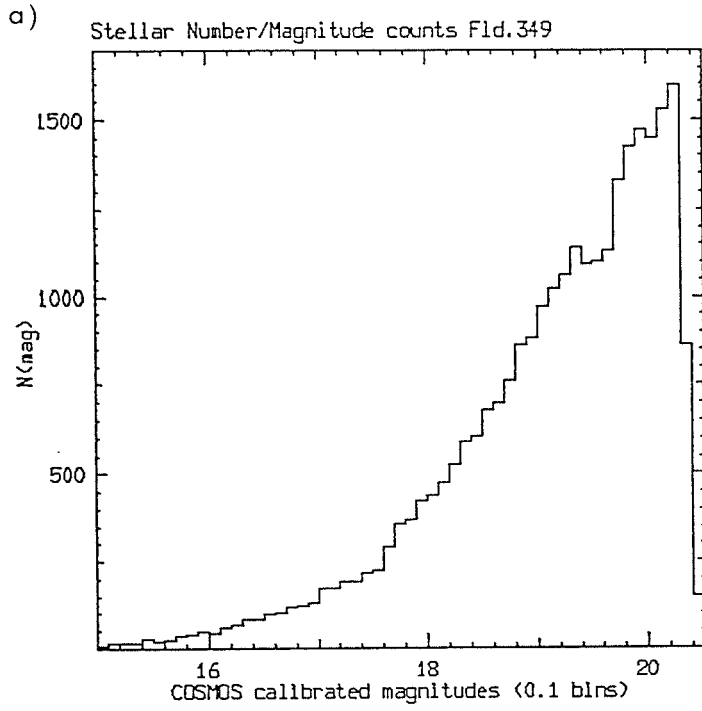


Figure 6.22a-b The number/magnitude histograms for the stars and galaxies to  $b_j = 20.5$  in field 349.

A comparison between the (N-m) counts in this field and those for the SGP from the data of MacGillivray and Dodd (1980), (hereafter MD80), was made since a comparison between two closely-separated fields could confirm the presence of a large-scale feature in field 349. Consequently figure 6.24 gives the log of the (N-m) counts per square degree versus the calibrated *Cosmos*  $b_j$  magnitudes for field 349 and field 413 (MD80 results). A number of features are worthy of note. Firstly, there is excellent agreement between the counts down to  $b_j \sim 18.2$ , even at  $b_j \sim 15.0$  where the Poisson error bars are significant. This agreement over three magnitudes confirms the magnitude calibration for these data since serious magnitude offsets between the data sets would shift the points along the abscissa. Furthermore, the agreement confirms the deficiency at  $b_j \sim 16.0$  found by MD80 and supported by data provided by Oemler (1974). The 20 Mpc void found in this field and described in the first half of this chapter could account for this deficiency. In agreement with MD80, the apparent deficiency at  $b_j \sim 17.5$  detected by Brown (1974), in the NGP, is absent in these data, confirming the anisotropy in the galaxy counts between the NGP and SGP regions (de Vaucouleurs 1977). The apparent deficiencies in Brown's counts at the NGP and the counts of MD80 at the SGP have been interpreted as due to the edge of the LSC being encountered. The fact that the observed deficiencies occur at different apparent magnitudes is interpreted as the result of the non-central position of our galaxy with respect to the LSC.

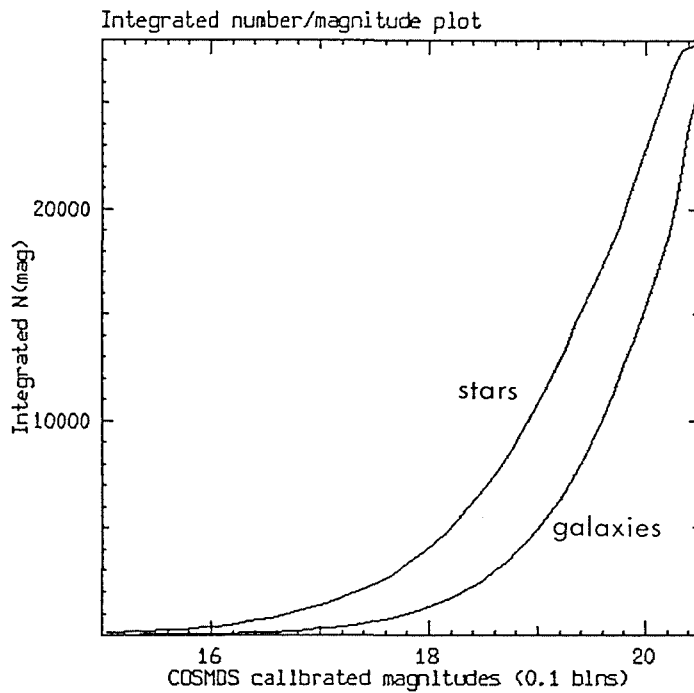


Figure 6.23 The integrated number/magnitude plot for both stars and galaxies to  $b_j = 20.5$  in field 349.

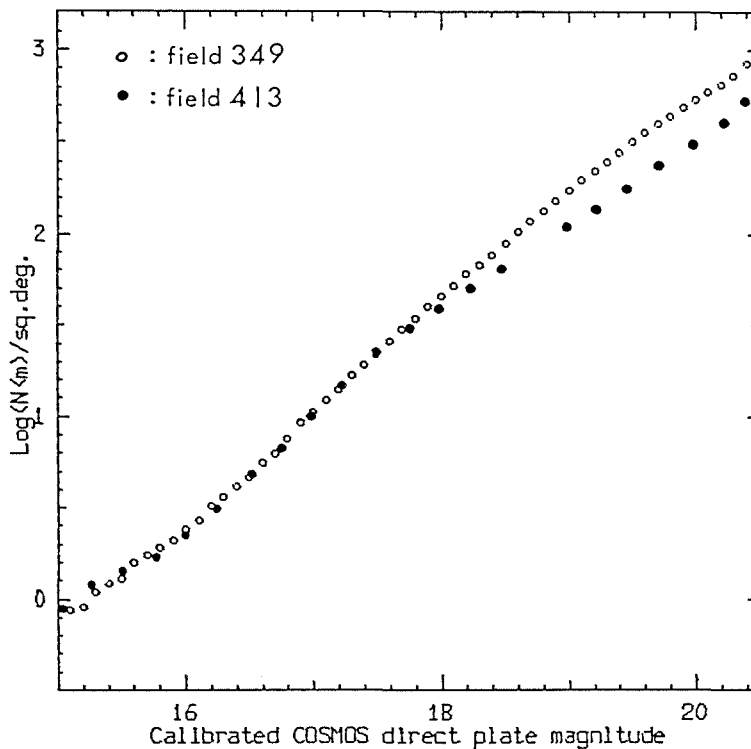


Figure 6.24 Comparison of the log of the number/magnitude counts per square degree versus the calibrated COSMOS  $b_j$  magnitudes for field 349 (this study), and field 415 (MD80 results).

A further interesting feature of figure 6.24 is that fainter than  $b_j \sim 18.2$  there is an excess in field 349 compared with field 413, present to the limit of the sample in field 349. At  $b_j \sim 18.5$  the counts in field 413 amount to 70% of those in field 349. This fraction decreases to  $\sim 60\%$  at  $b_j \sim 20.0$  but then increases again to  $\sim 63\%$  at  $b_j \sim 20.5$ . The obvious inference is that the excess is due to the large-scale structure in this field mentioned earlier. The  $\sim 20\%$  stellar contamination of the direct-plate star/galaxy separation revealed in chapter 5 is insufficient to account for all this excess. In any case the contamination exists over the entire magnitude range covered in approximately the same proportion so its effect should be manifest at brighter limits too. However, since the counts are in excellent agreement to  $b_j \sim 18.0$ , and since the star/galaxy separation was performed in the same manner on both plates, it seems likely that such contamination is also present in field 413. This suggests that the excess at  $b_j > 18.2$  is real compared with the SGP and indeed would be expected if there was a SC present in this field.

A further test performed compared observed counts at magnitudes  $b_j$  with those at  $b_j + \Delta b_j$  ( $\Delta b_j = 0.1$ ) and compared the resultant ratio with that expected if  $N(b_j) \propto 10^{0.6b_j}$ , the law for a uniform, homogeneous galaxy distribution. It is well known that faint galaxy counts increase with  $b_j$  less quickly than the expected law. The discrepancy is usually seen as the result of the need to apply K-corrections and also possibly of systematic magnitude errors. In fact deep galaxy counts, e.g. those of Ellis (1980), seem to vary roughly as  $10^{0.45b_j}$  with the deviation about that expected from the K-corrections. Figure 6.25 gives integrated ratios of the numbers of galaxies at  $b_j$  and  $b_j + \Delta b_j$  in 0.1 magnitude intervals as a function of magnitude, together with those expected from the  $10^{0.6b_j}$  and  $10^{0.45b_j}$  relations. There is much closer agreement of the observed ratios with the  $10^{0.45b_j}$  relation, especially at fainter limits.

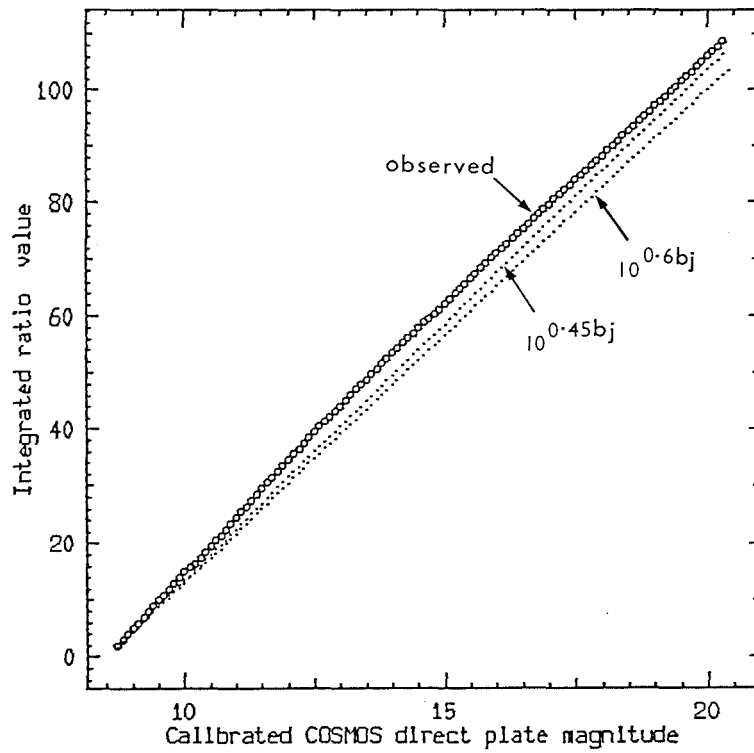


Figure 6.25 The integrated, observed ratios of the numbers of galaxies at  $b_j$  and  $b_j + \Delta b_j$  (0.1 magnitude intervals) as a function of magnitude, together with the lines expected from the  $10^{0.6b_j}$  and  $10^{0.45b_j}$  relations.

The curvature in the observed integrated ratios could be the effect of the large-scale density irregularities present in this field. Analysis of the projected 2-D distribution of galaxies in this field to  $b_j = 20.5$  will now be considered.

### 6.3.2. The 2-D statistical analysis of the projected galaxy distribution.

Individual galaxy positions will not generally be considered as statistics applied to large numbers of such objects require excessive amounts of CPU time. Instead the positional data are degraded by dividing the plate area into a 2-D array of cells, the size of which is chosen bearing in mind the typical separation between galaxies, the projected dimensions of interesting features such as clusters and the computing resources required. For this work the maximum array size used was 128 by 128 cells.

#### 6.3.2.1. Simple binning analysis.

The simplest test applied to such binned data was the construction of a histogram giving the frequency distribution of  $M$  cells containing  $N$  galaxies each. This distribution can be compared with that expected for a random distribution with the same mean and total number of objects as observed, i.e. a Gaussian with standard deviation which is the square root of the average number of galaxies per cell. The Chi-square test could be applied to test the significance of any deviations from random. Such tests have been used in the past to demonstrate that galaxies were non-randomly distributed and that significant galaxy clustering did exist, e.g. Abell (1958). However, the reliability and applicability of such tests have been questioned (see chapter 1). Moreover, the statistic produced with the Chi-square test does not indicate whether scaling of any clustering evident is present or furnish checks on isotropy. This test is

consequently of low statistical power. Nevertheless, figure 6.26 gives the histogram and corresponding overlaid Gaussian for the observed galaxy sample in field 349 to  $b_j = 20.5$ , even though no information of the details of the clumpy nature of the galaxy distribution is given. The galaxy X,Y positions were binned into a 70 by 70 array which, for the  $5.35^\circ$  by  $5.35^\circ$  plate area considered, is equivalent to  $5'$  by  $5'$  cells on the sky. The step wedge area was excluded from the analysis. Although at first glance the agreement between the observed and Gaussian relations appeared good, the frequency in each bin and the associated  $\sqrt{N}$  errors reveals that the excesses and paucities are highly significant. Indeed the resultant Chi-square statistic was  $\sim 1,200$  for 14 degrees of freedom indicating there is an exceedingly small probability that the observed distribution could have occurred by chance (e.g. the 99.9% quantile of the Chi-square statistic is 36.12). Other non-parametric statistics such as the Lilliefors test also led to rejection of the null hypothesis, 'Ho', that the observed distribution could have come from a random one, at very high confidence limits, i.e.  $\gg 99.99\%$ . These results are not surprising since the galaxy number/density contour plot of figure 5.8 reveals a clumpy galaxy distribution in this field and the presence of rich clusters. This is confirmed by the excess of cells containing  $> 15$  members compared with the Gaussian in figure 6.26. What is required is the application of more informative statistical tests which can reveal something more quantitative about the detailed nature of the galaxy distribution in this field, how it varies with angular scale, limiting magnitude and, ideally, depth. For the purposes of this thesis, 3 statistical tests designed to provide such information, at least in part, were employed, specifically, the 2-point angular correlation function, power spectrum analysis and Meads analysis. The results from the applying of each of these tests are described below.

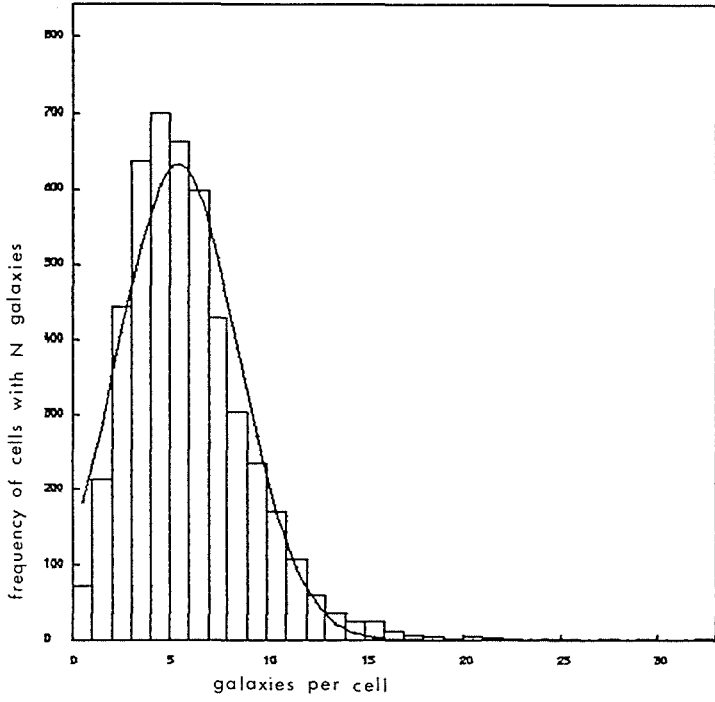


Figure 6.26 Histogram and corresponding Gaussian for the observed galaxy sample to  $b_j = 20.5$ .

### 6.3.2.2. Application of the 2-point angular correlation function.

Correlation functions, and in particular the 2-point spatial and angular correlation functions have been the most widely used statistical measures for studying the distribution of galaxies in recent years. In effect the 2-point correlation functions are simply the average of the product of the object density at point 'a' say, compared with that some fixed linear or angular distance away in a randomly chosen direction. They have been applied to all major galaxy catalogues generated so far (e.g. the CGCG of Zwicky et al, 1961-68, the Lick counts, Shane and Wirtanen, 1967, Seldner et al 1977, and the Jagellonian field, Rudnicki et al 1973). Properties of these catalogues and results from the application of the 2-point correlation functions were summarised by Groth (1980). The major contribution to the development of such statistics has been due to the efforts of a group of workers at Princeton (see Peebles, 1980, for a thorough description of the development, concepts and theory of correlation analysis). Remarkably the results from all the analyses seem to follow a simple power law of the form:-

$$\xi(r) = (r/r_0)^{-\gamma} \dots \dots \dots 6.18$$

where  $\gamma = 1.77 \pm 0.04$  and  $r_0 \sim 4.7 h^{-1} \text{Mpc}$  over the regions  $0.05 < r < 9 h^{-1} \text{Mpc}$  for the spatial function (e.g. Groth, 1980), or:-

$$W(\theta) = A\theta^{1-\gamma} \dots \dots \dots 6.19$$

for the angular function, over the scales  $10' < \theta < 3^\circ$ . Here 'A' is a constant which is strongly dependent on the depth of the sample since at greater depths there is a large increase in the number of overlapping structures seen in projection which causes the amplitude of  $W(\theta)$  to decrease correspondingly. On larger scales there seems to be a break from the power law behaviour although the position of this 'break' has been found to vary with the estimator used to furnish the correlation function results and with the data base and sample depth, e.g.  $3 h^{-1} \text{Mpc}$ , Shanks et al (1980), and  $9 h^{-1} \text{Mpc}$ , Groth and Peebles

(1977). Such discrepancies in 'break point' position between the shallow and deep samples may have serious cosmological implications since the power-law behaviour of the 2-point correlation functions are generally interpreted as due to there being no preferred galaxy clustering scales, i.e. the distribution of cluster size and density is continuous up to the break point. This picture is compatible with the gravitational instability and isothermal (matter only) theory of galaxy formation, Peebles (1974), where a power law exponent of 1.8 is predicted, in good agreement with the observed index. The break observed in the 2-point correlation function has been interpreted as the transition between linear (at larger scales than the break), and non-linear growth of density fluctuations (e.g. Davis et al, 1977). Furthermore, if the 2-point angular correlation function becomes significantly negative on larger scales, then this would indicate an anticlustering, in that the scale over which continuous clustering appears to hold is surrounded by regions deficient in galaxies, i.e. voids.

However, Hewett (1982), has shown that results from previous 2-point angular correlation analyses such as those of Shanks et al (1980), and MacGillivray and Dodd (1979), are sensitive both to the exact form of estimator used to derive the function and the type of edge correction employed. Discrepancies in the break point may thus, at least in part, be attributable to such effects. Hewett showed that an ensemble estimator of  $W(\theta)$ , such as that used by Peebles (1975), should be employed instead of direct or filtered estimators (e.g. Shanks et al 1980). This was because significantly different  $W(\theta)$  results were obtained with direct estimators, depending on the edge correction employed (such edge corrections are necessary when dealing with bound data such as a Schmidt field). The ensemble estimator though, proved to be unbiased and was little affected by use of different edge corrections. Fortunately, the direct estimators can be

reduced to the ensemble form by use of a further correction factor initially suggested by Sharp (1979), and described in detail by Hewett (1982).

Ideally, the 2-point spatial correlation function  $\xi(r)$  should be used to study the galaxy distribution. This is simply defined as the joint probability of finding two galaxies within volume elements  $dV_1$  and  $dV_2$  which are separated by distance  $r_{12}$ , i.e.:-

$$dP = N^2[1 + \xi(r_{12})]dV_1 dV_2 \dots \dots \dots 6.20$$

where  $N$  is the mean number density of galaxies per unit volume. In practice, since the physical separations between galaxies in most catalogues are unknown, the 2-point angular correlation function  $W(\theta)$  is employed. This is defined as the joint probability of finding an object within solid angle  $d\Omega_1$  and another within  $d\Omega_2$  at an angular separation  $\theta$  from  $d\Omega_1$  i.e.:-

$$dP = N'^2[1 + W(\theta)]d\Omega_1 d\Omega_2 \dots \dots \dots 6.21$$

where  $N'$  is the mean surface density of sample galaxies.

Limber (1953), derived the functional relation between the spatial and angular 2-point correlation functions which is further generalised by Phillips et al (1978). Essentially the angular functions can be written as integrals of the spatial function along the line of sight. For the purposes of this work no estimation of the spatial function is attempted and discussion is confined to application of the 2-point angular correlation function to various limiting magnitudes.

An ensemble estimator of the form employed by Peebles and Hauser (1974), was used, following the recommendations of Hewett (1982), and using his suggested edge corrector. This estimator was incorporated within a multi-purpose analysis programme written by H.T. MacGillivray and modified slightly by the author. The galaxy positional data were binned into a 128 by 128 cell array. The estimator was:-

$$\hat{W}(\theta) = \langle N_i N_j \rangle / \langle (N_i + N_j) / 2 \rangle - 1 \dots 6.22$$

where angular brackets denote averages over all cells with separations between  $\theta - \Delta\theta/2$  and  $\theta + \Delta\theta/2$  and  $N_i$  and  $N_j$  refer to the observed counts in the  $i$ th and  $j$ th cells. Figure 6.27 gives the results of applying the ensemble estimator to both the galaxy and stellar data in field 349. A square  $4^\circ$  sub-area excluding the step wedge region was used. Each cell of the array corresponded to  $\sim 1.9'$  by  $1.9'$  on the sky, and 15,064 galaxies and 16,018 stars from the original sample were included. The results from a random simulation with the same number of sources as the observed galaxy sample is also included in the plot. The galaxy, stellar and random simulation results are labelled a, b, and c respectively.

Although 20% stellar contamination of the galaxy sample has been revealed, this should not seriously affect the correlation results if the stars are randomly distributed as they add a random background which will depress the amplitude but not the shape of  $W(\theta)$ . As expected, the random simulation results are essentially flat with small, random fluctuations about zero on all scales. A flat stellar distribution is also expected if the stars were randomly distributed across the field. Any significant correlations in the stellar results could reflect galaxy contamination or plate sensitivity variations, clumpy, high galactic latitude obscuration or some other extrinsic effect. In fact, on scales  $< 0.5^\circ$ , small, positive values of  $W(\theta)$  were obtained for the stellar results.

However, their amplitude was only ~5% that of the galaxy sample. A similar effect was found by Beard (1984). Chapter 5 has shown that the stellar sample is probably free from galaxy contamination and so the small positive correlation could be the effect of weak, clumped extinction which cannot be ruled out even at such high galactic latitudes. Small-scale, localised sensitivity variations also seem an unlikely candidate for the effect, given the well-behaved nature of the sky background variation on the plate (see figure 5.8 chapter 5). The small-scale, weak, positive correlation may simply reflect the tendency for stars to form binaries. Absence of significant structure in the stellar results on scales  $> 0.5^\circ$ , illustrates that no large scale obscuration is present (unless of course it covers the entire field in a uniform manner). This is consistent with the findings of McFadzean et al (1982). Furthermore, any small scale, patchy obscuration that may be present has only a small effect. The lack of structure in the stellar sample on the same scales at which structure is evident in the galaxy results is further evidence for there being no significant galaxy contamination of the stellar sample.

Compared with the stellar and random sample results, the galaxy results appear strongly correlated and follow a fairly well-defined relation until  $-2^\circ$ , when a distinct break is evident (arrowed in the diagram). Longward of this break small but significant negative values of  $W(\theta)$ , which imply an anticorrelation, continue until the limit set by the data area. Similar weak anticorrelation longward of the break was also found by Hewett (1982), in the application of the ensemble estimator to the Jagellonian field and to a field centred on the SGP. The approximate scales at which the negative  $W(\theta)$  occurred in his data was  $1.5^\circ-1.7^\circ$ , equivalent to 10 and 11  $h^{-1}$ Mpc respectively for his derived sample depths.

For this field a typical value of  $\theta$  on which  $W(\theta)$  is most negative is  $\sim 2.5^\circ$ . If we consider the redshifts of the SC in the field at  $Z \sim 0.11$  (see later and Parker et al 1984 a,b), then this corresponds to  $14 h^{-1}\text{Mpc}$  and the break point at  $2^\circ$  corresponds to  $\sim 11.5 h^{-1}\text{Mpc}$ , in fairly good agreement with the break point of  $\sim 10 h^{-1}\text{Mpc}$  found by Davis et al (1977), from a somewhat shallower sample ( $B_{\text{lim}} = 18.6$ ), and that found for the Lick sample of  $9 h^{-1}\text{Mpc}$ , Groth and Peebles (1977).

An advantage of the ensemble estimator of  $W(\theta)$  is that it allows examination of sample properties which are unrelated to the field boundaries, since any large-scale gradients are removed by the estimation procedure (see Hewett, 1982). Hence  $W(\theta)$  should be unaffected by any large-scale gradients whether intrinsic to the galaxy distribution or due to some effect such as vignetting. Nevertheless, it is possible that the negative correlation observed at large angular scales in this field is due to the presence of the large-scale structure found. Larger samples from other UKST plates are needed before this anticlustering effect can be confirmed.

Figure 6.28 gives the result of fitting a power law of form given by equation 6.19 to the galaxy data in figure 6.27. The power index  $\gamma = 1.8$  was used together with a best fit 'A' value of 0.0175. The observed relation fits the power law well between  $0.2^\circ < \theta < 1.0^\circ$ . Longward of  $\sim 1.0^\circ$ ,  $W(\theta)$  decreases with  $\theta$  more rapidly than the power law until the distinct break at  $\sim 2.0^\circ$ .

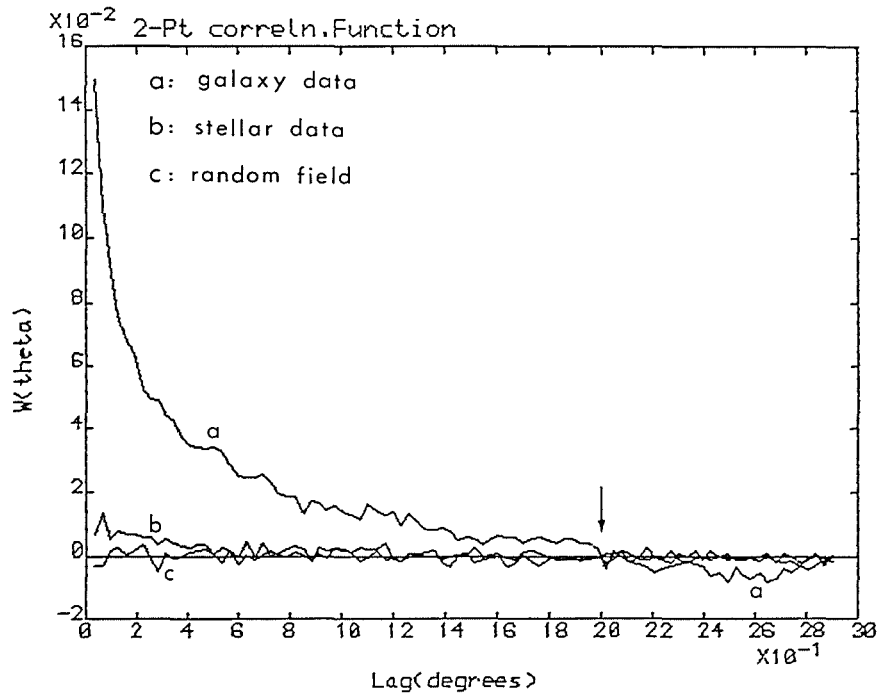


Figure 6.27 The 2-point angular correlation function results from the application of the ensemble estimator to both the stellar and galaxy data to  $b_j=20.5$ .

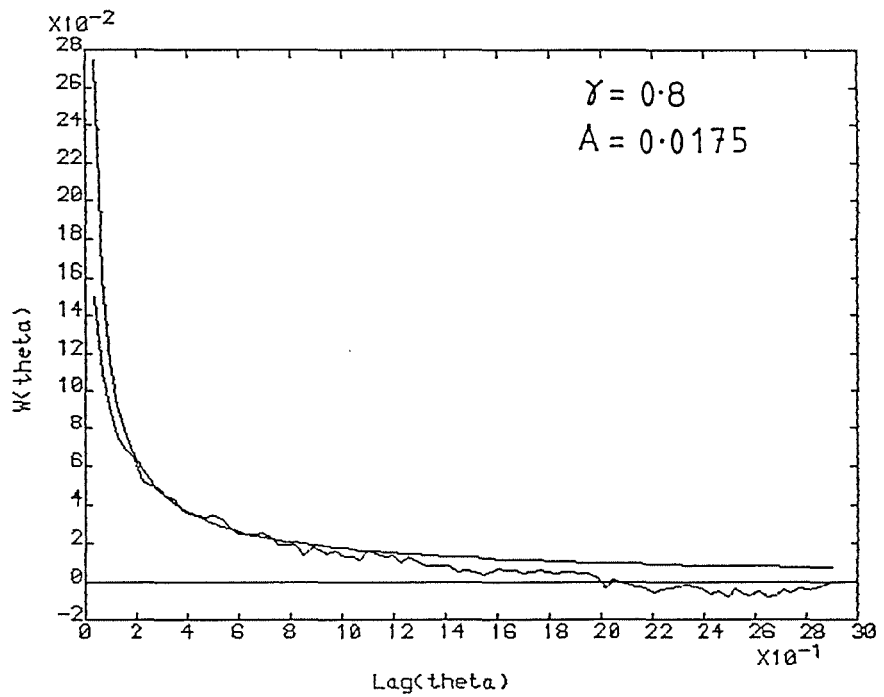


Figure 6.28 Result of fitting a power law of index  $\gamma = 1.8$  to the galaxy data of figure 6.27, following the form of equation 6.19.

Figure 6.29 gives the ensemble estimator results for the galaxy data to different limiting magnitudes, i.e.  $b_j < 20.5$ ,  $20.0$ , and  $19.0$ , labelled a, b and c in the plot. The same general shape of angular function is obtained with  $W(\theta)$  amplitude decreasing with increasing magnitude as expected. This indicates a scaling of the function with magnitude limit and consequently sample depth. Individual features are reproduced in all 3 curves, particularly curves b and c. Furthermore, the break point at  $\sim 2.0^\circ$  is reproduced in all cases, as is the negative depression between  $\sim 2.0^\circ - 2.9^\circ$ . Similarly, the type of correlation function found for the shallow Zwicky catalogue was also reproduced in the deeper Lick and Jagellonian catalogues. The  $W(\theta)$  results from the different depth catalogues have been compared using a scaling relation, i.e. if the effective depth of a catalogue penetrating to apparent magnitude  $m_0$  is:-

$$D = \log [0.2(m_0 - M) - 5] \dots \dots \dots 6.23$$

where  $M$  is the typical absolute magnitude of a galaxy, then the scaling relation (see Groth, 1980), is:-

$$W(\theta) = W(\theta D)/D \dots \dots \dots 6.24$$

Without knowledge of the luminosity function and typical sample depths for the magnitude-limited samples, the 2-point angular correlation functions for different 0.5 magnitude intervals were considered. The results are given in figures 6.30a-e. The most striking feature is progression of the 'break point' or scale where the  $W(\theta)$  results become consistently negative or zero. This varies from about  $2.4^\circ$  for  $18.0 < b_j < 18.5$ , to  $\sim 0.8^\circ$  for  $20.0 < b_j < 20.5$ , although it is difficult to say where the break point occurs in all cases due to the scatter in  $W(\theta)$ . Since the magnitude interval samples are crude depth samplings, then if the break point was occurring at a similar physical size for different depths, we would expect the angular size of the break to scale accordingly.

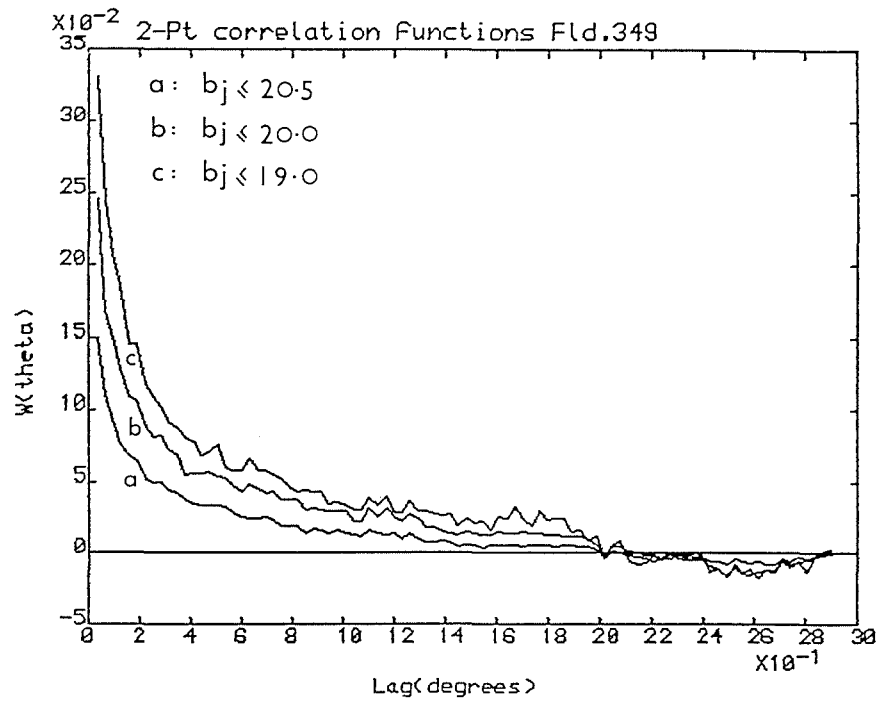


Figure 6.29 Results of applying the ensemble estimator of the 2-point angular correlation function to the galaxy data at different limiting magnitudes.

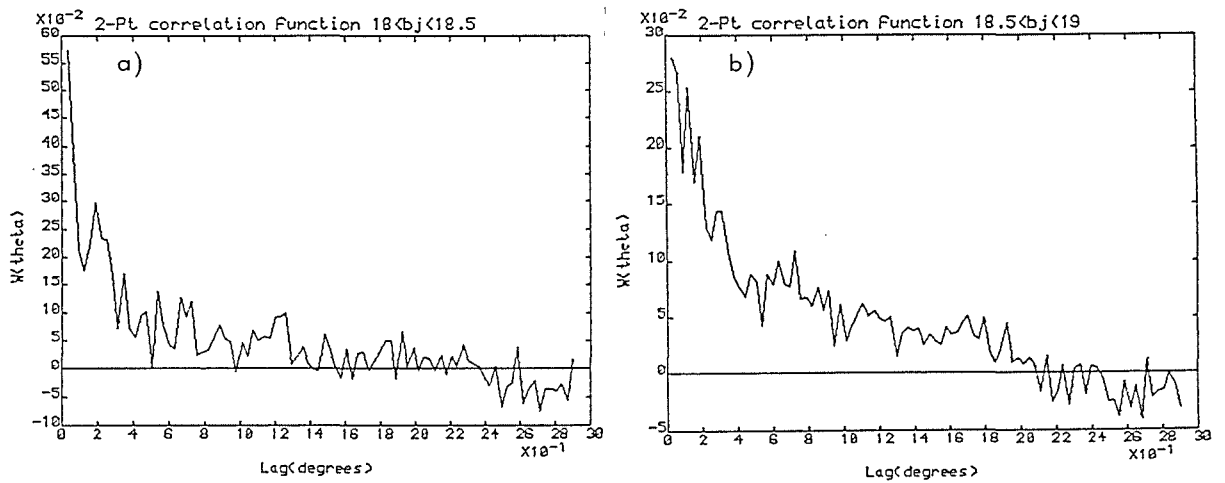


Figure 6.30a-b Results from application of the ensemble estimator to the galaxy data within various magnitude intervals.

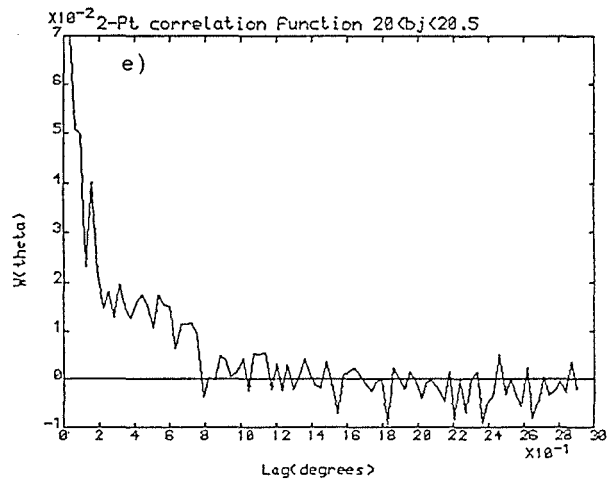
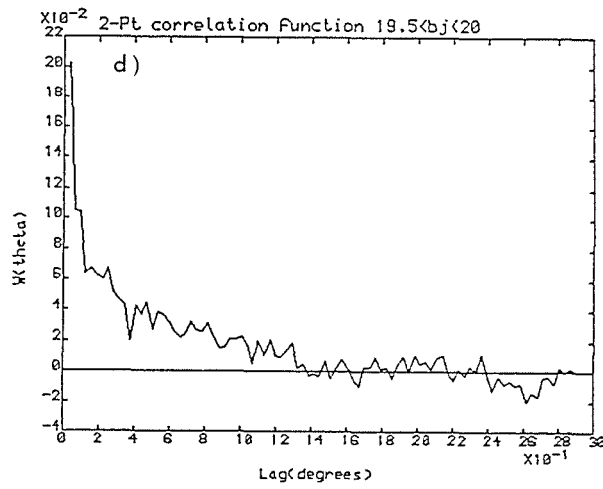
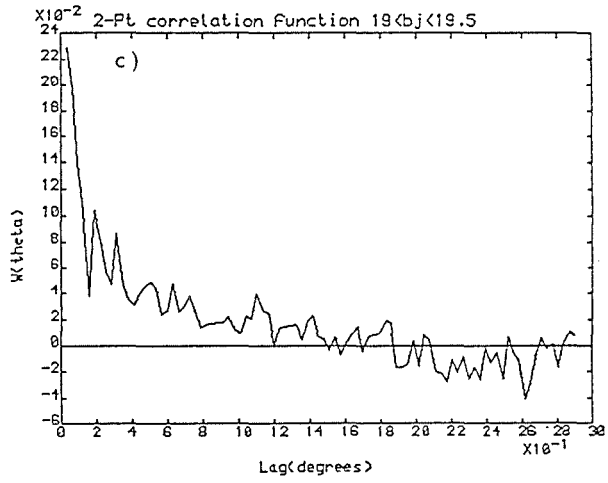


Figure 6.30a-e Results from application of the ensemble estimator to the galaxy data within various magnitude intervals.

A simple test of this supposition was performed. Firstly, a typical redshift for galaxies in the interval  $18.0 < b_j < 18.5$  was obtained by examining the objective-prism redshift histogram (figure 6.31), for all galaxies in this interval that yielded INTERZED objective-prism redshifts (see later). The redshift peak was at  $Z \sim 0.11 \pm 0.01$ . Using an apparent magnitude of  $b_j = 18.25$ , the distance derived from the typical redshift and the distance modulus formula, yielded a 'typical' absolute magnitude for the sample of  $M_{b_j} = -19.34$ . This magnitude was used for all the other magnitude interval samples. The mid-range apparent magnitude for each sample was used to determine a typical depth for each sample from the distance modulus. This technique is inherently crude given the assumption of absolute-magnitude constancy for each deeper sample, i.e. that a universal luminosity function applies over the entire sample depth, and an apparent magnitude choice for each sample that lies in the mid-range of magnitude covered. Hence the numbers of objects in each interval will be dominated by contributions from the fainter end of the range covered. Nevertheless, once a typical depth 'r' for each sample was obtained, this was used with the formula  $S = r\theta$  ( $\theta$  in radians), where  $\theta$  is the angular scale of the break point in each case, to yield the physical size 'S' of the break point. The results are summarised in table 6.3. The errors associated with each 'S' value of  $\sim 1.5$  Mpc were only calculated on the basis of  $\pm 0.01$  errors in redshift and  $\pm 0.1$  errors in selected break point position, which, in the latter case at least, are probably optimistic. No account was made for any variation in typical absolute magnitude employed nor the effect of using a mid-range of apparent magnitude in the distance modulus formula. Consequently, considering these uncertainties and the assumptions made, the results of table 6.3 appear remarkably consistent, with the observed break-point position in each sample apparently scaling quite well with depth.

table 6.3

$b_j$	$b_j$	$d(\text{mpc})$	$Z_{\text{typ}}$	$b(\theta)$	$S_b(\text{Mpc})$
18.25	$18.0 < b_j < 18.5$	330	0.11	$2.4^\circ$	$13.8 \pm 1.4$
18.75	$18.5 < b_j < 19.0$	415	0.14	$2.1^\circ$	$15.2 \pm 1.4$
19.25	$19.0 < b_j < 19.5$	522	0.17	$1.9^\circ$	$17.3 \pm 1.4$
19.75	$19.5 < b_j < 20.0$	646	0.21	$1.4^\circ$	$16.1 \pm 1.4$
20.25	$20.0 < b_j < 20.5$	828	0.28	$0.8^\circ$	$11.6 \pm 1.5$

Where:-

- 1) 'd' refers to an approximate sample depth for the appropriate magnitude interval  $b_j$ .
- 2) 'Z<sub>typ</sub>' is a typical redshift for the given magnitude interval.
- 3) '  $b(\theta)$ ' refers to the selected position of the break point.
- 4) 'S<sub>b</sub>' refers to the calculated physical scale of the break points.

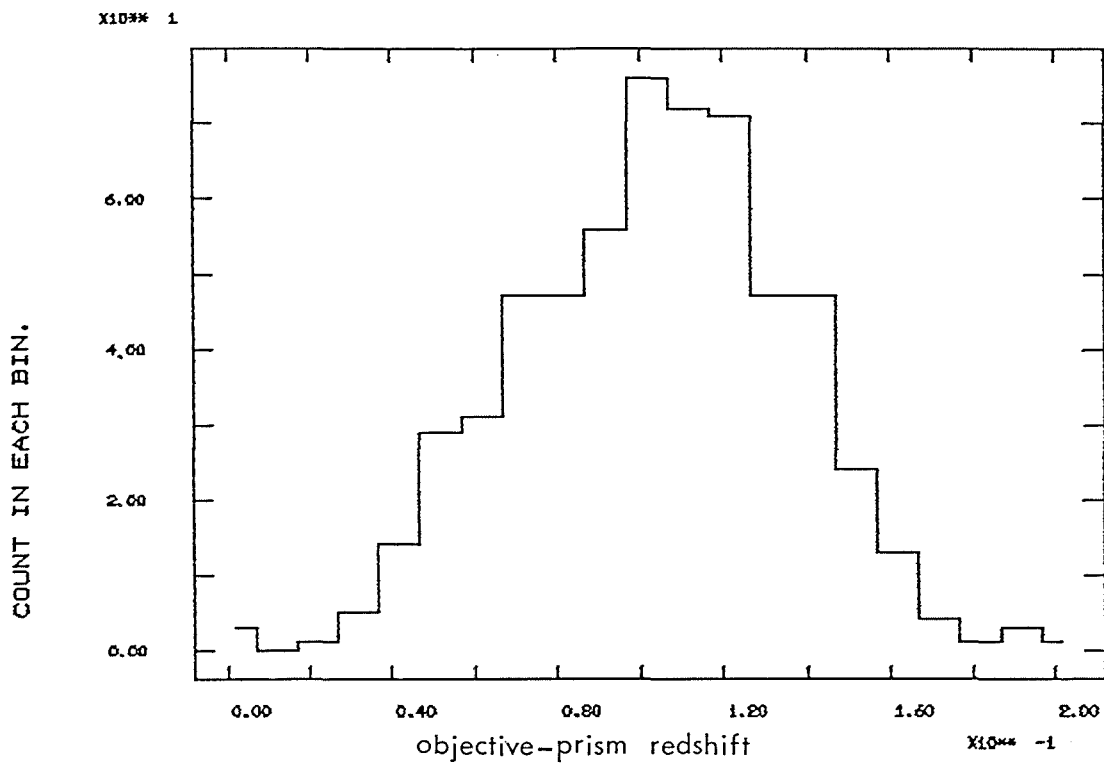


Figure 6.31 Redshift histogram for galaxies in the magnitude range  $18.0 < b_j < 18.5$  from INTERZED measures.

Such consistency in the correlation function over a wide range of sample depth has previously been demonstrated from the analyses of the Zwicky, Lick and Jagellonian catalogues. This was surprising considering the difficulties in correctly allowing for effects of variable extinction and plate-to-plate variations encountered in the shallower Zwicky and Lick catalogues (which covered wide expanses of the celestial sphere), and other selection effects. Fortunately, most of these problems are absent in this study since only a single Schmidt field is considered, although analyses of narrow-angle, deep samples are susceptible to effects of plate emulsion sensitivity variations, vignetting, measuring machine inaccuracies and even small-scale, clumped galactic extinction. A further limitation is that the projected physical extent of the field is small compared to the depth sampled. For a depth of  $\sim 830$  Mpc, corresponding to  $Z = 0.28$ , the X,Y extent would be only 60 by 60  $h^{-1}$  Mpc. Hewett (1982), states that the correlation results from such samples would significantly affect the estimates of  $W(\theta)$  if the field contained some large-scale feature and as a result would not be a 'fair' sample of the Universe.

An interesting observation is that the break point in figure 6.30b occurs at  $\theta \sim 2.1^\circ$ , in fair agreement with that in figure 6.29. This confirms that the contribution to  $W(\theta)$  at bright limits is dominating the fainter sample's break-point position. As will be shown later in the section on objective-prism redshifts, this is probably due to the presence of a foreground SC at  $Z \sim 0.05$ . In conclusion, the 2-point angular correlation function for galaxies to  $b_j = 20.5$  in this field seem to indicate a break point at  $\sim 15 h^{-1}$  Mpc (c.f. 9  $h^{-1}$  Mpc for the Lick catalogue), which seems to scale with depth. The functions' power-law nature is demonstrated to  $\theta \sim 1.0^\circ$ , with a reasonable fit to a  $\gamma \sim 1.8$  exponent for the sample to  $b_j = 20.5$ . This can be interpreted as strong evidence for continuous, hierarchical, galaxy clustering. The stellar sample results though,

indicate a possible extrinsic effect on the data but the magnitude of this effect is small.

Although correlation functions have been used extensively in galaxy-clustering studies, the amount of information furnished is relatively small. No specific details regarding individual structures or clusters is obtained, apart perhaps indirectly from statistical irregularities in the observed function. A measure of the average degree of irregularity as a function of characteristic scale length is given however, and this in itself is an interesting parameter that arises naturally in the theory of evolution of irregularities in an expanding Universe. However, a main disadvantage of the 2-point correlation function techniques is that they seem relatively insensitive to certain features that may be intrinsic to the galaxy distribution, such as the existence of voids, filaments and sheets. These features may themselves yield important information concerning the likely galaxy formation process.

Even the spatial 2-point galaxy correlation function  $\xi(r)$  is relatively insensitive to the manner in which clustering has evolved, (e.g. see Dekel and Aarseth, 1984). However, there is a more general problem associated with the correlation function in that the observed function at a given scale depends on effects in the data that may have a number of different scale lengths, see Tukey (1967), and Peebles (1973). For instance in the Lick catalogue, which covered  $\sim 11,000$  square degrees, there were inevitably large-scale variations in the observed galaxy number density due to effects of galactic obscuration and confusion. Inevitably, the derived correlation function at large scales would be affected. This large-scale coherence influences the apparent correlation function on small scales too. Such mixing of effects at different scales affects many statistical measures making a meaningful analysis difficult.

However, Peebles (1973), found that the "power spectrum", which is the square of the Fourier transform of the density distribution in flat space, can alleviate this problem to some extent. The power spectrum gives an immediate display of irregularity as a function of characteristic scale length and is considered a more powerful test for clustering than other statistical tests such as the correlation function, binning analysis and nearest-neighbour analysis (e.g. Bogart and Wagoner, 1973). For instance, Webster (1975), stresses that the NNA is greatly inferior to power spectrum analysis (hereafter PSA) in both flexibility and power as there is no way of applying the NNA to check on scaling or isotropy of any clustering revealed by the test. Furthermore only the nearest-neighbour distance of a given point is investigated, whereas the PSA uses information on the separation of all pairs of points. Consequently this test was also applied to the sample under study.

6.3.2.3 Results from a Power Spectrum analysis of the galaxy distribution.

Details of the techniques of PSA can be found in Peebles (1973), and Webster (1975,1982). Briefly, the distribution of galaxies can be considered replaced with a distribution of delta functions, then the square of the Fourier transform of this function is its power spectrum. As a 1-D example, if  $m$  points are scattered along a line of length  $2\pi$ , each of position  $X_j$ ,  $j = 1,2,3\dots m$ , with the origin at the line's mid-point, then if a delta function is considered at each point of strength  $\pi$ , a function representing these points can be defined as:-

$$f(X) = \pi \sum_{j=1}^m \delta(X - X_j) \dots \dots \dots 6.25$$

The Fourier transform of this is:-

$$F(u) = \sum_{j=1}^n e^{(i u x_j)} \dots \dots \dots 6.26$$

Following Webster (1975), we obtain the basic 1-D PSA statistic:-

$$I(u) = \frac{2}{n} | F(u) |^2 \dots\dots\dots 6.27$$

This is the normalised modulus of the square of equation 6.26 above. If the 2-D distribution of galaxies on the sky in true spherical co-ordinates is considered, then the exponential in equation 6.26 is replaced by a spherical harmonic, making the situation much more complicated, Peebles (1980). Considering the small angular extent of this field a projection of objects from the celestial sphere onto a 2-D surface was used in a Fourier PSA following Webster (1975,1980). This has the great advantage that the Fourier analysis is much easier to perform. Consequently, a 2-D PSA program was written by the author following the mathematical description of Webster (1975). Webster has shown that  $I(u)$ , is asymptotically distributed as Chi-square with 2 degrees of freedom, with the null hypothesis,  $H_0$ , that the 2-D distribution of objects is uniform, random and independent. To test for clustering on a scale size  $\lambda_c$ , say, the  $N$  values of  $I_u$  (excluding  $I_{-u} = I_u$ ) with  $\lambda_u > \lambda_c$ , are summed to form  $\Sigma I$ , i.e.:-

$$\Sigma I = \sum_{u=1}^n I_u \dots\dots\dots 6.28$$

This is distributed as  $\chi^2_{2u}$  with  $\Sigma v = 2N$  degrees of freedom to a good approximation. The final PSA statistic was defined as:-

$$Q = \Sigma I / \Sigma v \dots\dots\dots 6.29$$

Consequently, the expectation value of  $Q$  is 1 on the null hypothesis, and from the properties of Chi-square the standard deviation of  $Q$  is  $\sqrt{2/\Sigma v}$ . Thus, in the presence of clustering, the expectation value of  $Q$ ,  $E(Q)$ , gives the mean number of objects per cluster,  $\langle q \rangle$ . The scale size  $\lambda_c$  is not known beforehand and so statistics:-

$$Q' = \Sigma I' / \Sigma v' \dots\dots\dots 6.30$$

are formed initially, where the primed summations are over equal intervals in  $1/\lambda$ . A plot of  $Q'$  versus  $1/\lambda$  is then produced from which  $\lambda_c$ , the significant clustering scale of the sample can be isolated. The characteristic scale of any clustering is assessed by points greater than unity  $\pm \sigma$  ( $\sigma$  is independent of the number of objects in the sample). The significance of this clustering is then considered from the sum of  $Q'$  for all terms up to the scale on which  $Q' = 1$ .

A further advantage of PSA is that well-established means exist for determining the amount of contamination in the observed power spectrum, caused for instance, by sensitivity variations between plates where the PSA is carried out over a wide area (e.g. Peebles, 1973). Spurious effects in those PSA statistics whose wavelength is comparable with or greater than the diameter of a plate ( $\sim 5^\circ$ ) are expected. In 2-D the equivalent of equation 6.26 is:-

$$F_{uv} = \sum_{j=1}^m \exp i (uX_j + vY_j) \dots\dots\dots 6.31$$

where  $(X_j, Y_j)$  are the co-ordinates of the  $j$ th point and 'u' may be zero or any positive integer and 'v' may be any positive or negative integer (except if  $u = 0$ , in which case 'v' may only be positive). We get:-

$$I_{uv} = 2/m |F_{uv}|^2, \Sigma I = \sum_{u,v} I_{uv}, \Sigma_v = \sum_{u,v} 2 \dots\dots 6.32a-c$$

In a 2-D projection the purely 1-D terms, i.e. those with  $u = 0$  and  $v = 0$ , are routinely excluded to avoid the effects of any artificial stripes that might exist because of the special directions of the co-ordinate axes.

Application of the 2-D PSA to the galaxy data in this study was based on the RA's and Dec's of the galaxy sample to  $b_j = 20.5$ . As for the 2-point correlation function, 2-D PSA would be performed to different magnitude limits and over various 0.5 magnitude intervals. Projection of the galaxy celestial co-ordinates onto a 2-D surface was required. For this purpose a suitable tangent-plane projection program was kindly provided by Dr.R.G.Clowes. Final object co-ordinates were in degrees relative to the field centre. The resultant co-ordinates for each galaxy sample were then read to the author's 2-D PSA program. The assumptions are that if galaxies were uniformly distributed on the celestial sphere then their projection will also be uniformly distributed, and also that no artificial density irregularities would be introduced by use of such a projection. For the size of field considered here, over a narrow range of declination, these assumptions will be a good approximation. The 2-D PSA is applied over the largest rectangular area of X and Y that can be accommodated without exceeding the bounds of the data, since artificial density irregularities at the edges could introduce spurious effects into the PSA results. Thus a square  $\sim 4^\circ$  sub-area excluding the step wedge region was used.

As a test, the 2-D PSA was initially applied to the stellar data to  $b_j = 20.5$ . A flat power spectrum with small  $\pm 1\sigma$  fluctuations about  $Q' \sim 1$  (the expectation value at all scales on the null hypothesis), might be expected if the stars were randomly distributed and if non-intrinsic effects on the projected stellar distribution were small (e.g. such as vignetting). In figure 6.27 though, some excess of power in  $W(\theta)$  at scales  $< 0.5^\circ$  was observed for the same stellar sample so a similar excess in the PSA results might also be expected. In fact, if anything the converse situation holds. Figure 6.32a gives the 2-D PSA results for the stellar sample to  $b_j = 20.5$  in the  $4^\circ$  by  $4^\circ$  area. The power spectrum is essentially flat between

$1.35 < 1/\lambda < 6.2$ , corresponding to scale lengths between  $0.7^\circ$  and  $0.15^\circ$ . Between  $2.1 < 1/\lambda < 3.0$  though, covering scales from  $\sim 0.5^\circ$  to  $\sim 0.3^\circ$ , there is evidence of some feature in the power spectrum since the PSA switches from  $\sim 2\sigma$  below unity to  $\sim 2\sigma$  above unity. On scales  $> 0.73^\circ$  up to  $\sim 2.7^\circ$ , quite significant deviations from unity of up to  $5\sigma$  were obtained. A maximum of  $Q' \sim 3$  is attained at  $\theta \sim 1.6^\circ$ . This denotes the average multiplicity of objects in each cluster. From figure 6.32a the scale of significant clustering can be considered to be  $\lambda_c \sim 0.73^\circ$ . The sum of  $Q$  up to this  $\lambda_c$  value is  $2.073 \pm 0.141$ . Now the PSA statistic used is very sensitive to weak clustering. Consequently the effect in the 2-D stellar PSA results at large scales might not be evident in the 2-point correlation function. The reality of the stellar clustering scale of  $\sim 0.73^\circ$  is dubious and is likely due to some extrinsic effect. Although the magnitude of these extrinsic effects on the projected stellar distribution may be small, so that they are not revealed in the 2-point correlation function results (figure 6.27), which was flat and indistinguishable from a random field on scales  $0.5^\circ < \theta < 2.9^\circ$ , the increased sensitivity of the 2-D PSA statistic may have been sufficient to pick up the results of such effects on larger scales.

However, the 2-D PSA does not pick up any excess of power at small scales i.e.  $\theta < 0.5^\circ$ , over that expected for a random distribution as found in the 2-point correlation function results. This may be an artefact of the way the data was treated in each case, since objects were binned into a 128 by 128 celled array for the correlation analysis whereas individual object positions were considered for the 2-D PSA. Furthermore, the PSA results cover equal intervals of  $1/\lambda$  (in this case the bin width was  $0.25 \text{ deg}^{-1}$ ), which correspond to unequal intervals in  $\theta$ . Also the last 15 points plotted between  $3 < 1/\lambda < 6$  only cover  $\sim 0.2^\circ$  so that their significance is small.

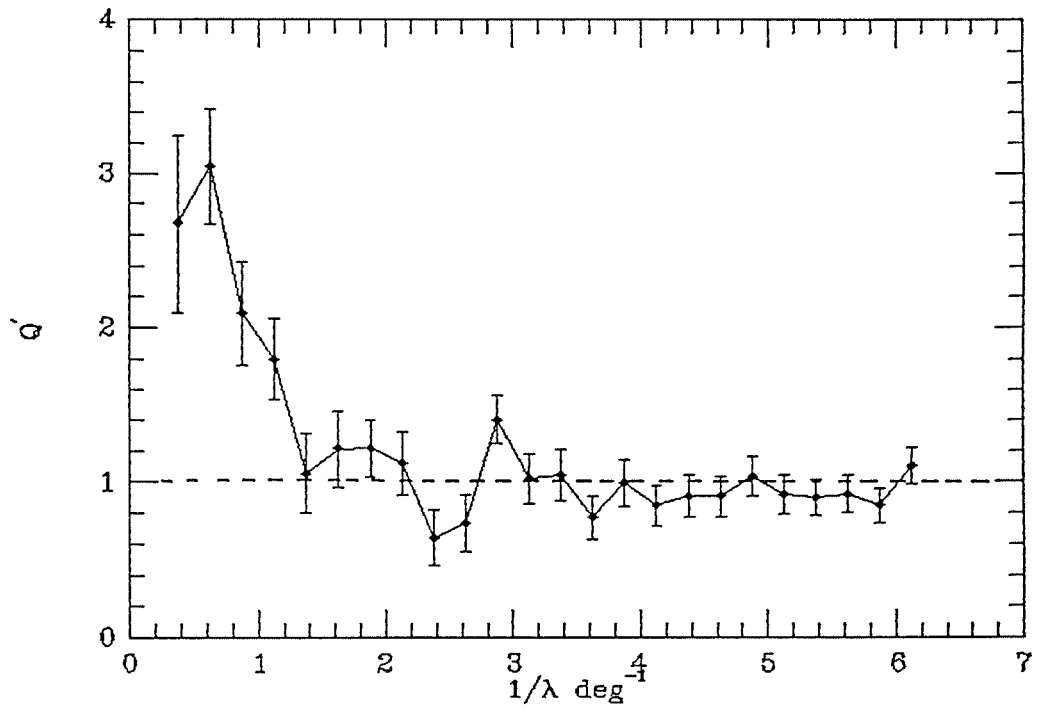


Figure 6.32a The 2-D PSA results for the stellar sample to  $b_j = 20.5$  in the  $4^\circ$  square sub-area of the field which excludes the step wedge region.

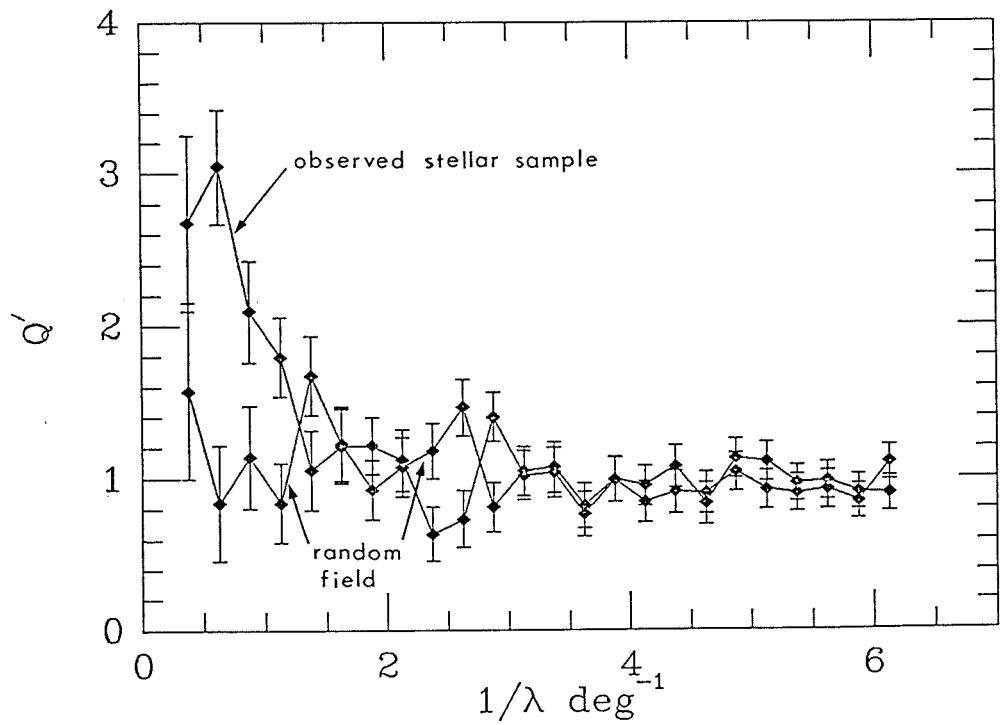


Figure 6.32b The 2-D PSA results for a random field superimposed on the observed stellar results.

To determine whether the excess in the 2-D PSA at larger scales was an artefact of the algorithm, a random field was generated with the same X,Y limits and total number of objects as for the stellar sample so that the results should be directly comparable. Figure 6.32b gives the 2-D PSA results from the random and stellar fields superimposed. For  $1/\lambda < 3$ , i.e.  $\theta < 0.3^\circ$ , the results are in excellent agreement whereas at  $1/\lambda < 3$  till  $1/\lambda \sim 1$  the random and stellar samples appear almost mirror-imaged about the  $Q' = 1$  line expected for unclustered objects. This suggests that the apparent feature in the 2-D PSA for the stellar field between  $2.1 < 1/\lambda < 3.0$  might not be an unlikely result from a random field. Nevertheless, although PSA results for the stellar and random fields are in good agreement between  $\sim 0.16^\circ$  and  $\sim 0.9^\circ$ , with the discrepancy generally  $< 1\sigma$  (but never more than  $2\sigma$ ), the excess of power in the stellar results on larger scales does seem to be real, since although the fluctuations in  $Q'$  about  $Q' = 1$  increase in amplitude on larger scales in both cases, the random field results still lie within  $\pm 1\sigma$  of unity. Consequently, there must be some effect on the stellar distribution causing this excess of power over that expected for a random point distribution. Bearing these initial results in mind, the results from the 2-D PSA on the galaxy data are considered.

Figure 6.33 gives 2-D PSA results for the galaxy sample in the  $4^\circ \times 4^\circ$  sub-area to  $b_j < 20.5, 20.0, 19.5$  and  $18.5$ , (labelled a,b,c,d and 'e' on the plot). In all cases, the power deviates significantly from unity, at  $1/\lambda < 2.0$ , though the amplitude increases with sample depth. The smallest  $1/\lambda$  point plotted corresponds to a scale of  $\sim 2.7^\circ$ . The similarity in results at  $1/\lambda > 3.4$ , regardless of sample magnitude limit, indicate that little useful information is being furnished by these points (corresponding to scales  $< 0.3^\circ$ ). However, at  $\theta > 0.3^\circ$ , the different samples do begin to reveal substantial differences in  $Q'$  amplitude (as one might expect).

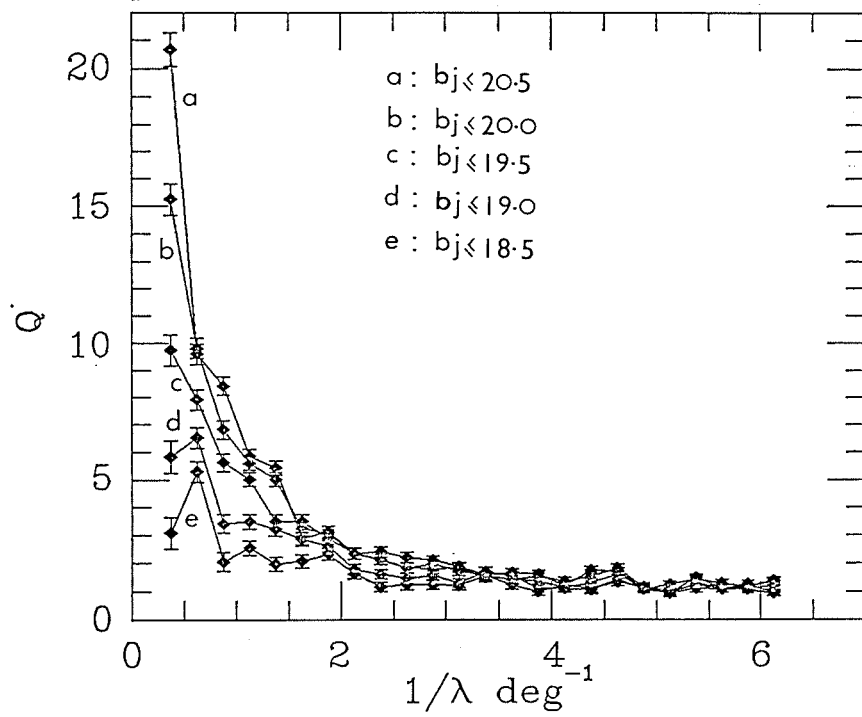


Figure 6.33 The 2-D PSA results for the galaxy sample to different magnitude limits, curves labelled a-e.

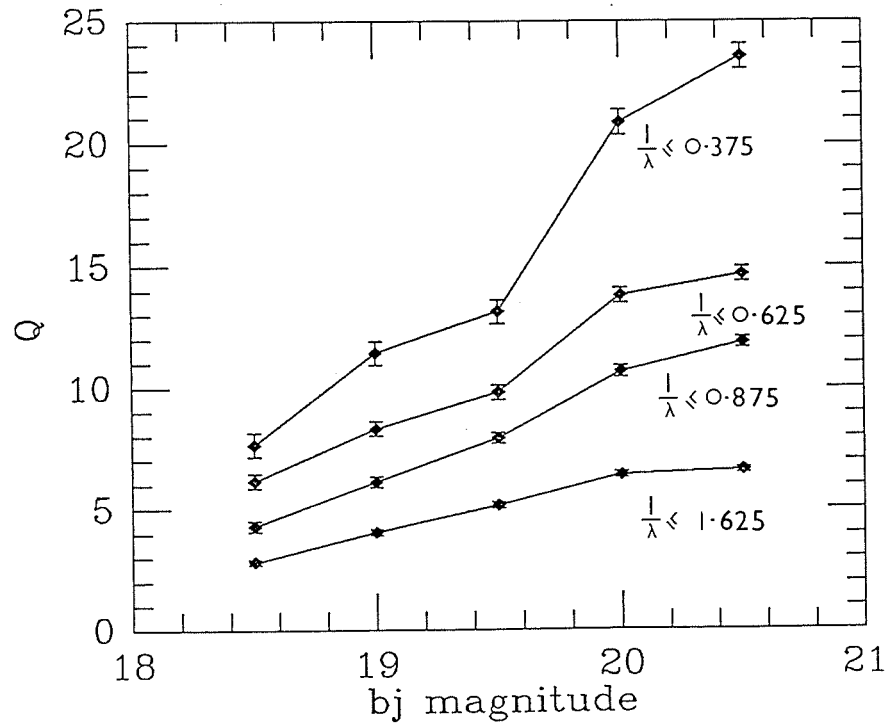


Figure 6.34 Plot of Q versus limiting  $b_j$  magnitude for four values of  $\lambda_c$ .

If the clustering was scaling with depth, the characteristic size should shift to smaller scales as fainter galaxies are included, since more distant clusters are being sampled. Consequently any significant feature evident at bright limits should move to larger  $1/\lambda$  values with increasing magnitude limit. If there were clustering of objects in some hierarchical fashion, then this ought to be manifest as distinct peaks in the PSA results at  $1/\lambda$  values that correspond most closely to the preferred clustering scale.

Such a feature is evident in the different magnitude-limited samples of figure 6.32 as a sudden jump in  $Q'$  amplitude in going from larger to smaller values of  $1/\lambda$ , i.e. smaller to larger angular scales. The smaller fluctuations in  $Q'$  values at  $1/\lambda > 2$  is perhaps not surprising since equal  $0.25 \text{ deg}^{-1}$  intervals in  $1/\lambda$  correspond to decreasing angular scales, whereas for  $1/\lambda < 2$ , each decrement in  $1/\lambda$  corresponds to a larger jump in angular scale. Thus, if clustering were present on some preferred scale in excess of any clustering there might be on other scales, then a jump in  $Q'$  at the  $1/\lambda$  which corresponds most closely to this scale might not be unexpected. This jump does shift to smaller scales on going from curve 'e' to 'a', expected if the clustering was scaling with depth. For curves 'd' and 'e', this jump defines a power spectrum peak at  $\sim 1.6^\circ$ , particularly pronounced in curve 'e'. There is no corresponding dip in the power spectrum for the fainter samples at scales  $> 1.6^\circ$ , probably because for the brighter samples the next largest physical scale of clustering is outside the bounds of the area covered. This PSA peak for the  $b_j < 18.5$ , and  $b_j < 19.0$  samples, occurs at about the same angular scale of  $\sim 1.6^\circ$  as the large projected feature evident from the surface number-density contour plot of this field of figure 5.8, chapter 5 and noted by Parker et al (1984a,b). The  $Q$  values for the samples with  $b_j < 18.5$  and  $b_j < 19.0$ , at  $\lambda_c \sim 1.6^\circ$ , were  $6.15 \pm 0.30$  and  $8.31 \pm 0.30$  respectively. The errors are the  $\pm 1\sigma$  values

calculated on the basis of the null hypothesis.

A final consideration is the behaviour of  $Q$  at a given  $\lambda_c$  value for different magnitude limited samples. Peebles (1973), notes that  $Q$  is expected to increase with apparent magnitude limit for a given  $\lambda_c$  if the observed clustering is indeed an intrinsic property of the galaxy distribution. This is because although more clusters will appear at fainter limits, those already evident in the brighter samples by their most luminous members will also become more populated. Consequently figure 6.34 is the run of  $Q$  with limiting  $b_j$  magnitude for four values of  $\lambda_c$ , (specifically 2.67, 1.60, 1.14 and 0.60, curves a,b,c and d in the diagram respectively). An increase in  $Q$  with increasing magnitude limit is indeed seen for all  $\lambda_c$ . The galaxy distribution appears strongly clustered for all magnitude-limited samples although the very large  $Q$  values at large angular scales must, at least in part, be due to superposition effects from different clusters along the line of sight. Nevertheless, the break point position in the different magnitude-limited samples does behave as if the clustering was scaling with depth, varying from  $\sim 0.6^\circ$  at  $b_j < 20.5$  to  $\sim 1.15^\circ$ - $1.6^\circ$  at  $b_j < 18.5$ .

As with the 2-point correlation function, the PSA was also performed on the galaxy data in successive 0.5 magnitude intervals. The results are given in figure 6.35a-e. This was a crude attempt to lessen the contributions to the PSA statistics from superposition of objects from widely different depths. An interesting feature of figure 6.35 is the jump in  $Q'$  from  $\sim 1$  to  $\sim 2.5$  in a,b,c and from  $Q' \sim 2 \sim 4.5$  in figure 6.35d. These jumps in  $Q'$  are unlikely due to larger increments in  $\lambda_c$  since the jump position is different for each sample and generally moves to smaller scales with fainter magnitude range, expected if such a feature was scaling with depth.

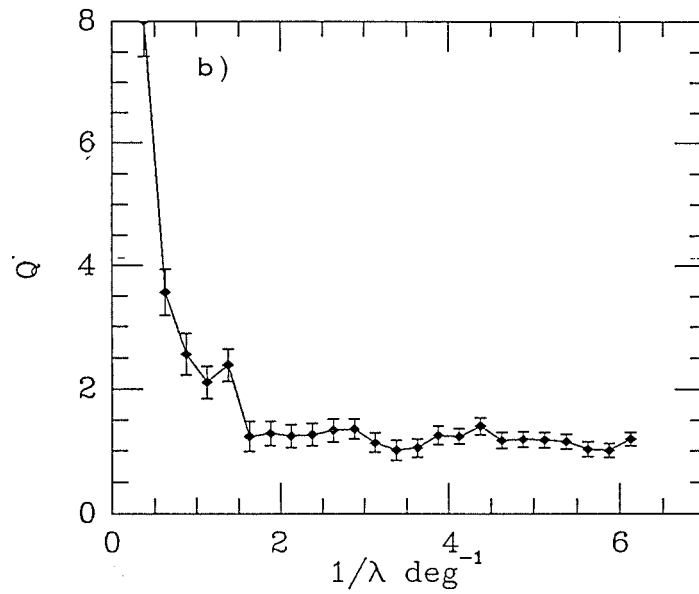
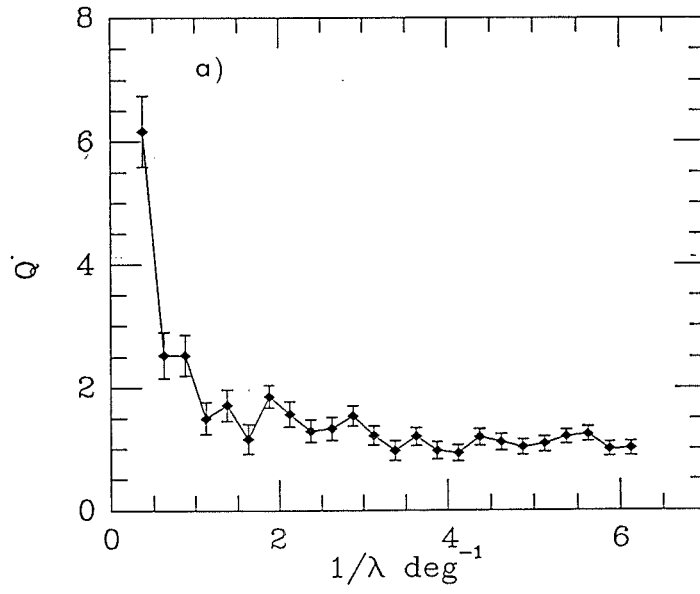


Figure 6.35a-b PSA results for different magnitude range galaxy samples.

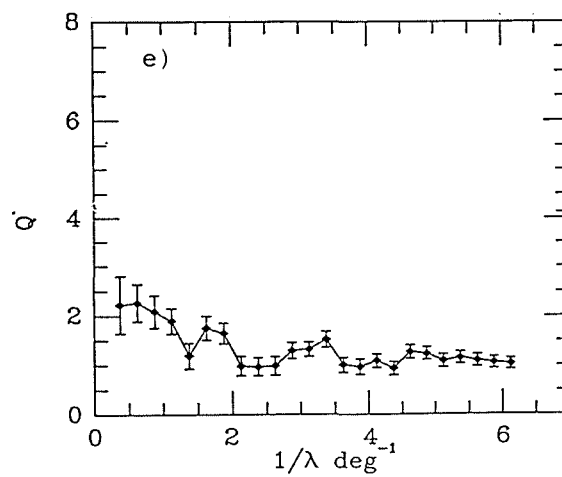
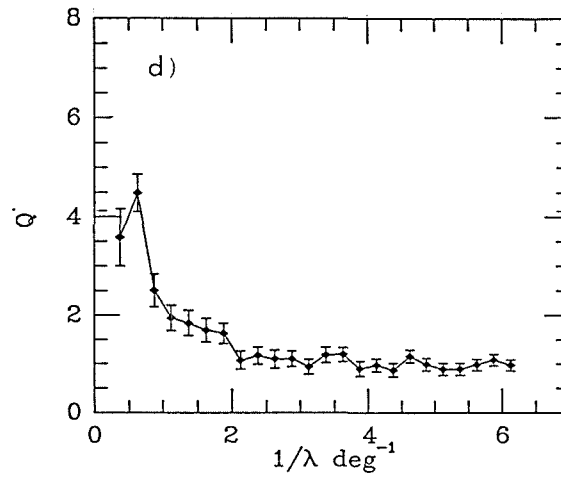
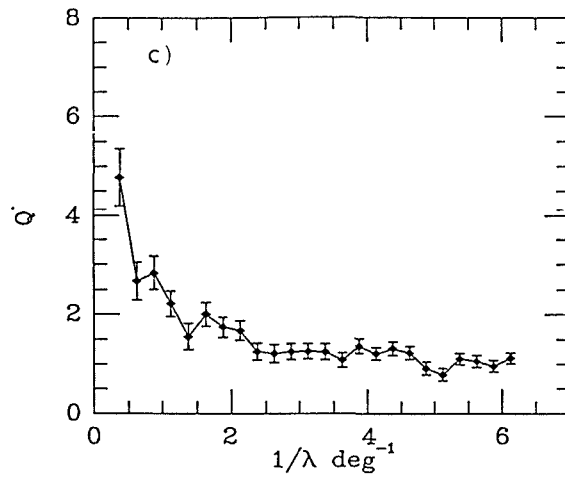


Figure 6.35c-e PSA results for different magnitude range galaxy samples.

In fact, apart from curve 'a', the break positions correspond closely to positions of equivalent 'breaks' in figure 6.33. Figure 6.35d exhibits a peak in the PSA statistic in the same position as in curve 'd' of figure 6.33, again presumably for the same reason as mentioned earlier. No significant break is evident in figure 6.35e for the brightest range covered, although comparison of the PSA results with a corresponding random field, (figure 6.36), does indicate clustering with an average of 2 members per cluster on scales  $> 0.89^\circ$  ( $Q = 2.13 \pm 0.17$ ), a  $5\sigma$  deviation from unity. In no case does  $Q'$  exceed  $\sim 8$  when the galaxy data is considered in 0.5 magnitude intervals. Furthermore, the largest  $Q'$  value is attained not for the faintest sample (figure 6.35a), but for the next faintest sample (figure 6.35b). Because each sample is magnitude, not depth limited, and since no cluster luminosity function is adopted,  $Q$  is only a relative indication of average cluster membership.

In conclusion, the 2-D PSA of the galaxy distribution over various magnitude intervals and limits seems to reveal the following information.

(1). Galaxies in this field are clustered on scales  $> 0.3^\circ$ , even for the brightest magnitude sample. The clustering strength, assessed by the deviation of  $Q'$  from unity at a given value of  $1/\lambda$ , increases at all  $\theta > 0.3^\circ$  for each magnitude limited sample so that the average number of objects per cluster,  $Q (= \langle q \rangle)$ , at a given  $\lambda_c > 0.3^\circ$  also increases with fainter limits.

(2). Although clustering on all scales  $\theta > 0.3^\circ$  is evident, particularly on the largest scales, there is distinct evidence of a feature or 'jump' in the clustering significance at specific  $\lambda_c$  values. This jump position moves to larger angular scales with decreasing magnitude limit, expected if the clustering was scaling with depth.

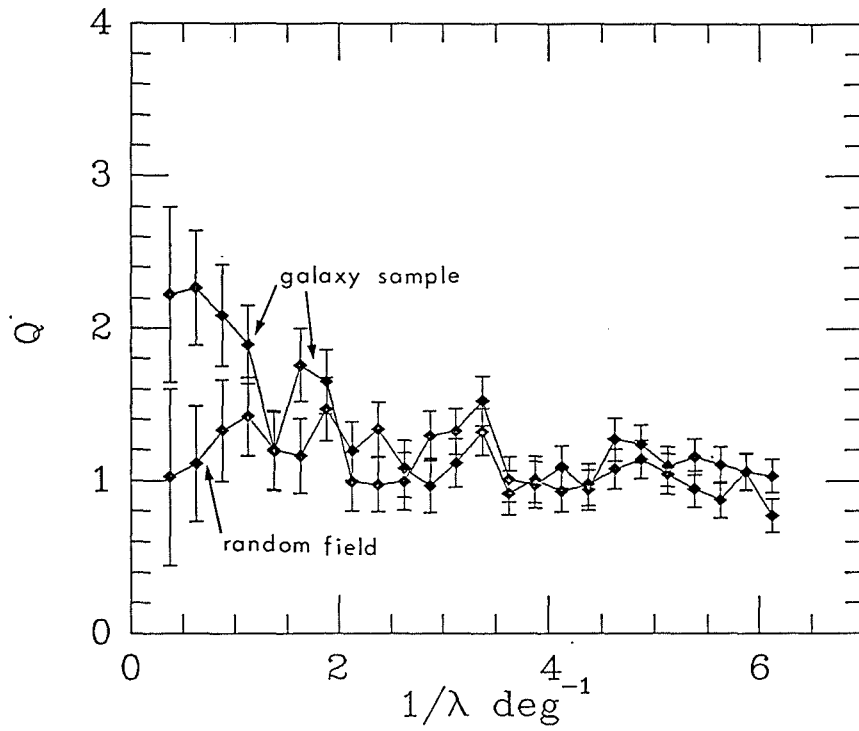


Figure 6.36 Comparison of PSA results between the galaxy sample with  $b_j < 18.5$  and a corresponding random field.

Furthermore, if 0.5 magnitude intervals are considered, then although the observed  $Q'$  amplitude decreases compared with that of the equivalent magnitude limited sample, the position of the feature in the 2-D PSA is little affected. This is reminiscent of the scaling of the apparent breaks in the 2-point correlation function over the same magnitude limits (although the break denoted the end of the clustering regime where  $W(\theta)$  tended to zero or negative values).

What is perplexing and apparently contradictory, is that for the 2-point correlation function the largest correlations occurred on the smallest scales where the equivalent 2-D PSA statistics were of marginal significance. Furthermore, small or even negative correlations occurred on the largest scales where the 2-D PSA statistics were the most significant. The same situation was uncovered to a lesser extent for the 2-point correlation function and 2-D PSA results for the stellar sample in the field. The Zwicky, Lick and Jagellonian counts also yield the greatest correlations on the smallest angular scales.

#### 6.3.2.4 Application of Meads analysis to the galaxy distribution in field 349.

Application of Meads<sup>3</sup> analysis was the last statistical test considered for the 2-D galaxy distribution. This is a simple though powerful means of detecting clustering on particular scales, e.g. Mead (1974). Shanks (1979), was responsible for first applying this statistic to galaxy data and further details and references can be found in that paper. Essentially though, as for the 2-point correlation function, the field is divided into a 2-D grid of  $N$  by  $N$  cells, where  $N$  must be a power of 2. Again a 128 by 128 array was considered. Clustering can then be tested on the 6 possible scales corresponding to cells grouped into sub-units of  $2^N \times 2^N$  elements,

(N = 1,2,..6,) , i.e. initially on scales of 2 X 2 elements and finally on 4 units of 64 X 64 elements. For instance, for the first scale that can be tested, of 2 X 2 cell areas, a square consisting of 4 units of 2 X 2 cells is considered. Following Shanks (1979), each cell 'Ai' i = 1,2..4, contains a 2 X 2 cell area aj, j = 1,2,..4. The counts of each 'aj' in each 'Ai' are then totalled. The statistic  $T_{B_1}^{(1)}$  is obtained from adding the differences between all possible combinations of any of the Ai units, i.e.:-

$$T_{B_1}^{(1)} = |A_4 - A_3| + |A_4 - A_2| + |A_4 - A_1| + |A_3 - A_2| + |A_3 - A_1| + |A_2 - A_1| \dots 6.33$$

Each 4 units of Ai form a larger square 'Bi' so that the above procedure is repeated for all squares of size Bi in the grid. The sum for each  $T_{B_i}$  is then obtained:-

$$T_B^{(1)} = \sum_i T_{B_i}^{(1)} \dots 6.34$$

This should be large if clustering was present on scales Ai. The above routine was incorporated into the general galaxy distribution program written by H.T.Macgillivray.

To determine the significance of any clustering detected from equation 6.33 above, individual galaxy counts in each cell 'ai' are randomised in each B square. The process in equations 6.33 and 6.34 is then repeated to form an analogous statistic  $T_B^{(2)}$ . Ninety-nine such randomisations were performed. The whole process is then repeated for the next scale up to the final 64 by 64 celled elements from the 128 by 128 array. Following Shanks (1979), a statistic 'S' is formed from the number of standard deviations the observed  $T_B^{(1)}$  for the real data, differed from the Tmean from the 99 random simulations, i.e.:-

$$S = (T_B^{(1)} - T_{mean}) / S_A \dots 6.35$$

where

$$S_A = (1/99.98 \sum_{i=2}^{100} (T^{(i)} - T_{mean})^2)^{1/2} \dots 6.36$$

The relatively small number of scales and the fact that the scale size doubles at each step so that any clustering on intermediate scales may be underestimated, is the main disadvantage of this technique. However, Shanks lists several features of this test which justify its inclusion as an appropriate tool for analysing the galaxy distribution. Specifically:-

(1) Obtaining significant results at small scales does not invalidate the test on larger scales. The test is thus sensitive to the presence of superclustering or hierarchical clustering on preferred scales. Conversely, detection of clustering on large scales in no way prejudices small scale results because Meads' analysis contrasts density enhancements locally and not globally.

(2) Only one type of deviation from randomness is tested so that interpretation of the results should be more straightforward.

(3) The technique can be used to compare real data with random simulations and different clustering models, e.g. a hierarchical or single scale clustering scenario. Shanks (1979), showed that Meads analysis was a more sensitive discriminant between hierarchical or power-law clustering than the 2-point correlation function which was unable to discriminate between these alternatives. Shanks showed that results from Meads analysis on real data and static 'N'-body simulations of different galaxy distribution models indicated that the hierarchical model (the natural consequence of isothermal perturbations), is less consistent with observation than a simple power-law model with clustering on a preferred scale (not incompatible with the adiabatic theory).

Figure 6.37 gives the Meads' analysis for the galaxy distribution in the  $4^\circ$  by  $4^\circ$  sub-area of field 349 to  $b_j = 20.5$ , compared with that from 2 random simulations with the same total number of galaxies as the observed sample and with the results for the stellar sample to the same limiting magnitude. The galaxy results reveal significant clustering, with a shape similar to that obtained by Shanks (1979), compatible with a power-law cluster model but not one of continuous hierarchical clustering. The random field results give the expected behaviour with  $S \sim 0.0$ . However, the stellar results although giving good agreement with the random field results over the first few scales, do show indications of clustering on larger scales (though the statistic is flat on a scales between  $\sim 1.0^\circ$  and  $\sim 2.0^\circ$ ). This 'clustering' of the stellar data on large scales agrees qualitatively with the 2-D PSA on the same stellar sample in figure 6.32a-b, which also gave small but significant excess of power on larger scales.

The Meads' results for the galaxy data in figure 6.37 exhibit 3 significant features. Firstly a gently rising S statistic until a cell size of  $\sim 0.5^\circ$ , then a significant drop at  $\sim 1.0^\circ$  followed by a sharp rise to the largest S value at a scale of  $\sim 2.0^\circ$ . Whether S would subsequently drop to smaller values on larger scales could only be determined if a larger area were surveyed. These results imply that there are two preferred scales of clustering in the data, the first at  $\theta \sim 0.5^\circ$  and the second and more significant clustering on a scale of at least  $2.0^\circ$ . If the equivalent 2-D PSA and 2-point correlation function results are examined, it is seen that for the magnitude limited galaxy sample to  $b_j = 20.5$ , the 2-D PSA exhibited a jump in  $Q'$  values roughly corresponding to the first peak in the Meads' analysis results with most power occurring on the largest scales, also in qualitative agreement with the Meads' results. For the 2-point correlation function though, most correlation occurred on the smaller scales. However, the observed break in the correlation function

occurs at  $\sim 2.0^\circ$ , just the scale on which the Meads' statistic is the most significant. A similar result was obtained by Shanks (1979), when he compared the 2-point correlation function and Meads' results for the Jagellonian catalogue, where the observed peak in the Meads' statistic occurred on the same scale as the drop in  $W(\theta)$ . Consequently, care must be exercised in interpreting these breaks and peaks in terms of maximum correlation lengths. For instance Shanks (1979), found that simulations with clusters of 50 Mpc diameter gave rise to a Meads' peak at  $\sim 10$  Mpc. The Meads' peak and  $W(\theta)$  break only correspond to the diameter outside which the cluster contrast is too small to be picked up by the statistics at the assumed depth of the survey, Shanks (1979). The physical size corresponding to the  $W(\theta)$  break and the Meads' peak gives a maximum clustering contrast length not a maximum possible correlation length since only the cores of clusters may stand out against the background galaxies for ever more distant clusters. Shanks stresses that the important point is not the size of the preferred scale but the shape of the Meads' result. For even deeper galaxy samples such as those of Ellis et al (1977), Shanks found that the highest Meads' statistic peak did not occur on the scales where the corresponding  $W(\theta)$  values were high but on the scale where  $W(\theta)$  was lower, again in agreement with the results of figure 6.37.

Figure 6.38 gives the Meads' results for the galaxy data to the same limiting magnitudes as employed for the earlier analyses. Interestingly, the same general Meads' shape is obtained in each case, though the significance of individual troughs and peaks diminishes at brighter limits. Perhaps the largest structure in this field is being detected even for the brighter samples where any large-scale feature would only be delineated by the most luminous members of the structure.

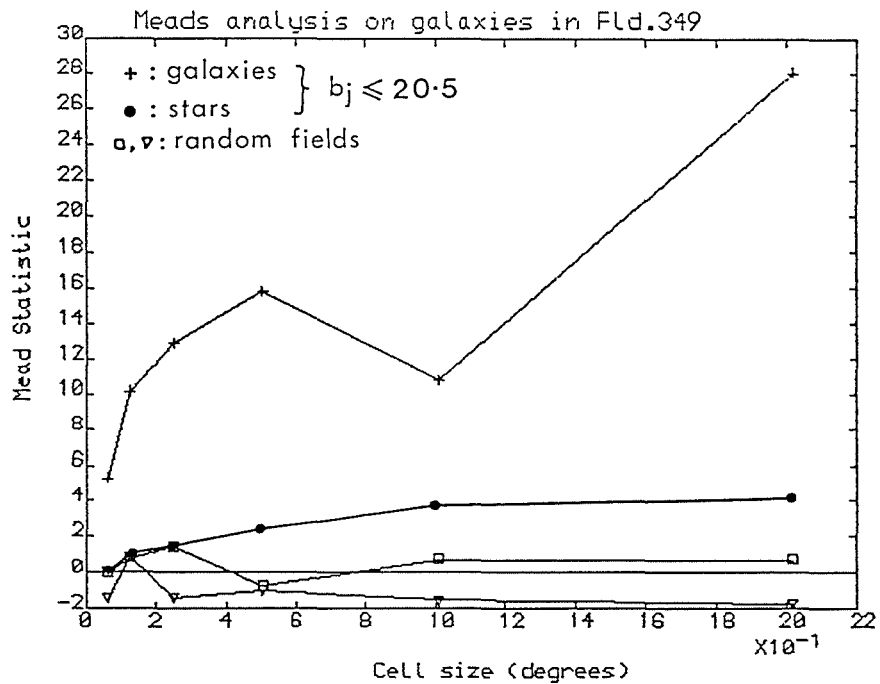


Figure 6.37 Comparison of Meads' results for the galaxy distribution to  $b_j = 20.5$  over the  $4^\circ$  square sub-area with 2 equivalent random simulations and the corresponding stellar results to the same limiting magnitude.

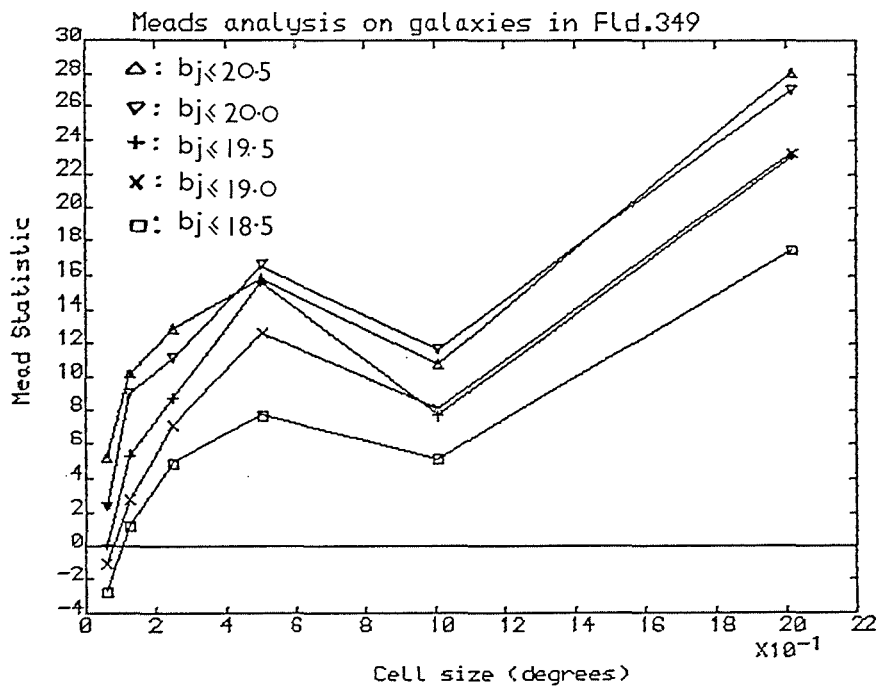


Figure 6.38 Meads analysis results for different magnitude limited galaxy samples.

As fainter magnitudes are considered though, increasing numbers of cluster and filament members are contributing to the enhancement of the feature. This is reflected by increasing 'S' values (and greater power in the 2-D PSA results at the same scale). A large-scale feature is indeed evident in figure 5.8 chapter 5 as a loop of enhanced galaxy density, and is of a diameter which closely matches the scale at which the Mead's statistic is maximum, on which the 2-D PSA gave the greatest power and where the break point occurred in the 2-point correlation function for the different magnitude limited samples.

Perhaps the first peak in the Mead's statistic, occurring at  $\theta \sim 0.6^\circ$  in each magnitude-limited sample, corresponds to the mean galaxy cluster size in the field and which may even be detected at bright limits. If the clusters are assumed to form part of the SC at a redshift of  $Z \sim 0.11$ , then the angular cluster size corresponds to a projected physical extent of  $3.4 h^{-1} \text{Mpc}$ , while the angular diameter of the large-scale feature itself corresponds to  $\sim 11.5 h^{-1} \text{Mpc}$ . Consequently, as deeper samples are considered, the clusters become better defined and populated so that their Mead's statistic is increased. Also, even though the projected angular extent of the clusters may increase in size somewhat with fainter magnitude limit (unless the most luminous cluster members were evenly distributed throughout each cluster), the large increments over which the clustering scales must necessarily lie tested with this technique, means that this might not be reflected in the position of the observed Mead's analysis peaks. The initial dip in Mead's statistic in figure 6.38 for all the magnitude limited samples also occurs at the same angular scale of  $\sim 1.0^\circ$ . This could correspond to the gap between the preferred clustering scales. The next largest scale, which can be considered as clustering of clustering, corresponds to the largest values of the Mead statistic in figure 6.38 at  $\sim 2.0^\circ$ . Here the Mead's

analysis is picking out the SC evident in this field (see next section). Indeed, the clustering scale of  $\sim 2.0^\circ$  agrees very well with the estimated diameter of the large-scale feature in figure 5.8 chapter 5. Since Mead's analysis is particularly sensitive to clustering of clustering and because results for small scales do not affect that for larger scales, the ability to pick out both clustering and superclustering is not surprising. Shanks (1979), obtained high Mead's statistics for the Ellis deep-galaxy sample attributed to a large-scale inhomogeneity in the galaxy counts. This was not however, due to any intrinsic feature of the galaxy distribution but was due to variations in the plate emulsion sensitivity. In this case though, direct-plate sky-background variations (see figure 5.8, chapter 5), do not reveal any such effect. Furthermore, the effect from the slight vignetting at the plate edges is reduced by choice of a  $4^\circ$  by  $4^\circ$  sub-area of the plate.

Another feature of figure 6.38 is that for the brighter magnitude limited samples, the Mead's statistic goes slightly negative on the smallest scales. This is not unexpected, since many cells in the array will be empty. Consequently, because the distribution of the sample to  $b_j = 18.5$  is also non-random, significant 'gaps' in the 2-D distribution are evident. This could lead to the observed anti-clustering effect.

The next stage in the analysis was to apply Mead's analysis over the same magnitude intervals as for the 2-point correlation function and 2-D PSA. The results are given in figure 6.39. Some very interesting features arise from this exercise. Firstly, the Mead's statistics for the faintest magnitude interval sample, i.e.  $20.0 < b_j < 20.5$ , which also contains the most objects, shows little obvious structure, apart from a slight depression at  $\theta \sim 1^\circ$  and a small rise at  $\sim 2^\circ$ .

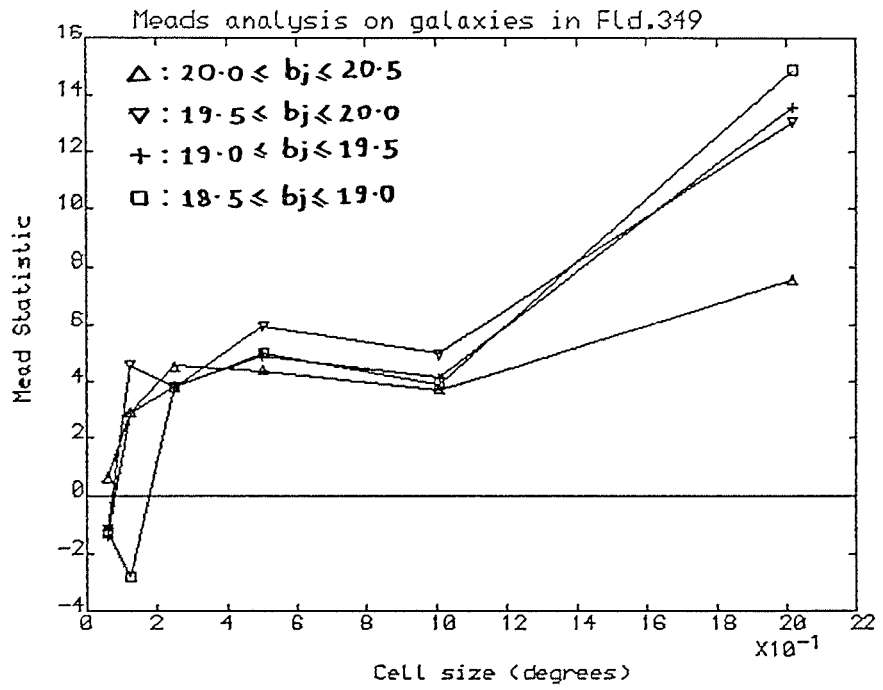


Figure 6.39 Meads' analysis results for different magnitude range galaxy samples.

On small scales the statistic does descend to small S values however. This result implies that the main contribution to the clustering is from the brighter samples and that the faintest galaxies lie 'behind' the SC. Similarly, the 2-point correlation function break point was at the same scale ( $\theta \sim 2.0^{\circ}$ ), in the magnitude-limited samples but occurred at different scales when the magnitude-interval samples were considered (see figures 6.29 and 6.30). For the correlation function results the position of the break point was indeed dominated by the brighter galaxies, i.e.  $18.5 < b_j < 19.5$ , when the  $W(\theta)$  results from the different magnitude samples were examined. Another feature of the results from the magnitude-interval samples is that even the most significant S value is only  $\sim 1/2$  what it was for the magnitude-limited samples. Obviously that is because the cluster population is restricted by the magnitude intervals chosen so that the density enhancements with respect to non-cluster regions are lower so the Mead statistic is lower also. Even so, it is the brightest magnitude intervals which give the most significant Mead's statistic on the largest scale of  $\theta \sim 2.0^{\circ}$ . This would not be the case if the large Mead's statistic at large scales was due to sky background or large-scale emulsion-sensitivity variations which would mainly affect the faint galaxy distribution. Furthermore, the peak at  $\sim 0.6^{\circ}$  is not as significant as the depression at  $\theta \sim 1.0^{\circ}$ , probably because the clusters are less well defined when magnitude intervals are considered. In fact the Mead's 'peak' for the faintest sample does not occur at  $\theta \sim 0.6^{\circ}$ , but at  $\theta \sim 0.3^{\circ}$ , and more structure is evident at smaller scales for the brighter magnitude-interval samples also.

The three main techniques used to analyse the 2-D projected galaxy distribution have given some insight into the anisotropy and large-scale structure present. Such structure was even evident from the surface number-density plot, but these statistical tests have put this observation on a more quantitative basis. Each statistic has its own particular merits and approach which reveal different aspects of the properties of the projected matter distribution. That there is significant structure is beyond doubt. The statistical deviations from a random field have been clearly demonstrated by all the techniques employed and have been shown to be highly significant. The 2-point correlation function results are perhaps the least informative for describing the nature and size of individual features of the galaxy distribution. Indeed the effect of the estimator used was to remove the effects of large-scale density gradients that may exist in the counts (Hewett, 1982), although the break at  $2^{\circ}$  must surely be connected to the size of the supercluster "loop" discovered. The 2-D power spectrum and Mead's analysis yielded more precise information on structure in the field (and its apparent scaling with depth), with both statistics giving significant power on large scales whilst also showing intermediate structure that varied with magnitude limit and magnitude interval as described above.

However, the tests employed say nothing about any single cluster or group of galaxies, although the size of the average cluster and the projected dimensions of the SC filament may be parameters available from the analysis. The tests analyse the data in a more global sense and so give parameters which describe the general properties of the 2-D projected distribution. Furthermore, as noted in chapter 1, it is dangerous to base conclusions on the clustering or structure in one field from purely 2-D information. Some means of 3-D analysis would enable a less-biased description of the galaxy distribution. In this respect the large numbers of objective-prism redshifts obtained for

this field should prove valuable. Although inherently crude, the results of chapters 3 and 4 have shown objective-prism redshifts may provide spatial information which is sufficiently accurate for the detection of cluster redshift peaks, large-scale density enhancements and voids. This information could be coupled with the 2-D data to verify the existence of the large-scale structure in this field and reveal if the visual impression of a filamentary supercluster gained from the 2-D plot is a true physical phenomenon. In fact, a preliminary analysis of this field by Parker et al, (1984a-b), using objective-prism redshifts for the rich clusters, has suggested the existence of a SC at  $Z \sim 0.11$ , together with some foreground structure at  $Z \sim 0.05$ . A more detailed analysis using Cosmos machine data and the INTERZED technique for the whole plate sample will now be described.

6.3.3. Analysis of the objective-prism galaxy redshift results for field 349 to  $b_j = 18.7$ .

Details of the reduction techniques employed in obtaining objective-prism galaxy redshifts from Cosmos data of the high quality, original plate UJ6535P of this field are given in chapter 5. From the paired direct/prism plate sample all galaxies to  $b_j = 18.7$ , flagged as such from the star/galaxy separation on the direct plate, had their objective-prism spectra examined using the INTERZED technique (Beard, 1984). The original intention was to obtain a sample to  $b_j = 19.0$ . However, an error was discovered by the author in the Haggis COSMAGCAL routine which had led to the magnitude estimates furnished by this routine being  $\sim 0.3$  magnitudes too faint. Although the software has been corrected, time constraints rule out further INTERZED measures of fainter galaxy spectra and subsequent modification to diagrams, results etc, since it was felt that sufficient data had already been obtained. In fact 1,539 galaxies to  $b_j = 18.7$  had yielded

of the  $\sim 2,900$  examined. Chapter 5 gives details of how the assigned feature -weights, and how the fraction of the total sample examined that yield redshifts, change with magnitude. This final section of the chapter concentrates on the further analysis of these data.

### 6.3.3.1 Comparison of the objective-prism redshift sample with a random simulation.

Figure 6.40a gives the redshift histogram for all galaxies yielding objective-prism redshifts to  $b_j = 18.7$  in this field, regardless of assigned feature weight, together with a sub-histogram giving the frequency distribution of objective-prism redshifts with top feature weights. No striking feature is apparent although there are indications of a redshift excess at  $Z \sim 0.11-0.13$  compared with the general trend, particularly noticeable in the results for the top feature weights. Obviously, without the benefit of comparison with some simulation or model of the redshift histogram that might be expected according to some favoured clustering description, the peak at  $Z \sim 0.11$  might simply be because the objective-prism selection function is a maximum over this redshift range. This question will be dealt with shortly. Firstly though, figures 6.40b-c give similar histograms for sub-sets of the objective-prism redshift sample over two broad magnitude ranges; specifically  $18.2 < b_j < 18.7$  in figure 6.40b and  $b_j < 18.2$  in figure 6.40c. The brighter sample is dominated by a low-redshift distribution peaking at  $Z \sim 0.05$ , whilst the fainter sample peaks at  $Z \sim 0.11-0.12$ . Generally speaking, the brightest galaxies will be of low redshift and the faintest of higher redshift, according to some luminosity function. The fact that the objective-prism redshift histograms for the bright and fainter samples are dominated by low and high redshift galaxies gives a simple though rough confirmation of the technique's validity.

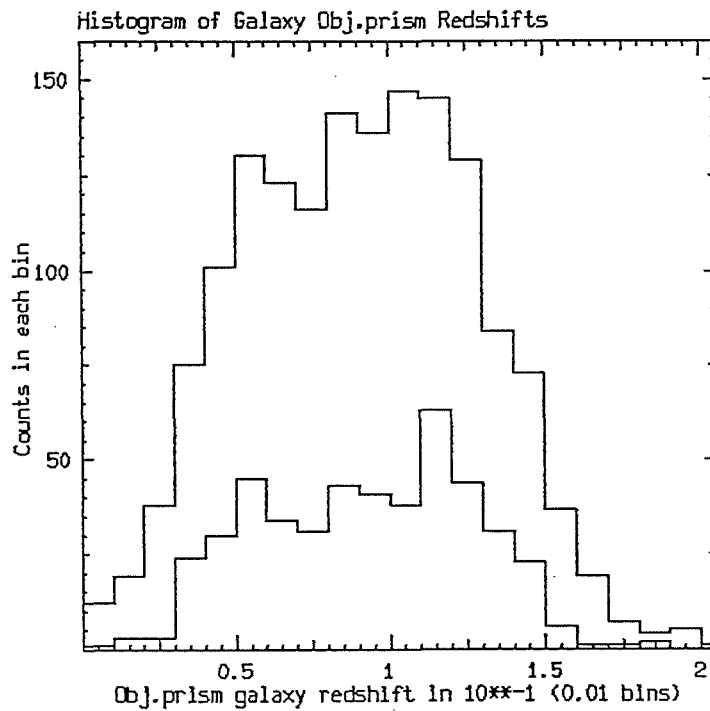


Figure 6.40a Redshift histogram for the total galaxy sample to  $b_j = 18.7$  that possess objective-prism redshifts, regardless of assigned feature weight.

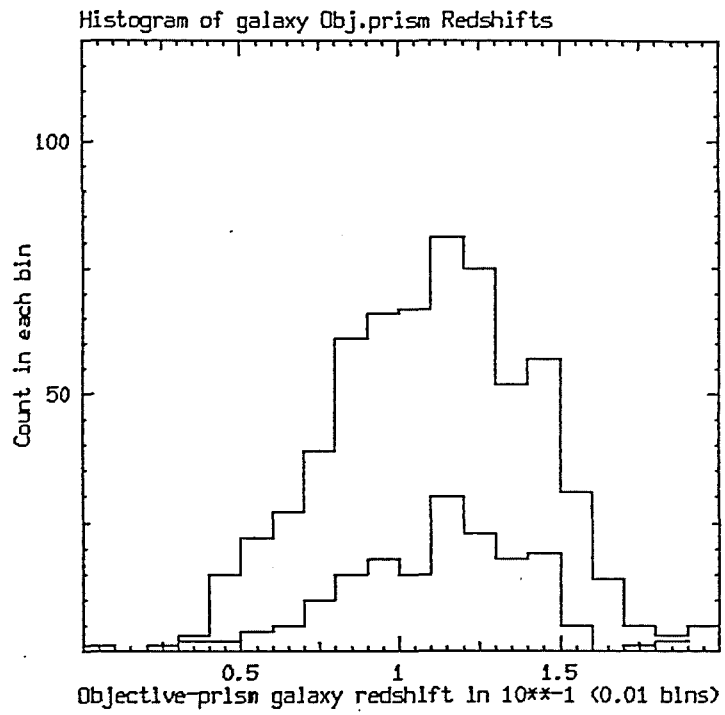


Figure 6.40b Redshift histogram for galaxies over the magnitude range  $18.2 < b_j < 18.7$ .

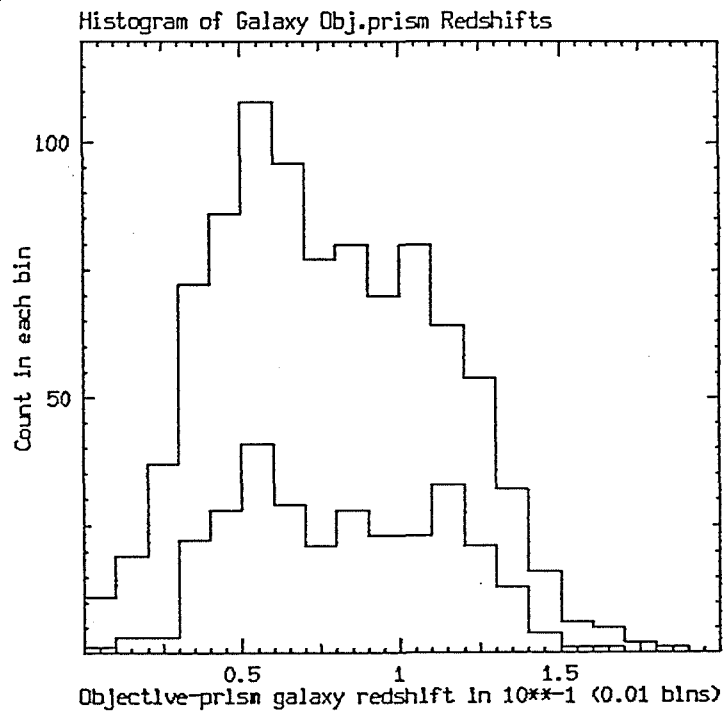


Figure 6.40c Redshift histogram for galaxies with  $b_j < 18.2$ .

In all cases in figures 6.40a-c, and as was found in chapter 3, the redshift distribution of galaxies with top-weight features essentially mimics that from the low weight feature results. Thus, although some low-weight redshifts will undoubtedly be discrepant, inclusion of the low-weight sample is considered worthwhile. This is because contamination by an unknown but small fraction of incorrectly assigned objective-prism redshifts is outweighed by the statistical benefits afforded by a much larger sample.

The objective-prism redshift selection function affects the observed sample size for given image parameters, with magnitude, image diameter, surface brightness and morphological type variations playing an important role. Comparison of observed data with a realistic selection function is important if the significance of the redshift histograms are to be correctly assessed. Firstly, the data in figure 6.40 were tested against a Gaussian distribution using the Chi-square test and the authors general statistics/graphics package. This led to rejection of the null hypothesis with  $\gg 99.9\%$  confidence. Similarly, the Lilliefors test led to rejection of 'Ho', the hypothesis that the observed redshift histogram could have arisen by chance, at  $\gg 99.99\%$  confidence. However, this is not to say that convolution of the objective-prism redshift selection function with a random distribution could not have produced the observed redshift histogram. It would be desirable to test the observed sample with some simulation convolved with the selection function. This requires knowledge of the selection function, the determination of which is itself a non-trivial problem.

Obviously, not all galaxy objective-prism spectra will yield a 4000Å feature suitable for measurement. The presence of such a feature in galaxy spectra is a function not only of galaxy morphology but also of other image properties as mentioned above. The final objective-prism redshift sample is a sub-set of the initial galaxy sample. If a galaxy is too bright, whether because of proximity or intrinsic luminosity, then the objective-prism spectrum is saturated and no features are discernable. If the galaxy angular diameter is large, then even though the spectrum might not be saturated any features will be smeared out by the blurring effects of the image profile. Also, if the galaxy is too faint then the spectrum will be dominated by noise. These extrinsic effects, together with the intrinsic effect that the 4000Å feature on which the redshift determinations depend, is only prominent in elliptical and early-type spiral galaxies, reduce the size of the galaxy sample yielding redshifts. Bearing these considerations in mind and coupled with the experience in measuring large numbers of objective-prism spectra gained by the author and others such as Cooke (1981), and Beard (1984), a set of restrictive criteria was generated in an attempt to emulate the objective-prism redshift selection function. Specifically, galaxies might be expected to yield objective-prism redshifts if they fulfilled the following conditions:-

- (a). Magnitude range  $15.8 \leq b_j \leq 19.0$ . (for our purposes the magnitude limit of 18.7 was adopted in application to the simulation results).
- (b). Morphological type range:- E, S0, Sa, Sb, although the elliptical galaxies will usually yield the strongest 4000Å features.
- (c). Galaxy images with diameters  $< 300 \mu\text{m}$  on the direct plate.

The above criterion were applied to a Monte-Carlo simulation of a 3-D segment of the Universe (MacGillivray and Dodd, 1982), projected onto the area of a UKST plate. The simulation, using software developed by

H.T. MacGillivray, was performed for the same number of galaxies as obtained from the star/galaxy separation on the direct plate and for a clustering description where galaxies were in randomly distributed clusters. Apart from the effects of luminosity evolution, all factors affecting the light from distant galaxies were taken into account, as were factors leading to the inclusion of the galaxy in a machine-determined catalogue.

The data from ten such simulations were averaged in an attempt to smooth out effects of individual clusters. Furthermore, a Gaussian error of  $3\sigma$  ( $\sigma = 0.01$ ), in redshift was applied to the simulated redshifts to try to allow for the expected measurement errors. The resultant model curve was generated for  $q_0 = 1$  and  $H_0 = 75 \text{ Kms}^{-1} \text{ Mpc}^{-1}$ . The fraction of overlapping spectra, that thus prevent objective-prism redshift determination, were not included as a parameter in the restrictive criteria applied to the simulation data as the contribution from this problem is variable and difficult to estimate, although in general it will be quite small. Cases of overlap only become serious in crowded areas such as with dense, rich clusters. This situation is exacerbated with fainter and more remote clusters where the projected object separations are smaller for a given intrinsic cluster concentration. Since rich clusters tend to be dominated by elliptical galaxies, e.g. Strom and Strom (1979), the potential objective-prism redshift cluster sample may be somewhat reduced. This could be partially alleviated by use of another prism plate of the same field but with the dispersion direction at right angles to the previous alignment although such an exercise will not generally be worthwhile.

Figure 6.41 gives the comparison of the observed frequency of galaxies with  $b_j \leq 18.7$  yielding redshifts, compared with the numbers expected from an average of 10 simulations after convolution with the assumed objective-prism redshift selection function. The simulation peak occurs at  $Z \sim 0.07 - 0.08$ , in disagreement with the observed peak. Even considering the uncertainties in some of the selection function parameter values, the discrepancy is quite marked. A strong excess of redshifts between  $Z \sim 0.08$  and  $Z \sim 0.13$  is evident at the  $3\sigma$  level. Elsewhere the agreement is not unreasonable, although there is an underestimate of high redshifts from the observations compared with the simulations and there is also evidence of an excess at  $Z \sim 0.05$ . An obvious conclusion from this comparison is that the large excess at  $0.08 \leq Z \leq 0.13$  and that at  $Z \sim 0.05$  could be due to large-scale structure in the galaxy distribution in this field (see section 6.3.2).

However, even if the model clustering scenario and selection function were well matched to the Universe 'seen' with this technique, the observed distribution would not be expected to follow the model curve exactly. A decision as to the level at which the deviations from the model curve are significant has to be made. Care must be taken in attempting to understand the importance of the results, bearing in mind the underlying assumptions of the model, which assumes that all galaxies that fulfil the selection criteria will yield a redshift. In fact, because of overlapping spectra etc, the actual numbers in the simulation should be slightly smaller, enhancing the  $3\sigma$  peaks already detected. Consequently a Chi-square test (with 19 d.o.f.) was applied to the data in figure 6.41. This yielded  $\chi_{19}^2 = 197.7$ , showing that it is extremely unlikely that the observed distribution could have arisen from the model one. The observed galaxy distribution is thus incompatible with the particular combination of simulation and assumed selection function employed.

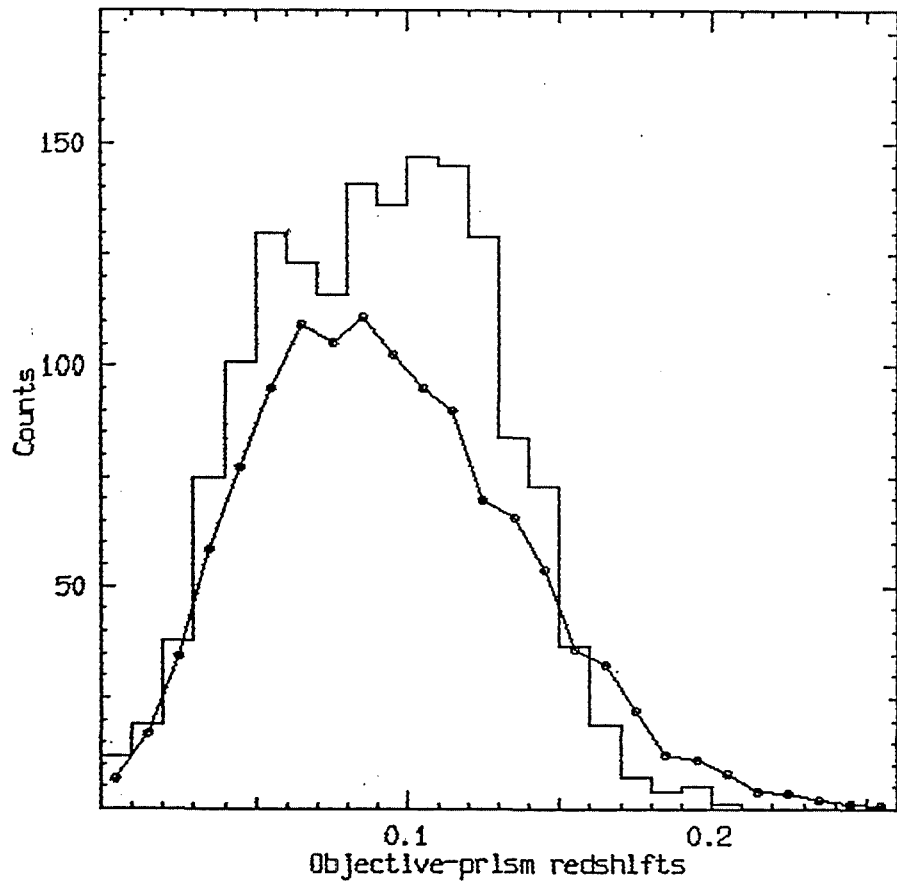


Figure 6.41 Comparison of the observed frequency of galaxies yielding objective-prism redshifts to  $b_j = 18.7$  compared with the number expected from an average of ten simulations which have been convolved with a chosen objective-prism redshift selection function.

### 6.3.3.2 Study of the objective-prism redshifts of selected clusters.

The next step in the analysis was to select all major regions of enhanced galaxy density from a dot plot of the galaxy distribution to  $b_j = 20.5$ , (see chapter 5, figure 5.8). These in the main correspond to the rich clusters analysed by Parker et al (1984a-b), although a different objective-prism plate of the same field and a different reduction technique were employed. In this study, small rectangular areas around the enhanced regions were extracted from the main Haggis data catalogue. All galaxies within the selected regions with objective-prism redshifts could then be examined. The cluster nomenclature of Parker et al (1984b), was adopted for easier result comparison.

The redshift results for each cluster area are given in figure 6.42a, whilst the equivalent results from Parker et al (1984b), are given in figure 6.42b. The associated isoplethal plot is given as figure 6.43 for comparison with that of figure 5.8, chapter 5, and for ease of cluster identification. The clusters referred to in figures 6.42a-b are shown numbered in figure 6.43, as are 5 control areas. The general agreement between the two sets of cluster data, derived using different data reduction techniques and plate material, is very encouraging, especially for cluster 1 (see Carter, 1980), and clusters 8, 9, and 15.

This independent confirmation of the main features described by Parker et al (1984b), vindicates the usefulness of the technique for determining cluster peak redshifts. Furthermore, the indications of a filamentary type SC at  $Z \sim 0.11$  are re-affirmed in this cluster study by the agreement between the peak redshifts for clusters 1, 2 and 15. The lack of obvious cluster peaks at  $Z \sim 0.11$  for clusters 4, 6 and 13 prevent a strong statement on the reality of the 'loop' structure in this field suggested by the results of Parker et al (1984b).

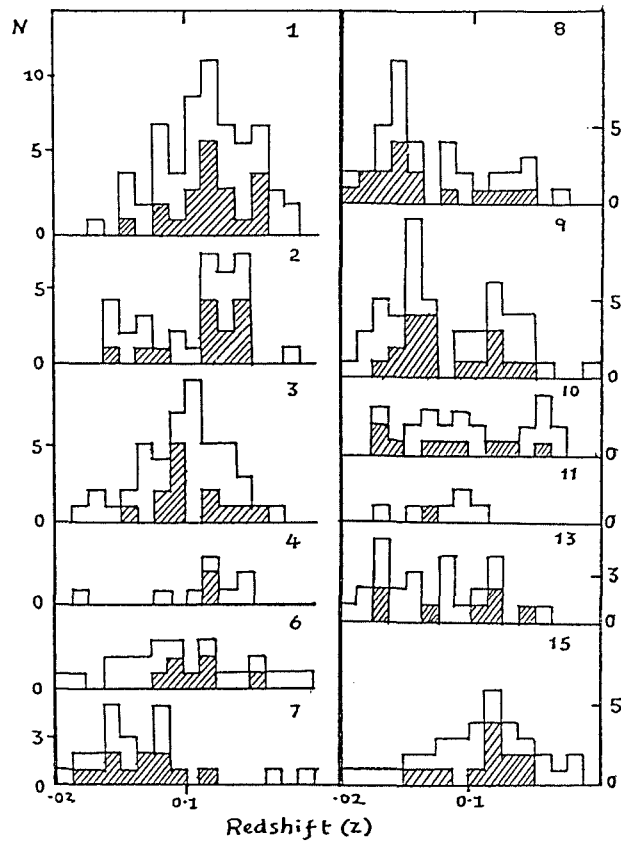


Figure 6.42a Redshift histograms from the cluster (rectangular) areas selected from the COSMOS data used in this study.

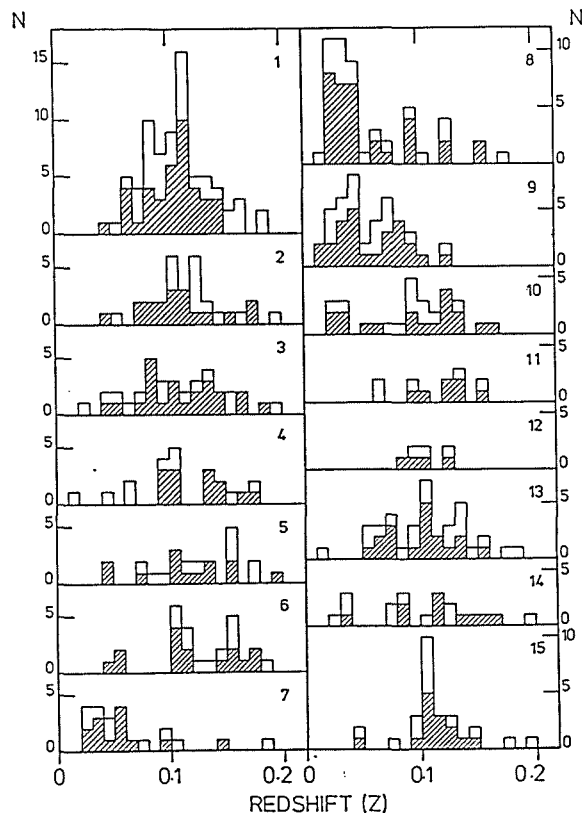


Figure 6.42b Equivalent cluster redshift histograms taken from Parker et al (1984b).

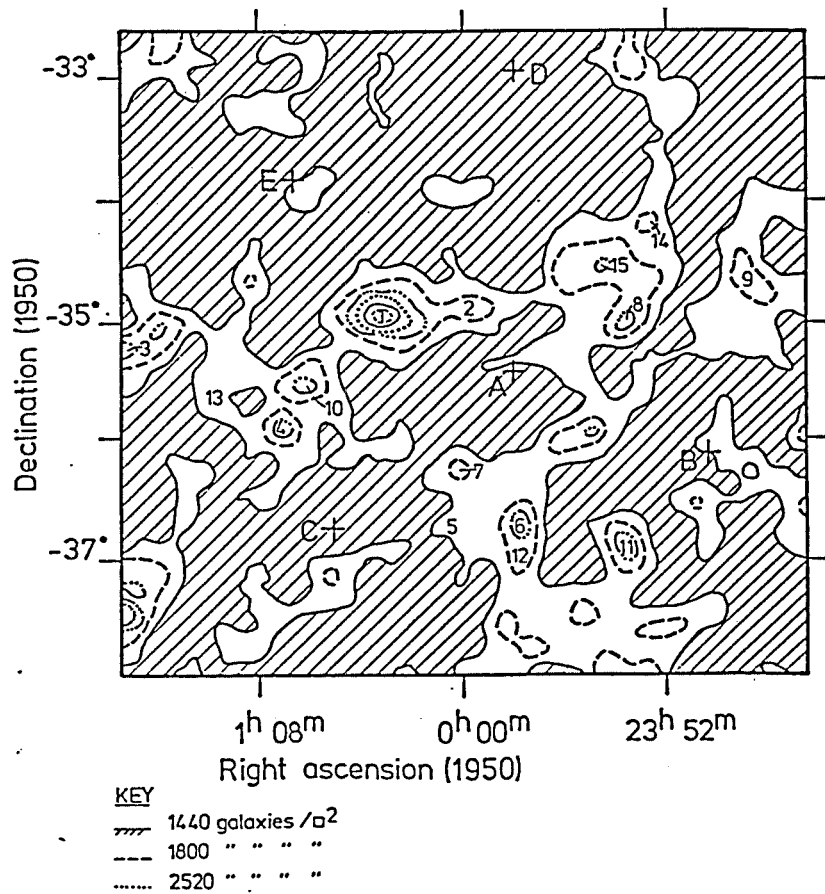


Figure 6.43 Isoplethal plot of the galaxy distribution in field 349 as determined by Parker et al (1984b), for comparison with figure 5.8. The position of the Control Areas described in the text are also indicated.

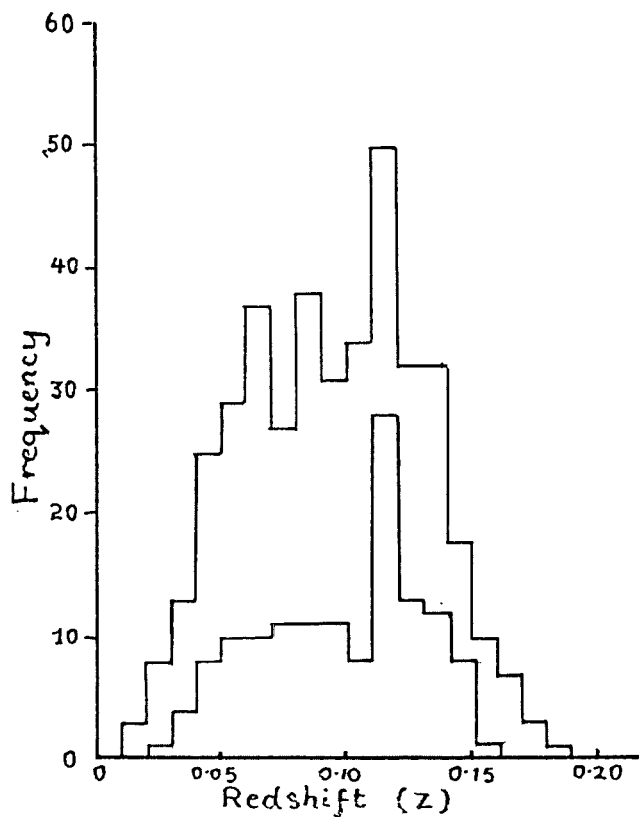


Figure 6.44 Combined objective-prism redshift histogram from the rectangular cluster areas selected in this study.

However, cluster 3 does exhibit a strong peak at  $Z \sim 0.10$ , suggesting an extension of the horizontal 'filament' to the left edge of the field. Foreground structure, typified by the low redshift peaks for clusters 8 and 9 is also confirmed. The results for cluster 9 in fact reveal a second redshift peak at  $Z \sim 0.11$ , implying that the foreground structure may be superimposed on a further extension of the horizontal filament to the right edge of the field.

If a combined cluster redshift histogram is constructed (figure 6.44), then a peak at  $Z \sim 0.11-0.12$  is evident, being particularly striking if only top-feature redshift results are considered. This is significant because these top-weight results are likely to be the most reliable. These results do indeed show a preference for galaxies with measurable  $4000\text{\AA}$  features to yield objective-prism redshifts at  $Z \sim 0.11$ , at least for the selected clusters.

The results for 5 control areas, each of side 50' and chosen in regions avoiding rich clusters, is given as a combined histogram in figure 6.45a. These control areas were selected in similar locations to those marked in figure 6.43. No significant structure is obvious from these areas. This conflicts with the results of Parker et al (1984b), where a peak at  $Z \sim 0.11$  was detected and interpreted as evidence for a dispersed component at the same redshift as the supposed supercluster 'filament'. This combined control-area redshift histogram is given in figure 6.45b. Such a dispersed component is not confirmed by the control areas chosen in this more objective study from Cosmos data of an original plate of high quality, where measurement of individual spectra were made without regard to the location of the galaxy on the plate. However, due to the relatively small numbers of galaxies involved, this discrepancy may be due to small differences in the sizes and locations of the control areas selected in each case.

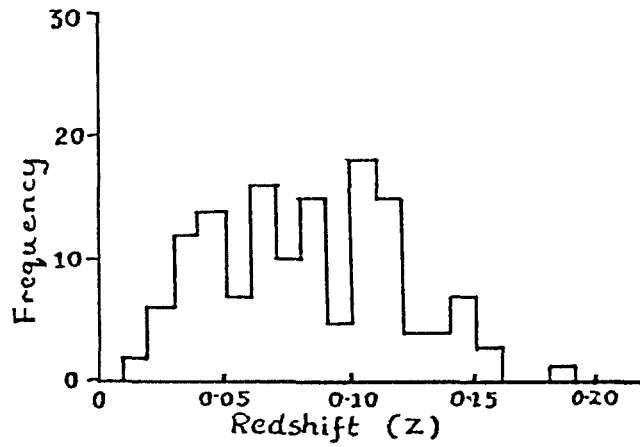


Figure 6.45a Combined objective-prism redshift histogram from the control areas selected from the Cosmos data used in this study.

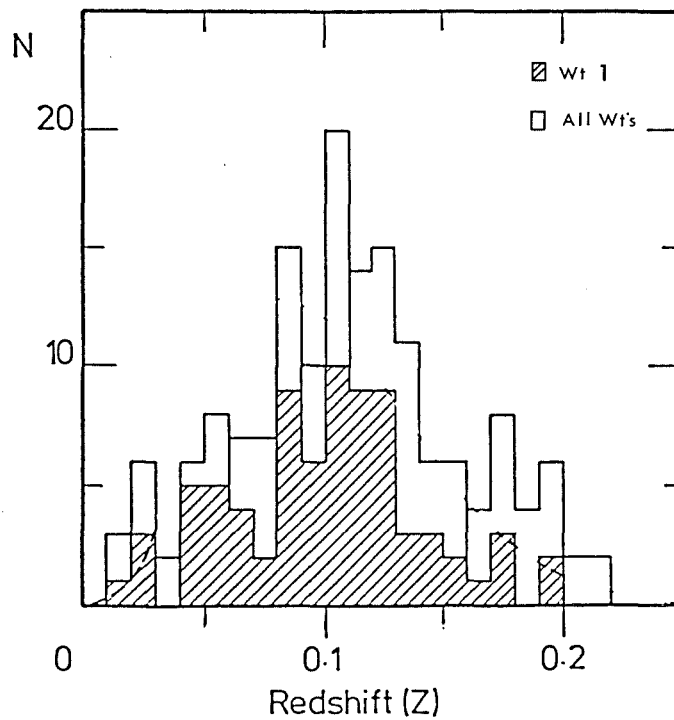


Figure 6.45b Combined objective-prism redshift histogram of the control areas from the data of Parker et al (1984b).

The situation may become clearer when the whole plate objective-prism redshift sample is examined (see later), although the results illustrated by figures 6.40a-c, and the slit-spectra results from the first half of this chapter, have already indicated that structure over preferred redshift ranges is present in this field.

An interesting feature of these results is that the same cluster redshift peaks as given by Parker et al (1984b), were obtained for the richer clusters, even though the clusters in this study were extracted as rectangular areas where all galaxies with objective-prism redshifts contained therein were used in constructing the cluster redshift histograms. This compares with individual cluster membership selection based on visual inspection of the plate, used by Parker et al (1984a-b). Such agreement of the cluster redshift peaks might be expected, since although inclusion of all results within a given cluster rectangle will inevitably lead to inclusion of non-cluster members (which might be largely eliminated if a visual selection of likely cluster galaxies was made), the galaxies in rectangles placed around rich clusters should still be dominated by cluster members. Furthermore, this approach imposes no subjective assessment of likely cluster membership on the sample. Of course the size of cluster rectangle selected for each identified cluster is a subjective choice in itself. The redshift peaks for some of the less rich clusters in this study though, (see figure 6.42b, results for clusters 6, 10 and 13), are not in good agreement with Parker et al (1984a-b), probably because more foreground and background galaxies are included which mask the true cluster peaks.

The selected cluster results presented here have nevertheless confirmed the validity and repeatability of the technique for determining cluster redshifts, even when different plate material and reduction techniques are employed (see chapter 3), and at least when rich clusters are considered. This initial limited, but selective, use of the cluster redshift data from the larger whole-plate sample, suggests the existence of a filamentary type SC at  $Z \sim 0.11$ , extending for at least  $\sim 4.0^\circ$  from cluster 3 to 15 and which corresponds to a physical extent of  $\sim 23 h^{-1} \text{Mpc}$ . This does not include a possible extension to the edge of the field, suggested by the second redshift peak of cluster 9. Significant foreground structure was also revealed at  $Z \sim 0.05 - 0.06$ , by clusters 8 and 9 which confirms the suggestion of such a feature from figure 6.40c.

The possibility that the background SC 'filament' at  $Z \sim 0.11$  branches at cluster 15 to form a 'loop' connected to clusters 6 and 12, as implied by the isoplethal plots of figure 5.8 and 6.44, and the cluster redshift results of figure 6.42b, is not confirmed in this study because the redshifts obtained for clusters 6 and 12, which lie along this 'extension', exhibit no obvious peaks. In fact, the enhanced density region between clusters 15 and 8 and clusters 6 and 12 could be due solely to the foreground structure at  $Z \sim 0.05-0.06$  and typified by the results for clusters 8 and 9. This situation may be clarified from study of the whole-plate objective-prism redshift sample over the appropriate redshift ranges. The reality of an underlying SC however, cannot be ruled out from the mere 2-D projected positions of galaxies possessing  $4000\text{\AA}$  features.

Thus, as the objective-prism redshifts presented so far for the selected clusters in this field represent a small fraction of the total sample obtained, examination of the 'whole plate' sample is the next stage of the analysis.

#### 6.3.3.3 Examination of the whole plate objective-prism sample.

Firstly, a 2-D, X-Y plot of all 1,539 galaxies with objective-prism redshifts was produced. Since Giovanelli et al (1982), have shown that elliptical galaxies may be important tracers of filamentary structure (see chapter 1), the objective-prism redshift sample may reveal any such structure in this field more clearly than might be expected from number/density considerations alone. This is because galaxies with objective-prism redshifts are usually ellipticals. Indeed, it was hoped that the filament evident in the number/density plots of figure 6.43 and figure 5.8 might be better delineated by this procedure. Furthermore, since rich clusters are dominated by ellipticals, a higher proportion of galaxies with objective-prism redshifts are expected in cluster regions which may also make weak cluster identification easier.

Figure 6.46a gives the X-Y plot of the entire objective-prism redshift sample to  $b_j = 18.7$ . This plot does appear to highlight the chain-like structure running mid-way through the field, as in figure 5.8, as well as other clumps and groupings. The most striking feature though, is the concentration of galaxies at the right-hand edge of this 'filament' and extending perpendicular to it. Whether or not this 'string' and the elongated enhancement at its right edge is physically meaningful, or is only a visual impression gained from the 2-D projection, may be determined by considering the objective-prism redshifts for galaxies in these features.

However, even without utilising the objective-prism redshifts, a further potential use of galaxy prism spectra with  $4000\text{\AA}$  features, as a means of detecting filamentary structure, is proposed. Such a technique may be useful for application to faint galaxy samples when direct plate morphological classification is difficult and colour information unavailable. Furthermore, if the galaxy objective-prism redshifts obtained were used, filament searches over particular redshift ranges could be performed.

A further insight into the structure in this field is obtained if the plot for all galaxies to  $b_j = 18.7$  possessing objective-prism redshifts (figure 6.46a), is compared with the galaxy sample with no objective-prism redshifts, to the same magnitude limit (figure 6.46b). Whilst the concentration of objects along the 'horizontal filament' and the extended feature at the right hand end of the filament, are obvious in figure 6.46a, the presence of these large-scale features is considerably less obvious in figure 6.46b, where the distribution of galaxies appears much more random. The two samples represent 53% and 47% of the total sample of 2,903 galaxies to  $b_j = 18.7$ , for galaxies with and without measurable  $4000\text{\AA}$  features respectively. Hence the observed structure in figure 6.46a cannot be attributed to a significant number/density disparity between the samples.

The differences between the galaxy distributions of figures 6.46a and 6.46b implies that it is the galaxies with  $4000\text{\AA}$  features, i.e. mainly the ellipticals, which are contributing most to the observed impression of filamentary and clumped structure in the projected 2-D plots as might be expected (see above). These results are encouraging signs for the use of galaxies possessing  $4000\text{\AA}$  features as a means of detecting 'filaments' and large-scale galaxy clumpings, which also have the potential for further resolution in depth.

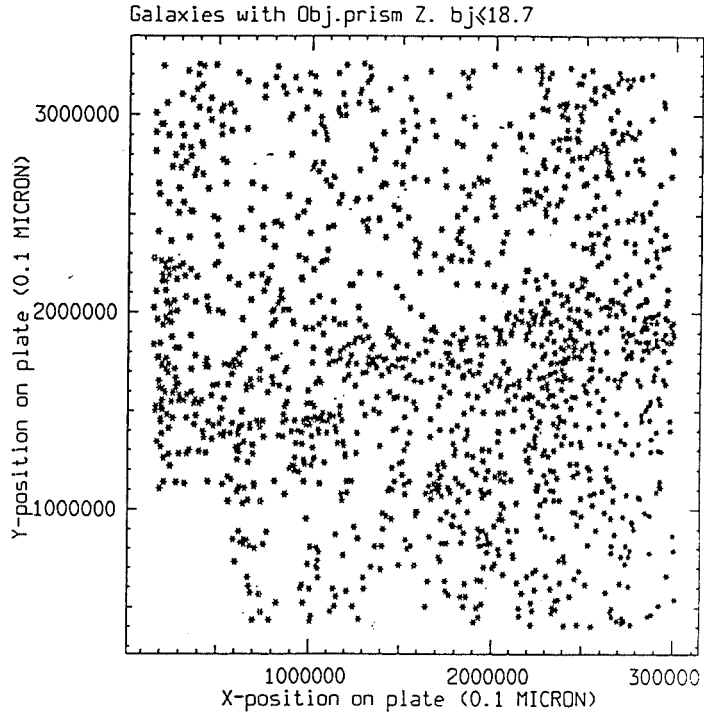


Figure 6.46a The 2-D X-Y plot of the entire galaxy sample with objective-prism redshifts to  $b_j = 18.7$ .

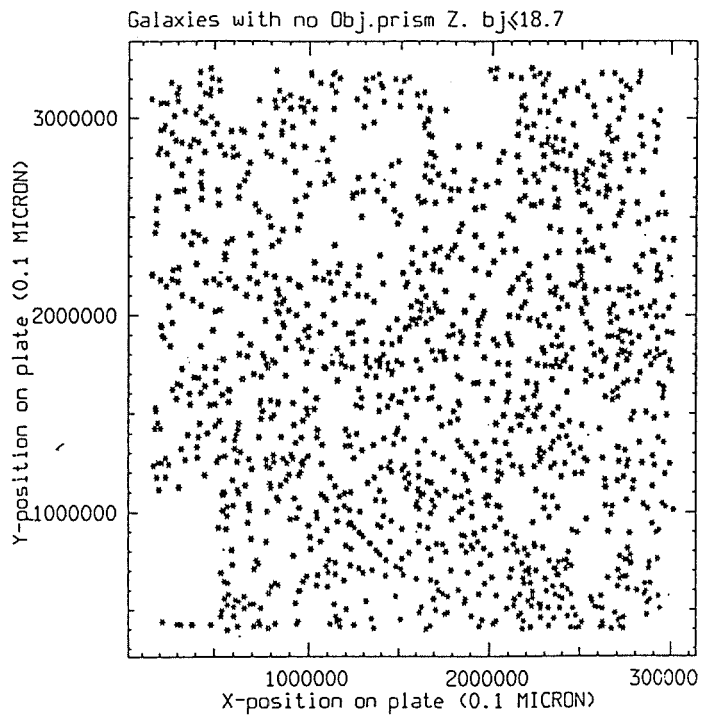


Figure 6.46b The 2-D X-Y plot of the galaxies to  $b_j = 18.7$  that have no measurable 4000Å features.

Further work and results from fields with known filamentary structure is required to confirm this proposal as a viable and worthwhile procedure. Finally, figures 6.46a and 6.46b can be compared with the X-Y plot for all galaxies detected to  $b_j < 18.7$  given in figure 6.46c. This merely confirms the role that galaxies with objective-prism redshifts play in highlighting features, since the structure evident in figure 6.46a is not further enhanced in figure 6.46c.

Returning to figure 6.46a, the strongest density of galaxies with objective-prism redshifts is at the right edge of the suspected filament and is probably mainly due to contributions from the foreground structure at  $Z \sim 0.06$  described in the cluster study, (clusters 8 and 9), and as such is not part of an extension of the 'filament' into a 'loop'. This is essentially confirmed in figure 6.47, the X-Y plot of all galaxies with objective prism redshifts. Each galaxy position is plotted with a circle whose diameter decreases with increasing redshift. The larger-diameter circles, representing the lower-redshift galaxies, dominate the enhancement at the right-hand end of the filament. Furthermore, use of circles of varying diameter to represent galaxy positions leads to considerable overlap in the denser regions. This in turn results in a more striking impression of clumped galaxy distribution than was given by figure 6.46a, because galaxies become connected to their nearest neighbours forming clumps and chains. For instance the vertical structure at the extreme left of the field is more apparent. The eye also tends to associate circles of similar diameter together and since the circle size is proportional to redshift, features of similar redshift are highlighted, with the lowest redshift features being most obvious.



Care must be taken in too readily interpreting these features as real since the eye is good at joining objects to form linear patterns, even from plots of random fields (e.g. Barrow et al, 1985). Nevertheless, the additional resolution given by the varying circle sizes means that such effects should be more restricted to different redshift intervals. In fact it could be argued, that for the lowest redshift galaxies at least, the plotted circles form a crude type of minimum spanning tree, revealing the natural pattern of galaxy clustering (see this chapter, page 345), since only galaxies whose projected positions are closer than the plotted circle diameters will overlap to form groups and chains. However, due to the concentration of foreground objects at the right edge of the field, it is difficult to see if an extended, underlying, high redshift component is also present in this region, which is compatible with the structure at  $Z \sim 0.11$  as suggested from the cluster studies.

A clearer picture is obtained if two broad redshift ranges are considered which encompass the foreground and background structure revealed from the preliminary cluster study. Consequently, figures 6.48a-b give the projected X-Y distribution for the galaxy redshift sample over the ranges  $0.04 < Z < 0.08$  and  $0.10 < Z < 0.14$ . Circles plotted for each galaxy decrease in diameter with increasing redshift to give some further depth resolution in each plot. In figure 6.48a, as expected, the enhancement at the right edge of the 'filament' is due mainly to contributions from lower redshift galaxies. Furthermore, in comparison to the rest of the sample over the same redshift range, this density enhancement is very striking and dominates the galaxy distribution. This foreground feature is elongated extending for  $\sim 1.07^\circ$ . The similarity of circle sizes indicate close redshift agreement for galaxies in this feature within the 0.04 redshift range covered.

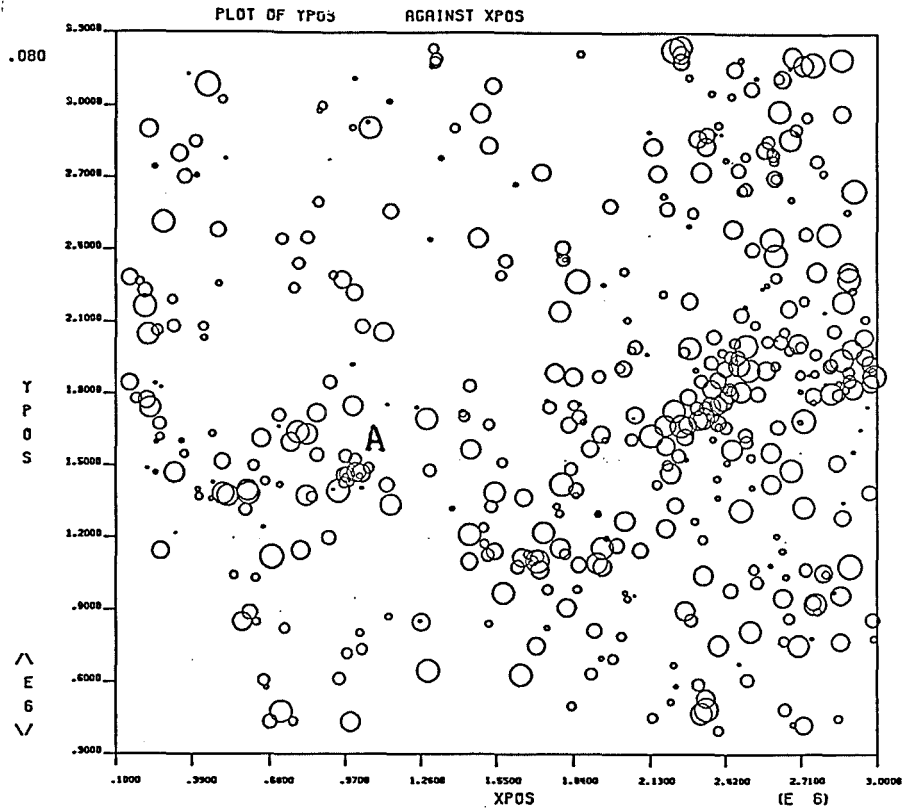


Figure 6.48a The 2-D X-Y plot for all galaxies over the redshift range  $0.04 \leq Z \leq 0.08$ .

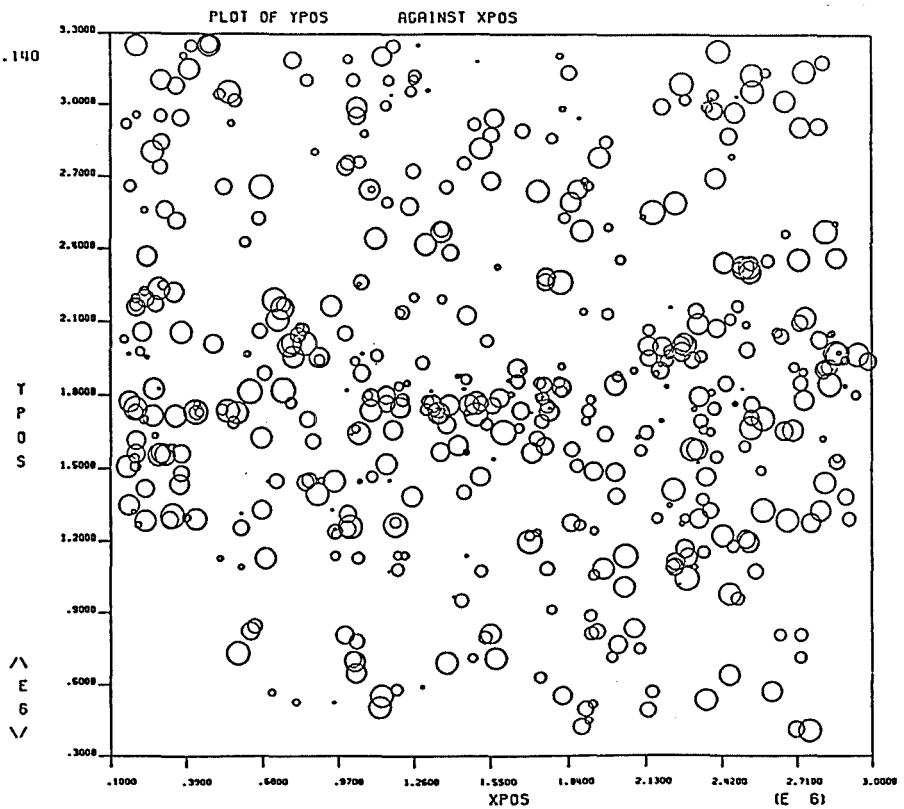


Figure 6.48b The 2-D X-Y plot for galaxies over the redshift range  $0.08 < Z \leq 0.12$ .

Assuming a mean redshift for this feature of  $Z \sim 0.055$  (from the average of the redshift peaks for clusters 8 and 9 which lie on the region of enhanced density), then this 'cigar shaped' feature extends for  $\sim 3.1 h^{-1} \text{Mpc}$  across the line of sight. This may be compared with the mean diameter of  $\sim 1.5 h^{-1} \text{Mpc}$  for groups surveyed within  $\sim 20 h^{-1} \text{Mpc}$  by de Vaucouleurs (1974). How far this feature might extend in depth may be investigated by examining the cone diagrams in X and Y for the area including this projected structure (see later). This cigar shaped cluster may form part of a larger structure, as there is another significant grouping of similar redshift at  $\sim 0.46^\circ$  to the right of the main feature (i.e. about  $1.3 h^{-1} \text{Mpc}$  away), at the very edge of the field.

Apart from a small clump labelled 'A' in figure 6.48a, the left-hand side of the field appears sparsely populated at these redshifts when compared with the structure exhibited in the right half of the field. Regions of  $\sim 3 h^{-1} \text{Mpc}$  in diameter are evident in which no galaxies yielding objective-prism redshifts are found over this 0.04 redshift range ( $=120 h^{-1} \text{Mpc}$ ). Note however, the presence of the step-wedge region at the bottom left of the diagram and hence the absence of galaxies in this particular area. The lack of galaxies with objective-prism redshifts over quite large areas in figure 6.48a indicates a paucity of elliptical galaxies over the covered redshift range. It would be interesting to enlarge the objective-prism redshift survey to the adjacent field (SERC survey field 408), to see if the foreground structure does indeed extend to lower R.A's.

Referring back to figure 6.2, the 2-D distribution of galaxies with  $b_j \leq 16.5$ , and figure 6.5, the associated slit-spectra redshift histogram, it can be seen that this foreground structure detected with the objective-prism redshifts is almost co-incident with the projected bright galaxy concentration in figure 6.2. Furthermore, the main peak of the second slit-spectra redshift distribution ( $V \sim 16,000$  Km/s), is in good agreement with the objective-prism redshifts obtained for the foreground structure in figure 6.46a of  $Z \sim 0.055$ .

As an additional exercise, the galaxies in figure 6.48a were segregated into two smaller redshift intervals; viz  $0.04 \leq Z \leq 0.06$  and  $0.06 \leq Z \leq 0.08$ , to see if further structure is revealed. The results are presented in the X-Y plots of figures 6.49a and 6.49b, where galaxy positions are again denoted by circles whose diameter decreases with increasing redshift. This proved to be an interesting undertaking as the plots suggest that the cigar shaped cluster, still evident in figure 6.49a, 'loops back' to higher redshifts in figure 6.49b before reappearing in the lower redshift interval again at the right edge of the field in figure 6.49a. The depth covered by both plots combined of  $\sim 120 h^{-1} \text{Mpc}$  is  $\sim 4X$  that of the expected uncertainty in the objective-prism redshifts of  $\sim 30 h^{-1} \text{Mpc}$  so that the curved 'filament' is unlikely due solely to the redshift measurement uncertainties of  $\pm 0.01$ . In fact, the excellent agreement between the circle sizes for the galaxies in the higher redshift extension of the cigar shaped cluster in figure 6.49a imply almost identical prism redshifts, since the full range of circle size used in the plot only covers 0.02 in redshift. The effect may however, be less pronounced than indicated by figures 6.49a-b since the observed structure could span the junction between the 2 redshift ranges selected.

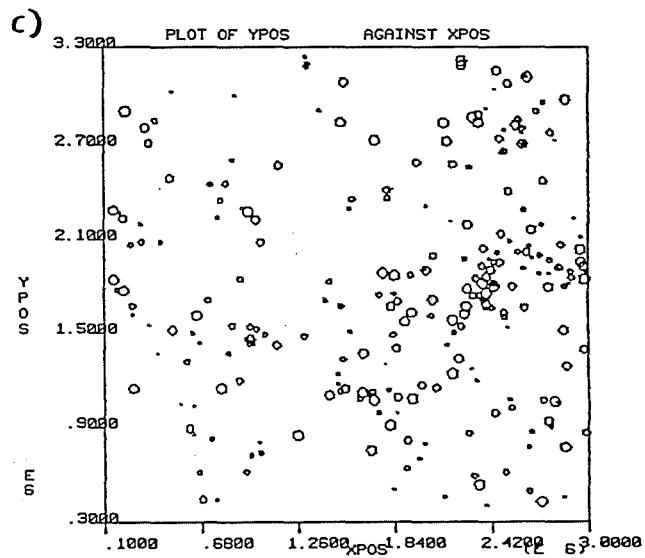
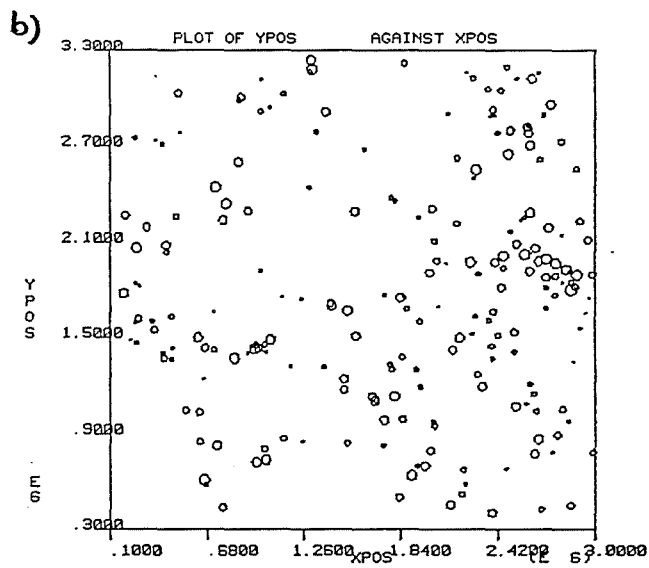
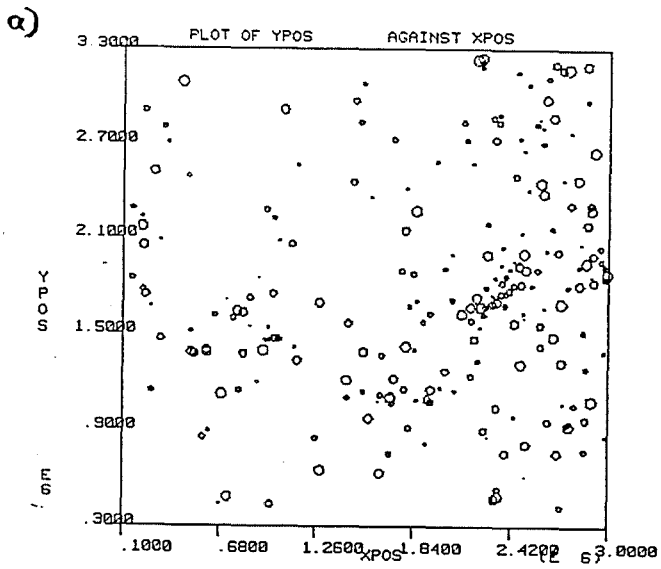


Figure 6.49a-c The 2-D X-Y plots of galaxies over the redshift ranges:  
 a)  $0.04 < Z < 0.06$   
 b)  $0.06 < Z < 0.08$   
 c)  $0.05 < Z < 0.07$

Consequently, figure 6.49c gives the X-Y plot for the galaxies over the redshift interval  $0.05 \leq Z \leq 0.07$ , which can be compared with figures 6.49a-b. It can be seen from the plotted circle diameters in this figure, that the cigar shaped region does appear to be connected to the small grouping at the extreme right edge of the field by a string of higher redshift galaxies which are consistently of smaller diameter than those in the features to which it is 'connected'. Furthermore, it is tempting to believe that figure 6.49c also indicates a curved 'tail' at the bottom left of the cigar shaped cluster of almost identical redshift to the main foreground enhancement.

The foreground structure revealed in figures 6.49a-c corresponds closely to the chosen cluster areas 8 and 9 of figure 6.43. The redshift histograms for clusters 8 and 9 in figure 6.42a gave main cluster peaks of  $Z \sim 0.05$  and  $0.06$  respectively, which also confirms the more remote nature of the connecting structure in figure 6.49b. In conclusion, it does seem likely from the results of figures 6.49a-c and from the redshift histograms for clusters 8 and 9, that these clusters are part of a larger feature that twists in depth and probably extends into the adjacent field. Finally, figure 6.50 gives the redshift histogram for all galaxies within a  $2.24^\circ$  square area of the plate encompassing the foreground structure. The contribution from the foreground structure at  $Z \sim 0.05 - 0.07$  dominates the distribution, as expected, although a secondary peak at  $Z \sim 0.10$  is also evident. This may be considered as evidence for the extension of the SC at  $Z \sim 0.11$  under this region.

IMPOSED LIMITS:-  
 XMIN : .180E 7 TO .300E 7  
 YICEN : .140E 7 TO .260E 7  
 Z : .000 TO .180

REJECTED OBJECTS IGNORED

NUMBER INCLUDED:-  
 GALAXIES: 414  
 REJECTS: 0  
 STARS: 0

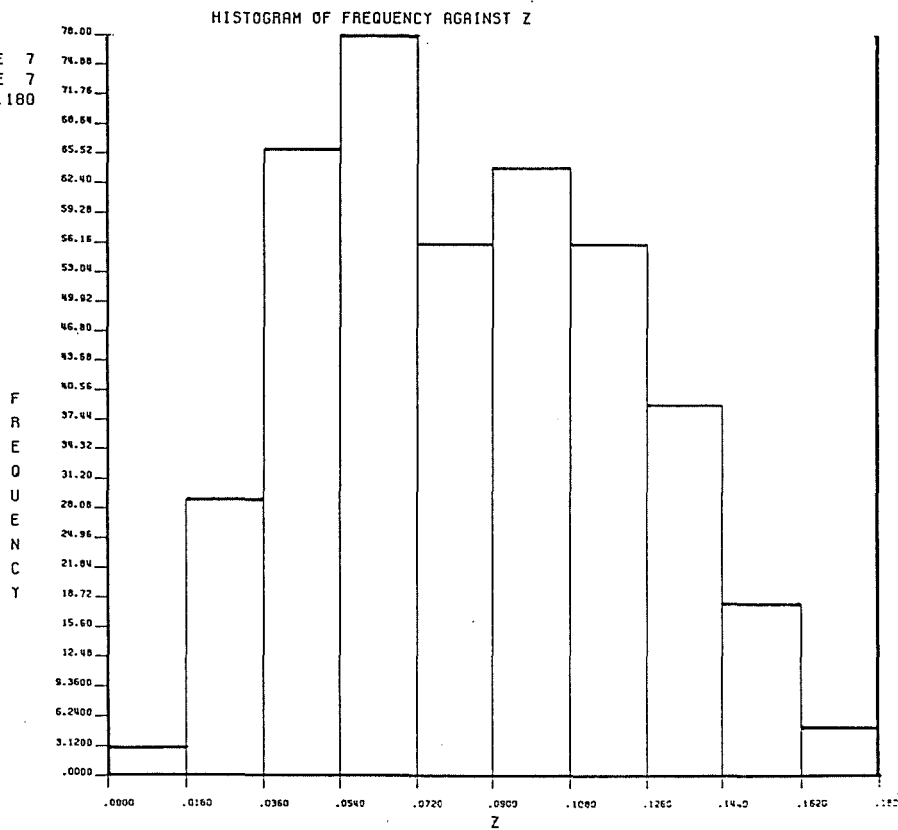


Figure 6.50 Redshift histogram for the galaxies within a  $2.24^\circ$  square area encompassing the 'foreground' structure.

Returning to figure 6.48b, the X-Y plot for galaxies over the redshift interval  $0.10 < Z < 0.14$  (chosen to cover the redshift range of the suspected SC at  $Z \sim 0.11$  implied by the cluster results), this 'filament' is indeed evident as a number-density enhancement running mid-way through the field in declination. The high redshift component of foreground cluster 9 (see figure 6.42a), can also be seen at the extreme right of the field centre. Compared with figure 6.48a, the galaxies in this redshift interval are generally more uniformly distributed over the field. The contribution from this 'enhancement' can be clearly seen however, if two strips  $\sim 1.5^\circ$  wide are chosen in the Y (declination) direction, where one strip covers the region of the 'filament' and the other is a strip running parallel to the first but over a range of Y-position avoiding the step-wedge region (as this would bias the counts). Redshift histograms for these strips are presented in figures 6.51a-b for the 'filament' and comparison strips respectively. All galaxies with objective-prism redshifts in these regions are included and the bin widths of 0.01 correspond to the expected resolution of the objective-prism redshift technique.

The first point to note is that the total number of galaxies with prism redshifts within the 'filament' strip is  $\geq 3X$  that for the comparison strip, i.e. 1,014 galaxies compared with 317, confirming the strong density enhancement in this strip. Secondly, both histograms exhibit two main peaks although these peaks are much more pronounced for the 'filament' region. The first peak in both histograms corresponds to the redshift of the foreground structure evident in figures 6.49a-b though the significance of this peak in the comparison strip is marginal. The peak from the foreground structure is expected in the 'filament' strip since this strip incorporates the main foreground clump in figure 6.46a.

IMPOSED LIMITS:-  
 YICEN : .150E 7 TO .230E 8  
 Z : .000 TO .180  
 REJECTED OBJECTS IGNORED  
 NUMBER INCLUDED:-  
 GALAXIES: 1014  
 REJECTS: 0  
 STARS: 0

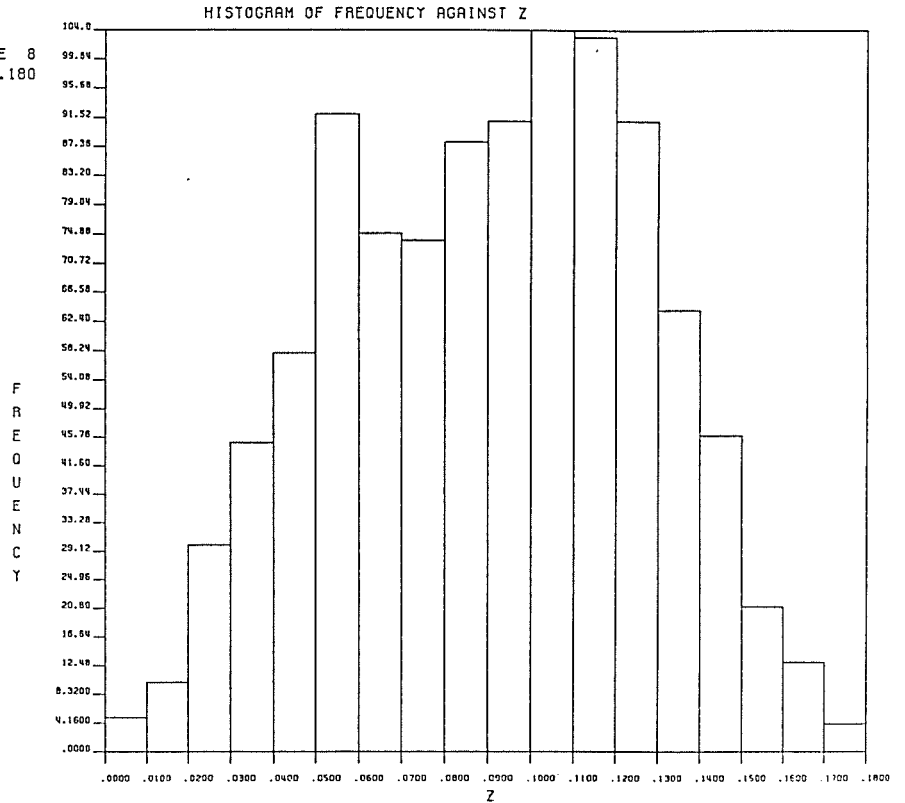


Figure 6.51a Redshift histogram for a 1.5° wide strip in declination through field 349, incorporating the SC 'filament' at  $Z \sim 0.11$ .

IMPOSED LIMITS:-  
 YICEN : .230E 7 TO .310E 7  
 Z : .000 TO .180  
 REJECTED OBJECTS IGNORED  
 NUMBER INCLUDED:-  
 GALAXIES: 317  
 REJECTS: 0  
 STARS: 0

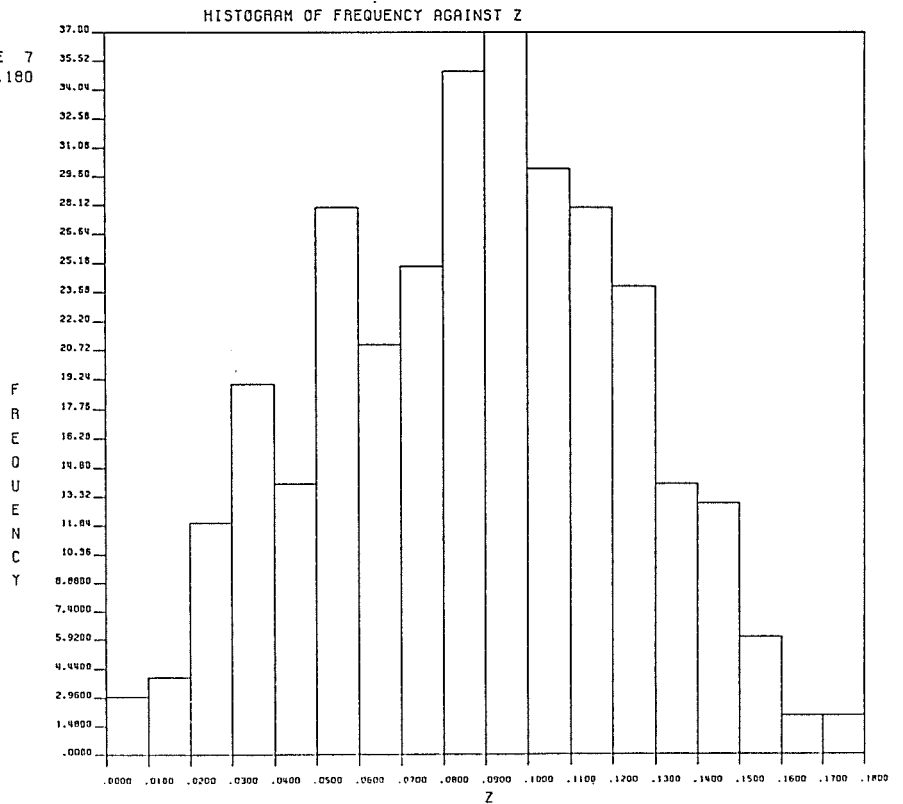


Figure 6.51b Comparison redshift histogram for an equivalent, parallel 1.5 strip in declination.

The second peak for the 'filament' strip, at  $Z \sim 0.10 - 0.12$ , is compatible with that of the SC at  $Z \sim 0.11$ , whilst that in figure 6.51b is of lower redshift, i.e.  $0.08 - 0.10$ . Although there is a contribution from the foreground structure, the density enhancement of figure 6.51a over that of figure 6.51b is dominated by the contributions from the high-redshift component, confirmed by comparing the relative heights of the high-redshift bins. Consequently, the reality of filamentary type SC is given further credence by these results.

Finally, figures 6.52a-b gives the cone diagrams for all 1,539 galaxies with objective-prism redshifts over field 349 to  $b_j = 18.7$ , which illustrates how the galaxy sample is distributed in redshift and X and Y position. The diagrams were generated by GALPLOT, a program kindly made available to the author by Dr.S.M.Beard. Figure 6.52a gives the plot of redshift (or distance) against X plate position (=R.A.), and figure 6.52b gives the corresponding results for Y plate position (=DEC). Each galaxy is plotted as a circle whose radius increases with decreasing magnitude so that the more luminous galaxies at a given redshift are evident. The most obvious and striking feature of these diagrams is the tendency for galaxies to be concentrated in fairly narrow X,Y regions with changing redshift. A strongly clumped agglomeration is evident in both plots, which lies in the mid DEC range in figure 6.52a but at the low R.A. range in figure 6.52b. This corresponds to the position of the foreground structure of figure 6.46a at  $Z \sim 0.05 - 0.06$ . However, this feature extends for  $> 150 h^{-1} \text{Mpc}$  from  $Z \sim 0.02-0.07$ , spanning the redshift range of the two foreground clusters 8 and 9 in figure 6.44. This not only confirms the existence of the foreground SC but also illustrates that the projected physical size of the feature, which could be as large as  $7 h^{-1} \text{Mpc}$  (see figure 6.49a-c), is small compared with its apparent distribution in depth.

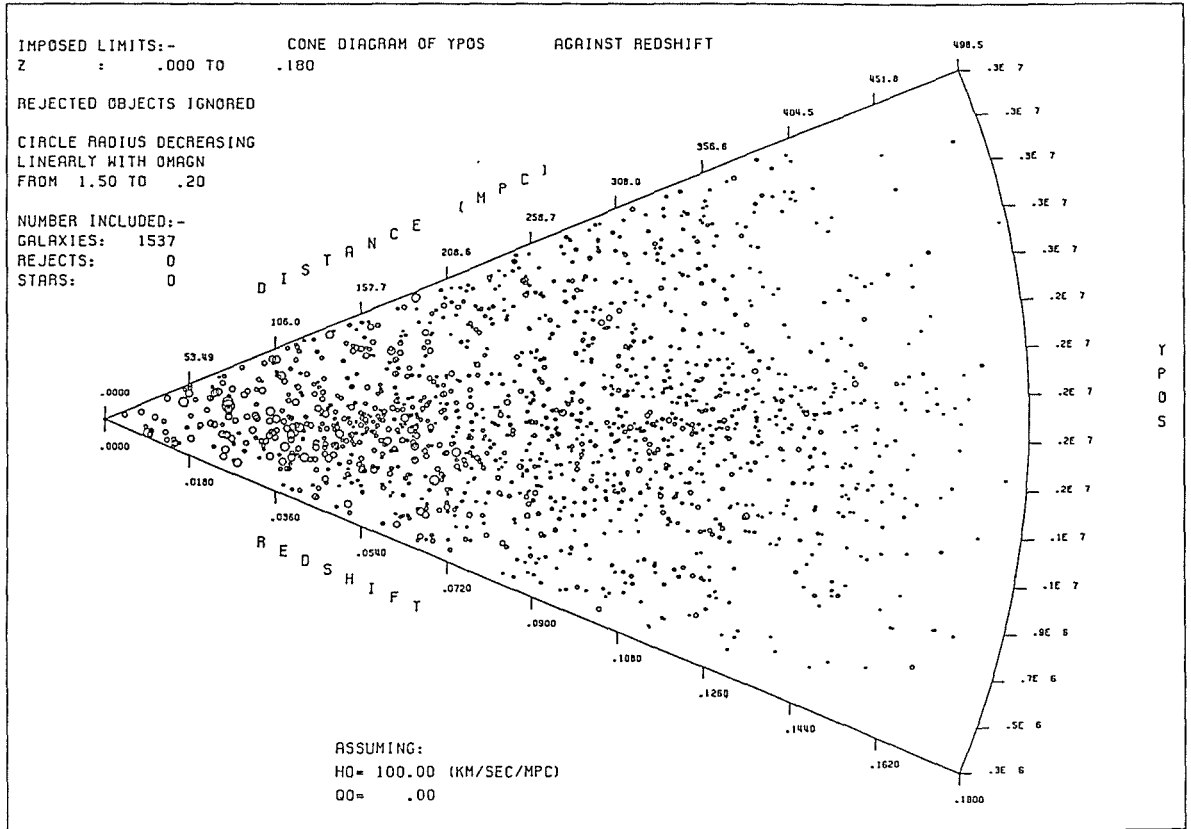


Figure 5.52a Cone diagram of X-plate position against redshift/depth for the entire objective-prism redshift sample.

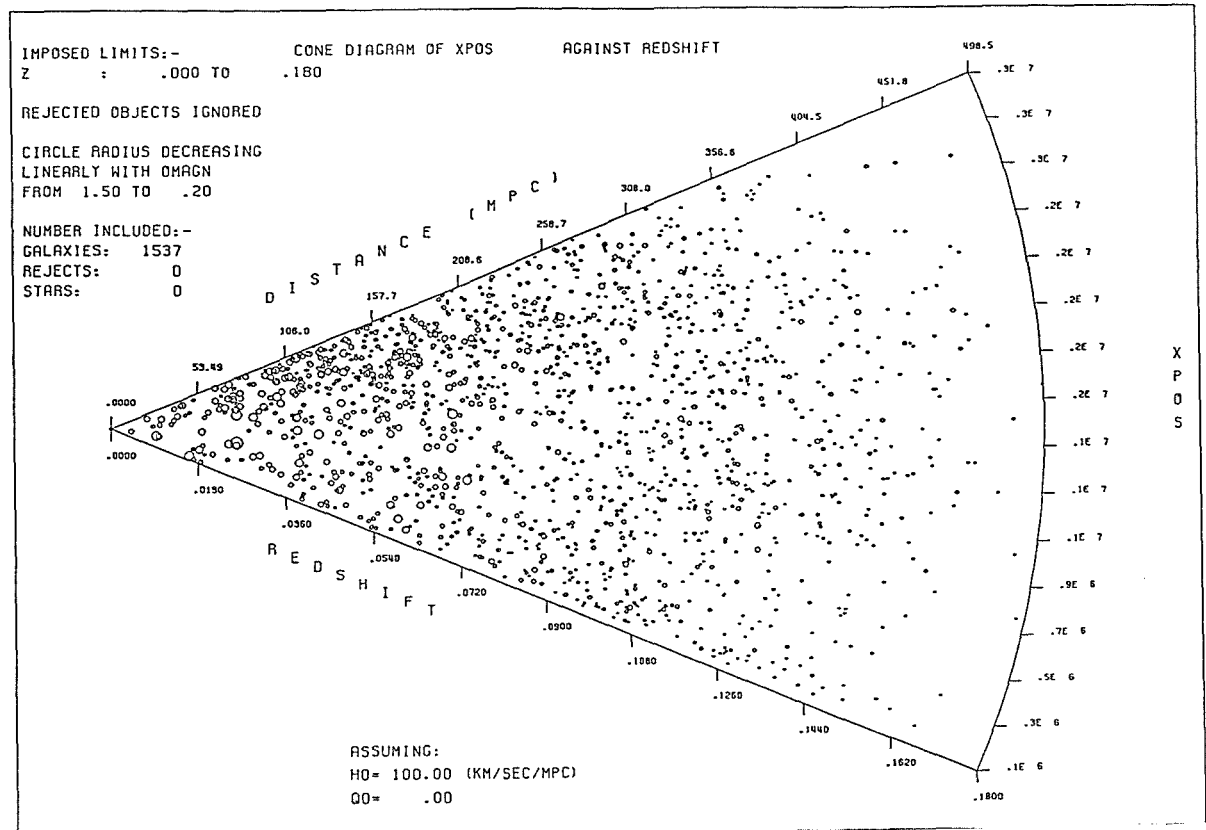


Figure 5.52b Cone diagram of Y-plate position against redshift/depth for the entire objective-prism redshift sample.

Although the resolution in depth is  $\sim 30 h^{-1} \text{Mpc}$ , due to the inherent crudeness of the objective-prism redshifts, this is unable to account for the observed elongation of the density enhancement. Indeed it is this 'foreground' SC and not the background SC at  $Z \sim 0.11$  which is striking in the cone diagrams. In figure 6.52b though, there is a suggestion that the foreground, elongated feature, which seems to fade at  $Z \sim 0.07$ , reappears at  $Z \sim 0.11$ , the redshift of the background SC, since these two concentrations seem to lie long the same line of sight. However, this does not imply, necessarily, that these two structures are in any way related. In fact the observed effect is because the filamentary structure at  $Z \sim 0.11$ , which runs across the field in the X-direction is overlaid by the foreground structure at the right edge of the field. Consequently, as figure 6.52a gives Y-position against redshift, the contributions from the galaxies in the filament are not resolved in X and appear as a density enhancement in the Y-direction in figure 6.52a. The SC at  $Z \sim 0.11$  is absent in figure 6.52b because in this case there is no resolution in the Y-direction so that the 'horizontal filament', which occurs over a narrow range of Y-positions, is lost within the contributions from the rest of the field.

The fact that the filamentary SC at  $Z \sim 0.11$  is not more obvious in the cone diagrams is also because galaxies in this feature, initially picked out from the cluster redshift peaks and evident in figure 6.48b, only constitute a small fraction of the total galaxy sample, and also because the redshifts would need to be more strongly clumped in both X and Y in order to show up. Furthermore, the majority of galaxies which constitute the SC may be too faint for inclusion in the objective-prism redshift sample so that only the most luminous cluster and filament members are evident.

As well as the striking large-scale structure revealed in figures 6.52a-b, areas deficient in galaxies are also apparent. The detection of the observed pattern of galaxy density enhancement and paucity on such large scales is the most important and cosmologically significant result furnished by the objective-prism redshift technique. The most significant result for this field, from a magnitude-limited, whole-plate sample, is the large density enhancement over the redshift range  $Z \sim 0.02-0.07$ . This feature extends for  $\sim 150 h^{-1}\text{Mpc}$  in depth and is projected over a  $2^\circ$  square area of the plate. An underlying 'filamentary-type' SC at  $Z \sim 0.11$ , with a projected extent along the main branch of at least  $23 h^{-1}\text{Mpc}$ , is also detected. Consequently, with large numbers of objective-prism redshifts the technique can thus be used to test for such large-scale features to depths of at least  $400 h^{-1}\text{Mpc}$  over entire UKST fields. Beyond this the selection function begins to seriously reduce the numbers of galaxies yielding measurable  $4000\text{\AA}$  features.

In conclusion, the objective-prism redshift results from this field to  $b_j = 18.7$ , have revealed the existence of significant large-scale features in the galaxy distribution and as such indicate that the technique is a useful probe of such features to depths of  $\sim 400 h^{-1}\text{Mpc}$ . Although only the largest features are resolved, the size and overall nature of these gross features in the galaxy distribution, probed by the objective-prism redshift technique, may still provide useful information since the observed sizes of SC's and the existence of filaments and chains must be compatible with appropriate cosmological theory (see chapter 1). A simple descriptive approach to the results from the large sample of objective-prism redshifts obtained has been given. More sophisticated and precise analysis techniques, such as application of the spatial 2-point correlation function, are not warranted at this stage due to the inherent crudeness of the redshifts.

General conclusions and future suggested work.

Although consisting of several sections which can, if desired, be considered separately from the rest of the work, the over-riding and connecting theme throughout the thesis has been an attempt to describe, in detail, the distribution of visible matter in one particular UKST field. The original vision had been to study the galaxy distribution of a number of adjacent fields near the SGP in order to obtain a significant and hopefully representative segment of the Universe for analysis, which would yield important information for improving our understanding of the distribution of matter on small ( $<20 h^{-1}\text{Mpc}$ ), up to very large ( $\sim 500 h^{-1}\text{Mpc}$ ), scales.

This study would initially consist of obtaining complete, or near complete, magnitude-limited samples of accurate, slit-spectra radial velocities for galaxies to  $b_j \sim 16.5$ . Such a sample would allow a detailed description of the small-scale relationship between galaxies and groups to moderate ( $\sim 150 h^{-1}\text{Mpc}$ ), depth, such as is given in chapter 6. Indeed, the radial velocities, accurate to  $\sim 75 \text{ Km/s}$  as demonstrated in chapter 2, are sufficient for determination of other properties of the galaxy distribution such as the luminosity function, M/L ratios, galaxy cluster/group virial parameters etc. Although such studies are outside the brief of this thesis they are of undoubted interest and would make a worthwhile investigation in their own right. It is hoped that the author will be able to undertake this project from the data obtained in field 349 in the near future.

The chosen magnitude limit of  $b_j \sim 16.5$  for this slit-spectra redshift survey is also compatible with that of the Durham redshift survey (e.g. Shanks et al. 1983), and would be a useful addition to their 'pencil beam' surveys. This would be especially true if slit-spectra data from a number of adjacent UKST fields were obtained. This is because the broad scale structure of the Universe cannot be satisfactorily recovered from views of a few narrow cones, Chincarini and Rood (1979).

The 2-point spatial correlation function, techniques of hierarchical clustering, nearest neighbour analysis and other sophisticated methods with which to describe the 3-D galaxy distribution could be applied to the high quality 3-D data. Obviously, the more fields which can be studied in this way the more important the results and statistics will be for understanding and unravelling properties of the galaxy distribution.

Apart from a precise investigation of the galaxy distribution to  $b_j \sim 16.5$  ( $\sim 150$  galaxies per UKST field), the Cosmos machine would be used to provide large amounts of data from scans of both direct and objective-prism plates for faint galaxies to  $b_j \sim 20.5$  and  $b_{uj} \sim 19.0$  respectively. The direct plate, faint galaxy sample would allow 2-D statistical analysis of the projected galaxy distribution whilst the objective-prism data would provide crude spatial information for galaxies to  $b_{uj} \sim 19.0$ , to depths of at least  $400 - 500 h^{-1}$  Mpc. The spatial resolution is sufficient to describe large scale density enhancements, voids and to obtain cluster redshift peaks.

Unfortunately, this ambitious program was restricted to a single UKST field as far as this thesis was concerned because of the time required to accumulate, reduce, assess and interpret the large quantity of data obtained even from this single field. The tools and methods developed and described in this work for performing the analysis of the galaxy data of field 349 can however, be directly applied to other fields when the data becomes available. Nevertheless, the results from analysis of the 2-D and 3-D galaxy data for this field have proved to be very interesting and informative. Perhaps the best way to continue is to consider the contributions made by each chapter in turn.

Chapter 1 was basically a review essay giving an account of the development in our understanding of the large-scale structure of the Universe, together with the cosmological theories constructed to address the implications of the observed structure. Chapter 2 described the steps involved in selecting a magnitude limited sample of galaxies from Cosmos data of the field, observing the sample with the RPCS and ITS of the SAAO 1.9m telescope and reducing their slit spectra at  $210 \text{ \AA/mm}$  to obtain accurate radial velocities. The observed sample of 107 galaxy radial velocities amounts to 80% of all galaxies detected by Cosmos to  $b_j \sim 16.5$  in the field and as such presents a valuable data base to a high level of completeness. The cross-correlation technique was once more shown to be a powerful means of deriving accurate velocities, which was further enhanced by giving careful attention to all stages of the data reduction and by using a wide selection of stellar and galaxy templates.

One of the prime reasons for obtaining accurate slit-spectra radial velocities for galaxies in this field was to provide a calibration sample for the objective-prism redshift technique (chapter 4). Although the faintest galaxies with slit-spectra velocities at  $b_j \sim 16.5$  were near the extreme bright limit of the useful range of the technique of  $b_j \sim 16.0$ , as determined by Cooke (1980), prism redshifts for all possible galaxies with slit-spectra in the field were examined. This led to an increase in the calibration sample by a factor of two over that previously available. Indeed, application of a surface-brightness correction to the prism redshifts demonstrated that the objective-prism redshift technique could be extended to a brighter limit of  $b_j \sim 15.5$ . Good agreement between the slit-spectra and corresponding objective-prism spectra redshifts were obtained to within the expected uncertainties of  $Z \pm 0.01$  at these magnitudes. However, these results have only improved the calibration at the bright end. Accurate slit-spectra redshifts are required for much fainter galaxies to  $b_j \sim 19.0$  to test and improve the calibration of the objective-prism redshift technique at faint limits also. The fibre-optic system on the AAT and UKST would be ideally suited for this task.

Since it was envisaged that the objective-prism redshift technique would play a significant role in investigating the distribution of faint galaxies it was important to ascertain whether useful and reliable spatial information, accurate to within the expected uncertainties, could in fact be obtained. Consequently, a major section of this thesis was concerned with the careful assessment of the viability of the objective-prism redshift technique as a means of probing the galaxy distribution to depths of  $\sim 500 h^{-1}$  Mpc. Although much work has already been done by Cooke (1980), and Beard (1984), no thorough investigation into the reliability, consistency and repeatability of the technique with changes in plate material,

measuring machine and reduction method had been undertaken.

Chapter 3 thus described the results of such an investigation using copy and original plates of field 349 and using J-L and Cosmos data. Though the J-L technique appears to give the best objective-prism redshift results, this method is impractical for whole plate samples due to the inordinate amount of time required to measure the large numbers of spectra present. Since the advantage of the technique lies in the potential to obtain large numbers of objective-prism redshifts, which to an extent compensate for the low redshift accuracy, a means of obtaining these results quickly and efficiently is required. Using data from scans of objective-prism plates obtained with fast measuring machines such as Cosmos seems to be the answer and the semi-interactive redshift measurement techniques such as INTERZED (Beard, 1984), give a substantial time saving over the laborious, manual J-L measures. Even so, the time needed to measure a whole plate sample to  $b_j \sim 19.0$ , the faint magnitude limit of the technique, is still prohibitive and is impractical for surveys over many fields. Furthermore, the interactive methods contain a certain amount of subjective judgement on the part of the observer and considerable experience and skill is required to obtain consistent results, as shown in chapter 3.

Consequently, the development of a reliable, automatic objective-prism redshift technique, such as that envisaged by Cooke (1984), and for which development work has already been undertaken, would be required. Such a technique, once properly implemented, would be fast, efficient and objective. Moreover, since it is based on a pattern matching process it would be fairly straightforward to include a selection of stellar template spectra of various spectral types. This would also enable the automatic technique to be applied to the stellar prism plate sample and provide rough spectral type

classifications for thousands of stars per field (see UKST objective-prism handbook). Such data could prove valuable in studies of galactic structure. Moreover, inclusion of stellar templates of zero redshift with the galaxy templates, could enable automatic rejection of any stellar contaminants in a galaxy sample based on a star/galaxy separation of the direct-plate data and the subsequent pairing with the prism - plate data. The results of chapter 5 have already shown that such contamination is a serious problem in the galaxy sample from a star/galaxy separation of the direct-plate Cosmos data of this field. This stellar contamination, which amounted to 20% of "classified" galaxies, was revealed by examination of the magnitude-magnitude plot of the paired direct-and prism - plate galaxy samples. This plot (figure 5.18), exhibited two distinct components with an upper curve lying directly along the single curve obtained when the equivalent stellar classified mag/mag plot is considered (figure 5.17). The stellar nature of objects lying on the upper curve of the galaxy mag/mag plot was independently confirmed from study of the galaxy objective-prism spectra where identified stellar contaminants were flagged (see figure 5.19). This result could have important consequences for number - magnitude counts and their interpretation, when based on star/galaxy separation from direct plate Cosmos data. Results from galaxy 2-point correlation function studies should not be adversely affected however, because the stellar contaminants should simply add a random background. Similar two component mag/mag plots were obtained by Beard (1984), though he attributes this effect to compact galaxies. This contamination is thus unlikely to be a peculiarity of the particular direct plate star/galaxy separation used for this field. Thus yet another potential use for objective-prism plate data as a more reliable means of star/galaxy separation, when paired with the corresponding direct plate data, is suggested.

The whole plate sample of  $\sim 1,500$  objective-prism redshifts presented in this thesis was obtained with the interactive INTERZED technique (see Beard, 1984). The data were from the high quality original objective-prism plate UJ6535P to  $b_j \sim 18.7$ . An original plate was used since the empirical studies of chapter 3 revealed significant problems if Cosmos data of copy plates were employed. The recommendation is that only original plates should be used for carrying out objective-prism redshift surveys with Cosmos data.

A new use of galaxies with  $4000\text{\AA}$  features as a means of detecting filamentary structure and galaxy clumping has also been demonstrated (see section 6.3 of chapter 6). This is due to the fact that such galaxies will be mainly ellipticals, and follows the suggestion of Giovanelli et al. (1982), that early type galaxies may be important tracers of such features. The results presented in figures 6.46a-c of chapter 6 well illustrate this new application. Compared to the projected distribution of galaxies without objective-prism redshifts, those with redshifts do indeed reveal the existence of clumps and chains in a more striking manner than from examination of number/density plots. For instance the SC 'filament' at  $Z \sim 0.11$  is clearly highlighted.

This work has shown once and for all that providing the limitations of the plate material and measuring machine are understood and allowed for, consistent objective-prism redshift samples can be obtained. The technique is thus a useful tool for probing the large-scale distribution of matter and can provide  $> 2,000$  crude redshifts per UKST field. The results described in chapter 3 contradict the assertion of Hewett (1984), that "in no case have two (objective-prism) plates of the same area of sky been measured and even simple internal errors investigated" (sic).

Perhaps the most useful application of the objective-prism redshift technique would be to complement the generation of a 2-D galaxy/cluster catalogue of the southern hemisphere from Cosmos data of UKST direct plates. The generation of the catalogue is already underway by workers at the ROE and should provide a wealth of information for performing a detailed statistical analysis of the large-scale structure in the Universe from the 2-D projected galaxy distribution. However, the very 2-D nature of such a catalogue limits its usefulness and may even give a false impression of galaxy clustering due to super-position effects, e.g. Perenod and Lesser (1980). Obtaining slit-spectra radial velocities, even if only for galaxies in the rich clusters in each field of the survey, would still require vast amounts of telescope time with conventional spectrographs. The advent of fibre-optic systems on the AAT and UKST is a potential means of overcoming the 2-D inadequacies of the catalogue, although it is unlikely that more than 100 redshifts per field would be obtained in any one exposure.

The objective-prism redshift technique though, could provide sufficient 3-D resolution to complement the 2-D data, since although crude, the technique is sufficiently accurate to enable large-scale density enhancements, rich cluster redshift peaks, and large voids to be detected and could also be used for filament detection over different redshift intervals. The detection of such gross features in the galaxy distribution, especially if they extend into adjacent fields, as is suggested from the results from field 349 described in chapter 6, has important cosmological implication. Study of such structures may yield information on the nature of any density fluctuations that may have occurred during the early stage of the Universe and thus give insight into the manner in which the largest structures may have formed. Of course, if this technique is to be a useful complement to the 2-D data then many more objective-prism

plates would need to be taken. The lack of high - quality objective-prism plates is the major limitation to a more widespread application of this technique at present.

Finally, chapter 6 describes the results of the 3-D analysis of the high-quality positional data for galaxies to  $b_j \sim 16.5$ , using the accurate slit-spectra radial velocities, and the results of an investigation into the 2-D projected faint galaxy distribution to  $b_j \sim 20.5$  from Cosmos direct plate data. These 2-D data are supplemented with a crude 3-D investigation from consideration of objective-prism redshifts for galaxies to  $b_j \sim 18.7$ .

Section 6.2.4 of chapter 6 details the main findings from analysis of the bright galaxy sample to  $b_j \sim 16.5$  in field 349. In brief however, two main redshift groupings were found in the galaxy distribution from this near-complete magnitude-limited sample, which was also characterised by the existence of two significant voids. The voids seemed to have depths of 20 and 80  $h^{-1}$  Mpc and projected physical dimensions of 6 X 11 and 5 X 9  $h^{-1}$  Mpc respectively, from the survey sample depth of  $\sim 180 h^{-1}$  Mpc. As described in chapter 1, such features are becoming increasingly apparent in the results from studies of the 3-D galaxy distribution when based on increasing samples of accurate radial velocities. Since these void volumes were minimum values, restricted by the size of the field studied, an extension of the radial - velocity survey to adjacent fields is suggested so that the full extent of these features can be ascertained. Furthermore, it would be interesting to obtain redshifts for fainter galaxies in the void regions to see if they are actually populated by low-luminosity galaxies.

Techniques of hierarchical clustering analysis were applied to the two main redshift groupings for the sample to  $b_j \sim 16.5$ , as well as application of the minimum - spanning - tree (MST), construct (see chapter 6). These techniques have been shown to be extremely useful and powerful means of classifying the observed galaxies into groups in a hierarchical fashion and for detecting field galaxies. The MST construct on the other hand can be used to reveal the natural degree of connectedness between galaxies and can consequently be used as a filament-detecting algorithm. Such methods have been rarely employed for astronomical purposes in the past but they are highly recommended for future use with accurate redshift surveys. A potentially important result was the existence of a characteristic 'break' in the fusion co-efficient from the hierarchical clustering analysis. This occurred at the same value for both redshift groupings and may be indicative of preferred levels of hierarchy for galaxies in this field.

Section 6.3.2 of chapter 6 describes the results of application of the 2-point correlation function, power spectrum analysis and Meads' analysis to the projected 2-D galaxy distribution in field 349 to different magnitude limits and over various 0.5 magnitude intervals. The distribution of galaxies was initially shown to be highly non-random from a simple binning analysis. Compared to the corresponding stellar sample to the same magnitude limit, and for an equivalent random sample, the 2-point correlation function of the 2-D galaxy data was strongly correlated and followed a fairly well - defined relation until  $\sim 2^\circ$  when a distinct break was evident. There was also evidence of anti-correlation at larger angular scales. This break point position corresponds to a physical size of  $\sim 11.5 h^{-1} \text{Mpc}$  (if the redshift of the SC at  $Z \sim 0.11$ , discovered from the objective-prism redshifts in this field, is used), and also appears to scale fairly well with depth (see table 6.3). The results of figure 6.29 and 6.30b

also indicate that it is the contribution to  $W(\theta)$  from the brighter galaxies which is dominating the observed break-point position in the results for the faint galaxy sample to  $b_j \sim 20.5$ . This is probably the result of the presence of the foreground structure also found in the field. This structure is centred at  $Z \sim 0.055$  and was also revealed from study of the objective-prism redshift results (see later).

The results from the 2-D PSA, which is considered a more powerful and sensitive test for galaxy clustering than other statistical methods such as nearest-neighbour analysis and correlation function analysis, indicates that the galaxies in this field are clustered on scales  $> 0.3^\circ$ , (see figure 6.33). The clustering strength increases at all  $\theta > 0.3^\circ$  for each magnitude-limited sample. An interesting feature of the PSA results is that they show evidence of a 'jump' in the clustering strength, as given by the  $Q'$  amplitude, at specific  $\lambda_c$  values. Furthermore, the position of this jump moves to larger angular scales with decreasing sample magnitude limit. Such behaviour is expected if the observed clustering was scaling with depth and is thus in qualitative agreement with the scaling of the break-point position observed in the 2-point correlation function results.

The last major statistical test applied to the 2-D galaxy data was Mead's analysis which is a powerful though simple technique for detecting clustering. The main disadvantage is that it only tests for clustering over a limited number of scales (e.g. see Mead, 1974). The results from this test also reveal significant clustering of the galaxy data when compared with equivalent random simulations and the corresponding stellar sample. The shape of the Mead's curve obtained from the galaxy data to  $b_j \sim 20.5$  was similar to that obtained by Shanks (1979), when he applied the statistic to a simulation of the galaxy distribution that follows a power-law cluster model, but not

one of continuous hierarchical clustering. Two preferred scales of clustering were indicated at  $\theta \sim 0.5^\circ$  and  $\theta \sim 2.0^\circ$ , although the exact scales are not known due to the limited number and resolution of scale sizes tested. The first Meads' peak at  $\theta \sim 0.5^\circ$  obtained from the galaxy data to  $b_j \sim 20.5$ , is at a similar scale to the jump observed in the  $Q'$  values in the equivalent 2-D PSA results. This peak may correspond to the mean cluster size in the field. If these clusters are considered part of the SC at  $Z \sim 0.11$ , then this corresponds to a physical extent of  $\sim 3.5 h^{-1} \text{Mpc}$ , not an unreasonable size for such clusters. The second peak at  $\theta \sim 2.0^\circ$  corresponds to the next preferred scale of clustering, and is picking out the SC in this field evident from the objective-prism redshifts. The clustering scale of  $\theta \sim 2.0^\circ$  agrees well with the conservative estimate of the diameter of the looped filamentary feature evident in figure 5.8. Interestingly, the same general Meads' curve was obtained for each galaxy sample to the different magnitude limits considered, although the amplitudes of the observed peaks and troughs did vary. This could be because the largest structure in the field (see figure 5.8), is dominating the statistics over a wide magnitude range (figure 6.38).

The above results from the study of the 2-D galaxy data have thus revealed significant anisotropy and structure in the projected galaxy distribution on scales at least as large as  $15 h^{-1} \text{Mpc}$ . Preferred clustering scales are also implied which seem to scale quite well with depth.

Analysis of the whole-plate objective-prism redshifts obtained in this field have also revealed significant features in the galaxy distribution. A foreground supercluster has been discovered which extends for  $\gg 150 h^{-1}\text{Mpc}$ , from  $Z \sim 0.02-0.07$ , particularly evident in the cone diagrams of figures 6.52a-b. A background 'filamentary' supercluster was also detected at  $Z \sim 0.11$ . This confirms the results from an initial objective-prism cluster study of this field by Parker et al. (1984b). This SC may extend right across the field in R.A. for  $\sim 5^\circ$ , corresponding to a distance of at least  $23 h^{-1}\text{Mpc}$ .

The existence of these large-scale features are compatible with the theory that superclusters developed from a truncated spectrum of adiabatic fluctuations of baryons or massive neutrinos with an excess of power on large scales. The presence of large voids, long filaments and extensive, elongated SC's as main features of the galaxy distribution in this field revealed by this investigation is difficult to reconcile with isothermal theory where structure is formed from gravitational interactions in a 'bottom up', hierarchical fashion. Furthermore, the fact that galaxies with objective-prism redshifts, i.e. mainly the ellipticals, highlight the filamentary SC, thus implying a morphological segregation of galaxies in these features, is a strong indication in favour of the adiabatic scenario of galaxy, cluster and supercluster formation (see Oort, 1984).

## References

- Aarseth, S.J., Gott, J.R., & Turner, E.L., 1978. *Ap.J.*, 228, 664.
- Abell, G.O., 1958. *Ap.J. Suppl.*, 31, 27.
- Abell, G.O., 1961. *Astron.J.*, 66, 607.
- Abell, G.O., 1962. In "Problems of extragalactic research.", Ed. G.C. McVittie (New York: MacMillan), p213.
- Abell, G.O., 1965. *Ann. Rev. Astron. & Astrophys.*, 3, 1.
- Abell, G.O., 1965. Stars & Stellar Systems volume IX, p601, Eds. Sandage, A., Sandage, M., & Kristian, J., University of Chicago press.
- Abell, G.O., & Seligman, C.E., 1965. *Astron.J.*, 70, 317.
- Abell, G.O., & Seligman, C.E., 1967. *Astron.J.*, 72, 288.
- Anderberg, M.R., 1973. Cluster analysis for applications, Academic Press, New York.
- Barrow, J.D., Bhavsar, S.P., & Sonoda, D.H., 1985, *Mon. Not. R. astr. Soc.*, 216, 17.
- Bautz, L.P., & Morgan, W.W., 1970. *Ap.J. Lett.*, 162, L149.
- Beard, S.M., 1983. In "Workshop on Astronomical measuring machines", p219, Eds. Stobie, R.S., & McInnes, B., Edinburgh, Scotland.
- Beard, S.M., 1984. Ph.D. thesis, University of Edinburgh.
- Beard, S.M., Cooke, J.A., Emerson, D., MacGillivray, H.T., & Kelly, B.D., 1985. *Mon. Not. R. Astr. Soc.*, submitted.
- Bevington, P.R., 1969. Data reduction & error analysis for the physical sciences, McGraw Hill book company.
- Bingelli, B., 1982. *Astron. Astrophys.*, 107, 338.
- Blair, M., & Gilmore, G., 1982. *P.A.S.P.*, 94, 742.
- Bogart, R.S., & Wagoner, R.V., 1973. *Ap.J.*, 181, 609.
- Brault, J.M., & White, O.R., 1971. *Astron. & Astrophys.*, 13, 169.
- Brown, G.S., 1974. Ph.D. thesis, University of Texas at Austin.
- Bruck, M.T., & Waldron, J.D., 1984.
- Burbidge, G.R., 1970, *Ann. Rev. Astron. & Astrophys.*, 8, 369.
- Burstein, D., & Heiles, C., 1982. *Astron.J.*, 87, 1165.
- Carter, D., 1980. *Mon. Not. R. Astr. Soc.*, 190, 307.
- Carter, D., Teague, P.F., & Gray, P.M., 1984.  
In "Clusters & groups of galaxies", p93, Eds. Mardirossian, F., Giuricin, G., & Mezetti, M., D. Reidel, Dordrecht, Holland.

- Charlier, C.V.L., 1922. Meddel.Lund.Astron.Obs., 98.
- Chincarini, G., 1978. Nature., 272, 515.
- Chincarini, G., & Rood, H.J., 1976. Ap.J., 206, 30.
- Chincarini, G., & Rood, H.J., 1979. Ap.J., 230, 648.
- Chincarini, G., et al., 1981. Ap.J.Lett., 249, L47.
- Clowes, R.G., 1983. AAS Photobulletin, 32, 14.
- Clowes, R.G., 1985. Automated Quasar Detection in SGP, in preparation.
- Cooke, J.A., 1980. Ph.D. thesis, University of Edinburgh.
- Cooke, J.A., Emerson, D., Kelly, B.D., MacGillivray, H.T., & Dodd, R.J., 1981. Mon.Not.R.astr.Soc., 196, 397.
- Cooke, J.A., Emerson, D., Beard, S.M., & Kelly, B.D., 1983. In "Workshop on Astronomical measuring machines", p209, Eds. Stobie, R.S., & McInnes, B., Edinburgh, Scotland.
- Cooke, J.A., Kelly, B.D., Beard, S.M., & Emerson, D., 1984. In "Astronomy with Schmidt-type telescopes", IAU collq. 67, p209, Ed. Cappacioli, M., D.Reidel, Dordrecht, Holland.
- Conover, W.J., 1971. Practical non-parametric statistics, John Wiley and sons inc.
- Corwin, H.G., 1974. Astron.J., 79, 1356.
- Corwin, H.G., 1981. Ph.D. thesis, University of Edinburgh.
- Corwin, H.G., & Emerson, D., 1982. Mon.Not.R.Astr.Soc., 200, 621.
- Cousins, A.W.J., 1980. Mon.Notes.Astr.Soc.Southern.Africa., 39, 22.
- Cowie, L.L., & Songaila, A., 1977. Nature., 226, 501.
- Dall'Oglio, G., de Bernardis, P., Masi, F., Melchiori, F., Moreno, G., & Trabalza, R., 1985. Ap.J., 289, 609.
- Davis, M., & Geller, M.J., 1976. Ap.J., 208, 13.
- Davis, M., Groth, E.J., & Peebles, P.J.E., 1977. Ap.J., 212, L107.
- Davis, M., Geller, M.J., & Huchra, J., 1978. Ap.J., 221, 1.
- Davis, M., Huchra, J.P., Latham, D.W., & Tonry, J., 1981. Ap.J., 253, 423.
- Dawe, J.A., & Watson, F.G., 1984. In "Astronomy with Schmidt-type telescopes", IAU collq. 67, p125, Ed. Cappacioli, M., D.Reidel, Dordrecht, Holland.
- Dekel, A., West, M.J., & Aarseth, S.J., 1984. Ap.J., 279, 1.
- Dekel, A., & Aarseth, S.J., 1984. Ap.J., 283, 1.
- de Vaucouleurs, G., 1953. Astron.J., 58, 30.
- de Vaucouleurs, G., 1956. Vistas in Astron., 2, 1584.

- de Vaucouleurs, G., 1958. *Astron.J.*, 63, 253.
- de Vaucouleurs, G., 1960. *Sov.Astron.*, 3, 897.
- de Vaucouleurs, G., 1961. *Astron.J.*, 66, 629.
- de Vaucouleurs, G., 1963. *Ap.J.Suppl.*, 74, 8.
- de Vaucouleurs, G., 1972. *IAU symp.* 44, p353,  
Ed. Evans, D.S, D.Reidel, Dordrecht.
- de Vaucouleurs, G., 1974. *Stars & Stellar Systems volume IX*, p557,  
Eds. Sandage, A., Sandage, M., & Kristian, J.,  
University of Ghicago press.
- de Vaucouleurs, G., 1975. *Ap.J.*, 202, 319.
- de Vaucouleurs, G., & Corwin, H.G., 1975. *Ap.J.*, 202, 327.
- de Vaucouleurs, G., de Vaucouleurs, A., & Corwin, H.G., 1976.  
Second reference catalogue of bright galaxies, University of Texas.
- de Vaucouleurs, G., 1977. *Occ.Rep.Roy.Obs.Edin.*, No.2.
- de Vaucouleurs, G., 1978. In "The large scale structure of the  
Universe", *IAU symp.* 79, p205, Eds. Longair, M.S,  
& Einasto, J., D.Reidel, Dordrecht, Holland.
- Doreshkevich, A.G., & Shandarin, S.F., 1977. *Soviet.Astron.*, 21, 414.
- Doreshkevich, A.G., Sunyaev, R.A., & Zeldovich, Ya.B., 1974.  
In "Confrontation of Cosmological theories with observational data",  
*IAU symp.* 63, p213, Ed. Longair, M.S., D.Reidel, Dordrecht, Holland.
- Doreshkevich, A.G., & Shandarin, S.F., 1976.  
*Mon.Not.R.astr.Soc.*, 175, 15p.
- Dressler, A., 1980. *Ap.J.*, 236, 351
- Eastmond, T.S., & Abell, G.O., 1978. *P.A.S.P.*, 90, 367.
- Eccles, M.J., Sim, M.E., & Tritton, K.P., 1983. Low light level  
detectors in Astronomy, Cambridge University press.
- Efstathiou, G., & Eastwood, J.W., 1981. *Mon.Not.R.astr.Soc.*, 194, 503.
- Einasto, J., Joeveer, M., Kivila, A., & Tago, E., 1975.  
*Astr.Circ.USSR.*, 895, 2.
- Einasto, J., Joeveer, M., & Saar, E., 1980. *Mon.Not.R.Astr.Soc.*, 193, 353.
- Einasto, J., Klypin, A.A., Saar, E., & Shandarin, S.F., 1984.  
*Mon.Not.R.astr.Soc.*, 206, 529.
- Ellis, R.S., Fong, R., & Phillipps, S., 1977.  
*Mon.Not.R.astr.Soc.*, 181, 163.
- Ellis, R.S., 1980. In "Objects of high redshift", *IAU symp.* 92,  
p23, Eds. Abell, G.O., & Peebles, P.J.E., D.Reidel, Dordrecht, Holland.

- Ellis, R.S., Gray, P.M., Carter, D., & Godwin, J., 1984. *Mon. Not. R. astr. Soc.*, 206, 285.
- Emerson, D., 1982. "Simulations of U.K. Schmidt Objective-prism spectra II: Stars", University of Edinburgh, Internal report.
- Emerson, D., 1983. "Simulations of U.K. Schmidt Objective-prism spectra III: Elliptical galaxies", University of Edinburgh, Internal report.
- Faber, S.M., & Dresler, A., 1976. *Ap. J. Lett.*, 210, L65.
- Faber, S.M., & Dresler, A., 1977. *Astron. J.*, 82, 187.
- Fall, S.M., & Jones, B.J.T., 1976. *Nature.*, 262, 457.
- Fay, T.D., Stein, W.L., & Warren, W.H., 1974. *P.A.S.P.*, 86, 772.
- Felten, J.E., 1977. *Astron. J.*, 82, 861.
- Fesenko, B.I., 1979a, *Astrophysics.*, 15, 402.
- Fesenko, B.I., 1979b, *Astron. Zh.*, 54, 1202.
- Fesenko, B.I., 1983. *Soviet. Astron.*, 27, 624.
- Fontanelli, P., 1982. In "The comparative HI content of normal galaxies, Eds. Haynes, M., & Giovanelli, R.
- Ford, H., Harms, R., Bartko, F., Ciardullo, R., & Eason, E., 1980. In "Objects of high Redshift", IAU symp. 92, p65, Eds. Abell, G.O., & Peebles, P.J.E., D.Reidel, Dordrecht, Holland.
- Freeman, K.C., 1975. Stars & Stellar Systems volume IX, p409, Eds. Sandage, A., Sandage, M., & Kristian, J., University of Chicago press.
- Fullerton, W., & Hoover, P., 1972. *Ap. J.*, 172, 9.
- Geller, M.J., & Beers, T.C., 1982. *P.A.S.P.*, 94, 421.
- Geller, M.J., & Huchra, J.P., 1983. *Ap. J. Suppl.*, 52, 61.
- Giovanelli, R., & Haynes, M.P., 1982. *Astron. J.*, 87, 1355.
- Gott, J.R., & Thuan, T.X., 1976. *Ap. J.*, 204, 649.
- Gray, P.M., 1983. *Proc. SPIE. Int. Soc. Opt. Eng.*, 374.
- Gregory, S.A., & Thompson, L.A., 1978. *Ap. J.*, 222, 784.
- Gregory, S.A., Thompson, L.A., & Tifft, W.G., 1981. *Ap. J.*, 243, 411.
- Gregory, S.A., & Thompson, L.A., 1984. *Ap. J.*, 286, 422.
- Groth, E.J., & Peebles, P.J.E., 1977. *Ap. J.*, 217, 385.
- Groth, E.J., 1980. In "Objects of high redshift", IAU symp. 92, p31, Eds. Abell, G.O., & Peebles, P.J.E., D.Reidel, Dordrecht, Holland.
- Gunn, J.E., & Gott, J.R., 1972. *Ap. J.*, 176, 1
- Hauser, M.G., & Peebles, P.J.E., 1977. *Ap. J.*, 185, 757.

- Hewett, P.C., 1982. *Mon.Not.R.astr.Soc.*, 201, 867.
- Hewett, P.C., 1982. Ph.D. thesis, University of Edinburgh.
- Hewett, P.C., 1984. In "Astronomy from measuring machines", Royal Greenwich Observatory, p118, 22-24th August 1984.
- Holmberg, E., 1937. *Lund. Ann.*, 6.
- Holmberg, E.B., 1974. *Astr. Astrophys.*, 35, 121.
- Hubble, E., 1934. *Ap.J.*, 79, 8.
- Huchra, J.P., & Sargent, W.L.W., 1973. *Ap.J.*, 186, 433.
- Huchra, J.P., Davis, M., Latham, D.W., & Tonry, J., 1983. *Ap.J. Suppl.*, 52, 89.
- Humason, M.L., Mayall, N.U., & Sandage, A.R., 1956. *Astron.J.*, 61, 97 & 138.
- Joeveer, M., Einasto, J., & Tago, E., 1978. *Mon.Not.R.astr.Soc.*, 185, 357.
- Joeveer, M., Einasto, J., 1978. In "The large scale structure of the Universe", IAU symp. 79, p241, Eds. Longair, M.S., & Einasto, J., D.Reidel, Dordrecht, Holland.
- Jones, B.J.T., 1976. *Mon.Not.R.astr.Soc.*, 174, 429.
- Kalinkov, M., Dermendjiev, V., Staikov, B., Kaneva, I., Tomov, B., & Stavrev, K., 1978. In "The large scale structure of the Universe", IAU symp. 79, p276, Eds. Longair, M.S., & Einasto, J., D.Reidel, Dordrecht, Holland.
- Karachentsev, I.D., 1966. *Astrophysics.*, 2, 307.
- Karachentsev, I.D., Tsaverskaya, R.L., & Shcherbanovskii, A.L., 1976. *Soviet.Astron.*, 19, 606.
- Karachentsev, I.D., & Scherbanovskii, A.L., 1978. *Soviet.Astron.*, 22, 257.
- Kiang, J., 1967. *Mon.Not.R.astr.Soc.*, 135, 1.
- Kiang, J., & Saslaw, W.C., 1969. *Mon.Not.R.astr.Soc.*, 143, 129.
- Kibblewhite, E., Bridgeland, M., & Bunclark, P., 1984. In "Astronomy with Schmidt-type telescopes", IAU collq. 67, p89, Ed. Cappacioli, M., D.Reidel, Dordrecht, Holland.
- King, C.R., & Ellis, R.S., 1985. *Ap.J.*, 288, 456.
- Kirshner, R.P., Oemler, A., & Shecter, P.L., 1979. *Astron.J.*, 84, 951.
- Kirshner, R.P., Oemler, A., Shecter, P.L., & Shectmann, S.A., 1983. *Ap.J. Lett.*, 248, L57.
- Krug, P.A., Morton, D.C., & Tritton, K.P., 1980. *Mon.Not.R.astr.Soc.*, 190, 237.
- Kuhn, J.R., & Uson, J.M., 1982. *Ap.J. Lett.*, 263, L47.

- Limber, D.N., 1953. *Ap.J.*, 117, 385.
- Materne, J., 1974. *Astron.Astrophys.*, 33, 451.
- Materne, J., 1978. *Astron.Astrophys.*, 63, 401.
- Materne, J., 1979. *Astron.Astrophys.*, 74, 235.
- Materne, J., & Tammann, G.A., 1974. *Astron.Astrophys.*, 37, 383.
- MacFadzean, A.D., Hilditch, R.W., & Hill, G., 1982.  
*Mon.Not.R.astr.Soc.*, 205, 525.
- MacGillivray, H.T., Martin, R., Pratt, N.M., Reddish, V.C., Seddon, H.,  
Alexander, L.W.G., Walker, G.S., & Williams, P.R., 1976.  
*Mon.Not.R.astr.Soc.*, 176, 265.
- MacGillivray, H.T., & Dodd, R.J., 1979. *Mon.Not.R.astr.Soc.*, 186, 69.
- MacGillivray, H.T., & Dodd, R.J., 1980. *Astrophys.Sp.Sci.*, 72, 315.
- MacGillivray, H.T., & Dodd, R.J., 1982. *Astrophys.Sp.Sci.*, 86, 437.
- MacGillivray, H.T., & Dodd, R.J., 1983.  
In "Workshop on Astronomical measuring machines, p195,  
Eds. Stobie, R.S., & McInnes, B., Edinburgh, Scotland.
- MacGillivray, H.T., & Dodd, R.J., 1984a, In IAU collq. 67, p125,  
"Astronomy with Schmidt-type telescopes",  
Ed. Cappacioli, M., D.Reidel, Dordrecht, Holland.
- MacGillivray, H.T., & Dodd, R.J., 1984b, In "Clusters & groups  
of galaxies", p589, Eds. Mardirossian, F., Giuricin, G., & Mezetti, M.,  
D.Reidel, Dordrecht, Holland.
- MacGillivray, H.T., & Stobie, R.S., 1985. *Vistas in Astronomy.*, 27, 433.
- McCrea, W.H., 1964. *Mon.Not.R.astr.Soc.*, 128, 335.
- Mead, R., 1974. *Biometrics*, 30, 295.
- Melnick, J., & Sargent, W.L.W., 1977. *Ap.J.*, 215, 401.
- Mezetti, M., Pisani, A., Giuricin, G., & Mardirossian, F., 1985.  
*Astron.Astrophys.*, 143, 188.
- Miller, R.H., 1984. *Astron.Astrophys.*, 138, 121.
- Moody, J.E., Turner, E.L., & Gott, J.R., 1983. *Ap.J.*, 273, 16.
- Murray, S.S., Forman, W., Jones, C., & Giacconi, R., 1978.  
*Ap.J.Lett.*, 219, L89.
- Nandy, K., Reddish, V.C., Tritton, K.P., Cooke, J.A., & Emerson, D.,  
1977. *Mon.Not.R.astr.Soc.*, 178, 639.
- Neyman, J., Scott, E.L., & Shane, C.D., 1953. *Ap.J.*, 117, 92.
- Neyman, J., Scott, E.L., & Shane, C.D., 1954. *Ap.J.Suppl.*, 1, 269.
- Nilsen, P., 1973. *Uppsala General Catalogue of Galaxies*,  
*Uppsala Astron.Obs.Ann.*, 6.

- Oemler, A.Jr., 1973. Ap.J., 180, 11.
- Oemler, A.Jr., 1974. Ap.J., 194, 1.
- Oemler, A.Jr., 1974. Ph.D. thesis, University of California.
- Oort, J.H., 1984. Ann.Rev.Astr.& Astrophys., 21, pp373-428.
- Ozernoy, L.M., 1974. IAU symp 58, p85, "The formation & dynamics of galaxies", Ed. Shakeshaft, J.R., D.Reidel, Dordrecht, Holland.
- Palmer, J.B., 1984. Ph.D. thesis, University of Edinburgh.
- Parker, Q.A., MacGillivray, H.T., Dodd, R.J., Cooke, J.A., Beard, S.M., Kelly, B.D., & Emerson, D., 1983. In "Workshop on Astronomical measuring machines", p233, Eds. Stobie, R.S., & McInnes, B., Edinburgh, Scotland.
- Parker, Q.A., MacGillivray, H.T., Dodd, R.J., Cooke, J.A., Beard, S.M., Kelly, B.D., & Emerson, D., 1984a, In "Astronomy with Schmidt-type telescopes", IAU. coll. 67., p405, Ed. Cappacioli, M., D.Reidel, Dordrecht, Holland.
- Parker, Q.A., MacGillivray, H.T., & Dodd, R.J., 1984b, In "Clusters & Groups of Galaxies", p595, Eds. Mardirossian, F., Giuricin, G., & Mezzetti, M., D.Reidel, Dordrecht, Holland.
- Parker, Q.A., 1986. Mon.Not.R.astr.Soc., in press.
- Parker, Q.A., & Beard, S.M., "An improved calibration of the objective-prism redshift technique", in preparation.
- Parker, Q.A., & Beard, S.M., "a new method of star/galaxy separation from matched prism & direct plates", in preparation.
- Peebles, P.J.E., 1972. Comm.Astrophys.Sp.Phys., 4, 53.
- Peebles, P.J.E., 1973. Ap.J., 185, 413.
- Peebles, P.J.E., & Hauser, M.G., 1974. Ap.J.Suppl., 28, 19.
- Peebles, P.J.E., 1974a. Ap.J.Lett., 189, L51.
- Peebles, P.J.E., 1974b. Astr.Astrophys., 32, 197.
- Peebles, P.J.E., 1975. Ap.J., 196, 647.
- Peebles, P.J.E., 1980. "The large scale structure of the Universe", Princeton University Press, New Jersey.
- Perrenod, S.C., & Lesser, M.P., 1980. P.A.S.P., 92, 764.
- Phillips, S., Fong, R., Ellis, R.S., Fall, S.M., & MacGillivray, H.T., 1978. Mon.Not.R.astr.Soc., 182, 673.
- Pritchett, C., & Van den Bergh, S., 1977. Ap.J.Suppl., 34, 101.
- Rainey, G.W., 1977. Ph.D. thesis, University of California.
- Reid, I.N., & Gilmore, G., 1982. Mon.Not.R.astr.Soc., 201, 73.
- Reiz, A., 1941. Lund. Ann., 9.

- Reynolds, J.H., 1921. Mon.Not.R.astr.Soc., 81, 129 & 598.
- Reynolds, J.H., 1934. Mon.Not.R.astr.Soc., 94, 196.
- Ridgway, S.T., & Brault, J.M., 1984. Ann.Rev.Astron.Astrophys., 22, 291.
- Rood, H.J., & Dickel, J.R., 1976. Ap.J., 205, 346.
- Rood, H.J., & Dickel, J.R., 1978. Ap.J., 224, 724.
- Rubin, V.C., 1954. Proc.Nat.Acad.Sci., 40, 451.
- Rubin, V.C., Ford, W.K., Thonnard, N., Roberts, M.S., & Graham, J.A., 1976. Astron.J., 81, 687.
- Rudnicki, K., 1964. Acta.Astron., 14, 273.
- Rudnicki, K., & Zieba, S., 1978. In IAU symp 79, p229, "The large scale structure of the Universe", Eds. Longair, M.S., & Einasto, J., D.Reidel, Dordrecht, Holland.
- Rudnicki, K., 1984. Sky & Telescope, Aug, P123.
- Sandage, A., Tammann, G.A., & Hardy, E., 1972. Ap.J., 172, 253.
- Sandage, A., & Tammann, G.A., 1974. Ap.J., 194, 559.
- Sandage, A., & Tammann, G.A., 1975. Ap.J., 197, 265.
- Sandage, A., Tammann, G.A., & Yahil, A., 1979. Ap.J., 232, 352.
- Sandage, A., Tammann, G.A., 1981. A Revised Shapley Ames Catalogue of Bright Galaxies, Carnegie Institution of Washington publication 635.
- Sarazin, C.L., Rood, H.J., & Strubble, M.F., 1982. Astron.Astrophys., 108, L7.
- Schechter, P.L., 1976. Ap.J., 203, 297.
- Schechter, P.L., 1977. Astron.J., 82, 569.
- Scott, E.L., 1968. In "Problems of extragalactic research", Ed. McVittie, G.C., MacMillan, New York.
- Scott, E.L., Shane, C.D., & Swanson, M.D., 1954. Ap.J., 119, 91.
- Seares, F.H., 1925. Ap.J., 62, 168.
- Seldner, M., Siebers, B., Groth, E.J., & Peebles, P.J.E., 1977. Astron.J., 61, 292.
- Seldner, M., & Uson, J.M., 1983. Ap.J., 264, 1.
- Sersic, J.L., 1980. Extragalactic Astronomy, D.Reidel, Dordrecht, Holland.
- Shandarin, S.F., 1983. Soviet.Astron.Lett., 9, 104.
- Shane, C.D., & Wirtanen, C.A., 1954. Astron.J., 59, 302.
- Shane, C.D., 1956. Astron.J., 61, 292.

- Shane, C.D., & Wirtanen, C.A., 1967. Pub.Lick.Obs., 22, 1.
- Shane, C.D., 1976. Stars & Stellar Systems volume IX, p647, Eds. Sandage, A., Sandage, M., & Kristian, J., University of Ghicago press.
- Shanks, T., 1979. Mon.Not.R.astr.Soc., 186, 583.
- Shanks, T., Fong, R., Ellis, R.S., & MacGillivray, H.T., 1980. Mon.Not.R.astr.Soc., 192, 209.
- Shanks, T., 1983. Mon.Not.R.astr.Soc., 202, 1245.
- Shanks, T., Bean, A.J., Efsthathiou, G., Ellis, R.S., Fong, R., & Peterson, B.A., 1983. Ap.J., 274, 529.
- Shanks, T., Stevenson, P.R.F., Fong, R., & MacGillivray, H.T., In IAU collq. 67, p489, "Astronomy with Schmidt-type telescopes", Ed. Cappacioli, M., D.Reidel, Dordrecht, Holland.
- Shanks, T., Stevenson, P.R.F., Fong, R., & MacGillivray, H.T., 1984. Mon.Not.R.astr.Soc., 206, 767.
- Shapiro, S.L., 1971. Astron.J., 76, 291.
- Shapley, H., 1938. Bull.Harv.Col.Obs., 908, 1.
- Sharp, N.A., 1979. Astr.Astrophys., 74, 312.
- Shectman, S.A., 1985. Ap.J., Suppl. 57, 77.
- Silk, J., 1975. Ap.J., 193, 525.
- Soniera, R.M., & Peebles, P.J.E., 1977. Ap.J., 211, 1.
- Soniera, R.M., & Peebles, P.J.E., 1978. Astron.J., 83, 845.
- Standon, P.R., & Tritton, K.P., 1979. Occ.Rep.of.R.O.E., 5.
- Stevenson, P.R.F, Shanks, T., & Fong, R., 1984. In "Clusters & Groups of Galaxies", p565, Eds. Mardirossian, F., Giuricin, G & Mezzetti, M., D.Reidel, Dordrecht, Holland.
- Stevenson, P.R.F, Shanks, T., & Fong, R., 1985. Mon.Not.R.astr.Soc., 213, 953.
- Stewart, J.M., & Sciama, D.N., 1967. Nature., 216, 742.
- Stobie, R.S., 1980. Soc.Photo-Optical.Instr.Eng., 264, 208.
- Strom, K.M., & Strom, S.E., 1979. Sci.Am., April, pp72-82.
- Struble, M.F., & Peebles, P.J.E., 1985. Astron.J., 90, 582.
- Sunyaev, R.A., & Zeldovich, Ya.B., 1972. Astr.Astrophys., 20, 189.
- Tago, E., Einasto, J., & Saar, E., 1984. Mon.Not.R.Astr.Soc., 206, 559.
- Tarenghi, M., Tifft, W.G., Chincarini, G., Rood, H.J., & Thompson, L.A., 1978. In "The large scale structure of the Universe", IAU symp. 79, p241, Eds. Longair, M.S, & Einasto, J., D.Reidel, Dordrecht, Holland.

- Tarenghi, M., Tifft, W.G., Chincarini, G., Rood, H.J., & Thompson, L.A., 1979. *Ap.J.*, 234, 793.
- Tarenghi, M., Chincarini, G., Rood, H.J., & Thompson, L.A., 1980. *Ap.J.*, 235, 724.
- Thanisch, P.F., McNally, B.V., & Robin, A., 1984. *Image & Vision Computing.*, 2, 191.
- Tifft, W.G., & Gregory, S.A., 1976. *Ap.J.*, 205, 696.
- Tifft, W.G., & Gregory, S.A., 1978. In *IAU symp 79*, p267, "The large scale structure of the Universe", Eds. Longair, M.S., & Einasto, J., D.Reidel, Dordrecht, Holland.
- Tonry, R., & Davis, M., 1979. *Astron.J.*, 84, 1511.
- Tully, R.B., & Fisher, J.R., 1975. In "Proceedings III European Astronomical Meeting", p481, Ed. Kharadze, E.K., Tbilisi.
- Tully, R.B., & Fisher, J.R., 1978. In *IAU symp 79*, p31, "The large scale structure of the Universe", Eds. Longair, M.S., & Einasto, J., D.Reidel, Dordrecht, Holland.
- Tully, R.B., 1980. *Ap.J.*, 237, 390.
- Tully, R.B., 1982. *Ap.J.*, 257, 389.
- Turner, E.L., & Gott, J.R., 1976. *Ap.J.Lett.*, 197, L89.
- Van den Bergh, S., 1960. *Astrophys.*, 131, 565.
- Van den Bergh, S., 1967. *Astron.J.*, 72, 70.
- Ward, J.H., 1963. *J.Amer.Stat.Ass.*, 58, 236.
- Webster, A., 1976. *Mon.Not.R.astr.Soc.*, 175, 61.
- Webster, A., 1976. *Mon.Not.R.astr.Soc.*, 199, 683.
- Welch, G.A., Chincarini, G., & Rood, H.J., 1975. *Astron.J.*, 80, 77.
- Wertz, J.R., 1971. *Ap.J.*, 164, 227.
- Wesson, P.S., 1975. *Astrophys.Sp.Sci.*, 32, 273 & 315.
- West, R.M., & Barbier, R., 1982. *Astron. & Astrophys.*, 106, 53.
- Wishart, D., 1969. *Biometrics.*, 22, 165.
- Yahil, A., & Vidal, N.V., 1977. *Ap.J.*, 214, 347.
- Yahil, A., Sandage, A.R., & Tammann, G.A., 1980. *Ap.J.*, 242, 448.
- Yu, J.T., & Peebles, P.J.E., 1969. *Ap.J.*, 158, 103.
- Zeldovich, Ya.B., 1978. In *IAU symp 79*, p31, "The large scale structure of the Universe", Eds. Longair, M.S., & Einasto, J., D.Reidel, Dordrecht, Holland.
- Zeldovich, Y.B., Einasto, J., & Shandarin, S.F., 1982, *Nature*, 300, 407.

Zwicky, F., 1938. P.A.S.P., 50, 218.

Zwicky, F., 1957. Morphological Astronomy, Springer-Verlag, Berlin.

Zwicky, F., 1959. Encyclopedia of Phys., 53, 392.

Zwicky, F., Herzog, E., Wild, P., Karpowicz, M., & Kowal, C.T., 1961-68,  
Catalogue of Galaxies & Clusters of Galaxies, in six volumes,  
California Institute of Technology, Pasadena.

Zwicky, F., & Rundnicki, K., 1963. Ap.J., 137, 707.

Zwicky, F., & Berger, J., 1965. Ap.J., 141, 34.

Zwicky, F., & Rundnicki, K., 1966. Z.f.Astrphys., 66, 246.